The origin of terrestrial neon : an experimental study of isotopic fractionation of Neon during basalt degassing

Elena Nunez

▶ **To cite this version:**

Elena Nunez. The origin of terrestrial neon : an experimental study of isotopic fractionation of Neon during basalt degassing. Other. Université d'Orléans, 2024. English. NNT : 2024ORLE1030 . tel-04826333

HAL Id: tel-04826333

https://theses.hal.science/tel-04826333v1

Submitted on 9 Dec 2024

HAL is a multi-disciplinary open access archive for the deposit and dissemination of scientific research documents, whether they are published or not. The documents may come from teaching and research institutions in France or abroad, or from public or private research centers.

L'archive ouverte pluridisciplinaire **HAL**, est destinée au dépôt et à la diffusion de documents scientifiques de niveau recherche, publiés ou non, émanant des établissements d'enseignement et de recherche français ou étrangers, des laboratoires publics ou privés.

UNIVERSITÉ D'ORLÉANS

ÉCOLE DOCTORALE EMSTU - Energie, Matériaux, Sciences de la Terre et de l'Univers -
ISTO - Institut des Sciences de la Terre d'Orléans

THÈSE présentée par :

NUNEZ Elena

Soutenue le : **04 octobre 2024**

Pour obtenir le grade de : **Docteur de l'Université d'Orléans**

Discipline/ Spécialité : Sciences de l'Univers

The origin of terrestrial neon

An experimental study of isotopic fractionation of Neon during basalt degassing.

THÈSE dirigée par :

M. MOREIRA Manuel	Professeur des Universités, Université d'Orléans
M. SCAILLET Bruno	Directeur de recherche, CNRS

RAPPORTEURS :

M. CARTIGNY Pierre	Directeur de recherche CNRS, Université de Paris - IPGP
M. SAAL Alberto	Professeur des Universités, Université de Brown (USA)

JURY :

Mme. ROSE Estelle	Directrice de recherche CNRS, ISTO-CNRS, Président du jury
M. SARDA Philippe	Professeur des Universités, Université Paris-Sud
Mme. PÉRON Sandrine	Chargée de recherche CNRS, ISTO- CNRS

« Pendant l'obscurité totale je fus extrêmement frappé du vif éclat des raies protubérantielles ; la pensée me vint aussitôt qu'il serait possible de les voir en dehors des éclipses.... Je lis dans un livre fermé jusqu'ici pendant les éclipses, je lis dans un livre fermé jusqu'ici pour tous. C'est le 19 août que j'ai fait cette découverte, aussi la véritable éclipse a eu lieu pour moi le 19 et non le 18 »

Pierre Janssen découvreur du premier gaz rare et du premier gaz extraterrestre avec Joseph Norman Lockyer.

Acknowledgements

Les deux premières personnes que je voudrais remercier sont mes directeurs de thèse Manuel et Bruno. Toute cette histoire a commencé en octobre 2019 lorsque Bruno et Juan m'ont donné l'opportunité de participer au cours de pétrologie expérimentale ici à Orléans. À cette époque, j'avais déjà commencé à m'intéresser aux gaz rares et à la volcanologie, mais la pétrologie expérimentale était quelque chose de totalement nouveau et intéressant pour moi. À cette époque, Bruno m'a dit que Manuel quittait l'IPGP pour s'installer à Orléans, mais je n'ai pas eu le plaisir de le rencontrer en personne. Des mois plus tard, Bruno m'a contacté et j'ai eu le premier entretien avec Manuel et, à ce moment-là, le sujet m'a semblé très intéressant : les gaz rares et l'expérimentation ? Et c'est parti pour l'aventure : expériences, lancement de ballons pour des mesures de gaz dans la stratosphère (Kiruna), prélèvement d'échantillons dans une éruption active in situ (La Palma), prélèvement d'échantillons de gaz dans des sources au Massif central et, enfin, l'Islande. Mais sans aucun doute l'opportunité de travailler sur ce sujet très intéressant et que, bien qu'il n'ait pas été proposé par moi, Manuel et Bruno ont fait en sorte qu'il soit le mien, en me donnant une totale liberté pour y travailler.

Merci également aux membres du jury, a Alberto Saal por la cercanía y los consejos tanto momentos previos a la defensa ("ya está hecho, tranquila") como durante la discusión después de la defensa. A Pierre Cartigny pour son enthousiasme lors de la correction du manuscrit et lors de la discussion, merci pour les conseils et les idées pour l'avenir. A Philippe Sarda (« papa des popping rocks ») pour la discussion et l'inspiration, qui sont venues bien avant ce projet, lorsque j'ai eu le premier contact avec les gaz nobles. A Sandrine Péron, pour sa gentillesse et son implication lors de la défense, de la discussion et de la correction du manuscrit, qui n'aurait certainement pas cette version finale. Et à Estelle, pour m'avoir montré non seulement les bonnes choses mais aussi les « mauvaises » ou améliorables du manuscrit, mais aussi pour avoir été si attentive en tant que présidente du jury.

Gracias Juanito, por todas nuestras charlas y bromas, por el café y por todas esas galletas bretonas de mantequilla que mantuvieron el azúcar alto durante estos cuatro años, mi español favorito :D. Pero, sobre todo, gracias por ayudarme a patear el autoclave en todos los experimentos donde el quench no funcionaba.

Grazie a Ida per i suoi ottimi consigli prima e dopo la difesa della tesi. Per le sessioni EMPA, la pazienza e le posizioni NO TOUCH che hanno reso possibili le analisi, ma soprattutto per aver messo l'essenza italiana in ogni intervento. A Florian, pour sa disponibilité et son accessibilité dès le premier jour. A Aneta, pour m'avoir permis de trouver facilement des «culitos» dans mes verres :D

Merci à Philipe et Laurent pour tout le travail de tomographie. Aux gars de l'atelier pour leur disponibilité et leur patience lorsque je devais demander quelque chose en anglais et/ou en français, en particulier Frédéric et son grand sourire.

A toutes les personnes de l'ISTO qui, bien que je ne le précise pas ici, ont d'une manière ou d'une autre contribué moralement, techniquement et avec des suggestions pendant ces quatre années (Giada, Fabrice, Ken, Julien...).

Thanks to all the PhD and postdoc community at ISTO, to those who are and were there, for all the parties/climbing/coffees/canoes/laser/beers/barbecues/hiking /conferences... we have done so many activities together that it is impossible to remember them all. To 'Gomboló' for always having the house available for dinner or a birthday, to 'Chiquito' for always having me present for Fontaimbleu/VerticalArt or some Croatian dinner, but above all for the little coffees and the hugs "Qué rico verte!" To Gigi, for your young and crazy spirit, because climbing with you is always fun and because you enjoy every single "tattoo" I leave you in the verticalArt sessions (we still have some repotting sessions to do). A Dile, per aver trasformato il caffè di ogni mattina in una terapia di tesi e altri doppi sensi e per essere il miglior partner di conferenza che si possa desiderare. Grazie per Lyon e per i "baci perugina". To Carolina, for suddenly coming in and bringing me all that irony and malice, even though inside you are a sweet piece of cake, for giving so much without expecting anything in return and for filling my office with more plants muejeje. To Romain for "looking" so innocent and being a stubborn apprentice. To Khadija, for our coffees, lunches and confidences (it's all over and we did it together!). A Hectorcito por el "chismesito" y estar siempre a la orden para el desorden (y todas esas cosas que lograste para mi…). To Jason Momoa for your big hugs and support. To Val, Fabien, Bence, David, Nathan, Zara, Alessandra, Amelie, Gabriel and Gabriel... you guys are so many that it is impossible not to forget someone, and not because you are not important.

To all those wonderful people who were present during these four years, who do not belong to the ISTO but thanks to it we were able to coincide in some way and get to know each other and form a beautiful friendship. Especially Blondy and Matejita, few people are as sweet as you and at the same time so funny. So that we continue sharing trips, concerts and dances. To Albancito, for being the first to break the French cliché and for having become a great friend and not just a climbing buddy. A mi colombiana favorita, por todos nuestros brunch y mensajitos de bizcochos y pipiflan, pero también por ser una gran amiga. A Claudio, per l'ampia conoscenza della bestemmia italiana che sarà sempre presente nella mia vita e per tutto il cibo delizioso che hai portato nella mia vita.

Gracias a mis "preferiti": Fede, Moni e Viktor, perché Orleans non sarebbe stata Orleans senza di voi, siete incisi con l'inchiostro sulla mia pelle ma anche nel mio cuore. I ringraziamenti che potrei scrivere per voi sono così grandi che la tesi sarebbe meno del dieci per cento di quello che ho scritto. Grazie per tutto, grazie per il sostegno incondizionato, gli abbracci, le lacrime, le risate, i postit, le chiamate in ritardo, i consigli... Abbiamo fatto numerosi viaggi, alcuni brevi (le vacanze) e altri lunghi (la tesi), ma senza dubbio il più importante per tutti noi deve ancora arrivare.. Grazie per essere diventati la mia famiglia e per avermi scelto come vostra famiglia.

A la pequeña familia que dejé atrás y que estuvieron presentes en cada pequeño paso que daba, celebrándolo cada momento (Javi, Mª Luisa, Evaristo, Manu y Eva), de todo corazón gracias. A la nouvelle famille qui se crée, qui m'accueille comme une

fille/sœur malgré ma mauvaise communication en français (Françoise, Bruno, Damien y Elodie). A mi familia, tito y tita, porque desde el día que nací han sido como unos segundos padres para mí. A papá y mamá por estar pegados al teléfono día y noche, por hacer que toda la distancia que nos separa sea nada con una simple videollamada para contar nada y todo. Porque el orgullo que yo puedo sentir de mi misma se debe al que veo en sus propios ojos. À Simon, pour m'avoir relevée quand je tombais et pour m'avoir relevée à nouveau, pour avoir été si patient. Parce que tu es arrivé au moment le plus difficile et que tu as décidé de rester. A Noe y Kathy, porque nadie podría imaginar que siendo personas tan diferentes podríamos ser tan compatibles y perfectamente imperfectas las unas para las otras. Porque no importa la distancia ni el tiempo, siempre somos y seremos nosotras y el resto del mundo 💔💔💔.

Index

Chapitre 1 Aperçu général

L'origine des éléments volatils sur Terre demeure un sujet de controverse, compte tenu de ses implications pour notre compréhension de l'évolution du système solaire primitif, de la formation de la Terre et de son atmosphère, ainsi que de la vie sur Terre. Les gaz rares sont des outils essentiels en tant que traceurs des principales espèces volatiles, telles que le CO_2 et le H_2O dans le manteau, en raison de leur inertie et de leur grande volatilité.

Les caractéristiques des gaz rares dans les panaches du manteau, notamment dans les sources de néon des Galápagos, d'Hawaï et d'Islande, suggèrent une combinaison de néon de type solaire acquis lors de l'accrétion de la Terre. Deux modèles principaux ont été proposés pour expliquer l'origine du néon dans le manteau : le premier modèle suggère que le néon a été incorporé dans un océan magmatique à la suite de la capture gravitationnelle d'une atmosphère primaire dense (Mizuno et al., 1980; Sasaki and Nakazawa, 1990; Harper Jr and Jacobsen, 1996; Yokochi and Marty, 2004; Mukhopadhyay, 2012; Williams and Mukhopadhyay, 2019). Le second modèle propose que le néon ait été acquis lors de l'accrétion de la Terre à partir de planétésimaux irradiés par le Soleil primitif (Trieloff et al., 2000; Ballentine et al., 2005; Raquin and Moreira, 2009; Kurz et al., 2009; Moreira, 2013; Colin et al., 2015; Moreira and Charnoz, 2016; Péron et al., 2016, 2017, 2018).

Cependant, il est difficile de déterminer l'abondance du néon et les compositions isotopiques dans les fusions du manteau primaire en raison de sa faible abondance et du fractionnement isotopique possible pendant les processus de transport et de dégazage. Les basaltes des dorsales médio-océaniques (MORB) et les basaltes des îles océaniques (OIB) ont été identifiés comme provenant de deux domaines distincts avec des compositions isotopiques et des histoires de dégazage différentes, les OIB suggérant la présence d'un ancien réservoir primordial dans les profondeurs de la Terre.

La concentration résiduelle des volatils du manteau (y compris les gaz rares) dans les roches et minéraux volcaniques est souvent déterminée par des processus secondaires, reflétant l'histoire de l'éruption ou la distribution des vésicules (ou des inclusions fluides)

plutôt que par la concentration primaire dans le manteau (Staudacher et al., 1989; Sarda and Graham, 1990; Moreira and Sarda, 2000; Sarda and Moreira, 2002; Aubaud et al., 2004; Chavrit, 2010; Chavrit et al., 2012). Dans la plupart des basaltes océaniques, la phase volatile du magma est dominée par le CO_2, et il est généralement admis que les concentrations de gaz rares dans la phase volatile ne varient pas entre les vésicules et que leur variation dans le magma dépend de l'ampleur et du mécanisme de la perte de gaz du magma (Burnard, 1999, 2001; Marty and Zimmermann, 1999).

Des travaux pionniers tels que ceux de Burnard (2001), qui ont utilisé l'ablation laser pour analyser des vésicules individuelles, ont suggéré que la composition isotopique des premières vésicules nucléées, les plus grandes vésicules piégées dans la matière fondue, serait similaire aux compositions "initiales" de la matière fondue. En revanche, les vésicules plus petites, qui sont normalement libérées au cours des dernières étapes de l'écrasement, correspondraient aux dernières vésicules nucléées congelées au cours de la trempe et seraient donc plus susceptibles de subir un fractionnement cinétique. En outre, il a indiqué que lors du broyage séquentiel d'un verre basaltique, le gaz libéré appartient à des vésicules de plus en plus petites.

Des travaux expérimentaux ont été menés sur le dégazage de systèmes magmatiques en équilibre ou en déséquilibre (Le Gall, 2015; Le Gall and Pichavant, 2016a; Pichavant et al., 2013, 2018). *Dans ce contexte, l'équilibre est compris comme un état où les espèces volatiles suivent les lois de solubilité pour une gamme spécifique de pression et de température. Lors de la décompression, l'objectif était d'étudier le partage d'une ou plusieurs espèces volatiles (H_2O et CO_2) entre le gaz et la matière fondue. Les résultats indiquent que, lors de la décompression, lorsque deux espèces volatiles sont impliquées, elles présentent une déviation par rapport à l'équilibre (CO_2).*

L'objectif de la présente étude est d'intégrer les observations de Burnard sur le fractionnement de l'hélium et de l'argon dans des vésicules de différentes tailles avec des études expérimentales impliquant plusieurs espèces volatiles. Le principal défi de ce travail est d'étudier le partage et le fractionnement isotopique du néon entre la phase gazeuse et la masse fondue. Cet objectif sera atteint grâce à l'analyse directe de vésicules individuelles, qui seront ensuite analysées par spectrométrie de masse. Il s'agit d'un double défi technique, qui implique d'une part la synthèse d'un verre sans bulles et l'homogénéisation ultérieure du néon dissous, et d'autre part le déclenchement de la

nucléation d'une bulle et de la croissance qui s'ensuit, pour être ensuite analysée. Comme nous le verrons plus loin, les vésicules seront limitées à des tailles micrométriques (moins de 200 μm) en raison de l'espace restreint de la capsule dans laquelle les expériences sont réalisées.

Les petites dimensions des vésicules nécessitent l'utilisation d'instruments à haute résolution spatiale et d'une ligne d'extraction bien purifiée, étant donné que la quantité de néon disponible dans chaque bulle est extrêmement faible. Ceci est illustré par le fait que le gaz libéré par chaque vésicule ne dépasse jamais 1,7 x 10^{-5} bar, le CO_2 représentant plus de 99% de cette pression.

En outre, l'objectif de cette étude est d'explorer le comportement des isotopes du néon dans diverses circonstances qui peuvent être extrapolées à des scénarios naturels, tels qu'un système dans lequel la décompression est initiée (un MORB régulier) et un système affecté par l'apport d'un flux/fusion riche en CO_2 (tel que Stromboli ; Pichavant et al., 2009).

La détermination du rapport isotopique du néon dans le manteau est fondamentale pour comprendre le mécanisme d'incorporation des gaz rares dans la Terre silicatée et ce travail vise à y contribuer en comprenant le comportement des isotopes du néon pendant les processus de dégazage.

Chapter 1: General Overview

The origin of volatile elements on Earth continues to be a contentious issue, as it has significant implications for our understanding of the early Solar System's evolution, the formation of the Earth and its atmosphere, and the development of life. Noble gases serve as essential tracers for major volatile species, such as CO_2 and H_2O in the mantle, due to their inertness and high volatility. This makes them reliable indicators of volatile behavior in the Earth's mantle, particularly in relation to volcanic degassing and mantle dynamics.

The noble gas characteristics of mantle plumes, particularly in the Galapagos, Hawaiian and Icelandic sources of neon, suggest a combination of solar-type neon acquired during Earth's accretion. Two main models have been proposed to explain the origin of neon in the mantle: The first model proposes that a primitive solar nebula was dissolved into the magma ocean and captured before the end of the planetary accretion (Mizuno et al., 1980; Sasaki and Nakazawa, 1990; Harper Jr and Jacobsen, 1996; Yokochi and Marty, 2004; Mukhopadhyay, 2012; Williams and Mukhopadhyay, 2019). The second model proposes that neon was acquired during Earth's accretion from planetesimals irradiated by the early Sun (Trieloff et al., 2000; Ballentine et al., 2005; Raquin and Moreira, 2009; Kurz et al., 2009; Moreira, 2013; Colin et al., 2015; Moreira and Charnoz, 2016; Péron et al., 2016, 2017, 2018). During the accretion phase, some volatiles, including noble gases, could be retained due to the temperature and pressure conditions prevailing at that time.

However, it is challenging to determine the neon abundance and isotopic compositions in primary mantle melts due to the low abundance and the possible isotopic fractionation during transport and degassing processes. Mid-ocean ridge basalts (MORBs) and oceanic island basalts (OIBs) have been identified as sourced from two distinct domains with different isotopic compositions and degassing histories, with the OIBs suggesting the presence of an ancient primordial reservoir in the deep Earth.

The residual concentration of mantle volatiles (including noble gases) in volcanic rocks and minerals is frequently determined by secondary processes, reflecting the

eruption history or vesicle (or fluid inclusion) distribution rather than by the primary concentration in the mantle (Staudacher et al., 1989; Sarda and Graham, 1990; Moreira and Sarda, 2000; Sarda and Moreira, 2002; Aubaud et al., 2004; Chavrit, 2010; Chavrit et al., 2012). In most oceanic basalts the volatile phase of the magma is dominated by CO_2, and it is generally assumed that noble gas concentrations in the volatile phase are not subject to variations between vesicles and that their variation in the magma is dependent on the extent and mechanism of gas loss from the magma (Burnard, 1999, 2001; Marty and Zimmermann, 1999).

Pioneering research by Burnard (2001), utilizing laser ablation to analyse individual vesicles, indicated that the isotopic composition of the initial nucleated vesicles—specifically, the larger vesicles trapped within the melt—would closely resemble the "initial" melt compositions. The nucleation and growth of vesicles occur continuously while the magma remains saturated with CO_2, leading to the formation of distinct generations of bubbles that can be differentiated by their sizes. Conversely, the smaller vesicles typically released during the later stages of crushing represent the last nucleated vesicles, which are frozen during quenching and are consequently more susceptible to kinetic fractionation. Furthermore, Burnard demonstrated that during the sequential crushing of basaltic glass, the gases released are derived from progressively smaller vesicles.

Some experimental works have been conducted on the degassing of magmatic systems in either equilibrium or disequilibrium (Le Gall, 2015; Le Gall and Pichavant, 2016a; Pichavant et al., 2013, 2018). In this context, bulk equilibrium is understood as a state where volatile species follow the solubility laws for a specific pressure and temperature range. During decompression, the objective was to study the partitioning of one or more volatile species (H_2O and CO_2) between the gas and the melt. The findings indicated that, during decompression, when two volatile species were involved, they exhibited a deviation from equilibrium (CO_2).

The objective of the present study is to integrate Burnard's observations of helium and argon fractionation in different vesicle sizes with experimental studies involving multiple volatile species. The main challenge of this work is to study the behaviour and isotopic fractionation of neon, during the nucleation and the bubble growth. This will be attempted through the direct analysis of individual vesicles, which will then be analysed

with mass spectrometry. This is a double technical challenge, which involves first the synthesis of a glass free of bubbles and the subsequent homogenisation of the dissolved neon, and second the triggering of a bubble nucleation and ensuing growth to be subsequently analysed. As will be observed later, the vesicles will be limited to micrometric sizes (less than 200 μm) due to the limited space of the capsule, in which the experiments are carried out.

The small dimensions of the vesicles necessitate the utilisation of instruments with high-spatial resolution and a well-purified extraction line, given that the quantity of neon available in each bubble is exceedingly small.

Furthermore, the objective of this study is to explore the behavior of neon isotopes under various conditions that can be extrapolated to natural scenarios, such as a system in which decompression is initiated (a typical MORB) and a system influenced by the input of a CO2-rich flow or melt (such a Stromboli; Pichavant et al. (2009).

Determining the mantle neon isotopic ratio is fundamental to understanding the mechanism of incorporation of noble gases in the silicate Earth and this work aims to contribute to it by understanding the behaviour of neon isotopes during degassing processes.

1.1. Noble gasses: discovery, chemical origin, and abundance:

The term "noble gases" is derived from their inability to engage in chemical reactions with other elements due to the full occupancy of their outermost shell with electrons. Consequently, they are unable to form chemical bonds with other atoms, which is why they are also known as “inert elements”. These elements are trace components found in geological materials and are sometimes referred to as “rare gases” due to their scarcity.

The noble gases were discovered fortuitously during a solar eclipse in 1868. Pierre Janssen, a French astronomer, observed a bright yellow flash in the chromosphere (**Figure 1.1**). The English astronomer Joseph Norman Lockyer observed the same protuberances and concluded that they must be an unknown solar element. The element was named Helium, derived from the Greek word *ἥλιος*, meaning Helios (Sun) (Pierre Jules César

Janssen, 1908). This discovery marked the first time a chemical element was discovered outside of Earth, making Helium the first extraterrestrial element.

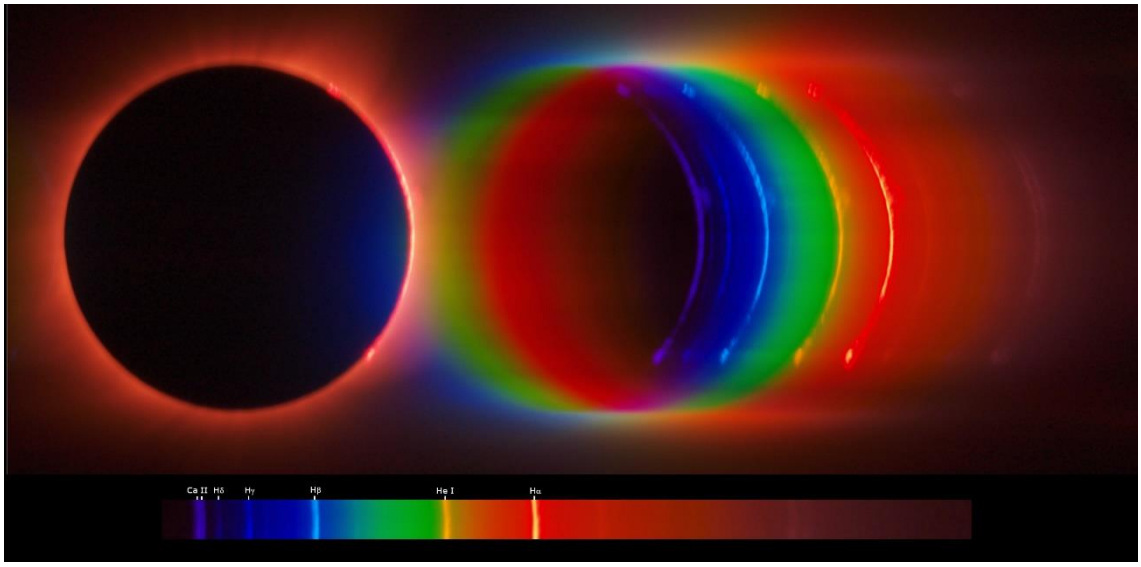

Figure 1.1: chromosphere flash spectrum captured during a total solar eclipse (ESA/M. Castillo-Fraile). Hydrogen shows the most intense emission with the red hydrogen-alpha emission at the far right and blue and purple to the left. In between, helium bright yellow.

The importance of noble gases in planetary science lies in their inertness, the widespread variations of their isotopic compositions, and their abundance.

Their overall depletion makes rare gases sensitive recorders of several types of nuclear processes (Dickin, 2018) involving relatively more abundant parent elements. In cosmochemistry, significant research has been conducted to understand both the source and distribution of volatiles in the solar system, to identify nucleosynthetic anomalies in meteorites, and to chronologically constrain the formation of the solar system (e.g. (Bauer, 1947; Burbidge et al., 1957; Porcelli et al., 2002). Noble gasses into the Earth's interior, make them excellent isotopic tracers. Tracers for the origin of volatile elements in the Earth and Earth's formation, tracers for the mantle degassing over time, tracers for mixing between mantle reservoirs, and tracers of the history of atmosphere formation for example (Mizuno et al., 1980; Allègre et al., 1983; Kurz, 1986; Zhang and Zindler, 1989; Moreira et al., 1998; Sasaki and Nakazawa, 1990; Trieloff et al., 2000; Moreira and Sarda, 2000; Burnard, 2001; Ballentine et al., 2005; Ruzié and Moreira, 2010; Mukhopadhyay, 2012; Péron et al., 2017; Jaupart et al., 2017; Marty, 2020, 2022).

In addition, isotopic ratios of noble gases have been used to describe the evolution of the crust, hydrological systems, and ocean basins, and to date tectonic events (e.g. Kendrick and Burnard (2013), Kipfer et al. (2002), Schlosser and Winckler (2002), Ballentine and Burnard (2002).

Helium, neon, argon, krypton, xenon, and radon are classified as highly volatiles and all except radon, which has only radioactive isotopes, have stable isotopes. Their physicochemical properties vary according to their atomic weight, Noble gases in the Earth are broadly derived from three sources: (i) Trapped during the accretionary process, which are classified as 'primitive', 'juvenile' or 'primordial'. (ii) Generated by nuclear reactions, such as neutron capture, spallation, radioactive decay, and fission (e.g., Ballentine et al., 2002; Ballentine and Burnard, 2002; Marty, 2020). (iii) A cometary source and/or a chondritic component added during the Late Veneer of material to the Earth (i.e. after the core was formed), and the continuous recycling of heavy noble gases through subduction and mantle processes (e.g. Busemann et al., 2000; Marty and Yokochi, 2006; Holland and Ballentine, 2006a; Holland et al., 2009; Marty, 2012). So, in this respect, they are extremely versatile, used for a variety of purposes, ranging from geochronology to the origin and history of the material in which they are found.

In what follows, only the stable isotopes of the noble gases are presented:

- *Helium:* With two stable isotopes, ^{3}He and ^{4}He, helium is the second in abundances and the second lightest element in the universe. In stars like our sun, ^{4}He and ^{3}He are produced through the fusion of hydrogen and cycling reactions of carbon, nitrogen, and oxygen nuclei, a process known as nucleosynthesis (Clayton, 1983; Rolfs and Rodney, 1988; Wieler, 2002; Dickin, 2018). In the Earth's mantle and crust, ^{4}He is produced through the radioactive decay of U and Th. The presence of ^{3}He in the mantle is generally considered to be primordial. However, ^{3}He on the Earth's surface may also result from spallation reactions caused by cosmogenic neutrons.

- *Neon:* Neon has three stable isotopes ^{20}Ne, ^{21}Ne and ^{22}Ne, either generated by nucleogenesis in stars, or related to the concentration of elements like uranium and thorium. Instead, they are produced through the reaction of their α and *n* particles with the nuclei of other isotopes, such as ^{18}O, ^{17}O, ^{25}Mg, ^{24}Mg, and ^{19}F (Wetherill, 1954a; B. M. Kennedy et al., 1990). But as Yatsevich and Honda

(1997) have shown, ^{20}Ne and ^{22}Ne production rates in the mantle are negligible and they are mostly considered as having a primordial origin in the earth mantle. But ^{21}Ne, being so scarce, is more susceptible to nucleogenesis. As with ^{3}He, the production of Ne at the surface of the Earth can be a product of spallation.

- *Argon:* In the mantle, there is no significant production of ^{36}Ar and ^{38}Ar (Krummenacher, 1970). In the crust, ^{36}Ar is not produced in significant quantities by radioactive processes (Ballentine et al., 2002; Ballentine and Burnard, 2002). ^{40}Ar is produced mainly by the radioactive decay of ^{40}K by capturing electrons and emitting positrons. Then in the mantle, ^{36}Ar and ^{38}Ar isotopes are considered primordial, and in the crust, they can also be products of spallation.

- *Krypton:* krypton has six stable isotopes: ^{78}Kr, ^{80}Kr, ^{82}Kr, ^{83}Kr, ^{84}Kr and, ^{86}Kr. The components in the solar system have significant variations in krypton isotopic composition, normally associated with nucleosynthesis inherited from the solar nebula. ^{83}Kr, ^{84}Kr and, ^{86}Kr isotopes can be produced in the mantle by spontaneous fission of ^{238}U and ^{244}Pu. All six are produced in the crust by spallation, but in both cases, this pathway of production is negligible (Wieler, 2002).

- *Xenon:* xenon is the heaviest noble gas with nine stable isotopes: ^{124}Xe, ^{126}Xe, ^{128}Xe, ^{129}Xe, ^{130}Xe, ^{131}Xe, ^{132}Xe, ^{134}Xe and ^{136}Xe. The heaviest 4th are fission products of ^{238}U and ^{244}Pu and ^{129}Xe is produced from the extinct ^{129}I (radiogenic). ^{124}Xe, ^{126}Xe, ^{128}Xe, and ^{130}Xe are non-radiogenic isotopes and primordial in the mantle (Wetherill, 1953a; Kuroda, 1960; Butler et al., 1963; Dickin, 2018).

Regarding noble gas element trends, the Earth generally exhibits a depletion in concentration and a greater isotopic fractionation in ‰ · amu^{-1} of light noble gases (He and Ne) compared to heavy noble gases (Ar, Kr, and Xe) relative to the solar component, except for Xe (Dauphas and Morbidelli, 2014). The concentrations of noble gases in Earth and in other planets are orders of magnitude lower than those in meteorites and the solar wind (**Table 1.1** and **1.2**. And **Figure 1.2**) although for Venus its noble gas abundances and isotopic compositions remain very uncertain (Donahue and Russell, 1997).

But overall, for the noble gases, the greatest differences between solar system bodies are observed in the ratios $^{20}Ne/^{22}Ne$. The stable isotopes of neon, ^{20}Ne, ^{21}Ne and ^{22}Ne, vary substantially in nature, which, along with its inertness, make neon an exceptional tool for tracing the origin of terrestrial volatiles. This is because of the solar-

like component in the Earth's mantle ($^{20}Ne/^{22}Ne \geq 12.5$) which is drastically different from that of the atmosphere ($^{20}Ne/^{22}Ne=9.8$).

Source	^{20}Ne (mol/g)	^{36}Ar (mol/g)	^{84}Kr (mol/g)	^{130}Xe (mol/g)
Solar Wind	8.4E-05	2.2E-06	8.7E-10	6.4E-12
Venus (surface)	1.6E-11	6.8E-11	6.1E-14	3.7E-15
Earth	4.9E-13	9.3E-13	1.9E-14	1.1E-16
Mars (surface)	8.9E-16	9.1E-15	2.0E-16	1.5E-18
CI chondrites	1.6E-11	4.3E-11	4.8E-13	6.5E-14
Comets*	3.3E-08	8.2E-07	3.9E-08	3.9E-10

Table 1.1: Noble gases abundances in the solar wind and selected reservoirs from Dauphas and Morbidelli (2014) (References there in). * Cometary concentrations derived from noble gas-trapping experiments in amorphous ice.

	Abundances related to solar				***F* (‰/amu)**			
Source	**20**	**36**	**84**	**130**	**Ne**	**Ar**	**Kr**	**Xe**
Solar wind	0	0	0	0	0.0	0	0.0	0.0
Venus (surface)	-6.72	-4.50	-4.16	-3.24	72	-8		
Earth	-8.24	-6.36	-4.66	-4.79	146	16	7.8	40.0
Mars (surface)	-10.97	-8.37	-6.64	-6.64	246	211	-11.8	33.3
CI chondrites	-6.71	-4.70	-3.26	-2.00	173	6	9.8	2.6
Comets	-3.40	-0.42	1.65	1.78				

Table 1.2.: Noble gases abundances normalized to the solar wind composition *log* (C_{source}/C_{sw}) and fractionation factor (‰ $\cdot amu^{-1}$) for Venus, Mars, Earth, CI chondrites type and Comets from Dauphas et al. (2014). The cometary concentrations were determined from noble gas trapping experiments in amorphous ice (calculated at 55 K; see more details in Dauphas *et al.* (2014)). $F_{Ne} = [(^{20}Ne/^{22}Ne)_{reservoir} / (^{20}Ne/^{22}Ne)_{Solar} - 1] \times 1000/(22–20)$, $F_{Ar} = [(^{38}Ar/^{36}Ar)_{reservoir}/(^{38}Ar/^{36}Ar)_{Solar} - 1] \times 1000/(38–36)$, $F_{Kr} = [(^{83}Kr/^{84}Kr)_{reservoir}/(^{83}Kr/^{84}Kr)_{Solar} - 1] \times 1000/(83–84)$, $F_{Xe} = [(^{128}Xe/^{130}Xe)_{reservoir}/(^{128}Xe/^{130}Xe)Solar - 1] \times 1000/(128–130)$.

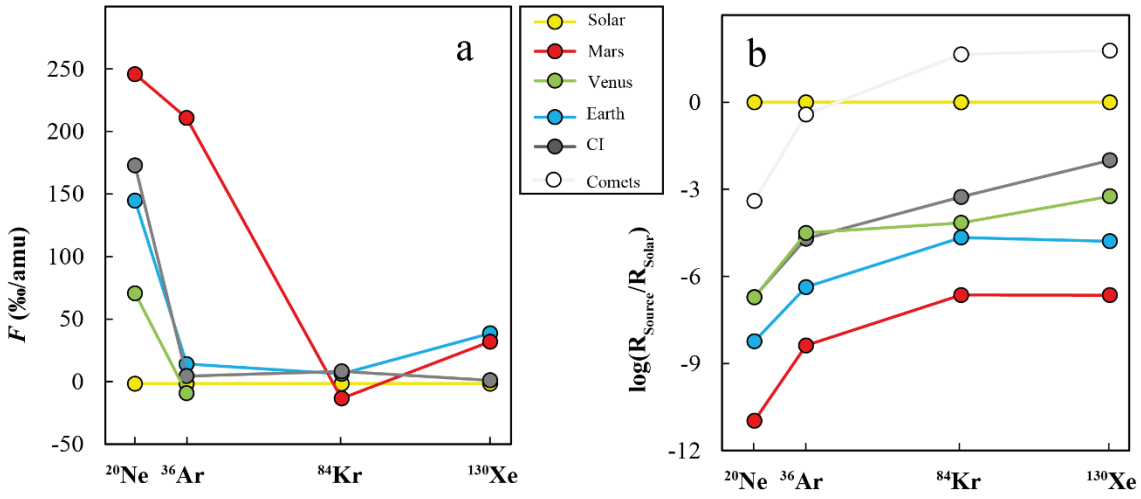

Figure 1.2: Relative elemental abundances of the four noble gases in Venus, Mars, and Earth's atmosphere Comets, and CI Chondrites relative to the solar wind abundances. (**a**) illustrate the fractionation factor of noble gases for various solar reservoirs and (**b**) the relative concentration concerning the composition of the solar wind. Data from **Table 1.2** from Dauphas and Morbidelli (2014) and references here in.

As previously described, the production rates of ^{20}Ne and ^{22}Ne in the mantle are negligible, and thus they are considered as essentially primordial in origin in the Earth's mantle. In this context, an excess of ^{20}Ne in mantle samples, giving high $^{20}Ne/^{22}Ne$ ratios, would mainly imply a primordial origin, i.e. a contribution from the solar Ne-component. In contrast, an excess of the ^{21}Ne would be attributed to nuclear reactions within the mantle. The following chapters will demonstrate how fractionation can also influence the neon isotopic ratios.

In this context, the diagram of the three stable isotopes of neon (Reynolds and Turner, 1964) provides a clear view of the contribution of each of the components involved in the gas being analysed by illustrating a line of mixing between them or by showing a possible fractionation of the isotopes involved. In this diagram, and thanks to the contribution made by the effort of numerous scientific studies of meteorites, lunar regolith, solar wind collectors, gas samples from mantle-derived hot springs, as well as the collection of representative samples from the upper and lower mantle (including CO_2 well-gas, bubbles trapped in glass, mineral melt inclusions, xenoliths, kimberlites, etc...) and samples where the Earth/ocean crust is involved in partial melting processes, the end members are broadly defined (Moreira et al., 1998; Kunz, 1999; Ballentine et al., 2005; Sumino et al., 2006; Heber et al., 2009, 2012; Pepin et al., 2012; Farrell et al., 2015; Péron et al., 2016; Williams and Mukhopadhyay, 2019).

Despite the solar-like neon in the mantle and the correlation between the two different mantle sources (convective well stirred and degassed upper mantle; and poorly degassed and heterogeneous lower mantle) are well-differentiated, a still open question is*: what is the exact isotopic composition of the mantle? and what is its origin?* This is a matter of concern for the scientific community.

1.2. Neon isotope ratios in the different solar components. The Bulk Solar System Composition:

1.2.1. The Sun:

The outer convective zone of the Sun and the photosphere are believed to preserve a composition close to that of the original solar nebula, which is the cloud of gas and dust from which the Sun and the rest of the solar system formed. The Sun contains more than 99.8% of the mass of the solar system being therefore representative of the composition of the material from which the planets and their building blocks are formed.

Due to the impossibility of direct sampling of the Sun, the solar wind provides the most reliable sample of the solar noble gas composition The abundance of the light elements in the solar wind is fractionated compared to their abundance in the solar photosphere (Wieler, 1998; Grimberg et al., 2006; Heber et al., 2009, 2012). This is because the elements in the solar wind are affected by an atom-ion separation process in the upper chromosphere. The $^{20}Ne/^{22}Ne$ ratio of 13.78 seems to be fractionated from the sun value due to the acceleration of the solar wind ions (Johannes Geiss et al., 1970; Bodmer and Bochsler, 2000), and that fractionation will depend on the energy of the solar event. Therefore, to obtain the composition of the solar nebula, it is necessary to correct for the composition of the solar wind.

Neon isotope data collected during different solar events allowed an estimate of the Ne-solar $^{20}Ne/^{22}Ne$: 13.36±0.10 (Heber et al., 2012). This ratio derived from the solar wind is believed to represent the initial solar nebula composition.

1.2.2. The Solar Wind:

The continuous flow of charged particles belonging to the Sun's photosphere has been studied on several occasions, thanks to the various Apollo expeditions using foils on the surface of the Moon (Bühler et al., 1969; Eberhardt et al., 1970; Geiss et al., 2004; J Geiss et al., 1970); and solar wind collectors in the case of Genesis (Heber et al., 2009; Grimberg et al., 2006; Heber et al., 2012).

Other ways of studying noble gases in the solar wind have been based on the analysis of gas trapped in meteorites from the surface of asteroids and samples of lunar regolith (Reynolds and Turner, 1964; Pepin et al., 1970; Reynolds et al., 1970; Becker and Pepin, 1994; Wieler, 1998; Hashizume et al., 2000).

The solar wind isotopic ratios of Ne were precisely estimated by the collectors of the last Genesis mission by (Heber et al., 2012) and give the value for $^{20}Ne/^{22}Ne$ of 13.703 ± 0.012 and 13.818 ± 0.013, fast and slow solar wind respectively, updating the previous measurements on Apollo foils or lunar grains exposed to solar wind.

1.2.3. Ne-B. The Solar Wind Implantation and Sputtering Component:

Another solar neon component has been identified in lunar regolith (Bühler et al., 1969; Eberhardt et al., 1970, 1972; McDonnell and Flavill, 1974) and gas-rich meteorites, being characterised by the preservation of noble gases with a solar signature before the compaction of the meteorite.

This component, defined as *Component B*, originated from the implantation of the mass-fractionated solar wind into the dust grain. It consists of micro-size grains that are exposed to solar corpuscular radiation (the solar wind), leading to their irradiation. The ions are implanted at different depths according to their kinetic energy (heavier isotopes implanted deeper than lighter), i.e. the same effect as for the collectors of the *Genesis mission* (Grimberg et al., 2006), resulting in a different isotopic ratio than that of the solar wind. Black and Pepin (1969) defined this isotopic composition of $^{20}Ne/^{22}Ne$ in gas-rich meteorites as 12.52 ± 0.18. When energetic particles, like ions from the solar wind, collide the surface of the microsize-grains, they cause atoms or molecules to be ejected, initiating the process known as sputtering, which gradually erodes the material's surface, starting with the outermost atomic layer. This phenomenon has been observed on the lunar regolith, (e.g. McDonnell and Flavill (1974).

In the case of lunar regolith, the surface of the Moon is constantly bombarded by the solar wind, which carries particles and gases, including noble gases like neon. The solar wind implants these noble gases into the upper layers of lunar soil. Raquin and Moreira (2009) calculated the Ne-B component via numerical modelling to be $^{20}Ne/^{22}Ne$ to be 12.73, a value that is slightly higher than that estimated by Black (1972), although consistent with the uncertainties and similar to the lunar soil (Eberhardt et al., 1972). Moreover, Moreira and Charnoz (2016) argue that if the implantation and sputtering processes do not achieve a steady state, i.e. for low exposure ages such as dust in the solar system (by a few Kyr), these values could be even higher than 12.73.

1.3. Neon isotope geochemistry of the Mantle:

1.3.1. The mantle structure and the isotopic Ne relationships with other terrestrial components:

Early neon isotopic measurements indicated a difference in isotopic composition between the earth's mantle ($^{20}Ne/^{22}Ne \geq 12.5$) and atmosphere ($^{20}Ne/^{22}Ne = 9.8$). During volcanic degassing, noble gases, including neon, are released from the mantle into the atmosphere. Over time, lighter isotopes like ^{20}Ne could have preferentially escaped into space (Craig and Lupton, 1976; Honda et al., 1987, 1991; Ozima and Zashu, 1988a; Poreda and di Brozolo, 1984; Sarda et al., 1988). The atmosphere and the ocean act as air-sea gas exchange systems, making the atmosphere the main source of noble gases in the ocean.

A further distinction between this terrestrial reservoir and others is that the ^{21}Ne signature in the upper mantle differs from those observed in the atmosphere. Additionally, the ^{21}Ne and ^{22}Ne isotopes are up to 1000 times more abundant in the crust than in the mantle, due to the high concentration of U and Th series decay (Wetherill, 1954b, 1953b). This implies that the atmosphere is not simply the complementary reservoir of the depleted MORB source. In comparison with the upper and lower mantle and with the air, the crustal rocks exhibit low $^{20}Ne/^{22}Ne$ and high $^{21}Ne/^{22}Ne$ ratios (Zadnik and Jeffery, 1985; B. Kennedy et al., 1990; Azuma et al., 1993). The origin of the volatiles, which include noble gases, in the atmosphere suggests the involvement of models other than those of the mantle, which will not be discussed in this chapter.

1.3.2. The upper mantle:

MORBs are primarily sourced from the upper mantle and erupted at mid-ocean ridges. The upper mantle is relatively homogeneous isotopically and has undergone extensive degassing, resulting in a depletion of volatile elements (Honda et al., 1991; Allegre et al., 1995). The process of degassing results in differences in the concentrations and isotopic compositions of noble gases between MORBs and OIBs.

In terms of neon, the isotopic composition of the basaltic rocks in the upper mantle is characterized by the MORB straight trend that passes through the composition of the *Air*, with $^{20}Ne/^{22}Ne = 9.8$ and $^{21}Ne/^{22}Ne = 0.0290$ values (Ozima and Podosek, 2002) and extend to values of $^{20}Ne/^{22}Ne = 12.48$ and $^{21}Ne/^{22}Ne = 0.0599$ (Moreira et al., 1998), this last due to the nucleogenic production of the ^{21}Ne isotope which generates higher isotopic $(U+Th)/^{22}Ne$ ratios (Yatsevich and Honda, 1997b). Contamination of MORBs by atmospheric Ne, as well as other noble gases (Ar, Kr, and Xe) can be extensive, as can be observed by the trend line which shows the mixing between the two components (MORB and *Air*; **Figure 1.3**).

1.3.3. Lower mantle as a reservoir of primordial noble gases:

In contrast, OIBs originate from the undegassed lower mantle, which is more heterogeneous isotopically (Allegre et al., 1995). The composition of volatiles in a primary mantle melt, i.e. before any gas loss, may vary due to compositional differences in the mantle or fractionation during the melting of the mantle. While the composition of the upper mantle is relatively well-defined, that of the plume source remains a matter of debate.

The lower mantle has undergone less degassing and retains higher concentrations of primordial noble gases, hinting at the presence of an ancient, primordial composition. The plume source exhibits different trend in neon isotopic composition relative to the low ^{21}Ne content (refers to; **Figure 1.3**), with values up to $^{20}Ne/^{22}Ne = 13.03 \pm 0.04$ and $^{21}Ne/^{22}Ne = 0.0368 \pm 0.0007$ for *Discovery anomaly* (*EW9309-5D*; Williams and Mukhopadhyay, 2019) and up to $^{20}Ne/^{22}Ne = 13.07 \pm 0.27$ and $^{21}Ne/^{22}Ne = 0.0353 \pm 0.0026$ in Galapagos hot spot (Péron et al., 2017) but the sample analysed at the *Discovery*

anomaly show Rayleigh distillation based on the $^{4}He/^{40}Ar$ and $^{3}He/^{22}Ne$ ratios (Moreira and Sarda, 2000); and the values from Galapagos show a large uncertainty. However, (Péron et al., 2017) determined the isotopic composition of the source of the hotspot in Galapagos to be $^{20}Ne/^{22}Ne = 12.65 \pm 0.04$ and $^{21}Ne/^{22}Ne = 0.0345 \pm 0.0004$ by applying Gaussian distribution to the values obtained in the analysed single vesicles not affected by contamination.

1.3.4. Local mantle variability:

Sometimes, the presence of the two mantle sources in the same eruptive event is documented. For example, the Shona and Discovery anomalies, situated in the southern Mid-Atlantic Ridge (Moreira et al., 1995; Sarda et al., 2000), present less nucleogenic ^{21}Ne in regions of higher $^{3}He/^{4}He$ (non-radiogenic helium) ratios. The observed bathymetric anomalies and the variations in the Ne and He isotope concentrations in these zones are consistent with plume material feeding into the sub-ridge mantle from nearby hotspot sources. This indicates the presence of a mantle blob that was entrained into the upper mantle flow. The trend line of these samples can be considered to reflect mixing between two sources, which lie intermediate between the two-mantle end-member trends. One of the samples associated with the *Discovery* anomaly was subjected to further analyses by step crushing, as described by Williams and Mukhopadhyay (2019) and is presented in **Figure 1.3** (sample 25D-discovery).

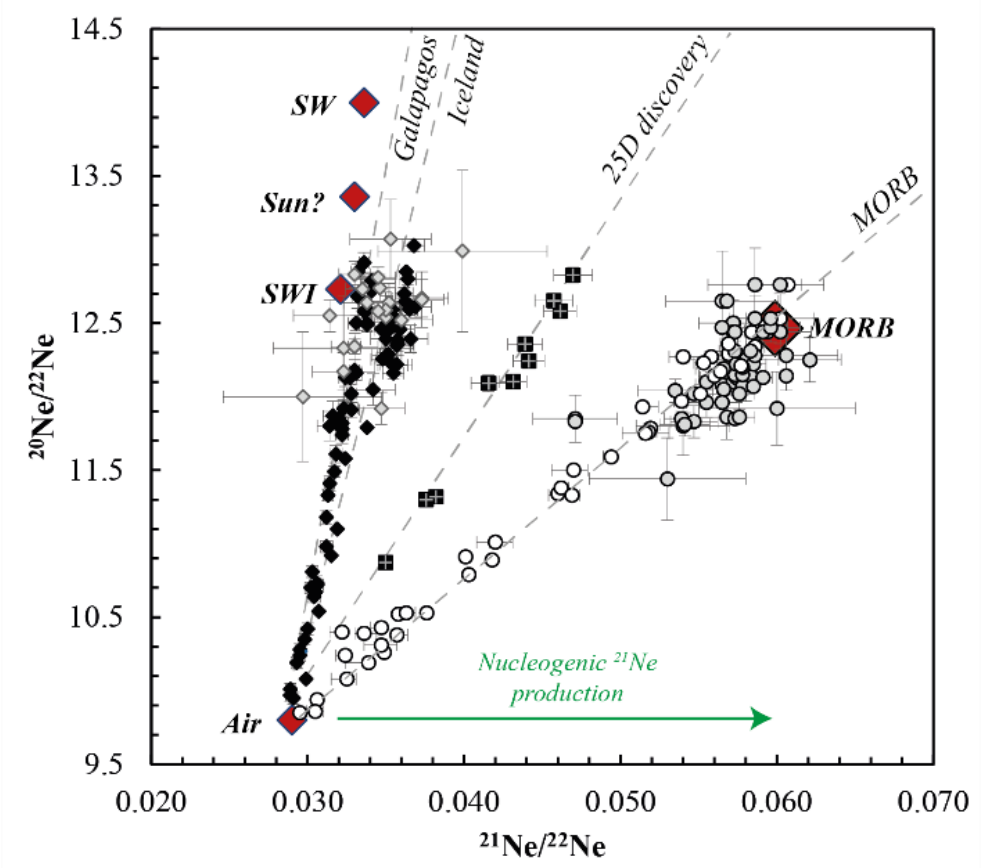

Figure 1.3: Three neon isotope diagram for MORBs: grey (vesicles) and white (crush) dots from: Moreira et al. (1998), Kurz (1999), Moreira and Sarda (2000), Tucker et al. (2012), Péron et al. (2019); OIBs black (crush) and grey (vesicles) diamonds from: Trieloff et al. (2000), Péron et al. (2016, 2017) and Williams and Mukhopadhyay (2019) and *25D-Discovery* (black squares with cross) from Williams and Mukhopadhyay (2019). The end-members are plotted with red diamonds for comparison: air from Ozima and Podosek (2002), SW from Pepin et al. (2012), Ne-B from Moreira and Charnoz (2016) Sun from (Heber et al., 2012) and MORB from Moreira et al. (1998)**.** The distinction between the two mantle sources (upper mantle and lower mantle) becomes visible with the significative nucleogenic production in MORBs of the ^{21}Ne isotope which generates higher isotopic $(U+Th)/^{22}Ne$ ratios (green arrow, ;Yatsevich and Honda, 1997b)**.**

1.4. Which solar component? The origin of Ne in the Earth's mantle:

The formation of the terrestrial planets begins with the collapse of dust in the gas-rich solar nebula during its early stages (3-5 Myr; Dauphas and Chaussidon, 2011). This process started approximately 4567 million years ago; the age of the oldest Calcium-Aluminium Inclusions (CAIs) found in the most primitive meteorites. Most of the mass contained in the solar disc ends up concentrating towards the centre of the solar disc, forming the proto-Sun (about 1 Myr). When the temperature inside of the start is high

enough, ca. 10^7 K, the nucleosynthesis starts (H-burning (D'E Atkinson and Houtermans, 1929).

The initial stage of planetary formation begins with the aggregation of dust particles into concentrated planes at vortices regions within the disk (i.e. regions where dust and gas accumulate and rotate), driven by turbulence in the accretion disk (Johansen et al., 2007, 2011; Cuzzi et al., 2008; Morbidelli et al., 2009; Chambers, 2010; Johansen and Klahr, 2011). Planetesimal accretion continues, forming embryos of approximately 0.1 Earth masses (M_E) in a few million years while the stellar nebula persists (Dauphas and Pourmand, 2011).

Once the gas has been removed from the system by accretion onto the Sun and by photoevaporation, the embryos rapidly become unstable and their orbits make them to collide with other bodies (Hollenbach et al., 2000). The gas nebula exerts a stabilising influence on the system of embryos and planetesimals, as it continuously attenuates their orbital eccentricities through tidal and friction drag effects. The growth of terrestrial planets, such as Earth, is thought to have proceeded via a different process than these planetesimals, i.e. via larger impacts between embryos (gravitational attraction), for approximately 50 Myr. For comparison, the Moon is thought to have formed approximately 50–150 Myr after CAI, by the same process (Canup and Asphaug, 2001; Raymond et al., 2009). It is postulated that a molten Earth embryo existed during the planetesimal accretion period, as the impact and core segregation generated heat, which in turn facilitated the degassing and the formation of the core and triggering a convective regime (e.g. magma ocean). Subsequently, the convective regime of the magma ocean is replaced by the convective regime of plate tectonics, during which the formation of the Earth's crust will result in a mantle depleted in incompatible elements, and the major cycles of elements will occur.

Having previously outlined the solar and terrestrial components that have similarities with each other and their respective neon isotopic composition, the question that has been the subject of much debate within the scientific community once again emerges. Neon isotopic composition is solar-like in the mantle but, it is sourced from which solar component?

The parent bodies of the terrestrial planets were formed from material condensed relatively close to the Sun, depleted in volatile elements.

Two main hypotheses have been proposed to explain the origin of light noble gases in the earth's mantle:

1.4.1. Capture of nebular gas during Earth's accretion in the mantle:

In the late 1980s and early 1990s, Honda et al. (1987, 1991), Sarda et al. (1988) and Ozima and Zashu (1988b, 1991) discovered ^{20}Ne values that were significantly higher than those observed in the current atmosphere in diamonds and basaltic glasses. This observation led to the formulation of the initial hypothesis regarding the origin of neon. Ozima and Zashu, and Sasaki (1999) proposed that the diamonds from the mantle exhibited solar values, while the current atmosphere exhibited a depletion in ^{20}Ne due to mass fractionation. They explained the difference between the two reservoirs (mantle and atmosphere), by arguing that the present atmosphere had been fractionated from the original solar-type ratio ($^{20}Ne/^{22}Ne = 13.6$) down to the present ratio ($^{20}Ne/^{22}Ne = 9.8$) by extensive loss (blow-off) of the proto-atmosphere at an early stage of the Earth's history. And that the actual atmosphere would be the product of a late-veneer, (volatile-rich material), and mantle degassing. **Figure 1.4** shows a representative scheme of this hypothesis (Olson and Sharp, 2019).

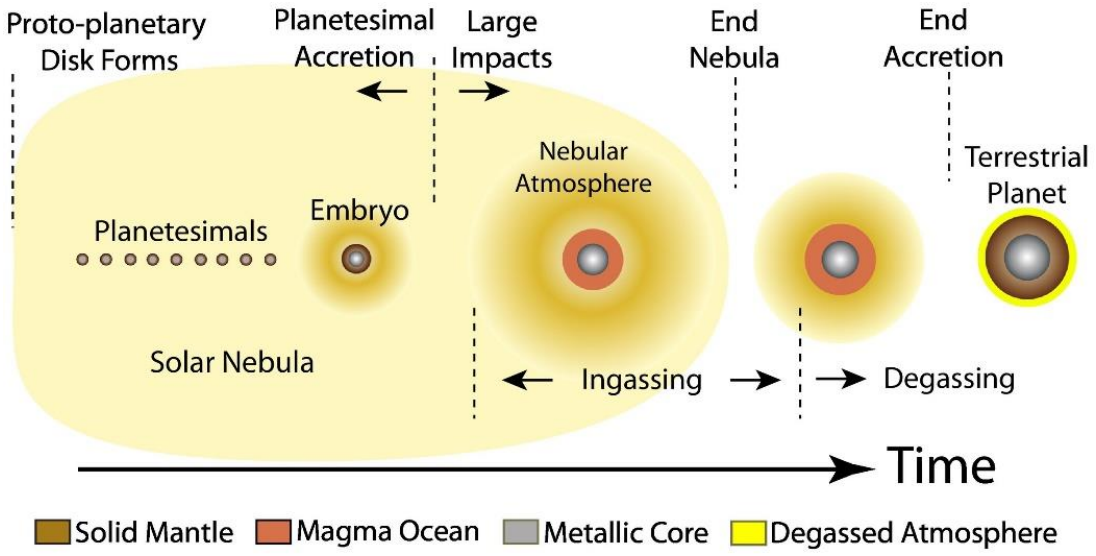

Figure 1.4: schematic evolution of a terrestrial planet in the solar nebular gas from (Olson and Sharp, 2019).

Numerous studies support this hypothesis (e.g. Mizuno et al. (1980), Sasaki and Nakazawa (1990), Harper and Jacobsen (1996), Yokochi and Marty (2004), Mukhopadhyay (2012), Williams and Mukhopadhyay (2019), Olson and Sharp (2019).

Some new high-quality neon data show $^{20}Ne/^{22}Ne$ ratios as high as 13.04±0.04 from the *Discovery ridge anomaly*, close to those of the solar nebula (Williams and Mukhopadhyay, 2019), and could be used as evidence that the solar nebula was dissolved during this period of the magma ocean. However, kinetic processes involved during vesiculation, could produce $^{20}Ne/^{22}Ne$ ratios higher than the magmatic ratio. (Ruzié and Moreira, 2010) proposed a model of fractionation during vesiculation, which could lead to higher isotopic compositions than the magma itself, and latter (Péron et al., 2017) showed higher isotopic compositions in some of the single vesicles analysed from Galapagos, which could be due either to slight heterogeneities in the samples or to the size of the bubbles.

Certain conditions must be met in order to make the solar nebula gas dissolution into a magma ocean a plausible scenario:

In order for the solar nebula to be effectively dissolved, it would have to be captured during the initial few million years of the formation of the Solar System, before it dissipates. However, Jaupart et al. (2017) demonstrated that bodies smaller than 0.2 M_E, as estimated for this period, are unlikely to capture significant amounts of gas. For this mechanism to be effective, the nebular atmosphere would have to be accreted rapidly and thermodynamically equilibrated between the magma ocean and the solar nebula, with atmospheric pressures between 10 and 100 bar (Porcelli et al., 2001; Yokochi and Marty, 2004).

Furthermore, the isotopic composition of neon and argon (which is not discussed here) in the mantle should be similar to that of the solar wind or solar ratios (Péron et al., 2018). Nevertheless, this is not the case, as the mantle ratio is markedly lower (**Figure 1.3** and *Sections 1.2* and *1.3*). To explain the lower isotope ratios observed in the current mantle, a significant amount of atmospheric neon would have to have subducted into the mantle. However, several studies have demonstrated that this is an unlikely scenario (Staudacher and Allègre, 1988; Moreira et al., 2003; Holland and Ballentine, 2006b), and thus it cannot account for the observed neon budget in the Earth's mantle.

Similarly, the analysis of single bubbles from natural samples will not yield any atmospheric gas record unless these are affected by microfractures (**Figure 1.5**) or the samples have been exposed to atmospheric contamination during the eruption (Péron et al., 2016, 2019).

The above arguments appear to preclude the solar nebula as the primary source of neon of the Earth's mantle, even if a minor contribution from solar gas cannot be ruled out.

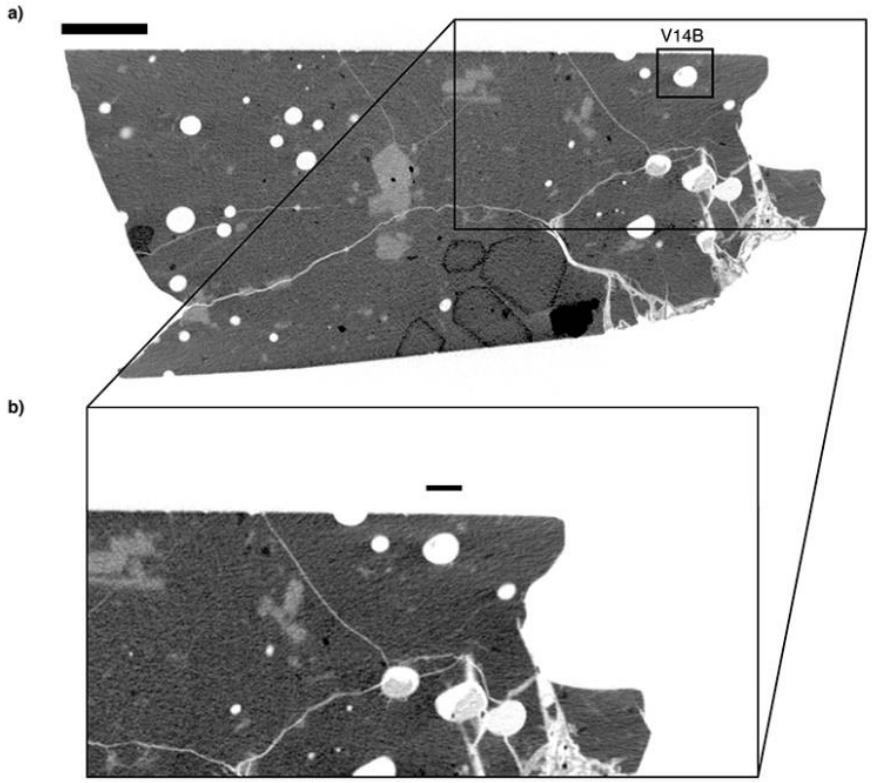

Figure 1.5: X-ray microtomography image of the sample *AHA-NEMO2-D22B* from Péron et al. (2017) where some fractures connected to vesicles can be observed

1.4.2. Solar Wind Implantation:

The second proposed model for the origin of volatile elements in the Earth's mantle proposes that the solar-like neon was carried out by solar wind and got implanted in planetary precursors (Trieloff et al., 2000; Ballentine et al., 2005; Raquin and Moreira, 2009; Kurz et al., 2009; Moreira, 2013; Colin et al., 2015; Moreira and Charnoz, 2016; Péron et al., 2016, 2017, 2018).

As explained earlier with the Ne-B component, this model assumes solar wind-derived neon implantation of the dust immersed in the solar disk. The solar escape velocity, i.e. the velocity of the isotopes in the solar wind, is the same, so the implantation depth will depend mainly on kinetic energy, and therefore the mass of the isotopes, with heavy isotopes being implanted deeper (Grimberg et al., 2006). The model presented by Raquin and Moreira (2009) and Moreira and Charnoz, (2016) was based on neon implantation profiles in the *Genesis* collectors (Grimberg et al. 2006). Linked to this solar wind implantation is assumed to be a sputtering process in which the surface layers of the grains (the first atomic layer) are eroded and after a few thousand years a static state is reached. The model gives a Ne-B isotopic composition of $^{20}Ne/^{22}Ne = 12.73$ using a $^{20}Ne/^{22}Ne = 14.00 \pm 0.02$ for the solar wind measured by Pepin et al. (2012) or $^{20}Ne/^{22}Ne = 12.53$ using a $^{20}Ne/^{22}Ne = 13.78$ (Heber et al., 2009).

Péron et al. (2018) provided a summary of the most representative isotopic and elemental compositions of the samples that are more similar to the solar and terrestrial components. (**Table 1.3**). They showed that the $^{20}Ne/^{22}Ne$ ratio from the different plume sources (Moreira et al., 1998; Trieloff et al., 2000; Kurz et al., 2009; Mukhopadhyay, 2012; Colin et al., 2015; Péron et al., 2016, 2017) ranges between 12.6 and 12.9 while the B component ranges between 12.65 and 12.9 (lunar bulk soils and gas-rich meteorites respectively).

The similarities between the plume source and the components suggest that a large part of the mantle light noble gases could derive from the solar wind implantation at the early stages of the Solar System. The issue of this model is related to the uncertainty of knowing the final noble gases composition of the Earth's parent bodies since it will depend on the irradiation and equilibrium time as well as the loss gas by diffusion.

Another important point is how the Implanted Solar Wind signature, SWI, was maintained during accretion and resisted heating. During accretion, the materials could have experienced varying degrees of heating. If the processes that led to the formation of certain rocks or regolith allowed them to retain low-temperature conditions, the original solar wind signatures might be preserved. A rapid cooling after accretion could also help maintain these signatures.

The two hypotheses are not mutually exclusive, and the concept of a hybrid model for the origin of terrestrial neon could be a potential solution.

	$^{20}Ne/^{22}Ne$	s	$^{38}Ar/^{36}Ar$	s
Lower mantle	12.65	0.04	0.1887	0.0006
Bulk lunar soils	12.64	0.08	0.1878	0.0008
Ilmenites	12.89	0.15	0.1933	0.0024
Sun	13.36	0.09	0.1857	0.001
Solar wind	13.75–14.00		0.1814–0.1823	
Solar wind (Heber et al., 2009)	13.78	0.03	0.1828	0.0003
Carbonaceous chondrites	8.2	0.4	0.1842	0.0044
Atmosphere	9.8	0.188	2.33	3
Mixing (0.64 CC + 0.36 LM)	9.8	0.012	0.051	

Table 1.3: from (Péron et al., 2018). Summary of Neon and Argon Isotopic Compositions for the Galapagos Mantle Source, Lunar Soils, Sun, Solar Wind, Carbonaceous Chondrites and mixing between the lower mantle 36% and carbonaceous chondrites 64%. References here in.

1.5. Processes that may control the isotopic compositions of the noble gases in the mantle:

The solubilities of noble gases in silicate liquids obey Henry`s law and are a strong function of the composition and the physical properties of the melt. Their different masses, solubilities, and atomic sizes as well as the pressure and temperature allow elemental and isotopic fractionations during physical processes (Lux, 1987; Jambon et al., 1986; Carroll and Webster, 1994; Nuccio and Paonita, 2000; Paonita et al., 2000; Iacono-Marziano et al., 2010).

The composition's dependency is determined by the melt's ionic porosity and the noble gases' ionic radii. Ionic porosity refers to the number of interstitial sites available in the melt for accommodating atoms of a particular size. Experiments conducted by Jambon et al. (1986) and Iacono-Marziano et al. (2010) demonstrated a preference for solubility in noble gases with a lower ionic radius. Furthermore, it was observed that solubility increases in melts with higher silica content due to the greater availability of voids resulting from the free space in the silicate network.

The solubility of noble gases increases as the ionic radius decreases, with the order being He > Ne > Ar > Kr > Xe. Temperature also affects the solubility. As highlighted by Iacono-Marziano et al. (2010), in mafic melts, an increase in temperature leads to an increase in solubility, while in more silicic melts, which have a more complex and polymerized structure compared to mafic melts, an increase in temperature leads to a decrease in noble gas solubility due to the structural characteristics of these melts.

The solubility of noble gases is also affected by the content of H_2O and CO_2 dissolved in the melt (Nuccio and Paonita, 2000, 2001; Paonita et al., 2000; Paonita, 2005). H_2O increases the solubility of noble gases because it acts as a network destroyer in mafic melts. Conversely, CO_2 dissolved in the magma decreases the solubility of noble gases.

Bubble nucleation is initiated at the point of volatile saturation in a magma and is subsequently promoted by decompression, heating, and the crystallisation of volatile-poor or volatile-free minerals. Bubbles grow in size and become more buoyant as a result of the processes of decompressive expansion, coalescence, and diffusive growth. The composition of these melts can be only preserved by quenching to glass during submarine eruptions or under thick ice layers.

The diffusion of noble gases exhibits a comparable linear relationship to solubility (Behrens, 2010; Lux, 1987) as noble gases follow different pathways depending on the phases present in the melt. These pathways include diffusion along grain boundaries, diffusion into newly formed vesicles when a major volatile phase is exsolved from the melt, and diffusion through a pre-existing melt when, for example, a new magma input is injected into the magma chamber. Similarly, the different isotopes for a same element will fractionate due to the mass, and this phenomenon will be more fully elucidated in *Chapter 4*.

Noble gases are lost from the melt silicate melts according to their solubilities. Mid-ocean ridge basalts are continuously degassing by exsolving CO_2, being progressively lost by partitioning into bubbles. The heavier volatile species are more enriched in the vapour phase than lighter ones due to their higher degree of incompatibility. (Pepin, 1991; Tolstikhin and O'Nions, 1994; Graham, 2002; Dauphas and Morbidelli, 2014).

When nucleation of vesicles starts, and CO_2 starts to exsolve from the melt, noble gases are rapidly partitioned toward the gas phase (Jambon et al., 1986) and are elementally fractionated (Burnard, 2001; Sarda and Moreira, 2002, 2002; Aubry et al., 2013). However, if the time to reach equilibrium is insufficient, and diffusion cannot be completed for all species, lighter volatile species, such as lighter noble gases and lighter isotopes, may partition faster to the gas phase. During the initial stages of nucleation and bubble growth, some authors thus propose that kinetic fractionation may occur (Aubaud et al., 2004; Ruzié and Moreira, 2010).

1.6. Purpose of this work:

There are two main technical approaches used for analysing basaltic rocks: (i) the conventional analytical approach, involving total crushing or total fusion, yields an average composition of gases entrapped within basalt vesicles; and analysis of single vesicles by laser ablation previously scanned by micro-CT which will give more accurate information about the gas evolution (Burnard et al., 1997; Burnard, 1999; Raquin et al., 2008; Péron et al., 2016).

The step crushing of basaltic glass releases volatiles from vesicles of varying sizes, representing different stages in the volatile evolution. This process can be employed to determine the volatile trajectory of each particular sample (Burnard, 1999). Sequential crushing releases gases from progressively smaller vesicles. The small vesicles tend to trap more fractionated magmatic volatiles than large vesicles. This could result in isotopic values that diverge significantly from the original values of the source.

An example could be shown by Péron et al. (2016, 2017). In this study, the authors compared the isotopic ratios obtained from the same sample, the Fernandina source, using two different methods: step crushing and bubble-by-bubble laser ablation. In the case of the single vesicles analysis, the vesicles exhibited a range of 12.17 ± 0.13 and 12.83 ± 0.09 for the $^{20}Ne/^{22}Ne$ ratios, in contrast, the highest $^{20}Ne/^{22}Ne$ ratios obtained by step crushing were found to be 12.91 ± 0.07. The authors proposed averaging the total number of bubbles analysed (excluding those affected by microfractures and providing an atmospheric value) to obtain a more representative value for the magma source $^{20}Ne/^{22}Ne$ = 12.65 ± 0.04 rather than taking the highest isotopic value obtained by step crushing.

This is because the latter can be influenced by kinetic fractionation in single vesicles or heterogeneities, as Burnard (1999) previously proposed.

Given the considerable uncertainty associated with such high isotopic ratios, both in single vesicles and in sequential crushing, this work aims to provide a more detailed analysis of the behaviour of neon when partitioning between the gas phase and the melt and before eruption occurs. *How neon isotopic signature can be affected during the vesiculation process?*

In order to achieve this, several experimental series have been conducted in which natural eruptive systems were recreated. To facilitate analysis, two single volatiles, Ne, and CO_2, constitute the volatile compounds. To eliminate the possibility that atmospheric contamination could be a determining factor, the experiments were conducted using a neon-rich synthetic glass with an atmospheric composition. The following chapters provide more details on each synthesis and experiment.

1.7. References:

Aiuppa, A., Federico, C., Giudice, G., Giuffrida, G., Guida, R., Gurrieri, S., Liuzzo, M., Moretti, R., Papale, P., 2009. The 2007 eruption of Stromboli volcano: insights from real-time measurement of the volcanic gas plume CO2/SO2 ratio. J. Volcanol. Geotherm. Res. 182, 221–230.

Allegre, C.J., Manhes, G., Göpel, C., 1995. The age of the Earth. Geochim. Cosmochim. Acta 59, 1445–1456.

Allègre, C.J., Staudacher, T., Sarda, P., Kurz, M., 1983. Constraints on evolution of Earth's mantle from rare gas systematics. Nature 303, 762–766. https://doi.org/10.1038/303762a0

Aubaud, C., 2022. Carbon stable isotope constraints on CO2 degassing models of ridge, hotspot and arc magmas. Chem. Geol. 605, 120962.

Aubaud, C., Pineau, F., Jambon, A., Javoy, M., 2004. Kinetic disequilibrium of C, He, Ar and carbon isotopes during degassing of mid-ocean ridge basalts. Earth Planet. Sci. Lett. 222, 391–406.

Aubry, G.J., Sator, N., Guillot, B., 2013. Vesicularity, bubble formation and noble gas fractionation during MORB degassing. Chem. Geol. 343, 85–98.

Azuma, S., Ozima, M., Hiyagon, H., 1993. Anomalous neon and xenon in an Archaean anorthosite from West Greenland. Earth Planet. Sci. Lett. 114, 341–352.

Ballentine, C.J., Barfod, D.N., 2000. The origin of air-like noble gases in MORB and OIB. Earth Planet. Sci. Lett. 180, 39–48.

Ballentine, C.J., Burgess, R., Marty, B., 2002. Tracing fluid origin, transport and interaction in the crust.

Ballentine, C.J., Burnard, P.G., 2002. Production, Release and Transport of Noble Gases in the Continental Crust. Rev. Mineral. Geochem. 47, 481–538. https://doi.org/10.2138/rmg.2002.47.12

Ballentine, C.J., Marty, B., Sherwood Lollar, B., Cassidy, M., 2005. Neon isotopes constrain convection and volatile origin in the Earth's mantle. Nature 433, 33–38.

Bauer, C.A., 1947. Production of helium in meteorites by cosmic radiation. Phys. Rev. 72, 354.

Becker, R.H., Pepin, R.O., 1994. Solar wind noble gases and nitrogen in metal from lunar soil 68501. Meteoritics 29, 724–738.

Behrens, H., 2010. Noble gas diffusion in silicate glasses and melts. Rev. Mineral. Geochem. 72, 227–267.

Behrens, H., Misiti, V., Freda, C., Vetere, F., Botcharnikov, R.E., Scarlato, P., 2009. Solubility of H2O and CO2 in ultrapotassic melts at 1200 and 1250 C and pressure from 50 to 500 MPa. Am. Mineral. 94, 105–120.

Behrens, H., Zhang, Y., 2001. Ar diffusion in hydrous silicic melts: implications for volatile diffusion mechanisms and fractionation. Earth Planet. Sci. Lett. 192, 363–376.

Black, D., Pepin, R., 1969. Trapped neon in meteorites—II. Earth Planet. Sci. Lett. 6, 395–405.

Black, D.C., 1972. On the origins of trapped helium, neon and argon isotopic variations in meteorites—I. Gas-rich meteorites, lunar soil and breccia. Geochim. Cosmochim. Acta 36, 347–375.

Blank, J.G., Brooker, R.A., 1994. Experimental studies of carbon dioxide in silicate melts; solubility, speciation, and stable carbon isotope behavior. Rev. Mineral. Geochem. 30, 157–186.

Bodmer, R., Bochsler, P., 2000. Influence of Coulomb collisions on isotopic and elemental fractionation in the solar wind acceleration process. J. Geophys. Res. Space Phys. 105, 47–60.

Bottinga, Y., Richet, P., 1981. High pressure and temperature equation of state and calculation of the thermodynamic properties of gaseous carbon dioxide. Am. J. Sci. 281, 615–660.

Bühler, F., Eberhardt, P., Geiss, J., Meister, J., Signer, P., 1969. Apollo 11 solar wind composition experiment: First results. Science 166, 1502–1503.

Burbidge, E.M., Burbidge, G.R., Fowler, W.A., Hoyle, F., 1957. Synthesis of the elements in stars. Rev. Mod. Phys. 29, 547.

Burnard, P., 2001. Correction for volatile fractionation in ascending magmas: noble gas abundances in primary mantle melts. Geochim. Cosmochim. Acta 65, 2605–2614.

Burnard, P., 1999. The bubble-by-bubble volatile evolution of two mid-ocean ridge basalts. Earth Planet. Sci. Lett. 174, 199–211.

Burnard, P., Graham, D., Turner, G., 1997. Vesicle-specific noble gas analyses of" popping rock": implications for primordial noble gases in Earth. Science 276, 568–571.

Busemann, H., Baur, H., Wieler, R., 2000. Primordial noble gases in "phase Q" in carbonaceous and ordinary chondrites studied by closed-system stepped etching. Meteorit. Planet. Sci. 35, 949–973.

Butler, W., Jeffery, P., Reynolds, J., Wasserburg, G., 1963. Isotopic variations in terrestrial xenon. J. Geophys. Res. 68, 3283–3291.

Canup, R.M., Asphaug, E., 2001. Origin of the Moon in a giant impact near the end of the Earth's formation. Nature 412, 708–712.

Carroll, M.R., Webster, J.D., 1994. Solubilities of sulfur, noble gases, nitrogen, chlorine, and fluorine in magmas. Rev. Mineral. 30, 231–231.

Chambers, J., 2010. Planetesimal formation by turbulent concentration. Icarus 208, 505–517.

Chavrit, D., 2010. Cartographie globale des flux de CO2 à l'axe des dorsales océaniques: une approche pétrologique.

Chavrit, D., Humler, E., Morizet, Y., Laporte, D., 2012. Influence of magma ascent rate on carbon dioxide degassing at oceanic ridges: Message in a bubble. Earth Planet. Sci. Lett. 357, 376–385.

Clayton, D.D., 1983. Principles of stellar evolution and nucleosynthesis. University of Chicago press.

Colin, A., Moreira, M., Gautheron, C., Burnard, P., 2015. Constraints on the noble gas composition of the deep mantle by bubble-by-bubble analysis of a volcanic glass sample from Iceland. Chem. Geol. 417, 173–183.

Craig, H., Lupton, J., 1976. Primordial neon, helium, and hydrogen in oceanic basalts. Earth Planet. Sci. Lett. 31, 369–385.

Cuzzi, J.N., Hogan, R.C., Shariff, K., 2008. Toward planetesimals: Dense chondrule clumps in the protoplanetary nebula. Astrophys. J. 687, 1432.

Dauphas, N., Burkhardt, C., Warren, P.H., Fang-Zhen, T., 2014. Geochemical arguments for an Earth-like Moon-forming impactor. Philos. Trans. R. Soc. Math. Phys. Eng. Sci. 372, 20130244.

Dauphas, N., Chaussidon, M., 2011. A perspective from extinct radionuclides on a young stellar object: the Sun and its accretion disk. Annu. Rev. Earth Planet. Sci. 39, 351–386.

Dauphas, N., Morbidelli, A., 2014. Geochemical and planetary dynamical views on the origin of Earth's atmosphere and oceans. ArXiv Prepr. ArXiv13121202.

Dauphas, N., Pourmand, A., 2011. Hf–W–Th evidence for rapid growth of Mars and its status as a planetary embryo. Nature 473, 489–492.

D'E Atkinson, R., Houtermans, F., 1929. Transmutation of the Lighter Elements in Stars. Nature 123, 567–568.

Di Carlo, I., Pichavant, M., Rotolo, S.G., Scaillet, B., 2006. Experimental crystallization of a high-K arc basalt: the golden pumice, Stromboli volcano (Italy). J. Petrol. 47, 1317–1343.

Dickin, A.P., 2018. Radiogenic isotope geology. Cambridge university press.

Dixon, J.E., Pan, V., 1995a. Determination of the molar absorptivity of dissolved carbonate in basanitic glass. Am. Mineral. 80, 1339–1342.

Dixon, J.E., Pan, V., 1995b. Determination of the molar absorptivity of dissolved carbonate in basanitic glass. Am. Mineral. 80, 1339–1342.

Dixon, J.E., Stolper, E.M., Holloway, J.R., 1995. An experimental study of water and carbon dioxide solubilities in mid-ocean ridge basaltic liquids. Part I: calibration and solubility models. J. Petrol. 36, 1607–1631.

Donahue, T., Russell, C., 1997. The Venus atmosphere and ionosphere and their interaction with the solar wind: An overview. Venus II Geol. Geophys. Atmosphere Sol. Wind Environ. 3.

Douglass, J., Schilling, J., Fontignie, D., 1999. Plume-ridge interactions of the Discovery and Shona mantle plumes with the southern Mid-Atlantic Ridge (40°-55° S). J. Geophys. Res. Solid Earth 104, 2941–2962.

Eberhardt, P., Geiss, J., Graf, H., Grögler, N., Krähenbühl, U., Schwaller, H., Schwarzmüller, J., Stettler, A., 1970. Trapped solar wind noble gases, exposure age and K/Ar-age in Apollo 11 lunar fine material. Presented at the Geochimica et Cosmochimica Acta Supplement, Volume 1. Proceedings of the Apollo 11 Lunar Science Conference held 5-8 January, 1970 in Houston, TX. Volume 2: Chemical and Isotope Analyses. Edited by AA Levinson. New York: Pergammon Press, 1970., p. 1037, p. 1037.

Eberhardt, P., Geiss, J., Graf, H., Grögler, N., Mendia, M., Mörgeli, M., Schwaller, H., Stettler, A., Krähenbühl, U., Von Gunten, H., 1972. Trapped solar wind noble gases in Apollo 12 lunar fines 12001 and Apollo 11 breccia 10046. Bern Univ.(Switzerland).

Farrell, W.M., Hurley, D.M., Zimmerman, M.I., 2015. Solar wind implantation into lunar regolith: Hydrogen retention in a surface with defects. Icarus 255, 116–126.

Fine, G., Stolper, E., 1985. The speciation of carbon dioxide in sodium aluminosilicate glasses. Contrib. Mineral. Petrol. 91, 105–121.

Frost, B.R., 2018. Introduction to oxygen fugacity and its petrologic importance, in: Oxide Minerals. De Gruyter, pp. 1–10.

Geiss, J., Bühler, F., Cerutti, H., Eberhardt, P., Filleux, C., Meister, J., Signer, P., 2004. The Apollo SWC experiment: results, conclusions, consequences. Space Sci. Rev. 110, 307–335.

Geiss, J, Eberhardt, P., Bühler, F., Meister, J., Signer, P., 1970. Apollo 11 and 12 solar wind composition experiments: Fluxes of He and Ne isotopes. J. Geophys. Res. 75, 5972–5979.

Geiss, Johannes, Hirt, P., Leutwyler, H., 1970. On acceleration and motion of ions in corona and solar wind. Sol. Phys. 12, 458–483.

Giordano, D., Russell, J.K., Dingwell, D.B., 2008. Viscosity of magmatic liquids: a model. Earth Planet. Sci. Lett. 271, 123–134.

Gonnermann, H.M., Manga, M., 2007. The fluid mechanics inside a volcano. Annu Rev Fluid Mech 39, 321–356.

Graham, D.W., 2002. Noble Gas Isotope Geochemistry of Mid-Ocean Ridge and Ocean Island Basalts: Characterization of Mantle Source Reservoirs. Rev. Mineral. Geochem. 47, 247–317. https://doi.org/10.2138/rmg.2002.47.8

Grimberg, A., Baur, H., Bochsler, P., Bühler, F., Burnett, D.S., Hays, C.C., Heber, V.S., Jurewicz, A.J., Wieler, R., 2006. Solar wind neon from Genesis: Implications for the lunar noble gas record. Science 314, 1133–1135.

Harper Jr, C.L., Jacobsen, S.B., 1996. Noble gases and Earth's accretion. Science 273, 1814–1818.

Hashizume, K., Chaussidon, M., Marty, B., Robert, F., 2000. Solar wind record on the Moon: deciphering presolar from planetary nitrogen. Science 290, 1142–1145.

Heber, V.S., Baur, H., Bochsler, P., McKeegan, K.D., Neugebauer, M., Reisenfeld, D.B., Wieler, R., Wiens, R.C., 2012. Isotopic mass fractionation of solar wind: Evidence from fast and slow solar wind collected by the Genesis mission. Astrophys. J. 759, 121.

Heber, V.S., Wieler, R., Baur, H., Olinger, C., Friedmann, T.A., Burnett, D.S., 2009. Noble gas composition of the solar wind as collected by the Genesis mission. Geochim. Cosmochim. Acta 73, 7414–7432.

Holland, G., Ballentine, C.J., 2006a. Seawater subduction controls the heavy noble gas composition of the mantle. Nature 441, 186–191.

Holland, G., Ballentine, C.J., 2006b. Seawater subduction controls the heavy noble gas composition of the mantle. Nature 441, 186–191.

Holland, G., Cassidy, M., Ballentine, C.J., 2009. Meteorite Kr in Earth's mantle suggests a late accretionary source for the atmosphere. Science 326, 1522–1525.

Hollenbach, D.J., Yorke, H.W., Johnstone, D., 2000. Disk dispersal around young stars. Protostars Planets IV 401, 12.

Honda, M., McDougall, I., Patterson, D.B., Doulgeris, A., Clague, D.A., 1991. Possible solar noble-gas component in Hawaiian basalts. Nature 349, 149–151.

Honda, M., Reynolds, J., Roedder, E., Epstein, S., 1987. Noble gases in diamonds: Occurrences of solarlike helium and neon. J. Geophys. Res. Solid Earth 92, 12507–12521.

Iacono-Marziano, G., Paonita, A., Rizzo, A., Scaillet, B., Gaillard, F., 2010. Noble gas solubilities in silicate melts: new experimental results and a comprehensive model of the effects of liquid composition, temperature and pressure. Chem. Geol. 279, 145–157.

Jambon, A., Weber, H., Braun, O., 1986. Solubility of He, Ne, Ar, Kr and Xe in a basalt melt in the range 1250–1600 C. Geochemical implications. Geochim. Cosmochim. Acta 50, 401–408.

Jaupart, E., Charnoz, S., Moreira, M., 2017. Primordial atmosphere incorporation in planetary embryos and the origin of Neon in terrestrial planets. Icarus 293, 199–205.

Javoy, M., Pineau, F., 1991. The volatiles record of a "popping" rock from the Mid-Atlantic Ridge at 14 N: chemical and isotopic composition of gas trapped in the vesicles. Earth Planet. Sci. Lett. 107, 598–611.

Jiménez-Mejías, M., Andújar, J., Scaillet, B., Casillas, R., 2021. Experimental determination of H $ _ {{2}} $ O and CO $ _ {{2}} $ solubilities of mafic alkaline magmas from Canary Islands. Comptes Rendus Géoscience 353, 289–314.

Johansen, A., Klahr, H., 2011. Planetesimal formation through streaming and gravitational instabilities. Earth Moon Planets 108, 39–43.

Johansen, A., Klahr, H., Henning, T., 2011. High-resolution simulations of planetesimal formation in turbulent protoplanetary discs. Astron. Astrophys. 529, A62.

Johansen, A., Oishi, J.S., Low, M.-M.M., Klahr, H., Henning, T., Youdin, A., 2007. Rapid planetesimal formation in turbulent circumstellar disks. Nature 448, 1022–1025.

Kendrick, M.A., Burnard, P., 2013. Noble gases and halogens in fluid inclusions: a journey through the Earth's crust. Noble Gases Geochem. Tracers 319–369.

Kennedy, B., Hiyagon, H., Reynolds, J., 1990. Crustal neon: a striking uniformity. Earth Planet. Sci. Lett. 98, 277–286.

Kennedy, B.M., Hiyagon, H., Reynolds, J.H., 1990. Crustal neon: a striking uniformity. Earth Planet. Sci. Lett. 98, 277–286. https://doi.org/10.1016/0012-821X(90)90030-2

Kipfer, R., Aeschbach-Hertig, W., Peeters, F., Stute, M., 2002. Noble gases in lakes and ground waters. Rev. Mineral. Geochem. 47, 615–700.

Kress, V.C., Carmichael, I.S., 1991. The compressibility of silicate liquids containing Fe 2 O 3 and the effect of composition, temperature, oxygen fugacity and pressure on their redox states. Contrib. Mineral. Petrol. 108, 82–92.

Krummenacher, D., 1970. Isotopic composition of argon in modern surface volcanic rocks. Earth Planet. Sci. Lett. 8, 109–117.

Kunz, J., 1999. Is there solar argon in the Earth's mantle? Nature 399, 649–650. https://doi.org/10.1038/21352

Kuroda, P., 1960. Nuclear fission in the early history of the earth. Nature 187.

Kurz, M.D., 1986. Cosmogenic helium in a terrestrial igneous rock. Nature 320, 435–439. https://doi.org/10.1038/320435a0

Kurz, M.D., Curtice, J., Fornari, D., Geist, D., Moreira, M., 2009. Primitive neon from the center of the Galápagos hotspot. Earth Planet. Sci. Lett. 286, 23–34.

Lange, R.A., 1994a. Volatiles in Magmas, in: Carroll, M.R., Holloway, J.R. (Eds.), . De Gruyter, pp. 331–370. https://doi.org/10.1515/9781501509674-015

Lange, R.A., 1994b. Volatiles in Magmas, in: Carroll, M.R., Holloway, J.R. (Eds.), . De Gruyter, pp. 331–370. https://doi.org/10.1515/9781501509674-015

Le Gall, N., 2015. Ascension et dégazage des magmas basaltiques: approche expérimentale.

Le Gall, N., Pichavant, M., 2016a. Experimental simulation of bubble nucleation and magma ascent in basaltic systems: Implications for Stromboli volcano. Am. Mineral. 101, 1967–1985.

Le Gall, N., Pichavant, M., 2016b. Homogeneous bubble nucleation in H2O-and H2O-CO2-bearing basaltic melts: results of high temperature decompression experiments. J. Volcanol. Geotherm. Res. 327, 604–621.

Le Roux, P., Le Roex, A., Schilling, J.-G., Shimizu, N., Perkins, W., Pearce, N., 2002. Mantle heterogeneity beneath the southern Mid-Atlantic Ridge: trace element evidence for contamination of ambient asthenospheric mantle. Earth Planet. Sci. Lett. 203, 479–498.

Lensky, N.G., Niebo, R.W., Holloway, J.R., Lyakhovsky, V., Navon, O., 2006. Bubble nucleation as a trigger for xenolith entrapment in mantle melts. Earth Planet. Sci. Lett. 245, 278–288.

Lux, G., 1987. The behavior of noble gases in silicate liquids: Solution, diffusion, bubbles and surface effects, with applications to natural samples. Geochim. Cosmochim. Acta 51, 1549–1560.

Mangan, M., Sisson, T., 2000. Delayed, disequilibrium degassing in rhyolite magma: decompression experiments and implications for explosive volcanism. Earth Planet. Sci. Lett. 183, 441–455.

Marsh, B.D., 2007. Crystallization of silicate magmas deciphered using crystal size distributions. J. Am. Ceram. Soc. 90, 746–757.

Marsh, B.D., 1988. Crystal size distribution (CSD) in rocks and the kinetics and dynamics of crystallization: I. Theory. Contrib. Mineral. Petrol. 99, 277–291.

Marty, B., 2022. Meteoritic noble gas constraints on the origin of terrestrial volatiles. Icarus 381, 115020.

Marty, B., 2020. Origins and early evolution of the atmosphere and the oceans. Geochem. Perspect. 9, 135–136.

Marty, B., 2012. The origins and concentrations of water, carbon, nitrogen and noble gases on Earth. Earth Planet. Sci. Lett. 313, 56–66.

Marty, B., Yokochi, R., 2006. Water in the early Earth. Rev. Mineral. Geochem. 62, 421–450.

Marty, B., Zimmermann, L., 1999. Volatiles (He, C, N, Ar) in mid-ocean ridge basalts: Assesment of shallow-level fractionation and characterization of source composition. Geochim. Cosmochim. Acta 63, 3619–3633.

McDonnell, J., Flavill, R., 1974. Sputter Erosion on the Lunar Surface: Measurements and Features Under Simulated Solar He+ Bombardment. Lunar Planet. Sci. V Houst. Lunar Planet Inst 478.

Mizuno, H., Nakazawa, K., Hayashi, C., 1980. Dissolution of the primordial rare gases into the molten Earth's material. Earth Planet. Sci. Lett. 50, 202–210.

Morbidelli, A., Bottke, W.F., Nesvorný, D., Levison, H.F., 2009. Asteroids were born big. Icarus 204, 558–573.

Moreira, M., 2013. Noble gas constraints on the origin and evolution of Earth's volatiles. Geochem. Perspect. 2, 229–230.

Moreira, M., Blusztajn, J., Curtice, J., Hart, S., Dick, H., Kurz, M.D., 2003. He and Ne isotopes in oceanic crust: implications for noble gas recycling in the mantle. Earth Planet. Sci. Lett. 216, 635–643.

Moreira, M., Charnoz, S., 2016. The origin of the neon isotopes in chondrites and on Earth. Earth Planet. Sci. Lett. 433, 249–256. https://doi.org/10.1016/j.epsl.2015.11.002

Moreira, M., Kunz, J., Allegre, C., 1998. Rare gas systematics in popping rock: isotopic and elemental compositions in the upper mantle. Science 279, 1178–1181.

Moreira, M., Rouchon, V., Muller, E., Noirez, S., 2018. The xenon isotopic signature of the mantle beneath Massif Central. Geochem Perspect Lett 6, 28–32.

Moreira, M., Sarda, P., 2000. Noble gas constraints on degassing processes. Earth Planet. Sci. Lett. 176, 375–386.

Moreira, M., Staudacher, T., Sarda, P., Schilling, J.-G., Allègre, C.J., 1995. A primitive plume neon component in MORB: The Shona ridge-anomaly, South Atlantic (51–52° S). Earth Planet. Sci. Lett. 133, 367–377.

Moretti, R., Papale, P., Ottonello, G., 2003. A model for the saturation of COHS fluids in silicate melts. Geol. Soc. Lond. Spec. Publ. 213, 81–101.

Mourtada-Bonnefoi, C., Laporte, D., 2002. Homogeneous bubble nucleation in rhyolitic magmas: an experimental study of the effect of H2O and CO2. J. Geophys. Res. Solid Earth 107, ECV-2.

Mourtada-Bonnefoi, C.C., Laporte, D., 2004. Kinetics of bubble nucleation in a rhyolitic melt: an experimental study of the effect of ascent rate. Earth Planet. Sci. Lett. 218, 521–537.

Mukhopadhyay, S., 2012. Early differentiation and volatile accretion recorded in deep-mantle neon and xenon. Nature 486, 101–104. https://doi.org/10.1038/nature11141

Nowak, M., Schreen, D., Spickenbom, K., 2004. Argon and CO2 on the race track in silicate melts: a tool for the development of a CO2 speciation and diffusion model. Geochim. Cosmochim. Acta 68, 5127–5138.

Nuccio, P., Paonita, A., 2001. Magmatic degassing of multicomponent vapors and assessment of magma depth: application to Vulcano Island (Italy). Earth Planet. Sci. Lett. 193, 467–481.

Nuccio, P., Paonita, A., 2000. Investigation of the noble gas solubility in H2O–CO2 bearing silicate liquids at moderate pressure II: the extended ionic porosity (EIP) model. Earth Planet. Sci. Lett. 183, 499–512.

Olson, P.L., Sharp, Z.D., 2019. Nebular atmosphere to magma ocean: a model for volatile capture during Earth accretion. Phys. Earth Planet. Inter. 294, 106294.

Ozima, M., Podosek, F.A., 2002. Noble gas geochemistry. Cambridge University Press.

Ozima, M., Zashu, S., 1991. Noble gas state of the ancient mantle as deduced from noble gases in coated diamonds. Earth Planet. Sci. Lett. 105, 13–27.

Ozima, M., Zashu, S., 1988a. Solar-type Ne in Zaire cubic diamonds. Geochim. Cosmochim. Acta 52, 19–25.

Ozima, M., Zashu, S., 1988b. Solar-type Ne in Zaire cubic diamonds. Geochim. Cosmochim. Acta 52, 19–25.

Paonita, A., 2005. Noble gas solubility in silicate melts: a review of experimentation and theory, and implications regarding magma degassing processes. Ann. Geophys.

Paonita, A., Gigli, G., Gozzi, D., Nuccio, P., Trigila, R., 2000. Investigation of the He solubility in H2O–CO2 bearing silicate liquids at moderate pressure: a new experimental method. Earth Planet. Sci. Lett. 181, 595–604.

Pepin, R., Nyquist, L., Phinney, D., Black, D.C., 1970. Isotopic composition of rare gases in lunar samples. Science 167, 550–553.

Pepin, R.O., 1991. On the origin and early evolution of terrestrial planet atmospheres and meteoritic volatiles. Icarus 92, 2–79.

Pepin, R.O., Schlutter, D.J., Becker, R.H., Reisenfeld, D.B., 2012. Helium, neon, and argon composition of the solar wind as recorded in gold and other Genesis collector materials. Geochim. Cosmochim. Acta 89, 62–80.

Péron, S., Moreira, M., Agranier, A., 2018. Origin of light noble gases (He, Ne, and Ar) on Earth: A review. Geochem. Geophys. Geosystems 19, 979–996.

Péron, S., Moreira, M., Colin, A., Arbaret, L., Putlitz, B., Kurz, M.D., 2016. Neon isotopic composition of the mantle constrained by single vesicle analyses. Earth Planet. Sci. Lett. 449, 145–154. https://doi.org/10.1016/j.epsl.2016.05.052

Péron, S., Moreira, M., Putlitz, B., Kurz, M., 2017. Solar wind implantation supplied light volatiles during the first stage of Earth accretion. Geochem. Perspect. Lett. 151–159.

Péron, S., Moreira, M.A., Kurz, M.D., Curtice, J., Blusztajn, J.S., Putlitz, B., Wanless, V.D., Jones, M.R., Soule, S.A., Mittelstaedt, E., 2019. Noble gas systematics in new popping rocks from the Mid-Atlantic Ridge (14° N): evidence for small-scale upper mantle heterogeneities. Earth Planet. Sci. Lett. 519, 70–82.

Pichavant, M., Di Carlo, I., Le Gac, Y., Rotolo, S.G., Scaillet, B., 2009. Experimental constraints on the deep magma feeding system at Stromboli volcano, Italy. J. Petrol. 50, 601–624.

Pichavant, M., Di Carlo, I., Rotolo, S.G., Scaillet, B., Burgisser, A., Le Gall, N., Martel, C., 2013. Generation of CO 2-rich melts during basalt magma ascent and degassing. Contrib. Mineral. Petrol. 166, 545–561.

Pichavant, M., Le Gall, N., Scaillet, B., 2018. Gases as precursory signals: experimental simulations, new concepts and models of magma degassing. Volcan. Unrest Adv Volcanol 139–154.

Pierre Jules César Janssen, 1908. . Mon. Not. R. Astron. Soc. 68, 245–249. https://doi.org/10.1093/mnras/68.4.245

Porcelli, D., Ballentine, C.J., Wieler, R., 2002. An overview of noble gas geochemistry and cosmochemistry. Rev. Mineral. Geochem. 47, 1–19.

Porcelli, D., Woolum, D., Cassen, P., 2001. Deep Earth rare gases: initial inventories, capture from the solar nebula, and losses during Moon formation. Earth Planet. Sci. Lett. 193, 237–251.

Poreda, R., di Brozolo, F.R., 1984. Neon isotope variations in Mid-Atlantic Ridge basalts. Earth Planet. Sci. Lett. 69, 277–289.

Raquin, A., Moreira, M., 2009. Atmospheric 38Ar/36Ar in the mantle: implications for the nature of the terrestrial parent bodies. Earth Planet. Sci. Lett. 287, 551–558.

Raquin, A., Moreira, M.A., Guillon, F., 2008. He, Ne and Ar systematics in single vesicles: mantle isotopic ratios and origin of the air component in basaltic glasses. Earth Planet. Sci. Lett. 274, 142–150.

Raymond, S.N., O'Brien, D.P., Morbidelli, A., Kaib, N.A., 2009. Building the terrestrial planets: Constrained accretion in the inner Solar System. Icarus 203, 644–662.

Reynolds, J., Hohenberg, C., Lewis, R., Davis, P., Kaiser, W., 1970. Isotopic analysis of rare gases from stepwise heating of lunar fines and rocks. Science 167, 545–548.

Reynolds, J., Turner, G., 1964. Rare gases in the chondrite Renazzo. J. Geophys. Res. 69, 3263–3281.

Rolfs, C.E., Rodney, W.S., 1988. Cauldrons in the cosmos: Nuclear astrophysics. University of Chicago press.

Roubinet, C., Moreira, M.A., 2018. Atmospheric noble gases in Mid-Ocean Ridge Basalts: identification of atmospheric contamination processes. Geochim. Cosmochim. Acta 222, 253–268.

Ruzié, L., Moreira, M., 2010. Magma degassing process during Plinian eruptions. J. Volcanol. Geotherm. Res. 192, 142–150.

Saltykov, S., 1967. Stereology: proceedings of the second international congress for stereology, chapter The determination of the size distribution of particles in an opaque material from a measurement of the size distribution of their sections.

Sarda, P., Graham, D., 1990. Mid-ocean ridge popping rocks: implications for degassing at ridge crests. Earth Planet. Sci. Lett. 97, 268–289.

Sarda, P., Moreira, M., 2002. Vesiculation and vesicle loss in mid-ocean ridge basalt glasses: He, Ne, Ar elemental fractionation and pressure influence. Geochim. Cosmochim. Acta 66, 1449–1458.

Sarda, P., Moreira, M., Staudacher, T., Schilling, J., Allègre, C.J., 2000. Rare gas systematics on the southernmost Mid-Atlantic Ridge: Constraints on the lower mantle and the Dupal source. J. Geophys. Res. Solid Earth 105, 5973–5996.

Sarda, P., Staudacher, T., Allègre, C.J., 1988. Neon isotopes in submarine basalts. Earth Planet. Sci. Lett. 91, 73–88. https://doi.org/10.1016/0012-821X(88)90152-5

Sasaki, S., 1999. Presence of a primary solar-type atmosphere around the earth: evidence of dissolved noble gas. Planet. Space Sci. 47, 1423–1431.

Sasaki, S., Nakazawa, K., 1990. Did a primary solar-type atmosphere exist around the proto-earth? Icarus 85, 21–42. https://doi.org/10.1016/0019-1035(90)90101-E

Scarpa, R., Tilling, R.I., Giggenbach, W., 1996. Chemical composition of volcanic gases. Monit. Mitig. Volcano Hazards 221–256.

Schlosser, P., Winckler, G., 2002. Noble gases in ocean waters and sediments. Rev. Mineral. Geochem. 47, 701–730.

Shinohara, H., Aiuppa, A., Giudice, G., Gurrieri, S., Liuzzo, M., 2008. Variation of H2O/CO2 and CO2/SO2 ratios of volcanic gases discharged by continuous degassing of Mount Etna volcano, Italy. J. Geophys. Res. Solid Earth 113.

Shishkina, T.A., Botcharnikov, R.E., Holtz, F., Almeev, R.R., Jazwa, A.M., Jakubiak, A.A., 2014. Compositional and pressure effects on the solubility of H2O and CO2 in mafic melts. Chem. Geol. 388, 112–129.

Sparks, R.S.J., 1978. The dynamics of bubble formation and growth in magmas: a review and analysis. J. Volcanol. Geotherm. Res. 3, 1–37.

Staudacher, T., Allègre, C.J., 1988. Recycling of oceanic crust and sediments: the noble gas subduction barrier. Earth Planet. Sci. Lett. 89, 173–183.

Staudacher, T., Sarda, P., Richardson, S., Allègre, C., Sagna, I., Dmitriev, L., 1989. Noble gases in basalt glasses from a Mid-Atlantic Ridge topographic high at 14 N: geodynamic consequences. Earth Planet. Sci. Lett. 96, 119–133.

Stolper, E., 1982. Water in silicate glasses: an infrared spectroscopic study. Contrib. Mineral. Petrol. 81, 1–17.

Stout, V.L., Gibbons, M.D., 1955. Gettering of gas by titanium. J. Appl. Phys. 26, 1488–1492.

Sumino, H., Kaneoka, I., Matsufuji, K., Sobolev, A.V., 2006. Deep mantle origin of kimberlite magmas revealed by neon isotopes. Geophys. Res. Lett. 33.

Tolstikhin, I., O'Nions, R., 1994. The Earth's missing xenon: A combination of early degassing and of rare gas loss from the atmosphere. Chem. Geol. 115, 1–6.

Trieloff, M., Kunz, J., Clague, D.A., Harrison, D., Allègre, C.J., 2000. The Nature of Pristine Noble Gases in Mantle Plumes. Science 288, 1036–1038. https://doi.org/10.1126/science.288.5468.1036

Warren, P.H., 1995. Extrapolated partial molar densities of SO3, P2O5, and other oxides in silicate melts. Am. Mineral. 80, 1085–1088.

Watson, E.B., Sneeringer, M.A., Ross, A., 1982. Diffusion of dissolved carbonate in magmas: experimental results and applications. Earth Planet. Sci. Lett. 61, 346–358.
Wetherill, G.W., 1954a. Variations in the isotopic abundances of neon and argon extracted from radioactive minerals. Phys. Rev. 96, 679.
Wetherill, G.W., 1954b. Variations in the isotopic abundances of neon and argon extracted from radioactive minerals. Phys. Rev. 96, 679.
Wetherill, G.W., 1953a. Spontaneous fission yields from uranium and thorium. Phys. Rev. 92, 907.
Wetherill, G.W., 1953b. Spontaneous fission yields from uranium and thorium. Phys. Rev. 92, 907.
Wieler, R., 2002. Cosmic-ray-produced noble gases in meteorites. Rev. Mineral. Geochem. 47, 125–170.
Wieler, R., 1998. The solar noble gas record in lunar samples and meteorites. Space Sci. Rev. 85, 303–314.
Williams, C.D., Mukhopadhyay, S., 2019. Capture of nebular gases during Earth's accretion is preserved in deep-mantle neon. Nature 565, 78–81. https://doi.org/10.1038/s41586-018-0771-1
Yatsevich, I., Honda, M., 1997a. Production of nucleogenic neon in the Earth from natural radioactive decay. J. Geophys. Res. Solid Earth 102, 10291–10298.
Yatsevich, I., Honda, M., 1997b. Production of nucleogenic neon in the Earth from natural radioactive decay. J. Geophys. Res. Solid Earth 102, 10291–10298.
Yokochi, R., Marty, B., 2004. A determination of the neon isotopic composition of the deep mantle. Earth Planet. Sci. Lett. 225, 77–88. https://doi.org/10.1016/j.epsl.2004.06.010
Yoshimura, S., 2015. Diffusive fractionation of H2O and CO2 during magma degassing. Chem. Geol. 411, 172–181.
Zadnik, M., Jeffery, P., 1985. Radiogenic neon in an Archaean anorthosite. Chem. Geol. Isot. Geosci. Sect. 52, 119–125.
Zhang, Y., Ni, H., Chen, Y., 2010. Diffusion data in silicate melts. Rev. Mineral. Geochem. 72, 311–408.
Zhang, Y., Xu, Z., 1995. Atomic radii of noble gas elements in condensed phases. Am. Mineral. 80, 670–675.
Zhang, Y., Xu, Z., Zhu, M., Wang, H., 2007. Silicate melt properties and volcanic eruptions. Rev. Geophys. 45.
Zhang, Y., Zindler, A., 1989. Noble gas constraints on the evolution of the Earth's atmosphere. J. Geophys. Res. Solid Earth 94, 13719–13737.

https://www.esa.int/About_Us/ESAC/The_colour_sphere_of_the_Sun

Chapitre 2 : Méthodes expérimentales et analytiques

Ce chapitre décrit en détail la méthodologie de développement d'expériences visant à étudier le comportement du néon et de ses isotopes dans les matériaux basaltiques sous certaines conditions de pression et de température. Il présente la composition du matériau de départ ainsi que la méthodologie utilisée pour enrichir ce matériau en néon à partir d'un verre basaltique sec afin de créer une matière fondue riche en CO_2 et des bulles de CO_2 pur.

Trois types d'expériences composent cette thèse :

- *Expériences statiques sur des verres basaltiques riches en CO_2 : utilisées pour étudier la composition d'un magma appauvri en CO_2 traversé par un flux riche en CO_2. Ces expériences visent à examiner la nucléation, la croissance et la coalescence des bulles dans des conditions isothermes et isobariques.*

- *Expériences statiques sur des verres basaltiques riches en CO_2 et en néon : destinées à étudier la composition isotopique du néon lorsqu'un flux de CO_2 traverse une masse fondue appauvrie en volatils.*

- *Expériences de décompression : où un magma contenant du CO_2 et du néon dissous de manière homogène commence à se décompresser en générant des bulles. Cela permettra d'étudier le fractionnement possible du néon pendant la décompression de la chambre magmatique jusqu'à quelques instants avant l'éruption.*

Les autoclaves seront utilisés comme instrument principal pour les expériences. Celles-ci consisteront en une capsule en $Au_{80}Pd_{20}$ de poudre de silicate sec, de verre enrichi en néon selon la méthode de Jambon et al. (1986), et d'oxalate d'argent comme support pour le CO_2, ce qui donnera lieu à la phase volatilisée.

Les échantillons feront l'objet de deux types d'analyses :

1. Analyse texturale : à l'aide de la tomographie à rayons X pour caractériser la distribution et la taille des bulles dans les échantillons, ainsi que pour encadrer les bulles qui seront analysées ultérieurement par ablation laser couplée à la spectrométrie de masse sous ultravide.

2. Analyse chimique : en utilisant (i) la microsonde électronique pour connaître la composition des éléments majeurs dans chacun des verres expérimentaux ; (ii) le FTIR pour déterminer la distribution et la teneur en CO_2 dissous dans le verre expérimental et la présence éventuelle d'eau ; (iii) la microscopie électronique à balayage pour caractériser certains des petits cristaux formés pendant les expériences, inaccessibles à l'analyse par microsonde ; (iv) les spectromètres de masse pour l'analyse l'abondance et la composition isotopique du néon dans les bulles des échantillons expérimentaux.

De plus, ce chapitre décrit brièvement les différents logiciels utilisés pour le traitement des images et des données obtenues par les techniques analytiques.

Chapter 2: Experimental and analytical methods

2.1 Starting material:

The initial material comprises basanitic scoria from the northeastern vent of Fasnia volcano, which erupted in January 1975 in Tenerife, Spain. The chemical composition of the glass is shown in **Table 2.1**. The synthetic glass used for all our experiments was developed from the same natural sample. The electron microprobe (EMPA) at the Institute of Earth Sciences, University of Orleans, France, was used to analyse the major element compositions and homogeneity of the resulting anhydrous glass.

To obtain the initial basaltic liquid before the decompression of the magmatic chamber starts, the natural sample was first crushed and powdered by using an agate mortar and acetone to prevent rubbing. Then, the powdered sample was melted at 1400°C and 1 bar for 4 hours in a platinum crucible and rapidly quenched in a water container at room temperature. The full process was repeated to ensure a homogeneous, anhydrous, and free of bubbles/crystals glass.

	Basanite FAS[a]	**sd**	**Starting mat.**	**sd**	**Neon-bearing glass**	**sd**
SiO_2	45.08	0.14	44.86	0.23	45.47	0.15
TiO_2	3.82	0.13	3.70	0.18	3.78	0.14
Al_2O_3	14.45	0.17	14.87	0.17	14.94	0.17
FeO[b]	12.51	0.27	12.39	0.24	11.49	0.43
MnO	0.28	0.05	0.17	0.07	0.11	0.06
MgO	7.15	0.22	7.80	0.05	7.80	0.11
CaO	10.82	0.17	10.38	0.10	10.43	0.16
Na_2O	3.6	0.1	3.63	0.07	3.77	0.08
K_2O	1.57	0.07	1.47	0.15	1.49	0.04
P_2O_5	0.71	0.07	0.73	0.09	0.71	0.05
$Na_2O + K_2O$	5.17		5.10		5.26	
Total	100		100		100	

Table 2.1.: Composition normalized to 100% from the whole rock, starting glass and Ne-bearing glass:
[a] Anhydrous melt (from Jiménez-Mejías *et al.,* 2021).
[b] All Fe is reported as FeO.
Oxide concentrations (wt.%) measured by EMPA at ISTO-France.

2.2 Ne-bearing glass:

After preparing the dry glass, it was powdered again to be used in the experiments conducted during the thesis and for the Ne-bearing glass. Two methods were used for the former, but although both were successful in enriching the neon in the glass, only one had the appropriate properties for the task we wanted to conduct: a glass free of bubbles with neon dissolved in it.

The first method involved an experiment using the Internally Heated Pressure Vessel (IHPV), which will be further described in section 2.4 of this chapter. To conduct the experiment, 60 mg of powdered dry glass was loaded into a platinum capsule that was half-welded, allowing air to circulate inside. The IHPV was then prepared for the experiment. The typical gases used to pressurize the autoclave include N_2, Ar, or H_2. The vessel was loaded with 1 bar of neon followed by 600 bars of nitrogen for the experiment. H_2 was not used to prevent the production of water resulting from the reduction of Fe_2O_3 present in the starting glass into FeO or the presence of small vesicles before the main experiments. Instead, the experiments were pressurised with nitrogen, as argon was avoided due to the capsule being placed in the vessel without welding. This means that the glass would be exposed to high pressures of argon, which would mask the signal of neon, making the analysis of neon impossible. How argon influences neon for the results will be described later in points *2.2.1.2*. and *2.8.6.1* of this chapter.

After one and a half hours, the experiment was stopped. The capsule was removed, and the top end was welded to create a closed system, preventing any exchange with air during the next experimental step. Following the welding, the capsule underwent a new experiment to ensure the homogeneity of the glass. The experimental conditions were set at 1200°C and 1700 bar for six hours in the IHPV.

The doping of the glass in neon was a success but the glass was full of vesicles making it useless for our purpose since the distribution of Ne is partitioned between the gas and the melt phase. An image of the resulting glass can be observed in *Figure 2.1*.

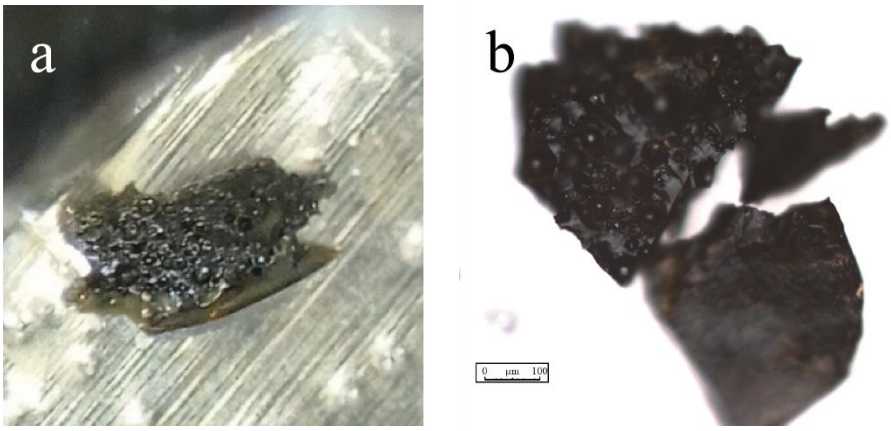

Figure 2.1. Chunk of the experimental sample 1Eb observed at the binocular lens (a) and microscope (b). A big portion of the sample was full of micrometric vesicles. The use of this glass would therefore provide a fractionation prior to the actual experiment and would therefore be useless.

However, despite the good results of the analysis of this sample obtained in the mass filter (tests 4-S4, -S6, -S7, and -S8), some of the chunks analysed (e.g., T4-S8) showed too high values, outside of the normal range, for the $^{20}Ne/^{22}Ne = 27.73$, indicating a non-homogeneous distribution of Ne in the glass due to the random ubiquity of microscopic bubbles. Therefore, the second method, as described below, was more accurate.

The second method and the one used for all subsequent experiments, was made following the same technique of Jambon et al., (1986).

First, the anhydrous basanitic starting powder was equilibrated in a temperature-regulated electric furnace at 1400 ^{O}C, under a constant flux of neon at 1 bar of pressure for 270 min. The furnace is equipped with a ceramic tube where the crucible is held (**Figure 2.2**.). As a neon source, we used a *"pure gases rare bottle (Ne-n50)*" provided by Air-liquid, whose properties are pressure at 15 ºC = 200 bar, charge = 9 M^3, He < 3 ppm, CO_2 < 500 ppb, CnHm < 500 ppb, O2 < 500 ppb, and N_2 < 500 ppb.

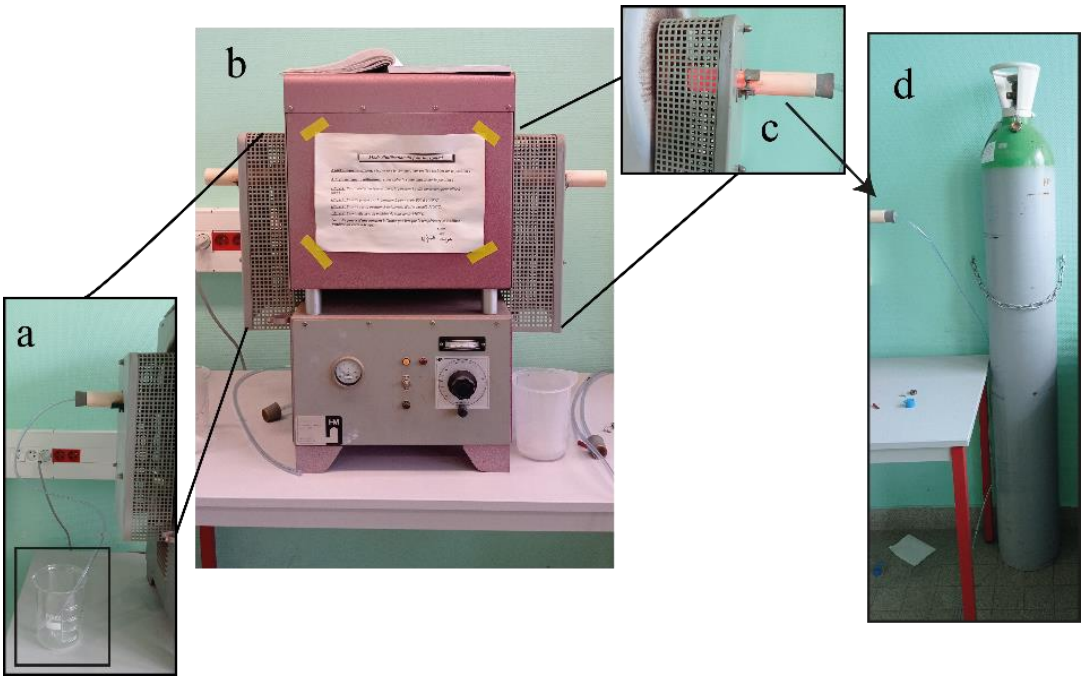

Figure 2.2. Temperature-regulated electric furnace. The flux of Ne is entering directly from the bottle (d) at pressure regulated at 1 bar to the furnace (b) by a cable connected to the ceramic tube (c). The exit of the gas is at the other extreme of the furnace (a) where another cable is ending in a baker with water to control that the flux of neon is still going on during the experiment.

The experiment consisted of a charge of 0.3236g of the powdered silicate loaded in a platinum crucible. According to the solubility laws and the experiments described by Jambon et al., (1986) a continuous flux of neon passing through 1cm^3 of silicate melt at 1300 ºC should reach the equilibrium after 278 hours. Subsequently, since the solubility of Ne at 1300°C is 2.5x10^{-4} cm^3 · g^{-1} · bar^{-1} and the concentration of Ne at 1 bar of partial pressure in equilibrium should be 2.5·10^{-4} cm^3 STP g^{-1} in line with Henry's law:

$$C_i = K_i * P_i$$

where C_i is the concentration of Ne, K_i is the solubility constant (in units of cm^3 STP·g^{-1}·bar^{-1}) of Ne and P_i is the partial pressure; we decide to prepare a crucible with a layer of 1-2 mm of the powdered starting material. The use of powder facilitates the Ne dispersion through the grain interstices before melting, and its diffusion within the small glass fragments (<100 microns), resulting in faster equilibrium (Lux, 1987). That way we could reduce the experiment time to 270 min. Then, the melt was quenched following the same procedure as we followed with the starting material. For comparison, an image of the starting material (dry glass) and the Ne-bearing glass after quenched are shown in

Figure 2.3. Furthermore, the composition of the Ne-bearing glass is also shown in **Table 2.1.**

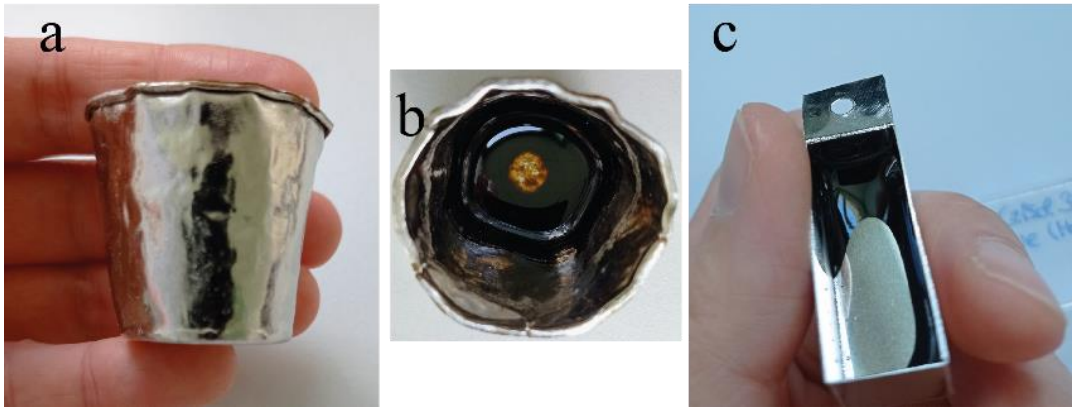

Figure 2.3. The images *a* and *b* show the crucible after quenching the starting material for dry glass, while the image *c* shows the crucible for Ne-bearing glass after quenching. Both crucibles are made of platinum in order to resist high temperatures.

2.2.1 QMS700 quadrupole type mass spectrometer:

Due to the much larger abundance of Ne in experimental glasses compared to its abundance in natural silicate melts, the use of high sensitivities mass spectrometer (with magnetic sectors as Noblesse or Helix type) is not recommended since we could oversaturate the detector. Instead, a mass filter was used, also called quadrupole mass analyser, for checking the homogeneity distribution of neon in the Ne-bearing glass that we will use for our experiments.

The QMS700 quadrupole-type mass spectrometer hosted at the *Institut de Sciences de la Terre d'Orléans* is designed to measure four noble gases (helium, neon, argon, and krypton). This type of mass filter separates ions based on the stability of their flight trajectory through an oscillating electric field in the quadrupole. It is composed of four cylindrical rods, set parallels to each other. A general scheme is shown in *Figure 2.4.* The electric field is generated when a radio frequency voltage is applied between one pair of opposing rods within the quadrupole. When the ions pass through the mass filter, they follow a trajectory that will depend on the applied voltage, and only the ions with the selected mass-to-charge ratio and stable trajectory will reach the detector.

Depending on the mass-to-charge ratio, the ions can be measured in two types of detectors: (i) a Faraday cup, doing a direct measurement of the ion current using an electrometer amplifier, or (ii) a Secondary Electron Multiplier, SEM. The Faraday cup will measure positive ions and the SEM will be used when a high sensitivity is required, multiplying incident charges to obtain at the end a shower of electrons that will be collected by the ion counter.

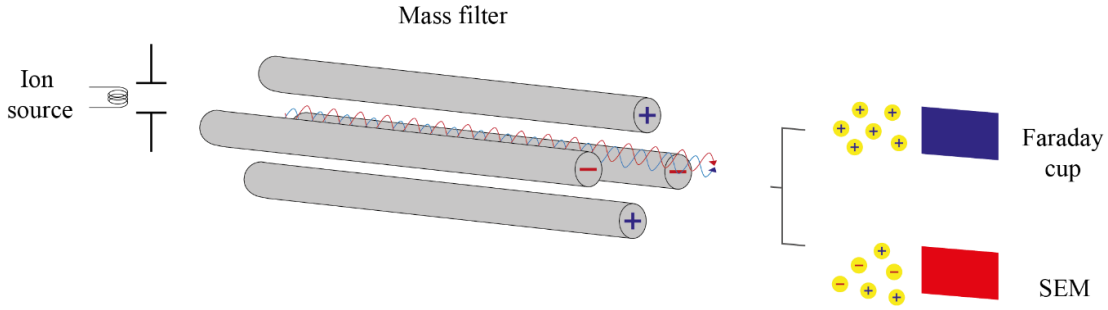

Figure 2.4. The voltage applied with the ion source will generate a current that will pass through the pair of opposing rods generating a magnetic field that will separate the ions and electrons based on the voltage. The specific collectors will then give us the signal we are testing.

2.2.1.1 Preparing the analysis:

Several chunks of about 0.1 mg of the Ne-enriched glass from several experiments were analysed at the QMS700. The chunks were carefully selected taking pieces from the top, middle, and bottom of the crucible/capsule (depending on the experiment) to ensure that the homogeneity is in the whole volume.

The sample holder where the chunks of glass were charged was baked at 100 ºC and pumped for at least one day to desorb all the noble gases of the glass after quenching, avoiding contamination from air. Once the analytical blank was low enough to start the analysis, a laser-type Ytterbium-doped fibre was used to melt the glass and release the volatiles dissolved. Each chunk analysed was shot with the laser for at least one minute and, when the laser stops, the liquid is immediately quenched to glass. An example of the resultant quenched glass is shown in **Figure 2.5**.

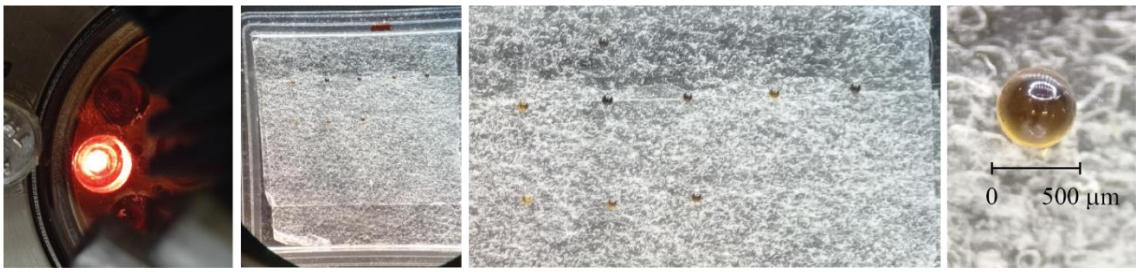

Figure 2.5. The first image in the left shows the chunk of glass while is being heated with the laser beyond the glass transition temperature. From left to right we zoom in the resultant glass after quenching and analysed with the laser and the QMS700.

2.2.1.2 Purification and analysis:

After the gas extraction, the gas is sent to the purification line by opening a manual valve. That is the only manual valve, the remaining of purification line system being controlled with automated valves via Python for every step of the gas expansion and line purification. A scheme of the purification line is shown in **Figure 2.6**.

The first gas purification stage consists of a SAES getter, a chemical trap that can sorb active gases such as H_2O, CO_2, CO, and H_2, by chemical reaction under vacuum. The SAES getter purifies the noble gases from other major gas components during 5 min at 400ºC. Then it is turned off in order to trap hydrogen at room temperature.

After the purification, heavy noble gases (Ar, Kr, and Xe) are captured by cryogenic adsorption using activated charcoal at liquid nitrogen temperature for 15 min. Finally, we obtain the gas ready to be released and measured for the mass filter.

As we explain in *Chapter 1*, this work will be focused only on neon isotopes and their possible physical fractionation during vesiculation. Moreover, our synthetic glasses will be only loaded with neon and not in other noble gases. The measurement of this noble gas is perhaps one of the most complicated in terms of the analysis due to the isobaric interference between ^{22}Ne and CO_2^{++} and ^{20}Ne and $^{40}Ar^{++}$, that is why, during the analysis, we measure masses 20, 21, 22, 40 and 44 in every cycle to correct later the interference in the signal.

The neon is introduced into the mass filter for 1 minute to allow equilibrium before the analytical cycles. Between twenty and twenty-five cycles of measurements were done for each chip of glass in the SEM configuration of the quadrupole.

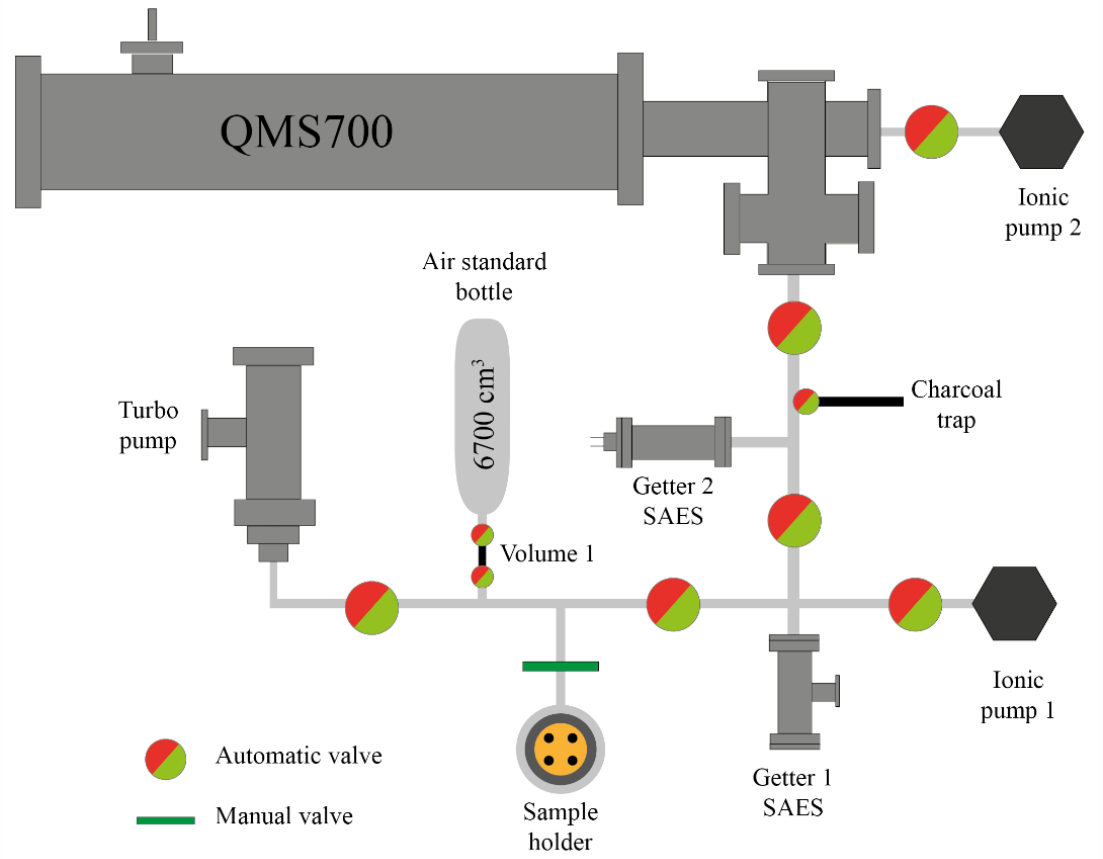

Figure 2.6. Representative scheme (not to scale) of the extraction and under-vacuum purification line. The expansion of the gas through the line is controlled electronically by a *python* configuration. Up to nine valves impede or allow passage of the gas while the large molecules and heavy noble gases are being trapped in the chemical traps. Two of them allow the cleaning of the line after the analysis by pumping the gas with an ionic and one turbo pups. The small volume located between the air standard bottle and the line has a volume of $V_1 = 2.47$ cm^3.

2.2.2. Analytical blank:

The analytical blank is an important parameter to measure to validate the results of the gas analysed since it checks if the molecules adhered to the line walls. The protocol to follow is the same as for the sample analysis, but without melting the sample, purifying the leftover gas that can be adsorbed to the line after pumping it. Moreover, we never start a sample or standard analysis after changing the sample until the blank is low enough to allow a precise measurement. The analytical blank is also measured using between 20 and 25 cycles.

Regarding the protocol, we want to highlight the importance to strictly follow the same equilibrium time and trapping time in every step, in order to have the most accurate results and corrections for analytical blanks, standards, and sample analysis.

2.2.3. Standard:

The standard analysis is essential to calibrate the sensitivity and mass discrimination of the mass filter. For neon analysis the sensitivity, *S,* of the mass spectrometer lies in the SEM, which is described as the ratio of the gas input into the mass filter (cm^3) and the gas measured (cps). The mass discrimination during the measurement can be expressed as the ratio between the real, *R*, and the measured, *r,* value of a given isotopic ratio *i/j*:

$$k_{(i/j)} = \frac{R_{i/j}}{r_{i/j}}$$

As we were not interested in knowing exactly the discriminated value of the isotopic ratio but the homogeneity of neon in our glass, we just ran some standards for the first tests.

The standard used comes from the dilution of a small volume of "one pipette" (V_1 = 2.47 cm^3) of air at 1bar pressure into an empty stainless-steel bottle V_B = 6700 cm^3 at ultra-high vacuum. Every run standard corresponds to *n* number of *pipettes,* and the neon concentration is calculated as:

$$X_{Ne} = \frac{V_1}{V_B} \cdot V_1 \cdot 18.18 \cdot n\ ppm$$

Where V_1/V_B correspond to the diluted air in the bottle. Then in each pipette the concentration of Ne will be $X_{Ne} = 1.66 \cdot 10^{-2}$ ppm. The volume of the standards analysed is here specified as the number of pipettes taken.

The results obtained from the analytical blank, standard, and glass are exported to an Excel file for the manual treatment. The mass filter in every cycle is calibrated to scan the signal from mass 19 to 22.98 [amu], 39 to 40.98 [amu], and 43 to 44.98 [amu], that way we can better localize where the wished mass is. After choosing the point we take

the resultant value in that point for every cycle. An example of the analytical blank and one of the tests of the glass scanned is shown in **Figure 2.7.**

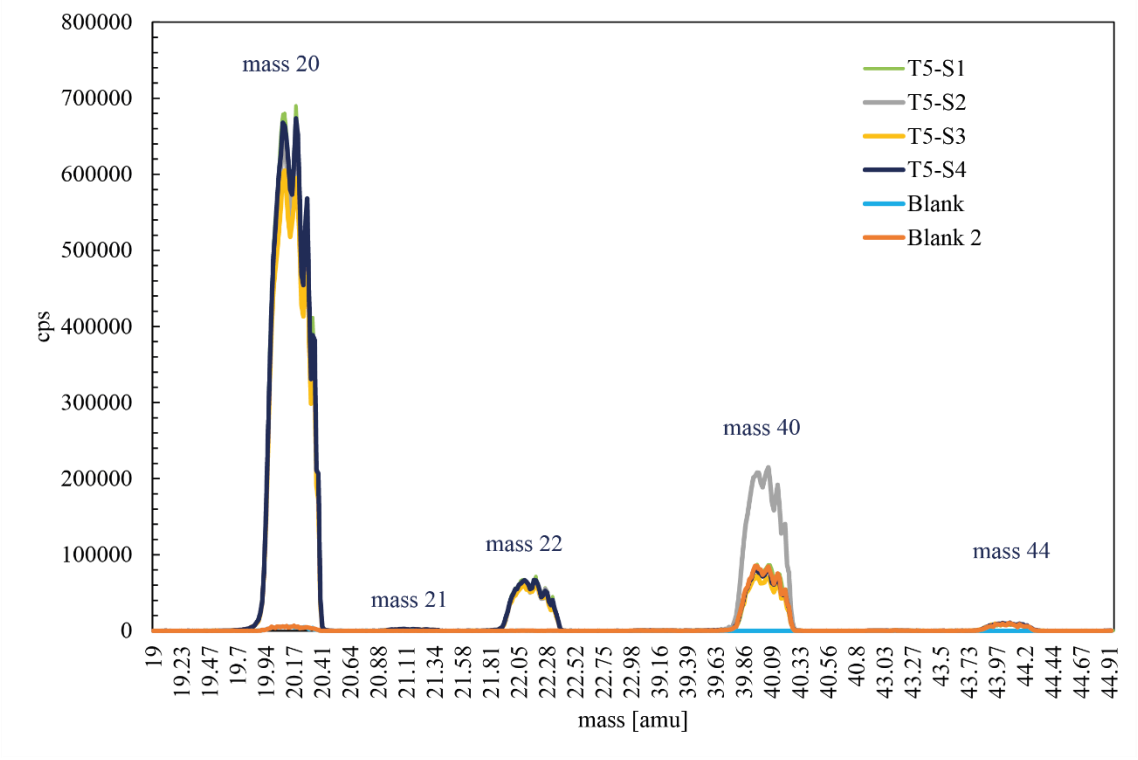

Figure 2.7. Mass scan run at the QMS700. Only one cycle of each test is shown as an example. For the blanks, at the same scale than the glass analyses, only the peaks of ^{20}Ne, ^{40}Ar and CO_2 are visible since ^{20}Ne is the most abundant isotope and Ar and CO_2 are never completely trapped by the chemical traps. The chemical traps can trap about 99% of the gas but a small fraction still remains and passes to the mass filter. In the case of the glass scan, the three peaks of neon isotopes are clear, as well as masses 40 and 44. This scan allow us to select the points to analyse. Before any treatment the scan illustrates a clear homogeneity for Ne isotopes.

Ne isotope abundances and isotopic ratios were corrected from CO_2^{++} and $^{40}Ar^{++}$ interferences as:

$$^{20}Ne = m_{20} - 0.075 \cdot m_{40} \rightarrow {}^{40}Ar^{++}$$

$$^{22}Ne = m_{22} - 0.0075 \cdot m_{44} \rightarrow CO_2^{++}$$

Where m_{20}, m_{22}, m_{40}, *and* m_{44} correspond with mass 20, 22, 40 and 44 since CO_2^{++} and $^{40}Ar^{++}$ represents around 10% and 1% of ^{20}Ne and ^{22}Ne signal respectively.

Figure 2.8. belongs to one chunk of glass of 0.116 mg (Test5-S4) shot with the laser for 1 minute 20 seconds. It shows an example of the result before and after interference correction for the 25 cycles.

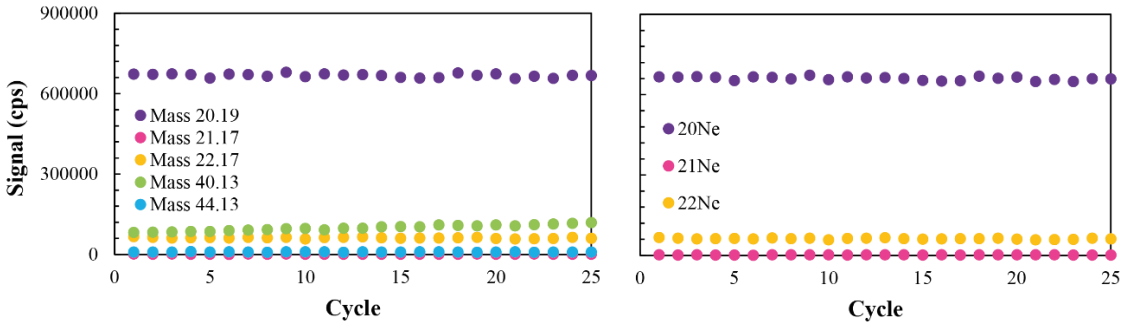

Figure 2.8. Twenty-five cycles run for T5-S4 before (a) and after (b) interference correction. Each colour represents the value obtained by scanning for the point selected from the scan in **Figure 2.7**. The exact point chosen for the scan is shown in the legend. As we can observe, the difference between both is not that high. The abundance of ^{21}Ne is small compared with the other isotopes which is coherent since it represents <0.3%. The signal for every mass is given in *cps* for the 25 cycles.

After CO_2^{++} and $^{40}Ar^{++}$ interferences correction, we average the result of each mass and calculate the one sigma error, as the standard deviation of all the cycles divided between the root square of the number of cycles and the $^{20}Ne/^{22}Ne$ and $^{21}Ne/^{22}Ne$ ratios. *Figure* 2.9. corresponds to a chunk of glass of 0.102 mg (*T4-S5*) shot for 1 minute after CO_2^{++} and $^{40}Ar^{++}$ correction. The mean and the one-sigma error for every isotope and ratio are shown in red.

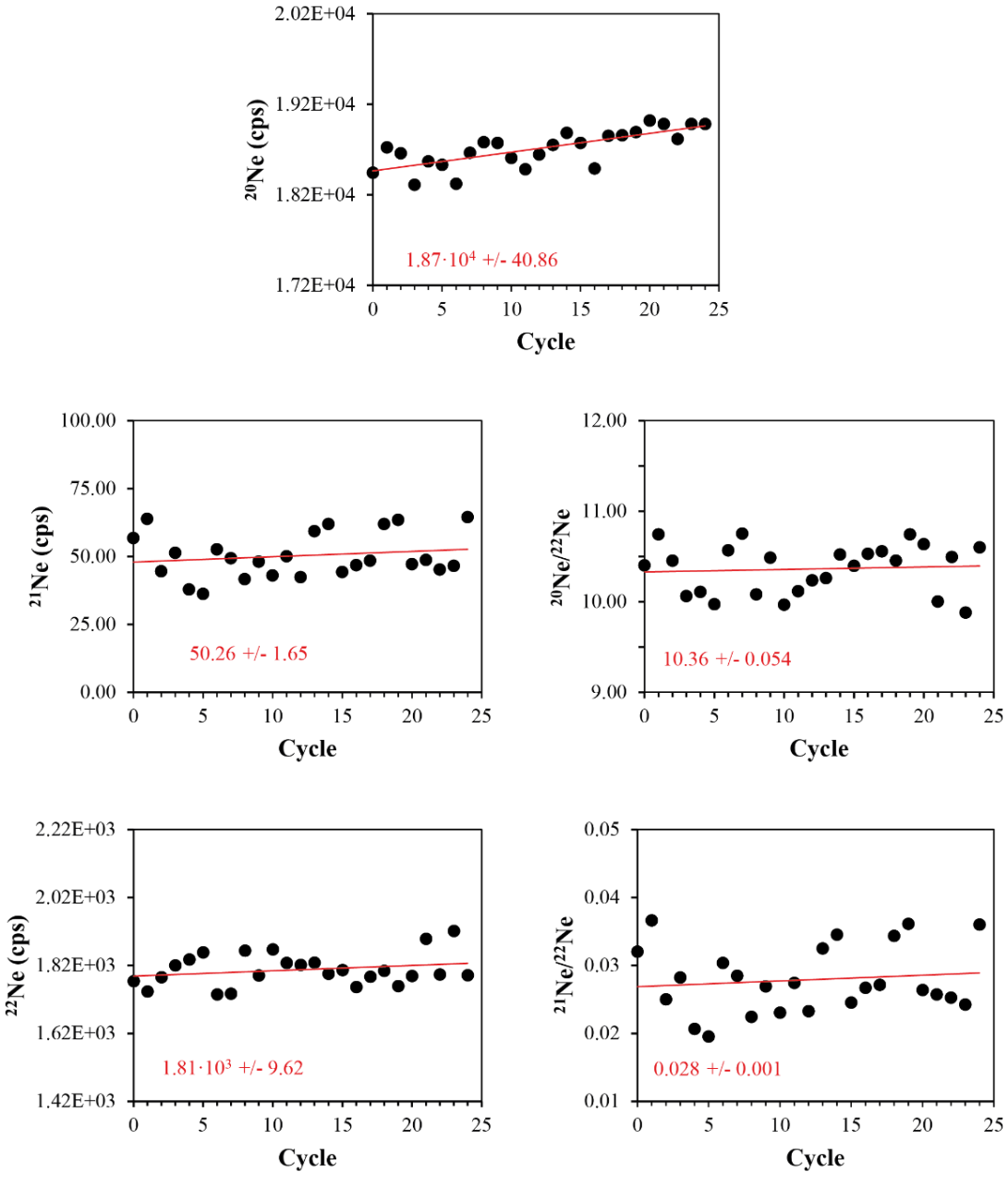

Figure 2.9. Example of data plotted as signal against cycle for T4-S5. The isotopic ratios and the signal for every isotope follow a linear trend with a sigma lower than 1%. The data are shown prior to the sensitivity and mass discrimination calculations.

2.3. Experimental capsules preparation:

The selection of the experimental container is particularly important. The alloy or metallic composition of the capsule plays a significant role in limiting chemical interactions with the synthetic glass composition. It must also limit the transfer of hydrogen molecules through the capsule as much as possible, minimize iron loss during

the experiments, and resist temperatures higher than 1200 °C. The capsule material fulfilling these conditions is an alloy made of Au_{80} Pd_{20} (Di Carlo et al., 2006; Pichavant et al., 2009).

The capsules are set up from a $Au_{80}Pd_{20}$ tube of 2.9 mm outer diameter, and 0.4 mm wall thickness. We cut the tube into 1.5 cm long capsules which were cleaned in a boiling solution of distilled water and hydrochloric acid 30% for at least 10 minutes, rinsing the capsules and repeating the process with distilled water only. Then, we dry and anneal them with a torch up to red colour for a few seconds.

The first step to making the capsule a closed system is welding the base by arc welding. About 60 mg of starting material was used for each capsule. As the CO_2 source, we used silver oxalate ($Ag_2C_2O_4$) which breaks down into Ag and CO_2 at about 200-300°C. As source of neon, we added the Ne-bearing glass described previously.

To calculate the quantity of the volatile species to be added in each capsule, for all the experiments only CO_2, the molar fraction of the CO_2 was calculated first. Since we introduce this species from silver oxalate:

$$wt.(\%)_i = \frac{m_i * n° \, atoms * 100}{m_{sol}}$$

Where the molecular mass of $Ag_2C_2O_4$ = 303.7554 g/mol, then:

$$Ag = \frac{107.8682 \frac{g}{mol} * 2}{303.7554 \frac{g}{mol}} * 100 = 71.02\%$$

$$C = \frac{12.0107 \frac{g}{mol} * 2}{303.7554 \frac{g}{mol}} * 100 = 7.91\%$$

$$O = \frac{15.9994 \frac{g}{mol} * 4}{303.7554 \frac{g}{mol}} * 100 = 21.07\%$$

Then, the 28.98 wt.% of $Ag_2C_2O_4$ added to the experiment correspond to CO_2.

For the Ne experiments, we took a small amount of Ne-bearing glass and added it to the capsule. How to calculate this amount will be described more in detail in *Chapter 4*.

At the end every species, *x*, introduced is reported as:

$$wt.\%_x = \frac{m_x}{m_{tot}} * 100$$

Finally, the capsules were arc-welded at the top to avoid the loss of volatiles during the experiment in the IHPV. Capsules were weight measured before and after arc welding and after IHPV experiments to guarantee that no volatile loss had occurred. A scheme of the experimental capsule is shown in **Figure 2.10**.

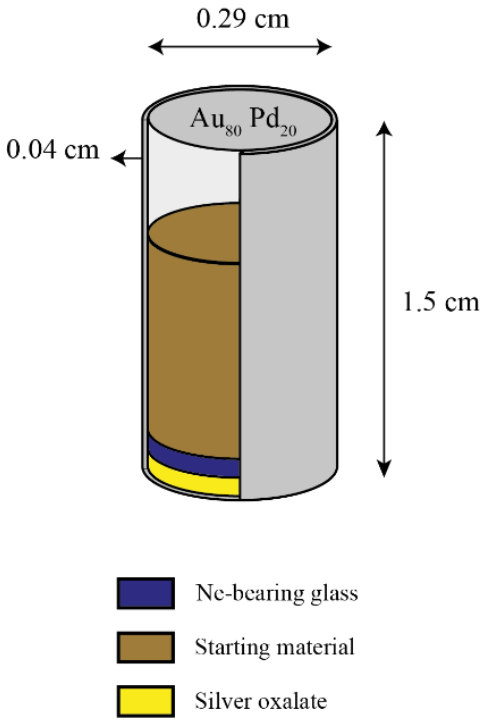

Figure 2.10. Representative scheme of the experimental capsule. The volatiles species are first introduced in the capsule for a better calculation of weight percentage and for avoiding the loss by evaporation while closing the capsule while welding. Here we present the capsule for the Ne-bearing glass experiments. The procedure is the same when the source of neon is not added.

There is a difference between the static experiments and the decompressed ones regarding the amount of CO_2. In the static experiments, the main goal was to oversaturate the system in CO_2 and create a highly vesiculated sample. For the decompression experiments, oversaturation of the sample during the decompression process could lead to an explosion within the capsule, resulting in the failure of the experiment. These experiments adhered to the solubility law and followed the methods used by Jiménez-Mejías et al. (2021). In their study, which had the same sample composition as the present experiments and was conducted at 1200 ºC and 2 kbar, the dissolved CO2 measured was 2713 ± 138 ppm.

It is important to note that no water was intentionally added to the capsules. However, after the experiments, some of the synthesized samples were found to contain a small amount of water dissolved in the glass (<1%). There are two possible explanations for this: (i) As explained in point 2.2, one of the gases used to pressurise the IHPV is hydrogen. Even if only argon is used in the experiments, hydrogen molecules from other experiments conducted prior to my experimental study may remain attached to the autoclave, diffuse through the capsule walls, and then react with the iron content of our basaltic powder as follows:

$$Fe_2O_3 + H_2 \underset{\leftarrow}{\rightarrow} FeO + H_2O$$

(ii) The second option for the presence of water could be due to silver oxalate, which in contact with air during sample preparation, can absorb a small but finite amount of H_2O.

2.4. Internally Heated and Pressured Vessel. Experiments to recreate the magmatic chamber conditions:

2.4.1. Static experiments:

For this thesis subject, a total of 24 experiments (for both statics and decompression experiments), have been conducted using Internally Heated and Pressured Vessels at the Institute of Earth Sciences of Orleans.

The previously set up capsules are placed inside of the autoclave which can recreate the *P-T* conditions similar to that of the nature. The IHPV is equipped with a system of rapid quench which prevents back reactions during cooling of the sample at the end of the experiment, freezing that moment in the experimental glass.

For the experiment's setup, up to four capsules are placed in a small ceramic bucket. The buck is hung by a platinum wire wrapped around two PtRh fine rods, see **Figure 2.11**. The temperature in the IHPV is controlled by the two thermocouples, where the gradient between the upper and the lower thermocouple is <10 ºC.

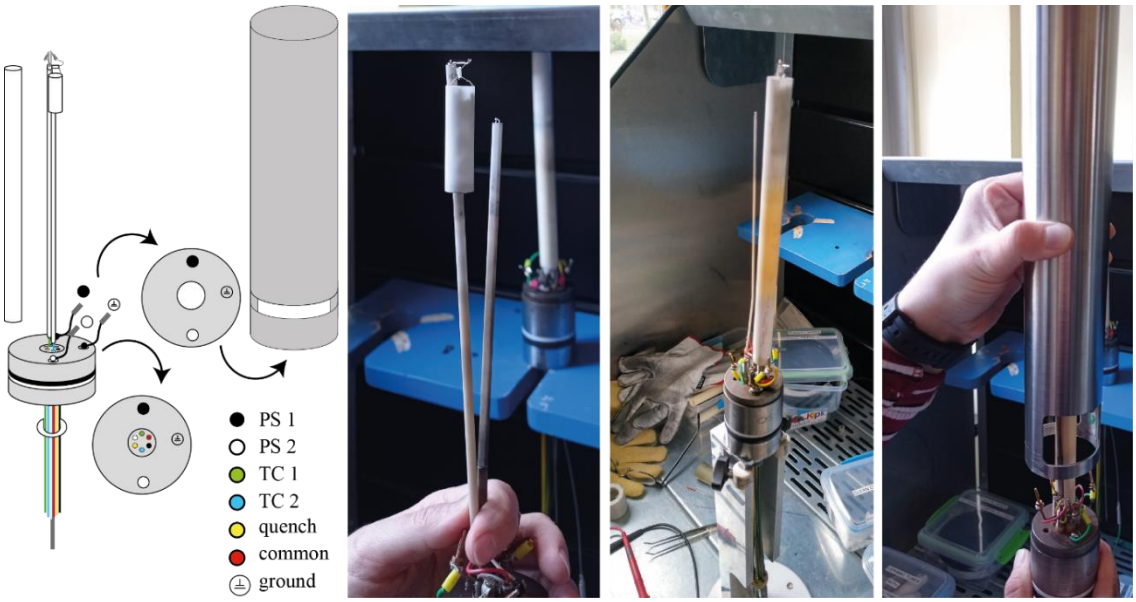

Figure 2.11. Schematic representation and real image of the closure nut and furnace that go inside the autoclave. The sample holder is made of a ceramic bucket hanged by a platinum wire. A ceramic tube is guiding the bucket for the fall during the quench. The colours represent the connections that allow the control of the experiment. PS = Power Supply, TC = Thermocouple. The cables connect the closure nut with the furnace and with the controller (**Figure 2.12**.)

When the quench button is actionized, an electrical current passes through the wire which holds the bucket, cutting the wire and letting the bucket to drop in the bottom and cold part of the vessel, thereby producing a fast quench of the capsules. To avoid the break of the ceramic bucket during its fall, the bucket is placed inside a ceramic tube filled with quartz wool at its bottom cold end. The closure nut is connected to the furnace with three wires that supply the current.

When the closure nut and the oven are connected and ready, they are introduced inside the IHPV in a horizontal position for the assembly of the wires with the controller (**Figure 2.12**.), at which the condition of the experiment are defined. After testing the electrical connectivity, the IHPV is rotated vertical and the vessel is pressurized to ~1200 bars with argon, which allows to reach ~2000 bar when temperature is increased to reach the final set point of 1200ºC, about 20-30 min. As explained above, the use of pure Ar instead of a mixture of Ar-H_2, avoid as much as possible the reduction of Fe^{3+} of the starting glass and the formation of water.

Figure 2.12. One of the autoclaves used to run the experiments. The upper part of the autoclave (left) is connected to the capillary that pressurize the experiment. In the lower part of the same image and the lower-middle image the connection exiting from the shutter and going to the controller (upper-middle and right image). The controller shows the conditions of two different experiments, while reaching the set-up conditions and while the experiment is running. In the right image, a voltmeter is controlling the quench connection. The small screen in the right shows the temperature if the upper and lower thermocouple and the screen in the middle part shows the pressure. The screen in the left allows us to control the intensity of the thermocouple's resistances.

After setting up the pressure the temperature of the experiment is raised to 1200 ºC, which is higher than the liquidus temperature of common basalts and wait till the experiment is ended by drop quenching the capsules. The experiments showed a fast-transient increase of the pressure of about forty bars upon the falling of the capsule (P_Q), indicating a successful quench when the bucket drops down. After the quenching, the experimental capsules were weighed to check that no gas was lost during the experiment and carefully opened to keep, as much as possible, the samples in large pieces (**Figure 2.13.**).

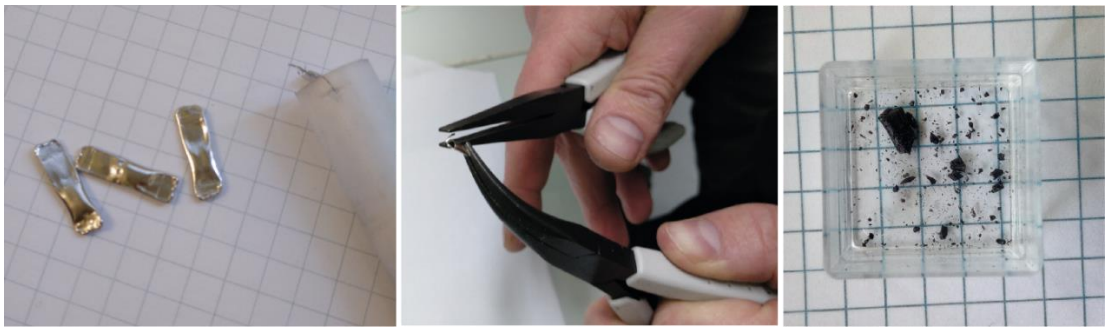

Figure 2.13. Resultant capsules after the experiment. As can be observed in the images, the preservation of the run product glass into a single piece is not easy due to the fragility of the glass (for the high vesicularity of it) and for the hardness of the capsule. The biggest pieces will be used for microtomography, and noble gases analysis. The tiniest pieces for SEM and EMPA, and the middles for FTIR.

2.4.2. Decompression experiments:

The static experiments were done to simulate the condition of the magmatic chamber when nucleation and growth of vesicles started (non-equilibrium), therefore the pressure was kept constant till the quench. In contrast, the decompression experiment aimed to simulate the rise and degassing of the magma to the surface and so, the fractionation of the neon isotopes during decompression driven degassing, if any. The last type was conducted after equilibrating the charges for at least 24 hours, prior to decompression.

To carry out the experiment, we had to follow three steps during every experience: (i) re-homogenise the synthetic glass and the volatile species – magmatic chamber -, (ii) decompression (the rise of the magma), and (iii) quench - close to the surface or at an established depth. An example of the three stages is shown with the P-T record acquired with the autoclave controller (**Figure 2.14.**).

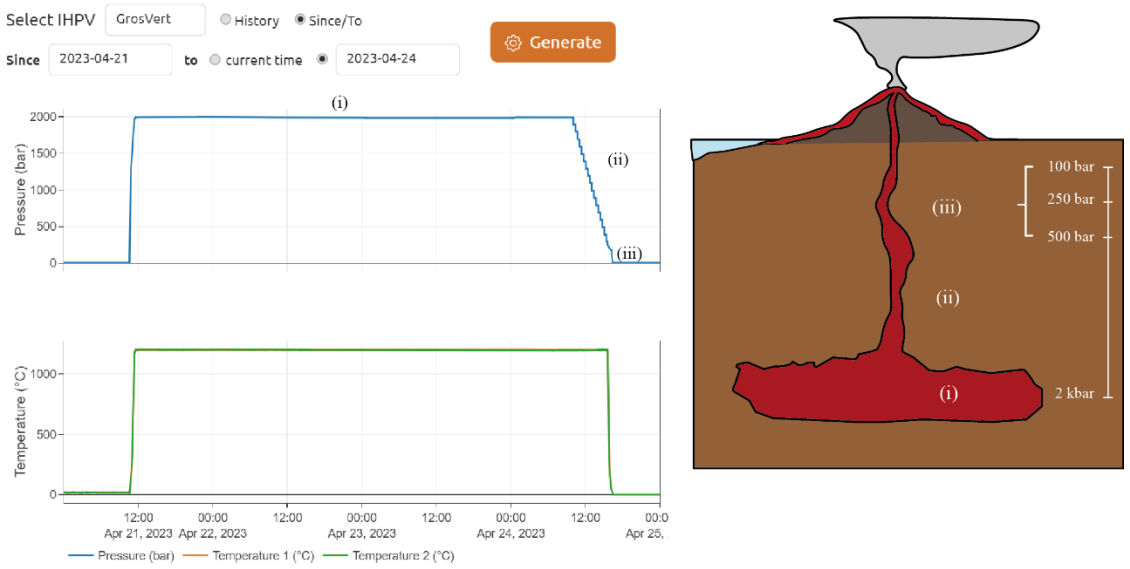

Figure 2.14. Record of autoclave for EN-E4 sample. The upper graphic shows the evolution of pressure with time. The lower graphic shows a constant temperature during the whole experiments. This evolution on time represents all the stages during the volcanic cycle. The experiment lasted for 43 hours and 10 minutes. The initial pressure, when the temperature is reached (1200 ºC) is 2 kbar, then, the re-homogenisation of the synthetic start (i) and last for 42h and 30 min. The decompression starts (ii) with a rate of 50 bar · min^{-1}. We quenched the glass at 100 bars, very close to the surface.

The first stage corresponds to the same protocol followed for the static samples without including the quench. We run this stage for at least 30 h: according to CO_2 melt diffusion calculations (Zhang et al., 2010), and the size of our charges, this time is enough to attain an equilibrium distribution of dissolved CO_2 in the glass.

The second stage of decompression runs just after the equilibrium was reached, used a ramp (decompression rate *dP/dt*) fixing the rate of magma ascent and final pressure. To release the pressure, a manual valve was sequentially opened to control the amount of argon released, via a manometer connected to the controller of the IHPV with an accuracy of ± 20 bar. To finish we drop quenched the experimental samples when the desired pressure was reached.

2.5. Fourier Transforms Infrared Spectroscopy (FTIR):

Infrared spectroscopy is the analysis of infrared light interacting with a molecule due to characteristic vibrations of the molecules in the spectrum. IR spectroscopy allows us to check the homogeneity, abundance, and distribution of H_2O and CO_2. The FTIR spectra were collected in transmission using a Nicolet 6700 FTIR spectrometer attached to an IR microscope (Nicolet Continuouμm) equipped with an MCT detector at the Institute of Earth's Sciences of Orleans.

One or two chunks of glass for every quenched glass were double polished for IR spectroscopy analyses to a thickness of 25 up to 107 μm (*Figure 2.15.*). The thickness was measured five times at each analysed point by using a LEITZ DMR optical microscope equipped with an electronic X-Y stage. We took pictures for every point analysed at the FTIR and these points were checked at this microscope averaging a total of five measurements in each spot. The electronic X-Y stage has an error of ± 2 μm, and together with the standard deviation of the 5 points measurements, they were included in the error propagation of the result.

Figure 2.15. Chunk of glass merged onto the epoxy resin ready for polishing (left) and some pieces ready for the FTIR analysis suspended on the NaCl glass of the microscope stage (right).

Carbonate bands (≈ 1430 and ≈ 1525 cm^{-1}) and OH-stretching vibration (≈ 3525 cm^{-1}) were obtained making a first subtraction with the spectrum of an anhydrous decarbonated sample (the starting material at the mid-infrared region (MIR), scaled at the same thickness and then drawing a linear baseline below the H_2O bending and carbonate vibration bands. An example of spectra treatment for sample ESFa-6A-CO_2 + Ne is shown

in *Figure 2.16*. Typically, 128 - 256 scans were collected for each spectrum in the range of 1000 to 4000 cm^{-1}, with a window aperture of 40 x 40 and 20 x 20 µm and spectral resolution of 4 cm^{-1}, collecting background on NaCl windows before each sample. Between three and six spots were acquired in various parts of the experimental glasses. Then, the results were averaged.

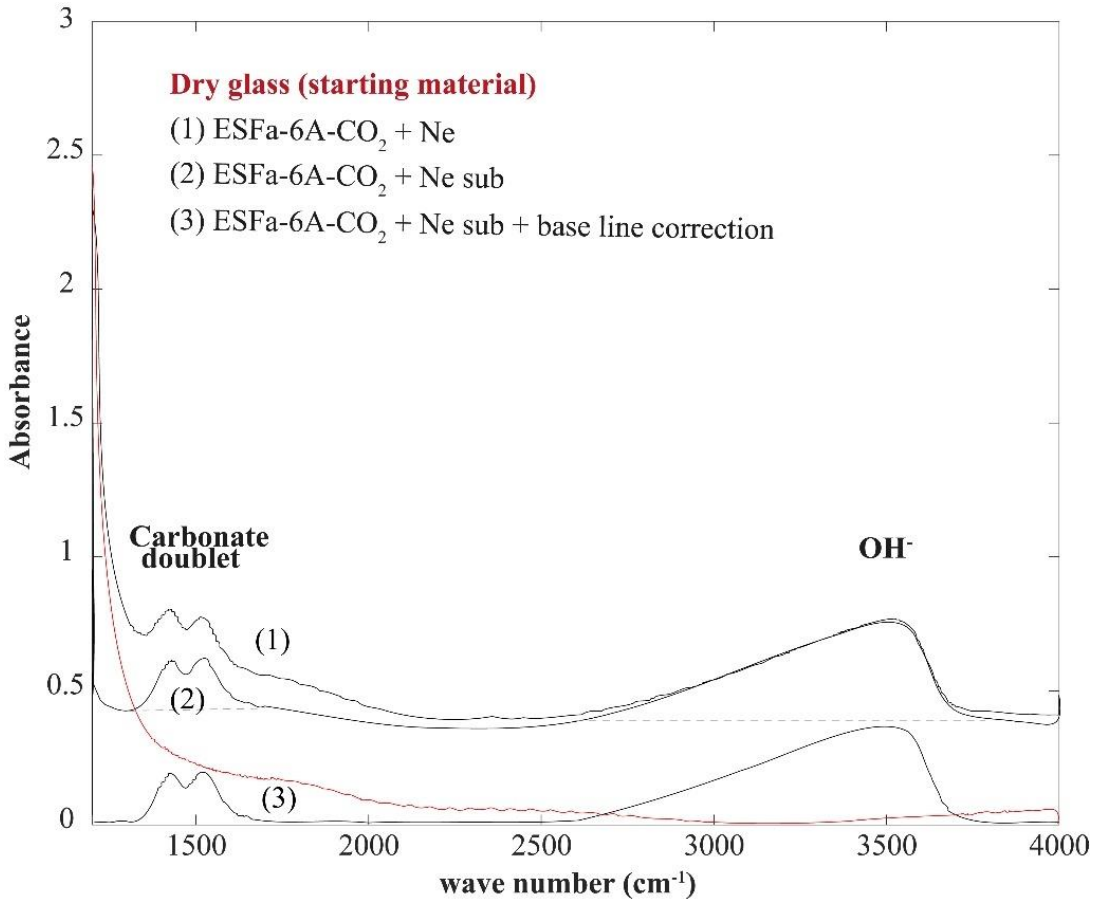

Figure 2.16. representative mid-infrared spectra for the *ESFa-6A-CO_2+Ne* sample. The red spectrum represents the dry glass used as starting material. Spectrum 1 represents the run in one of the points of the chunk of glass without correction. Spectrum 2 represents Spectrum 1 after the subtraction of the dry glass. Spectrum 3 represents the resultant spectra after the correction of the baseline (dashed line). The absorbance of the fundamental OH^- stretching vibration is about 3520 cm^{-1} and the double peak of carbonate at 1520 cm^{-1} and 1430 cm^{-1}.

The H_2O and CO_2 concentrations in the experimental glasses were determined using the Beer-Lambert law (Stolper, 1982):

$$C_i = 100 \frac{M_i \cdot A_j}{d \cdot \rho_{liq} \cdot \varepsilon_j}$$

Where C_i is the concentration of the species i in wt.%, M_i is the molecular weight of the species, A_j is the absorbance (peak height), d is the thickness of the section at each analysed point, ρ_{liq} is the density of the sample (in g · L^{-1}) and $\mathcal{E}_j$ is the absorption coefficient of band j (in L· mol^{-1} · cm^{-1}).

Despite that no water was added to the experimental samples, some FTIR spectra show a small amount of dissolved water. Thus, we decided to use the carbonate peak of 1430 cm^{-1}, since the 1525 cm^{-1} band is slightly affected by the H_2O bending at 1630 cm^{-1}, to calculate the amount of CO_2 dissolved into the glass. Hence, the absorption coefficient considered for the 1430 cm^{-1} peak is 283 ± 8 L · mol^{-1} · cm^{-1} (Dixon and Pan, 1995a).

Because powdered glass was used to prepare the capsules, the formation of bubbles during the synthesis of the experiment cannot be prevent, which could drive us to a false measurement of density by Archimedes' method. Thus, the density of the silicate liquid was determined with the model of Lange (1994) and Warren (1995). This model uses the composition of the glass analysed by electron microprobe, assuming that the density of a silicate liquid is an additive and linear function of the composition, temperature, and pressure.

In silica bearing-glasses, iron is present both in the ferrous (divalent, i.e. in olivine) and the ferric (trivalent) states, the latter being mostly incorporated into magnetite as indicated in the reaction:

$$3Fe_2SiO_4 + O_2 = 2Fe_3O_4 + 3SiO_2$$

fayalite magnetite

The equation above demonstrates that the change in Fe redox state is controlled by oxygen fugacity (fO2). As oxygen-controlled experiments are conducted using silica-bearing glass and variations in fO_2 can significantly affect magma phase equilibria and density, it is necessary to consider the solid assemblage quartz-fayalite-magnetite (QFM) to normalize the oxygen fugacity (oxygen buffer). Frost, (2018) provides the expression for the QFM buffer at equilibrium within the temperature range of 573 - 1200 °C.

$$Log\ fO_2 = \frac{A}{T} + B + \frac{C(P-1)}{T}$$

With A= -25096.3, B = 8.735 and C = 0.110, P in bars, and T in Kelvins.

At high pressures and temperatures, Fe-redox equilibrium in natural melts can be expressed empirically (Kress and Carmichael, 1991) as:

$$ln\left(\frac{X_{Fe_2O_3}}{X_{FeO}}\right) = a\ln(fO_2) + \frac{b}{T} + c + \sum_i d_i X_i + e\left[1 - \frac{T_o}{T} - ln\left(\frac{T}{T_o}\right)\right] + f\frac{P}{T} + g\frac{(T-T_o)P}{T} + h\frac{P^2}{T}$$

With values from *a* to *h* taken from (Kress and Carmichael, 1991) (*Table 2.2.*)**.** T_o is a reference temperature, and *T* and *P* are the temperature and pressure of the experiment. That way, knowing fO_2, we can obtain the distribution of Fe species from the total amount of FeO, FeO_t, obtained by electron microprobe analysis.

	Value	
a	0,196	
b	11492	(K)
c	-6,675	
$\mathbf{d_{Al2O3}}$	-2,243	
$\mathbf{d_{FeO}}$*	-1,828	
$\mathbf{d_{Cao}}$	3,201	
$\mathbf{d_{Na2O}}$	5,854	
$\mathbf{d_{K2O}}$	6,215	
e	-3,36	
f	-7,01E-07	($K \cdot Pa^{-1}$)
g	-1,54E-10	(Pa^{-1})
h	3,85E-17	($K \cdot Pa^{-2}$)
$\mathbf{T_o}$	1673	(K)

Table 2.2. Parameters values for Kress and Carmichael 1991.

Volume and expansion of silicate liquids at temperature T, $V_{liq}\ (T)$, can be described as a linear and additive function of composition (Lange, 1994b) where:

$$V_{liq}(T) = \sum X_i \left[\overline{V}_{i,T_o} + \frac{d\overline{V}_i}{dT}(T - T_o) \right]$$

and $\overline{V}_i$ is the partial molar volume of each oxide component. The volume and thermal data values are listed in **Table 2.3**.

	V_i,1673 K (cm^3/mole)	(dV_i/dT)1 bar ($1O^{-3}$ $cm^3 \cdot mole^{-1} \cdot K^{-1}$)	(dV_i/dP)1673 K (10^{-4} $cm^3 \cdot mole^{-1} \cdot bar^{-1}$)	$[(dV_i/dP)]/dT$ ($1O^{-7}$ $cm^3 \cdot mole^{-1} \cdot bar^{-1} \cdot K^{-1}$)
SiO_2	26.90 ± 0.06	0.00 ± 0.50	-1.89 ± 0.02	1.3 ± 0.1
TiO_2	23.16 ± 0.26	7.24 ± 0.46	-2.31 ± 0.06	-
Al_2O_3	37.11 ± 0.18	2.62 ± 0.17	-2.26 ± 0.09	2.7 ± 0.5
Fe_2O_3	42.13 ± 0.28	9.09 ± 3.49	-2.53 ± 0.09	3.1 ± 0.5
FeO	13.65 ± 0.15	2.92 ± 1.62	-0.45 ± 0.03	-1.8 ± 0.3
MgO	11.45 ± 0.13	2.62 ± 0.61	0.27 ± 0.07	-1.3 ± 0.4
CaO	16.57 ± 0.09	2.92 ± 0.58	0.34 ± 0.05	-2.9 ± 0.3
Na_2O	28.78 ± 0.10	7.41 ± 0.58	-2.40 ± 0.05	-6.6 ± 0.4
K_2O	45.84 ± 0.17	11.91 ± 0.89	-6.75 ± 0.14	-14.5 ± 1.5

Table 2.3.: Partial molar volumes, thermal expansions and compressibility of oxides components from Kress and Carmichael (1991b) and Lange (1994b).

Finally, we can convert the molar volume to the density of the silicate melt using the following relationship:

$$\rho_{liq}(T) = \frac{\sum X_i \cdot m_i}{V_{liq}(T)}$$

Where X_i is the molar fraction of each oxide component, m_i is the molecular mass of each oxide component.

2.6. Electron microprobe (EMPA) and Scanning Electron Microscope (SEM):

Up to three chips of the glass of every quenched experiment were embedded into epoxy resin, polished, and carbon coated for analysis with a Cameca SX-Five electron microprobe (**Figure 2.17.**). The analytical conditions were: 15kV accelerating voltage, a beam current of 10 nA, and a defocused beam of 5 µm and 1 µm of diameter for glass

and oxides analyses, respectively. The counting time for all pics (10 seconds) and for BGDs (5 seconds).

Figure 2.17. Example of epoxy before polishing (left) and ready for SEM and EMPA analysis (right).

At least five spots in each chunk of glass were analysed and averaged to evaluate the homogeneity of the glass. We selected only some samples to check the composition of the oxides and all of them had the same composition (magnetite). The obtained data were normalized on an anhydrous basis and after averaging the spot in each glass. We used the composition to obtain the density of every experimental sample as we explained previously (point 2.5. of this chapter).

The same resin mounts were used for SEM analyses with a ZEISS Merlin Compact microscope equipped with a GEMINI I column. Both EPMA and SEM analyses were done at the Earth Science Institute of the University of Orléans. The SEM tool allows to obtain a 2D image of the quenched glass surface and to characterize the texture of the experimental glass after the quench. In particular it shows the detail the shape and relationship between oxides and vesicle size allowing to compare it with the 3D image obtained with the micro-CT in terms of the detection limit for the smallest bubbles. Note that, as a curiosity, the oxides tend to crystallize near the bubbles or at the boundary between the glass and the bubble (**Figure 2.18**.). All the experimental glasses were characterized by this technique.

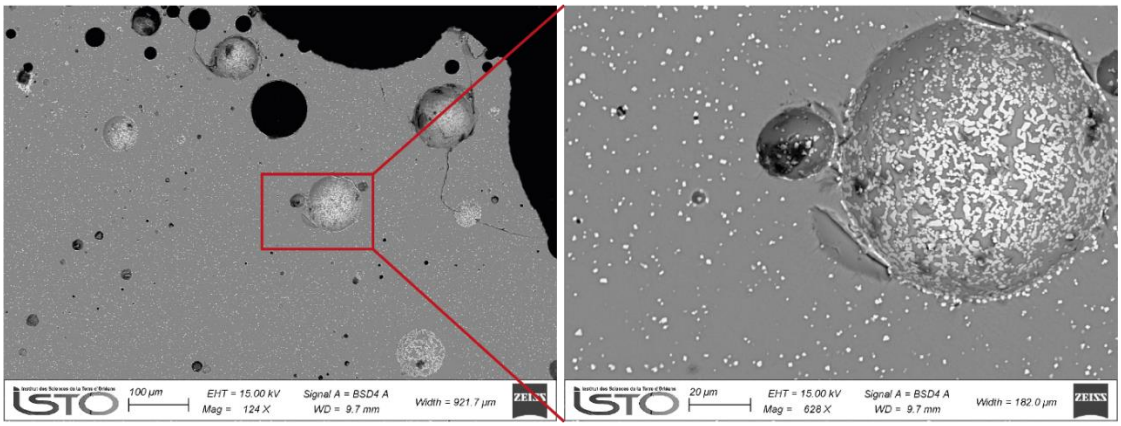

Figure 2.18. Example of SEM image corresponding to sample ESFa-2C-CO_2. This sample show an important amount of magnetite. The quality of the image allows us to have a 3D perspective of some of the vesicles. In addition to observing clusters of oxides in the bladder limits. The magnification range are 124 x (left) and 628 x (right).

2.7. 3-D microtomography:

X-ray computed tomography is a non-destructive technique that allows to precisely locate vesicles inside the experimental sample in 3D before piercing them to analyse the gas by mass spectrometry. Data were collected with a Nanotom Phoenix Micro-tomography equipped with a 180 kV X-ray tube with variable filament currents (40-170 µm) and operating voltage up to 120 kV (*Figure 2.19.*). The biggest piece of glass of every experimental capsule (sometimes several pieces at the same time) was mounted on a carbon fibre rod with a thermoplastic adhesive and then placed into the instrument to be rotated 360^{O} for the scan. Between 700 and 2000 projections were acquired with a resolution of 3 to 3.5 µm per pixel.

Figure 2.19. Nanotom Phoenix Micro-tomography. 1: Fibre rod with the sample adhered on the top; 2: source of X-ray; 3: rotating plate; 4: detector.

The reconstruction of the acquired images in stacks was made via 3D *VGStudioMax*. The first step is to correct for artefacts using a median filter and separating different density bands. Then we separate the portion of glass from vesicles and from the air surrounding the glass.

Some samples were analysed at the X-ray CT two times, before and after the gas acquisition by laser ablation. This allowed us to localize some of the pierced vesicles and estimate their corresponding volume with the pressure obtained by the manometer before the analysis in the mass spectrometer.

The microtomography images were processed using ImageJ. The 'analyse particles' plugin was used after adjusting the threshold to obtain the surface of the glass and vesicles independently in each slice of the 2D image stack. This allowed for the calculation of bubble density at the surface of the image ($nb \cdot mm^{-2}$). The surface data measurements were converted to volume using the procedure outlined by Sarda and Graham, (1990), and Chavrit, (2010). The vesicles were grouped by intervals of different diameters, following the model of Saltykov, (1967). Further details on these methods will be provided in Chapter 3. An example of the glass obtained after opening the capsule is shown in **Figure 2.20**, using 3D by *VGStudioMax* and *2D-Image plugging* treatments.

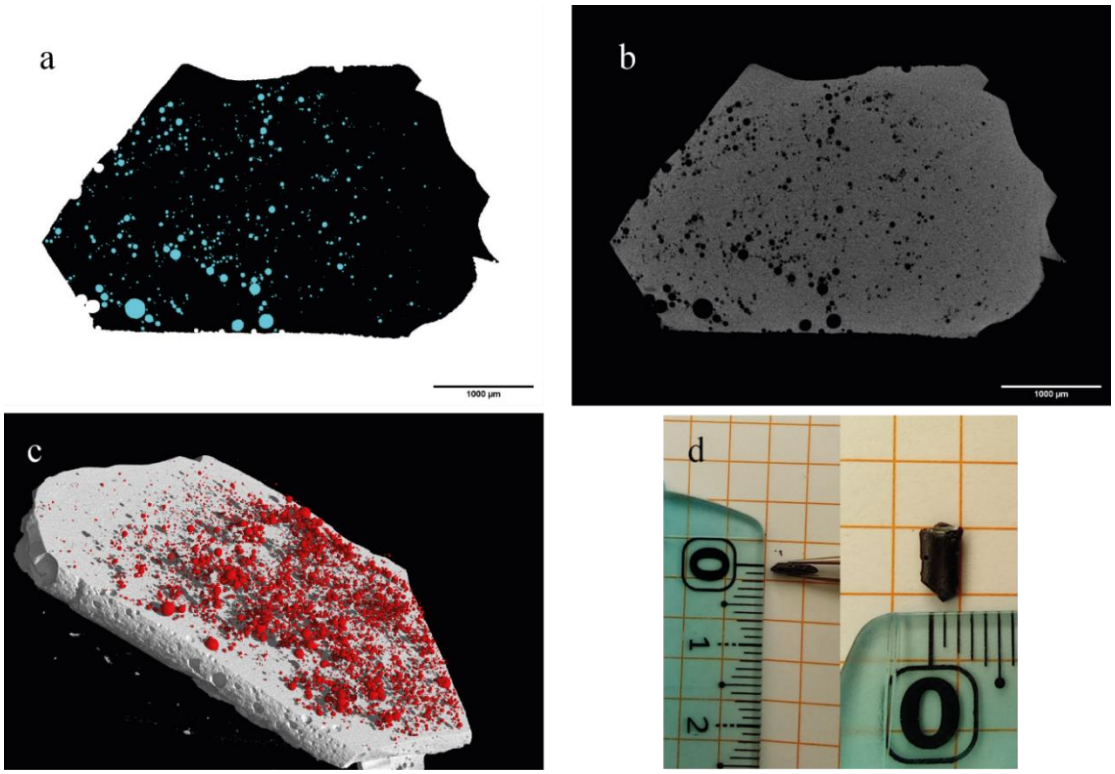

Figure 2.20. Images obtained after treatment by *ImageJ* in 2D (*a* and *b*) and *VGStudioMax* in 3D (*c*). The same sample (*ESFa-3B-CO_2+Ne*) is shown at scale (*d*). Image *a* was used to calculate the vesicle size distribution of the experimental sample. We applied the appropriate threshold to separate vesicles from glass before counting the particles. Image *b* is the image obtained directly from the micro-CT after correcting the artifacts. Image *c* was processed also to remove the artifacts and separate the densities of the two phases of the sample (gas and glass).

2.8. Helix-SFT mass spectrometer type:

2.8.1. Preparing the sample:

After the x-ray CT acquisition and a double-face soft polish, the biggest pieces of quenched glasses were embedded into acetone and ethanol to remove all the thermoplastic resin residues. We let them dry for some hours at 100 ºC in an oven to desorb all the volatiles adhering to the surface before inserting them into the mass spectrometer sample holder.

2.8.2. Gass extraction and purification:

Two methods were used for the gas extraction of the vesicles: the one on which this work is mainly based on (i), a bubble-by-bubble laser ablation (Péron et al., 2019);

and the most common technique for the analysis of the whole gas-trapped in the sample and to which a brief chapter will be dedicated (ii), the step crush.

2.8.2.1. Bubble-by-bubble laser ablation:

The experimental samples were loaded into the laser cell under vacuum and baked at 100 ºC for at least two days until the blank in the line was low enough (^{22}Ne αblank = 1.7%) to start with the analysis. Due to the number of experiments run and the difficulty of the analysis (low vesicularity and tiny size of the vesicles), only the most representative samples were selected for testing our hypothesis. The selection was based on (i) the experimental run time (for the static samples), at least one for each time series; (ii) the distribution of bubbles and vesicularity, with different sizes of bubbles and/or vesicularity; and (iii) the pressure at which the experiment was quenched (for the decompressed samples).

Due to the millimetric size of our experimental samples, the type of laser beam, as well as the diameter, having a good control over the movement of the spot becomes an important task. The drilling was done with a diode-pumped air-cooled Q-switched laser of 263 nm wavelength and 35µm diameter, which works by repetition of power plasma pulses. The holder cell is placed on a mobile base controlled by entering coordinates into the computer to which it is connected.

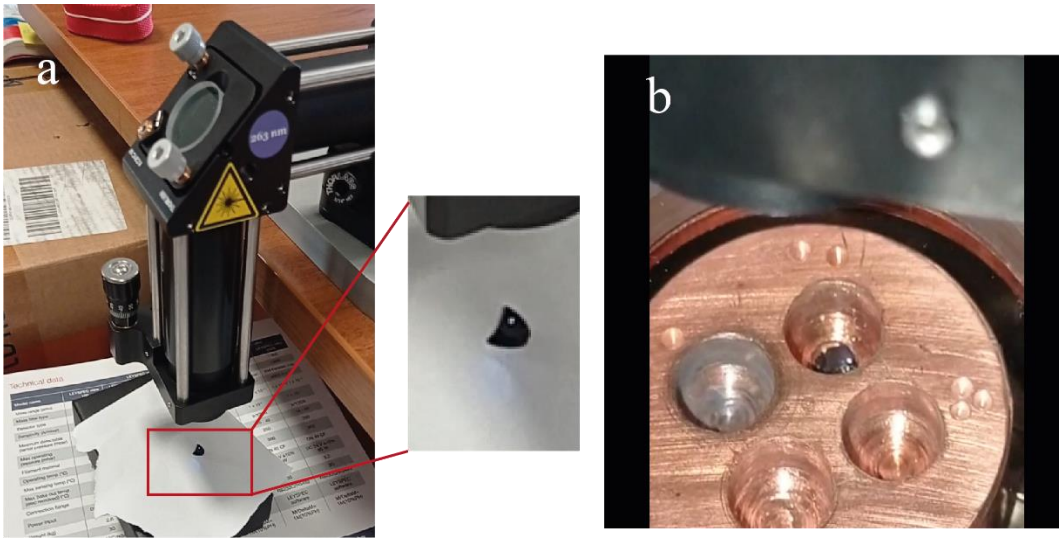

Figure 2.21. Images of different samples being pierced by the laser. Image a is the first test of the laser after setting up and the second image is piercing a sample under vacuum.

This tool allows us to prink our tiny samples and be very precise in reaching micrometric bubbles. The pressure in the laser cell was measured (in millibars) with a

manometer MKS Baratron® 1Torr full scale. When the laser ablation starts, a smooth increase in pressure happens (while the laser is consuming the matrix of the sample) while, when a bubble is reached, a sharp change in the pressure pops up in the manometer (**Figure 2.22**.), the ablation stops, and the purification of the gas starts along the line. Sometimes, due to a coalescence effect, the vesicles are very close one to each other causing a concatenation of pressure jumps, releasing two or even three bubbles with a single shot: yet the accuracy of the gauge is good enough to allow distinguish this jump in the pressure trend line and discard these values form the result (**Figure 2.23.**). In **Figure 2.24**. the surface of the experimental sample after the ablation is shown and an image in 3D with the path of the laser and the vesicles that have not yet been pierced (*ESFa-5B-CO_2+Ne* and *EN-E9* respectively).

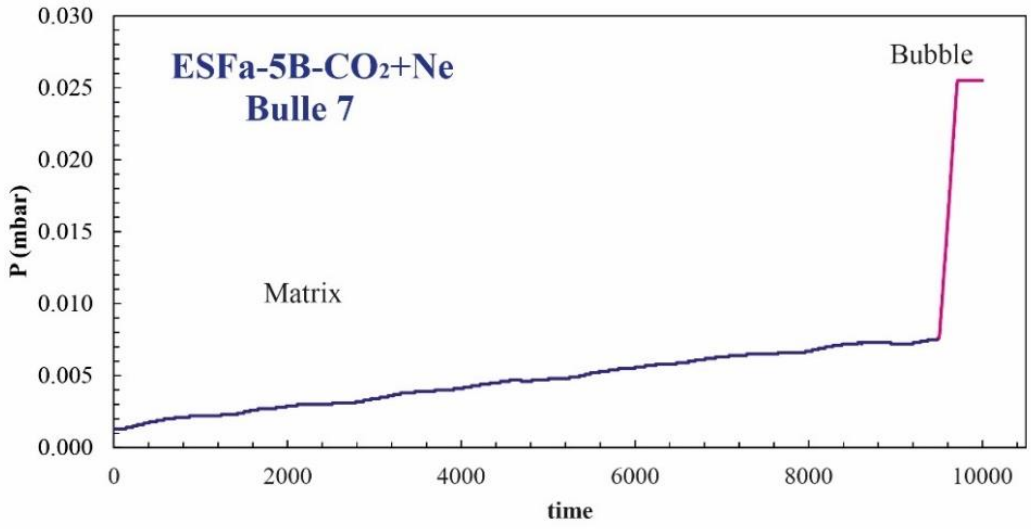

Figure 2.22. Pressure in mbars recorded by the manometer during laser ablation of the vesicle 7 in *ESFa-5B-CO_2* sample. The blue path represents the ablation of the matrix and the pink one the jump when the gas of the vesicle is released.

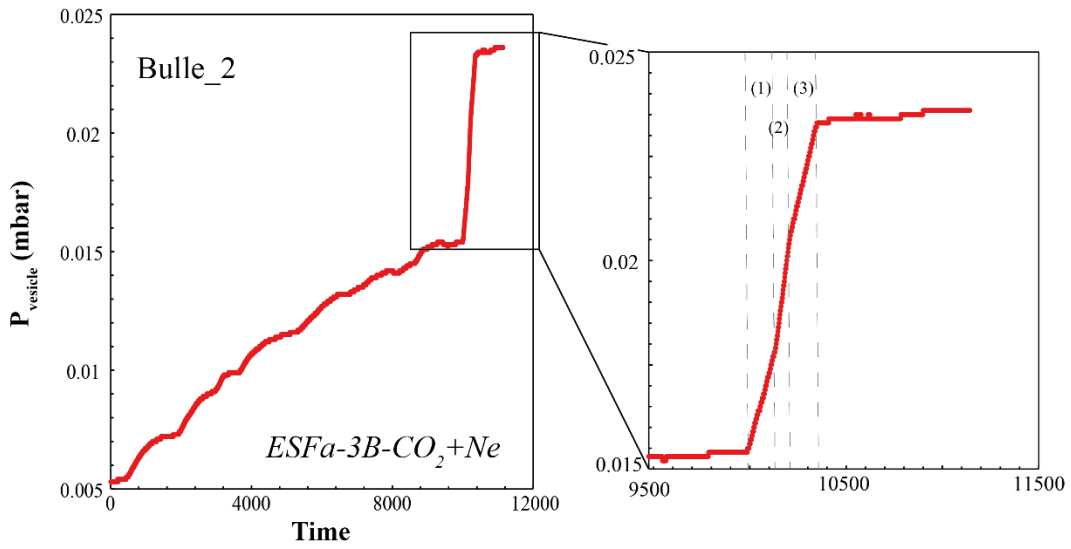

Figure 2.23. Pressure in mbars recorded by the manometer during laser ablation of three vesicles for sample *ESFa-3B-CO_2*. A zooming into the diagram shows three inflection points on the trend line where the pressure changes, indicating the bursting of three tiny vesicles occurring close to each other.

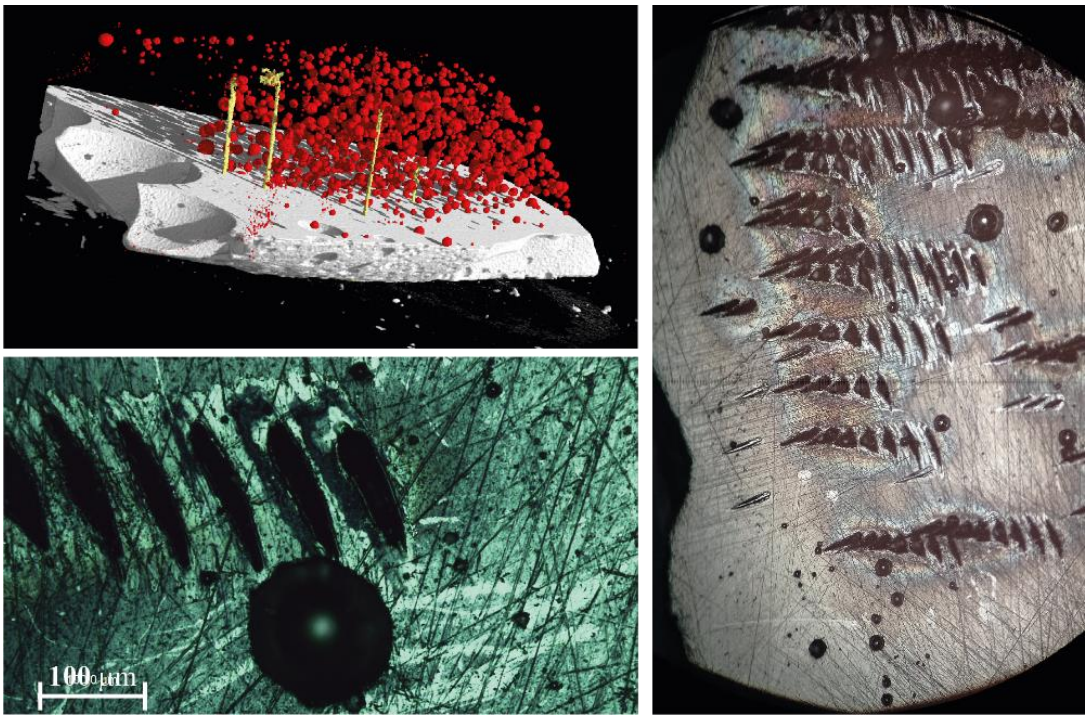

Figure 2.24. 3D-image obtained by *VGStudioMax* with vesicles in red, glass in grey and some laser path in yellow colours (upper left); and 2D- images observed at the microscope where can be observed the way we follow piercing the sample.

2.8.2.2. Step-crushing:

For the samples that were analysed using the step-crushing technique, we just took a small portion of the quenched glass. That is because our samples are oversaturated in Ne compared to nature and we had the risk to oversaturate the detector of the mass spectrometer.

The experimental samples were loaded into the crusher, which was baked under an ultra-high vacuum at 100-120 ºC for at least one night before starting the crushing. The crusher consisted of a stainless-steel finger tube with a heavy metallic ball inside. When the blank was low enough to start the analysis, we dropped the metal ball from the upper part of the finger tube using a powerful magnet. We let drop the ball up to three to four times for every step, controlling the increase of pressure with the manometer connected to the line. Sometimes, the gas amount released with the step crushing was so large that we had to reduce the volume introduced into the mass spectrometer. We will indicate when we had to do it in *Chapter 5* as well as the steps done for every sample.

2.8.3. Purification and analysis:

Once the gas is released from a pierced bubble or the crushed sample, the first stage of purification starts passing the gas through two getters-type Titanium sponges while the volume of the gas expands into the line. For five minutes, the first Ti-getter hot (above 700 ºC) is adsorbing chemical species like CO_2, O_2, and N_2 and then, the Ti-getter is switched off to trap H_2 for ten minutes in a T range of about 25 to 400 ºC (Stout and Gibbons, 1955). Big species such as H_2O and CH_4 are being sorbed while the getter is operating at both temperatures. A second Ti-getter repeats the process. The second step of purification consists of a *cold finger* composed of active charcoal which, when liquid nitrogen is present, traps heavy noble gases like Ar, Kr, and Xe at -195.8 ºC for 15 min, leaving Ne free to be analysed into the mass spectrometer. One cold finger is placed at the end of the purification line and one more at the beginning of the mass spec. A scheme of the purification line is shown in **Figure 2.25**.

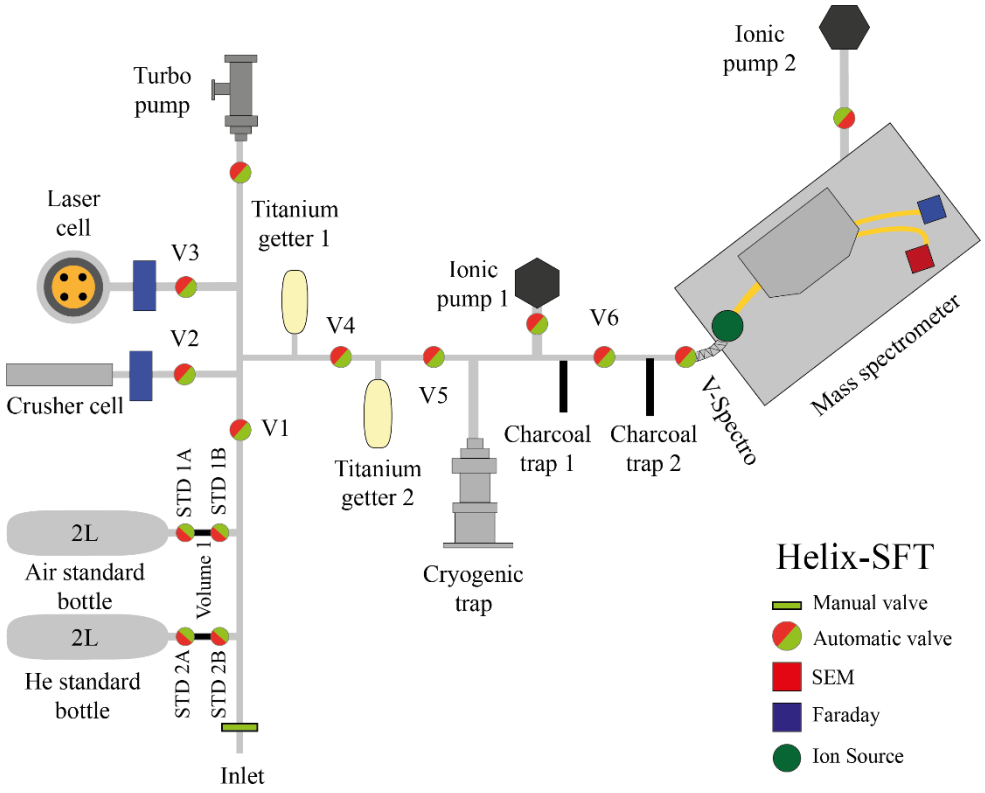

Figure 2.25. extraction and under-vacuum purification line attached to the Helix-SFT mass spectrometer type. The automatic valves are controlled by *LabVIEW* ©.

Once the gas is purified within the line, the residual noble gases are introduced into a HELIX-Split Flight Tube (ThermoFisher) mass spectrometer type. The Helix-SFT is a magnetic mass spectrometer designed for the analysis of noble gases in small samples. It is composed of an electron ionization source, a powerful magnetic sector static vacuum that will separate isotopes according to the mass; an electron multiplier, to measure small signals; and one electrically suppressed Faraday, detector for large signals.

Before neon is introduced at the end of the gas purification step, two cycles of measurement are done to stabilize the magnet of the mass spectrometer. These cycles measure the multi-collector background while the ionic pump linked to the mass spec is pumping. The magnet and the multi-collector are ready, the ionic pump is closed, and the gas is inserted.

Fifteen cycles of measurement were done for every single vesicle, step crushing, blank or standard. Ne was analysed using an acceleration voltage of 4.5 kV and a trap current of 250µA. The acquisition software and the data processing were home-made using *C#* and MATLAB© respectively.

The Helix has hysteresis problems, which is for the same mass, in this case twenty, the intensity of the magnetic field may vary. and its resolution does not discriminate the peaks of HF, ^{20}Ne and ^{40}Ar. To avoid them, mass 20 is analysed by mass-scan instead of placing the magnet in the field set for mass 20 (Moreira et al., 2018). **Figure 2.26**. (not at scale) shows an example schematized of the mass scan. The resultant line at the end is a sum of the three peaks (HF, ^{20}Ne and ^{40}Ar) and, since our work is focused on Ne, having a good discrimination of the peaks, becomes a crucial task.

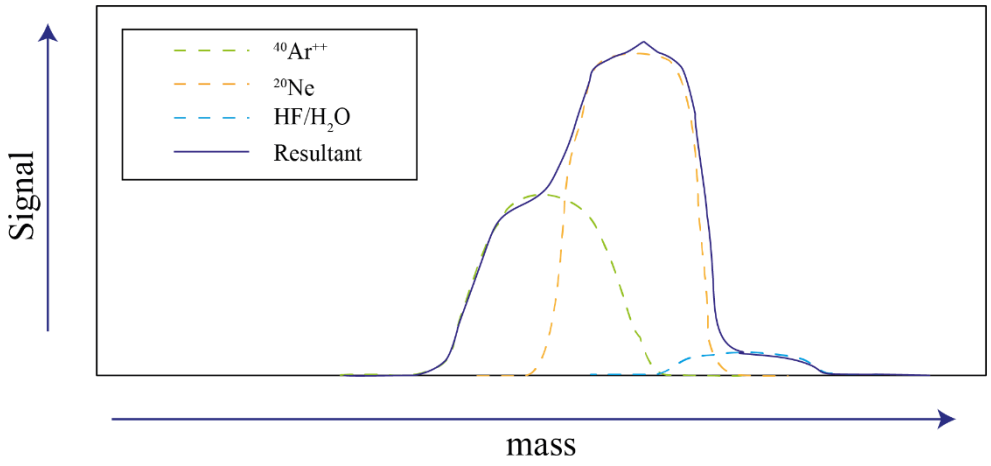

Figure 2.26. Representative scheme (not at scale) of a 20-mass scan in the mass spectrometer. The resultant signal (blue line) is the summatory of ^{20}Ne, Ar^{++} and HF.

2.8.4. Analytical blank:

As previously mentioned, the development of this experimental study encountered several challenges. One of these challenges is the small size of our bubbles, ranging from tens to a few hundred microns. The complexity is related to the ability to locate them and to have a sufficiently good instrumental resolution to conduct this analysis. The first problem can be reduced, although not completely solved, with 3D microtomography. Although tomography allows for the determination of the distribution of bubbles, locating them precisely is an impossible task. Therefore, the sample is drilled multiple times on the surface in areas where bubbles are most likely to be found until a pressure jump during ablation is observed.

When finding a vesicle, it is important to consider that the volume of gas released may not be equivalent to that of a vesicle from a natural sample due to differences in size. In natural samples, the diameter of the vesicles reaches hundreds of microns, whereas in experimental samples, they are reduced to tens of microns. Therefore, having a good

blank in the line is crucial. Fortunately, the concentration of Ne in our samples is high thanks to the synthetic glass developed, and the blank is often negligible. Results are provided in the Supplementary material. Furthermore, we conducted various matrix measurements by performing laser ablation at different drilling times to ensure that the data processing did not include any signal from the matrix.

2.8.5. Standard:

The air standard is connected at the Helix-SFT purification line (**Figure 2.25**.). It is the volume of one pipette (small volume of 0.1 cm^3) of a 2L bottle reservoir of diluted air from the room in the laboratory. To prepare that reservoir, we isolate the line from the bottle by closing V_1, V_2, V_3, V_4 and the turbo pump. Then we open the STD-1B valve, open, the inlet and, open the manual valve letting the air enter and equilibrate for two minutes. After the two minutes have elapsed, we close the STD-1B valve and open the STD-1A valve, equilibrating again for two minutes this small volume. Hereafter, we close the STD-1A valve and open the STD-1B valve and V1, waiting again for another two minutes. Finally, we close the STD-1B valve, screw the inlet, pump the line by the turbo pump and bake it. The same protocol for both, the samples and blank, was used.

As we explained for the QMS700, the standard analysis is essential to test the sensitivity of the mass spectrometer as well as the mass discrimination. The way to check the sensitivity and the mass discrimination in the mass spectrometer is to run standard for several days/weeks. As our experiments were conducted over three years, the spectrometer sometimes remained without analysis for a month or two at most. **Figures 2.27**. and **2.28** show the standards analysed for four months, while the static samples were being analysed. The standard analyses can be accurately reproduced even when the volume of gas introduced into the mass spectrometer is changed. The figures show a non-significant variation in Ne sensitivity and mass discrimination for the $^{20}Ne/^{22}Ne$ and $^{21}Ne/^{22}Ne$ ratios, so we can consider the mean and standard deviation as optimal for the data treatment, as well as the results of the samples run at the same period as the standards.

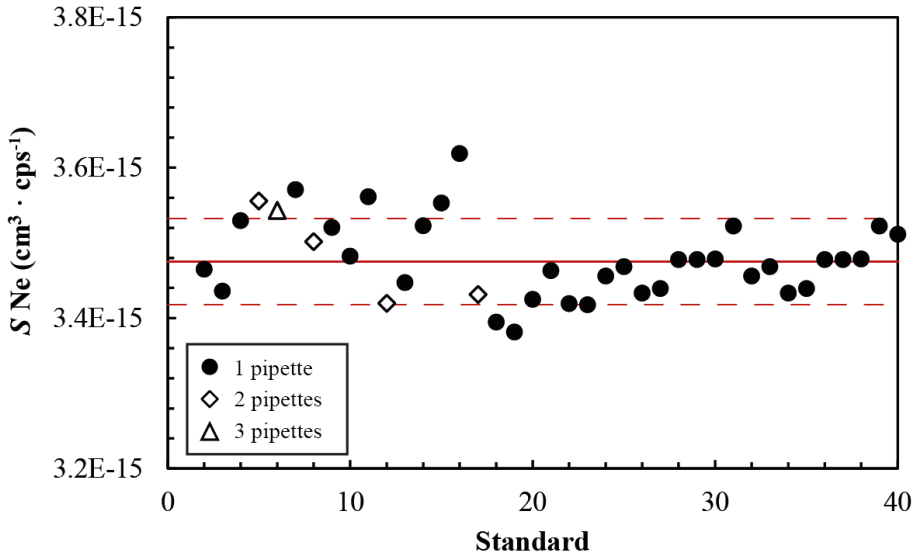

Figure 2.27. Standard measurements of the mass spectrometer. Up to 40 standards were analysed in a period of four months. The red line indicates the mean value up to 40 measurements and the dashed red lines the standard deviation (one sigma). The legend plots the volume analysed for every standard.

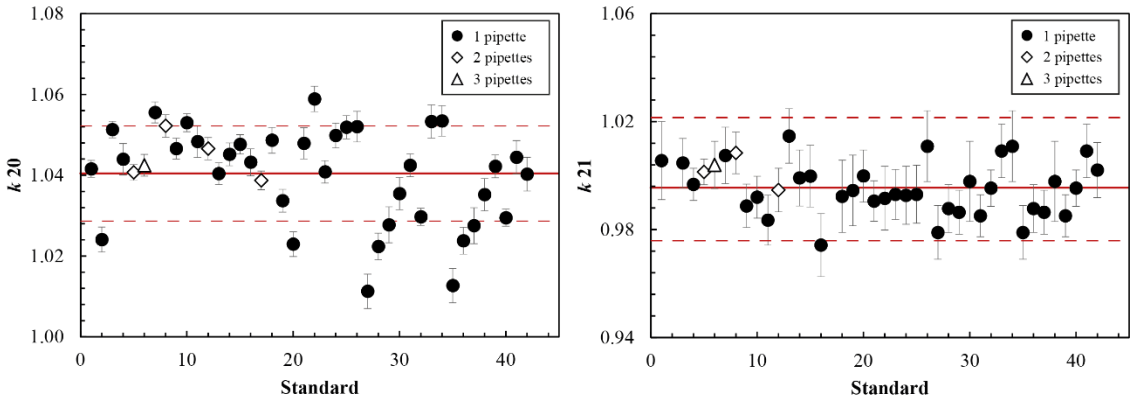

Figure 2.28. Mass discrimination, *k20* for $^{20}Ne/^{22}Ne$ isotopic ratio (left) and *k21* for $^{21}Ne/^{22}Ne$ isotopic ratio (right) in standard measured for four months. The one sigma error of every standard is shown with the corresponding symbol. The red line indicates the mean value of the 43 measurements and the dashed red lines the standard deviation. The legend plots the volume analysed for every standard.

Nevertheless, developing experiments in the autoclave and the microtomography scanning and image treatment takes time and, for a while, running the mass spectrometer is not possible. The **Figure 2.29**. shows a drift in these moments. When needed, we group the standards in similar groups (green dashed line) to use the mean of each one in the

samples analysed in the same periods. The blue lines show the total mean and the respective standard deviation for all the standards.

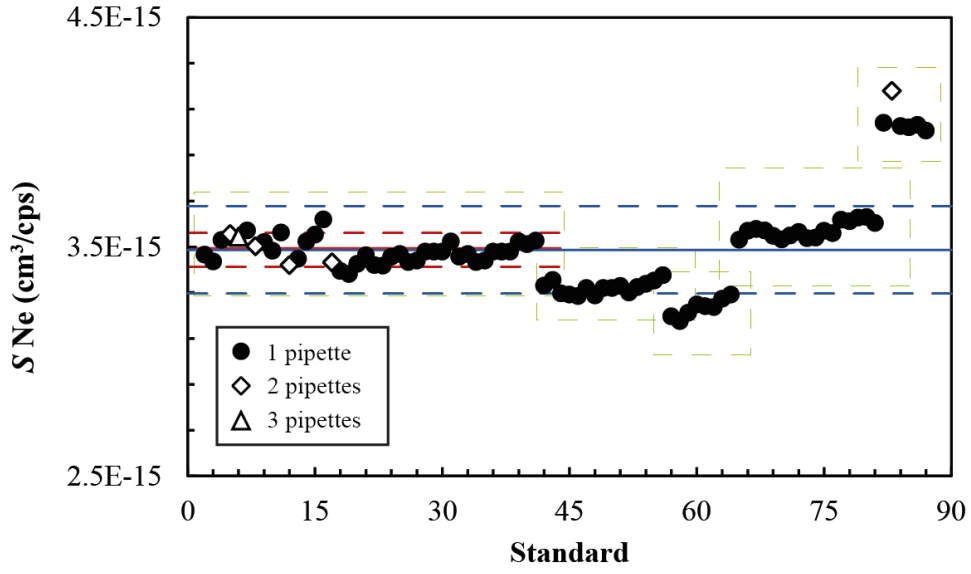

Figure 2.29. Standard measurements of the mass spectrometer along 3 years. The red line and the dashed line correspond to the mean of the first group of standards (*Figure 2.27*) and the blue and the dashed blue line corresponds to the mean and standard deviation of all the standards measured. Up to 5 groups of standards were selected for mass discrimination correction and Ne abundance for our experimental samples.

2.8.6. Data processing:

2.8.6.1. MATLAB©:

Returning to the hysteresis problem of the Helix spectrometer (explained in *2.8.3* point of this chapter), we use a MATLAB© code that allows us to select manually the point where the peak of ^{20}Ne is located. Here we present some examples of the first step of the obtained data treatment using this code.

Usually, this task is easy when Ne abundance is high enough compared to the signal of Ar^{++}, that can be filtered thanks to the help of the background, which is checked regularly. A good scan of ^{20}Ne would show a signal with a flat plateau **(Figure 2.30.c, d,** and **e).** But, sometimes, mostly for the analytical blank scans or when the signal of Ar^{++} is relatively high (e.g., in some samples conducted on decompressed experiments (**Figure 2.30.a** and **b**), it becomes a challenge. In these cases, the results are reported after data

treatment, but any results that are masked by Ar^{++} are excluded as they are not considered reliable.

The figures show that the flat plateau is replaced by a peak on the left side which decreases throughout the cycles until it becomes a flatter signal. Rather than considering this signal as representative of the analysis, we preserved the gas in the purification line without pumping it and analysed a second to fifth aliquots. For all samples where the signal of Ar^{++} was evident, we followed this procedure and selected the second and subsequent aliquots as representative of the step crushing.

In the case of the analytical blank is more difficult. The line is extremely clean, so much so that a background is used as a reference to set the point of the peak of Ne (**Figure 2.30.f**). The signal provided by the scan is so small that becomes mostly Ar^{++}, moreover, during the scan, the counts of the ^{21}Ne isotope are about or close to 0 cps. The same for the matrix of the samples, several parts of some of the quenched glasses were drilled for matrix analysis, shooting the glass with the laser for several minutes, and the resultant signal was similar or even less to the analytical blanks (**Figure 2.30.f**).

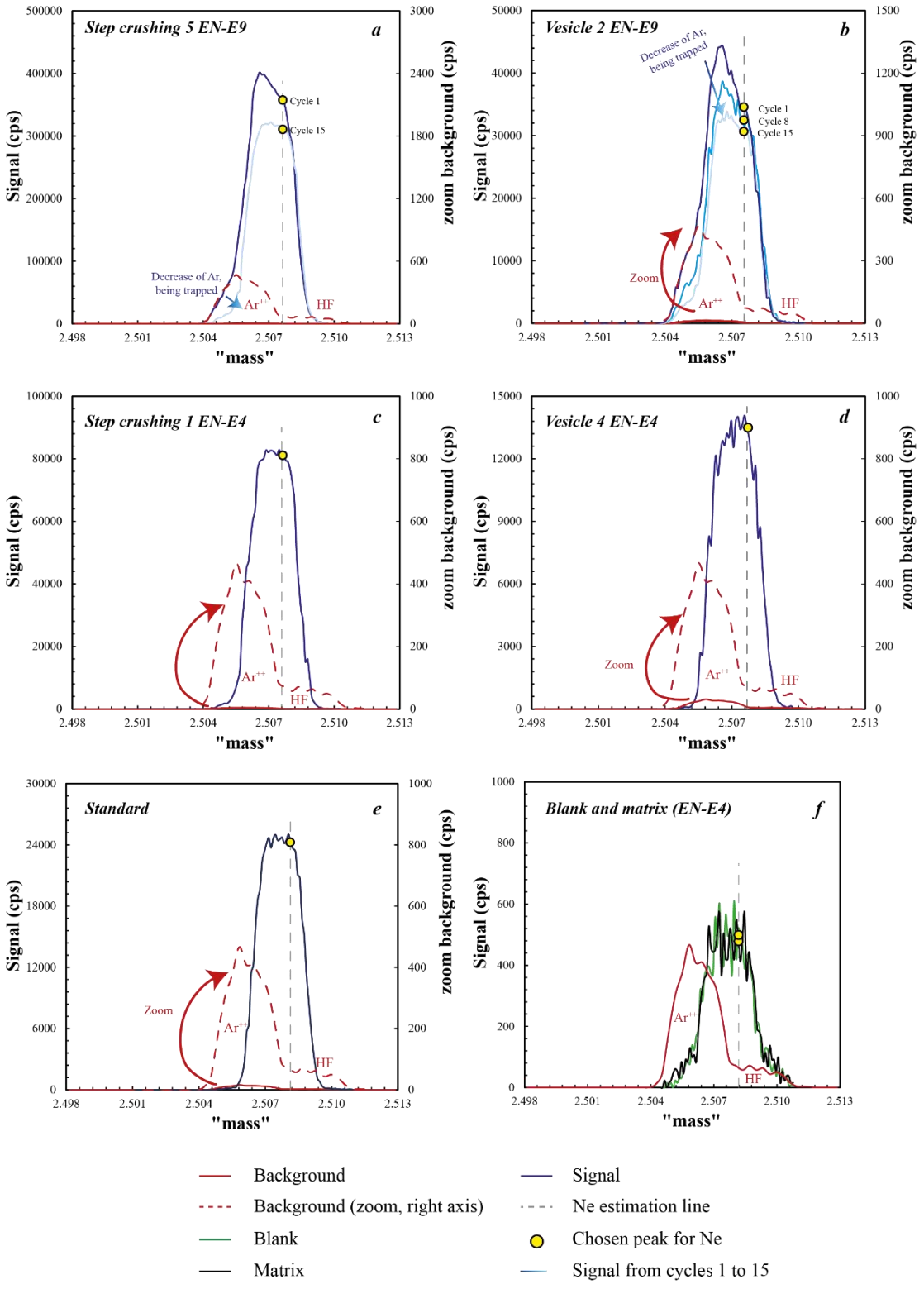

Figure 2.30. MATLAB© diagrams showing the point where the peak of ^{20}Ne is taken for: the samples with high concentration of Ar^{++} (**a** and **b**); normal analysis with a flat plateau (**c** and **d**); standard (**e**) and blank and matrix (**f**).The background of the mass spectrometer is marked in red but, as sometimes is really small comparing to the signal a second *y* exe, is added (right exe) to increase the scale for comparison.

The MATLAB© code also includes unit conversion. The Helix measures the signal in femtoAmps but, after the first step of treatments, we obtain the results in counts per second (number of electrons passing through the current per second). Since ne ion has an elemental charge q = $1.602176663 \cdot 10^{-19}$ coulomb and 1 coulomb/s = 1A, then $1 \cdot 10^{-15}$ amps = 6241.55 ions·sec^{-1} (cps).

As mentioned above, the background in the mass spectrometer is checked and estimated regularly so Ar^{++}/Ar^{+} and CO_2^{++}/CO_2^{+} ratios were modified when needed. For instance, the first experiments, the statics ones, were corrected by Ar^{++}/Ar^{+} and CO_2^{++}/CO_2^{+} partial contribution of 0.03 and 0.0015 respectively, but the latest experiments, decompression ones, were corrected with 0.03 and 0.0019, respectively.

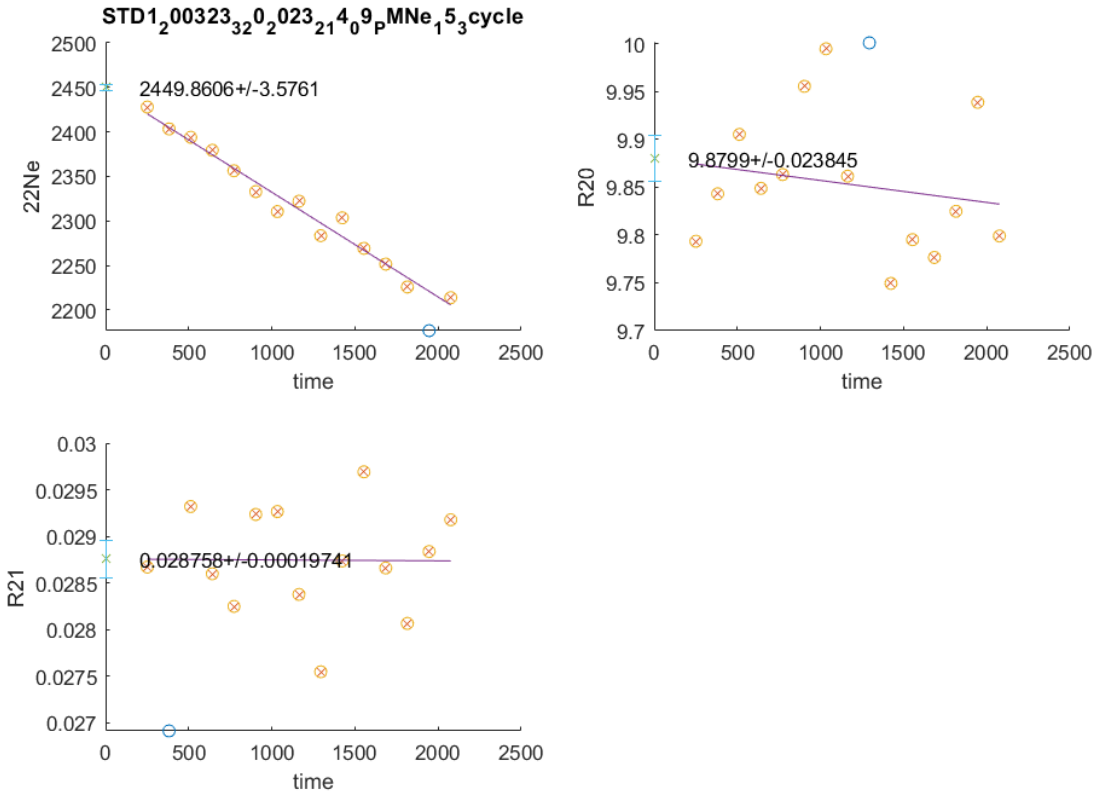

Figure 2.31. Example of result obtained after selecting ^{20}Ne peaks with MATLAB© code. ^{20}Ne signal is given in cps at the upper left diagram. The extrapolated mean and the standard deviation are shown next to the trend line. The same for $^{20}Ne/^{22}Ne$ and $^{21}Ne/^{22}Ne$ isotopic ratios. Only the yellow crossed points are considered for the extrapolated mean and the error.

After selecting the peak for the fifteen cycles, the code calculates and returns the average of the ^{22}Ne signal with the standard deviation, and the $^{20}Ne/^{22}Ne$ and $^{21}Ne/^{22}Ne$

extrapolated mean ratios and standard deviations. An example of the final results is shown in **Figure 2.31**.

2.8.6.2. Data spreadsheet processing:

For the treatment of the data processed by MATLAB© we use the following strategy. First, we calculate and correct the blank contribution, α_{blank}, in the standards and samples as:

$$\propto_{blank} = \frac{22Ne_{blank}}{22Ne_{measured}}$$

$$22Ne_{corrected} = 22Ne_{measured} - 22Ne_{blank}\ (cps)$$

We deduce the sensitivity of the instrument as:

$$\boldsymbol{S_{22Ne_{std}}} = \frac{[Ne]_{air} * NA_{22Ne_{air}} * \frac{{v_1}^2}{v_{bottle} + v_1}}{22Ne_{corrected(STD)}}\ (cm^3 * cps^{-1})$$

Where $[Ne]_{air}$ = 18.18·10^{-6} cm^3 (concentration of Ne in the air), NA $^{22}Ne_{air}$ = 0.0925 (natural abundance of ^{22}Ne isotope in the air), v_1= 0.1 cm^3 (volume of the pipette) and V_{bottle} = 2000 cm^3 (volume of the standard bottle).

For obtaining the ^{22}Ne abundance:

$$\boldsymbol{22Ne_{sample}} = 22Ne_{corrected(sample)} * sensitivity\ \ (cm^3STP)$$

For $^{20}Ne/^{22}Ne$ and $^{21}Ne/^{22}Ne$ correction of the α_{blank} in the standard and the sample we followed the same strategy as for $^{22}Ne_{corrected}$:

$$\boldsymbol{R_{i\ corrected}} = \frac{R_{i\ measured} - \propto_{blank} * R_{i\ blank}}{1 - \propto_{blank}}$$

And for the error propagation:

$$\boldsymbol{U_{i\ corrected}} = \sqrt{\left(\frac{\sigma_{measured}}{1 - \propto_{blank}}\right)^2 + \left[\left(\frac{\propto_{blank} * \sigma_{blank}}{1 - \propto_{blank}}\right)^2 + \frac{(R_{i\ measured} - R_{i\ blank})\ * 0.05 * \propto_{blank}}{(1 - \propto_{blank})^2}\right]^2}$$

Where U_i refers to the uncertainty of the isotopic ratio *i*.

The final isotopic ratio, and the uncertainty, σ, are obtained by using the mean and the standard deviation of the group of standards measured in a certain period:

$$\boldsymbol{k_i} = \frac{R_{i\ corrected\ (sample)}}{R_{i\ corrected\ (std)}{}_{mean}} * R_{i\ air}$$

$$\boldsymbol{\sigma_i} = \sqrt{\left(\frac{U_{i\ corrected\ (sample)}}{R_{i\ corrected\ (std)}{}_{mean}}\right)^2 + \left(\frac{R_{i\ corrected\ (sample)} * \sigma_{std}}{\left(R_{i\ corrected\ (std)}{}_{mean}\right)^2}\right)^2} * R_{i\ air}$$

2.9. References:

Aiuppa, A., Federico, C., Giudice, G., Giuffrida, G., Guida, R., Gurrieri, S., Liuzzo, M., Moretti, R., Papale, P., 2009. The 2007 eruption of Stromboli volcano: insights from real-time measurement of the volcanic gas plume CO2/SO2 ratio. J. Volcanol. Geotherm. Res. 182, 221–230.

Allegre, C.J., Manhes, G., Göpel, C., 1995. The age of the Earth. Geochim. Cosmochim. Acta 59, 1445–1456.

Allègre, C.J., Staudacher, T., Sarda, P., Kurz, M., 1983. Constraints on evolution of Earth's mantle from rare gas systematics. Nature 303, 762–766. https://doi.org/10.1038/303762a0

Aubaud, C., 2022. Carbon stable isotope constraints on CO2 degassing models of ridge, hotspot and arc magmas. Chem. Geol. 605, 120962.

Aubaud, C., Pineau, F., Jambon, A., Javoy, M., 2004. Kinetic disequilibrium of C, He, Ar and carbon isotopes during degassing of mid-ocean ridge basalts. Earth Planet. Sci. Lett. 222, 391–406.

Aubry, G.J., Sator, N., Guillot, B., 2013. Vesicularity, bubble formation and noble gas fractionation during MORB degassing. Chem. Geol. 343, 85–98.

Azuma, S., Ozima, M., Hiyagon, H., 1993. Anomalous neon and xenon in an Archaean anorthosite from West Greenland. Earth Planet. Sci. Lett. 114, 341–352.

Ballentine, C.J., Barfod, D.N., 2000. The origin of air-like noble gases in MORB and OIB. Earth Planet. Sci. Lett. 180, 39–48.

Ballentine, C.J., Burgess, R., Marty, B., 2002. Tracing fluid origin, transport and interaction in the crust.

Ballentine, C.J., Burnard, P.G., 2002. Production, Release and Transport of Noble Gases in the Continental Crust. Rev. Mineral. Geochem. 47, 481–538. https://doi.org/10.2138/rmg.2002.47.12

Ballentine, C.J., Marty, B., Sherwood Lollar, B., Cassidy, M., 2005. Neon isotopes constrain convection and volatile origin in the Earth's mantle. Nature 433, 33–38.

Bauer, C.A., 1947. Production of helium in meteorites by cosmic radiation. Phys. Rev. 72, 354.

Becker, R.H., Pepin, R.O., 1994. Solar wind noble gases and nitrogen in metal from lunar soil 68501. Meteoritics 29, 724–738.

Behrens, H., 2010. Noble gas diffusion in silicate glasses and melts. Rev. Mineral. Geochem. 72, 227–267.

Behrens, H., Misiti, V., Freda, C., Vetere, F., Botcharnikov, R.E., Scarlato, P., 2009. Solubility of H2O and CO2 in ultrapotassic melts at 1200 and 1250 C and pressure from 50 to 500 MPa. Am. Mineral. 94, 105–120.

Behrens, H., Zhang, Y., 2001. Ar diffusion in hydrous silicic melts: implications for volatile diffusion mechanisms and fractionation. Earth Planet. Sci. Lett. 192, 363–376.

Black, D., Pepin, R., 1969. Trapped neon in meteorites—II. Earth Planet. Sci. Lett. 6, 395–405.

Black, D.C., 1972. On the origins of trapped helium, neon and argon isotopic variations in meteorites—I. Gas-rich meteorites, lunar soil and breccia. Geochim. Cosmochim. Acta 36, 347–375.

Blank, J.G., Brooker, R.A., 1994. Experimental studies of carbon dioxide in silicate melts; solubility, speciation, and stable carbon isotope behavior. Rev. Mineral. Geochem. 30, 157–186.

Bodmer, R., Bochsler, P., 2000. Influence of Coulomb collisions on isotopic and elemental fractionation in the solar wind acceleration process. J. Geophys. Res. Space Phys. 105, 47–60.

Bottinga, Y., Richet, P., 1981. High pressure and temperature equation of state and calculation of the thermodynamic properties of gaseous carbon dioxide. Am. J. Sci. 281, 615–660.

Bühler, F., Eberhardt, P., Geiss, J., Meister, J., Signer, P., 1969. Apollo 11 solar wind composition experiment: First results. Science 166, 1502–1503.

Burbidge, E.M., Burbidge, G.R., Fowler, W.A., Hoyle, F., 1957. Synthesis of the elements in stars. Rev. Mod. Phys. 29, 547.

Burnard, P., 2001. Correction for volatile fractionation in ascending magmas: noble gas abundances in primary mantle melts. Geochim. Cosmochim. Acta 65, 2605–2614.

Burnard, P., 1999. The bubble-by-bubble volatile evolution of two mid-ocean ridge basalts. Earth Planet. Sci. Lett. 174, 199–211.

Burnard, P., Graham, D., Turner, G., 1997. Vesicle-specific noble gas analyses of" popping rock": implications for primordial noble gases in Earth. Science 276, 568–571.

Busemann, H., Baur, H., Wieler, R., 2000. Primordial noble gases in “phase Q” in carbonaceous and ordinary chondrites studied by closed-system stepped etching. Meteorit. Planet. Sci. 35, 949–973.

Butler, W., Jeffery, P., Reynolds, J., Wasserburg, G., 1963. Isotopic variations in terrestrial xenon. J. Geophys. Res. 68, 3283–3291.

Canup, R.M., Asphaug, E., 2001. Origin of the Moon in a giant impact near the end of the Earth’s formation. Nature 412, 708–712.

Carroll, M.R., Webster, J.D., 1994. Solubilities of sulfur, noble gases, nitrogen, chlorine, and fluorine in magmas. Rev. Mineral. 30, 231–231.

Chambers, J., 2010. Planetesimal formation by turbulent concentration. Icarus 208, 505–517.

Chavrit, D., 2010. Cartographie globale des flux de CO2 à l’axe des dorsales océaniques: une approche pétrologique.

Chavrit, D., Humler, E., Morizet, Y., Laporte, D., 2012. Influence of magma ascent rate on carbon dioxide degassing at oceanic ridges: Message in a bubble. Earth Planet. Sci. Lett. 357, 376–385.

Clayton, D.D., 1983. Principles of stellar evolution and nucleosynthesis. University of Chicago press.

Colin, A., Moreira, M., Gautheron, C., Burnard, P., 2015. Constraints on the noble gas composition of the deep mantle by bubble-by-bubble analysis of a volcanic glass sample from Iceland. Chem. Geol. 417, 173–183.

Craig, H., Lupton, J., 1976. Primordial neon, helium, and hydrogen in oceanic basalts. Earth Planet. Sci. Lett. 31, 369–385.

Cuzzi, J.N., Hogan, R.C., Shariff, K., 2008. Toward planetesimals: Dense chondrule clumps in the protoplanetary nebula. Astrophys. J. 687, 1432.

Dauphas, N., Burkhardt, C., Warren, P.H., Fang-Zhen, T., 2014. Geochemical arguments for an Earth-like Moon-forming impactor. Philos. Trans. R. Soc. Math. Phys. Eng. Sci. 372, 20130244.

Dauphas, N., Chaussidon, M., 2011. A perspective from extinct radionuclides on a young stellar object: the Sun and its accretion disk. Annu. Rev. Earth Planet. Sci. 39, 351–386.

Dauphas, N., Morbidelli, A., 2013. Geochemical and planetary dynamical views on the origin of Earth's atmosphere and oceans. ArXiv Prepr. ArXiv13121202.

Dauphas, N., Pourmand, A., 2011. Hf–W–Th evidence for rapid growth of Mars and its status as a planetary embryo. Nature 473, 489–492.

D'E Atkinson, R., Houtermans, F., 1929. Transmutation of the Lighter Elements in Stars. Nature 123, 567–568.

Di Carlo, I., Pichavant, M., Rotolo, S.G., Scaillet, B., 2006. Experimental crystallization of a high-K arc basalt: the golden pumice, Stromboli volcano (Italy). J. Petrol. 47, 1317–1343.

Dickin, A.P., 2018. Radiogenic isotope geology. Cambridge university press.

Dixon, J.E., Pan, V., 1995a. Determination of the molar absorptivity of dissolved carbonate in basanitic glass. Am. Mineral. 80, 1339–1342.

Dixon, J.E., Pan, V., 1995b. Determination of the molar absorptivity of dissolved carbonate in basanitic glass. Am. Mineral. 80, 1339–1342.

Dixon, J.E., Stolper, E.M., Holloway, J.R., 1995. An experimental study of water and carbon dioxide solubilities in mid-ocean ridge basaltic liquids. Part I: calibration and solubility models. J. Petrol. 36, 1607–1631.

Donahue, T., Russell, C., 1997. The Venus atmosphere and ionosphere and their interaction with the solar wind: An overview. Venus II Geol. Geophys. Atmosphere Sol. Wind Environ. 3.

Douglass, J., Schilling, J., Fontignie, D., 1999. Plume-ridge interactions of the Discovery and Shona mantle plumes with the southern Mid-Atlantic Ridge (40°-55° S). J. Geophys. Res. Solid Earth 104, 2941–2962.

Eberhardt, P., Geiss, J., Graf, H., Grögler, N., Krähenbühl, U., Schwaller, H., Schwarzmüller, J., Stettler, A., 1970. Trapped solar wind noble gases, exposure age and K/Ar-age in Apollo 11 lunar fine material. Presented at the Geochimica et Cosmochimica Acta Supplement, Volume 1. Proceedings of the Apollo 11 Lunar Science Conference held 5-8 January, 1970 in Houston, TX. Volume 2: Chemical and Isotope Analyses. Edited by AA Levinson. New York: Pergammon Press, 1970., p. 1037, p. 1037.

Eberhardt, P., Geiss, J., Graf, H., Grögler, N., Mendia, M., Mörgeli, M., Schwaller, H., Stettler, A., Krähenbühl, U., Von Gunten, H., 1972. Trapped solar wind noble gases in Apollo 12 lunar fines 12001 and Apollo 11 breccia 10046. Bern Univ.(Switzerland).

Farrell, W.M., Hurley, D.M., Zimmerman, M.I., 2015. Solar wind implantation into lunar regolith: Hydrogen retention in a surface with defects. Icarus 255, 116–126.

Fine, G., Stolper, E., 1985. The speciation of carbon dioxide in sodium aluminosilicate glasses. Contrib. Mineral. Petrol. 91, 105–121.

Frost, B.R., 2018. Introduction to oxygen fugacity and its petrologic importance, in: Oxide Minerals. De Gruyter, pp. 1–10.

Geiss, J., Bühler, F., Cerutti, H., Eberhardt, P., Filleux, C., Meister, J., Signer, P., 2004. The Apollo SWC experiment: results, conclusions, consequences. Space Sci. Rev. 110, 307–335.

Geiss, J, Eberhardt, P., Bühler, F., Meister, J., Signer, P., 1970. Apollo 11 and 12 solar wind composition experiments: Fluxes of He and Ne isotopes. J. Geophys. Res. 75, 5972–5979.

Geiss, Johannes, Hirt, P., Leutwyler, H., 1970. On acceleration and motion of ions in corona and solar wind. Sol. Phys. 12, 458–483.

Giordano, D., Russell, J.K., Dingwell, D.B., 2008. Viscosity of magmatic liquids: a model. Earth Planet. Sci. Lett. 271, 123–134.

Gonnermann, H.M., Manga, M., 2007. The fluid mechanics inside a volcano. Annu Rev Fluid Mech 39, 321–356.

Graham, D.W., 2002. Noble Gas Isotope Geochemistry of Mid-Ocean Ridge and Ocean Island Basalts: Characterization of Mantle Source Reservoirs. Rev. Mineral. Geochem. 47, 247–317. https://doi.org/10.2138/rmg.2002.47.8

Grimberg, A., Baur, H., Bochsler, P., Bühler, F., Burnett, D.S., Hays, C.C., Heber, V.S., Jurewicz, A.J., Wieler, R., 2006. Solar wind neon from Genesis: Implications for the lunar noble gas record. Science 314, 1133–1135.

Harper Jr, C.L., Jacobsen, S.B., 1996. Noble gases and Earth's accretion. Science 273, 1814–1818.

Hashizume, K., Chaussidon, M., Marty, B., Robert, F., 2000. Solar wind record on the Moon: deciphering presolar from planetary nitrogen. Science 290, 1142–1145.

Heber, V.S., Baur, H., Bochsler, P., McKeegan, K.D., Neugebauer, M., Reisenfeld, D.B., Wieler, R., Wiens, R.C., 2012. Isotopic mass fractionation of solar wind: Evidence from fast and slow solar wind collected by the Genesis mission. Astrophys. J. 759, 121.

Heber, V.S., Wieler, R., Baur, H., Olinger, C., Friedmann, T.A., Burnett, D.S., 2009. Noble gas composition of the solar wind as collected by the Genesis mission. Geochim. Cosmochim. Acta 73, 7414–7432.

Holland, G., Ballentine, C.J., 2006a. Seawater subduction controls the heavy noble gas composition of the mantle. Nature 441, 186–191.

Holland, G., Ballentine, C.J., 2006b. Seawater subduction controls the heavy noble gas composition of the mantle. Nature 441, 186–191.

Holland, G., Cassidy, M., Ballentine, C.J., 2009. Meteorite Kr in Earth's mantle suggests a late accretionary source for the atmosphere. Science 326, 1522–1525.

Hollenbach, D.J., Yorke, H.W., Johnstone, D., 2000. Disk dispersal around young stars. Protostars Planets IV 401, 12.

Honda, M., McDougall, I., Patterson, D.B., Doulgeris, A., Clague, D.A., 1991. Possible solar noble-gas component in Hawaiian basalts. Nature 349, 149–151.

Honda, M., Reynolds, J., Roedder, E., Epstein, S., 1987. Noble gases in diamonds: Occurrences of solarlike helium and neon. J. Geophys. Res. Solid Earth 92, 12507–12521.

Iacono-Marziano, G., Paonita, A., Rizzo, A., Scaillet, B., Gaillard, F., 2010. Noble gas solubilities in silicate melts: new experimental results and a comprehensive model of the effects of liquid composition, temperature and pressure. Chem. Geol. 279, 145–157.

Jambon, A., Weber, H., Braun, O., 1986. Solubility of He, Ne, Ar, Kr and Xe in a basalt melt in the range 1250–1600 C. Geochemical implications. Geochim. Cosmochim. Acta 50, 401–408.

Jaupart, E., Charnoz, S., Moreira, M., 2017. Primordial atmosphere incorporation in planetary embryos and the origin of Neon in terrestrial planets. Icarus 293, 199–205.

Javoy, M., Pineau, F., 1991. The volatiles record of a "popping" rock from the Mid-Atlantic Ridge at 14 N: chemical and isotopic composition of gas trapped in the vesicles. Earth Planet. Sci. Lett. 107, 598–611.

Jiménez-Mejías, M., Andújar, J., Scaillet, B., Casillas, R., 2021. Experimental determination of H $ _ {{2}} $ O and CO $ _ {{2}} $ solubilities of mafic alkaline magmas from Canary Islands. Comptes Rendus Géoscience 353, 289–314.

Johansen, A., Klahr, H., 2011. Planetesimal formation through streaming and gravitational instabilities. Earth Moon Planets 108, 39–43.

Johansen, A., Klahr, H., Henning, T., 2011. High-resolution simulations of planetesimal formation in turbulent protoplanetary discs. Astron. Astrophys. 529, A62.

Johansen, A., Oishi, J.S., Low, M.-M.M., Klahr, H., Henning, T., Youdin, A., 2007. Rapid planetesimal formation in turbulent circumstellar disks. Nature 448, 1022–1025.

Kendrick, M.A., Burnard, P., 2013. Noble gases and halogens in fluid inclusions: a journey through the Earth's crust. Noble Gases Geochem. Tracers 319–369.

Kennedy, B., Hiyagon, H., Reynolds, J., 1990. Crustal neon: a striking uniformity. Earth Planet. Sci. Lett. 98, 277–286.

Kennedy, B.M., Hiyagon, H., Reynolds, J.H., 1990. Crustal neon: a striking uniformity. Earth Planet. Sci. Lett. 98, 277–286. https://doi.org/10.1016/0012-821X(90)90030-2

Kipfer, R., Aeschbach-Hertig, W., Peeters, F., Stute, M., 2002. Noble gases in lakes and ground waters. Rev. Mineral. Geochem. 47, 615–700.

Kress, V.C., Carmichael, I.S., 1991. The compressibility of silicate liquids containing Fe 2 O 3 and the effect of composition, temperature, oxygen fugacity and pressure on their redox states. Contrib. Mineral. Petrol. 108, 82–92.

Krummenacher, D., 1970. Isotopic composition of argon in modern surface volcanic rocks. Earth Planet. Sci. Lett. 8, 109–117.

Kunz, J., 1999. Is there solar argon in the Earth's mantle? Nature 399, 649–650. https://doi.org/10.1038/21352

Kuroda, P., 1960. Nuclear fission in the early history of the earth. Nature 187.

Kurz, M.D., 1986. Cosmogenic helium in a terrestrial igneous rock. Nature 320, 435–439. https://doi.org/10.1038/320435a0

Kurz, M.D., Curtice, J., Fornari, D., Geist, D., Moreira, M., 2009. Primitive neon from the center of the Galápagos hotspot. Earth Planet. Sci. Lett. 286, 23–34.

Lange, R.A., 1994a. Volatiles in Magmas, in: Carroll, M.R., Holloway, J.R. (Eds.), . De Gruyter, pp. 331–370. https://doi.org/10.1515/9781501509674-015

Lange, R.A., 1994b. Volatiles in Magmas, in: Carroll, M.R., Holloway, J.R. (Eds.), . De Gruyter, pp. 331–370. https://doi.org/10.1515/9781501509674-015

Le Gall, N., 2015. Ascension et dégazage des magmas basaltiques: approche expérimentale.

Le Gall, N., Pichavant, M., 2016a. Experimental simulation of bubble nucleation and magma ascent in basaltic systems: Implications for Stromboli volcano. Am. Mineral. 101, 1967–1985.

Le Gall, N., Pichavant, M., 2016b. Homogeneous bubble nucleation in H2O-and H2O-CO2-bearing basaltic melts: results of high temperature decompression experiments. J. Volcanol. Geotherm. Res. 327, 604–621.

Le Roux, P., Le Roex, A., Schilling, J.-G., Shimizu, N., Perkins, W., Pearce, N., 2002. Mantle heterogeneity beneath the southern Mid-Atlantic Ridge: trace element evidence for contamination of ambient asthenospheric mantle. Earth Planet. Sci. Lett. 203, 479–498.

Lensky, N.G., Niebo, R.W., Holloway, J.R., Lyakhovsky, V., Navon, O., 2006. Bubble nucleation as a trigger for xenolith entrapment in mantle melts. Earth Planet. Sci. Lett. 245, 278–288.

Lux, G., 1987. The behavior of noble gases in silicate liquids: Solution, diffusion, bubbles and surface effects, with applications to natural samples. Geochim. Cosmochim. Acta 51, 1549–1560.

Mangan, M., Sisson, T., 2000. Delayed, disequilibrium degassing in rhyolite magma: decompression experiments and implications for explosive volcanism. Earth Planet. Sci. Lett. 183, 441–455.

Marsh, B.D., 2007. Crystallization of silicate magmas deciphered using crystal size distributions. J. Am. Ceram. Soc. 90, 746–757.

Marsh, B.D., 1988. Crystal size distribution (CSD) in rocks and the kinetics and dynamics of crystallization: I. Theory. Contrib. Mineral. Petrol. 99, 277–291.

Marty, B., 2022. Meteoritic noble gas constraints on the origin of terrestrial volatiles. Icarus 381, 115020.

Marty, B., 2020. ORIGINS AND EARLY EVOLUTION OF THE ATMOSPHERE AND THE OCEANS. Geochem. Perspect. 9, 135–136.

Marty, B., 2012. The origins and concentrations of water, carbon, nitrogen and noble gases on Earth. Earth Planet. Sci. Lett. 313, 56–66.

Marty, B., Yokochi, R., 2006. Water in the early Earth. Rev. Mineral. Geochem. 62, 421–450.

Marty, B., Zimmermann, L., 1999. Volatiles (He, C, N, Ar) in mid-ocean ridge basalts: Assesment of shallow-level fractionation and characterization of source composition. Geochim. Cosmochim. Acta 63, 3619–3633.

McDonnell, J., Flavill, R., 1974. Sputter Erosion on the Lunar Surface: Measurements and Features Under Simulated Solar He+ Bombardment. Lunar Planet. Sci. V Houst. Lunar Planet Inst 478.

Mizuno, H., Nakazawa, K., Hayashi, C., 1980. Dissolution of the primordial rare gases into the molten Earth's material. Earth Planet. Sci. Lett. 50, 202–210.

Morbidelli, A., Bottke, W.F., Nesvorný, D., Levison, H.F., 2009. Asteroids were born big. Icarus 204, 558–573.

Moreira, M., 2013. Noble gas constraints on the origin and evolution of Earth's volatiles. Geochem. Perspect. 2, 229–230.

Moreira, M., Blusztajn, J., Curtice, J., Hart, S., Dick, H., Kurz, M.D., 2003. He and Ne isotopes in oceanic crust: implications for noble gas recycling in the mantle. Earth Planet. Sci. Lett. 216, 635–643.

Moreira, M., Charnoz, S., 2016. The origin of the neon isotopes in chondrites and on Earth. Earth Planet. Sci. Lett. 433, 249–256. https://doi.org/10.1016/j.epsl.2015.11.002

Moreira, M., Kunz, J., Allegre, C., 1998. Rare gas systematics in popping rock: isotopic and elemental compositions in the upper mantle. Science 279, 1178–1181.

Moreira, M., Rouchon, V., Muller, E., Noirez, S., 2018. The xenon isotopic signature of the mantle beneath Massif Central. Geochem Perspect Lett 6, 28–32.

Moreira, M., Sarda, P., 2000. Noble gas constraints on degassing processes. Earth Planet. Sci. Lett. 176, 375–386.

Moreira, M., Staudacher, T., Sarda, P., Schilling, J.-G., Allègre, C.J., 1995. A primitive plume neon component in MORB: The Shona ridge-anomaly, South Atlantic (51–52° S). Earth Planet. Sci. Lett. 133, 367–377.

Moretti, R., Papale, P., Ottonello, G., 2003. A model for the saturation of COHS fluids in silicate melts. Geol. Soc. Lond. Spec. Publ. 213, 81–101.

Mourtada-Bonnefoi, C., Laporte, D., 2002. Homogeneous bubble nucleation in rhyolitic magmas: an experimental study of the effect of H2O and CO2. J. Geophys. Res. Solid Earth 107, ECV-2.

Mourtada-Bonnefoi, C.C., Laporte, D., 2004. Kinetics of bubble nucleation in a rhyolitic melt: an experimental study of the effect of ascent rate. Earth Planet. Sci. Lett. 218, 521–537.

Mukhopadhyay, S., 2012. Early differentiation and volatile accretion recorded in deep-mantle neon and xenon. Nature 486, 101–104. https://doi.org/10.1038/nature11141

Nowak, M., Schreen, D., Spickenbom, K., 2004. Argon and CO2 on the race track in silicate melts: a tool for the development of a CO2 speciation and diffusion model. Geochim. Cosmochim. Acta 68, 5127–5138.

Nuccio, P., Paonita, A., 2001. Magmatic degassing of multicomponent vapors and assessment of magma depth: application to Vulcano Island (Italy). Earth Planet. Sci. Lett. 193, 467–481.

Nuccio, P., Paonita, A., 2000. Investigation of the noble gas solubility in H2O–CO2 bearing silicate liquids at moderate pressure II: the extended ionic porosity (EIP) model. Earth Planet. Sci. Lett. 183, 499–512.

Olson, P.L., Sharp, Z.D., 2019. Nebular atmosphere to magma ocean: a model for volatile capture during Earth accretion. Phys. Earth Planet. Inter. 294, 106294.

Ozima, M., Podosek, F.A., 2002. Noble gas geochemistry. Cambridge University Press.

Ozima, M., Zashu, S., 1991. Noble gas state of the ancient mantle as deduced from noble gases in coated diamonds. Earth Planet. Sci. Lett. 105, 13–27.

Ozima, M., Zashu, S., 1988a. Solar-type Ne in Zaire cubic diamonds. Geochim. Cosmochim. Acta 52, 19–25.

Ozima, M., Zashu, S., 1988b. Solar-type Ne in Zaire cubic diamonds. Geochim. Cosmochim. Acta 52, 19–25.

Paonita, A., 2005. Noble gas solubility in silicate melts: a review of experimentation and theory, and implications regarding magma degassing processes. Ann. Geophys.

Paonita, A., Gigli, G., Gozzi, D., Nuccio, P., Trigila, R., 2000. Investigation of the He solubility in H2O–CO2 bearing silicate liquids at moderate pressure: a new experimental method. Earth Planet. Sci. Lett. 181, 595–604.

Pepin, R., Nyquist, L., Phinney, D., Black, D.C., 1970. Isotopic composition of rare gases in lunar samples. Science 167, 550–553.

Pepin, R.O., 1991. On the origin and early evolution of terrestrial planet atmospheres and meteoritic volatiles. Icarus 92, 2–79.

Pepin, R.O., Schlutter, D.J., Becker, R.H., Reisenfeld, D.B., 2012. Helium, neon, and argon composition of the solar wind as recorded in gold and other Genesis collector materials. Geochim. Cosmochim. Acta 89, 62–80.

Péron, S., Moreira, M., Agranier, A., 2018. Origin of light noble gases (He, Ne, and Ar) on Earth: A review. Geochem. Geophys. Geosystems 19, 979–996.

Péron, S., Moreira, M., Colin, A., Arbaret, L., Putlitz, B., Kurz, M.D., 2016. Neon isotopic composition of the mantle constrained by single vesicle analyses. Earth Planet. Sci. Lett. 449, 145–154. https://doi.org/10.1016/j.epsl.2016.05.052

Péron, S., Moreira, M., Putlitz, B., Kurz, M., 2017. Solar wind implantation supplied light volatiles during the first stage of Earth accretion. Geochem. Perspect. Lett. 151–159.

Péron, S., Moreira, M.A., Kurz, M.D., Curtice, J., Blusztajn, J.S., Putlitz, B., Wanless, V.D., Jones, M.R., Soule, S.A., Mittelstaedt, E., 2019. Noble gas systematics in new popping rocks from the Mid-Atlantic Ridge (14° N): evidence for small-scale upper mantle heterogeneities. Earth Planet. Sci. Lett. 519, 70–82.

Pichavant, M., Di Carlo, I., Le Gac, Y., Rotolo, S.G., Scaillet, B., 2009. Experimental constraints on the deep magma feeding system at Stromboli volcano, Italy. J. Petrol. 50, 601–624.

Pichavant, M., Di Carlo, I., Rotolo, S.G., Scaillet, B., Burgisser, A., Le Gall, N., Martel, C., 2013. Generation of CO 2-rich melts during basalt magma ascent and degassing. Contrib. Mineral. Petrol. 166, 545–561.

Pichavant, M., Le Gall, N., Scaillet, B., 2018. Gases as precursory signals: experimental simulations, new concepts and models of magma degassing. Volcan. Unrest Adv Volcanol 139–154.

Pierre Jules César Janssen, 1908. . Mon. Not. R. Astron. Soc. 68, 245–249. https://doi.org/10.1093/mnras/68.4.245

Porcelli, D., Ballentine, C.J., Wieler, R., 2002. An overview of noble gas geochemistry and cosmochemistry. Rev. Mineral. Geochem. 47, 1–19.

Porcelli, D., Woolum, D., Cassen, P., 2001. Deep Earth rare gases: initial inventories, capture from the solar nebula, and losses during Moon formation. Earth Planet. Sci. Lett. 193, 237–251.

Poreda, R., di Brozolo, F.R., 1984. Neon isotope variations in Mid-Atlantic Ridge basalts. Earth Planet. Sci. Lett. 69, 277–289.

Raquin, A., Moreira, M., 2009. Atmospheric 38Ar/36Ar in the mantle: implications for the nature of the terrestrial parent bodies. Earth Planet. Sci. Lett. 287, 551–558.

Raquin, A., Moreira, M.A., Guillon, F., 2008. He, Ne and Ar systematics in single vesicles: mantle isotopic ratios and origin of the air component in basaltic glasses. Earth Planet. Sci. Lett. 274, 142–150.

Raymond, S.N., O'Brien, D.P., Morbidelli, A., Kaib, N.A., 2009. Building the terrestrial planets: Constrained accretion in the inner Solar System. Icarus 203, 644–662.

Reynolds, J., Hohenberg, C., Lewis, R., Davis, P., Kaiser, W., 1970. Isotopic analysis of rare gases from stepwise heating of lunar fines and rocks. Science 167, 545–548.

Reynolds, J., Turner, G., 1964. Rare gases in the chondrite Renazzo. J. Geophys. Res. 69, 3263–3281.

Rolfs, C.E., Rodney, W.S., 1988. Cauldrons in the cosmos: Nuclear astrophysics. University of Chicago press.

Roubinet, C., Moreira, M.A., 2018. Atmospheric noble gases in Mid-Ocean Ridge Basalts: identification of atmospheric contamination processes. Geochim. Cosmochim. Acta 222, 253–268.

Ruzié, L., Moreira, M., 2010. Magma degassing process during Plinian eruptions. J. Volcanol. Geotherm. Res. 192, 142–150.

Saltykov, S., 1967. Stereology: proceedings of the second international congress for stereology, chapter The determination of the size distribution of particles in an opaque material from a measurement of the size distribution of their sections.

Sarda, P., Graham, D., 1990. Mid-ocean ridge popping rocks: implications for degassing at ridge crests. Earth Planet. Sci. Lett. 97, 268–289.

Sarda, P., Moreira, M., 2002. Vesiculation and vesicle loss in mid-ocean ridge basalt glasses: He, Ne, Ar elemental fractionation and pressure influence. Geochim. Cosmochim. Acta 66, 1449–1458.

Sarda, P., Moreira, M., Staudacher, T., Schilling, J., Allègre, C.J., 2000. Rare gas systematics on the southernmost Mid-Atlantic Ridge: Constraints on the lower mantle and the Dupal source. J. Geophys. Res. Solid Earth 105, 5973–5996.

Sarda, P., Staudacher, T., Allègre, C.J., 1988. Neon isotopes in submarine basalts. Earth Planet. Sci. Lett. 91, 73–88. https://doi.org/10.1016/0012-821X(88)90152-5

Sasaki, S., 1999. Presence of a primary solar-type atmosphere around the earth: evidence of dissolved noble gas. Planet. Space Sci. 47, 1423–1431.

Sasaki, S., Nakazawa, K., 1990. Did a primary solar-type atmosphere exist around the proto-earth? Icarus 85, 21–42. https://doi.org/10.1016/0019-1035(90)90101-E

Scarpa, R., Tilling, R.I., Giggenbach, W., 1996. Chemical composition of volcanic gases. Monit. Mitig. Volcano Hazards 221–256.

Schlosser, P., Winckler, G., 2002. Noble gases in ocean waters and sediments. Rev. Mineral. Geochem. 47, 701–730.

Shinohara, H., Aiuppa, A., Giudice, G., Gurrieri, S., Liuzzo, M., 2008. Variation of H2O/CO2 and CO2/SO2 ratios of volcanic gases discharged by continuous degassing of Mount Etna volcano, Italy. J. Geophys. Res. Solid Earth 113.

Shishkina, T.A., Botcharnikov, R.E., Holtz, F., Almeev, R.R., Jazwa, A.M., Jakubiak, A.A., 2014. Compositional and pressure effects on the solubility of H2O and CO2 in mafic melts. Chem. Geol. 388, 112–129.

Sparks, R.S.J., 1978. The dynamics of bubble formation and growth in magmas: a review and analysis. J. Volcanol. Geotherm. Res. 3, 1–37.

Staudacher, T., Allègre, C.J., 1988. Recycling of oceanic crust and sediments: the noble gas subduction barrier. Earth Planet. Sci. Lett. 89, 173–183.

Staudacher, T., Sarda, P., Richardson, S., Allègre, C., Sagna, I., Dmitriev, L., 1989. Noble gases in basalt glasses from a Mid-Atlantic Ridge topographic high at 14 N: geodynamic consequences. Earth Planet. Sci. Lett. 96, 119–133.

Stolper, E., 1982. Water in silicate glasses: an infrared spectroscopic study. Contrib. Mineral. Petrol. 81, 1–17.

Stout, V.L., Gibbons, M.D., 1955. Gettering of gas by titanium. J. Appl. Phys. 26, 1488–1492.

Sumino, H., Kaneoka, I., Matsufuji, K., Sobolev, A.V., 2006. Deep mantle origin of kimberlite magmas revealed by neon isotopes. Geophys. Res. Lett. 33.

Tolstikhin, I., O'Nions, R., 1994. The Earth's missing xenon: A combination of early degassing and of rare gas loss from the atmosphere. Chem. Geol. 115, 1–6.

Trieloff, M., Kunz, J., Clague, D.A., Harrison, D., Allègre, C.J., 2000. The Nature of Pristine Noble Gases in Mantle Plumes. Science 288, 1036–1038. https://doi.org/10.1126/science.288.5468.1036

Warren, P.H., 1995. Extrapolated partial molar densities of SO3, P2O5, and other oxides in silicate melts. Am. Mineral. 80, 1085–1088.

Watson, E.B., Sneeringer, M.A., Ross, A., 1982. Diffusion of dissolved carbonate in magmas: experimental results and applications. Earth Planet. Sci. Lett. 61, 346–358.

Wetherill, G.W., 1954a. Variations in the isotopic abundances of neon and argon extracted from radioactive minerals. Phys. Rev. 96, 679.

Wetherill, G.W., 1954b. Variations in the isotopic abundances of neon and argon extracted from radioactive minerals. Phys. Rev. 96, 679.
Wetherill, G.W., 1953a. Spontaneous fission yields from uranium and thorium. Phys. Rev. 92, 907.
Wetherill, G.W., 1953b. Spontaneous fission yields from uranium and thorium. Phys. Rev. 92, 907.
Wieler, R., 2002. Cosmic-ray-produced noble gases in meteorites. Rev. Mineral. Geochem. 47, 125–170.
Wieler, R., 1998. The solar noble gas record in lunar samples and meteorites. Space Sci. Rev. 85, 303–314.
Williams, C.D., Mukhopadhyay, S., 2019. Capture of nebular gases during Earth's accretion is preserved in deep-mantle neon. Nature 565, 78–81. https://doi.org/10.1038/s41586-018-0771-1
Yatsevich, I., Honda, M., 1997a. Production of nucleogenic neon in the Earth from natural radioactive decay. J. Geophys. Res. Solid Earth 102, 10291–10298.
Yatsevich, I., Honda, M., 1997b. Production of nucleogenic neon in the Earth from natural radioactive decay. J. Geophys. Res. Solid Earth 102, 10291–10298.
Yokochi, R., Marty, B., 2004. A determination of the neon isotopic composition of the deep mantle. Earth Planet. Sci. Lett. 225, 77–88. https://doi.org/10.1016/j.epsl.2004.06.010
Yoshimura, S., 2015. Diffusive fractionation of H2O and CO2 during magma degassing. Chem. Geol. 411, 172–181.
Zadnik, M., Jeffery, P., 1985. Radiogenic neon in an Archaean anorthosite. Chem. Geol. Isot. Geosci. Sect. 52, 119–125.
Zhang, Y., Ni, H., Chen, Y., 2010. Diffusion data in silicate melts. Rev. Mineral. Geochem. 72, 311–408.
Zhang, Y., Xu, Z., 1995. Atomic radii of noble gas elements in condensed phases. Am. Mineral. 80, 670–675.
Zhang, Y., Xu, Z., Zhu, M., Wang, H., 2007. Silicate melt properties and volcanic eruptions. Rev. Geophys. 45.
Zhang, Y., Zindler, A., 1989. Noble gas constraints on the evolution of the Earth's atmosphere. J. Geophys. Res. Solid Earth 94, 13719–13737.

Chapitre 3 : Nucléation et évolution de bulles dans un système basaltique : un premier test pour contraindre la vésiculation dans un système statique hors équilibre.

Dans une masse fondue de silicates, les éléments volatils sont les espèces chimiques dissoutes dans le liquide qui, lorsqu'elles sont sursaturées, passent dans la phase vapeur. Le magma atteint la sursaturation lorsque la pression des espèces volatiles devient supérieure à la pression du système, par exemple lorsque la pression change lors de la dépressurisation de la chambre magmatique. Les espèces volatiles les plus abondantes dans les systèmes magmatiques naturels sont H_2O, CO_2 et S sous forme de H_2S et SO_2. Le soufre peut devenir pertinent lorsque son pourcentage en poids dissous dépasse quelques dixièmes de pour cent. Les matières fondues silicatées dissolvent l'eau plus facilement que le CO_2, ce qui fait du CO_2 la première espèce volatile à former des bulles.

À mesure que la phase gazeuse s'exsolve, d'autres espèces volatiles mineures se répartissent entre le liquide et le gaz en fonction de leur solubilité et de leur diffusivité dans la masse fondue de silicates, y compris les gaz rares. Les espèces les moins solubles sont corrélées à une phase fondue de silicates appauvrie et à une concentration accrue dans la phase gazeuse.

Les magmas basaltiques ont une température élevée et une faible viscosité, permettant une diffusion rapide des éléments volatils. Lorsque ces éléments atteignent leur saturation dans la masse fondue, ils s'échappent rapidement vers la phase gazeuse en formant des vésicules. Les études ont constamment montré que la diffusivité des volatils suit la loi d'Arrhenius.

Selon le modèle de porosité ionique étendu (EIP) de Nuccio et Paonita (2000), pour des conditions de pression et de température données, la solubilité des gaz rares dans une fonte basaltique augmente à mesure que la quantité de CO_2 dissous diminue (voir figure 3.2). En raison de leur solubilité relativement faible par rapport à H_2O, les gaz rares se répartissent de plus en plus dans la phase gazeuse à mesure que la quantité

de CO_2 augmente. Le modèle suppose que le nombre d'atomes de gaz rares dissous est proportionnel au nombre de sites disponibles pouvant accueillir des atomes de cette taille.

Le modèle classique de dégazage dans les fontes basaltiques propose que le CO_2 soit en grande partie perdu dans la phase gazeuse du réservoir avant l'ascension du magma (Dixon et al., 1995).

Ce chapitre propose une approche expérimentale de la nucléation de vésicules de CO_2 pur avant que l'équilibre ne soit atteint pour mieux comprendre cette première étape de dégazage à travers leur nucléation, leur croissance et leur coalescence.

Chapter 3: Bubble nucleation and evolution in a basaltic system: a first test for constraining vesiculation in a non-equilibrium static system.

3.1. Introduction:

In a silicate melt, volatile elements are chemical species dissolved in the liquid. When the melt becomes supersaturated, these volatiles separate into the vapor phase. Supersaturation happens when the pressure of the volatile species exceeds the system's pressure, such as during depressurization of a magma chamber, when the pressure decreases. The most abundant volatile species in natural magmatic systems are H_2O, CO_2, and S in the form of H_2S and SO_2. Sulphur may be relevant when the wt.% dissolved exceeds a few tenths of a per cent (Moretti et al., 2003). Silicate melts dissolve water more readily than CO_2, resulting in CO_2 being the first volatile species to nucleate bubbles.

As the gas phase exsolves, other minor volatile species are partitioned between the liquid and gas depending on their solubility and diffusivity in the silicate melt (Scarpa et al., 1996; Paonita, 2005; Gonnermann and Manga, 2007), including noble gases. The less soluble species is correlated to a depleted silicate melt phase and an increased concentration in the gas phase. **Figure 3.1** provides an example of the residual fraction of volatile species in tholeiitic melt **a.** (Paonita, 2005) and basaltic melts **b** (Jambon et al., 1986)**.**

Following the extended ionic porosity model, EIP, from (Nuccio and Paonita, 2000), for given pressure and temperature conditions, noble gas solubility in a basaltic melt increases by increasing dissolved CO_2 (refers to **Figure 3.2.**). The model explains noble gas solubility based on the availability of appropriately sized interstitial holes in the silicate melt, which is influenced by the melt's composition (e.g., H_2O and CO_2 content) and the size of the noble gas atoms. Due to its small solubility compared to H_2O, noble gases are increasingly partitioned into the gas phase as the amount of CO_2 increases.

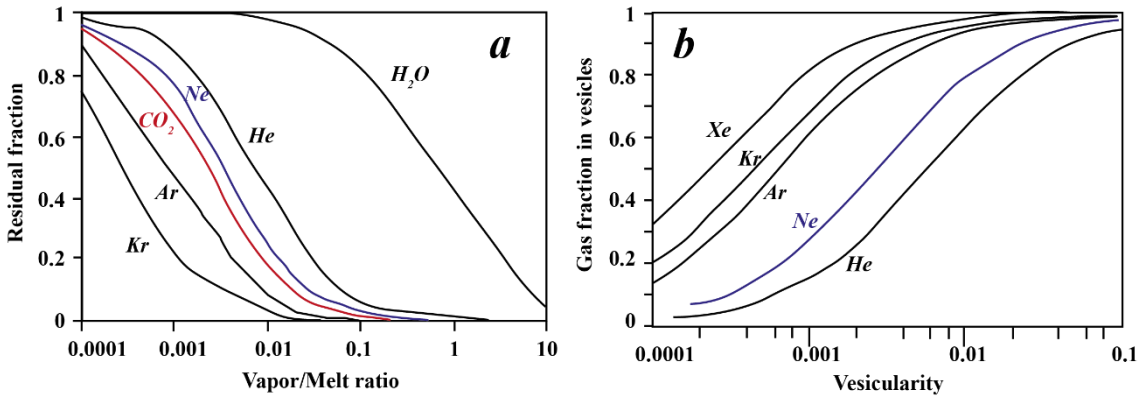

Figure 3.1.: (a) residual fraction of volatile elements remaining in a tholeiitic melt concerning the amount of exsolved vapor during closed system degassing (Paonita, 2005). **(b)** noble gas partitioned into the vesicles in a basaltic glass concerning the amount of exsolved vapor during closed system degassing (Jambon et al., 1986).

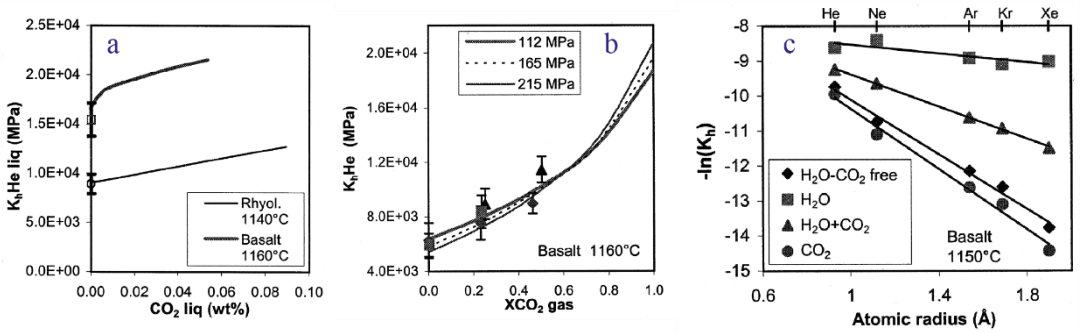

Figure 3.2.: Solubility of noble gasses in basaltic melts based on ionic porosity (Nuccio and Paonita, 2000). (**a**) The model shows the solubility of He, as K_h (Henry's constant), versus CO_2 dissolved in the glass in a CO_2-He-Silicate melt system. For two different composition (rhyolitic and basaltic) the increase of the CO_2 in the liquid increases the solubility of helium. In a basaltic melt. Figure (**b**) shows the how the solubility of He (K_h) increases with the molar fraction of CO2 in the vapor at different pressures: 112 MPa (thicker line), 165 MPa (dashed line and 215 MPa (thinner line). In **(c)** is show the model of Solubility of noble gases from the EIP model and is based on the relationship between the concentration of dissolved noble gas and ionic porosity of the melt. The model computed the noble gassed dissolved for different volatiles presence (H_2O and CO_2) in a basaltic melt at isothermal and isobaric conditions (1150 ºC and 200 MPa).

Basaltic magmas have an elevated temperature and low viscosity, which enables rapid diffusion of volatile elements. When these elements reach their saturation in the melt, they quickly escape to the gas phase forming vesicles. Studies have consistently shown that the volatile diffusivity follows Arrhenius's law. Therefore, the resulting diffusion coefficients can be expressed succinctly by the general equation:

$$D = D_0 exp\left(\frac{-E_a}{RT}\right)$$

Where D is the diffusion coefficient in $m^2 \cdot s^{-1}$, D_0 is the preexponential factor ($m^2 \cdot s^{-1}$), E_a is the activation energy in $J \cdot mol^{-1}$; R is the gas constant, 8.3143 $J \cdot K^{-1} \cdot mol^{-1}$, and T is the temperature in Kelvins.

In most silicate melts, CO_2 is the most abundant volatile species, dissolved either as CO_2 molecules or as carbonate groups (Fine and Stolper, 1985; Blank and Brooker, 1994). Unlike H_2O, CO_2 diffusion does not depend on the composition of the anhydrous magma and its concentration is a multi-species, as CO_2 and as CO_3^{2-}. The predominant C-bearing species in basaltic melts is CO_3^{2-} (Zhang et al., 2007). Perhaps because of the similarity in atomic size and mass to Ar, CO_2 diffusion is approximately the same as the chemical diffusivity of Ar in silicate melts (Zhang and Xu, 1995; Behrens and Zhang, 2001; Nowak et al., 2004; Zhang et al., 2007), and is described as:

$$\ln D_{CO_2} = -13.99 - \frac{17367 + 1.9448 * P}{T} + \frac{(855.2 + 0.2712P) * C_w}{T}$$

Where D_{CO2} is CO_2 diffusivity in $m^2 \cdot s^{-1}$, P is the pressure in MPa, T is the temperature in Kelvins, and C_w is the weight per cent of H_2O. It is important to highlight that this equation can be used to estimate diffusivity at T in the range of 773 – 1773 K, P ≤1 GPa and < 5wt.% H_2O. This is derived from the previous equation using an E_a = 144.4 $kJ \cdot mol^{-1}$.

In anhydrous magmas, like in alkaline basaltic melts, CO_2 can start nucleating at pressure oversaturation typically ranging from 20 to 100 MPa (Lensky et al., 2006). Homogeneous nucleation occurs when the melt reaches this high-pressure oversaturation. While, in hydrous magmas, the presence of water reduces the melt's viscosity and affects volatile behaviour, lowering the threshold for bubble nucleation. As a result, CO_2 can nucleate at significantly lower pressures than anhydrous systems, often below 20 MPa (Le Gall and Pichavant, 2016). The exact pressures vary depending on the melt

composition and volatile content, but water generally facilitates earlier CO_2 degassing by reducing the nucleation pressure threshold.

As mentioned earlier, CO_2 will exsolve first at high pressures, followed by H_2O at shallower depths. Consequently, neon is expected to partition into the gas phase during the early stages of vesiculation, when CO_2 starts exsolving. Given that neon is a volatile species that diffuses faster than CO_2, the key question is how this early bubble nucleation phase influences the initial neon isotopic composition in the melt. The timing and behaviour of neon exsolution could play a significant role in shaping the isotopic signature observed during degassing.

3.2. Experimental strategy:

The classical model of degassing in basalt melts proposes that CO_2 is largely lost to the gas phase in the reservoir before magma ascent, (Dixon et al., 1995). An experimental approach that investigates the nucleation of pure CO_2 vesicles before reaching equilibrium can provide valuable insights into the initial stages of degassing.

Based on the diffusion rates and solubility of CO_2, the aim is to adapt our experiments to different time ranges according to the composition and the grain size of the silicate powder used for the experiments.

For the initial set of experiments, before exploring how early nucleation and bubble growth affect minor species like neon, this chapter proposes a series of experiments lasting up to 19 hours—shorter than the time required for equilibrium (Pichavant et al., 2018). As demonstrated in the final experiments (*Chapter 5*), equilibrium of CO2 in the melt—the homogeneous distribution of it in the gas—is achieved after 30 hours. To preserve an out-of-equilibrium system, it is necessary to quench the experimental glass during the early stage of bubble nucleation, if it exists.

Using powdered starting material for the experiment facilitates rapid diffusion of CO_2 between the grains (Jambon et al., 1986). The size of the powdered silicate was about a few tens of microns. The composition of the synthetic glass is detailed in **Table 2.1**. in *Chapter 2.*

The experiments will be set up at the same conditions of P and T (≈ 2 kbars and 1200 ºC). The variables will be the run duration and the amount of CO_2 added to the capsule. To ensure the nucleation of vesicles in the liquid phase, the experimental capsules will be oversaturated with CO_2. The results will shed some light on nucleation under non-equilibrium conditions.

3.2.1: Experiments:

A total of thirty-three experimental capsules were conducted, with CO_2 concentrations varying between 0.7 and 7 wt.%. The experiments were carried out under high-*P-T* conditions described in **Table 3.1**. Some experiments were repeated due to issues with the autoclave. These experiments are indicated in the table with an asterisk.

		CO_{2added}	**T**	**P_{exp}**	**P_Q**	**$time_{exp}$**
Sample	Run	(wt. %)	(°C)	(bar)	(bar)	(min)
ESFa-4-CO₂	#2	1,18	1200	1598	44	30
ESFa-5-CO2	#2	2,51	1200	1598	44	30
ESFa-6-CO2	#2	2,34	1200	1598	44	30
ESFa-7-CO2	#2	6,11	1200	1598	44	30
ESFa-8-CO2	#3	1,38	1200	1609	50	240
ESFa-9-CO2	#3	2,72	1200	1609	50	240
ESFa-10-CO2	#3	7,18	1200	1609	50	240
ESFa-7E-CO2	#6	1,15	1200	1794	41	10
ESFa-8E-CO2	#6	3,02	1200	1794	41	10
ESFa-9E-CO2	#6	4,99	1200	1794	41	10
ESFa-10E-CO2	#7	1,38	1200	1726	51	1140
ESFa-1D-CO2	#7	2,87	1200	1726	51	1140
ESFa-2D-CO2	#7	5,45	1200	1726	51	1140
ESFa-3D-CO2	#8 + 9	0,68	1200	1725	55	130
ESFa-4D-CO2	#8 + 9	1,60	1200	1725	55	130
ESFa-5D-CO2	#8 + 9	5,07	1200	1725	55	130
ESFa-6D-CO2*	#10 +11	0,97	1200	1674	48	360
ESFa-7D-CO2*	#10 +11	1,94	1200	1674	48	360
ESFa-8D-CO2*	#10 +11	4,43	1200	1674	48	360

ESFa-10D-CO2	#12	1,03	1200	1671	48	10
ESFa-1C-CO2	#12	2,59	1200	1671	48	10
ESFa-2C-CO2	#12	5,20	1200	1671	48	10
ESFa-3C-CO2	#13	0,85	1200	1683	42	60
ESFa-4C-CO2	#13	1,48	1200	1683	42	60
ESFa-5C-CO2	#13	5,45	1200	1683	42	60
ESFa-6C-CO2	#14	0,69	1200	1605	38	240
ESFa-7C-CO2	#14	6,12	1200	1605	38	240
ESFa-8C-CO2	#14	4,20	1200	1660	30	10
ESFa-9C-CO2	#15	4,19	1200	1660	30	10
ESFa-10C-CO2	#15	1,30	1200	1605	38	240
ESFa-1B-CO2	#15	1,33	1200	1660	30	10
ESFa-3A-CO2	#16	5,16	1200	1669	31	10
ESFa-4A-CO2	#17	1,28	1200	1732	40	240

Table 3.1: Experimental conditions. # indicates the experimental run, the sum of two numbers indicates several runs done with the same capsule; CO_{2added} is the wt.% of CO_2 loaded into the capsule; P_{exp} is the pressure at which the experiment was quenched; P_Q indicates the transient pressure increase generated by the drop quench due to the change in temperature when the capsule falls into the cold bottom part of the vessel.

The sample containers were Au_{80} Pd_{20} capsules 1.5 cm long, 2.9 mm outer diameter and 0.4 mm wall thickness. The only volatile species is provided by $Ag_2C_2O_4$ which brings the required CO_2. The starting material consisted of a dry powdered basanite glass of approximately 60 mg loaded into the metal capsule. The capsules were arc-welded to avoid the loss of volatiles during the experimental phase and weighed before and after the experiments to ensure that no leaks occurred during the experiment.

The experiments were carried out in the IHPV working vertically and equipped with a drop quench for 10, 30, 60, 120, 240, 360 and 1140 min before quenching. The gas used to pressurise the autoclave was Ar. More general details of the autoclave and the experimental procedure are described in *2.4.1.* of this manuscript. Each autoclave experiment involves loading different experimental capsules (up to a maximum of four) for the same run, with varying amounts of CO2. Temperature and pressure were monitored regularly, the uncertainty for the two parameters were ± 5 ºC and ± 20 bar. The

signal from the quenching filament wire and the resistances of the thermocouples were also monitored throughout the experiments using a voltmeter.

3.3. Analytical methods:

After opening the capsules, the glass chips were separated by size for chemical and textural characterisation using various methods. The smaller chips were used for infrared spectroscopy through double-face polishing in micrometre thickness. For scanning electron microscopy and electron microprobe, some fragments were embedded in epoxy resin, polished and C-coated. The large pieces were analysed by X-ray microtomography. The textural and compositional analyses of the samples were conducted entirely at the Institute of Earth Sciences in Orléans (ISTO for its acronym in French).

FTIR analysis was not possible for all samples due to the presence of iron oxides in the glass which damped the IR signal (**Figure 3.3.**); The iron oxides were evenly distributed throughout the quenched glass, except for some accumulation near the vesicle boundaries. They were analysed by EMPA or by SEM when the size was too small (1-5µm) for EMPA analysis.

The dominant carbonaceous species in our synthetic samples is CO_3^{2-}. As water is occasionally present in some samples, the FTIR spectra may be slight to moderately affected by the H_2O bending at 1630 cm^{-1}, making it unsuitable for CO_2 quantification purposes (Behrens et al., 2009; Shishkina et al., 2014). Therefore, to calculate the amount of CO_2 dissolved in the glass, the 1430 cm^{-1} peak was the most suitable in all experimental glasses using an absorption coefficient of 283±8 $L \cdot mol^{-1} \cdot cm^{-1}$ (Dixon and Pan, 1995b). The concentrations of volatiles in the experimental glasses were calculated using the Beer-Lambert law:

$$C_i = 100 \frac{M_i \cdot A_j}{d \cdot \rho_{liq} \cdot \varepsilon_j}$$

Where C_i is the concentration of the species i in wt., %, M_i is the molecular weight of the species, A_j is the absorbance (peak height), d is the thickness of the section at each analysed point (cm), ρ_{liq} is the density of the sample (in $g \cdot L^{-1}$) and $\mathcal{E}_j$ is the absorption coefficient of band j (in $L \cdot mol^{-1} \cdot cm^{-1}$).

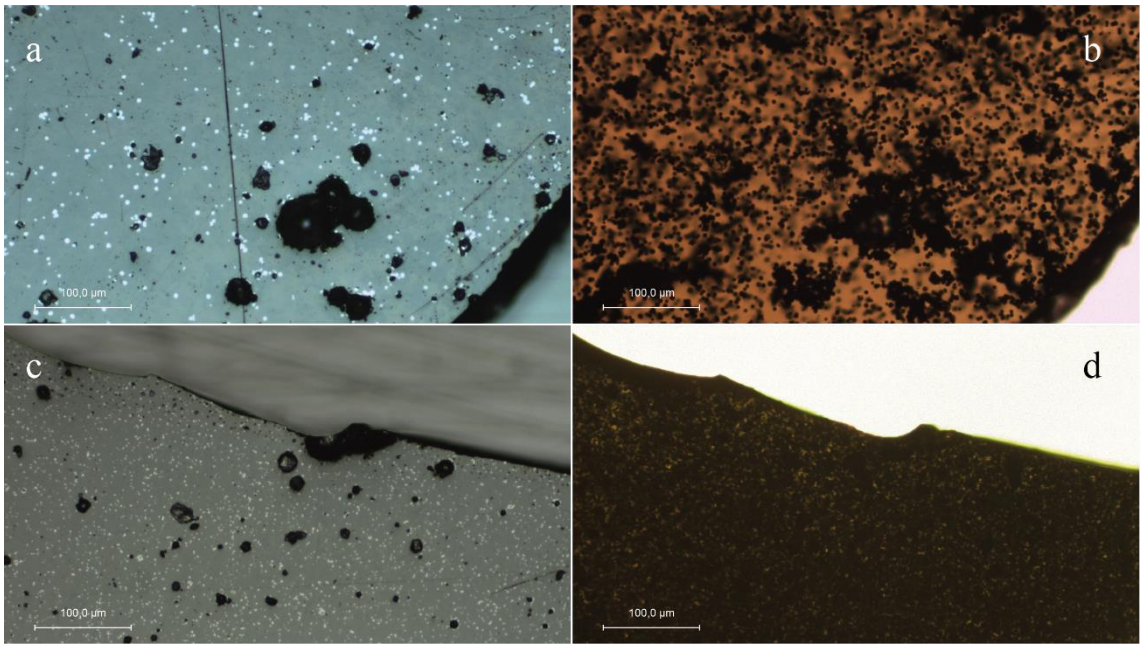

Figure 3.3.: a, b, c and **d** reflected and transmitted light of samples *ESFa-6D-CO_2* and *ESFa-7-CO_2* respectively showing the amount and distribution of oxides (white in reflected light and black in transmitted light).

3.3.1 X-ray microtomography and piercing of pure CO_2 vesicles:

X-ray microtomography was primarily used to characterise the sample's texture in terms of vesicularity and vesicle size distribution (VSD). It was also used to calculate the volume of the vesicles and compare it with the measured expanded gas after piercing them with the laser in the mass spectrometer's laser cell. This was the case for *ESFa-8-CO_2*, as detailed below, where the combination of micro-CT before and after laser ablation, along with pressure measurement using a manometer attached to the mass spectrometer, provided precise control of the *P/v* of the analysed vesicle.

3.3.1.1. Measuring pressure of vesicles:

ESFa-8-CO_2 consists of 60.1 mg of dry silicate powder doped with 2.9 mg of $Ag_2C_2O_4$ (1.4 wt. % of CO_2). The capsule was loaded to the autoclave under conditions set at 1609 bars and 1200 °C for 4 hours and drop quenched, which resulted in a pressure increase of +50 bars (**Table 3.1**).

A piece of 11.9 mg of glass was imaged by X-ray microtomography. Subsequently, it was cleaned with acetone and ethanol before being loaded into the laser cell connected to the vacuum line of the mass spectrometer. The laser cell was baked at 100°C overnight to desorb any volatiles attached to the surface of the sample. After the initial series of vesicle piercings, the sample was extracted from the laser cell, slightly polished, and reloaded to reach vesicles deeper than those pierced during the first step.

Due to the small size of the vesicles, the first step in locating them is to set the starting point in the sample [0,0,0] with the laser's coordinate reference system. Identification of the vesicles is a mixture of chance and practice, as there is no guarantee that the vesicles previously identified by microtomography will be hit by the laser. The average displacement chosen was about 0.05 - 0.100 mm in one direction of the surface (X or Y axis), adjusting the Z-axis displacement to focus the laser. Pressure changes during laser piercing are measured by a pressure gauge connected to the laser cell. The resulting pressure is plotted on a *P/time* graph (**Figure 3.4.**).

A total of eighteen bubbles were reached during the two drilling steps. The volume of each vesicle was obtained through microtomography imaging of the sample after the piercing.

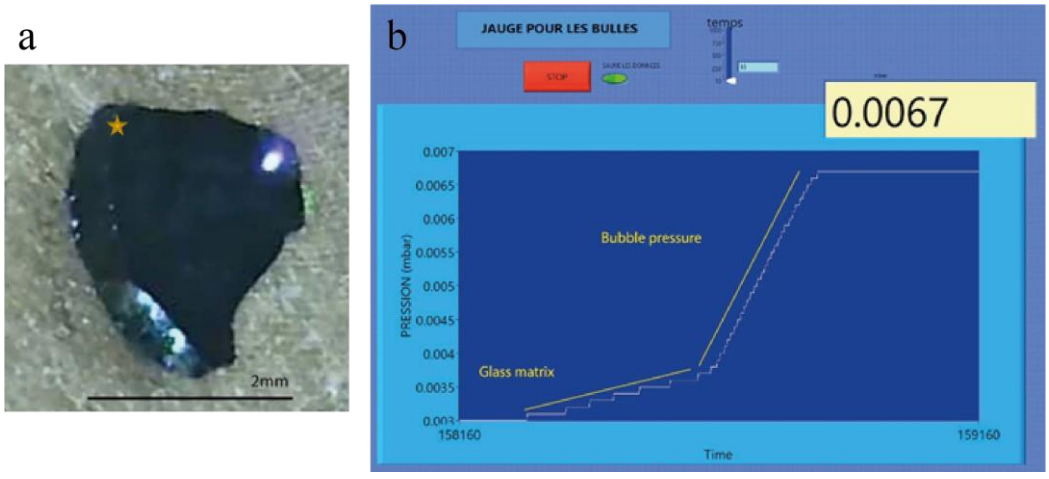

Figure 3.4.: The star in image **a** represents the reference point [0, 0, 0] for the sample in the coordinate axis. At the time the image was taken, the sample was being pierced at the spot where the spotlight is shining. Image **b** displays the computer screen during pressure control. A change in slope is observed when the matrix ablation stops, and the vesicle gas is released.

3.3.1.2. Localizing the pierced vesicles via 2D and 3D image:

After a second microtomography scan, the path taken by the laser during the ablation process becomes visible. An example of this is shown in **Figure 2.24**. The region of interest (ROI) for the image analysis is the selected volume where the punctured vesicles were placed (**Figure 3.5**.). The starting point [0, 0, 0] and the points where the vesicles were found in the laser coordinate reference system should be considered for the localization of the vesicles. The task of working with 2D and 3D images is long but simple. The scale can be adjusted from pixels (tomography resolution) to millimetres (laser displacement) using *Adobe Illustrator* for 3D images and *ImageJ* for 2D images.

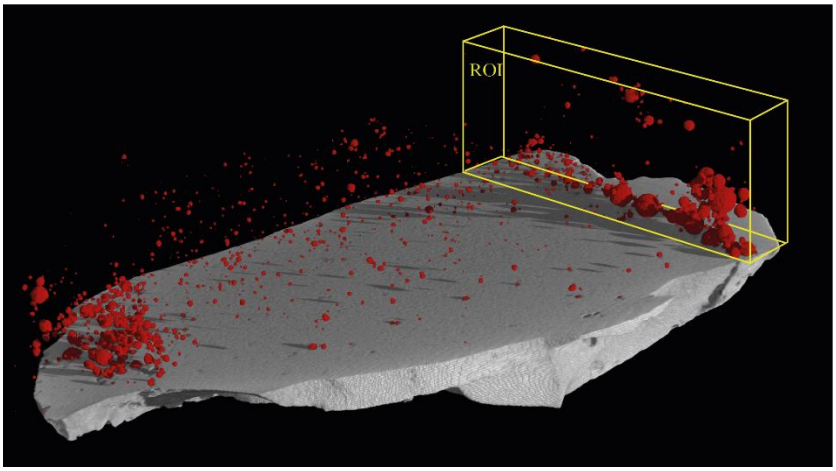

Figure 3.5.: The image highlights the Region of Interest (ROI) that was ablated by the laser in sample ESFa-8-CO_2. It was taken prior to the piercing, and the samples were polished twice to expose the vesicles located in the middle thickness of the sample.

The length and reference starting point of the specimen have been established and recorded in two 2D scans, one taken before piercing and one taken after piercing. The scale remains fixed as the slices are moved. An example of several slices with the scale and starting point is shown in **Figure 3.6.**

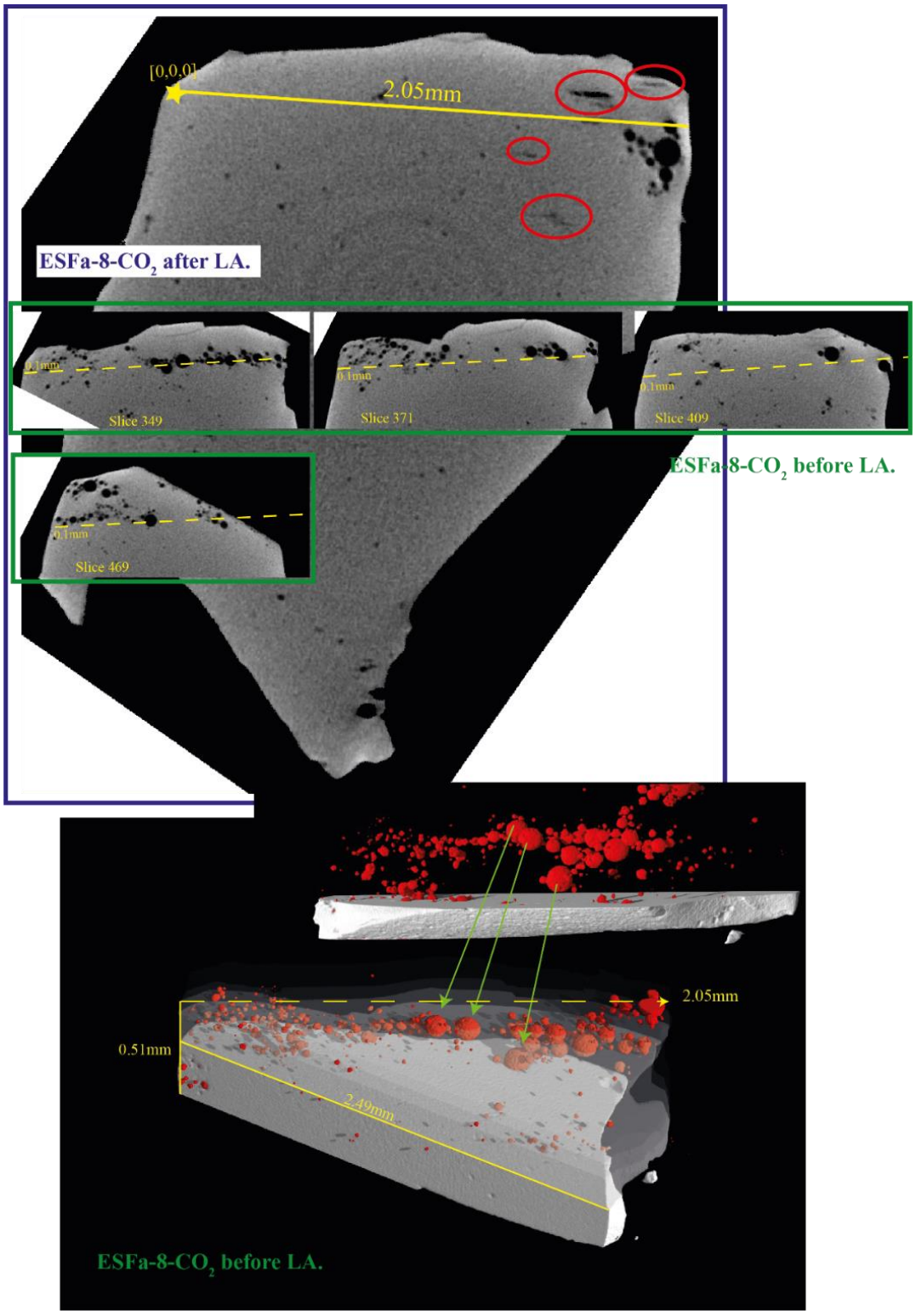

Figure 3.6: This is an example of an image being scaled and referenced during the search for pierced vesicles in different slices of a scanned image stack. On the top panel, the path of the laser is indicated by the red circles. The 3D image shows various perspectives of the sample, with the glass volume semi-transparent to highlight the vesicle distribution in the quenched glass.

After identifying the vesicles using the coordinates recorded in the notebook, the maximum diameter of each vesicle was measured in the 2D image of the corresponding slice of the stack obtained by the micro-CT. The volume of each bubble was calculated as the volume of a sphere from the diameter measured and compared with the corresponding measured pressure. The results are presented in **Table 3.2**.

				P (CO_2)	D	r	V
ESFa-8-CO₂		**[X, Y, Z]**		**(bars)**	**(µm)**	**(µm)**	**(cm^3)**
First set	1.10	-1.40	0.00	9.00E-07	18.0	9.0	3.05E-09
	0.95	-0.90	0.00	9.75E-07	18.0	9.0	3.05E-09
	1.20	-1.00	0.00	1.20E-06	28.5	14.3	1.21E-08
	1.10	-1.20	0.00	1.20E-06	48.0	24.0	5.79E-08
	0.80	-0.70	0.00	1.90E-06	57.0	28.5	9.70E-08
	0.75	-0.70	0.00	2.50E-06	66.0	33.0	1.51E-07
	0.03	0.15	0.05	4.30E-06	67.5	33.8	1.61E-07
Second set							
****1***	0.55	-0.10	0.93	7.00E-07	36.2	18.12	2.49E-08
****2***	1.55	0.20	0.72	1.30E-06	50.0	25.01	6.55E-08
****3***	0.95	0.15	3.00	5.00E-07	58.7	29.33	1.06E-07
****4***	1.25	0.15	1.60	1.00E-06	63.8	31.91	1.36E-07
****5***	1.30	0.15	0.80	2.20E-06	65.9	32.93	1.50E-07
****6***	1.45	0.20	1.80	4.00E-06	67.2	33.59	1.59E-07
****7***	1.45	0.20	1.53	5.00E-06	90.6	45.29	3.89E-07
****8***	1.00	0.15	2.80	6.20E-06	94.7	47.36	4.45E-07
****9***	1.60	0.20	1.41	9.00E-06	113.6	56.78	7.67E-07
****10***	1.10	0.20	2.40	8.00E-06	108.0	54.00	6.60E-07

Table 3.2: tracking of the pierced vesicles from *ESFa-8-CO_2* from the first and the second set of piercing. * Refers to the vesicles shown in **Figure 3.7**.; P_{CO2} is the measured pressure of the corresponding bubble (assumed to be pure CO_2); *D* is the diameter measured in the image slice in µm; *r* is the radius of the vesicle in µm; and *V* is the volume obtained in cm^3.

A linear trend with $r^2 = 0.92$ is shown when plotting the measured pressure against the calculated volume (**Figure 3.8**). This correlation coefficient provides a good fit to the regression line, allowing for the calculation of the volume of the analysed vesicles from the pressure measurement.

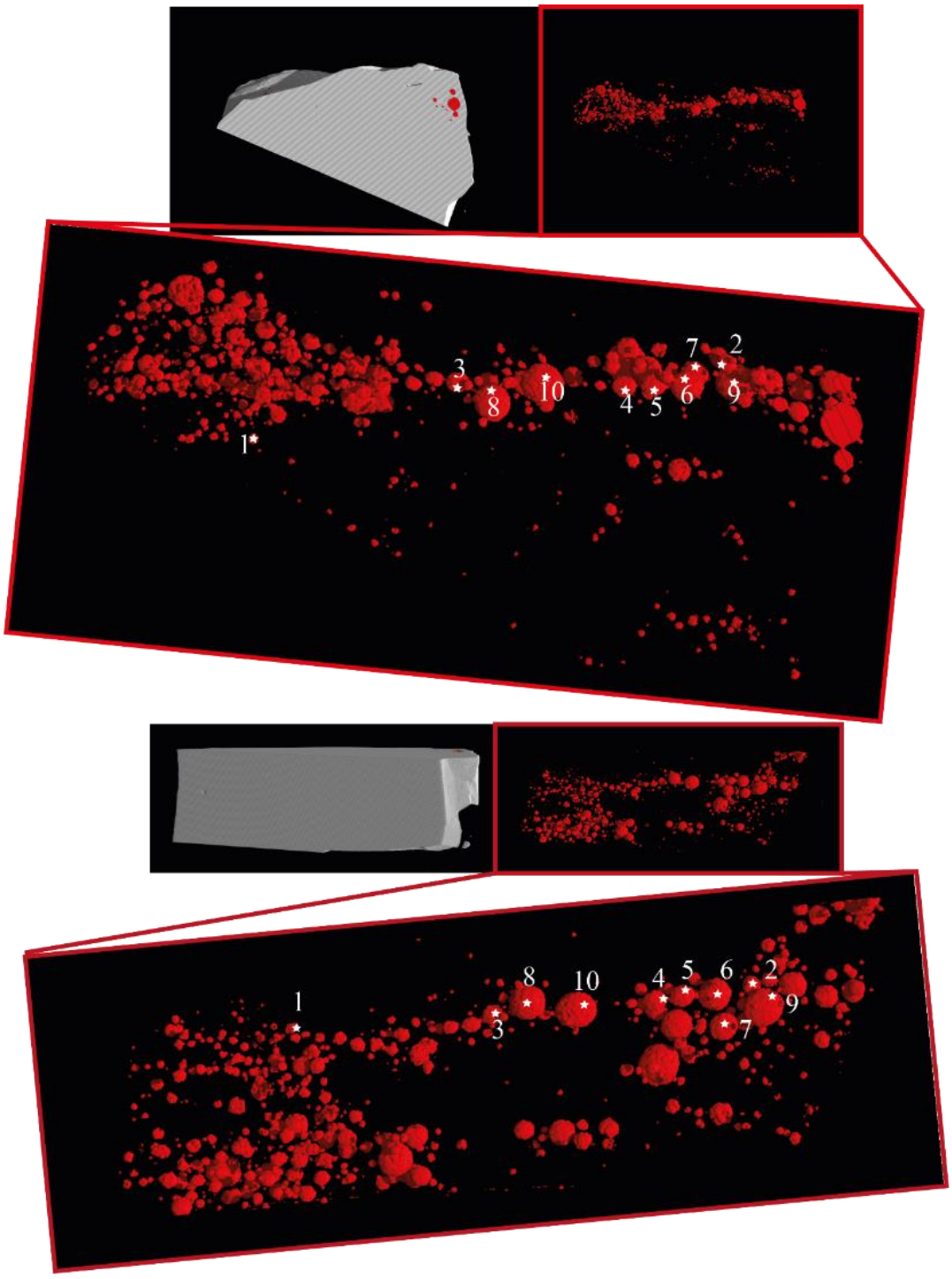

Figure 3.7: The location of ablated vesicles shown in **Table 3.2**. is depicted in the image. The image's top portion presents a perspective of the sample from above (X-Y plane), while the second portion displays a cut section of the sample in depth (X-Z plane).

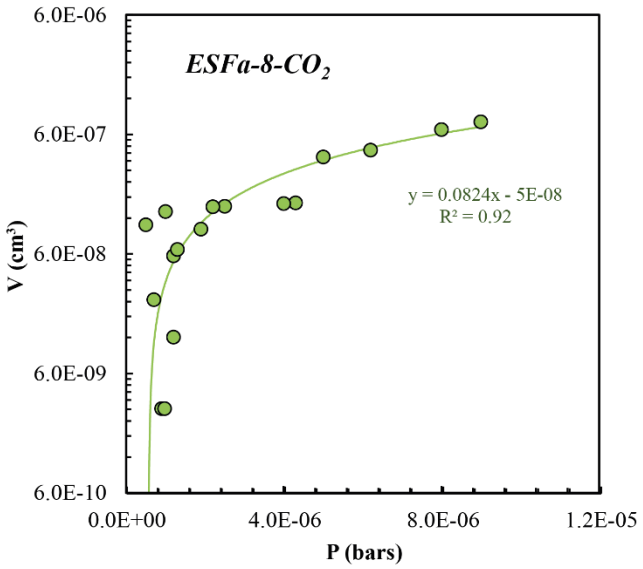

Figure 3.8: The graph displays the correlation between the measured pressure of the vesicles and their corresponding calculated volume. Note that the volume scale is logarithmic, yet the trend remains linear. The correlation coefficient is shown in the lower right-hand corner of the graphic, along with the equation of the fitted line.

3.4. 2D-Image analysis:

3.4.1. Vesicle Size Distribution (VSD):

The Vesicle Size Distribution, VSD, is based on Marsh's (1988) theoretical model for the Crystal Size Distribution, CSD, which assumes a steady state where the vesicular size distribution does not change with time. The experimental samples are classified into different types of VSD using Marsh's (Marsh, 1988) model as an exponential law, where different populations of bubbles of different sizes, *Ln(n),* are plotted against the maximum diameter of the bubble's population in the distribution.

The exponential model (**Figure 3.9.a.**) for the vesicle size distribution has limitation, the fact that the growth process is stationary and the nucleation and growth rates are constant. However, in nature, it is possible to observe different scenarios such as: (i) different populations of bubbles or coalescence phenomena causing sharp breaks in the VSD, and (ii) a cessation of nucleation and a decrease in it, where no new bubbles are formed, and larger bubbles grow at the expense of smaller ones. In the latter case, the graph displays the final limit as a curve with a shortage of small bubbles below a critical size, which is known as the 'Ostwald ripening' phenomenon.

Figure 3.9.b shows an example of the trend with different events of nucleation, coalescence, and Ostwald ripening phenomenon.

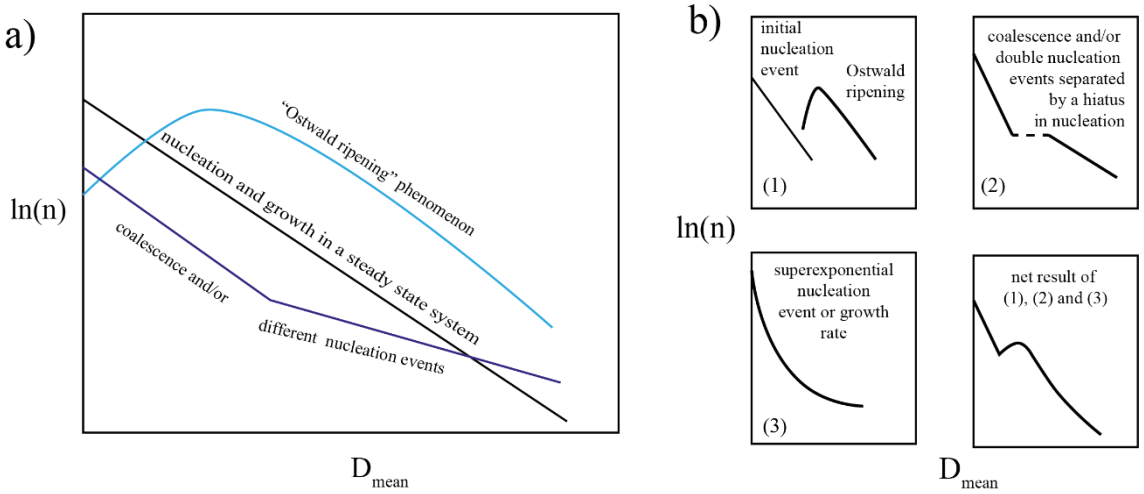

Figure 3.9.: a. Variability of VSD in exponential law from Chavrit (2010):and Marsh, (1988); **b.** effect of various nucleation events on the resulting VSD, from Marsh 1998.

The four types of VSD are classified based on the correlation coefficient, R^2, obtained from the trend line of the diagrams. This includes all sets of bubble sizes and the overall shape of the distribution. However, to classify the VSD by type, it is necessary to consider the classes at $ln(n) = 0$. Depending on the R^2 value, the VSD can be classified into (Chavrit, 2010):

- Type I: With $R^2 \geq 0.9$, these samples have a unique bubble population, where $Ln(n)$ decreases linearly with increasing size diameter.
- Type II: with $R^2 < 0.9$ all classes are plotted. The VSD trend is not perfectly linear. This may be due to (i) two different populations of bubbles, or (ii) the total number of bubbles in the area analysed is less than 100, making it difficult to clarify the type of VSD.
- Type III**:** This type is characterised by linear VSDs for the larger classes and curved downwards for the smaller classes. The trend of the point shows an Ostwald ripening shape.
- Type IV: Samples belonging to this type have less than 100 bubbles (IVa) or less than 20 (IVb) in the analysed surface. One or more classes are missing.

3.4.2. ImageJ:

The characteristics of vesicularity were obtained in the initial stage of processing a stack of images previously analysed with *VGStudioMax*. The 2D images were processed using ImageJ. However, the image stack format is too large for the software to manage. Therefore, the first step is to convert the images from TIFF to 8-bit, allowing the software to read the images in 256 levels of grey.

Due to scanning artefacts, the resulting image stack is not perfect. Therefore, some adjustments are necessary to slightly smooth and emphasise the contrast between the glass and the bubbles. For better analysis performance, an example of this adjustment is to modify the brightness and use a medium filter if necessary. Adjusting the threshold allows segmentation of the ROI with the same grey level, making it possible to distinguish between the boundary of the glass and the vesicles. The grey level threshold is adjusted twice in each stack. Firstly, select only the glass and measure the surface area it occupies. Secondly, select only the air within the glass and measure its surface.

The *Set Measurements* option enables the selection of data to be returned after running the *Analyse Particles* plugin. For the VSD study, the area and perimeter of each count of the same grey value within the threshold are sufficient. *Analyse Particles* is used to count areas of the same grey value, separated by the threshold option in each image. An example of each sample for both glass and bubble counting, filtered by the threshold, is shown in the *Appendix* of this manuscript. The plugin generates a table of data that can be further processed in an *Excel* spreadsheet.

It should be noted that while the software can count particles in 3D, the stack's information may be too large for the computer to process. However, analysing only a small volume of the sample to reduce this information may not accurately represent its vesicularity, as some samples may have vesicles concentrated in specific areas of the capsule. For instance, **Figure 3.10.** represents only a piece of 16.2 mm^3 and 1.4% vesicularity belonging to the quenched glass *ESFa-8D-CO2.* This work performs a 2D analysis of each sample in ImageJ and then transforms it into 3D to ensure that no relevant information is missed.

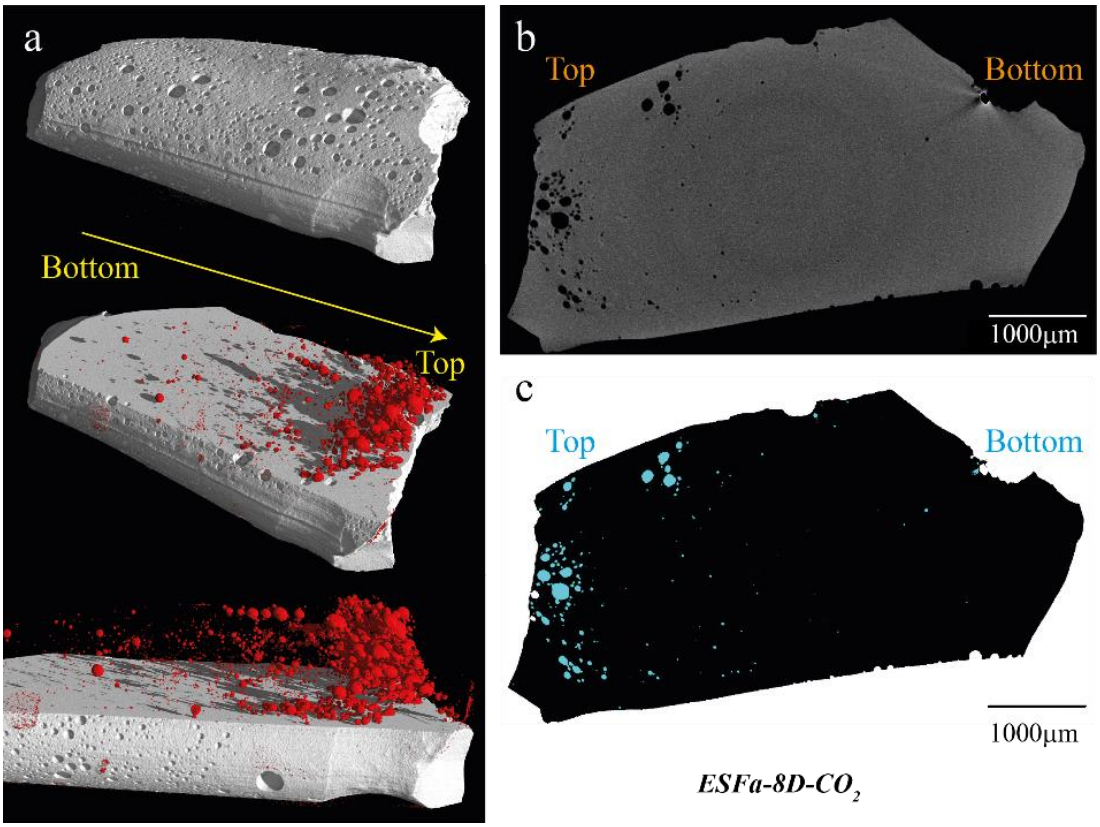

Figure 3.10.: a. A 3D image representing sample 8D. The glass is depicted in grey, the vesicles in red, and the path of the bubbles from the bottom to the top of the capsule in yellow. **b.** 2D image representing one slice of the image stack analysed by ImageJ already filtered and threshold adjusted. The terms 'bottom' and 'top' refer to the lower and upper parts of the experimental capsule.

The *ESFa-8D-CO2* experiment lasted for 6 hours. The results of the bubble distribution analysis indicate that the majority of the gas was released from the melt, with the remaining gas accumulating at the top of the capsule. It is important to note that the statement "almost" all the gas migration should be highlighted, as the experiment resulted in a decrease of vesicularity of approximately 21% compared to the amount of CO_2 loaded into the capsule. Section 3.6.5 will provide additional information on this phenomenon. The vesicles display a prolate shape in the direction of bubble flow.

Upon analysing the image in different coordinate axes provided by the micro-CT, it is evident that the most representative distribution of the vesicles can be obtained by taking the top and bottom of the capsule in the same orientation plane. This is due to the observed effect of coalescences and Ostwald ripening phenomena (refer to **Figures 3.10**. and **3.11**.)

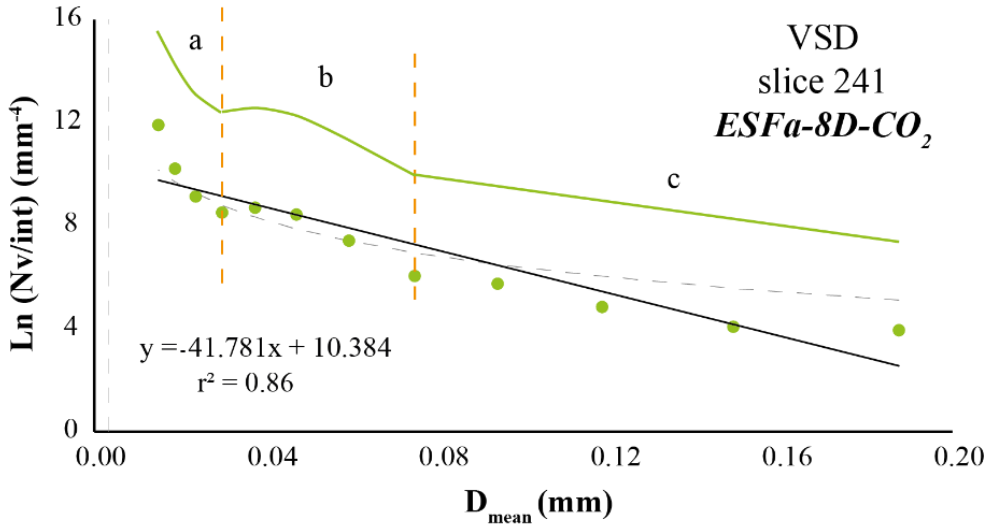

Figure 3.11.: Slice 241 from the stack of images of sample *ESFa-8D-CO₂* provides an example of fast nucleation (a), coalescence (slope rupture indicated by the orange dashed line between b and c), and Ostwald ripening phenomenon (b).

The use of 3D and 2D image analysis is a powerful tool for texture analysis of quenched glasses when analysing the total sample volume is necessary. In this study, VGStudioMax was used to calculate the vesicularity in the total volume of the sample and the distribution of the vesicles for laser ablation. ImageJ was used to characterise VSD by summarising the surfaces counted in each image of the stack and characterising single slices considered to be representative of the sample.

3.4.2.1 Textural analysis in 2D with excel sheet:

The calculus for the textural analysis was performed on a representative surface taken from one of the slices of each analysed sample using micro-CT. The image analyses were done in the transverse of the experimental glasses, where the top and the bottom of the capsule was always presents in order to have a better representation of the whole system. Further information on the selection of the representative sample can be found in the Appendix of this manuscript.

The *Analyse particles* function of *ImageJ* generates information in two tables. The first table provides information on the counted surfaces in each image of the stack, while the second table summarises the area and count of each slice analysed. The first table is used to calculate the diameter of each vesicle in every slice by deconvoluting the formula

for the area of a circle, while the second table reports the mean diameter and information required to calculate the bubble density and vesicularity in each slice as:

- *Bubble density, $N_b \cdot cm^{-2}$:* corresponds to the number of bubbles, N_b, per surface unit. This parameter is an indicator of nucleation processes. It was calculated in every slice but also applied to the whole stack of the sample.

- *Vesicularity, Ves (%):* is defined as the surface occupied for the vesicles inside the glass. This parameter can be calculated as:

$$Ves = \frac{V_b}{V_b + V_m} * 100$$

Where V_b is the volume of the air occupied by the vesicles and V_m is the volume of the glass. Or using the bubble density (described above) and the mean diameter in cm (Chavrit, 2010):

$$Ves = \frac{Nb}{cm^2} * \pi * \left(\frac{D}{2}\right)^2 * 100$$

VSD in our synthetic glasses is obtained by determining the 3D distribution from 2D measurements in some selected slices of the microtomography images, which are considered to be representative of the whole volume. The number of vesicles per unit volume, *Nv*, is calculated from the measured number per unit area according to Saltykov (1967) as follows:

- *Interval:* the first stage consists of setting the intervals for defining the population of vesicles, in statistics defined as classes:

$$Int_i = D_{max_i} * (1 - 10^{-0.1})$$

$$D_{max_i} = D_{max_{i-1}} - Int_{i-1}$$

where D_{max} corresponds to the maximum diameter in the interval *i*, taking the first value of the interval as the biggest diameter of the bubble.

- *Number of bubbles $(Nb)_i$:* defines the number of bubbles for each population interval. It calculates the frequency of each population of bubbles for a given range.

$$Range = D_{max_i} - Int_i$$

- *Number of bubbles per unit of area $(N_a)_i$*:

$$(N_a)_i = \frac{(N_b)_i}{mm^2}$$

- *Number of bubbles per unit of volume, $(N_v)_i$*:

$$(N_v)_i = \left(\frac{1}{D_{max\,i}}\right)[1.6461 * (N_a)_i - 0.4561 * (N_a)_{i-1} - 0.1162 * (N_a)_{i-2} - 0.0415 * (N_a)_{i-3} - 0.0173 * (N_a)_{i-4} - 0.0079 * (N_a)_{i-5} - 0.0038 * (N_a)_{i-6} - 0.0018(N_a)_{i-7} - 0.0010 * (N_a)_{i-8} - 0.0003 * (N_a)_{i-9} - 0.0002 * (N_a)_{i-10} - 0.0002 * (N_a)_{i-11}]$$

Note that all terms are used only when the twelfth-class interval is calculated.

- *ln(n):* the bubble density for a selected population of vesicles, *n*, is calculated and plotted as $ln(n)_i$ versus D_{max}:

$$ln(n)_i = ln\left(\frac{N_{v_i}}{Int_i}\right)$$

The value of the correlation coefficient, R^2, of the exponential trend line in the diagram represents the global point distribution of VSD.

3.4.3. Vesicularity of the system and vesicularity of the sample:

It is important to note that the vesicularity referred to in this work pertains to the sample after the capsule has been opened, not the system as a whole. The fragility of the glass, as opposed to the hardness of the capsule, often results in multiple fragments of quenched glass when removed from the capsule.

Although the analysed glass sample may be representative of the entire experiment, it is important to note that some information may be lost from the non-analysed small fragments of glass when the recovered part is not large enough. To solve the problem of unmeasurable CO_2 loss from the melt due to the unavailability of tools to open the metallic capsules under vacuum, the theoretical vesicularity of the system, $Ves_{the.}$ was calculated based on the amount of CO_2 loaded into the capsule.

The difference in between the measured vesicularity (by microtomography) and the theoretical vesicularity, represents the gas accumulated at the melt-capsule interphase:

$$Ves_{diff} = Ves_{the.} - Ves_s$$

$$Ves_{the.} = \frac{V_b}{V_{mag}} * 100$$

$$V_{mag} = V_b + V_{liq}$$

$$V_b = \frac{m_{co_2} - \left(m_{tot} * co_{2_{dis.}}\right)}{\rho_{CO_{2_b}}}$$

$$V_{liq} = \frac{m_{sil} - \left(m_{tot} * co_{2_{dis.}}\right)}{\rho_{mag}}$$

$$m_{tot} = m_{co_2} + m_{sil.}$$

Where Ves_s is the measured vesicularity of the sample; V_b is the volume of the bubble; V_{liq} is the volume of the liquid; ρ_{CO2} is the density of the CO_2 at the pressure and temperature conditions of the experiment (determined by Bottinga and Richet, (1981) $\rho_{mag} = 2.7$ g·cm^{-3}; $CO_{2dis.} = 2.7 \cdot 10^{-6}$ g·cm^{-3} for this composition and at 2 kbars and 1200ºC (Jiménez-Mejías et al., 2021); m_{CO2} is the mass of CO_2 loaded to the capsule; $m_{sil.}$ is the mass of the silica powder loaded into the capsule; and $m_{tot.}$ is the total mass loaded.

3.4.4. Bubble growth rates before decompression and rate of ascent:

An additional parameter that can provide useful information about our experimental samples is the growth rate of the bubbles, *G*. This parameter is independent of bubble size and gives information about the residence time of the bubbles in the magma during decompression, τ. Watson et al. (1982) calculated this value for basaltic melts using the diffusivity laws for dissolved CO_2, but (Sarda and Graham, 1990) showed that this value is strongly dependent on the initial CO_2 of the magma, which is unknown, and can then affect by several orders of magnitude the value of *G*.

Here the initial CO_2 is known. Furthermore, since this chapter focuses on the initial phase of nucleation and gas loss under isobaric conditions rather than during decompression, the formula used to calculate τ was deconvolved to calculate the bubble growth rate before decompression, G_0, and the residence time of the bubbles in the magma before the decompression starts, τ_0, was fixed at 1800 min. After this time, our run product glasses show no more vesicles (e.g. sample EN-E3 *Chapter 5*). This new parameter will

provide the growth rate for the first generation of vesicles formed before the decompression.

The aim of obtaining this parameter is to find any relationship with the CO_2 dissolved into the glass, the diffusion, the vesicularity or any other parameter of the VSD.

$$G_0 = \frac{1}{\tau_0 * -a}$$

Where *a* is the slope of the VSD trend in μm for each experimental sample.

However, there is still debate regarding the assimilation capacity of a system when a CO_2-rich melt or gas suddenly enters the magmatic system (i.e. Shinohara et al. (2008); Aiuppa et al. (2009). The capsules were loaded with a significant amount of CO_2, and as the starting material is a dry glass, it creates an ideal environment to observe the ascent rate of bubbles, v_b, and CO_2 diffusion simultaneously for comparison.

The diffusion of CO_2 was calculated for each experiment where FTIR analysis was possible, considering the amount of dissolved water when present, using the formula described at the beginning of this chapter.

The bubble ascent rate, v_b, was calculated using Stokes' Law, which describes the motion of a spherical particle through a viscous fluid:

$$v_b = -\frac{2}{9} * \frac{r^2 * g * (\rho_b - \rho_L)}{\eta}$$

Where *r* is the mean radius of the vesicles in each sample in meters, *g* is the gravity in $m \cdot s^{-1}$, ρ_b and ρ_L are the densities of the bubble and the liquid respectively in $kg \cdot m^3$, and η is the viscosity of the magma in $Pa \cdot s^{-1}$, calculated for each experiment regarding the amount of dissolved water and the pressure following the method of Giordano et al. (2008).

3.5. Results:

3.5.1. Major elements:

The quenched glasses were analysed for major elements and here the average is shown along with that of the starting material (dry glass). Except for a small loss of iron,

the run product glasses do not change anything in the composition (**Table 3.3.**). The main interests for checking the run product compositions were first to calculate the density of the glass using the (Lange, 1994b) method as was explained in *Chapter 2* and to know the composition of the iron oxides that adsorb the signal of the FTIR. When the analysis with the EMPA was not possible, the iron oxides were analysed Using the SEM (**Table 3.4.**). Only some samples were analysed for oxides since all presented the same composition.

	Na_2O	MgO	SiO_2	Al_2O_3	CaO	K_2O	TiO_2	FeO	MnO	P_2O_5	$Na_2O + K_2O$	Total
Average *ESFa*	3.8	7.5	45.2	15.1	10.7	1.5	3.6	11.6	0.2	0.8	5.3	100.0
sd	0.1	0.2	0.7	0.2	0.3	0.1	0.1	1.0	0.0	0.0		
Starting mat	3.6	7.8	44.9	14.9	10.4	1.5	3.7	12.4	0.2	0.7	5.1	100.0
sd	0.1	0.0	0.2	0.2	0.1	0.1	0.2	0.2	0.1	0.1		

Table 3.3.: Average chemical composition of the of the whole set of experimental samples and the starting material. The chemical composition of each experimental sample is provided in the *Appendix* of the manuscript.

	MgO	sd	Al_2O_3	sd	TiO_2	sd	FeO	sd
ESFa-5-CO2*	15.27	0.48	12.12	0.15	2.58	0.05	65.24	1.63
ESFa-6-CO2*	14.6	0.34	11.63	0.27	2.66	0.07	66.28	1.32
ESFa-10-CO2	15.24		10.28		2.72		65.68	
ESFa-10-CO2*	16.03	0.02	12.23	0.25	2.63	0.05	66.21	1.45
ESFa-7D-CO2	14.57	0.92	12.49	0.42	2.30	0.06	66.26	1.37
ESFa-3C-CO2*	14.86	0.33	12.26	0.09	2.65	0.02	67.22	1.18
ESFa-5C-CO2	14.61	0.61	12.21	0.02	2.85	0.08	61.61	2.09
ESFa-9C-CO2*	12.65	0.21	12.48	0.1	3.47	0.08	63.37	1.59

Table 3.4.: chemical composition of the oxides analysed by *SEM and EMPA. To calculate the standard deviation of sample 10 analysed by EMPA was not possible due to the tiny size of the crystal but the only possible analysis is shown here to compare with the analysis of the SEM.

3.5.2. CO_2 and H_2O content:

The results of IR Spectroscopy are given in **Table 3.5**. The dissolved carbon concentration varies from 585 - 1710 ppm and, despite no water being added, seven of

the experimental glasses show less than 1 wt.% H_2O. This water is generated through the reduction of Fe^{3+} of the melt during the synthesis. This effect was already explained in *Chapter 2*.

The distribution of dissolved CO_2 in the experimental glasses was heterogeneous, as evidenced by the significant values for experiments of the same run duration and the standard deviation in every sample. The analysis was challenging due to the number of oxides that absorbed the signal in some of the quenched glasses, resulting in unclear FTIR analysis spots. In some cases, it was impossible to take more than one spot. For example, samples *ESFa-4C-CO₂* and *ESFa-1B-CO₂* had completely dark chunks under the microscope. Some analysed spots are attached to the Appendix of this manuscript.

Sample	n[a]	Thickness	sd	δ	sd	A_{3525}	sd	H_2O	sd	A_{1430}	sd	$[CO_2]$	sd
		µm		(g/cc)	(g/cc)	(cm^{-1})		(wt.%)	(wt.%)	(cm^{-1})		(ppm)	(ppm)
ESFa-4-CO₂	2	42	13	2722.3	14.9					0.0485	0.0157	722	429
ESFa-5-CO2				2744.6	5.4								
ESFa-6-CO2				2751.6	12.8								
ESFa-7-CO2				2726.8	35.5								
ESFa-8-CO2	1	56	1	2716.5	7.2	0.0626	0.0015	0.13	0.00	0.0870	0.0047	893	0
ESFa-9-CO2				2711.0	6.6								
ESFa-10-CO2	3	56	6	2734.1	41.4	0.0504	0.0114	0.10	0.03	0.0987	0.0134	1022	252
ESFa-7E-CO2				2728.5	36.1								
ESFa-8E-CO2				2752.9	16.7								
ESFa-9E-CO2				2766.4	53.5								
ESFa-10E-CO2	4	54	5	2739.0	4.3	0.2261	0.0109	0.47	0.04	0.1229	0.0091	1315	169
ESFa-1D-CO2				2751.0	3.1								
ESFa-2D-CO2	3	86	1	2751.0	6.9	0.3045	0.0312	0.39	0.04	0.1605	0.0158	1059	111
ESFa-3D-CO2	3	50	17	2772.3	43.5					0.0778	0.0132	925	200
ESFa-4D-CO2				2724.5	4.7								
ESFa-5D-CO2	4	50	1	2764.3	15.3					0.0589	0.0064		
ESFa-6D-CO2				2713.3	5.1								
ESFa-7D-CO2				2753.2	11.9								
ESFa-8D-CO2	6	97	5	2734.8	42.6					0.1202	0.0244	702	114
ESFa-10D-CO2				2732.8	21.6								
ESFa-1C-CO2	3	58	7	2762.2	56.4					0.1022	0.0302	971	159
ESFa-2C-CO2	3	56	6	2760.9	30.7							668	304
ESFa-3C-CO2				2752.2	12.8								
ESFa-4C-CO2	1	26	2	2742.3	18.5					0.0796	0.0052	1710	3

ESFa-5C-CO2	1	50	2	2753.6	31.7					0.0634	0.0030	722	0
ESFa-6C-CO2	5	69	2	2730.3	20.6					0.0846	0.0095	700	84
ESFa-7C-CO2	5	65	10	2772.8	56.9					0.1038	0.0089	915	137
ESFa-8C-CO2				2756.6	39.2								
ESFa-9C-CO2	4	45	5	2761.5	11.6	0.0844	0.0060	0.21	0.04	0.0464	0.0161	585	178
ESFa-10C-CO2	3	53	1	2731.3	12.6					0.0865	0.0107	931	97
ESFa-1B-CO2	3	47	3	2731.1	12.9	0.1031	0.0195	0.24	0.04	0.0597	0.0251	707	267
ESFa-3A-CO2				2751.2	12.4								
ESFa-4A-CO2	2	73	2	2732.8	20.3	0.4675	0.0225	0.72	0.05	0.1826	0.0099	1429	111
Starting material				2738.7	2.7								

Table 3.5.: FTIR data. Average of H_2O and CO_2 concentration calculated from n^a (number of analytical spots in each sample) whenever possible. δ is the density of the sample and the thickness belongs to the chunk of glass analysed.

3.5.3. 3D Micro-CT:

29 out of 33 experimental glasses were recovered from the capsule and were deemed suitable for analysis using micro-CT. Note that not all the scanners display the total volume of the experimental samples, but only the largest piece that was recovered. The glasses were then sorted into diverse groups based on their run duration **Figures 3.16., 3.17., 3.18**. and **3.19.**:

- <u>*Group 10 minutes of experiment*</u>: The size of the bubbles in that group of samples, varies, ranging from mere nuclei to vesicles measuring three hundred microns. Two of the samples are particularly noteworthy due to the presence of one or two particularly large vesicles: *ESFa-2C-CO_2* (**Figure 3.12.**) has two large vesicles connected to the capsule-melt interface (CO_2 exsolved from the melt located between the glass and the capsule), appearing as empty spaces in the glass in **Figure 3.16**. The vesicles have a diameter of about 1000 and 550µm; *ESFa-3A-CO_2* (**Figure 3.13.**) has two vesicles located at the contact with the capsule, measuring about 1200 and 800µm.

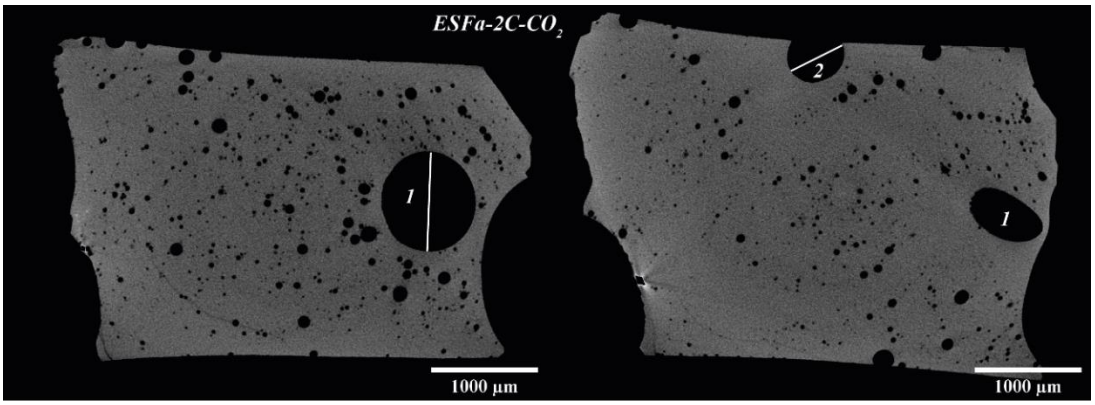

Figure 3.12.: *ESFa-2C-CO_2* in two different slices showing the maximum diameter of two bubbles connected to the external part of the quenched glass. Vesicle *1* has a diameter of about 1000µm and vesicle 2 of 550µm.

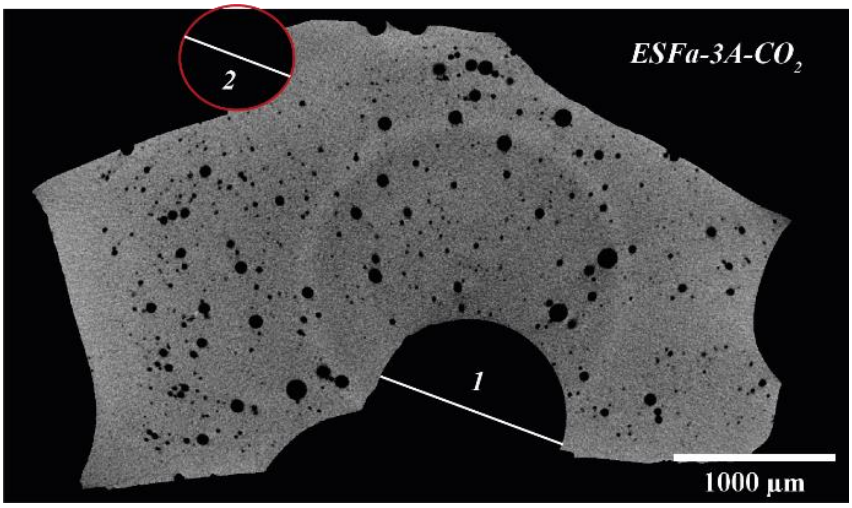

Figure 3.13.: *ESFa-3A-CO_2* shows the slice of the image stack with the maximum diameter of one bubble located at the melt-capsule interphase. Vesicle *1* has a diameter of about 1200µm and vesicle 2 of 800µm.

The vesicles are distributed homogeneously throughout the glass, except for *ESFa-7E-CO_2*, where they are closer to the edge of the capsule (laterally, not on the top or bottom). The nucleation of vesicles is also observed to be homogeneous throughout the glass. After only 10 minutes of experimentation, vesicle coalescence is already occurring. This can be observed by the proximity of a trains of vesicles, with some of them being noticeably larger than the others.

- *Group 30 minutes:* Even though the difference with the first group of samples may not be immediately apparent, upon closer inspection, several accumulations of large vesicles can be observed in groups along the glass. Additionally, new

vesicles have nucleated and are dispersed throughout the glass in the 30-minute group of experiments. As previously observed, one of the experimental samples, *ESFa-7-CO_2,* contains a large vesicle that is in contact with one of the limits of the capsule, measuring approximately 940µm (**Figure 3.14**.). This effect is present in several experiments at different lengths and was already explained in *Chapter 2*.

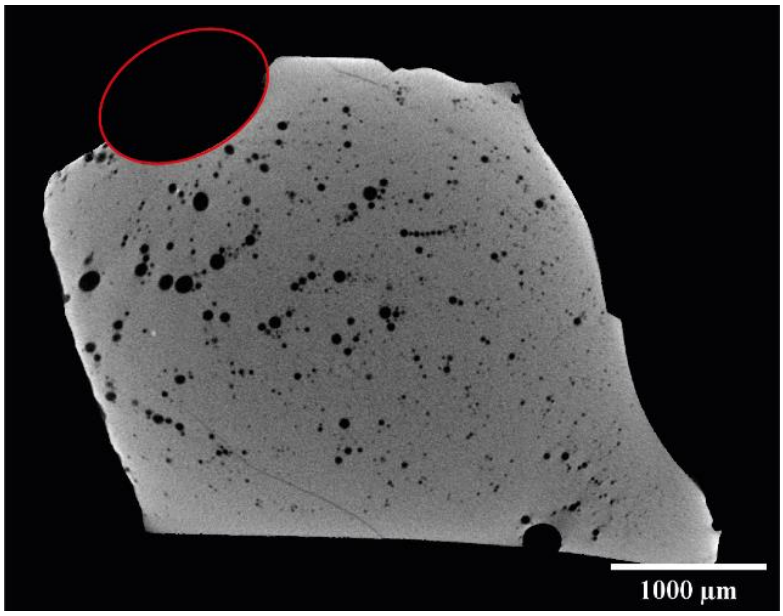

Figure 3.14.: *ESFa-7-CO_2* showing the slice of the image stack with the maximum diameter of one bubble connected to the external part of the quenched glass with a diameter of 940µm.

- *Group 60 minutes of the experiment:* In contrast to the previous two run durations, the vesicles in this new time group, 60 minutes, begin to experience a gravitational effect. Although not as pronounced as in later observations, the larger bubbles move towards the upper part of the capsule, while bubble nucleation is more prominent in the lower part. It is important to note that this effect is not as obvious as in subsequent longer runs. In this group of samples, large bubbles can also be found in some of the glasses that are located at the edges of the capsule (e.g. *ESFa-5C-CO_2*).
- *Group 130 minutes of experiment*: This group of samples, 130 minutes of the experiment, is not significantly different from groups 3 and 5 in terms of the effect of gravity. The distribution of the vesicles is also similar to the previous groups.

In some samples (e.g. *ESFa-5D-CO_2,* ***Figure 3.15.***), the accumulation of vesicles at the top creates a distinctive shape, but it is not as pronounced as it will be in groups 5 and 6.

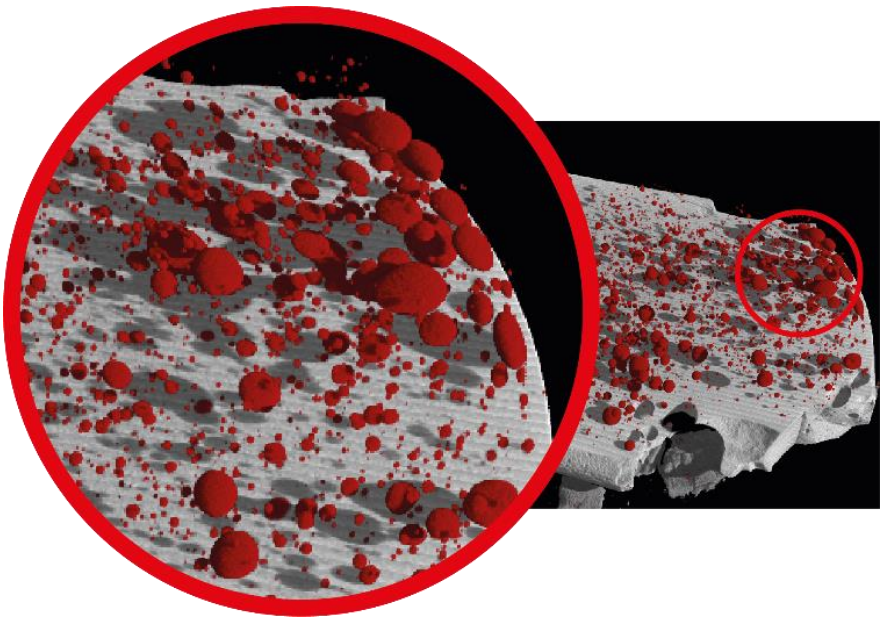

Figure 3.15.: 3D image of sample *ESFa-5D-CO_2* (group 130 minutes of experiment) with a zoom on a group of vesicles whose shape becomes deformed in the upper part of the capsule.

- *Group 240 minutes of the experiment:* This group of experimental glasses, 240 minutes of the experiment, exhibits an accumulation of larger bubbles in the upper part of the capsule, which becomes more pronounced towards the centre than at the sides. Although bubble nucleation is still occurring, the populations of large bubbles due to coalescence are more noticeable, as well as the elongated shape of the bubbles located in the upper part of the glass. The sample *ESFa-10-CO_2* did not fragment during the opening of the capsule and the image analysis could be performed on the entire volume of the glass. However, the sample *ESFa-7C-CO_2* exhibits the same effect but unfortunately, it was not possible to scan more than a third of the glass in a large piece.

- *Group 360 min of experiment:* In this run, bubble nucleation is minimal, and the size of the bubbles is increasing. During the experiment, an important event occurred where most of the vesicles accumulated at the top of the glass, leaving a significant portion of the lower part free of bubbles. This resulted in a lower vesicularity compared to previous samples. It is possible that a significant amount

of the gas phase escaped from the melt, accumulating on the top of the capsule, at the melt-capsule interface.

- *Group 1140 minutes of experiment:* This group is notable for the lack of bubble nucleation and the accumulation of bubbles at one end of the capsule. Sample *ESFa-10E-CO_2* was fully recoverable, while only the upper part of the *ESFa-2D-CO_2* was available for analysis. However, both samples exhibit the same characteristics. The possibility of a larger gas transfer toward the top of the capsule in these samples is more evident.

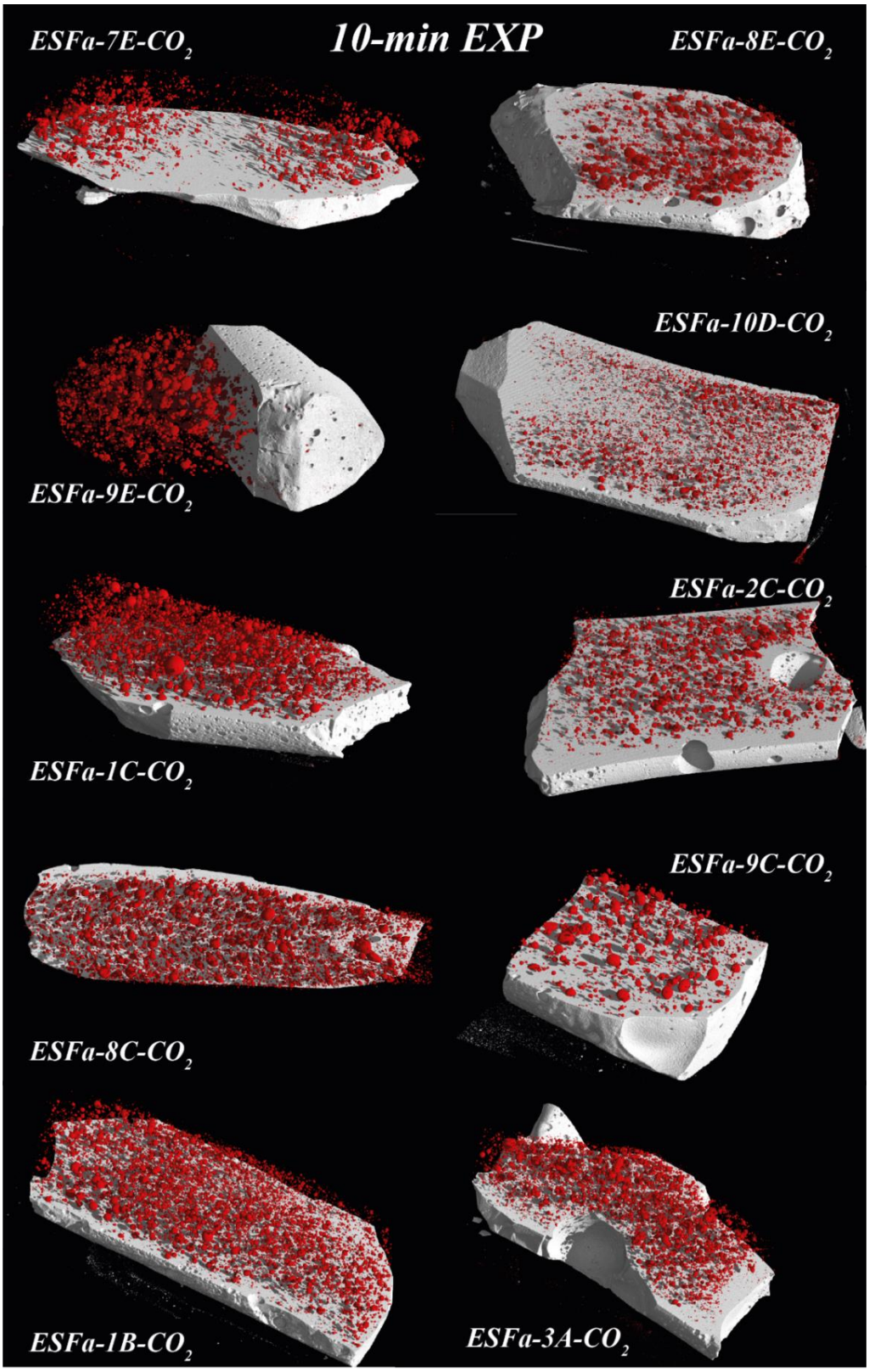

Figure 3.16.: This section presents 3D images of group 1, which consisted of ten charges of 10-minute experiments. The images illustrate the distribution of vesicles in the glass, although only a portion of the glass volume is shown. The details regarding the scale and volume are provided in the manuscript's *appendix*, along with additional information.

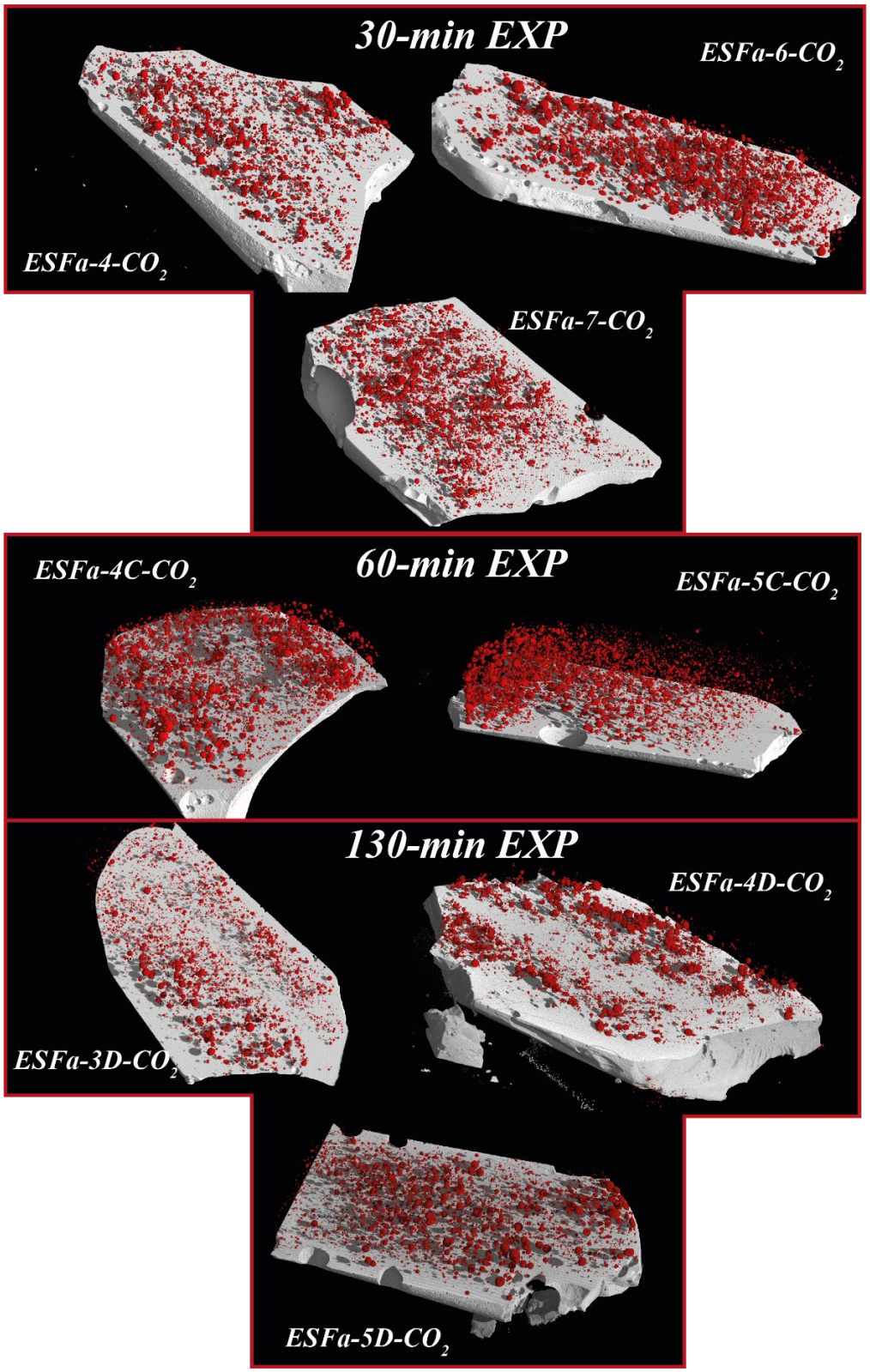

Figure 3.17.: This section presents 3D images of groups 2, 3 and 4, which consisted of three, two, and three samples of 30-, 60-, and 130-minute experiments respectively. The images illustrate the distribution of vesicles in the glass, although only a portion of the glass volume is shown. The details regarding the scale and volume are provided in the manuscript's *appendix*, along with additional information.

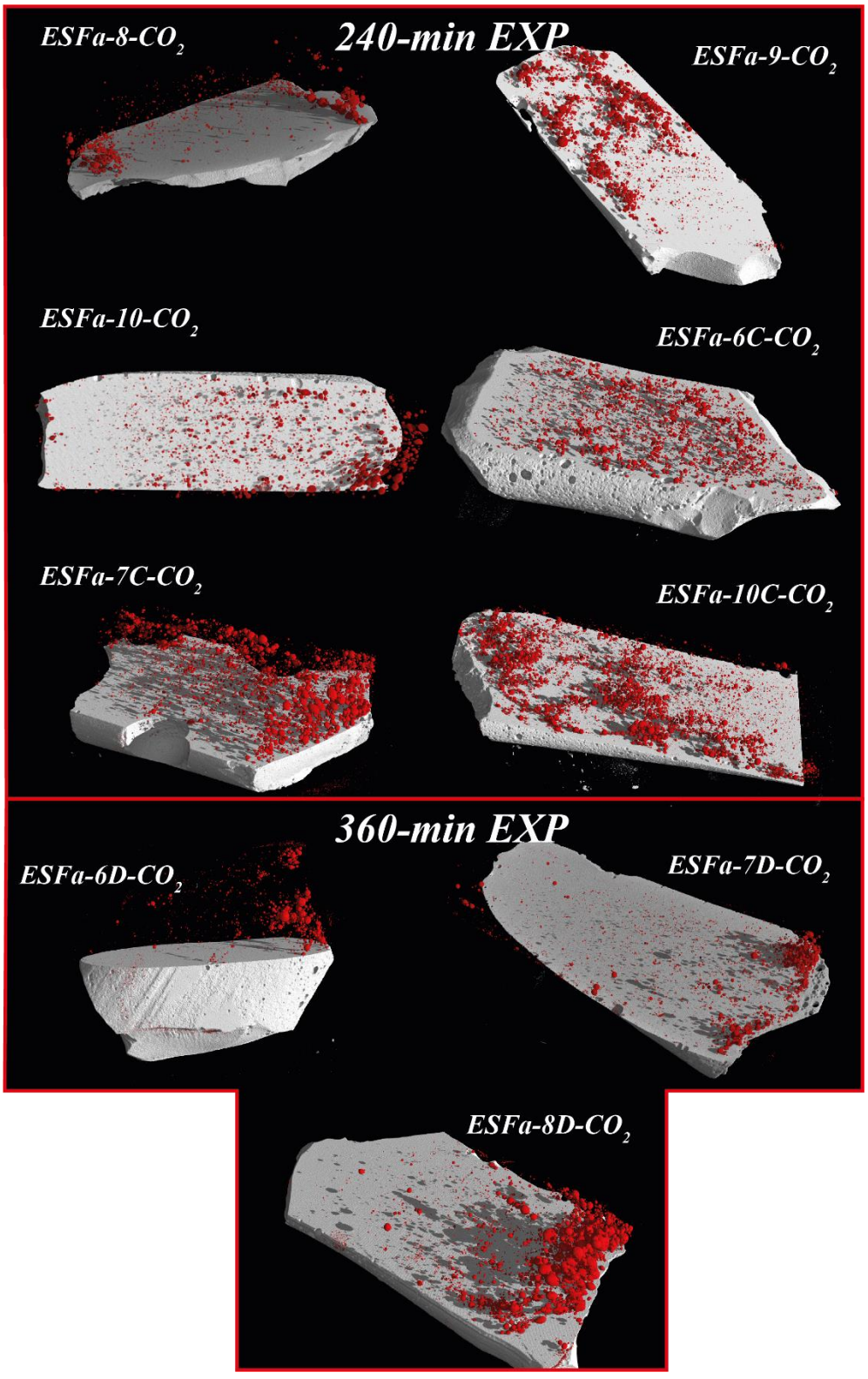

Figure 3.18.: This section presents 3D images of groups 5, and 6, which consisted of six, and three samples of 240-, and 360-minute experiments, respectively. The images illustrate the distribution of vesicles in the glass, although only a portion of the glass volume is shown. The details regarding the scale and volume are provided in the manuscript's *appendix*, along with additional information.

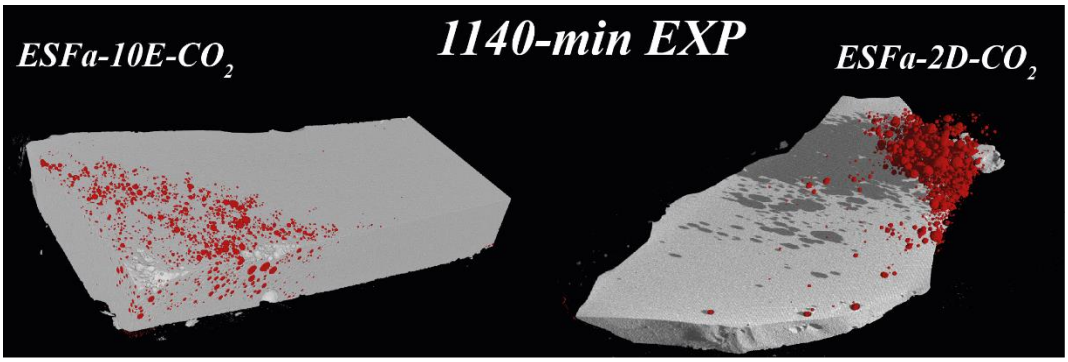

Figure 3.19.: This section presents 3D images of group 7, which consisted of two, samples of 1140-minute experiments respectively. The images illustrate the distribution of vesicles in the glass, although only a portion of the glass volume is shown. The details regarding the scale and volume are provided in the manuscript's *appendix*, along with additional information.

3.5.4. VSD textural analysis from the surface of the study to the volume of the sample:

3.5.4.1. Bubble density, vesicularity and mean diameter in 2D:

Following the same sorting as in the previous section, the characteristics of vesicularity for each group are:

- *Group 10 minutes of experiment:* exhibits a wide range of vesicularity, from 2.5% to 9.6%, with the highest vesicularity recorded in sample *ESFa-8E-CO₂*. The range of bubble density is also wide, from 40.7 mm^{-2} to 88.95 mm^{-2}, with the highest bubble density observed in sample *ESFa-7E-CO₂*. The mean diameter ranges from 14.71 µm to 27.95µm. In contrast to vesicularity and bubble density, this group of samples has the smallest mean bubble diameter of all experimental samples, including sample *ESFa-7E-CO₂*. This can be attributed to the high number of small bubbles and a high degree of nucleation.

- *Group 30 minutes of the experiment*: This group has still an important level of vesicularity compared to the longer run duration experiments groups, with a range from 2.07% to 6.77%. The range of bubble density remains wide, from 42.11 mm^{-2} to 53.75 mm^{-2}, with the highest value observed in *ESFa-6-CO₂*. The mean bubble diameter is similar to that of the previous group, ranging from 19.83 µm to 28.14 µm. It should be noted that the surface area analysed for sample *ESFa-6-CO₂* is larger than that of the other samples in this group, which suggests that the piece is more complete.

- *Group 60 minutes of experiment*: With only two samples the vesicularity of this group is between 3 and 4%. The bubble density is similar to that of the previous group, with 41.1 mm^{-2} and 52.54 mm^{-2}, respectively, as well as the mean diameter of the vesicles, which is 18.6 µm and 24.45 µm.
- *Groups 130 and 240 minutes of experiment*: These temporal series show a slight increase in vesicularity, and bubble density compared to the previous group, up to 5% and 63.61 mm^{-2} respectively, while the mean diameter remains within a similar range of around 22 µm.
- *Groups 360 and 1140 minutes of experiment*: After 360 minutes of the experiment, the vesicularity of these groups, decreased to less than 2%, and the density of vesicles also decreased to 10.83 mm^{-2}(e.g. *ESFa-2D-CO_2*).

3.5.4.2. VSD, from 2D to volume:

In the previous section, the experimental samples were sorted into seven groups based on the duration of the experiment. In this section, the samples are sorted into three *types* based on Marsh (1988) and Chavrit (2010) for the Vesicle Size Distribution using logarithmic plots of bubble density versus maximum diameter for each range (**Table 3.6.** and **Figures 3.20., 3.21., and 3.22.)**. Furthermore, the analysed surfaces are presented in the Appendix of this manuscript along with the textural characteristics of each sample.

The analysis was attempted on small pieces of glass where the micro-CT analysis was not possible by using SEM images. However, due to their size, the characterization was not representative. The provenance of the pieces inside the capsules could not be located. These pieces, marked by the two asterisks in **Table 3.6**., are not considered for the results and the discussion.

In general, all the experimental samples show a large vesicle size distribution with a coefficient correlation $R^2 > 0.8$, only one sample has a R^2 lower than it and is classified in *type III*, due to a strong effect of Ostwald ripening effect, which is the case of *ESFa-2D-CO_2*.

- *Type I:* Twelve of the quenched glasses were positioned in this type of VDS. This type of VDS is characterised by the absence of an intermediate population of

vesicles between the smallest and largest detected ones. The coefficient ratio here is 0.9 or greater and all-time series are classified within this type.

- *Type II:* this type of VSD is characterised by a coefficient ratio lower than 0.9 but, as can be observed, the R^2 of most of the samples classified here is close to 0.9. The fact of having a constant nucleation of vesicles so fast before the gas can be degassed or vesicles can coalesce gives a large value of R^2 to the smallest population of vesicles, lowering the coefficient ratio.

- *Type III:* even if it was evident in most of the slices analysed, here the samples are classified where the Ostwald ripening phenomenon was more evident for the *Ln(n)* vs D_{max} curve. The graphs show a sharp jump after the third or fourth population of smaller vesicles, where the trend of the logarithmic data increases and curves towards the side of the smaller to medium-sized vesicles. In this type of VSD, it can be observed that the longer test series have the steepest curve.

Sample	Exp. Time (min)	Resolution (µm)	Nb	Area (mm^2)	Bubbles density (mm^{-2})	D_{max} (µm)	D_{mean} (µm)	Ves Image slice (%)	Ln(n) (mm^{-4})	sd	a (mm-1)	sd	R^2	$D_{mean\ th}$ (-1/a) (µm)	G_0 (µm/min)	VSD group
ESFa-4-CO₂	30	3	376	8.98	42.11	99.85	19.83	2.07	12.5	0.3	-66.9	5.8	0.93	15.0	8.3E-03	III
ESFa-5-CO2*	30		71	1.25	57.0	48.05	21.40	2.05								
ESFa-6-CO2	30	3.5	712	13.36	53.75	185.26	28.14	6.77	11.7	0.4	-40.6	4.9	0.88	24.6	1.4E-02	II
ESFa-7-CO2	30	3	472	9.37	52.54	118.58	20.84	3.25	12.5	0.4	-59.5	6.4	0.90	16.8	9.3E-03	III
ESFa-8-CO2	240	3	145	4.82	30.71	118.77	19.48	1.90	12.0	0.4	-63.7	7.8	0.87	15.7	8.7E-03	II
ESFa-9-CO2	240	3	639	12.54	51.35	173.21	24.00	4.74	12.0	0.4	-47.4	4.8	0.91	21.1	1.2E-02	I
ESFa-10-CO2	240	3	196	12.11	16.52	108.32	21.32	1.04	11.3	0.4	-62.9	7.7	0.87	15.9	8.8E-03	II
ESFa-7E-CO2	10	3	553	6.28	88.95	98.58	14.71	3.09	13.5	0.4	-78.7	9.0	0.88	12.7	7.1E-03	II
ESFa-8E-CO2	10	3	751	9.57	78.62	309.61	25.40	9.60	11.2	0.5	-31.4	3.6	0.88	31.8	1.8E-02	II
ESFa-9E-CO2	10	3	352	5.69	62.59	155.05	21.06	4.74	12.3	0.5	-53.1	7.3	0.84	18.8	1.0E-02	II
ESFa-10E-CO2	1140	3	497	12.83	39.0	102.79	20.12	2.14	12.3	0.3	-63.6	6.8	0.90	15.7	8.7E-03	I
ESFa-1D-CO2*	1140		11	1.78	6.19	24.04	14.10	0.10								
ESFa-2D-CO2	1140	3	64	2.93	10.83	179.70	33.09	1.36	10.3	0.6	-36.4	7.2	0.72	27.4	1.5E-02	III
ESFa-3D-CO2	130	3	555	11.42	39.14	139.98	23.07	2.58	12.3	0.2	-56.1	3.7	0.96	17.8	9.9E-03	I
ESFa-4D-CO2	130	3	655	10.38	63.61	131.93	21.04	4.12	12.5	0.4	-56.6	5.9	0.90	17.7	9.8E-03	I
ESFa-5D-CO2	130	3	705	15.29	51.87	246.26	22.29	4.94	10.9	0.7	-36.1	5.7	0.80	27.7	1.5E-02	II
ESFa-6D-CO2	360	3	96	6.15	16.09	97.47	20.46	1.01	11.6	0.4	-70.5	8.1	0.88	14.2	7.9E-03	III
ESFa-7D-CO2	360	3	282	14.57	19.49	157.36	24.00	1.84	11.0	0.5	-46.8	6.7	0.83	21.4	1.2E-02	III
ESFa-8D-CO2	360	3	209	13.39	15.68	229.74	24.95	1.64	10.7	0.4	-46.0	3.8	0.94	21.7	1.2E-02	I
ESFa-10D-CO2	10	3	1207	15.12	79.95	122.66	16.30	2.93	13.2	0.4	-69.5	6.3	0.92	14.4	8.0E-03	I
ESFa-1C-CO2	10	3	583	10.40	56.1	322.30	27.95	7.88	10.87	0.51	-30.20	3.37	0.89	33.1	1.8E-02	II
ESFa-2C-CO2	10	3	400	11.82	35.20	140.43	22.02	2.47	12.38	0.49	-63.21	6.08	0.92	15.8	8.8E-03	I
ESFa-3C-CO2*	60		273	1.27	215.62	59.45	15.87	4.27								
ESFa-4C-CO2	60	3	332	5.15	64.66	143.98	18.16	3.14	13.39	0.55	-80.62	8.01	0.91	12.4	6.9E-03	I
ESFa-5C-CO2	60	3	490	12.00	41.09	159.39	24.45	3.69	11.84	0.40	-49.53	5.30	0.90	20.2	1.1E-02	I
ESFa-6C-CO2	240	3	451	12.88	35.08	163.54	15.53	1.26	12.44	0.44	-73.74	5.72	0.94	13.6	7.5E-03	I
ESFa-7C-CO2	240	3	223	9.76	23.04	158.13	23.25	1.96	11.31	0.52	-52.31	6.88	0.85	19.1	1.1E-02	III

ESFa-8C-CO2	10	3	633	10.93	57.99	201.92	22.44	4.62	11.84	0.50	-43.87	5.21	0.88	22.8	1.3E-02	II
ESFa-9C-CO2	10	3	257	4.94	52.61	168.48	26.40	5.93	11.89	0.47	-45.66	5.91	0.86	21.9	1.2E-02	II
ESFa-10C-CO2	240	3	524	16.09	32.81	159.17	24.92	2.78	11.77	0.30	-52.50	4.04	0.94	19.0	1.1E-02	I
ESFa-1B-CO2	10	3	732	12.77	57.56	170.10	20.33	3.47	12.88	0.48	-67.37	5.93	0.93	14.8	8.2E-03	I
ESFa-3A-CO2	10	3	348	8.62	40.72	165.80	23.76	3.56	11.89	0.43	-51.40	5.41	0.90	19.5	1.1E-02	III

Table 3.6.: VSD parameter of the experimental samples analysed by micro-CT and image treated by ImageJ and Excel. $Exp._{time}$ refers to the duration of the experiment; *Nb* represents the number of counted bubbles in the slice; D_{max} and D_{mean} correspond to the maximum and mean diameter of the vesicles in the analysed slice; $Ves_{ImageJ\ slice}$ indicates the vesicularity of the analysed area in the slice; *Ln(n)* is the density of the population of vesicles obtained by the linear trend of the graph *Ln(n)* vs (D_{max}); *a* is the slope of the trend line; R^2 is the correlation coefficient of the trend line; $D_{mean\ th\ (-1/a)}$ is the theoretical mean diameter for this sample obtained by the inverse of the slope; Additionally, the growth rate of the vesicles is represented by G_0.

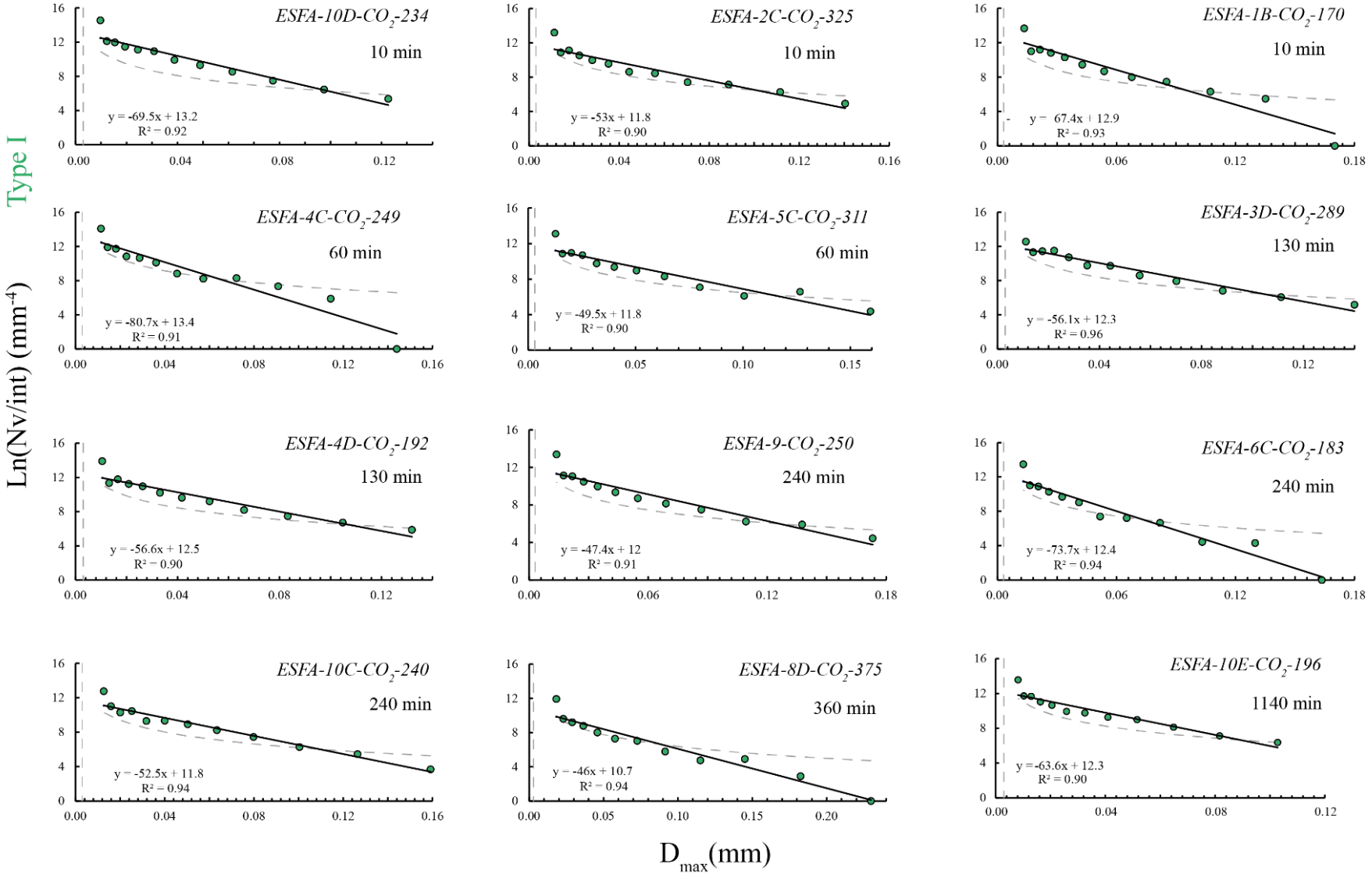
Type I
Ln(Nv/int) (mm-4)
ESFA-10D-CO2-234
10 min
y = -69.5x + 13.2
R² = 0.92
ESFA-2C-CO2-325
10 min
y = -53x + 11.8
R² = 0.90
ESFA-1B-CO2-170
10 min
y = 67.4x + 12.9
R² = 0.93
ESFA-4C-CO2-249
60 min
y = -80.7x + 13.4
R² = 0.91
ESFA-5C-CO2-311
60 min
y = -49.5x + 11.8
R² = 0.90
ESFA-3D-CO2-289
130 min
y = -56.1x + 12.3
R² = 0.96
ESFA-4D-CO2-192
130 min
y = -56.6x + 12.5
R² = 0.90
ESFA-9-CO2-250
240 min
y = -47.4x + 12
R² = 0.91
ESFA-6C-CO2-183
240 min
y = -73.7x + 12.4
R² = 0.94
ESFA-10C-CO2-240
240 min
y = -52.5x + 11.8
R² = 0.94
ESFA-8D-CO2-375
360 min
y = -46x + 10.7
R² = 0.94
ESFA-10E-CO2-196
1140 min
y = -63.6x + 12.3
R² = 0.90
Dmax(mm)

Figure 3.20.: Population density plots as a function of the maximum diameter of each interval for samples grouped in VSD type I. This type is characterized by a population density value > 0.9 and the Ostwald ripening phenomenon is not observed. The dashed grey curve is a way of illustration for a minimum number of 4 bubbles per interval. The vertical dashed grey line is the limit of detection of the tomography. In this group, the population of smaller size of bubbles stands out above the other and further away from the trend line.

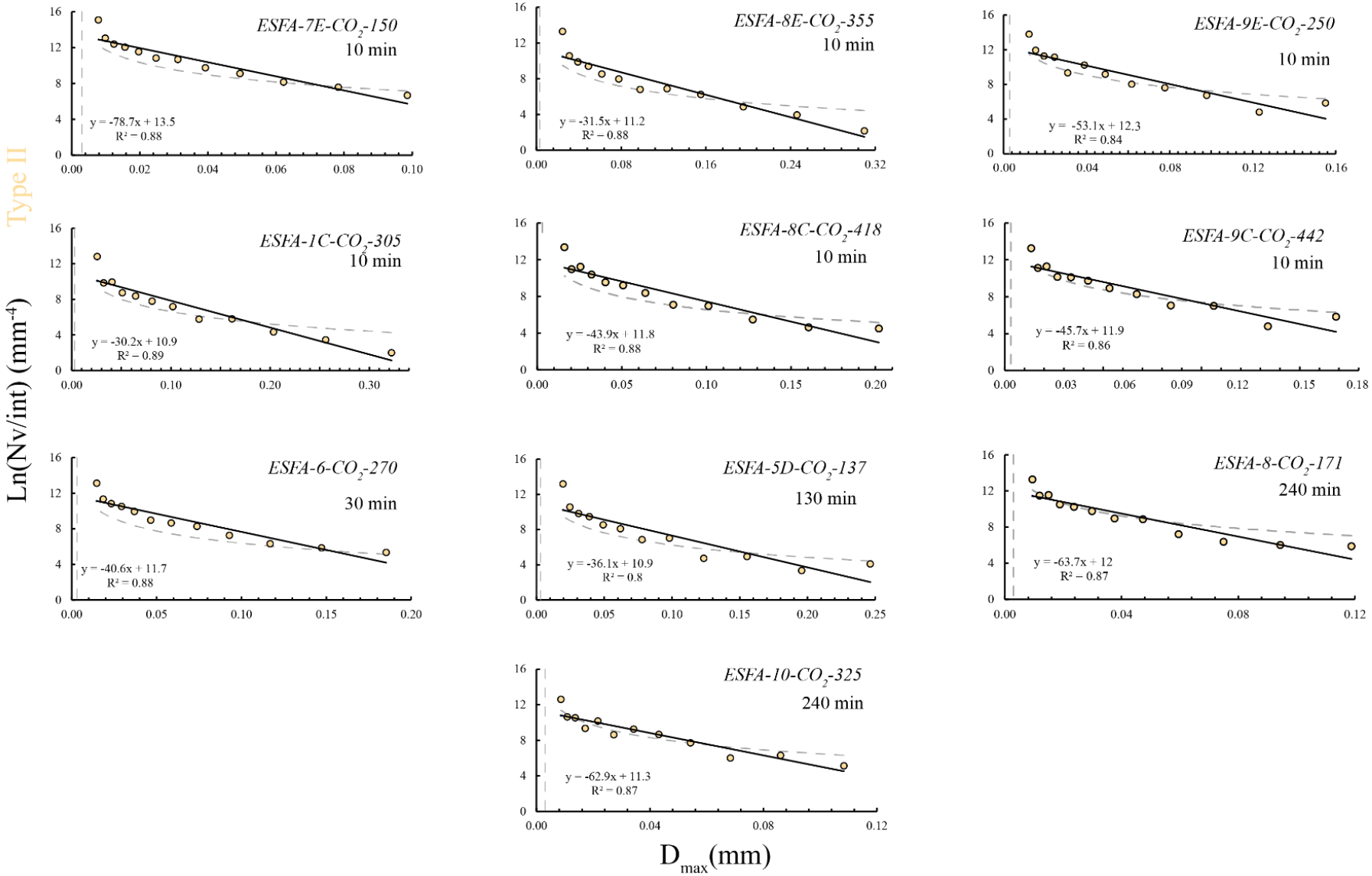
Type II
Ln(Nv/int) (mm-4)
ESFA-7E-CO2-150
10 min
y = -78.7x + 13.5
R² = 0.88
ESFA-8E-CO2-355
10 min
y = -31.5x + 11.2
R² = 0.88
ESFA-9E-CO2-250
10 min
y = -53.1x + 12.3
R² = 0.84
ESFA-1C-CO2-305
10 min
y = -30.2x + 10.9
R² = 0.89
ESFA-8C-CO2-418
10 min
y = -43.9x + 11.8
R² = 0.88
ESFA-9C-CO2-442
10 min
y = -45.7x + 11.9
R² = 0.86
ESFA-6-CO2-270
30 min
y = -40.6x + 11.7
R² = 0.88
ESFA-5D-CO2-137
130 min
y = -36.1x + 10.9
R² = 0.8
ESFA-8-CO2-171
240 min
y = -63.7x + 12
R² = 0.87
ESFA-10-CO2-325
240 min
y = -62.9x + 11.3
R² = 0.87
Dmax(mm)

Figure 3.21.: Population density plots as a function of the maximum diameter of each interval for samples grouped in VSD type II. This type is characterized by a population density value < 0.9 and the Ostwald ripening phenomenon is not observed. The dashed grey curve is a way of illustration for a minimum number of 4 bubbles per interval. The vertical dashed grey line is the limit of detection of the tomography.

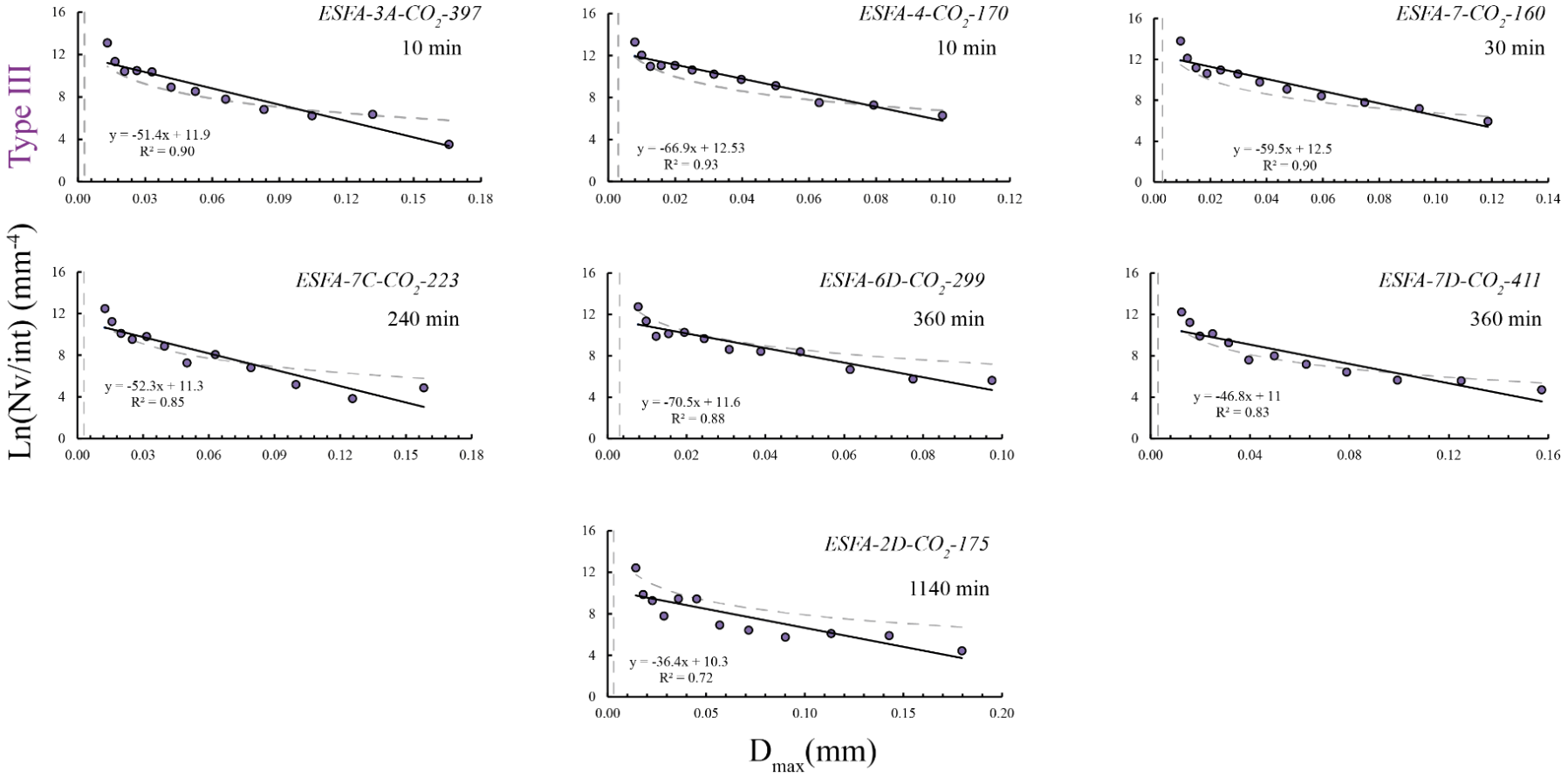

Figure 3.22.: Population density plots as a function of the maximum diameter of each interval for samples grouped in VSD type III. This type is characterized by Ostwald ripening phenomenon curve from the 3rd or 4th population of vesicles. The dashed grey curve is a way of illustration for a minimum number of 4 bubbles per interval. The vertical dashed grey line represents the limit of detection for the tomography. Up until the Ostwald ripening curve, the slope of the smaller population is continuous and detectable.

In **Figure 3.23.a**. when comparing the bubble population density with the mean diameter measured in our samples, a steep slope is observed. The population density decreases as the mean sample diameter increases, while the sample population density increases with the measured bubble density. The theoretical maximum diameter (-1/*a*) also shows an inverse relationship with the population density, *Ln(n)* (**Figure 3.23.b)**. The mean diameter estimated from the slope of the VSD plots, -1/*a*, is slightly smaller than the measured mean diameter.

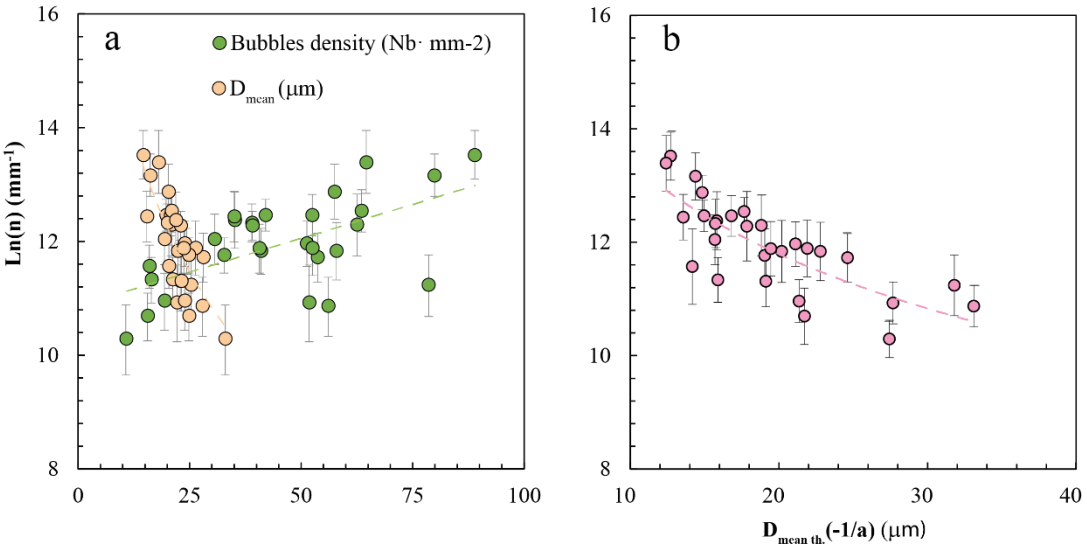

Figure 3.23: (a) The graphic displays the population density of vesicles of various sizes for each sample, plotted against the bubble density (green dots) and the measured mean diameter (salmon dots). The dashed lines are indicative of the trend for each parameter. The units are shown in the legend **(b)** Density of population of each sample vs the theoretical mean diameter of each sample and the logarithmic trend line by way of example. The standard deviation of *Ln(n)* is also plotted for every sample in this graphic.

3.5.5. Theoretical Vesicularity and Growth Rate:

The result of the lost vesicularity is shown in **Table 3.7.** Measuring vesicularity using either *ImageJ* (green in the figure and calculated from surface to volume) or *VGStudioMax* (purple in the diagram measured in 3D) does not make a significant difference for this study. The vesicularity measured using *ImageJ* is larger because it includes some bubbles located between the quenched glass and the capsule some part of the volume of the system.

Figure 3.24. illustrates a direct correlation between the amount of CO_2 loaded into the capsule and the increase in Ves_{lost}. The upper graphic shows that the vesicularity remaining in the sample is not influenced by the amount of CO_2 dissolved into the glass, as it remains stable. Therefore, there must be another factor influencing the vesicularity.

Upon closer inspection, **Figure 3.24.** shows three samples where the theoretical vesicularity and the one measured in the glass become closer than the other samples. These samples, represented by the three green and/or purple dots outside the trend line, correspond to a 10-minute interval during the experiment (*ESFa-8E-CO₂*, *ESFa-1C-CO₂,* and *ESFa-9C-CO₂*). As these samples correspond to different experimental runs, it can be concluded that this is not an artefact of the experiment.

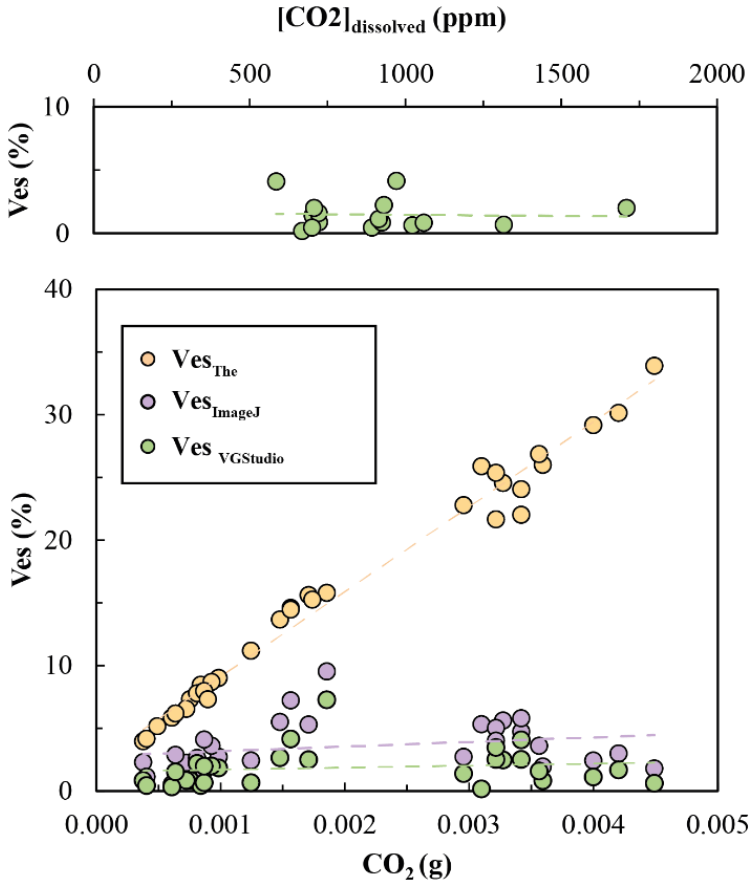

Figure 3.24.: relation between vesicularity of the system and/or vesicularity of the sample and the CO_2 dissolved or loaded into the experimental capsules. Salmon dots represent the vesicularity of the system, the expected vesicularity based on the amount of CO_2 loaded. The purple and green dots represent the vesicularity measured in the whole volume of the sample by ImageJ from the sum of the total area, and in green the one obtained by VGStudioMax.

Sample	P (bar)	St.mat (g)	CO_2 (g)	m_{total} (g)	V_{liq} (cm^3)	V_b (cm^3)	V_{magma} (cm^3)	V_{the} (%)	Ves_{ImageJ} (%)	$Ves_{VGSTudio}$ (%)	V_{diff} (%)
ESFa-4-CO2	1546	0.0632	0.0008	0.0640	0.0232	0.0018	0.0251	7.4	1.6	0.9	6.5
ESFa-5-CO2	1546	0.0607	0.0016	0.0623	0.0221	0.0038	0.0260	14.8			
ESFa-6-CO2	1546	0.0618	0.0015	0.0633	0.0225	0.0036	0.0261	13.9	5.5	2.7	11.2
ESFa-7-CO2	1546	0.0646	0.0042	0.0688	0.0237	0.0103	0.0340	30.3	3.0	1.7	28.6
ESFa-8-CO2	1558	0.0601	0.0008	0.0609	0.0221	0.0021	0.0242	8.5	1.1	0.5	8.0
ESFa-9-CO2	1558	0.0612	0.0017	0.0629	0.0226	0.0042	0.0268	15.7	5.3	2.5	13.2
ESFa-10-CO2	1558	0.0581	0.0045	0.0626	0.0213	0.0110	0.0323	34.2	1.8	0.6	33.5
ESFa-7E-CO2	1776	0.0622	0.0007	0.0629	0.0228	0.0016	0.0244	6.6	2.3	0.9	5.7
ESFa-8E-CO2	1776	0.0596	0.0019	0.0615	0.0217	0.0041	0.0258	16.1	9.6	7.3	8.8
ESFa-9E-CO2	1776	0.0651	0.0034	0.0685	0.0235	0.0076	0.0312	24.5	4.8	2.5	22.0
ESFa-10E-CO2	1747	0.0620	0.0009	0.0629	0.0226	0.0020	0.0246	8.0	1.6	0.7	7.3
ESFa-1D-CO2	1747	0.0588	0.0017	0.0605	0.0214	0.0039	0.0253	15.5			
ESFa-2D-CO2	1747	0.0623	0.0036	0.0659	0.0226	0.0081	0.0308	26.4	2.0	0.8	25.5
ESFa-3D-CO2	1746	0.0552	0.0004	0.0556	0.0199	0.0008	0.0208	4.1	2.3	0.9	3.2
ESFa-4D-CO2	1746	0.0605	0.0010	0.0615	0.0222	0.0022	0.0244	9.1	2.7	1.9	7.2
ESFa-5D-CO2	1746	0.0613	0.0033	0.0646	0.0222	0.0074	0.0296	25.0	5.6	2.5	22.5
ESFa-6D-CO2	1638	0.0622	0.0006	0.0628	0.0229	0.0014	0.0244	5.9	0.6	0.4	5.5
ESFa-7D-CO2	1638	0.0629	0.0012	0.0641	0.0228	0.0029	0.0258	11.4	2.5	0.7	10.7
ESFa-8D-CO2	1638	0.0637	0.0030	0.0667	0.0233	0.0070	0.0303	23.0	2.7	1.4	21.6
ESFa-10D-CO2	1631	0.0615	0.0006	0.0621	0.0225	0.0015	0.0240	6.2	2.9	1.5	4.7
ESFa-1C-CO2	1631	0.0589	0.0016	0.0605	0.0213	0.0037	0.0250	14.7	7.2	4.2	10.6
ESFa-2C-CO2	1631	0.0565	0.0031	0.0596	0.0205	0.0073	0.0278	26.3	5.3	0.2	26.1
ESFa-3C-CO2	1643	0.0575	0.0005	0.0580	0.0209	0.0012	0.0220	5.2			
ESFa-4C-CO2	1643	0.0618	0.0009	0.0627	0.0225	0.0022	0.0247	8.8	3.6	2.0	6.8
ESFa-5C-CO2	1643	0.0618	0.0036	0.0654	0.0224	0.0084	0.0308	27.2	3.6	1.6	25.6
ESFa-6C-CO2	1663	0.0586	0.0004	0.0590	0.0215	0.0009	0.0224	4.2	1.1	0.5	3.8
ESFa-7C-CO2	1663	0.0613	0.0040	0.0653	0.0221	0.0093	0.0315	29.7	2.4	1.1	28.6
ESFa-8C-CO2	1663	0.0734	0.0032	0.0766	0.0266	0.0075	0.0341	22.0	5.0	2.5	19.5
ESFa-9C-CO2	1613	0.0782	0.0034	0.0816	0.0283	0.0082	0.0365	22.4	5.8	4.1	18.3
ESFa-10C-CO2	1613	0.0618	0.0008	0.0626	0.0226	0.0019	0.0246	7.9	2.6	2.2	5.6
ESFa-1B-CO2	1613	0.0646	0.0009	0.0655	0.0237	0.0021	0.0257	8.1	4.1	2.0	6.1
ESFa-3A-CO2	1677	0.0591	0.0032	0.0623	0.0215	0.0074	0.0289	25.7	4.0	3.5	22.2
ESFa-4A-CO2	1740	0.0692	0.0009	0.0701	0.0253	0.0020	0.0273	7.4			

Table 3.7.: specification of the amount of material loaded in each capsule and of the calculation of the theoretical vesicularity. *P* is the pressure of the experiment when it was quenched; *St.mat* refers to the weight of the loaded starting material; *CO2* is the weight of CO2 loaded in the capsule; m_{total} is the sum of all components; V_{liq} is the calculated volume of the melt; V_b is the calculated volume of the CO2 in the vesicles from the amount of CO2 loaded for this pressure and density of the sample; and V_{magma} is the volume of the magma; additionally Ves_{the} and Ves_{diff} represent the theoretical vesicularity and the lost vesicularity by subtracting the Ves calculated by VGStudioMax.

The coalescence of bubbles can be observed in all quenched glasses, whether on a local part of the sample or in the whole sample. Please refer to the *Appendix* for images of *ImageJ* treatment. A rapid nucleation of vesicles, their quick ascension due to gravity, and a significant decrease of vesicularity may indicate extensive degassing or gas segregation. Therefore, it is important to calculate the rate of growth of the vesicles, G_0 and see the relationship with other parameters already explained.

Figure 3.25. compares the growth rate with the CO_2 dissolved in the, the vesicularity, and the mean bubble diameter of each sample glass (**Tables 3.6** and **3.5**). The trends for the two groups of data indicate not correlation between the mean diameter and the dissolved CO_2 with this new parameter.

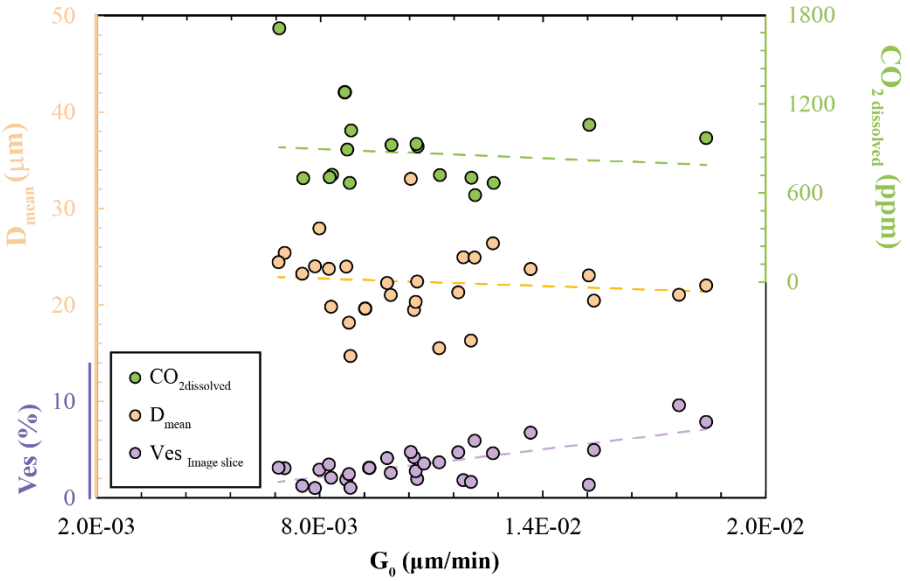

Figure 3.25. The relationship between the vesicularity of the sample, the amount of CO_2 dissolved in the glass, and the mean diameter of the vesicles was analysed to determine their relationship with the growth rate of the vesicles in each quenched glass. The mean diameter is represented by salmon dots and the trend line is shown in the same colour. The amount of CO_2 dissolved in the glass is represented by green dots and the trend line is shown in the same colour. The vesicularity was measured in the volume of the sample using *ImageJ*, by summing the total area, and is represented by purple dots.

In contrast, vesicularity is more markedly correlated. The samples with the highest vesicularity are those with the fastest growth rate. It is important to note that this growth rate parameter is calculated based on a fixed/constant residence time, which is the same for all samples (the experimental duration upon which no more bubbles are found in the sample for these pressure and temperature conditions – *EN-E3, Chapter 5*), and the slope of the VSD.

3.5.6. CO_2 diffusion and bubble rise rate:

To ensure maximum rigour, we only calculated CO_2 diffusion in magma (following the formula showed in *Section 3.1* for CO_2 diffusion) and bubble ascent velocity for samples where FTIR analysis and tomography were possible. As expected, the diffusion values remain constant since the magma composition does not change and the maximum water content in the samples does not exceed 1% (less than 0.5% for this set of samples). The values range from $9.07 \cdot 10^{-12}$ to $9.25 \cdot 10^{-12}$ $m^2 \cdot s^{-1}$ (**Table 3.8.**).

Sample	Exp. Time (min)	r (m)	ηL (Pa/s)	D_{CO2} (m^2/s^1)	v_b m/s	R_{exp} cm	D_{exp} cm	G_r cm
ESFa-4-CO2	30	9.92E-06	40.81	9.23E-12	1.21E-08	0.002	0.013	1.25E-05
ESFa-8-CO2	240	9.74E-06	25.79	9.25E-12	1.84E-08	0.027	0.036	1.05E-04
ESFa-10-CO2	240	1.07E-05	28.16	9.24E-12	2.04E-08	0.029	0.036	1.06E-04
ESFa-10E-CO2	1140	1.01E-05	13.53	9.21E-12	3.74E-08	0.256	0.079	4.98E-04
ESFa-2D-CO2	1140	1.65E-05	15.16	9.19E-12	9.08E-08	0.621	0.079	8.69E-04
ESFa-3D-CO2	130	1.15E-05	40.81	9.07E-12	1.65E-08	0.013	0.027	6.44E-05
ESFa-8D-CO2	360	1.25E-05	40.81	9.13E-12	1.91E-08	0.041	0.044	2.17E-04
ESFa-1C-CO2	10	1.40E-05	40.81	9.14E-12	2.43E-08	0.001	0.007	9.20E-06
ESFa-2C-CO2	10	1.10E-05	40.81	9.14E-12	1.51E-08	0.001	0.007	4.39E-06
ESFa-4C-CO2	60	9.08E-06	40.81	9.12E-12	1.02E-08	0.004	0.018	2.07E-05
ESFa-5C-CO2	60	1.22E-05	40.81	9.12E-12	1.85E-08	0.007	0.018	3.36E-05
ESFa-6C-CO2	240	7.76E-06	40.81	9.22E-12	7.44E-09	0.011	0.036	9.04E-05
ESFa-7C-CO2	240	1.16E-05	40.81	9.22E-12	1.70E-08	0.024	0.036	1.27E-04
ESFa-9C-CO2	10	1.32E-05	21.11	9.21E-12	4.20E-08	0.003	0.007	6.08E-06
ESFa-10C-CO2	240	1.25E-05	40.81	9.22E-12	1.92E-08	0.028	0.036	1.27E-04
ESFa-1B-CO2	10	1.02E-05	19.79	9.22E-12	2.62E-08	0.002	0.007	4.12E-06

Table 3.8. Results obtained for CO_2 diffusion and bubble velocity for the composition of our experimental samples and from the CO_2 and H_2O dissolved in the glass for the respective conditions of pressure. *Exp.Time* is the experimental time, *r* is the mean radius of the vesicles obtained from the mean diameter from the VSD parameters, η_L is the viscosity of the melt, D_{CO2} is the CO_2 diffusion, v_b is the velocity of the bubbles, R_{exp} is the distance covered by the vesicle at *Exp.Time*, D_{exp} is the distance covered by the CO_2 diffusion at *Exp.Time* and G_r is the bubble radius growth at *Exp.Time*.

However, the presence of water affects the viscosity of the liquid, causing it to decrease by a few tens of $Pa \cdot s^{-1}$ as the water content increases. This results in an increased rate of ascent velocity for samples (**Figure 3.26.**).

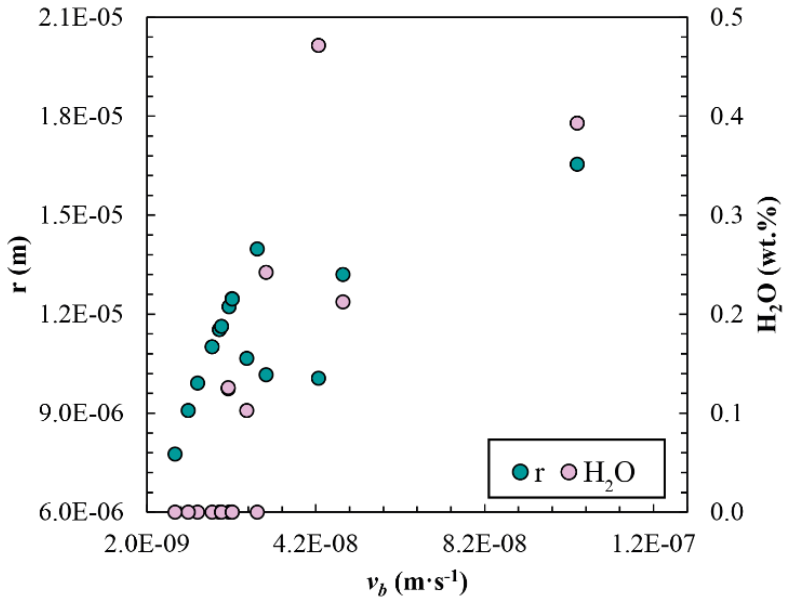

Figure 3.26. The diagram plots the bubble velocity as a function of the mean vesicle radius (left axis, green dots) and the percentage of H_2O dissolved in the glass (right axis, pink dots).

3.6. Discussion:

3.6.1. Vesicularity and CO_2 dissolved in time:

A useful method for illustrating the evolution of vesicularity and bubble distribution in our time series is to draw a graph that displays a sample from each group, ordered by duration from shortest to longest. The advantage of using X-ray tomography and image analysis is that it allows us to visualise this evolution in the quenched samples.

Although the images may not be at the same scale, the increase in the population of larger diameter bubbles and the disappearance of smaller populations from shorter to longer experiments are well apparent in **Figure 3.27** and **VSD graphics** (the scale of the D_{max} population of vesicles trend to increase in time). In addition, the distribution of vesicles is more homogeneous in shorter experiments compared to longer ones, where they tend to accumulate towards one end of the capsule (the upper part). Bubble coalescence is present in all samples, but it is more noticeable in shorter experiments, where the nucleation is stronger and vesicularity higher.

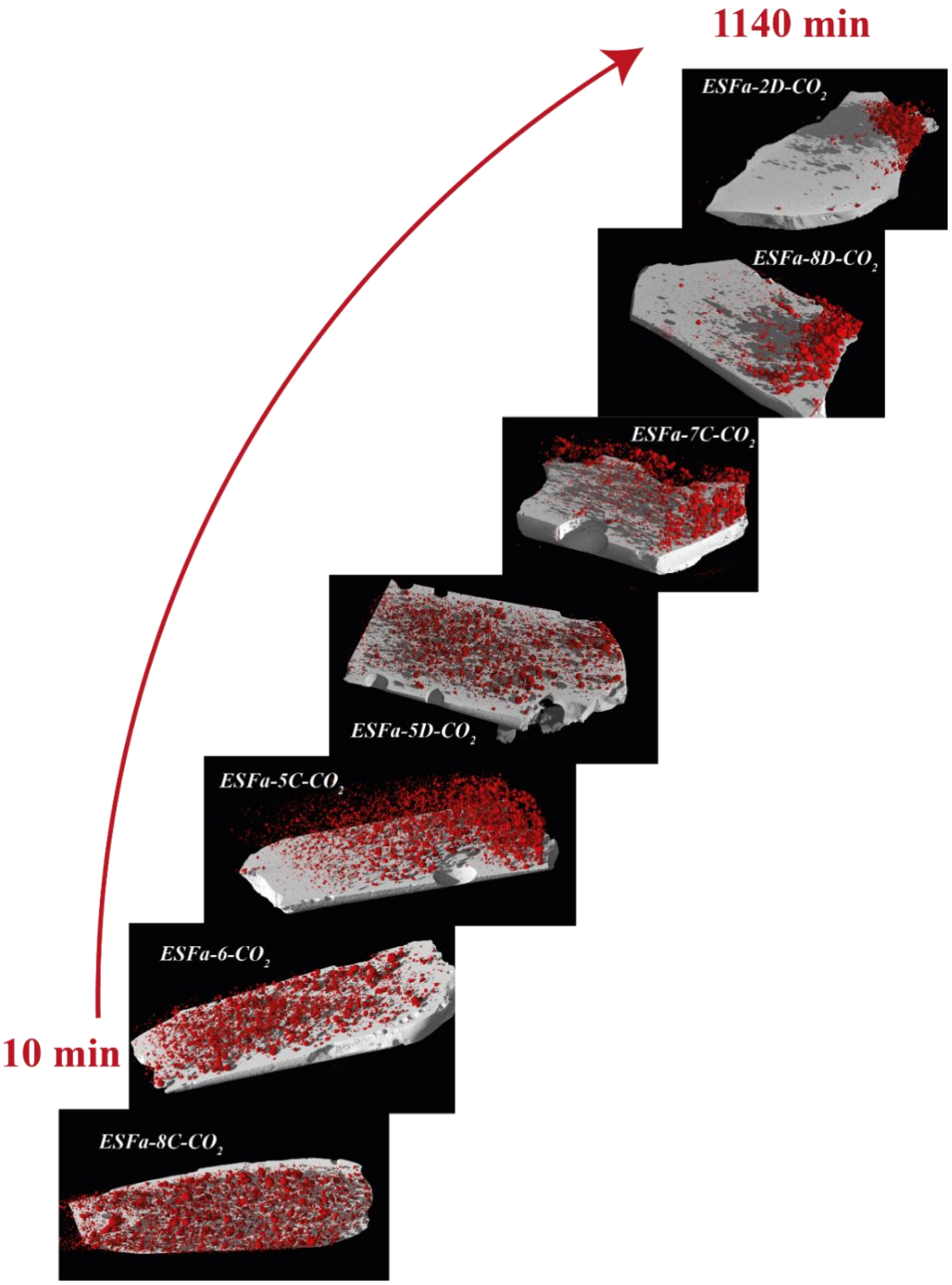

Figure 3.27.: For this figure and the general discussion, the most representative sample volumes of each of the experimental groups have been selected, separated by time. The experiment time increases from 10 to 1140 minutes, from the sample on the bottom to the sample on the top.

The decrease of vesicularity from the shorter to the longer experiments, together with the accumulation of larger vesicles towards the top of the capsule and the near

disappearance of bubble nucleation in the main volume of melt in the 1140 min experiments, suggest (i) the total dissolution of CO_2 in the glass and/or (ii) a possible magma gas segregation. Considering that the magma is in a closed system (the sealed capsule).

The **Figure 3.28.** displays the samples analysed using both FTIR and microtomography to investigate the relationship between CO_2 dissolved in the glass and vesicularity. The vesicularity represented here is the same as that obtained with the 3D image of the experimental glasses. This provides a better reference for comparing to **Figure 3.27**.

Although a significant amount of CO_2 was added in the solid form of silver oxalate, the maximum vesicularity achieved was only 7.3% in sample *ESFa-8E-CO_2* during the 10-minute experiment (refer to **Table 3.7**). For instance, samples *ESFa-10E-CO_2* and *ESFa-2D-CO_2* contained 1.38 and 5.45 wt.% of CO_2, respectively, but ended up with a vesicularity of less than 1%.

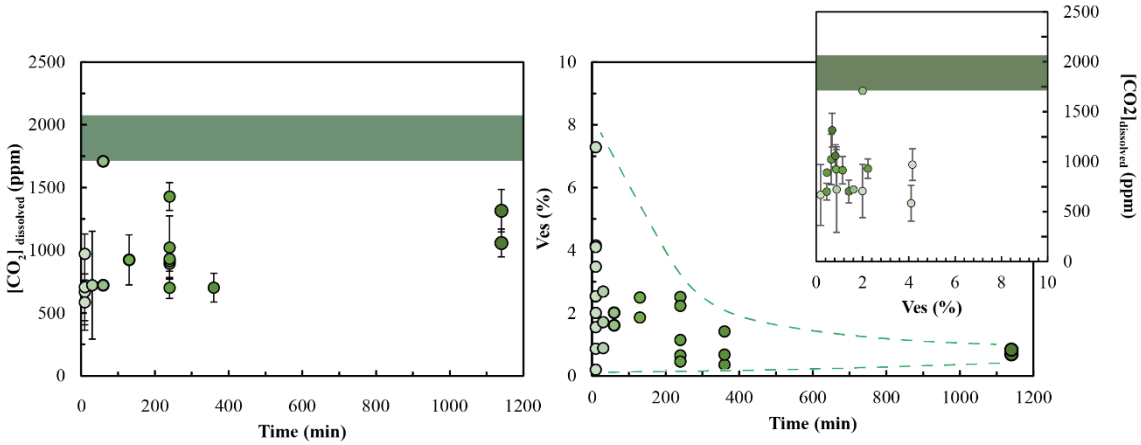

Figure 3.28.: The green area of the figures points out the maximum CO_2 dissolved expected in the samples for the composition of the magma and the conditions of the experiments (1200ºC and 1.5-1.7 kbars) regarding to (Jiménez-Mejías et al., 2021). The darkness of the dots in the green scale increases with the duration of the experiment. The dashed green lines show the field of vesicularity dispersion over time.

The distribution of CO2 in the glass becomes more homogeneous over time, as shown in **Figure 3.28**. by the dispersion of the samples, the incorporation of CO_2 into the glass and the decrease in the standard deviation. According to the solubility laws and experimental conditions, and according to Jiménez-Mejías et al. (2021), our composition should reach between 1750-2100 ppm of dissolved CO_2 at 1200 ºC and 1.5-1.7 kbars once

equilibrium is achieved (green area in the graphics). Despite being in the same conditions as P and T, the CO_2 dissolved into the quenched glasses does not reach what it is supposed to. This is likely because the time to reach the equilibrium in the experiment is not long enough as noted by Pichavant et al. (2018).

Similarly to the CO_2 dissolved in the glass, vesicularity decreases over time and its value becomes less dispersed. One observation from comparing the vesicularity and dissolved CO_2 in the quenched glass at different run times is the lack of correlation between the two parameters in non-equilibrium experiments.

3.6.2. VSD in time:

When comparing the calculated VSD parameters (**Figure 3.29.**), it can be observed that the density of bubbles decreases as the duration of the experiments increases, in parallel with the vesicularity. A proportional trend can be seen when representing the vesicularity against the density of bubbles per mm^2 of the sample. In contrast, our experiments show an increase in the average size of the bubbles over time, which was also noticeable in the 3D images of the tomography.

The decrease in vesicularity and bubble density, coupled with an increase in average diameter and a relatively heterogeneous but constant distribution of dissolved CO_2 in the glasses, suggests that the flux of CO_2, produced when the oxalate reached the temperature to release it, is being transferred toward the top of the capsule faster than the time that the melt has to assimilate it. Additionally, the decrease of vesicularity indicates that gas segregation becomes more significant as the initial starting composition is richer in CO_2.

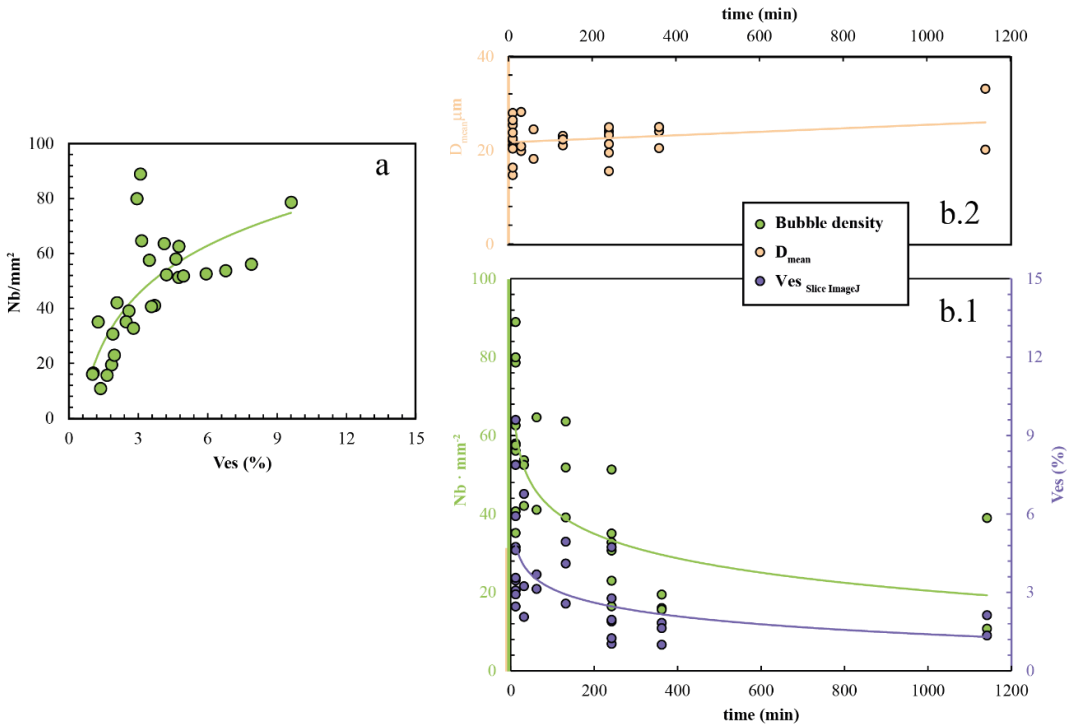

Figure 3.29. VSD parameters in time. Graph ***a***. and ***b.1***. show the direct relationship between bubble density and vesicularity. In ***b.1***. Both parameters display a logarithmic trend line over time with bubble density on the left axis and vesicularity on the right axis. Graph **b.2**, on the other hand, shows an increasing linear trend.

3.6.3. Competition between diffusion and particle velocities:

The comparison of VSD parameters and dissolved CO_2, sorted by time, led us to consider the competition between particle velocity (bubbles) and diffusion. When translating textural data into physical values by applying the diffusion laws (*Section 3.1.*) and bubble transfer (*Section 3.5.1.)* it is observed that during the first six hours of the experiments and for an equal period, diffusion dominates the physical process of CO_2 partitioning, reaching greater distances than bubble mobility (refers to **Figure 3.30**.). However, after about six hours, the distance travelled by the bubbles R_{exp} becomes more important than diffusion D_{exp}.

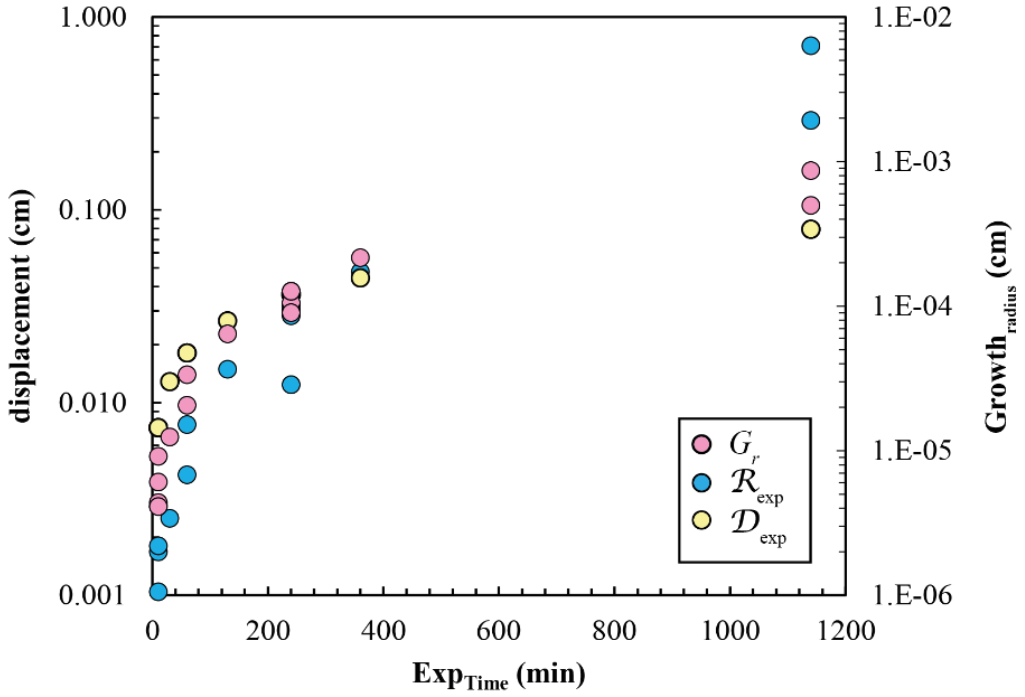

Figure 3.30. The diagram illustrates the displacement of CO_2 through diffusion (yellow dots) or in bubbles (blue dots) on the left axis, and the growth of the bubble radius (pink dots) on the right axis over time. For better visualisation, logarithmic scales are used on the axes.

The experiments in this series rely heavily on the results of CO_2 diffusion and particle velocity. These results are influenced by the viscosity of a melt with a small water content and the diameter of the bubbles that move through it.

The size of the bubbles and the time they take to form are the main factors that determine CO_2 partitioning in our experiments, despite the impact of dissolved water on particle velocity. As shown by the VSD parameters, increasing the experiment's duration results in a larger mean bubble diameter and, consequently, a faster v_s.

As discussed in section *3.5.5*, G_0 is associated with vesicularity and, to a lesser extent, other VSD parameters. In shorter experiments, G_0 was faster, but it became progressively slower in longer experiments where the nucleation of new vesicles was rare or absent. As nucleation decreases, v_s increases because the vesicles grow at the expense of coalescence of larger vesicles. The effect can be observed in **Figure 3.30**., where the growth of the radius over time, G_r, indicated by the pink dots, follows the same trend as the displacement of the vesicles over time, R_{exp}.

3.7. Conclusions, implications for a natural system and perspectives:

It is crucial to emphasize the significance of studying vesicularity in the entire sample obtained from experiments. Taking a small portion of the sample's volume may result in less rigorous data. This is demonstrated by the distribution of bubbles in certain parts of the capsule.

When conducting a study on natural samples, such as using thermodynamics as a tool, it is possible to locate the samples in various parts of the volcanic conduit or magmatic chamber and create a 'representative' scheme. However, as demonstrated by the treated tomography images, even a small omission of volume from the experimental samples can result in a significant difference.

Due to the large amount of data provided by the volume under study (in terms of processing), a complementary 3D and 2D analysis is a powerful tool for characterizing the textural properties of the samples.

Regarding the parameters of vesicularity, the shorter experiments have a higher vesicularity compared to those lasting 1140 minutes. This results in more homogeneous VSD distributions, unlike samples where bubble nucleation decreases or where coalescence dominates over nucleation.

This chapter examines the behaviour of an initial dry basaltic melt under pre-established *P-T* conditions when exposed to a sudden influx of CO_2. This study aimed to investigate the changes in VSD parameters over time and the physical laws that govern the presence of CO_2 in the system, including bubble nucleation, vesicularity, gas diffusion and transport, and gas saturation of the melt over time under non-equilibrium conditions and before decompression.

The experiment simulated the sudden injection of a CO_2 column into a dry liquid and the various effects on dissolution and vesicularity. The samples were subjected to textural analysis, which revealed a continuous nucleation process and a rapid rate of bubble growth in the newly formed vesicles. This resulted in a wide range of bubble sizes and a varied distribution throughout the glass in shorter-time experiments. Towards the final stages before reaching equilibrium, bubble nucleation is rare or absent. Although the number of bubbles continues to increase, their growth rate slows down.

The samples indicate that during the initial stages of nucleation and growth of vesicles, CO_2 diffusion dominates the physical process over vesicle transport, despite the vesicularity reaching its peak during these stages.

Diffusion is a parameter affected by the concentration of a compound in the melt. At time zero, the initial material has a CO_2 concentration of 0 ppm and begins to release CO2 from the silver oxalate once the melting temperature is reached (around 140ºC). This allows CO2 to diffuse through the grains more quickly than vesicle transport, as shown in **Figure 3.30**.

During nucleation, the bubble transport through the top pf the capsule is dependent on the size of the bubbles, resulting in a slow rise. As time passes, the vesicles increase in size and the concentration of CO_2 in the liquid increases, causing diffusion to slow down until equilibrium is reached. However, the particles continue to increase in size, making their displacement more effective and increasing the rate of rise about diffusion.

The low vesicularity in the liquid before reaching equilibrium (group 1140-min of experiments), the slowdown of G_0, even with the presence of CO_2 in the system, and the homogenisation tendency of CO_2 in the glass indicate that equilibrium is approaching. The cessation of bubble nucleation in the longest experiments, even with an excess of CO_2, and the sub saturation of CO_2 in the glass, suggest the accumulation of gas at the top of the capsule in the melt-capsule interface, while diffusion is still taking place.

In a basaltic system, where CO_2 is the predominant volatile phase, our results suggest that:

- With the arrival of a new influx of magma/gas rich in CO_2 in a basaltic system, the CO_2 will initially diffuse faster towards the old melt present in the magmatic chamber until the size of the new bubbles reaches a critical size (approximately 5 μm in diameter according to our experiments). Once this critical size is reached, the vesicles will transport the CO_2 to the surface faster than the time it takes for CO_2 to diffuse in the melt and reach equilibrium in the system.
- The results demonstrate that CO_2 fractionation can occur under non-equilibrium conditions before decompression of the magmatic chamber. This process may lead to a greater gas loss than the magma can dissolve before assimilation.

Therefore, when discussing the diffusion of CO_2 and the faster bubble ascension rate that precedes decompression, it becomes more feasible to consider the possibility of noble gas fractionation at these levels. This leads to the next experimental stage, which involves searching for fractionation in the initial vesicles of neon isotopes, the main goal of this thesis. This work will be further developed in the next chapters.

3.8. References:

Aiuppa, A., Federico, C., Giudice, G., Giuffrida, G., Guida, R., Gurrieri, S., Liuzzo, M., Moretti, R., Papale, P., 2009. The 2007 eruption of Stromboli volcano: insights from real-time measurement of the volcanic gas plume CO2/SO2 ratio. J. Volcanol. Geotherm. Res. 182, 221–230.

Allegre, C.J., Manhes, G., Göpel, C., 1995. The age of the Earth. Geochim. Cosmochim. Acta 59, 1445–1456.

Allègre, C.J., Staudacher, T., Sarda, P., Kurz, M., 1983. Constraints on evolution of Earth's mantle from rare gas systematics. Nature 303, 762–766. https://doi.org/10.1038/303762a0

Aubaud, C., 2022. Carbon stable isotope constraints on CO2 degassing models of ridge, hotspot and arc magmas. Chem. Geol. 605, 120962.

Aubaud, C., Pineau, F., Jambon, A., Javoy, M., 2004. Kinetic disequilibrium of C, He, Ar and carbon isotopes during degassing of mid-ocean ridge basalts. Earth Planet. Sci. Lett. 222, 391–406.

Aubry, G.J., Sator, N., Guillot, B., 2013. Vesicularity, bubble formation and noble gas fractionation during MORB degassing. Chem. Geol. 343, 85–98.

Azuma, S., Ozima, M., Hiyagon, H., 1993. Anomalous neon and xenon in an Archaean anorthosite from West Greenland. Earth Planet. Sci. Lett. 114, 341–352.

Ballentine, C.J., Barfod, D.N., 2000. The origin of air-like noble gases in MORB and OIB. Earth Planet. Sci. Lett. 180, 39–48.

Ballentine, C.J., Burgess, R., Marty, B., 2002. Tracing fluid origin, transport and interaction in the crust.

Ballentine, C.J., Burnard, P.G., 2002. Production, Release and Transport of Noble Gases in the Continental Crust. Rev. Mineral. Geochem. 47, 481–538. https://doi.org/10.2138/rmg.2002.47.12

Ballentine, C.J., Marty, B., Sherwood Lollar, B., Cassidy, M., 2005. Neon isotopes constrain convection and volatile origin in the Earth's mantle. Nature 433, 33–38.

Bauer, C.A., 1947. Production of helium in meteorites by cosmic radiation. Phys. Rev. 72, 354.

Becker, R.H., Pepin, R.O., 1994. Solar wind noble gases and nitrogen in metal from lunar soil 68501. Meteoritics 29, 724–738.

Behrens, H., 2010. Noble gas diffusion in silicate glasses and melts. Rev. Mineral. Geochem. 72, 227–267.

Behrens, H., Misiti, V., Freda, C., Vetere, F., Botcharnikov, R.E., Scarlato, P., 2009. Solubility of H2O and CO2 in ultrapotassic melts at 1200 and 1250 C and pressure from 50 to 500 MPa. Am. Mineral. 94, 105–120.

Behrens, H., Zhang, Y., 2001. Ar diffusion in hydrous silicic melts: implications for volatile diffusion mechanisms and fractionation. Earth Planet. Sci. Lett. 192, 363–376.

Black, D., Pepin, R., 1969. Trapped neon in meteorites—II. Earth Planet. Sci. Lett. 6, 395–405.

Black, D.C., 1972. On the origins of trapped helium, neon and argon isotopic variations in meteorites—I. Gas-rich meteorites, lunar soil and breccia. Geochim. Cosmochim. Acta 36, 347–375.

Blank, J.G., Brooker, R.A., 1994. Experimental studies of carbon dioxide in silicate melts; solubility, speciation, and stable carbon isotope behavior. Rev. Mineral. Geochem. 30, 157–186.

Bodmer, R., Bochsler, P., 2000. Influence of Coulomb collisions on isotopic and elemental fractionation in the solar wind acceleration process. J. Geophys. Res. Space Phys. 105, 47–60.

Bottinga, Y., Richet, P., 1981. High pressure and temperature equation of state and calculation of the thermodynamic properties of gaseous carbon dioxide. Am. J. Sci. 281, 615–660.

Bühler, F., Eberhardt, P., Geiss, J., Meister, J., Signer, P., 1969. Apollo 11 solar wind composition experiment: First results. Science 166, 1502–1503.

Burbidge, E.M., Burbidge, G.R., Fowler, W.A., Hoyle, F., 1957. Synthesis of the elements in stars. Rev. Mod. Phys. 29, 547.

Burnard, P., 2001. Correction for volatile fractionation in ascending magmas: noble gas abundances in primary mantle melts. Geochim. Cosmochim. Acta 65, 2605–2614.

Burnard, P., 1999. The bubble-by-bubble volatile evolution of two mid-ocean ridge basalts. Earth Planet. Sci. Lett. 174, 199–211.

Burnard, P., Graham, D., Turner, G., 1997. Vesicle-specific noble gas analyses of" popping rock": implications for primordial noble gases in Earth. Science 276, 568–571.

Busemann, H., Baur, H., Wieler, R., 2000. Primordial noble gases in “phase Q” in carbonaceous and ordinary chondrites studied by closed-system stepped etching. Meteorit. Planet. Sci. 35, 949–973.

Butler, W., Jeffery, P., Reynolds, J., Wasserburg, G., 1963. Isotopic variations in terrestrial xenon. J. Geophys. Res. 68, 3283–3291.

Canup, R.M., Asphaug, E., 2001. Origin of the Moon in a giant impact near the end of the Earth’s formation. Nature 412, 708–712.

Carroll, M.R., Webster, J.D., 1994. Solubilities of sulfur, noble gases, nitrogen, chlorine, and fluorine in magmas. Rev. Mineral. 30, 231–231.

Chambers, J., 2010. Planetesimal formation by turbulent concentration. Icarus 208, 505–517.

Chavrit, D., 2010. Cartographie globale des flux de CO2 à l’axe des dorsales océaniques: une approche pétrologique.

Chavrit, D., Humler, E., Morizet, Y., Laporte, D., 2012. Influence of magma ascent rate on carbon dioxide degassing at oceanic ridges: Message in a bubble. Earth Planet. Sci. Lett. 357, 376–385.

Clayton, D.D., 1983. Principles of stellar evolution and nucleosynthesis. University of Chicago press.

Colin, A., Moreira, M., Gautheron, C., Burnard, P., 2015. Constraints on the noble gas composition of the deep mantle by bubble-by-bubble analysis of a volcanic glass sample from Iceland. Chem. Geol. 417, 173–183.

Craig, H., Lupton, J., 1976. Primordial neon, helium, and hydrogen in oceanic basalts. Earth Planet. Sci. Lett. 31, 369–385.

Cuzzi, J.N., Hogan, R.C., Shariff, K., 2008. Toward planetesimals: Dense chondrule clumps in the protoplanetary nebula. Astrophys. J. 687, 1432.

Dauphas, N., Burkhardt, C., Warren, P.H., Fang-Zhen, T., 2014. Geochemical arguments for an Earth-like Moon-forming impactor. Philos. Trans. R. Soc. Math. Phys. Eng. Sci. 372, 20130244.

Dauphas, N., Chaussidon, M., 2011. A perspective from extinct radionuclides on a young stellar object: the Sun and its accretion disk. Annu. Rev. Earth Planet. Sci. 39, 351–386.

Dauphas, N., Morbidelli, A., 2013. Geochemical and planetary dynamical views on the origin of Earth's atmosphere and oceans. ArXiv Prepr. ArXiv13121202.

Dauphas, N., Pourmand, A., 2011. Hf–W–Th evidence for rapid growth of Mars and its status as a planetary embryo. Nature 473, 489–492.

D'E Atkinson, R., Houtermans, F., 1929. Transmutation of the Lighter Elements in Stars. Nature 123, 567–568.

Di Carlo, I., Pichavant, M., Rotolo, S.G., Scaillet, B., 2006. Experimental crystallization of a high-K arc basalt: the golden pumice, Stromboli volcano (Italy). J. Petrol. 47, 1317–1343.

Dickin, A.P., 2018. Radiogenic isotope geology. Cambridge university press.

Dixon, J.E., Pan, V., 1995a. Determination of the molar absorptivity of dissolved carbonate in basanitic glass. Am. Mineral. 80, 1339–1342.

Dixon, J.E., Pan, V., 1995b. Determination of the molar absorptivity of dissolved carbonate in basanitic glass. Am. Mineral. 80, 1339–1342.

Dixon, J.E., Stolper, E.M., Holloway, J.R., 1995. An experimental study of water and carbon dioxide solubilities in mid-ocean ridge basaltic liquids. Part I: calibration and solubility models. J. Petrol. 36, 1607–1631.

Donahue, T., Russell, C., 1997. The Venus atmosphere and ionosphere and their interaction with the solar wind: An overview. Venus II Geol. Geophys. Atmosphere Sol. Wind Environ. 3.

Douglass, J., Schilling, J., Fontignie, D., 1999. Plume-ridge interactions of the Discovery and Shona mantle plumes with the southern Mid-Atlantic Ridge (40°-55° S). J. Geophys. Res. Solid Earth 104, 2941–2962.

Eberhardt, P., Geiss, J., Graf, H., Grögler, N., Krähenbühl, U., Schwaller, H., Schwarzmüller, J., Stettler, A., 1970. Trapped solar wind noble gases, exposure age and K/Ar-age in Apollo 11 lunar fine material. Presented at the Geochimica et Cosmochimica Acta Supplement, Volume 1. Proceedings of the Apollo 11 Lunar Science Conference held 5-8 January, 1970 in Houston, TX. Volume 2: Chemical and Isotope Analyses. Edited by AA Levinson. New York: Pergammon Press, 1970., p. 1037, p. 1037.

Eberhardt, P., Geiss, J., Graf, H., Grögler, N., Mendia, M., Mörgeli, M., Schwaller, H., Stettler, A., Krähenbühl, U., Von Gunten, H., 1972. Trapped solar wind noble gases in Apollo 12 lunar fines 12001 and Apollo 11 breccia 10046. Bern Univ.(Switzerland).

Farrell, W.M., Hurley, D.M., Zimmerman, M.I., 2015. Solar wind implantation into lunar regolith: Hydrogen retention in a surface with defects. Icarus 255, 116–126.

Fine, G., Stolper, E., 1985. The speciation of carbon dioxide in sodium aluminosilicate glasses. Contrib. Mineral. Petrol. 91, 105–121.

Frost, B.R., 2018. Introduction to oxygen fugacity and its petrologic importance, in: Oxide Minerals. De Gruyter, pp. 1–10.

Geiss, J., Bühler, F., Cerutti, H., Eberhardt, P., Filleux, C., Meister, J., Signer, P., 2004. The Apollo SWC experiment: results, conclusions, consequences. Space Sci. Rev. 110, 307–335.

Geiss, J, Eberhardt, P., Bühler, F., Meister, J., Signer, P., 1970. Apollo 11 and 12 solar wind composition experiments: Fluxes of He and Ne isotopes. J. Geophys. Res. 75, 5972–5979.

Geiss, Johannes, Hirt, P., Leutwyler, H., 1970. On acceleration and motion of ions in corona and solar wind. Sol. Phys. 12, 458–483.

Giordano, D., Russell, J.K., Dingwell, D.B., 2008. Viscosity of magmatic liquids: a model. Earth Planet. Sci. Lett. 271, 123–134.

Gonnermann, H.M., Manga, M., 2007. The fluid mechanics inside a volcano. Annu Rev Fluid Mech 39, 321–356.

Graham, D.W., 2002. Noble Gas Isotope Geochemistry of Mid-Ocean Ridge and Ocean Island Basalts: Characterization of Mantle Source Reservoirs. Rev. Mineral. Geochem. 47, 247–317. https://doi.org/10.2138/rmg.2002.47.8

Grimberg, A., Baur, H., Bochsler, P., Bühler, F., Burnett, D.S., Hays, C.C., Heber, V.S., Jurewicz, A.J., Wieler, R., 2006. Solar wind neon from Genesis: Implications for the lunar noble gas record. Science 314, 1133–1135.

Harper Jr, C.L., Jacobsen, S.B., 1996. Noble gases and Earth's accretion. Science 273, 1814–1818.

Hashizume, K., Chaussidon, M., Marty, B., Robert, F., 2000. Solar wind record on the Moon: deciphering presolar from planetary nitrogen. Science 290, 1142–1145.

Heber, V.S., Baur, H., Bochsler, P., McKeegan, K.D., Neugebauer, M., Reisenfeld, D.B., Wieler, R., Wiens, R.C., 2012. Isotopic mass fractionation of solar wind: Evidence from fast and slow solar wind collected by the Genesis mission. Astrophys. J. 759, 121.

Heber, V.S., Wieler, R., Baur, H., Olinger, C., Friedmann, T.A., Burnett, D.S., 2009. Noble gas composition of the solar wind as collected by the Genesis mission. Geochim. Cosmochim. Acta 73, 7414–7432.

Holland, G., Ballentine, C.J., 2006a. Seawater subduction controls the heavy noble gas composition of the mantle. Nature 441, 186–191.

Holland, G., Ballentine, C.J., 2006b. Seawater subduction controls the heavy noble gas composition of the mantle. Nature 441, 186–191.

Holland, G., Cassidy, M., Ballentine, C.J., 2009. Meteorite Kr in Earth's mantle suggests a late accretionary source for the atmosphere. Science 326, 1522–1525.

Hollenbach, D.J., Yorke, H.W., Johnstone, D., 2000. Disk dispersal around young stars. Protostars Planets IV 401, 12.

Honda, M., McDougall, I., Patterson, D.B., Doulgeris, A., Clague, D.A., 1991. Possible solar noble-gas component in Hawaiian basalts. Nature 349, 149–151.

Honda, M., Reynolds, J., Roedder, E., Epstein, S., 1987. Noble gases in diamonds: Occurrences of solarlike helium and neon. J. Geophys. Res. Solid Earth 92, 12507–12521.

Iacono-Marziano, G., Paonita, A., Rizzo, A., Scaillet, B., Gaillard, F., 2010. Noble gas solubilities in silicate melts: new experimental results and a comprehensive model of the effects of liquid composition, temperature and pressure. Chem. Geol. 279, 145–157.

Jambon, A., Weber, H., Braun, O., 1986. Solubility of He, Ne, Ar, Kr and Xe in a basalt melt in the range 1250–1600 C. Geochemical implications. Geochim. Cosmochim. Acta 50, 401–408.

Jaupart, E., Charnoz, S., Moreira, M., 2017. Primordial atmosphere incorporation in planetary embryos and the origin of Neon in terrestrial planets. Icarus 293, 199–205.

Javoy, M., Pineau, F., 1991. The volatiles record of a "popping" rock from the Mid-Atlantic Ridge at 14 N: chemical and isotopic composition of gas trapped in the vesicles. Earth Planet. Sci. Lett. 107, 598–611.

Jiménez-Mejías, M., Andújar, J., Scaillet, B., Casillas, R., 2021. Experimental determination of H $ _ {{2}} $ O and CO $ _ {{2}} $ solubilities of mafic alkaline magmas from Canary Islands. Comptes Rendus Géoscience 353, 289–314.

Johansen, A., Klahr, H., 2011. Planetesimal formation through streaming and gravitational instabilities. Earth Moon Planets 108, 39–43.

Johansen, A., Klahr, H., Henning, T., 2011. High-resolution simulations of planetesimal formation in turbulent protoplanetary discs. Astron. Astrophys. 529, A62.

Johansen, A., Oishi, J.S., Low, M.-M.M., Klahr, H., Henning, T., Youdin, A., 2007. Rapid planetesimal formation in turbulent circumstellar disks. Nature 448, 1022–1025.

Kendrick, M.A., Burnard, P., 2013. Noble gases and halogens in fluid inclusions: a journey through the Earth's crust. Noble Gases Geochem. Tracers 319–369.

Kennedy, B., Hiyagon, H., Reynolds, J., 1990. Crustal neon: a striking uniformity. Earth Planet. Sci. Lett. 98, 277–286.

Kennedy, B.M., Hiyagon, H., Reynolds, J.H., 1990. Crustal neon: a striking uniformity. Earth Planet. Sci. Lett. 98, 277–286. https://doi.org/10.1016/0012-821X(90)90030-2

Kipfer, R., Aeschbach-Hertig, W., Peeters, F., Stute, M., 2002. Noble gases in lakes and ground waters. Rev. Mineral. Geochem. 47, 615–700.

Kress, V.C., Carmichael, I.S., 1991. The compressibility of silicate liquids containing Fe 2 O 3 and the effect of composition, temperature, oxygen fugacity and pressure on their redox states. Contrib. Mineral. Petrol. 108, 82–92.

Krummenacher, D., 1970. Isotopic composition of argon in modern surface volcanic rocks. Earth Planet. Sci. Lett. 8, 109–117.

Kunz, J., 1999. Is there solar argon in the Earth's mantle? Nature 399, 649–650. https://doi.org/10.1038/21352

Kuroda, P., 1960. Nuclear fission in the early history of the earth. Nature 187.

Kurz, M.D., 1986. Cosmogenic helium in a terrestrial igneous rock. Nature 320, 435–439. https://doi.org/10.1038/320435a0

Kurz, M.D., Curtice, J., Fornari, D., Geist, D., Moreira, M., 2009. Primitive neon from the center of the Galápagos hotspot. Earth Planet. Sci. Lett. 286, 23–34.

Lange, R.A., 1994a. Volatiles in Magmas, in: Carroll, M.R., Holloway, J.R. (Eds.), . De Gruyter, pp. 331–370. https://doi.org/10.1515/9781501509674-015

Lange, R.A., 1994b. Volatiles in Magmas, in: Carroll, M.R., Holloway, J.R. (Eds.), . De Gruyter, pp. 331–370. https://doi.org/10.1515/9781501509674-015

Le Gall, N., 2015. Ascension et dégazage des magmas basaltiques: approche expérimentale.

Le Gall, N., Pichavant, M., 2016a. Experimental simulation of bubble nucleation and magma ascent in basaltic systems: Implications for Stromboli volcano. Am. Mineral. 101, 1967–1985.

Le Gall, N., Pichavant, M., 2016b. Homogeneous bubble nucleation in H2O-and H2O-CO2-bearing basaltic melts: results of high temperature decompression experiments. J. Volcanol. Geotherm. Res. 327, 604–621.

Le Roux, P., Le Roex, A., Schilling, J.-G., Shimizu, N., Perkins, W., Pearce, N., 2002. Mantle heterogeneity beneath the southern Mid-Atlantic Ridge: trace element

evidence for contamination of ambient asthenospheric mantle. Earth Planet. Sci. Lett. 203, 479–498.

Lensky, N.G., Niebo, R.W., Holloway, J.R., Lyakhovsky, V., Navon, O., 2006. Bubble nucleation as a trigger for xenolith entrapment in mantle melts. Earth Planet. Sci. Lett. 245, 278–288.

Lux, G., 1987. The behavior of noble gases in silicate liquids: Solution, diffusion, bubbles and surface effects, with applications to natural samples. Geochim. Cosmochim. Acta 51, 1549–1560.

Mangan, M., Sisson, T., 2000. Delayed, disequilibrium degassing in rhyolite magma: decompression experiments and implications for explosive volcanism. Earth Planet. Sci. Lett. 183, 441–455.

Marsh, B.D., 2007. Crystallization of silicate magmas deciphered using crystal size distributions. J. Am. Ceram. Soc. 90, 746–757.

Marsh, B.D., 1988. Crystal size distribution (CSD) in rocks and the kinetics and dynamics of crystallization: I. Theory. Contrib. Mineral. Petrol. 99, 277–291.

Marty, B., 2022. Meteoritic noble gas constraints on the origin of terrestrial volatiles. Icarus 381, 115020.

Marty, B., 2020. ORIGINS AND EARLY EVOLUTION OF THE ATMOSPHERE AND THE OCEANS. Geochem. Perspect. 9, 135–136.

Marty, B., 2012. The origins and concentrations of water, carbon, nitrogen and noble gases on Earth. Earth Planet. Sci. Lett. 313, 56–66.

Marty, B., Yokochi, R., 2006. Water in the early Earth. Rev. Mineral. Geochem. 62, 421–450.

Marty, B., Zimmermann, L., 1999. Volatiles (He, C, N, Ar) in mid-ocean ridge basalts: Assesment of shallow-level fractionation and characterization of source composition. Geochim. Cosmochim. Acta 63, 3619–3633.

McDonnell, J., Flavill, R., 1974. Sputter Erosion on the Lunar Surface: Measurements and Features Under Simulated Solar He+ Bombardment. Lunar Planet. Sci. V Houst. Lunar Planet Inst 478.

Mizuno, H., Nakazawa, K., Hayashi, C., 1980. Dissolution of the primordial rare gases into the molten Earth's material. Earth Planet. Sci. Lett. 50, 202–210.

Morbidelli, A., Bottke, W.F., Nesvorný, D., Levison, H.F., 2009. Asteroids were born big. Icarus 204, 558–573.

Moreira, M., 2013. Noble gas constraints on the origin and evolution of Earth's volatiles. Geochem. Perspect. 2, 229–230.

Moreira, M., Blusztajn, J., Curtice, J., Hart, S., Dick, H., Kurz, M.D., 2003. He and Ne isotopes in oceanic crust: implications for noble gas recycling in the mantle. Earth Planet. Sci. Lett. 216, 635–643.

Moreira, M., Charnoz, S., 2016. The origin of the neon isotopes in chondrites and on Earth. Earth Planet. Sci. Lett. 433, 249–256. https://doi.org/10.1016/j.epsl.2015.11.002

Moreira, M., Kunz, J., Allegre, C., 1998. Rare gas systematics in popping rock: isotopic and elemental compositions in the upper mantle. Science 279, 1178–1181.

Moreira, M., Rouchon, V., Muller, E., Noirez, S., 2018. The xenon isotopic signature of the mantle beneath Massif Central. Geochem Perspect Lett 6, 28–32.

Moreira, M., Sarda, P., 2000. Noble gas constraints on degassing processes. Earth Planet. Sci. Lett. 176, 375–386.

Moreira, M., Staudacher, T., Sarda, P., Schilling, J.-G., Allègre, C.J., 1995. A primitive plume neon component in MORB: The Shona ridge-anomaly, South Atlantic (51–52° S). Earth Planet. Sci. Lett. 133, 367–377.

Moretti, R., Papale, P., Ottonello, G., 2003. A model for the saturation of COHS fluids in silicate melts. Geol. Soc. Lond. Spec. Publ. 213, 81–101.

Mourtada-Bonnefoi, C., Laporte, D., 2002. Homogeneous bubble nucleation in rhyolitic magmas: an experimental study of the effect of H2O and CO2. J. Geophys. Res. Solid Earth 107, ECV-2.

Mourtada-Bonnefoi, C.C., Laporte, D., 2004. Kinetics of bubble nucleation in a rhyolitic melt: an experimental study of the effect of ascent rate. Earth Planet. Sci. Lett. 218, 521–537.

Mukhopadhyay, S., 2012. Early differentiation and volatile accretion recorded in deep-mantle neon and xenon. Nature 486, 101–104. https://doi.org/10.1038/nature11141

Nowak, M., Schreen, D., Spickenbom, K., 2004. Argon and CO2 on the race track in silicate melts: a tool for the development of a CO2 speciation and diffusion model. Geochim. Cosmochim. Acta 68, 5127–5138.

Nuccio, P., Paonita, A., 2001. Magmatic degassing of multicomponent vapors and assessment of magma depth: application to Vulcano Island (Italy). Earth Planet. Sci. Lett. 193, 467–481.

Nuccio, P., Paonita, A., 2000. Investigation of the noble gas solubility in H2O–CO2 bearing silicate liquids at moderate pressure II: the extended ionic porosity (EIP) model. Earth Planet. Sci. Lett. 183, 499–512.

Olson, P.L., Sharp, Z.D., 2019. Nebular atmosphere to magma ocean: a model for volatile capture during Earth accretion. Phys. Earth Planet. Inter. 294, 106294.

Ozima, M., Podosek, F.A., 2002. Noble gas geochemistry. Cambridge University Press.

Ozima, M., Zashu, S., 1991. Noble gas state of the ancient mantle as deduced from noble gases in coated diamonds. Earth Planet. Sci. Lett. 105, 13–27.

Ozima, M., Zashu, S., 1988a. Solar-type Ne in Zaire cubic diamonds. Geochim. Cosmochim. Acta 52, 19–25.

Ozima, M., Zashu, S., 1988b. Solar-type Ne in Zaire cubic diamonds. Geochim. Cosmochim. Acta 52, 19–25.

Paonita, A., 2005. Noble gas solubility in silicate melts: a review of experimentation and theory, and implications regarding magma degassing processes. Ann. Geophys.

Paonita, A., Gigli, G., Gozzi, D., Nuccio, P., Trigila, R., 2000. Investigation of the He solubility in H2O–CO2 bearing silicate liquids at moderate pressure: a new experimental method. Earth Planet. Sci. Lett. 181, 595–604.

Pepin, R., Nyquist, L., Phinney, D., Black, D.C., 1970. Isotopic composition of rare gases in lunar samples. Science 167, 550–553.

Pepin, R.O., 1991. On the origin and early evolution of terrestrial planet atmospheres and meteoritic volatiles. Icarus 92, 2–79.

Pepin, R.O., Schlutter, D.J., Becker, R.H., Reisenfeld, D.B., 2012. Helium, neon, and argon composition of the solar wind as recorded in gold and other Genesis collector materials. Geochim. Cosmochim. Acta 89, 62–80.

Péron, S., Moreira, M., Agranier, A., 2018. Origin of light noble gases (He, Ne, and Ar) on Earth: A review. Geochem. Geophys. Geosystems 19, 979–996.

Péron, S., Moreira, M., Colin, A., Arbaret, L., Putlitz, B., Kurz, M.D., 2016. Neon isotopic composition of the mantle constrained by single vesicle analyses. Earth Planet. Sci. Lett. 449, 145–154. https://doi.org/10.1016/j.epsl.2016.05.052

Péron, S., Moreira, M., Putlitz, B., Kurz, M., 2017. Solar wind implantation supplied light volatiles during the first stage of Earth accretion. Geochem. Perspect. Lett. 151–159.

Péron, S., Moreira, M.A., Kurz, M.D., Curtice, J., Blusztajn, J.S., Putlitz, B., Wanless, V.D., Jones, M.R., Soule, S.A., Mittelstaedt, E., 2019. Noble gas systematics in new popping rocks from the Mid-Atlantic Ridge (14° N): evidence for small-scale upper mantle heterogeneities. Earth Planet. Sci. Lett. 519, 70–82.

Pichavant, M., Di Carlo, I., Le Gac, Y., Rotolo, S.G., Scaillet, B., 2009. Experimental constraints on the deep magma feeding system at Stromboli volcano, Italy. J. Petrol. 50, 601–624.

Pichavant, M., Di Carlo, I., Rotolo, S.G., Scaillet, B., Burgisser, A., Le Gall, N., Martel, C., 2013. Generation of CO 2-rich melts during basalt magma ascent and degassing. Contrib. Mineral. Petrol. 166, 545–561.

Pichavant, M., Le Gall, N., Scaillet, B., 2018. Gases as precursory signals: experimental simulations, new concepts and models of magma degassing. Volcan. Unrest Adv Volcanol 139–154.

Pierre Jules César Janssen, 1908. . Mon. Not. R. Astron. Soc. 68, 245–249. https://doi.org/10.1093/mnras/68.4.245

Porcelli, D., Ballentine, C.J., Wieler, R., 2002. An overview of noble gas geochemistry and cosmochemistry. Rev. Mineral. Geochem. 47, 1–19.

Porcelli, D., Woolum, D., Cassen, P., 2001. Deep Earth rare gases: initial inventories, capture from the solar nebula, and losses during Moon formation. Earth Planet. Sci. Lett. 193, 237–251.

Poreda, R., di Brozolo, F.R., 1984. Neon isotope variations in Mid-Atlantic Ridge basalts. Earth Planet. Sci. Lett. 69, 277–289.

Raquin, A., Moreira, M., 2009. Atmospheric 38Ar/36Ar in the mantle: implications for the nature of the terrestrial parent bodies. Earth Planet. Sci. Lett. 287, 551–558.

Raquin, A., Moreira, M.A., Guillon, F., 2008. He, Ne and Ar systematics in single vesicles: mantle isotopic ratios and origin of the air component in basaltic glasses. Earth Planet. Sci. Lett. 274, 142–150.

Raymond, S.N., O'Brien, D.P., Morbidelli, A., Kaib, N.A., 2009. Building the terrestrial planets: Constrained accretion in the inner Solar System. Icarus 203, 644–662.

Reynolds, J., Hohenberg, C., Lewis, R., Davis, P., Kaiser, W., 1970. Isotopic analysis of rare gases from stepwise heating of lunar fines and rocks. Science 167, 545–548.

Reynolds, J., Turner, G., 1964. Rare gases in the chondrite Renazzo. J. Geophys. Res. 69, 3263–3281.

Rolfs, C.E., Rodney, W.S., 1988. Cauldrons in the cosmos: Nuclear astrophysics. University of Chicago press.

Roubinet, C., Moreira, M.A., 2018. Atmospheric noble gases in Mid-Ocean Ridge Basalts: identification of atmospheric contamination processes. Geochim. Cosmochim. Acta 222, 253–268.

Ruzié, L., Moreira, M., 2010. Magma degassing process during Plinian eruptions. J. Volcanol. Geotherm. Res. 192, 142–150.

Saltykov, S., 1967. Stereology: proceedings of the second international congress for stereology, chapter The determination of the size distribution of particles in an opaque material from a measurement of the size distribution of their sections.

Sarda, P., Graham, D., 1990. Mid-ocean ridge popping rocks: implications for degassing at ridge crests. Earth Planet. Sci. Lett. 97, 268–289.

Sarda, P., Moreira, M., 2002. Vesiculation and vesicle loss in mid-ocean ridge basalt glasses: He, Ne, Ar elemental fractionation and pressure influence. Geochim. Cosmochim. Acta 66, 1449–1458.

Sarda, P., Moreira, M., Staudacher, T., Schilling, J., Allègre, C.J., 2000. Rare gas systematics on the southernmost Mid-Atlantic Ridge: Constraints on the lower mantle and the Dupal source. J. Geophys. Res. Solid Earth 105, 5973–5996.

Sarda, P., Staudacher, T., Allègre, C.J., 1988. Neon isotopes in submarine basalts. Earth Planet. Sci. Lett. 91, 73–88. https://doi.org/10.1016/0012-821X(88)90152-5

Sasaki, S., 1999. Presence of a primary solar-type atmosphere around the earth: evidence of dissolved noble gas. Planet. Space Sci. 47, 1423–1431.

Sasaki, S., Nakazawa, K., 1990. Did a primary solar-type atmosphere exist around the proto-earth? Icarus 85, 21–42. https://doi.org/10.1016/0019-1035(90)90101-E

Scarpa, R., Tilling, R.I., Giggenbach, W., 1996. Chemical composition of volcanic gases. Monit. Mitig. Volcano Hazards 221–256.

Schlosser, P., Winckler, G., 2002. Noble gases in ocean waters and sediments. Rev. Mineral. Geochem. 47, 701–730.

Shinohara, H., Aiuppa, A., Giudice, G., Gurrieri, S., Liuzzo, M., 2008. Variation of H2O/CO2 and CO2/SO2 ratios of volcanic gases discharged by continuous degassing of Mount Etna volcano, Italy. J. Geophys. Res. Solid Earth 113.

Shishkina, T.A., Botcharnikov, R.E., Holtz, F., Almeev, R.R., Jazwa, A.M., Jakubiak, A.A., 2014. Compositional and pressure effects on the solubility of H2O and CO2 in mafic melts. Chem. Geol. 388, 112–129.

Sparks, R.S.J., 1978. The dynamics of bubble formation and growth in magmas: a review and analysis. J. Volcanol. Geotherm. Res. 3, 1–37.

Staudacher, T., Allègre, C.J., 1988. Recycling of oceanic crust and sediments: the noble gas subduction barrier. Earth Planet. Sci. Lett. 89, 173–183.

Staudacher, T., Sarda, P., Richardson, S., Allègre, C., Sagna, I., Dmitriev, L., 1989. Noble gases in basalt glasses from a Mid-Atlantic Ridge topographic high at 14 N: geodynamic consequences. Earth Planet. Sci. Lett. 96, 119–133.

Stolper, E., 1982. Water in silicate glasses: an infrared spectroscopic study. Contrib. Mineral. Petrol. 81, 1–17.

Stout, V.L., Gibbons, M.D., 1955. Gettering of gas by titanium. J. Appl. Phys. 26, 1488–1492.

Sumino, H., Kaneoka, I., Matsufuji, K., Sobolev, A.V., 2006. Deep mantle origin of kimberlite magmas revealed by neon isotopes. Geophys. Res. Lett. 33.

Tolstikhin, I., O'Nions, R., 1994. The Earth's missing xenon: A combination of early degassing and of rare gas loss from the atmosphere. Chem. Geol. 115, 1–6.

Trieloff, M., Kunz, J., Clague, D.A., Harrison, D., Allègre, C.J., 2000. The Nature of Pristine Noble Gases in Mantle Plumes. Science 288, 1036–1038. https://doi.org/10.1126/science.288.5468.1036

Warren, P.H., 1995. Extrapolated partial molar densities of SO3, P2O5, and other oxides in silicate melts. Am. Mineral. 80, 1085–1088.

Watson, E.B., Sneeringer, M.A., Ross, A., 1982. Diffusion of dissolved carbonate in magmas: experimental results and applications. Earth Planet. Sci. Lett. 61, 346–358.

Wetherill, G.W., 1954a. Variations in the isotopic abundances of neon and argon extracted from radioactive minerals. Phys. Rev. 96, 679.

Wetherill, G.W., 1954b. Variations in the isotopic abundances of neon and argon extracted from radioactive minerals. Phys. Rev. 96, 679.

Wetherill, G.W., 1953a. Spontaneous fission yields from uranium and thorium. Phys. Rev. 92, 907.

Wetherill, G.W., 1953b. Spontaneous fission yields from uranium and thorium. Phys. Rev. 92, 907.

Wieler, R., 2002. Cosmic-ray-produced noble gases in meteorites. Rev. Mineral. Geochem. 47, 125–170.

Wieler, R., 1998. The solar noble gas record in lunar samples and meteorites. Space Sci. Rev. 85, 303–314.

Williams, C.D., Mukhopadhyay, S., 2019. Capture of nebular gases during Earth's accretion is preserved in deep-mantle neon. Nature 565, 78–81. https://doi.org/10.1038/s41586-018-0771-1

Yatsevich, I., Honda, M., 1997a. Production of nucleogenic neon in the Earth from natural radioactive decay. J. Geophys. Res. Solid Earth 102, 10291–10298.

Yatsevich, I., Honda, M., 1997b. Production of nucleogenic neon in the Earth from natural radioactive decay. J. Geophys. Res. Solid Earth 102, 10291–10298.

Yokochi, R., Marty, B., 2004. A determination of the neon isotopic composition of the deep mantle. Earth Planet. Sci. Lett. 225, 77–88. https://doi.org/10.1016/j.epsl.2004.06.010

Yoshimura, S., 2015. Diffusive fractionation of H2O and CO2 during magma degassing. Chem. Geol. 411, 172–181.

Zadnik, M., Jeffery, P., 1985. Radiogenic neon in an Archaean anorthosite. Chem. Geol. Isot. Geosci. Sect. 52, 119–125.

Zhang, Y., Ni, H., Chen, Y., 2010. Diffusion data in silicate melts. Rev. Mineral. Geochem. 72, 311–408.

Zhang, Y., Xu, Z., 1995. Atomic radii of noble gas elements in condensed phases. Am. Mineral. 80, 670–675.

Zhang, Y., Xu, Z., Zhu, M., Wang, H., 2007. Silicate melt properties and volcanic eruptions. Rev. Geophys. 45.

Zhang, Y., Zindler, A., 1989. Noble gas constraints on the evolution of the Earth's atmosphere. J. Geophys. Res. Solid Earth 94, 13719–13737.

Chapitre 4 : Dynamique du néon dans la vésiculation du magma dans des conditions hors équilibre.

Le chapitre précédent a analysé l'impact de l'introduction d'un nouveau flux de gaz ou d'une matière fondue riche en gaz dans un système de silicates fondus, sous des conditions spécifiques de pression et de température, simulant une chambre magmatique, avant l'atteinte de l'équilibre. Il a été observé que, lors de la nucléation et avant que les bulles n'atteignent une taille critique, le CO_2 se diffusait à travers les grains plus rapidement que la montée des bulles vers la surface, selon la loi de Stokes calculée pour nos échantillons expérimentaux. Par la suite, le gaz était perdu avant que la diffusion ne soit terminée.

Les bulles trouvées dans les verres basaltiques sont un outil crucial pour déterminer les processus de dégazage du magma, car elles en fournissent une preuve directe. Alors que la plupart des études sur les processus de dégazage se concentrent sur les traceurs géochimiques, cette étude propose une approche combinant traceurs géochimiques et analyse vésiculaire pour définir les processus de dégazage, depuis les premiers stades de la nucléation des bulles jusqu'à l'ascension du magma et juste avant le début de l'éruption. Cette technique permet de contraindre le comportement des gaz rares légers, en particulier le fractionnement des isotopes stables du néon.

La technique utilisée pour extraire le gaz des vésicules est cruciale pour l'interprétation des données obtenues. Une extraction séquentielle du gaz par broyage des échantillons libère le gaz des vésicules de différentes tailles, en commençant par les plus grandes et en continuant vers les plus petites. Dans les échantillons naturels, la méthode la plus courante pour extraire le gaz des vésicules consiste à écraser l'échantillon dans des conditions d'ultravide (par exemple, Sarda et al., 2000 ; Raquin et Moreira, 2009 ; Ruzié et Moreira, 2010 ; Williams et Mukhopadhyay, 2019). Cette méthode représente une technique d'acquisition de données plus efficace que l'ablation laser, permettant de déterminer la trajectoire volatile de chaque échantillon individuel et de réduire l'erreur analytique en fonction de la vésiculaire de l'échantillon et de la quantité de gaz. Cependant, avec cette technique, il est possible d'extraire des bulles de gaz contaminées par la présence de micro-fractures reliant les bulles à la surface de l'échantillon (Roubinet et Moreira, 2018 ; Ballentine et Barfod, 2000). De plus, cette

méthode présente l'inconvénient que la roche se brise aux endroits les plus fragiles lors du concassage, qui sont typiquement les plus grosses bulles. Cela entraîne l'exclusion de certaines populations de très petites bulles, correspondant souvent à différentes générations de bulles, conduisant à la perte d'informations cruciales.

Pour résoudre ce problème de contamination des bulles connectées à la surface de l'échantillon Colin et al. (2015), Burnard et al. (1997) et Péron et al. (2016) ont suggéré de scanner les échantillons avec une tomographie à rayons X pour localiser les bulles exemptes de contamination, puis d'utiliser l'ablation laser dans une technique d'ultravide pour libérer le gaz. L'information obtenue en traçant les rapports isotopiques dans le diagramme des trois isotopes du Ne montre une ligne de mélange entre les deux composantes (manteau et atmosphère) (Figure 4.1) jusqu'à des résultats plus étroitement liés à la source mantellique. Le problème s'est posé lorsque les résultats ont montré des vésicules avec des rapports isotopiques plus élevés que ceux obtenus précédemment. En pratique, on suppose que le taux le plus élevé mesuré lors des étapes de concassage est le moins contaminé. Cette approche a récemment été utilisée par certains auteurs pour suggérer qu'il pourrait s'agir du rapport isotopique réel de la source.

Est-ce le rapport isotopique correct de la source ? Ou existe-t-il un fractionnement cinétique qui se produit lors de la nucléation et de la vésiculation des bulles ?

Chapter 4: Neon Dynamics in Magma Vesiculation under Non-Equilibrium Conditions.

4.1. Introduction:

The previous chapter analysed the impact of a new gas flux or a gas-rich melt entering in a silicate melt system under specific pressure and temperature conditions, simulating a magma chamber, before reaching equilibrium. It was observed that, during nucleation and before the bubble size reached a critical size, CO_2 diffused through the grains faster than the buoyancy of the bubbles towards the surface, calculated for our experimental samples by Stokes' law. Subsequently, the gas was lost before the diffusion was completed.

Bubbles found in basaltic glasses are a crucial tool for determining magma degassing processes as they provide direct evidence of them. While most studies on degassing processes focus on geochemical tracers, this study proposes a combined approach of both geochemical tracers and vesicularity to define degassing processes from the early stages of bubble nucleation to magma ascent and moments right before the eruption starts. This technique enables the constraint of light noble gas behaviour, particularly the neon stable isotope fractionation.

The technique used to extract gas from vesicles is crucial in interpreting the obtained data. A sequential gas extraction by crushing the samples releases the gas from vesicles of varying sizes and progressively smaller vesicles. In natural samples, the most common method for extracting the gas from the vesicles is by crushing the sample under ultra-high vacuum conditions (e.g. Sarda et al., 2000; Raquin and Moreira, 2009; Ruzié and Moreira, 2010; Williams and Mukhopadhyay, 2019). This method represents a more efficient data acquisition technique than laser ablation enabling the determination of the volatile trajectory of each individual sample and reducing the analytical error depending on the vesicularity of the sample and the amount of gas. However, with this technique, it is possible to extract air-contaminated gas bubbles by the presence of micro-fractures connecting the bubbles to the sample surface (Roubinet and Moreira, 2018; Ballentine and Barfod, 2000). Furthermore, this method has a drawback in that the rock breaks up at the points of greatest fragility during crushing, which are typically the largest bubbles.

This results in the exclusion of some populations of very small bubbles, which often correspond to different bubble generations, leading to loss of crucial information.

To solve this problem regarding the contamination of bubbles connected to the sample surface Burnard et al. (1997) and Péron et al. (2016) suggested scanning the samples with X-ray tomography to locate the bubbles that should be free of contamination and then using laser ablation in ultra-high vacuum technique to release the gas. The information obtained by plotting the isotopic ratios in the three-Ne isotopes diagram shows a mixing line between the two components (mantle and atmosphere). (**Figure 4.1.**) to results that are more closely related to the mantle source. The issue arose when the results showed vesicles with isotopic ratios higher than previously obtained. In practice, it is assumed that the highest ratio measured during step crushing is the less contaminated one. This approach has been recently used by some authors for suggesting that this could be the actual isotopic ratio of the source. Is this the correct isotopic ratio of the source? Or is there a kinetic fractionation that occurs during the nucleation and vesiculation of the bubbles?

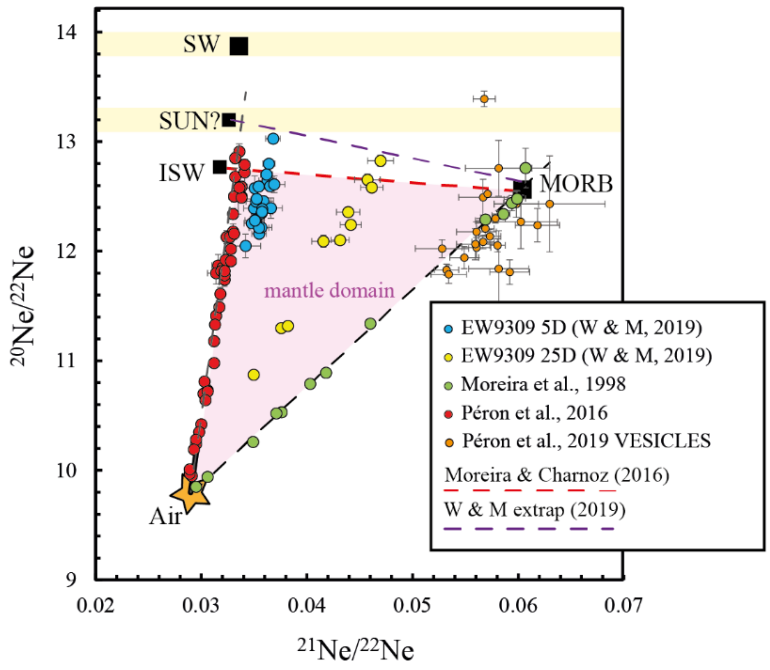

Figure 4.1.: The graph displays the analytical results for the three neon isotopes obtained through the crushing method (values extended in the air-mantle mixing line) and individual vesicle analysis (points accumulated near the mantle component). Data from: Moreira et al. (1998); Moreira and Charnoz (2016); Péron et al. (2016), (2019); Williams and Mukhopadhyay, (2019)

4.2. Experimental strategy:

This chapter implements, through experimental petrology, a simple theoretical model of vesiculation to study the kinetic fractionation of stable neon isotopes during nucleation and bubble growth in a closed system and non-equilibrium conditions. The same type of experiments as in the previous chapter have been followed: time series, with CO_2 overload as volatile species forming bubbles. Temperature of 1200ºC and pressures range between 1530 and 1800 bar. As a novelty, a neon source is provided from a glass that has been previously enriched with an air isotopic signature.

4.2.1. Ne-bearing glass:

The first task was to saturate the starting material in neon. The technique used was the same as that carried out by Jambon et al. (1986), as described in *Chapter 2*, bringing the melt to equilibrium with a flux of Ne at 1 bar of pressure and 1400ºC (as described in *section 2.2.*).

After the glass was quenched, an analysis was made of all the enriched experimental glasses, taking pieces from the various parts of the crucible in which the experiments were conducted, for checking the homogeneity of the neon in the glass. The glasses were analysed using the QMS700 mass spectrometer at the Institute of Earth Sciences of Orleans (ISTO in French).

As explained in *Chapter 2*, two methods were used to produce a neon-enriched glass, but only one of them is optimal for the type of experiments we want to perform due to the absence of bubbles.

The **Figure 4.2.** and **Table 4.1.** present three different tests and their corresponding data. *T4-1Eb* represents the experiment pressurised with N_2 and Ne, which resulted in the formation of bubbles. Upon closer inspection of the data, it is evident that the isotopic distribution in the sample is not homogeneous. Therefore, the use of this glass has been completely ruled out for the purpose of this work.

As for the glass pieces included in *T4-9D*, they were enriched using the (Jambon et al., 1986) system and pressurised in the autoclave with the capsule closed at 1700 bars and 1200ºC for 6 hours. This method gave a homogeneous distribution of neon in the

glass. Still, the prepared quantity of this glass was small, so the experiment was repeated, this time without pressurising the capsule, leaving only the neon flow through the melt for 4 hours at atmospheric pressure. The yellow dots in **Figure 4.2.** represent this glass, which was part of the T5 experiment. The distribution is homogeneous without pressurising the closed capsule inside the autoclave, which saves time in preparing the glass. This starting material will be used in static and decompression experiments to study the fractionation of neon during the nucleation and growth of bubbles in our experimental magmatic system.

	weight (mg)	^{22}Ne (cps/mg)	σ	^{20}Ne/^{22}Ne	σ	^{21}Ne/^{22}Ne	σ
T4-S2 9D	0.102	2.25E+04	1.23E+02	10.23	0.05	0.0276	0.0011
T4-S3 9D	0.106	2.56E+04	1.27E+02	10.13	0.05	0.0267	0.0009
T4-S5 9D	0.102	1.77E+04	9.43E+01	10.36	0.05	0.0279	0.0010
T4-S4 1Eb	0.12	9.40E+04	5.26E+02	10.43	0.05	0.0271	0.0003
T4-S6 1Eb	0.104	1.53E+05	4.83E+02	10.01	0.01	0.0270	0.0002
T4-S7 1Eb	0.118	3.29E+05	4.55E+02	9.84	0.01	0.0272	0.0002
T5-S1	0.102	6.27E+05	3.97E+03	10.47	0.06	0.0289	0.0011
T5-S2	0.110	5.34E+05	4.24E+03	10.59	0.09	0.0296	0.0014
T5-S3	0.106	5.30E+05	4.81E+03	10.59	0.10	0.0298	0.0009
T5-S4	0.116	5.38E+05	3.90E+03	10.61	0.07	0.0286	0.0012

Table 4.1.: Results obtained in the analysed glass for the two method for enriching the dry glass in neon**.** *Test 4-1Eb* corresponds to the first method of Ne-bearing glass setup in the IHPV and pressurized with N_2. *T4-9D* and *T5* correspond to the method of Jambon et al. (1986) plus pressuring the closed capsule at the autoclave in the case of *T4-9D*. Here are shown the raw data of each starting material without mass discrimination correction, since the main interest was to know the homogeneous distribution of neon in the starting glass.

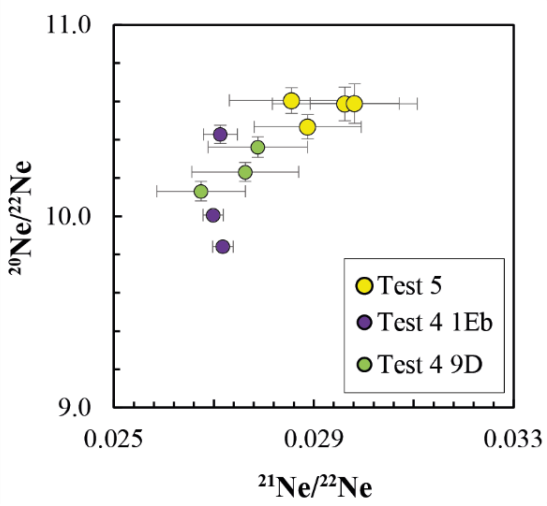

Figure 4.2: The diagram illustrates the three Ne isotopes pot. The experiment pressurised with N_2 and the capsule opened in the autoclave is represented by the purple dots. The yellow dots represent the experiment following the Jambon et al. (1986) method and has been used throughout this thesis. The green dots represent the experiment carried out using the Jambon et al. (1986) method, which was subsequently re-equilibrated in the autoclave with the capsule closed for 6 hours. This graph shows the raw data of each starting material without mass discrimination correction, since the main interest was to know the homogeneous distribution of neon in the starting glass.

An additional test was conducted to verify the solubility of the Ne-bearing glass used in the experiments, as the solubility of neon had not been previously tested for this particular composition. The results are shown in **Table 4.2.**

Sample	mass x 10^{-4} g	^{22}Ne x 10^{-9} $cm^3STP \cdot g^{-1}$	$^{21}Ne/^{22}Ne$	Solubility x10^{-4} cm^3 STP $\cdot$ g^{-1} $\cdot$ bar^{-1}
Test6-s1	2.32	9.67 ± 0.04	0.0296 ± 0.0015	3.26
Test6-s2	1.24	10.79 ± 0.04	0.0285 ± 0.0014	3.63
Test6-s3	2.04	8.86 ± 0.02	0.0299 ± 0.0015	2.98
Test6-s4	1.40	8.19 ± 0.02	0.0295 ± 0.0015	2.76
		9.38 ± 1.12	0.0294 ± 0.0006	3.16 ± 0.38

Table 4.2.: Results obtained in the four analysed chunk of glass with the method of Jambon et al. (1986) for enriching the dry glass in neon. The results are corrected for blank and CO_2^{++} interferences.

4.2.2. Theoretical model:

For any volatile species dissolved in a silicate melt in equilibrium conditions, the solubility law follows Henry's law, at low pressure. Solubility refers to the maximum

amount of a species that can be dissolved into the silicate melts for given pressure and temperature conditions, "S*aturation conditions"*. As was introduced in *Chapter 1* and *Chapter 3*, neon's content of the melt increases as the CO_2 partial pressure increases in the system due to the decrease in the partial pressure of neon.

The solubility of Ne for the composition of the starting material was calculated to be $K_{Ne} = 3.16 \cdot 10^{-4}$ $cm^3 \cdot g^{-1} \cdot bar^{-1}$ (**Table 4.2**). The $^{21}Ne/^{22}Ne$ ratio was measured to be 0.0294 ± 0.0006 $cm^3STP \cdot g^{-1}$.

Assuming a simple vesiculation model (**Figure 4.3.**), similar to that of (Ruzié and Moreira, 2010), where a magma consists of homogeneous spheres of silicate liquid with a central homogeneous vesicle of pure CO_2, the vesicularity of the magma can be calculated as:

$$Ves = \frac{V_b}{V_m} = \frac{\frac{4}{3}\pi r^3}{\frac{4}{3}\pi R^3} = \left(\frac{r}{R}\right)^3 \qquad [1]$$

Where V_b and V_m are the volume of the bubble and the magma spheres, respectively.

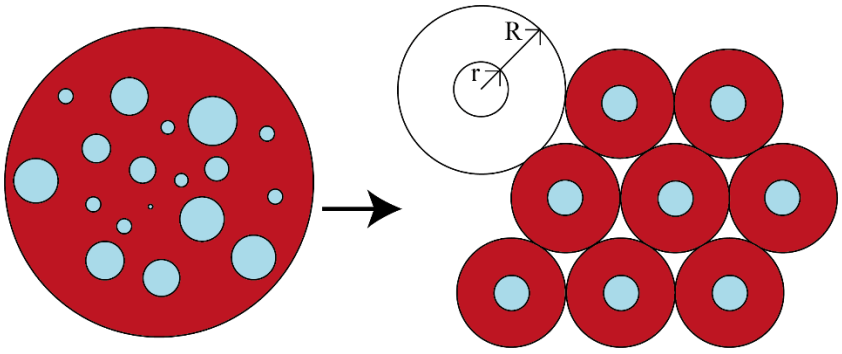

Figure 4.3.: This is a representative sketch of vesiculated magma composed of gas spheres surrounded by a finite volume of melt. *R* represents the radius of the magma, while *r* represents the radius of the vesicle. Modified from Ruzié and Moreira, (2010).

The pressure dependence of neon gas solubility obeys Henry's law (i.e. linear relationships between P_{Ne} and C_{Ne}) up to 1500 bars (e.g. Jambon et al., 1986; Lux, 1987; Nuccio and Paonita, 2000; Iacono-Marziano et al., 2010):

$$C_{Ne} = K_{Ne} * P_{Ne} \qquad [2]$$

Given the density of the starting material $\rho = 2.74 g/cm^3$, obtained using the model of Lange (1994) and Warren (1995) (see *Chapter 2* for more details), and a solubility

constant of $K_{Ne} = 3.16 \cdot 10^{-4}$ cm^3·g^{-1}·bar^{-1} (obtained for the composition of the glass), the volume of the gas inside of the vesicle can be calculated as:

$$V_{Ne} = \frac{4}{3}\pi(R^3 - r^3) * \rho * C_{Ne} \qquad [3]$$

Where C_{Ne} is the concentration of neon. Combining equations 2 and 3, the theoretical partial pressure of neon going to the gas phase can be calculated as:

$$P_{Ne} = \frac{V_{Ne}}{\frac{4}{3}\pi\left(\frac{r^3}{Ves} - r^3\right) * \rho * K_{Ne}} * X_{Ne} \qquad [4]$$

Where X_{Ne} is the molar fraction of neon. From equation (4), it can be seen that the gas pressure will depend on the size of the vesicles, *r*, and the vesicularity, *ves*, of the sample, which the experiment will control.

Figure 4.4. shows an example of the partial pressure of neon calculated for different vesicle sizes and vesicularities.

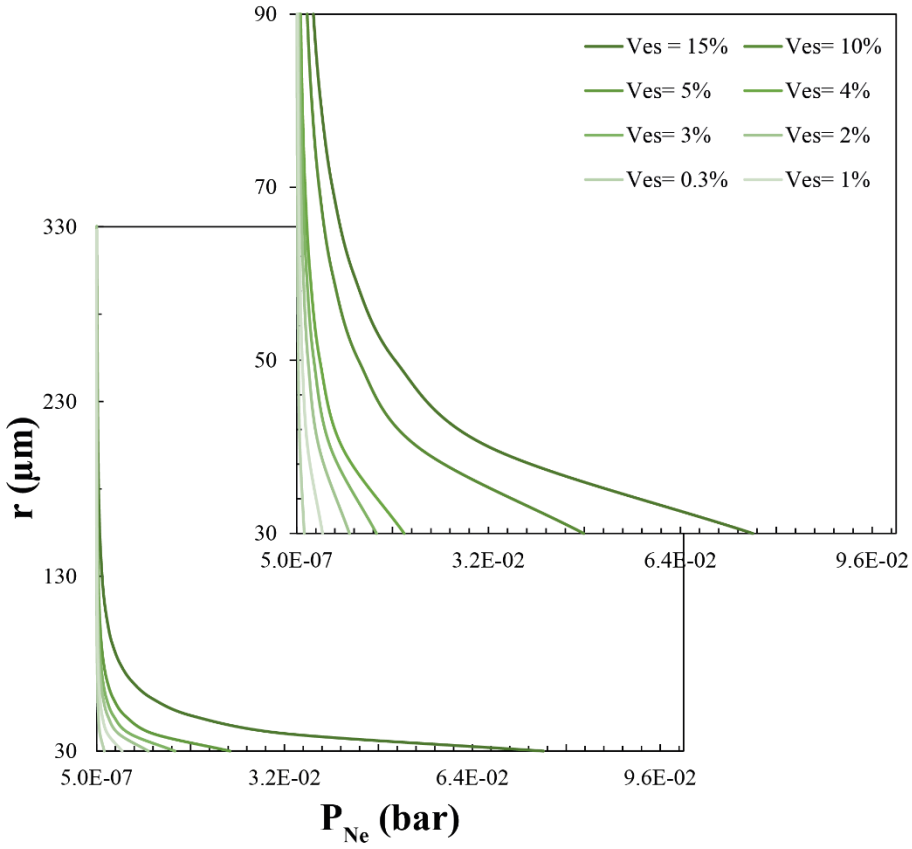

Figure 4.4.: The diagram illustrates the theoretical partial pressure of neon, P_{Ne}, in the vesicles, which depends on the vesicularity of the sample and the mean size of the vesicles, *r*. The pressure was obtained from the formula [4] with $K_{Ne} = 3.16 \pm 0.38$ cm^3 STP g^{-1}·bar^{-1} (**Table 4.2**).

Following the same model decomposed into magma spheres and considering the homogeneous concentration of Ne isotopes in the silicate melt with an air neon isotopic ratio of $^{20}Ne/^{22}Ne$= 9.8 (since our Ne-bearing glass is atmospheric in composition), a theoretical model of neon kinetic fractionation during nucleation and growth of vesicles can be calculated by assuming that ^{22}Ne isotope diffuses slower than ^{20}Ne by a factor of mass equal to $(22/20)^{1/2}$, with a maximum fractionation factor of (Graham's law):

$$F_{20\mathrm{Ne}/22\mathrm{Ne}} = \frac{20\mathrm{Ne}/22\mathrm{Ne}_s}{\sqrt{\frac{m_{22}}{m_{20}}}}$$

where m_{20} and m_{22} are neon isotope mass, and $^{20}Ne/^{22}Ne_s$ is the initial isotopic ratio dissolved into the glass (e.g. Craig and Lupton, 1976; Ruzié and Moreira, 2010).

This model also assumes that the exchange only occurs at the vesicle-magma interface, where Henry's Law [2] applies. It also assumes that the outer boundary of the magma sphere remains constant in terms of neon concentration (no gas enters or leaves the magma sphere) and that the bubbles are static, with no account taken of their growth or the nucleation of new populations. The neon isotopes diffuse from the magma into the bubbles from time t_1 to time t_n at different rates until they reach equilibrium. The time taken to reach equilibrium depends on the solubility constant, the distance travelled by the neon isotopes till the bubbles (i.e. the vesicularity of the magma) and the diffusivities of neon isotopes. The method used for the calculation is based on finite differences.

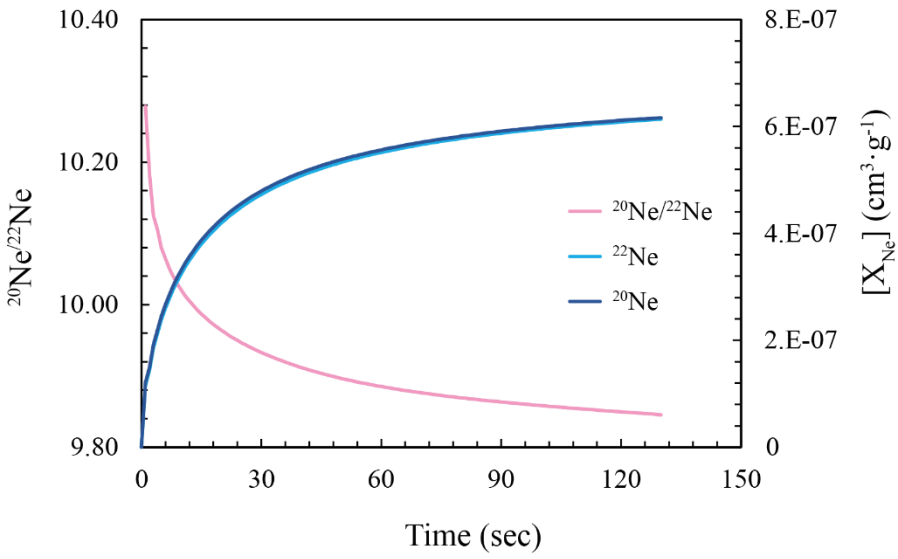

Figure 4.5.: model of kinetic fractionation that occurs in a magma sphere with a radius of r = 5 and R = 27 over time from t = 0 to t = 130. The diffusion of the ^{20}Ne isotope filling the vesicle in time is represented by the dark blue line, followed closely and almost overlapping by the ^{22}Ne isotope. The pink line represents the fractionation factor, which decreases with time while the isotopic ratio in the vesicle equals that of the melt when equilibrium is reached.

Figure 4.5 illustrates the kinetic fractionation that occurs in a pure CO_2 vesicle over time from t = 0 to t = 130 which has a constant radius of r = 5 which is immersed in a magma sphere with a radius R = 27 a homogeneous $^{20}Ne/^{22}Ne$ isotopic composition of = 9.8. These parameters have no units since r and R are synonymous with vesicularity [1]. As for t, the main interest is in comparing the concentration of both isotopes for an equal time. As can be seen, the ^{20}Ne isotopes diffuse more rapidly into the vesicle than ^{22}Ne isotopes. The difference in the isotopic ratio with time is plotted by the pink line of the $^{20}Ne/^{22}Ne$ ratio, which at first will show the theoretical maximum fractionation of $^{20}Ne/^{22}Ne$ =10.28 and will reach the equilibrium at time t_n = n with $^{20}Ne/^{22}Ne$ = 9.8.

In the context of a closed system with continuous nucleation and growth of vesicles, which to first order approaches our experimental conditions as described in the previous chapter, and where equilibrium has not yet been achieved, a significant kinetic fractionation record is anticipated.

4.2.3. Capsule preparation:

To investigate the Ne isotopic fractionation during vesiculation, this work proposes a simple experimental technique with the known proportion of rock powder, CO_2, and Ne. The experiments proposed for studying the kinetic fractionation of neon in

a silicate melt, where the major volatile species is CO_2, were the same as those used for studying vesicularity. Up to six experiments were conducted at the IHPV at the Institute of Earth Sciences of Orleans, ISTO. Eleven capsules were loaded with the conditions listed in **Table 4.3.**

Sample	Run	glass powder (mg)	CO2 (mg)	Ne (mg)	T (°C)	P_{exp} (bar)	P_Q (bar)	$time_{exp}$ (min)
ESFa-1B-CO2+Ne	#1	60.70	1.83	6.60	1200	1535	39	240
ESFa-2B-CO2+Ne	#1	63.80	0.84	6.50	1200	1535	39	240
ESFa-3B-CO2+Ne	#1	51.60	0.84	5.40	1200	1535	39	240
ESFa-4B-CO2+Ne	#2	61.70	1.65	6.70	1200	1573	73	10
ESFa-5B-CO2+Ne	#2	60.40	1.80	6.00	1200	1573	73	10
ESFa-6B-CO2+Ne	#2	63.50	3.74	6.30	1200	1573	73	10
ESFa-7B-CO2+Ne	#4	63.50	0.90	6.50	1200	1605	46	240
ESFa-10B-CO2+Ne	#4	64.10	3.83	6.30	1200	1605	46	240
ESFa-1A-CO2+Ne	#3	61.40	3.36	6.60	1200	1660	33	10
ESFa-2A-CO2+Ne	#4	59.90	0.96	6.30	1200	1605	46	240
ESFa-5A-CO2+Ne	#5	62.50	3.65	6.60	1200	1669	39	10
ESFa-6A-CO2+Ne	#6	56.90	0.87	6.60	1200	1732	48	240

Table 4.3: Experimental conditions. # indicates the experimental run; CO_{2added} is the CO_2 loaded into the capsule; Ne_{added} is the neon loaded into the capsule; P_{exp} is the temperature at which the experiment was quenched; P_Q indicates the transient pressure increase generated by the drop quench due to the change in temperature when the capsule falls into the cold bottom part of the vessel.

The experiments were conducted at pressures ranging from 1535 to 1732 ± 10 bars and a temperature of 1200ºC. A maximum of three capsules were loaded into the same experimental run. As in the previous static experiment, the capsules were loaded with excess CO_2 to ensure vesicularity (between 1.3 and 5.6 wt.% of CO_2). The estimated neon content in every capsule ranged from $4.14 \cdot 10^{-6} \pm 2.4 \cdot 10^{-7}$ wt.%. The run times selected for the analysis were 10 and 240 minutes.

All capsules were weighed before and after welding, as well as before and after each experiment, to check for any gas loss during pressurisation or during the experiment itself.

4.3. Analytical methods:

After quenching, the capsules were opened carefully to retrieve the largest possible piece of glass. Following the same methodology (see *Chapter 2*), the larger pieces of glass were kept for textural analyses with micro-CT and mass spectrometry

using the Helix-SFT mass spectrometer. The smaller pieces of glass were sorted for a range of compositional and textural analyses using EMPA and SEM, and for their dissolved volatiles using FTIR.

For EMPA and SEM analyses at least one piece of glass from each sample was used as representative of each sample and they were embedded in epoxy resin, polished and C-coated. Between five and ten points in every glass were pricked in order to evaluate the homogeneity of the major element compositions (refer to *Chapter 2* for more details).

OH- and CO_2^{3-} in the quenched glasses were determined by Fourier Transform Infrared Spectroscopy on doubly-face polished glass chips. FTIR analysis could not be performed on sample *ESFa-1A-CO_2+Ne* since the IR signal was absorbed by magnetite present in the glass (**Figure 4.6.**). The carbonate and the water species dissolved in the quenched glasses were quantified by using the Beer-Lambert law:

$$C_i = 100 \frac{M_i \cdot A_j}{d \cdot \rho_{liq} \cdot \varepsilon_j}$$

with absorption coefficients of ε_{3520} = 59.2 ± 4 L·mol^{-1} ·cm^{-1} for the OH-stretching vibration (~3520 cm^{-1}; Shishkina et al., 2014) and ε_{1430} = 283±8 L·mol^{-1} ·cm^{-1} (Dixon and Pan, 1995b) for the 1430 cm^{-1} peak in the mid-infrared (MIR) region.

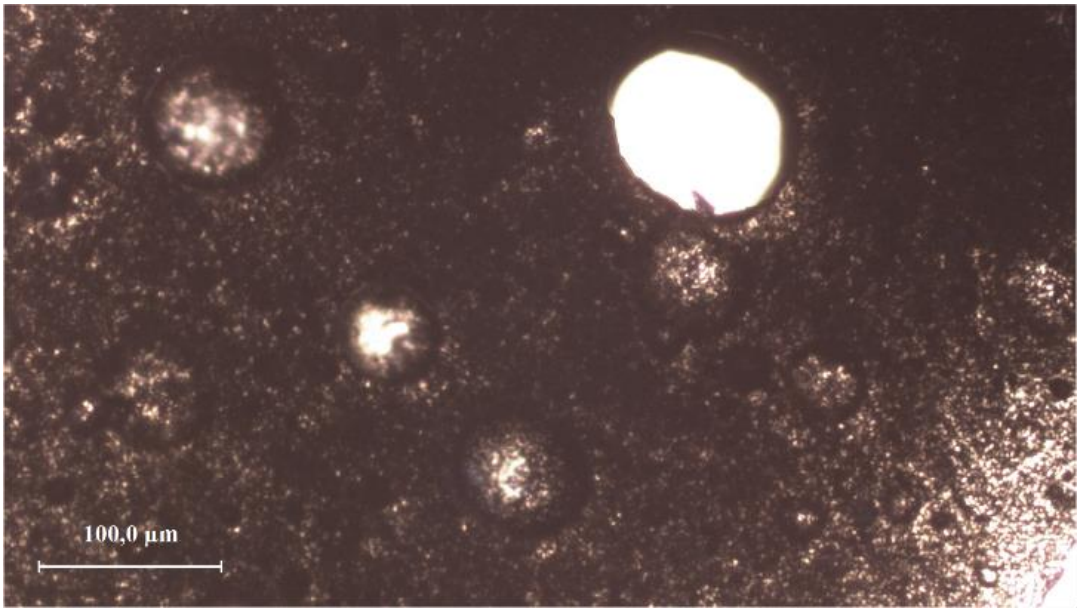

Figure 4.6.: Sample *ESFa-1A-CO_2+Ne* observed under transmitted light. Finding a space to analyse the dissolved volatiles in this glass was an impossible task due to the amount and distribution of magnetite absorbing the signal.

For microtomography, all samples were analysed at a resolution of 3µm as described in *Chapter 2*. Microtomography is a necessary tool not only for the study of vesicularity but also for the localization of vesicles analysed with the mass spectrometer. Accurately locating bubble populations for analysis is essential due to the micrometric size of the bubbles, which reduces analytical time in the mass spectrometer. It is worth noting that localizing bubbles with a laser coupled to the mass spectrometer is a time-consuming process. Randomness plays a significant role in this process, and it can take anywhere from three minutes to three weeks to find out a sizeable bubble, depending on the vesicularity of the sample and the distribution and size of the bubbles. As a result, due to the complexity of the bubble localization process, only three experimental samples were analysed to test the kinetic fractionation.

After acquiring X-ray CT scans and polishing the largest pieces with a double soft-face technique, they were embedded in acetone and ethanol for at least one day before being introduced into the mass spectrometer to eliminate any remaining thermoplastic resin. Subsequently, they were placed in a furnace at 120º to remove all moisture. Three representative samples were then loaded into the laser cell under vacuum and baked at 100 - 120 ºC for at least one night until the blank in the line was low enough ($^{22}Ne < 4.75 \cdot 10^{-13}$ cm^3) to begin the analysis.

Samples *ESFa-3B-CO_2+Ne*, *ESFa-5B-CO_2+Ne*, and *ESFa-6B-CO_2+N*e had 16, 10, and 3 pierced bubbles, respectively. The drilling was performed using a diode-pumped air-cooled Q-switched laser, and the pressure of each pierced vesicle was measured with a manometer connected to the laser cell. After purification along the line (refer to *Chapter 2*), the neon isotopes are measured using the Helix SFT mass spectrometer, which is optimized for noble gas isotope measurements at ISTO. Additionally, masses 40 and 44 are measured to correct for mass interferences. Neon abundances and isotopic ratios were then corrected for $^{40}Ar^{++}/^{40}Ar^{+}$ and CO_2^{++}/CO_2^{+} ionization ratios (around 0.1 and 0.01 respectively).

The volume of each analysed vesicle was calculated using the equation for the straight line obtained in *Section 3.3.1.2*:

$$V_b = 0.0824 * P_b - 5 * 10^{-8}$$

Where P_b is the total pressure measured with the manometer of the expanded gas when piercing a vesicle. The partial pressure of Ne, P_{Ne}, was obtained with the constant

solubility of K_{Ne} =3.16·10^{-4} obtained for the Ne-bearing glass and following Henry's law [2] assuming that all neon went to the gas phase. P_{CO2} was calculated by subtracting P_{Ne} from the total pressure, P_b, of the vesicle.

4.4. Results:

4.4.1. Major elements and scanning electron microscope:

The quenched glasses were analysed for major elements (**Table 4.4.**) to check the homogeneity of the experimental samples and to obtain the density of the liquid using the Lange, (1994) method, as explained in *Chapter 2*. The EMPA analyses indicate that the compositions of the run products are similar to the starting material except for the sample *ESFa-1B-CO_2+Ne*. This sample shows an increase in Al_2O_3 and K_2O and a decrease in FeO and MgO, most probably due to the presence of micro plagioclases in the quenched glasses that were hit during the analysis, despite efforts to avoid them.

	SiO_2	TiO_2	Al_2O_3	FeO	MnO	MgO	CaO	Na_2O	K_2O	P_2O5	$Na_2O + K_2O$	Total
ESFa-1B-CO2+Ne	45.17	4.15	20.12	7.54	0.18	5.98	9.38	3.93	2.52	1.03	6.44	100
	2.37	0.59	1.92	2.36	0.08	1.30	1.26	0.24	0.40	0.23		
ESFa-2B-CO2+Ne	45.15	3.76	15.81	10.97	0.22	7.36	10.31	3.83	1.73	0.87	5.55	100
	3.01	0.05	0.16	4.11	0.06	0.35	0.83	0.24	0.18	0.08		
ESFa-3B-CO2+Ne	47.51	3.57	15.31	8.52	0.21	7.09	11.15	4.09	1.76	0.80	5.85	100
	0.25	0.08	0.12	0.41	0.05	0.16	0.09	0.10	0.03	0.10		
ESFa-4B-CO2+Ne	44.51	3.60	15.09	12.18	0.24	7.76	10.43	3.78	1.62	0.78	5.40	100
	0.23	0.16	0.14	0.19	0.03	0.13	0.08	0.08	0.09	0.09		
ESFa-5B-CO2+Ne	44.92	3.80	15.25	11.86	0.19	7.68	10.32	3.55	1.65	0.79	5.19	100
	0.13	0.09	0.24	0.23	0.06	0.09	0.09	0.10	0.07	0.05		
ESFa-6B-CO2+Ne	44.59	3.58	15.16	12.08	0.23	7.74	10.41	3.72	1.64	0.85	5.37	100
	0.20	0.10	0.22	0.12	0.06	0.06	0.12	0.08	0.03	0.04		
ESFa-1A-CO2+Ne	45.13	3.63	15.26	11.34	0.19	7.48	10.72	3.81	1.63	0.80	5.44	100
	1.83	0.19	0.21	2.43	0.06	0.16	0.53	0.04	0.09	0.07		
ESFa-2A-CO2+Ne	46.48	3.70	15.57	9.71	0.18	7.15	10.81	3.84	1.63	0.93	5.47	100
	0.72	0.06	0.22	1.19	0.03	0.12	0.22	0.18	0.08	0.11		
ESFa-7B-CO2+Ne	45.96	3.70	14.99	10.43	0.18	7.45	10.80	4.02	1.62	0.84	5.64	100

	0.30	0.10	0.09	0.39	0.11	0.15	0.18	0.04	0.05	0.07		
ESFa-10B-CO2+Ne	46.97	3.73	15.41	9.23	0.20	7.18	10.96	3.77	1.61	0.94	5.38	100
	0.37	0.09	0.16	0.26	0.08	0.06	0.09	0.07	0.03	0.07		
ESFa-5A-CO2+Ne	46.26	3.67	15.37	9.74	0.21	7.42	10.89	3.91	1.63	0.90	5.55	100
	1.60	0.14	0.23	2.03	0.04	0.23	0.50	0.10	0.10	0.04		
ESFa-6A-CO2+Ne	44.46	3.49	15.20	12.24	0.18	7.75	10.45	3.79	1.62	0.81	5.41	100
	0.36	0.15	0.10	0.26	0.06	0.06	0.10	0.08	0.05	0.08		

Table 4.4.: Chemical composition of the whole set of experimental samples. The chemical composition of each experimental sample is provided in the *Appendix* of the manuscript.

Two of the analysed samples, *ESFa-1B-CO_2+Ne* and *ESFa-2B-CO_2+Ne*, contained different amounts of crystals. In the case of sample *ESFa-1B-CO_2* (**Figure 4.7.a.** and **b.),** they were abundant with sizes ranging from 5 to 100µm. In the case of *ESFa-2B-CO_2+Ne,* they were scarce with length <30µm (**Figure 4.7.c.** and **d.**).

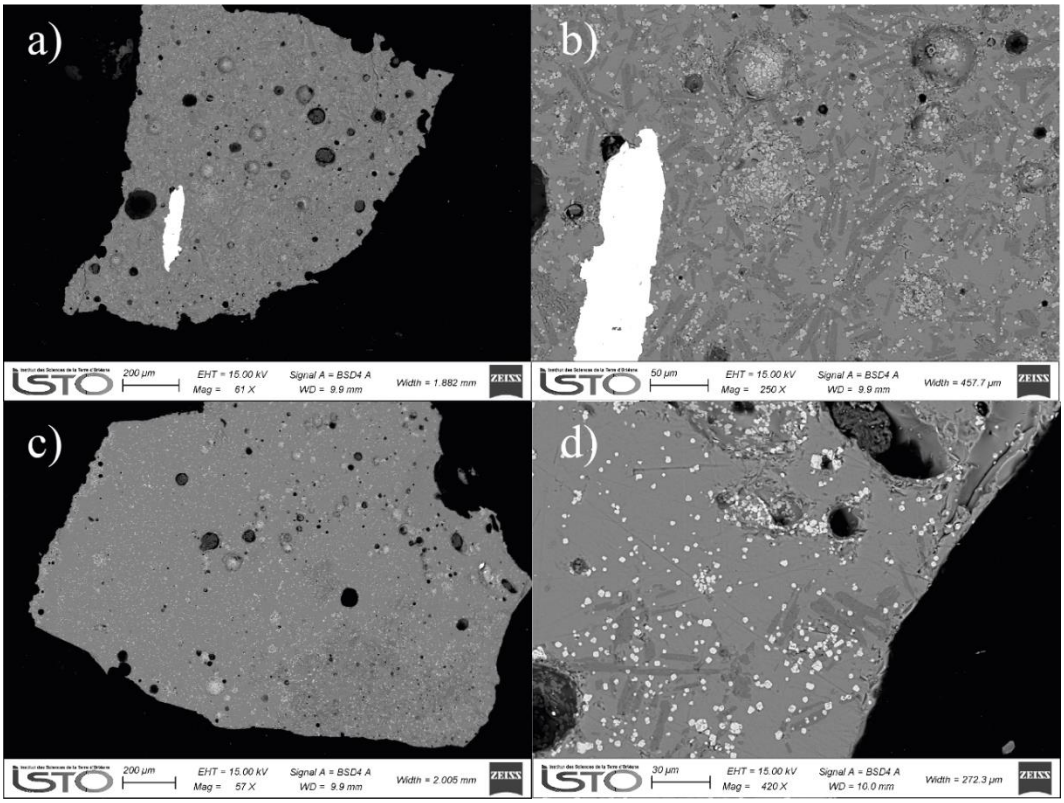

Figure 4.7.: Images ***a*** and ***b*** show a scanning electron microscope view of sample *ESFa-1B-CO2+Ne*, displaying the distribution of oxides and plagioclases at different scales. A large crystal of Ag (white) is also visible in the picture, originating from the silver oxalate used as a source of CO_2. Images ***c*** and ***d*** display the distribution and size of the plagioclase and magnetite crystals in sample *ESFa-2B-CO_2+Ne* at different scales.

4.3.2. CO_2 and H_2O content:

Between two and five points on each quenched glass were analysed using FTIR in the smallest chunk of glass. The results of the IR Spectroscopy are given in **Table 4. 5.** The dissolved CO_3^{2-} varies from 721–1705 ppm. Although no water was added to the charges, two samples showed a small amount of dissolved OH^- (0.3 and 0.64 wt.%; *ESFa-6B-CO2+Ne and ESFa-6A-CO2+Ne respectively*), most likely due to iron reduction of the oxidised starting glass, or to moisture of the silver oxalate loaded to the capsule, as described in *Chapters 2* and *3.*

Sample	Thickness (cm)	σ	Density (g · l^{-1})	σ	A_{1430}	σ	A_{3525}	σ	[CO_2] (ppm)	sd	CO_2 (wt.%)	σ	H_2O (wt.%)	sd
ESFa-1B-CO2+Ne.1	0.0050	0.0003	2678	46	0.1048	0.0104			1328	158				
ESFa-1B-CO2+Ne.2	0.0049	0.0003	2678	46	0.1220	0.0058								
ESFa-2B-CO2+Ne.1	0.0035	0.0002	2739	75	0.0794	0.0042			1023	259				
ESFa-2B-CO2+Ne.2	0.0035	0.0002	2739	75	0.0636	0.0057								
ESFa-2B-CO2+Ne.3	0.0041	0.0003	2739	75	0.0548	0.0040								
ESFa-3B-CO2+Ne.1	0.0082	0.0001	2691	7	0.0986	0.0025			721	188				
ESFa-3B-CO2+Ne.2	0.0082	0.0001	2691	7	0.1084	0.0013								
ESFa-3B-CO2+Ne.3	0.0082	0.0001	2691	7	0.1284	0.0022								
ESFa-3B-CO2+Ne.4	0.0073	0.0002	2691	7	0.0526	0.0091								
ESFa-3B-CO2+Ne.5	0.0057	0.0003	2691	7	0.0820	0.0035								
ESFa-4B-CO2+Ne.1	0.0045	0.0001	2760	3	0.0686	0.0029			1025	246				
ESFa-4B-CO2+Ne.2	0.0044	0.0004	2760	3	0.0932	0.0035								
ESFa-5B-CO2+Ne.1	0.0026	0.0002	2755	4	0.0812	0.0036			1705	101				
ESFa-5B-CO2+Ne.2	0.0027	0.0002	2755	4	0.0770	0.0037								
ESFa-6B-CO2+Ne.1	0.0042	0.0004	2758	3	0.0524	0.0018	0.1202	0.0004	880	240	0.3188	1.33E-03	0.30	0.025
ESFa-6B-CO2+Ne.2	0.0042	0.0004	2758	3	0.0774	0.0011	0.1070	0.0007			0.2838	1.06E-03		
ESFa-7B-CO2+Ne.1	0.0034	0.0002	2728	8	0.0900	0.0016			1546	66				
ESFa-7B-CO2+Ne.2	0.0034	0.0004	2728	8	0.0950	0.0030								
ESFa-10B-CO2+Ne.1	0.0039	0.0002	2707	5	0.0870	0.0038			1197	119				
ESFa-10B-CO2+Ne.2	0.0042	0.0002	2707	5	0.0810	0.0025								
ESFa-2A-CO2+Ne.1	0.0064	0.0002	2715	20	0.1196	0.0036			1023	63				
ESFa-2A-CO2+Ne.6	0.0033	0.0001	2715	20	0.0560	0.0021								
ESFa-5A-CO2+Ne.1	0.0034	0.0001	2720	36	0.0636	0.0029			1043	47				
ESFa-5A-CO2+Ne.2	0.0034	0.0001	2720	36	0.0600	0.0051								
ESFa-6A-CO2+Ne.1	0.0057	0.0003	2763	5	0.1468	0.0013	0.2986	0.0011	1605	220	0.5769	2.19E-03	0.64	0.084
ESFa-6A-CO2+Ne.2	0.0057	0.0003	2763	5	0.1770	0.0016	0.3575	0.0013			0.6956	3.24E-03		

Table 4.5: FTIR data. Average of H_2O and CO_2 concentrations calculated from the number of analytical spots in each sample, whenever possible. δ is the standard deviation of the density of the sample and of the thickness where the chunk of glass was analysed.

4.4.3. Micro-CT:

Ten out of twelve experimental samples were scanned using Micro-CT to study the vesicularity parameter and vesicle distribution for neon analysis with the mass spectrometer. Some of the quenched glasses were scanned using two or even three pieces in the same image scan, all belonging to the same experimental capsule. Others were scanned separately for analysis. For instance, in the case of the sample *ESFa-4B-CO_2+Ne*, the pieces retrieved from the capsule aperture were insufficient for image-scan analysis. Note that no scale is provided for the images and that the colours make references only to the two phases (glass and bubbles) of the experiments that the micro-CT can recognise at the imposed resolution and the size of the samples.

The glasses were then sorted into two diverse groups based on their run duration. In both groups, 10- and 240-minutes of the experiment, the vesicle distribution of the scanned glasses showed the same pattern as the temporal series studies in the previous chapter for bubbles containing pure CO_2.

4.4.3.1. 3D Data treatment by VGStudioMax:

- *Group of 10 minutes of the experiment:* The vesicles are distributed evenly throughout the glass, as shown in **Figure 4.8.**, except for sample *ESFa-6B-CO_2+Ne*, which tends for larger vesicles to accumulate at one end of the glass. Small vesicles are also present and scattered throughout the glass, indicating nucleation. Despite the mean size of the vesicles growing inside the melt, some of the experimental glasses in this group contain exceptionally large vesicles trapped between the glass-capsule interface, some of them bigger than 1 mm. In most cases, when the vesicles are large enough, they cause the glass to break during the capsule's aperture (**Figure 4.9.**).

  Two of the samples exhibit a higher density of bubbles compared to the others: *ESFa-1A-CO_2+Ne* and *ESFa-5A-CO_2+Ne*. Two samples belonging to this group were selected to analyse Ne composition in the bubbles *ESFa-5B-CO_2+Ne* and *ESFa-6B-CO_2+Ne.*

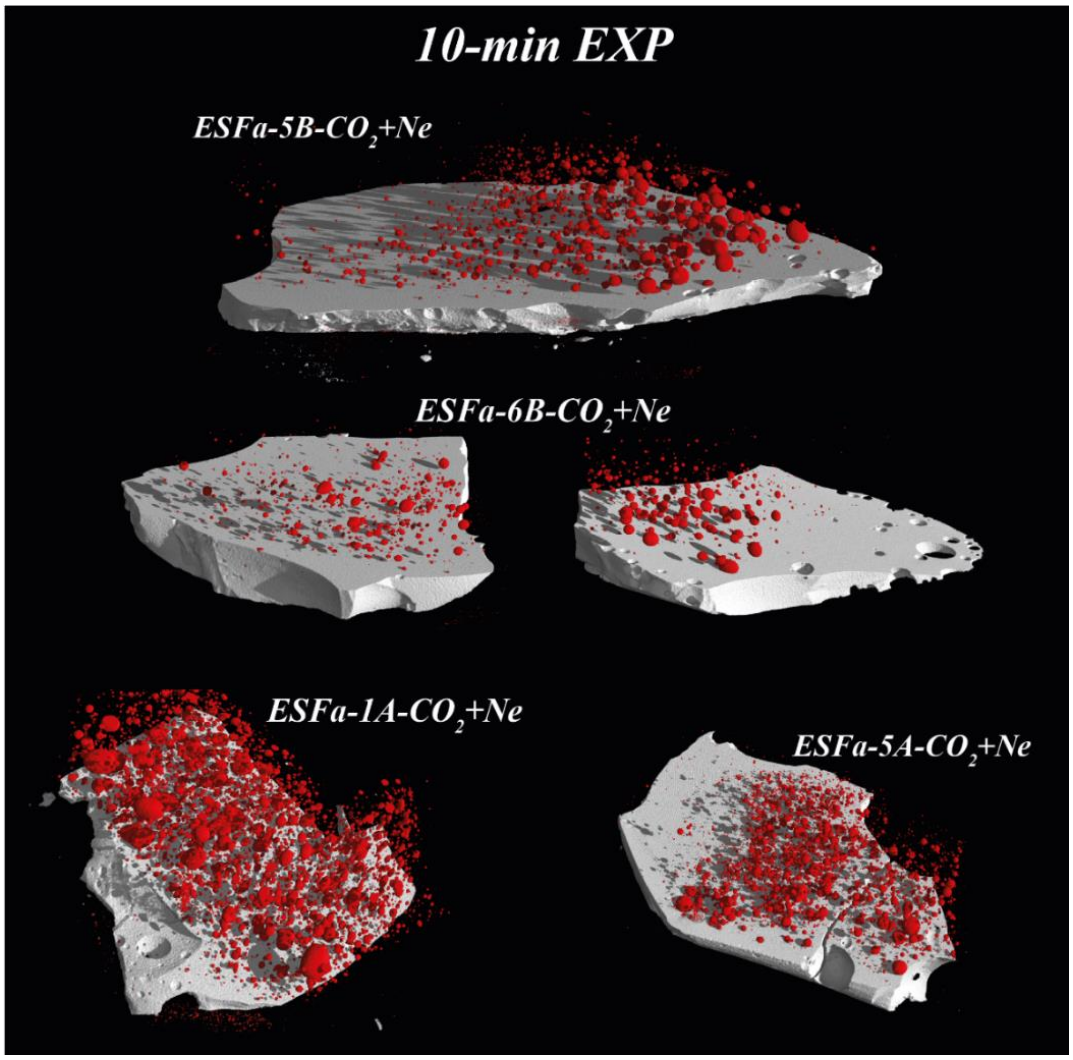

Figure 4.8.: 3D image of samples belonging to the 10-min group of experiments. The images illustrate the distribution of the vesicles (red) in the glass (grey). These images show only the larger pieces preserved for every experiment. Notice how some of the samples were scanned keeping two pieces of glass attached to each other to better understand the evolution of the system such as for the sample of *ESFa-5A-CO_2+Ne*. When this procedure was not possible, the pieces were image scanned separately (*ESFa-6B-CO_2+Ne)*.

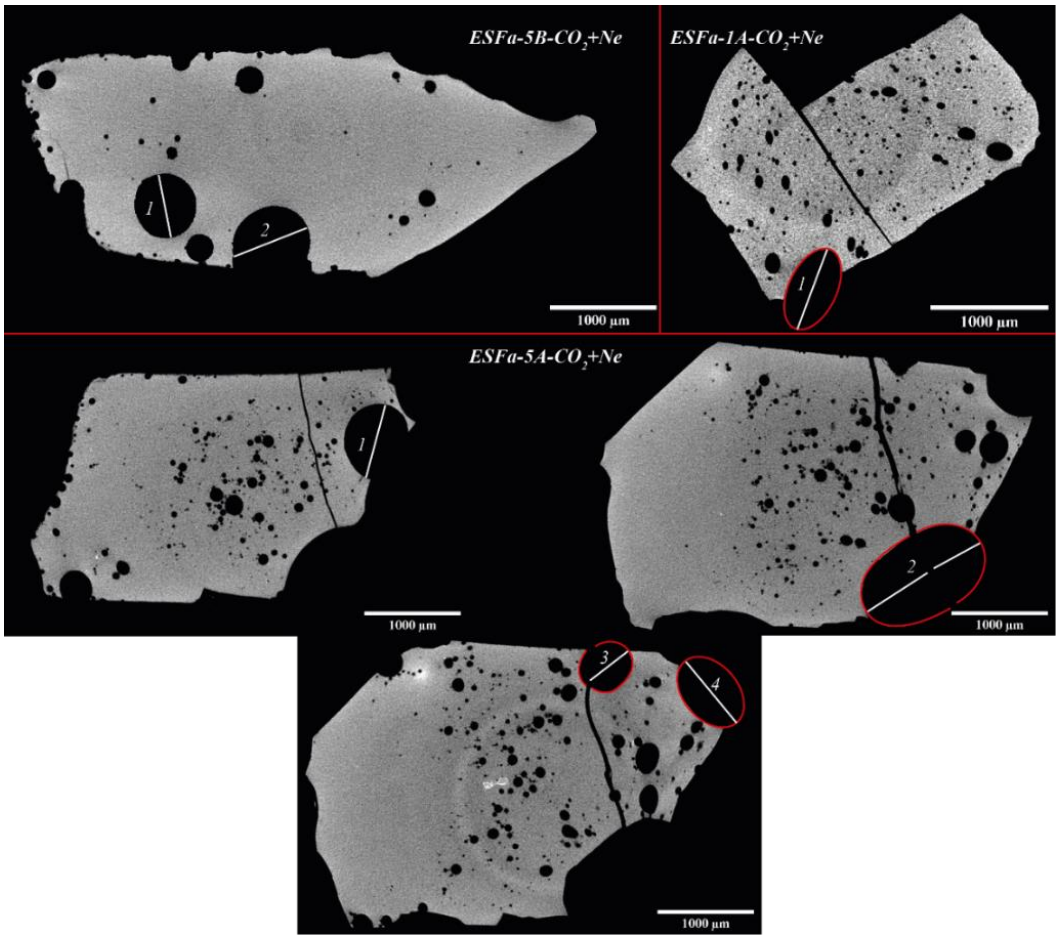

Figure 4.9.: ESFa-5B-CO_2+Ne showing the maximum diameter of two vesicles trapped between the glass interface and the capsule with radius of: 1 = 598µm and 2 = 761µm; Sample *ESFa-1A-CO_2+Ne* showing the maximum diameter of the biggest vesicle: 1 = 707µm; the three last slices show sample *ESFa-5A-CO_2+Ne* with the biggest vesicles founded: 1 = 775µm, 2 = 1407µmm 3 = 518µm and 4 = 920µm. The diameter of the vesicles was measured individually using ImageJ and taking in to account the break of the glass when it was present. Notice how these big bubbles create a rough surface.

- *Group of 240 minutes of experiment:* Although it is premature to observe significant changes, the gas bubbles in this time series, as with the samples where the gas phase was pure CO_2, tend to separate from the bottom of the capsule (**Figure 4.10.**). Bubble growth by coalescence becomes noticeable when populations of larger bubbles are surrounded by smaller bubbles (**Figure 4.11.**). The presence of tiny vesicles is noticeable in all the experimental glasses indicating a continuous nucleation.

  As with the previous group, two samples stand out due to the presence of bubbles larger than the general representation *ESFa-1B-CO_2+Ne* and *ESFa-10B-CO_2+Ne*

(**Figure 4.12.**). These bubbles are located at the capsule-glass interface in both cases.

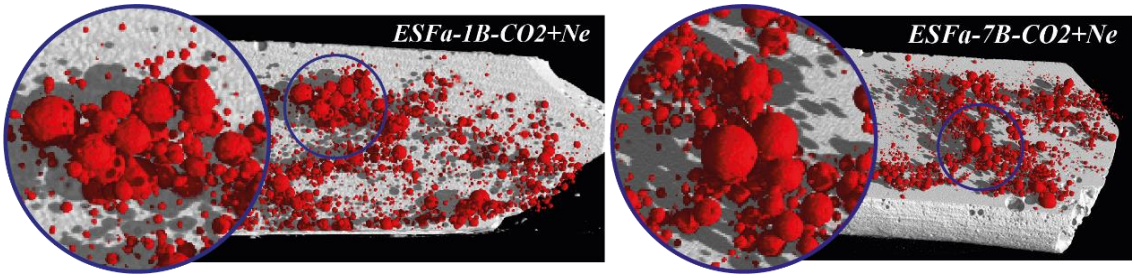

Figure 4.11: 3D image of samples *ESFa-1B-CO_2+Ne* and *ESFa-7B-CO_2+Ne* (group 240 minutes of experiment) with a zoom on a group of vesicles growing by coalescence of surrounded by smaller vesicles.

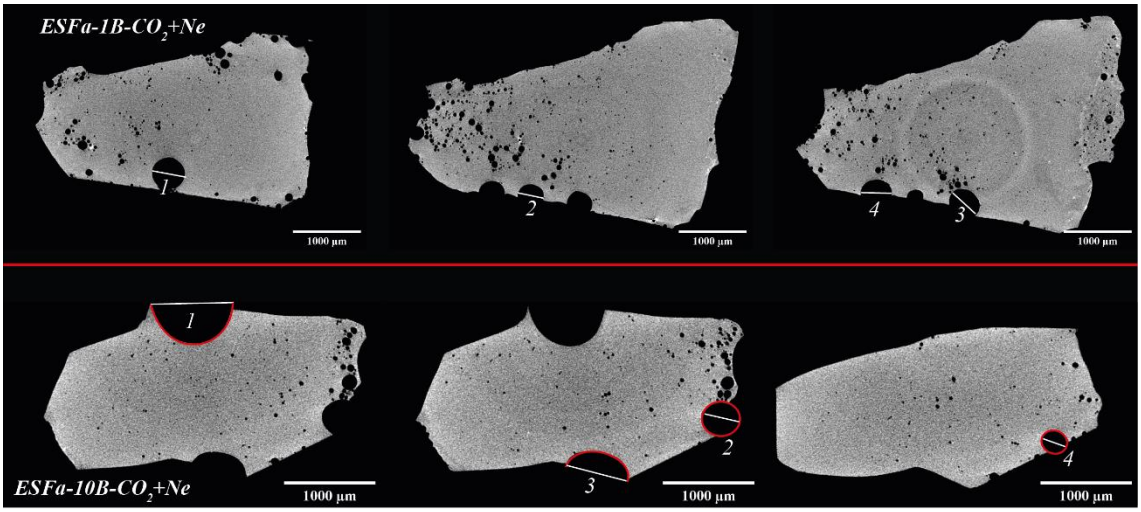

Figure 4.12.: *ESFa-1B-CO_2+Ne* showing the maximum diameter of four vesicles trapped between the glass interface and the capsule with radius of: 1 = 486µm, 2 = 390µm, 3 = 445µm and 4 = 460µm; Sample *ESFa-10B-CO_2+Ne* showing the maximum diameter of the biggest vesicles: 1 = 865µm, 2 = 368µmm 3 = 800µm and 4 = 256µm. The diameter of the vesicles was measured individually using ImageJ.

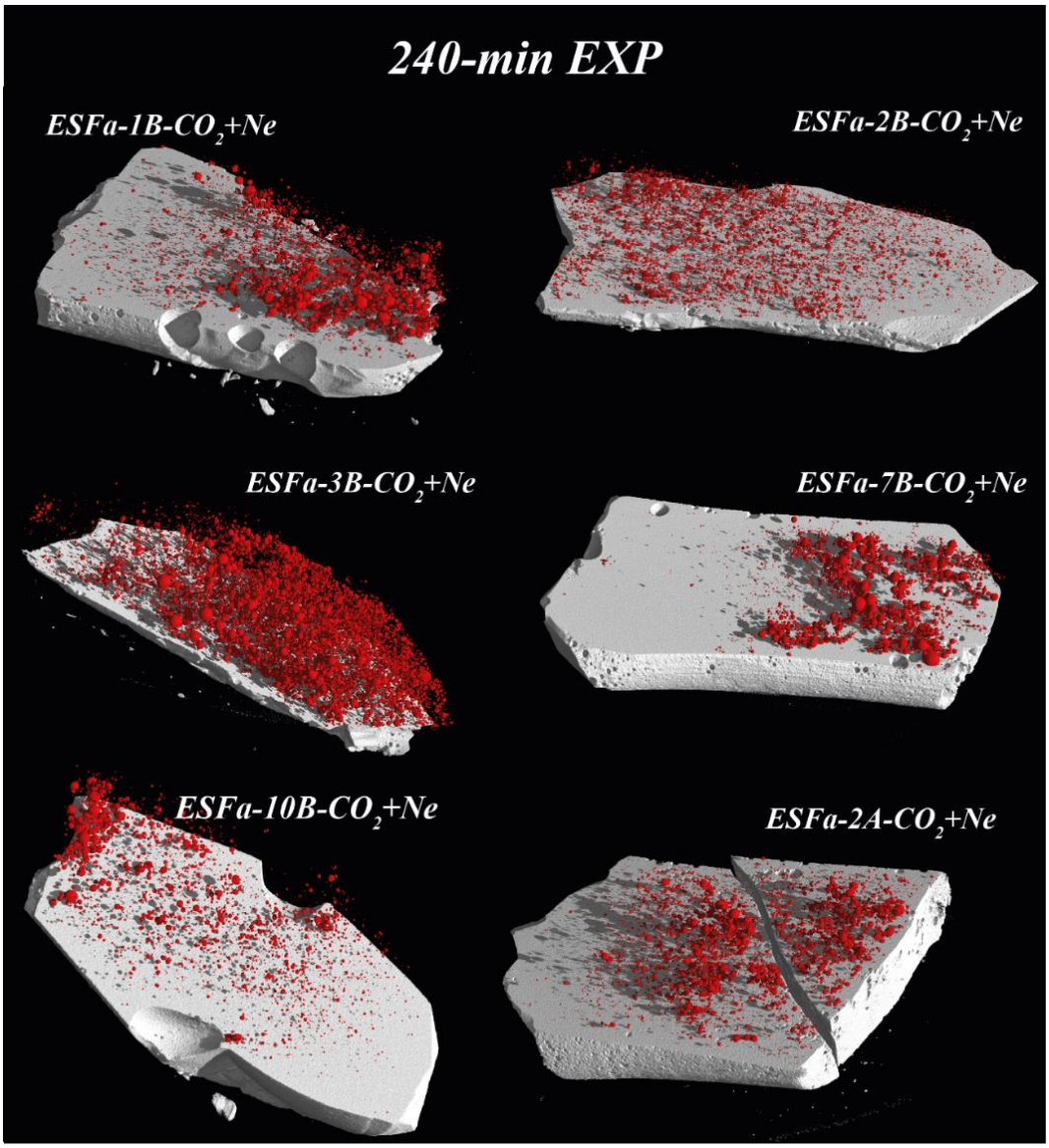

Figure 4.12.: 3D image of samples belonging to the 240-min group of experiments. The images illustrate the distribution of the vesicles (red) in the glass (grey). These images show only the larger pieces preserved by every experiment. The sample *ESFa-2A-CO_2+Ne* was scanned keeping two pieces of glass attached in other to better understand the system as a whole.

4.4.3.2. VSD textural analysis in 2D and 3D by ImageJ:

The tomography-derived image stacks were processed for 2D and 3D analyses using *ImageJ*, following the method of Marsh (1988) and Chavrit (2010), as described in *Chapter 3*. The experimental glasses were sorted into different vesicularity groups following the same classification. Results are shown in **Table 4.6.**

4.4.3.2.1. Bubble density, vesicularity and mean diameter in 2D:

It is important to note that, similar to the classifications in *Chapter 3*, the vesicularity, bubble density, and mean diameters presented in this table of results refer to those analysed in a representative area of the image stack obtained from the CT-scan.

- *Group of 10 minutes of experiment:* The bubble density of this group ranges from 7.47 to 88.94mm^{-2}. Sample *ESFa-1A-CO_2+Ne* has the highest bubble density. It is worth noting that although the analysed surface area, and so the volume, of the sample is small, it is unlikely to significantly influence the results due to the abundance of vesicles present and their homogeneous distribution. It is expected that the non-analysed portion of that sample will have a similar appearance. The mean diameter of the group ranges from 16.57 to 37.88µm. Sample *ESFa-5B-CO_2+Ne* has the largest mean diameter, which is 10µm larger on average than the same group of experimental samples ran with pure CO_2 in the volatile phase of the previous chapter. The vesicularity of this group ranges between 0.79 – 7.67 %, with sample *ESFa-5A-CO_2+Ne* having the higher vesicularity.

- *Group of 240 minutes of experiment:* The bubble density range of this group is bigger than in the earlier group, ranging from 33.57 to 80.25mm^{-2}, sample *ESFa-2B-CO_2+Ne*, having the higher density of bubble of the. However, the mean diameter of this group is smaller than the previous group and is consistent with the group that only used CO_2 as the volatile species for the same experimental time. The mean diameters range from 16.60 to 22.58µm, with sample *ESFa-7B-CO_2+Ne* having the largest mean diameter of the group. The vesicularity of this group ranges from 1.73 to 4.11%, sample *ESFa-3B-CO_2+Ne* being the most vesiculated one.

4.4.3.2.1. VSD, from 2D to volume:

The distinct types of Vesicle-Size-Distribution are represented in **Figure 4.13**. The experiments that lasted 240 minutes have higher correlation coefficients, with $R^2 > 0.88$, which is related to the number of bubbles counted (Chavrit, 2010). These experimental samples have more than 330 vesicles counted on the surface studied, indicating a good

representation of all the populations of bubbles. For more information, refer to *Section 3.4.1*.

For samples grouped as VSD type III, the effect of Ostwald ripening is observed several times in the same sample, where the slope breakage occurs not only in the smallest diameters but also in intermediate populations around 0.08 mm (sample *ESFa-5B-CO_2+Ne* and *ESFa-5A-CO_2+Ne*), 0.13 mm (samples *ESFa-5B-CO_2+Ne* and *ESFa-3B-CO_2+Ne*), and/or 0.17 mm (as in the case of sample *ESFa-5A-CO_2+Ne*).

VSD type IVa is represented by the sample *ESFa-6B-CO_2+Ne* with the absence of one intermediate-size vesicle population, but also with a curved trend line through the smaller vesicles to the intermediate sizes.

The VSD parameter was integrated into the graphic used for pure CO_2 vesicles in order to ascertain that they exhibited a similar tendency and that no changes were occurring as a result of the development of new experiments. The data are presented in **Figure 4.14**, with darker colours and larger dots.

Sample	Exp. Time (min)	Nb	Area (mm^2)	Bubbles density (mm^{-2})	D_{max} (µm)	D_{mean} (µm)	Ves Image slice (%)	Ln(n) (mm^{-4})	sd	a (mm-1)	sd	R^2	$D_{mean\ th}$ (-1/a) (µm)	G_0 (µm/min)	VSD group
ESFa-1B-CO_2+Ne	240	384	9.33	43.30	119.78	18.05	1.88	12.75	0.44	-70.19	5.43	0.94	14.25	7.92E-03	I
ESFa-2B-CO_2+Ne	240	1111	13.86	80.25	191.13	16.60	2.84	13.49	0.45	-77.08	4.95	0.96	12.97	7.21E-03	I
ESFa-3B-CO_2+Ne	240	953	10.63	70.99	161.78	18.47	4.11	12.91	0.54	-60.25	7.05	0.88	16.60	9.22E-03	III
ESFa-4B-CO2+Ne	10														
ESFa-5B-CO_2+Ne	10	133	11.26	11.99	196.57	37.88	2.61	9.54	0.58	-31.98	6.18	0.73	31.27	1.74E-02	III
ESFa-6B-CO_2+Ne	10	39	5.64	7.47	90.58	29.47	0.79	10.14	1.40	-51.68	11.56	0.69	19.35	1.08E-02	IVa
ESFa-7B-CO_2+Ne	240	494	13.30	37.37	166.22	22.58	3.13	11.65	0.44	-47.82	5.55	0.88	20.91	1.16E-02	II
ESFa-10B-CO_2+Ne	240	157	4.71	33.57	91.40	19.84	1.73	12.10	0.31	-63.42	7.24	0.88	15.77	8.76E-03	II
ESFa-1A-CO_2+Ne	10	333	3.73	88.94	122.29	16.57	4.11	13.32	0.39	-71.29	6.74	0.92	14.03	7.79E-03	I
ESFa-2A-CO_2+Ne	240	702	10.32	61.43	160.89	17.31	3.71	12.54	0.45	-56.70	5.91	0.90	17.64	9.80E-03	I
ESFa-5A-CO_2+Ne	10	308	8.12	38.30	273.67	30.35	7.67	10.50	0.68	-31.11	5.24	0.78	32.14	1.79E-02	III
ESFa-6A-CO2+Ne	240														

Table 4.6: VSD parameter of the experimental samples analysed by micro-CT and image treated by ImageJ and Excel. *$Exp._{time}$* refers to the duration of the experiment; *Nb* represents the number of counted bubbles in the slice; D_{max} and D_{mean} correspond to the maximum and mean diameter of the vesicles in the analysed slice; $Ves_{ImageJ\ slice}$ indicates the vesicularity of the analysed area in the slice; *Ln(n)* is the density of the population of vesicles obtained by the linear trend of the graph *Ln(n)* vs (D_{max}); *a* is the slope of the trend line; R^2 is the correlation coefficient of the trend line; $D_{mean\ th\ (-1/a)}$ is the theoretical mean diameter for this sample obtained by the inverse of the slope; Additionally, the growth rate of the vesicles is represented by G_0. There is not data available for samples sample *ESFa-4A-CO_2+Ne* and sample *ESFa-6A-CO_2+Ne* since the recovered pieces from the aperture of the capsule were not large enough for the scan.

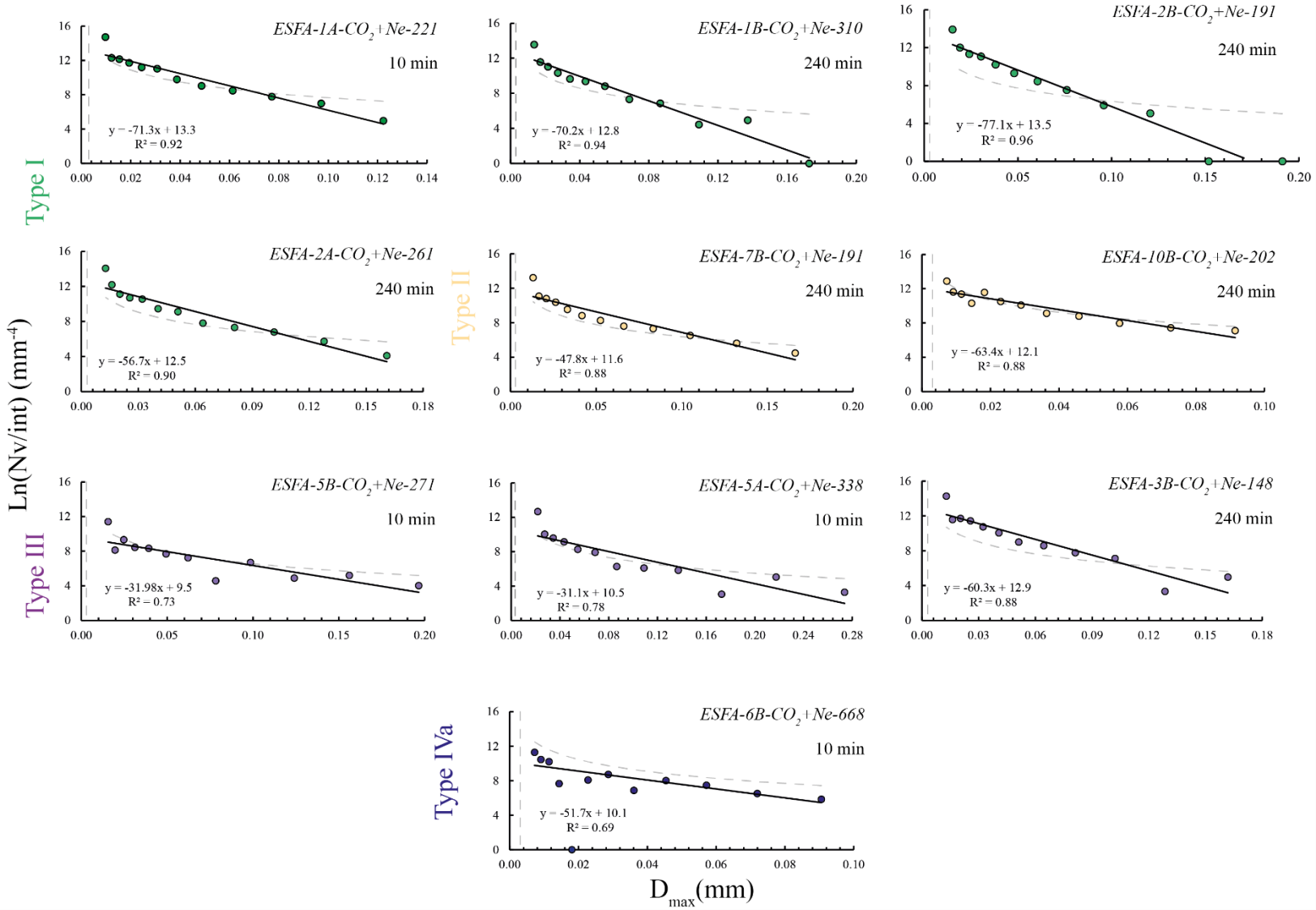
Type I
Type II
Type III
Type IVa
Ln(Nv/int) (mm-4)
Dmax(mm)
ESFA-1A-CO2+Ne-221
10 min
y = -71.3x + 13.3
R² = 0.92
ESFA-1B-CO2+Ne-310
240 min
y = -70.2x + 12.8
R² = 0.94
ESFA-2B-CO2+Ne-191
240 min
y = -77.1x + 13.5
R² = 0.96
ESFA-2A-CO2+Ne-261
240 min
y = -56.7x + 12.5
R² = 0.90
ESFA-7B-CO2+Ne-191
240 min
y = -47.8x + 11.6
R² = 0.88
ESFA-10B-CO2+Ne-202
240 min
y = -63.4x + 12.1
R² = 0.88
ESFA-5B-CO2+Ne-271
10 min
y = -31.98x + 9.5
R² = 0.73
ESFA-5A-CO2+Ne-338
10 min
y = -31.1x + 10.5
R² = 0.78
ESFA-3B-CO2+Ne-148
240 min
y = -60.3x + 12.9
R² = 0.88
ESFA-6B-CO2+Ne-668
10 min
y = -51.7x + 10.1
R² = 0.69

Figure 4.13.: Population density plots as a function of the maximum diameter of each interval for samples grouped in *VSD Type I* (green dots), *VSD Type II* (salmon dots), *VSD Type III* (purple dots) and *VSD Type IVa* (blue dots). The dashed grey curve is indicative for a minimum number of 4 bubbles per interval. The vertical dashed grey line is the limit of detection of the tomography.

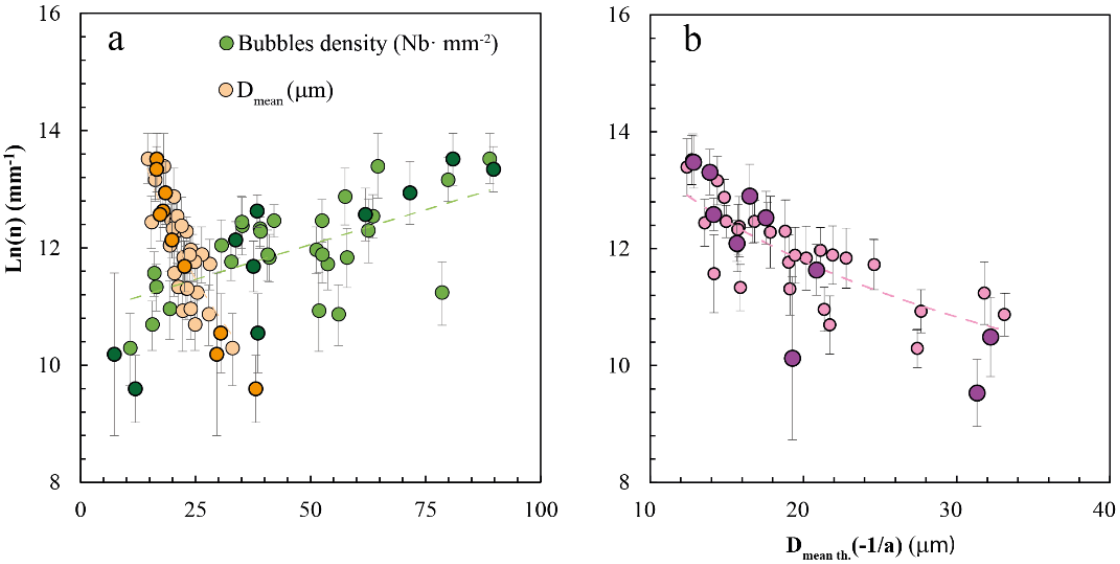

Figure 4.14.: **a.** Density of population of each sample against the bubble density of the samples (green dots) and the measured mean diameter (salmon dots). The difference in colour shade signals the pure CO_2 experiments (pale colours) and the experiments with neon (dark colours). The dashed lines indicate the trend for each parameter. The units are shown in the legend. **b.**The density of population of each sample is also plotted against the theoretical mean diameter of each sample, along with a logarithmic trend line as an example. The standard deviation of Ln(n) is also plotted for every sample in this graph.

4.4.4. CO_2 diffusion and bubble rise rate:

Like for the VSD parameters, the bubble velocity in the neon-rich experiments was calculated as a function of the vesicle radius and the water content of the experimental samples. The results are plotted **Figure 4.15.a**. Note that the water marked here refers to the water present in the glass of the sample analysed by FTIR.

Similarly, we calculated the diffusion of CO_2, the ascent distances of bubbles, and the average bubble growth as a function of experimental time (**Figure 4.15.b**). As expected, there are no noticeable changes compared to the neon-free experiments (*Chapter 3*).

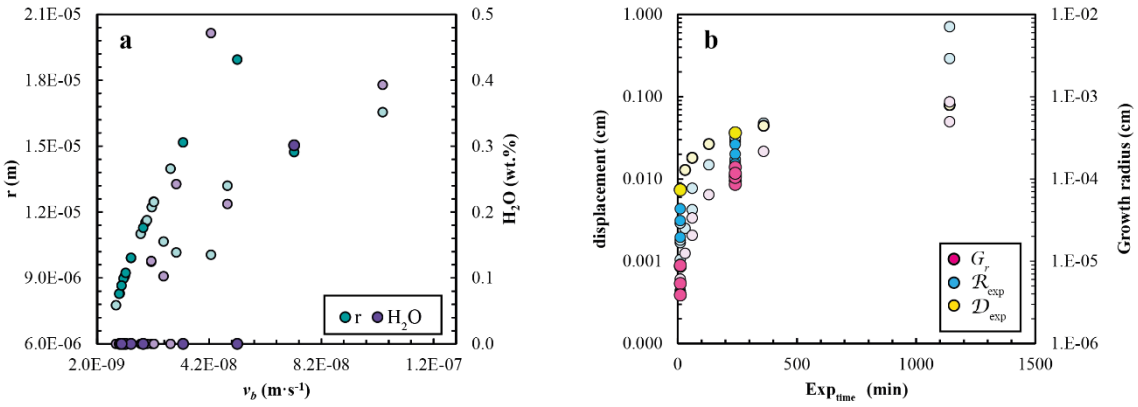

Figure 4.15.: The diagrams plot the new experiments integrated in the diagrams from *Chapter 3.* **a.** Bubble velocity as a function of the mean vesicle radius (left axis, green dots) and the percentage of H_2O dissolved in the glass (right axis, purple dots). **b.** Transport distance of CO_2 through diffusion (yellow dots) or in bubbles (blue dots) on the left axis, and the increase of bubble radius (pink dots) on the right axis over time. For better visualisation, logarithmic scales are used on both axes. For both diagrams the difference in colour shade signals the pure CO_2 experiments (pale colours) and the experiments with neon (dark colours).

4.4.5. Neon isotopic composition:

The samples were selected based on the experimental time, with at least one sample for each time series, and the distribution of bubbles and vesicularity. The vesicularity of the samples was 0.9% and 0.4% for *ESFa-5B-CO_2+Ne* and *ESFa-6B-CO_2+Ne*, respectively, while *ESFa-3B-CO_2+Ne* had a vesicularity of 1.7%. It is important to note that the vesicularity mentioned here refers to the measurement taken in the glass using VGStudioMax since the real vesicularity will be that obtained theoretically. The results of neon isotopic ratios and Ne abundance are shown in **Table 4.7.**

Eighteen vesicles were analysed for sample *ESFa-3B-CO_2+Ne*, but only seventeen will be considered for neon isotopic ratios. This is because three vesicles were pierced at the same time and a change in the pressure was revealed (*Bulle 9 ALA;* **Figure 2.23**.). Sixteen vesicles will be considered for Ne abundances since *Bulle 2* does not represent the entire gas content of the vesicles due to issues with manipulation during analysis. The neon isotopic ratios of sample *ESFa-3B-CO_2+Ne* range from $^{20}Ne/^{22}Ne$= 9.72±0.06 to 10.71±0.11, with some even approaching the maximum fractionation factor ($^{20}Ne/^{22}Ne$=10.28). Specifically, this is the case for *Bulle 2*, *Bulle 2ALA,* and *Bule 3ALA.*

ESFa-3B-CO2+Ne

Experimental conditions: t= 240 min, T = 1200° C, P = 1535±10 bar, ves = 1.7%

	Pb_{Tot}(bar)	D (µm)	V (cc)	^{22}Ne (ccSTP)		^{20}Ne/^{22}Ne	σ	^{21}Ne/^{22}Ne	σ	P_{Ne}(bar)	P_{CO2}(bar)
Bulle 1	4.00E-06	130.78	2.80E-07	4.69E-12	3.91E-13	9.97	0.06	0.0288	0.0006	1.49E-08	3.99E-06
Bulle 2**	7.90E-06	168.78	6.01E-07	6.11E-12	5.08E-13	10.28	0.05	0.0303	0.0006	1.93E-08	7.88E-06
Bulle 3	2.60E-06	109.53	1.64E-07	3.04E-12	2.53E-13	9.97	0.09	0.0303	0.0007	9.61E-09	2.59E-06
Bulle 4	2.20E-06	101.65	1.31E-07	3.73E-12	3.10E-13	9.80	0.06	0.0285	0.0007	1.18E-08	2.19E-06
Bulle 5	1.65E-05	218.81	1.31E-06	1.85E-11	1.54E-12	10.05	0.05	0.0296	0.0005	5.85E-08	1.64E-05
Bulle 6	1.40E-06	80.56	6.54E-08	2.18E-12	1.82E-13	9.75	0.08	0.0286	0.0007	6.91E-09	1.39E-06
Bulle 7	1.10E-06	68.76	4.06E-08	1.58E-12	1.32E-13	9.85	0.12	0.0282	0.0007	5.01E-09	1.09E-06
Bulle 1 ALA	1.90E-06	94.82	1.07E-07	1.84E-12	1.53E-13	9.82	0.08	0.0307	0.0007	5.83E-09	1.89E-06
Bulle 2 ALA	1.50E-06	83.82	7.36E-08	2.31E-12	1.92E-13	10.50	0.13	0.0303	0.0005	7.33E-09	1.49E-06
Bulle 3 ALA	3.50E-05	283.03	2.83E-06	3.69E-12	3.07E-13	10.26	0.10	0.0298	0.0004	1.17E-08	3.50E-05
Bulle 4 ALA	9.00E-07	57.82	2.42E-08	1.54E-12	1.28E-13	9.84	0.08	0.0294	0.0007	4.87E-09	8.95E-07
Bulle 5 ALA	1.10E-06	68.76	4.06E-08	1.47E-12	1.23E-13	9.88	0.10	0.0304	0.0009	4.66E-09	1.10E-06
Bulle 6 ALA	9.00E-07	57.82	2.42E-08	1.47E-12	1.23E-13	10.08	0.11	0.0282	0.0010	4.66E-09	8.95E-07
Bulle 7 ALA	1.30E-06	77.02	5.71E-08	7.09E-13	5.90E-14	10.06	0.09	0.0291	0.0007	2.24E-09	1.30E-06
Bulle 8 ALA	1.30E-06	77.02	5.71E-08	1.83E-12	1.52E-13	10.03	0.10	0.0292	0.0008	5.79E-09	1.29E-06
Bulle 9 ALA**	3.60E-06	125.43	2.47E-07	4.41E-12	3.67E-13	9.73	0.08	0.0292	0.0005	1.40E-08	3.59E-06
Bulle 10 ALA	3.50E-06	124.01	2.38E-07	5.81E-12	4.83E-13	9.76	0.07	0.0288	0.0004	1.84E-08	3.48E-06
Bulle 11 ALA	2.10E-06	99.47	1.23E-07	2.39E-12	1.99E-13	9.77	0.09	0.0287	0.0007	7.57E-09	2.09E-06

ESFa-5B-CO2+Ne

Experimental conditions: t= 10 min, T = 1200° C, P = 1573±10 bar, ves = 0.9%

	Pb_{Tot}(bar)	D (µm)	V (cm^3)	^{22}Ne (ccSTP)		^{20}Ne/^{22}Ne	σ	^{21}Ne/^{22}Ne	σ	P_{Ne}(bar)	P_{CO2}(bar)
Bulle 1	1.73E-05	222.43	1.38E-06	2.42E-11	1.75E-13	9.97	0.02	0.0289	0.0002	7.65E-08	1.72E-05
Bulle 2	1.90E-06	94.82	1.07E-07	2.63E-12	1.90E-14	10.03	0.04	0.0289	0.0004	8.33E-09	1.89E-06
Bulle 3	2.80E-06	113.07	1.81E-07	3.64E-12	2.63E-14	9.96	0.04	0.0290	0.0005	1.15E-08	2.79E-06
Bulle 4	1.80E-06	92.31	9.83E-08	2.27E-12	1.64E-14	10.24	0.05	0.0302	0.0005	7.18E-09	1.79E-06
Bulle 5	1.90E-06	94.82	1.07E-07	1.97E-12	1.42E-14	10.02	0.05	0.0284	0.0005	6.24E-09	1.89E-06
Bulle 6	2.80E-06	113.07	1.81E-07	3.30E-12	2.38E-14	9.80	0.03	0.0284	0.0004	1.04E-08	2.79E-06
Bulle 7	1.78E-05	224.62	1.42E-06	2.53E-11	1.83E-13	9.81	0.02	0.0293	0.0001	8.03E-08	1.77E-05
Bulle 10	2.00E-06	97.20	1.15E-07	2.75E-12	1.98E-14	9.62	0.04	0.0283	0.0003	8.70E-09	1.99E-06
Bulle 11	3.10E-06	118.01	2.05E-07	4.47E-12	3.23E-14	9.44	0.04	0.0296	0.0002	1.41E-08	3.09E-06
Bulle 12	2.30E-06	103.73	1.40E-07	3.42E-12	2.47E-14	9.73	0.05	0.0300	0.0005	1.08E-08	2.29E-06

ESFa-6B-CO2+Ne

Experimental conditions: t= 10 min, T = 1200° C, P = 1573±10 bar, ves =0.4 %

	Pb_{Tot}(bar)	D (µm)	V (cm^3)	^{22}Ne (ccSTP)		^{20}Ne/^{22}Ne	σ	^{21}Ne/^{22}Ne	σ	P_{Ne}(bar)	P_{CO2}(bar)
Bulle 1	9.00E-07	57.82	2.42E-08	1.11E-12	7.60E-15	9.40	0.08	0.0264	0.0009	3.51E-09	8.96E-07
Bulle 2	4.90E-06	141.45	3.54E-07	4.87E-12	3.34E-14	9.56	0.03	0.0297	0.0005	1.54E-08	4.88E-06
Bulle 3	9.00E-07	57.82	2.42E-08	1.07E-12	7.33E-15	9.58	0.07	0.0289	0.0008	3.39E-09	8.97E-07
Air						9.8		0.0290			
MFF_{Ne}						10.28		0.0297			

Table 4.7: P_{bTot} is the total pressure of the vesicle, V_b is the volume of the vesicle, P_{Ne} is the partial pressure of neon in the vesicle, and P_{CO2} is the CO_2 partial pressure. Neon isotopic composition and abundances were analysed by a HELIX-SFT mass spectrometer at ISTO-France, using laser extraction of single vesicles. All experimental glasses were corrected for blank. *[a] Part of the volume corresponding to this bubble was released before the analysis and *[b] the gas extracted belongs to three vesicles pierced at the same time, therefore, these results were not considered for the discussion and conclusion of this work. The units are shown in the table for each parameter.

In the *ESFa-5B CO2+Ne* sample, ten vesicles were analysed, with $^{20}Ne/^{22}Ne$ ranging from 9.45 ± 0.05 to 10.24 ± 0.06. Similarly to sample *ESFa-3B CO_2+Ne*, one of the analysed vesicles was found to be close to the maximum fractionation factor. This sample shows vesicle isotopic ratios lower than the sample of 240 minutes.

Only three vesicles were analysed in sample *ESFa-6B CO_2+Ne* due to the difficulty of finding them for the low vesicularity, 0.4%. Unlike the other samples, this one exhibit significantly lower isotope ratios $^{20}Ne/^{22}Ne < 9.58\pm0.07$.

The partial pressures of Ne and CO_2 are plotted against the volume of the respective analysed vesicles **(Figure 4.16.)**. Plotting the partial pressure of Ne against the volume of the vesicle reveals that it follows the correlation line obtained in *Chapter 3* for vesicles of pure CO_2. The only exception to this tendency is found in the sample *Bulle 3ALA* of sample *ESFa-3B-CO_2+Ne*, where the concentration of ^{22}Ne is smaller than in the other analysed vesicles.

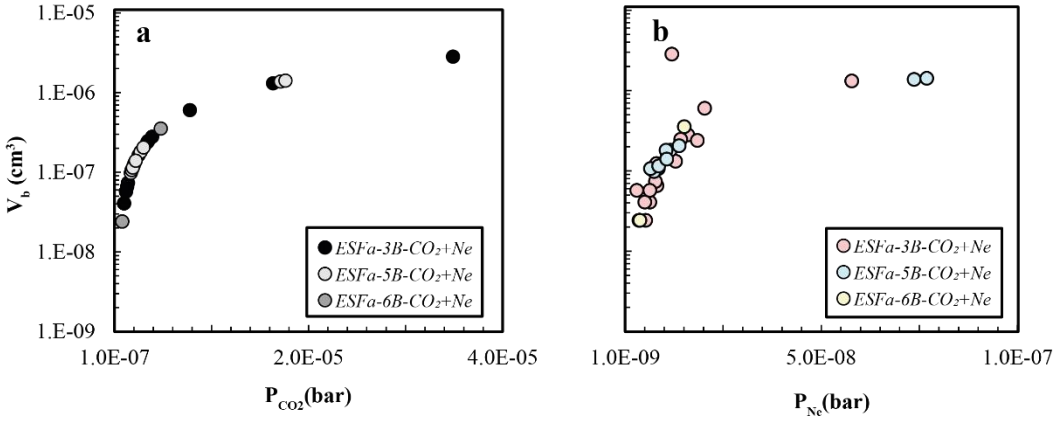

Figure 4.16.: Partial pressure of CO_2 (**a**) and Ne (**b**) vs volume of every analysed bubble. The partial pressure of Ne follows the same trend to the one of CO_2 with exception of one vesicle which is significantly deviated due to the lower concentration of ^{22}Ne. Notice that the volume of the vesicles is presented on a logarithmic scale.

4.5. Discussion:

4.5.1. Comparison of CO_2-bearing glass and CO_2+Ne-bearing glass experimental results:

To ensure consistency between the Ne+CO_2- and CO_2-static experiments, all samples underwent the same analyses and calculations. **Figure 4.17.** The relevance lies in the fact that the time series chosen to study the kinetic fractionation of neon during the vesiculation were quenched minutes before than the bubble buoyancy were more significant than CO_2 diffusion.

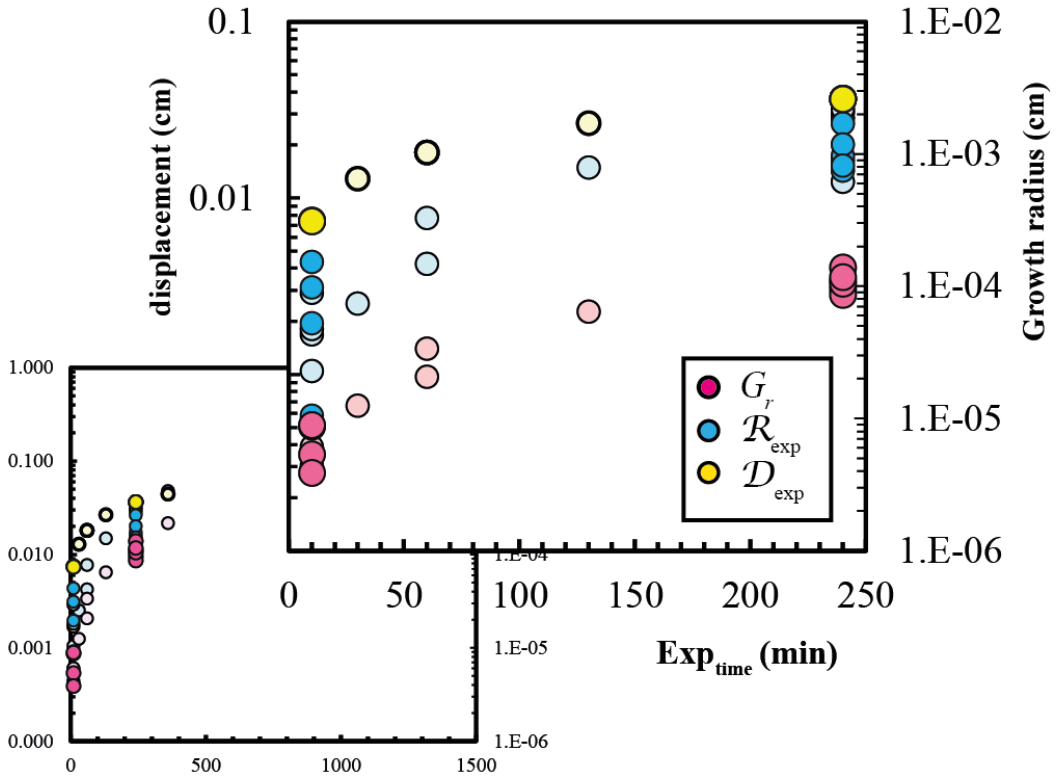

Figure 4.17. The diagram illustrates the displacement of CO_2 through diffusion (yellow dots) or in bubbles (blue dots) on the left axis, and the growth of the bubble radius (pink dots) on the right axis over time. For better visualization, logarithmic scales are used on the axes. The darker colours refer to the experiments with Ne+CO_2.

Neon is known to diffuse faster and to be more soluble than CO_2 (Jambon et al., 1986; Lux, 1987; Zhang and Xu, 1995; Behrens and Zhang, 2001; Nowak et al., 2004; Zhang et al., 2007). However, it quickly partitions into bubbles when present (Jambon et al., 1986; Paonita, 2005). The simple theoretical model presented previously assumes that lighter isotopes diffuse faster than heavier isotopes, resulting in higher isotopic ratios than

the starting material when the time to reach the equilibrium is not long enough. It is therefore expected that fractionation will occur until equilibrium is reached, and that it will be more pronounced in experiments of shorter duration.

It is important to note that the model of diffusion and rise of CO_2 bubbles (**Figure 4.17.**) refers to an average bubble radius. However, as shown in **Figure 4.9.** and **4.12.**, some bubbles may be large enough to effectively partition neon isotopes before moving towards the melt-capsule interface.

On this basis, it can be expected that as the magma becomes progressively more degassed in neon (following the degassing path of CO_2), neon will become increasingly concentrated in the vesicles and the gas accumulated at the capsule-melt interface. Bubbles with varying isotopic ratios will be present due to differences in the diffusion of neon isotopes, resulting in some bubbles having isotopic ratios similar to the starting material (those that have had more time to grow and have not yet been lost between the melt interface and the capsule.), while others have higher ratios (those that are nucleating or at an early growth stage before full diffusion occurs).

As the capsules form a completely closed system with a limited volume, the gas accumulating at the top during the experiment will continuously interact with the melt (**Figure 4.18.c** and **d**). This gas is expected to become enriched in lighter isotopes, while the melt becomes enriched in heavier isotopes. Additionally, bubbles formed from progressively neon-depleted magma would exhibit lower isotopic signals.

4.5.2. what do the analysed bubbles tell us?

Using the equation of the line obtained in chapter three to determine the volume of bubbles from the pressure and following the laws of solubility with a solubility constant K_{Ne}= 3.16 $\cdot 10^{-4}$, the partial pressure of each gas in each vesicle was estimated. It was observed that the partial pressure follows a similar trend to that of CO_2, albeit somewhat more irregular (**Figure 4.18.**). *Bulle 3ALA* in sample *ESFa-3B-CO_2+Ne* is the most apparent case.

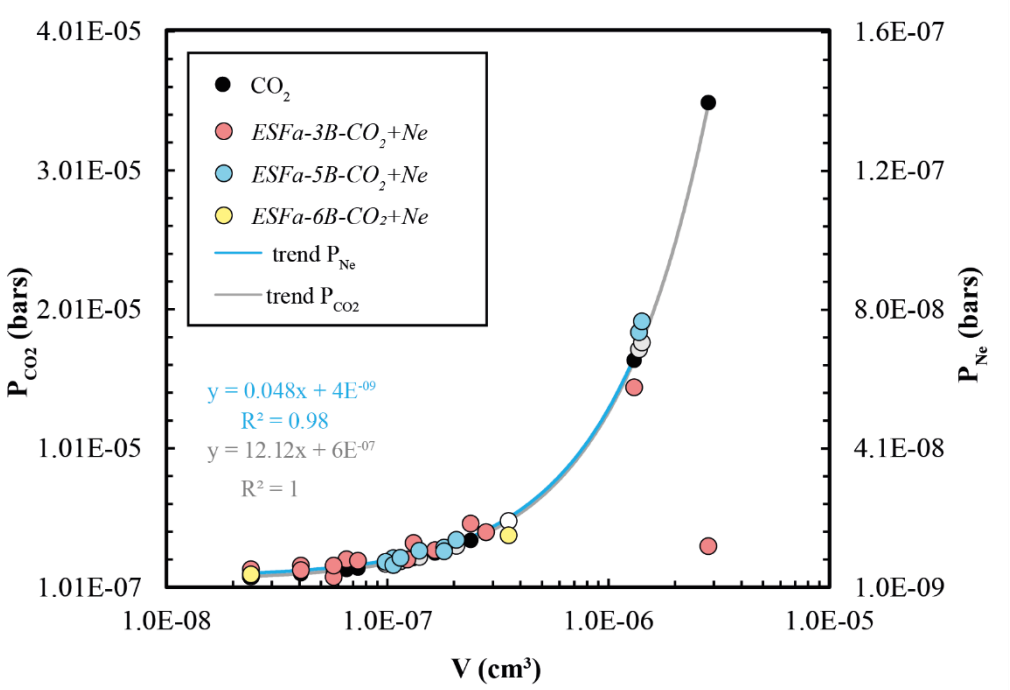

Figure 4.18.: The partial pressures of Ne and CO_2 in each vesicle are plotted against the volume of the vesicle. The scales were adjusted to better visualize the two gases present in the vesicles. The correlation coefficients of the equations of the lines are shown in their respective colours (see legend).

When plotting a diagram with the three neon isotopes, a notable spread in the isotopic signals of the analyzed bubbles is observed along the fractionation line. Some of them are even close to the maximum theoretical fractionation factor, MFF_{Ne}. Although the analytical error may be significant, the dispersion of the bubbles along this line is also considerable. The bubbles started from a homogeneous isotopic distribution in the magma. This fractionation is observed in the three analysed samples, where sample *ESFa-3B-CO_2+Ne* (240min of experiment) shows the highest ratios for $^{20}Ne/^{22}Ne$ and samples *ESFa-5B-CO_2+Ne* and *ESFa-6B-CO_2+Ne* the lowest. In the case of $^{21}Ne/^{22}Ne$ ratio, also *ESFa-6B-CO_2+Ne* is noteworthy for having a bubble with an exceptionally low ratio ($^{21}Ne/^{22}Ne$=0.0263), like *Bulle 1ALA* of sample *ESFa-3B-CO_2+Ne* ($^{21}Ne/^{22}Ne$=0.0271).

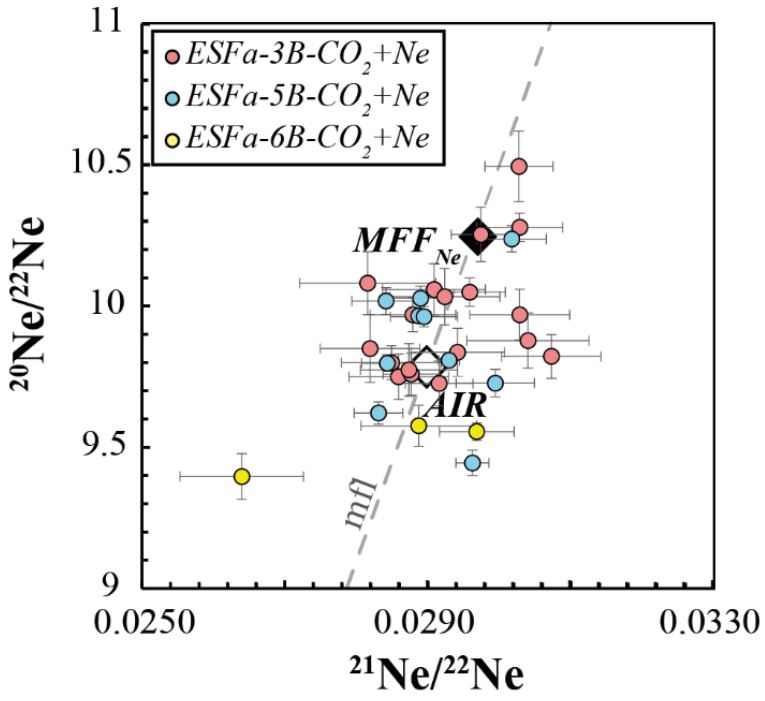

Figure 4.19.: Data of singles vesicles plotted as $^{20}Ne/^{22}Ne$ vs $^{21}Ne/^{22}Ne$ diagram. The black diamond represents the maximum theoretical fractionation factor, $\boldsymbol{MFF_{Ne}}$, expected for the reference value ($^{20}Ne/^{22}Ne$ = 10.28 and $^{21}Ne/^{22}Ne$ = 0.030); the white diamond represents the reference value taken from the standard $^{20}Ne/^{22}Ne$ = 9.8 and $^{21}Ne/^{22}Ne$ = 0.029 (air ratios). The dashed line represents the mass fractionation line, *mfl*. Data of sample *ESFa-3B CO_2+Ne* (red dots) have a wider spread over the mfl, Sample *ESFa-6B CO_2+Ne* (yellow dots) shows the lowest values related to the $^{20}Ne/^{22}Ne$ ratio. All the vesicle analysis with the exception of Bulle 2 and Bulle 9 ALA belonging to *ESFa-3B-CO2+Ne* are plotted with their respective 1σ

4.5.3. What might happen inside the capsules during the experiment?

In **Figure 4.20.a**, at t=0, the melt represents the three mixed components under the experimental conditions. Once CO_2 bubble nucleation begins, the neon dissolved in the magma rapidly escapes into the gas phase (**Figure 4.20.b**), leading to a progressively neon-depleted melt as the experiment advances. Meanwhile, a neon-rich gas phase accumulates at the top of the capsule. Bubbles forming at the bottom of the capsule will exhibit lower isotopic ratios, as lighter isotopes concentrate at the capsule-melt interface.

The experiment continues and the gas trapped at the interface between the melt and the capsule interacts with the melt (**Figure 4.20.c**). The lighter isotopes fill the new bubbles first due to their faster diffusion. Eventually, some of the bubbles reach equilibrium, but the new bubbles are still fractionated because enough time has not passed

for complete equilibrium to be achieved (**Figure 4.20.d**). When equilibrium is complete, the magma will have dissolved the maximum Ne and CO_2 due to overpressure into the bubbles and/or the vesicles will rise to the top of the capsule by Stoke`s law, and there will be no vesicles in the melt.

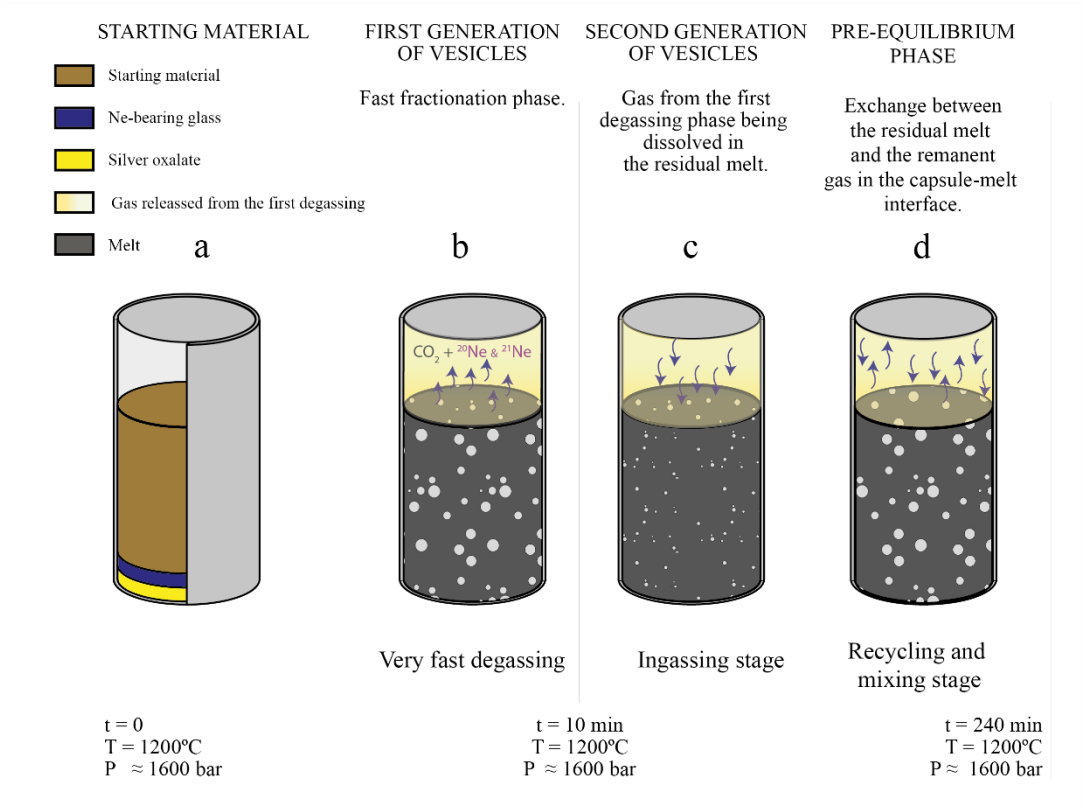

Figure 4.20 Representative scheme of the isotopic fractionation of the quenched glass during the experiment under non-equilibrium closed system conditions: this scheme explains the evolution of our quenched glasses during the experiment. The first capsule represents the start of the experiment, with the powdered starting material, the volatile component in the solid phase (silver oxalate) and the Ne-containing glass (whose mass percentage is so small that a more accurate balance was required).

4.6. Conclusions:

The preliminary results of this study suggest that the time when the vesicles are nucleated and quenched in the history of a magmatic eruption plays a key role when interpreting results for noble gases.

The previous chapter was referring to vesicle evolution and CO_2 diffusion in experiments where equilibrium had not yet been reached. It was found that diffusion was the main physical process in the shorter experiments. However, once the general size of

the vesicles was sufficient to overcome diffusion, buoyancy dominated, causing the velocity of the vesicles to exceed Ne diffusion. In our experiments, this occurred at around 240 minutes.

This chapter focuses on short experiments lasting between 10 and 240 minutes. Advancing further in the topic that interests us, the experiments went further and, in addition to the silver oxalate provided as CO_2 source, a fraction of homogeneous glass enriched in neon was introduced and the previous experiments were reproduced. Upon comparing the results, it is observed that the diffusion and buoyancy in the experimental samples remained consistent with the experimental series performed using pure CO_2. The experiments were successfully reproduced as also the vesicularity parameters were maintained.

The bubbles analysed have a small average diameter of only a few tens of microns. Therefore, the amount of gas inside the bubbles is not significant enough to cause a small analytical error. The bubble-to-bubble laser analytical method offers a more reliable result for fractionation studies. In a system with continuous nucleation of bubbles, the youngest generation of bubbles will tend to be more fractionated if the diffusion of all isotopes of the same element has not concluded. The same will happen with elements of different masses, such as two different noble gases.

4.7. References:

Aiuppa, A., Federico, C., Giudice, G., Giuffrida, G., Guida, R., Gurrieri, S., Liuzzo, M., Moretti, R., Papale, P., 2009. The 2007 eruption of Stromboli volcano: insights from real-time measurement of the volcanic gas plume CO2/SO2 ratio. J. Volcanol. Geotherm. Res. 182, 221–230.

Allegre, C.J., Manhes, G., Göpel, C., 1995. The age of the Earth. Geochim. Cosmochim. Acta 59, 1445–1456.

Allègre, C.J., Staudacher, T., Sarda, P., Kurz, M., 1983. Constraints on evolution of Earth's mantle from rare gas systematics. Nature 303, 762–766. https://doi.org/10.1038/303762a0

Aubaud, C., 2022. Carbon stable isotope constraints on CO2 degassing models of ridge, hotspot and arc magmas. Chem. Geol. 605, 120962.

Aubaud, C., Pineau, F., Jambon, A., Javoy, M., 2004. Kinetic disequilibrium of C, He, Ar and carbon isotopes during degassing of mid-ocean ridge basalts. Earth Planet. Sci. Lett. 222, 391–406.

Aubry, G.J., Sator, N., Guillot, B., 2013. Vesicularity, bubble formation and noble gas fractionation during MORB degassing. Chem. Geol. 343, 85–98.

Azuma, S., Ozima, M., Hiyagon, H., 1993. Anomalous neon and xenon in an Archaean anorthosite from West Greenland. Earth Planet. Sci. Lett. 114, 341–352.

Ballentine, C.J., Barfod, D.N., 2000. The origin of air-like noble gases in MORB and OIB. Earth Planet. Sci. Lett. 180, 39–48.

Ballentine, C.J., Burgess, R., Marty, B., 2002. Tracing fluid origin, transport and interaction in the crust.

Ballentine, C.J., Burnard, P.G., 2002. Production, Release and Transport of Noble Gases in the Continental Crust. Rev. Mineral. Geochem. 47, 481–538. https://doi.org/10.2138/rmg.2002.47.12

Ballentine, C.J., Marty, B., Sherwood Lollar, B., Cassidy, M., 2005. Neon isotopes constrain convection and volatile origin in the Earth's mantle. Nature 433, 33–38.

Bauer, C.A., 1947. Production of helium in meteorites by cosmic radiation. Phys. Rev. 72, 354.

Becker, R.H., Pepin, R.O., 1994. Solar wind noble gases and nitrogen in metal from lunar soil 68501. Meteoritics 29, 724–738.

Behrens, H., 2010. Noble gas diffusion in silicate glasses and melts. Rev. Mineral. Geochem. 72, 227–267.

Behrens, H., Misiti, V., Freda, C., Vetere, F., Botcharnikov, R.E., Scarlato, P., 2009. Solubility of H2O and CO2 in ultrapotassic melts at 1200 and 1250 C and pressure from 50 to 500 MPa. Am. Mineral. 94, 105–120.

Behrens, H., Zhang, Y., 2001. Ar diffusion in hydrous silicic melts: implications for volatile diffusion mechanisms and fractionation. Earth Planet. Sci. Lett. 192, 363–376.

Black, D., Pepin, R., 1969. Trapped neon in meteorites—II. Earth Planet. Sci. Lett. 6, 395–405.

Black, D.C., 1972. On the origins of trapped helium, neon and argon isotopic variations in meteorites—I. Gas-rich meteorites, lunar soil and breccia. Geochim. Cosmochim. Acta 36, 347–375.

Blank, J.G., Brooker, R.A., 1994. Experimental studies of carbon dioxide in silicate melts; solubility, speciation, and stable carbon isotope behavior. Rev. Mineral. Geochem. 30, 157–186.

Bodmer, R., Bochsler, P., 2000. Influence of Coulomb collisions on isotopic and elemental fractionation in the solar wind acceleration process. J. Geophys. Res. Space Phys. 105, 47–60.

Bottinga, Y., Richet, P., 1981. High pressure and temperature equation of state and calculation of the thermodynamic properties of gaseous carbon dioxide. Am. J. Sci. 281, 615–660.

Bühler, F., Eberhardt, P., Geiss, J., Meister, J., Signer, P., 1969. Apollo 11 solar wind composition experiment: First results. Science 166, 1502–1503.

Burbidge, E.M., Burbidge, G.R., Fowler, W.A., Hoyle, F., 1957. Synthesis of the elements in stars. Rev. Mod. Phys. 29, 547.

Burnard, P., 2001. Correction for volatile fractionation in ascending magmas: noble gas abundances in primary mantle melts. Geochim. Cosmochim. Acta 65, 2605–2614.

Burnard, P., 1999. The bubble-by-bubble volatile evolution of two mid-ocean ridge basalts. Earth Planet. Sci. Lett. 174, 199–211.

Burnard, P., Graham, D., Turner, G., 1997. Vesicle-specific noble gas analyses of" popping rock": implications for primordial noble gases in Earth. Science 276, 568–571.

Busemann, H., Baur, H., Wieler, R., 2000. Primordial noble gases in "phase Q" in carbonaceous and ordinary chondrites studied by closed-system stepped etching. Meteorit. Planet. Sci. 35, 949–973.

Butler, W., Jeffery, P., Reynolds, J., Wasserburg, G., 1963. Isotopic variations in terrestrial xenon. J. Geophys. Res. 68, 3283–3291.

Canup, R.M., Asphaug, E., 2001. Origin of the Moon in a giant impact near the end of the Earth's formation. Nature 412, 708–712.

Carroll, M.R., Webster, J.D., 1994. Solubilities of sulfur, noble gases, nitrogen, chlorine, and fluorine in magmas. Rev. Mineral. 30, 231–231.

Chambers, J., 2010. Planetesimal formation by turbulent concentration. Icarus 208, 505–517.

Chavrit, D., 2010. Cartographie globale des flux de CO2 à l'axe des dorsales océaniques: une approche pétrologique.

Chavrit, D., Humler, E., Morizet, Y., Laporte, D., 2012. Influence of magma ascent rate on carbon dioxide degassing at oceanic ridges: Message in a bubble. Earth Planet. Sci. Lett. 357, 376–385.

Clayton, D.D., 1983. Principles of stellar evolution and nucleosynthesis. University of Chicago press.

Colin, A., Moreira, M., Gautheron, C., Burnard, P., 2015. Constraints on the noble gas composition of the deep mantle by bubble-by-bubble analysis of a volcanic glass sample from Iceland. Chem. Geol. 417, 173–183.

Craig, H., Lupton, J., 1976. Primordial neon, helium, and hydrogen in oceanic basalts. Earth Planet. Sci. Lett. 31, 369–385.

Cuzzi, J.N., Hogan, R.C., Shariff, K., 2008. Toward planetesimals: Dense chondrule clumps in the protoplanetary nebula. Astrophys. J. 687, 1432.

Dauphas, N., Burkhardt, C., Warren, P.H., Fang-Zhen, T., 2014. Geochemical arguments for an Earth-like Moon-forming impactor. Philos. Trans. R. Soc. Math. Phys. Eng. Sci. 372, 20130244.

Dauphas, N., Chaussidon, M., 2011. A perspective from extinct radionuclides on a young stellar object: the Sun and its accretion disk. Annu. Rev. Earth Planet. Sci. 39, 351–386.

Dauphas, N., Morbidelli, A., 2013. Geochemical and planetary dynamical views on the origin of Earth's atmosphere and oceans. ArXiv Prepr. ArXiv13121202.

Dauphas, N., Pourmand, A., 2011. Hf–W–Th evidence for rapid growth of Mars and its status as a planetary embryo. Nature 473, 489–492.

D'E Atkinson, R., Houtermans, F., 1929. Transmutation of the Lighter Elements in Stars. Nature 123, 567–568.

Di Carlo, I., Pichavant, M., Rotolo, S.G., Scaillet, B., 2006. Experimental crystallization of a high-K arc basalt: the golden pumice, Stromboli volcano (Italy). J. Petrol. 47, 1317–1343.

Dickin, A.P., 2018. Radiogenic isotope geology. Cambridge university press.

Dixon, J.E., Pan, V., 1995a. Determination of the molar absorptivity of dissolved carbonate in basanitic glass. Am. Mineral. 80, 1339–1342.

Dixon, J.E., Pan, V., 1995b. Determination of the molar absorptivity of dissolved carbonate in basanitic glass. Am. Mineral. 80, 1339–1342.

Dixon, J.E., Stolper, E.M., Holloway, J.R., 1995. An experimental study of water and carbon dioxide solubilities in mid-ocean ridge basaltic liquids. Part I: calibration and solubility models. J. Petrol. 36, 1607–1631.

Donahue, T., Russell, C., 1997. The Venus atmosphere and ionosphere and their interaction with the solar wind: An overview. Venus II Geol. Geophys. Atmosphere Sol. Wind Environ. 3.

Douglass, J., Schilling, J., Fontignie, D., 1999. Plume-ridge interactions of the Discovery and Shona mantle plumes with the southern Mid-Atlantic Ridge (40°-55° S). J. Geophys. Res. Solid Earth 104, 2941–2962.

Eberhardt, P., Geiss, J., Graf, H., Grögler, N., Krähenbühl, U., Schwaller, H., Schwarzmüller, J., Stettler, A., 1970. Trapped solar wind noble gases, exposure age and K/Ar-age in Apollo 11 lunar fine material. Presented at the Geochimica et Cosmochimica Acta Supplement, Volume 1. Proceedings of the Apollo 11 Lunar Science Conference held 5-8 January, 1970 in Houston, TX. Volume 2: Chemical and Isotope Analyses. Edited by AA Levinson. New York: Pergammon Press, 1970., p. 1037, p. 1037.

Eberhardt, P., Geiss, J., Graf, H., Grögler, N., Mendia, M., Mörgeli, M., Schwaller, H., Stettler, A., Krähenbühl, U., Von Gunten, H., 1972. Trapped solar wind noble gases in Apollo 12 lunar fines 12001 and Apollo 11 breccia 10046. Bern Univ.(Switzerland).

Farrell, W.M., Hurley, D.M., Zimmerman, M.I., 2015. Solar wind implantation into lunar regolith: Hydrogen retention in a surface with defects. Icarus 255, 116–126.

Fine, G., Stolper, E., 1985. The speciation of carbon dioxide in sodium aluminosilicate glasses. Contrib. Mineral. Petrol. 91, 105–121.

Frost, B.R., 2018. Introduction to oxygen fugacity and its petrologic importance, in: Oxide Minerals. De Gruyter, pp. 1–10.

Geiss, J., Bühler, F., Cerutti, H., Eberhardt, P., Filleux, C., Meister, J., Signer, P., 2004. The Apollo SWC experiment: results, conclusions, consequences. Space Sci. Rev. 110, 307–335.

Geiss, J, Eberhardt, P., Bühler, F., Meister, J., Signer, P., 1970. Apollo 11 and 12 solar wind composition experiments: Fluxes of He and Ne isotopes. J. Geophys. Res. 75, 5972–5979.

Geiss, Johannes, Hirt, P., Leutwyler, H., 1970. On acceleration and motion of ions in corona and solar wind. Sol. Phys. 12, 458–483.

Giordano, D., Russell, J.K., Dingwell, D.B., 2008. Viscosity of magmatic liquids: a model. Earth Planet. Sci. Lett. 271, 123–134.

Gonnermann, H.M., Manga, M., 2007. The fluid mechanics inside a volcano. Annu Rev Fluid Mech 39, 321–356.

Graham, D.W., 2002. Noble Gas Isotope Geochemistry of Mid-Ocean Ridge and Ocean Island Basalts: Characterization of Mantle Source Reservoirs. Rev. Mineral. Geochem. 47, 247–317. https://doi.org/10.2138/rmg.2002.47.8

Grimberg, A., Baur, H., Bochsler, P., Bühler, F., Burnett, D.S., Hays, C.C., Heber, V.S., Jurewicz, A.J., Wieler, R., 2006. Solar wind neon from Genesis: Implications for the lunar noble gas record. Science 314, 1133–1135.

Harper Jr, C.L., Jacobsen, S.B., 1996. Noble gases and Earth's accretion. Science 273, 1814–1818.

Hashizume, K., Chaussidon, M., Marty, B., Robert, F., 2000. Solar wind record on the Moon: deciphering presolar from planetary nitrogen. Science 290, 1142–1145.

Heber, V.S., Baur, H., Bochsler, P., McKeegan, K.D., Neugebauer, M., Reisenfeld, D.B., Wieler, R., Wiens, R.C., 2012. Isotopic mass fractionation of solar wind: Evidence from fast and slow solar wind collected by the Genesis mission. Astrophys. J. 759, 121.

Heber, V.S., Wieler, R., Baur, H., Olinger, C., Friedmann, T.A., Burnett, D.S., 2009. Noble gas composition of the solar wind as collected by the Genesis mission. Geochim. Cosmochim. Acta 73, 7414–7432.

Holland, G., Ballentine, C.J., 2006a. Seawater subduction controls the heavy noble gas composition of the mantle. Nature 441, 186–191.

Holland, G., Ballentine, C.J., 2006b. Seawater subduction controls the heavy noble gas composition of the mantle. Nature 441, 186–191.

Holland, G., Cassidy, M., Ballentine, C.J., 2009. Meteorite Kr in Earth's mantle suggests a late accretionary source for the atmosphere. Science 326, 1522–1525.

Hollenbach, D.J., Yorke, H.W., Johnstone, D., 2000. Disk dispersal around young stars. Protostars Planets IV 401, 12.

Honda, M., McDougall, I., Patterson, D.B., Doulgeris, A., Clague, D.A., 1991. Possible solar noble-gas component in Hawaiian basalts. Nature 349, 149–151.

Honda, M., Reynolds, J., Roedder, E., Epstein, S., 1987. Noble gases in diamonds: Occurrences of solarlike helium and neon. J. Geophys. Res. Solid Earth 92, 12507–12521.

Iacono-Marziano, G., Paonita, A., Rizzo, A., Scaillet, B., Gaillard, F., 2010. Noble gas solubilities in silicate melts: new experimental results and a comprehensive model of the effects of liquid composition, temperature and pressure. Chem. Geol. 279, 145–157.

Jambon, A., Weber, H., Braun, O., 1986. Solubility of He, Ne, Ar, Kr and Xe in a basalt melt in the range 1250–1600 C. Geochemical implications. Geochim. Cosmochim. Acta 50, 401–408.

Jaupart, E., Charnoz, S., Moreira, M., 2017. Primordial atmosphere incorporation in planetary embryos and the origin of Neon in terrestrial planets. Icarus 293, 199–205.

Javoy, M., Pineau, F., 1991. The volatiles record of a "popping" rock from the Mid-Atlantic Ridge at 14 N: chemical and isotopic composition of gas trapped in the vesicles. Earth Planet. Sci. Lett. 107, 598–611.

Jiménez-Mejías, M., Andújar, J., Scaillet, B., Casillas, R., 2021. Experimental determination of H $ _ {{2}} $ O and CO $ _ {{2}} $ solubilities of mafic alkaline magmas from Canary Islands. Comptes Rendus Géoscience 353, 289–314.

Johansen, A., Klahr, H., 2011. Planetesimal formation through streaming and gravitational instabilities. Earth Moon Planets 108, 39–43.

Johansen, A., Klahr, H., Henning, T., 2011. High-resolution simulations of planetesimal formation in turbulent protoplanetary discs. Astron. Astrophys. 529, A62.

Johansen, A., Oishi, J.S., Low, M.-M.M., Klahr, H., Henning, T., Youdin, A., 2007. Rapid planetesimal formation in turbulent circumstellar disks. Nature 448, 1022–1025.

Kendrick, M.A., Burnard, P., 2013. Noble gases and halogens in fluid inclusions: a journey through the Earth's crust. Noble Gases Geochem. Tracers 319–369.

Kennedy, B., Hiyagon, H., Reynolds, J., 1990. Crustal neon: a striking uniformity. Earth Planet. Sci. Lett. 98, 277–286.

Kennedy, B.M., Hiyagon, H., Reynolds, J.H., 1990. Crustal neon: a striking uniformity. Earth Planet. Sci. Lett. 98, 277–286. https://doi.org/10.1016/0012-821X(90)90030-2

Kipfer, R., Aeschbach-Hertig, W., Peeters, F., Stute, M., 2002. Noble gases in lakes and ground waters. Rev. Mineral. Geochem. 47, 615–700.

Kress, V.C., Carmichael, I.S., 1991. The compressibility of silicate liquids containing Fe 2 O 3 and the effect of composition, temperature, oxygen fugacity and pressure on their redox states. Contrib. Mineral. Petrol. 108, 82–92.

Krummenacher, D., 1970. Isotopic composition of argon in modern surface volcanic rocks. Earth Planet. Sci. Lett. 8, 109–117.

Kunz, J., 1999. Is there solar argon in the Earth's mantle? Nature 399, 649–650. https://doi.org/10.1038/21352

Kuroda, P., 1960. Nuclear fission in the early history of the earth. Nature 187.

Kurz, M.D., 1986. Cosmogenic helium in a terrestrial igneous rock. Nature 320, 435–439. https://doi.org/10.1038/320435a0

Kurz, M.D., Curtice, J., Fornari, D., Geist, D., Moreira, M., 2009. Primitive neon from the center of the Galápagos hotspot. Earth Planet. Sci. Lett. 286, 23–34.

Lange, R.A., 1994a. Volatiles in Magmas, in: Carroll, M.R., Holloway, J.R. (Eds.), . De Gruyter, pp. 331–370. https://doi.org/10.1515/9781501509674-015

Lange, R.A., 1994b. Volatiles in Magmas, in: Carroll, M.R., Holloway, J.R. (Eds.), . De Gruyter, pp. 331–370. https://doi.org/10.1515/9781501509674-015

Le Gall, N., 2015. Ascension et dégazage des magmas basaltiques: approche expérimentale.

Le Gall, N., Pichavant, M., 2016a. Experimental simulation of bubble nucleation and magma ascent in basaltic systems: Implications for Stromboli volcano. Am. Mineral. 101, 1967–1985.

Le Gall, N., Pichavant, M., 2016b. Homogeneous bubble nucleation in H2O-and H2O-CO2-bearing basaltic melts: results of high temperature decompression experiments. J. Volcanol. Geotherm. Res. 327, 604–621.

Le Roux, P., Le Roex, A., Schilling, J.-G., Shimizu, N., Perkins, W., Pearce, N., 2002. Mantle heterogeneity beneath the southern Mid-Atlantic Ridge: trace element evidence for contamination of ambient asthenospheric mantle. Earth Planet. Sci. Lett. 203, 479–498.

Lensky, N.G., Niebo, R.W., Holloway, J.R., Lyakhovsky, V., Navon, O., 2006. Bubble nucleation as a trigger for xenolith entrapment in mantle melts. Earth Planet. Sci. Lett. 245, 278–288.

Lux, G., 1987. The behavior of noble gases in silicate liquids: Solution, diffusion, bubbles and surface effects, with applications to natural samples. Geochim. Cosmochim. Acta 51, 1549–1560.

Mangan, M., Sisson, T., 2000. Delayed, disequilibrium degassing in rhyolite magma: decompression experiments and implications for explosive volcanism. Earth Planet. Sci. Lett. 183, 441–455.

Marsh, B.D., 2007. Crystallization of silicate magmas deciphered using crystal size distributions. J. Am. Ceram. Soc. 90, 746–757.

Marsh, B.D., 1988. Crystal size distribution (CSD) in rocks and the kinetics and dynamics of crystallization: I. Theory. Contrib. Mineral. Petrol. 99, 277–291.

Marty, B., 2022. Meteoritic noble gas constraints on the origin of terrestrial volatiles. Icarus 381, 115020.

Marty, B., 2020. ORIGINS AND EARLY EVOLUTION OF THE ATMOSPHERE AND THE OCEANS. Geochem. Perspect. 9, 135–136.

Marty, B., 2012. The origins and concentrations of water, carbon, nitrogen and noble gases on Earth. Earth Planet. Sci. Lett. 313, 56–66.

Marty, B., Yokochi, R., 2006. Water in the early Earth. Rev. Mineral. Geochem. 62, 421–450.

Marty, B., Zimmermann, L., 1999. Volatiles (He, C, N, Ar) in mid-ocean ridge basalts: Assesment of shallow-level fractionation and characterization of source composition. Geochim. Cosmochim. Acta 63, 3619–3633.

McDonnell, J., Flavill, R., 1974. Sputter Erosion on the Lunar Surface: Measurements and Features Under Simulated Solar He+ Bombardment. Lunar Planet. Sci. V Houst. Lunar Planet Inst 478.

Mizuno, H., Nakazawa, K., Hayashi, C., 1980. Dissolution of the primordial rare gases into the molten Earth's material. Earth Planet. Sci. Lett. 50, 202–210.

Morbidelli, A., Bottke, W.F., Nesvorný, D., Levison, H.F., 2009. Asteroids were born big. Icarus 204, 558–573.

Moreira, M., 2013. Noble gas constraints on the origin and evolution of Earth's volatiles. Geochem. Perspect. 2, 229–230.

Moreira, M., Blusztajn, J., Curtice, J., Hart, S., Dick, H., Kurz, M.D., 2003. He and Ne isotopes in oceanic crust: implications for noble gas recycling in the mantle. Earth Planet. Sci. Lett. 216, 635–643.

Moreira, M., Charnoz, S., 2016. The origin of the neon isotopes in chondrites and on Earth. Earth Planet. Sci. Lett. 433, 249–256. https://doi.org/10.1016/j.epsl.2015.11.002

Moreira, M., Kunz, J., Allegre, C., 1998. Rare gas systematics in popping rock: isotopic and elemental compositions in the upper mantle. Science 279, 1178–1181.

Moreira, M., Rouchon, V., Muller, E., Noirez, S., 2018. The xenon isotopic signature of the mantle beneath Massif Central. Geochem Perspect Lett 6, 28–32.

Moreira, M., Sarda, P., 2000. Noble gas constraints on degassing processes. Earth Planet. Sci. Lett. 176, 375–386.

Moreira, M., Staudacher, T., Sarda, P., Schilling, J.-G., Allègre, C.J., 1995. A primitive plume neon component in MORB: The Shona ridge-anomaly, South Atlantic (51–52° S). Earth Planet. Sci. Lett. 133, 367–377.

Moretti, R., Papale, P., Ottonello, G., 2003. A model for the saturation of COHS fluids in silicate melts. Geol. Soc. Lond. Spec. Publ. 213, 81–101.

Mourtada-Bonnefoi, C., Laporte, D., 2002. Homogeneous bubble nucleation in rhyolitic magmas: an experimental study of the effect of H2O and CO2. J. Geophys. Res. Solid Earth 107, ECV-2.

Mourtada-Bonnefoi, C.C., Laporte, D., 2004. Kinetics of bubble nucleation in a rhyolitic melt: an experimental study of the effect of ascent rate. Earth Planet. Sci. Lett. 218, 521–537.

Mukhopadhyay, S., 2012. Early differentiation and volatile accretion recorded in deep-mantle neon and xenon. Nature 486, 101–104. https://doi.org/10.1038/nature11141

Nowak, M., Schreen, D., Spickenbom, K., 2004. Argon and CO2 on the race track in silicate melts: a tool for the development of a CO2 speciation and diffusion model. Geochim. Cosmochim. Acta 68, 5127–5138.

Nuccio, P., Paonita, A., 2001. Magmatic degassing of multicomponent vapors and assessment of magma depth: application to Vulcano Island (Italy). Earth Planet. Sci. Lett. 193, 467–481.

Nuccio, P., Paonita, A., 2000. Investigation of the noble gas solubility in H2O–CO2 bearing silicate liquids at moderate pressure II: the extended ionic porosity (EIP) model. Earth Planet. Sci. Lett. 183, 499–512.

Olson, P.L., Sharp, Z.D., 2019. Nebular atmosphere to magma ocean: a model for volatile capture during Earth accretion. Phys. Earth Planet. Inter. 294, 106294.

Ozima, M., Podosek, F.A., 2002. Noble gas geochemistry. Cambridge University Press.

Ozima, M., Zashu, S., 1991. Noble gas state of the ancient mantle as deduced from noble gases in coated diamonds. Earth Planet. Sci. Lett. 105, 13–27.

Ozima, M., Zashu, S., 1988a. Solar-type Ne in Zaire cubic diamonds. Geochim. Cosmochim. Acta 52, 19–25.

Ozima, M., Zashu, S., 1988b. Solar-type Ne in Zaire cubic diamonds. Geochim. Cosmochim. Acta 52, 19–25.

Paonita, A., 2005. Noble gas solubility in silicate melts: a review of experimentation and theory, and implications regarding magma degassing processes. Ann. Geophys.

Paonita, A., Gigli, G., Gozzi, D., Nuccio, P., Trigila, R., 2000. Investigation of the He solubility in H2O–CO2 bearing silicate liquids at moderate pressure: a new experimental method. Earth Planet. Sci. Lett. 181, 595–604.

Pepin, R., Nyquist, L., Phinney, D., Black, D.C., 1970. Isotopic composition of rare gases in lunar samples. Science 167, 550–553.

Pepin, R.O., 1991. On the origin and early evolution of terrestrial planet atmospheres and meteoritic volatiles. Icarus 92, 2–79.

Pepin, R.O., Schlutter, D.J., Becker, R.H., Reisenfeld, D.B., 2012. Helium, neon, and argon composition of the solar wind as recorded in gold and other Genesis collector materials. Geochim. Cosmochim. Acta 89, 62–80.

Péron, S., Moreira, M., Agranier, A., 2018. Origin of light noble gases (He, Ne, and Ar) on Earth: A review. Geochem. Geophys. Geosystems 19, 979–996.

Péron, S., Moreira, M., Colin, A., Arbaret, L., Putlitz, B., Kurz, M.D., 2016. Neon isotopic composition of the mantle constrained by single vesicle analyses. Earth Planet. Sci. Lett. 449, 145–154. https://doi.org/10.1016/j.epsl.2016.05.052

Péron, S., Moreira, M., Putlitz, B., Kurz, M., 2017. Solar wind implantation supplied light volatiles during the first stage of Earth accretion. Geochem. Perspect. Lett. 151–159.

Péron, S., Moreira, M.A., Kurz, M.D., Curtice, J., Blusztajn, J.S., Putlitz, B., Wanless, V.D., Jones, M.R., Soule, S.A., Mittelstaedt, E., 2019. Noble gas systematics in new popping rocks from the Mid-Atlantic Ridge (14° N): evidence for small-scale upper mantle heterogeneities. Earth Planet. Sci. Lett. 519, 70–82.

Pichavant, M., Di Carlo, I., Le Gac, Y., Rotolo, S.G., Scaillet, B., 2009. Experimental constraints on the deep magma feeding system at Stromboli volcano, Italy. J. Petrol. 50, 601–624.

Pichavant, M., Di Carlo, I., Rotolo, S.G., Scaillet, B., Burgisser, A., Le Gall, N., Martel, C., 2013. Generation of CO 2-rich melts during basalt magma ascent and degassing. Contrib. Mineral. Petrol. 166, 545–561.

Pichavant, M., Le Gall, N., Scaillet, B., 2018. Gases as precursory signals: experimental simulations, new concepts and models of magma degassing. Volcan. Unrest Adv Volcanol 139–154.

Pierre Jules César Janssen, 1908. . Mon. Not. R. Astron. Soc. 68, 245–249. https://doi.org/10.1093/mnras/68.4.245

Porcelli, D., Ballentine, C.J., Wieler, R., 2002. An overview of noble gas geochemistry and cosmochemistry. Rev. Mineral. Geochem. 47, 1–19.

Porcelli, D., Woolum, D., Cassen, P., 2001. Deep Earth rare gases: initial inventories, capture from the solar nebula, and losses during Moon formation. Earth Planet. Sci. Lett. 193, 237–251.

Poreda, R., di Brozolo, F.R., 1984. Neon isotope variations in Mid-Atlantic Ridge basalts. Earth Planet. Sci. Lett. 69, 277–289.

Raquin, A., Moreira, M., 2009. Atmospheric 38Ar/36Ar in the mantle: implications for the nature of the terrestrial parent bodies. Earth Planet. Sci. Lett. 287, 551–558.

Raquin, A., Moreira, M.A., Guillon, F., 2008. He, Ne and Ar systematics in single vesicles: mantle isotopic ratios and origin of the air component in basaltic glasses. Earth Planet. Sci. Lett. 274, 142–150.

Raymond, S.N., O'Brien, D.P., Morbidelli, A., Kaib, N.A., 2009. Building the terrestrial planets: Constrained accretion in the inner Solar System. Icarus 203, 644–662.

Reynolds, J., Hohenberg, C., Lewis, R., Davis, P., Kaiser, W., 1970. Isotopic analysis of rare gases from stepwise heating of lunar fines and rocks. Science 167, 545–548.

Reynolds, J., Turner, G., 1964. Rare gases in the chondrite Renazzo. J. Geophys. Res. 69, 3263–3281.

Rolfs, C.E., Rodney, W.S., 1988. Cauldrons in the cosmos: Nuclear astrophysics. University of Chicago press.

Roubinet, C., Moreira, M.A., 2018. Atmospheric noble gases in Mid-Ocean Ridge Basalts: identification of atmospheric contamination processes. Geochim. Cosmochim. Acta 222, 253–268.

Ruzié, L., Moreira, M., 2010. Magma degassing process during Plinian eruptions. J. Volcanol. Geotherm. Res. 192, 142–150.

Saltykov, S., 1967. Stereology: proceedings of the second international congress for stereology, chapter The determination of the size distribution of particles in an opaque material from a measurement of the size distribution of their sections.

Sarda, P., Graham, D., 1990. Mid-ocean ridge popping rocks: implications for degassing at ridge crests. Earth Planet. Sci. Lett. 97, 268–289.

Sarda, P., Moreira, M., 2002. Vesiculation and vesicle loss in mid-ocean ridge basalt glasses: He, Ne, Ar elemental fractionation and pressure influence. Geochim. Cosmochim. Acta 66, 1449–1458.

Sarda, P., Moreira, M., Staudacher, T., Schilling, J., Allègre, C.J., 2000. Rare gas systematics on the southernmost Mid-Atlantic Ridge: Constraints on the lower mantle and the Dupal source. J. Geophys. Res. Solid Earth 105, 5973–5996.

Sarda, P., Staudacher, T., Allègre, C.J., 1988. Neon isotopes in submarine basalts. Earth Planet. Sci. Lett. 91, 73–88. https://doi.org/10.1016/0012-821X(88)90152-5

Sasaki, S., 1999. Presence of a primary solar-type atmosphere around the earth: evidence of dissolved noble gas. Planet. Space Sci. 47, 1423–1431.

Sasaki, S., Nakazawa, K., 1990. Did a primary solar-type atmosphere exist around the proto-earth? Icarus 85, 21–42. https://doi.org/10.1016/0019-1035(90)90101-E

Scarpa, R., Tilling, R.I., Giggenbach, W., 1996. Chemical composition of volcanic gases. Monit. Mitig. Volcano Hazards 221–256.

Schlosser, P., Winckler, G., 2002. Noble gases in ocean waters and sediments. Rev. Mineral. Geochem. 47, 701–730.

Shinohara, H., Aiuppa, A., Giudice, G., Gurrieri, S., Liuzzo, M., 2008. Variation of H2O/CO2 and CO2/SO2 ratios of volcanic gases discharged by continuous degassing of Mount Etna volcano, Italy. J. Geophys. Res. Solid Earth 113.

Shishkina, T.A., Botcharnikov, R.E., Holtz, F., Almeev, R.R., Jazwa, A.M., Jakubiak, A.A., 2014. Compositional and pressure effects on the solubility of H2O and CO2 in mafic melts. Chem. Geol. 388, 112–129.

Sparks, R.S.J., 1978. The dynamics of bubble formation and growth in magmas: a review and analysis. J. Volcanol. Geotherm. Res. 3, 1–37.

Staudacher, T., Allègre, C.J., 1988. Recycling of oceanic crust and sediments: the noble gas subduction barrier. Earth Planet. Sci. Lett. 89, 173–183.

Staudacher, T., Sarda, P., Richardson, S., Allègre, C., Sagna, I., Dmitriev, L., 1989. Noble gases in basalt glasses from a Mid-Atlantic Ridge topographic high at 14 N: geodynamic consequences. Earth Planet. Sci. Lett. 96, 119–133.

Stolper, E., 1982. Water in silicate glasses: an infrared spectroscopic study. Contrib. Mineral. Petrol. 81, 1–17.
Stout, V.L., Gibbons, M.D., 1955. Gettering of gas by titanium. J. Appl. Phys. 26, 1488–1492.
Sumino, H., Kaneoka, I., Matsufuji, K., Sobolev, A.V., 2006. Deep mantle origin of kimberlite magmas revealed by neon isotopes. Geophys. Res. Lett. 33.
Tolstikhin, I., O'Nions, R., 1994. The Earth's missing xenon: A combination of early degassing and of rare gas loss from the atmosphere. Chem. Geol. 115, 1–6.
Trieloff, M., Kunz, J., Clague, D.A., Harrison, D., Allègre, C.J., 2000. The Nature of Pristine Noble Gases in Mantle Plumes. Science 288, 1036–1038. https://doi.org/10.1126/science.288.5468.1036
Warren, P.H., 1995. Extrapolated partial molar densities of SO3, P2O5, and other oxides in silicate melts. Am. Mineral. 80, 1085–1088.
Watson, E.B., Sneeringer, M.A., Ross, A., 1982. Diffusion of dissolved carbonate in magmas: experimental results and applications. Earth Planet. Sci. Lett. 61, 346–358.
Wetherill, G.W., 1954a. Variations in the isotopic abundances of neon and argon extracted from radioactive minerals. Phys. Rev. 96, 679.
Wetherill, G.W., 1954b. Variations in the isotopic abundances of neon and argon extracted from radioactive minerals. Phys. Rev. 96, 679.
Wetherill, G.W., 1953a. Spontaneous fission yields from uranium and thorium. Phys. Rev. 92, 907.
Wetherill, G.W., 1953b. Spontaneous fission yields from uranium and thorium. Phys. Rev. 92, 907.
Wieler, R., 2002. Cosmic-ray-produced noble gases in meteorites. Rev. Mineral. Geochem. 47, 125–170.
Wieler, R., 1998. The solar noble gas record in lunar samples and meteorites. Space Sci. Rev. 85, 303–314.
Williams, C.D., Mukhopadhyay, S., 2019. Capture of nebular gases during Earth's accretion is preserved in deep-mantle neon. Nature 565, 78–81. https://doi.org/10.1038/s41586-018-0771-1
Yatsevich, I., Honda, M., 1997a. Production of nucleogenic neon in the Earth from natural radioactive decay. J. Geophys. Res. Solid Earth 102, 10291–10298.
Yatsevich, I., Honda, M., 1997b. Production of nucleogenic neon in the Earth from natural radioactive decay. J. Geophys. Res. Solid Earth 102, 10291–10298.
Yokochi, R., Marty, B., 2004. A determination of the neon isotopic composition of the deep mantle. Earth Planet. Sci. Lett. 225, 77–88. https://doi.org/10.1016/j.epsl.2004.06.010
Yoshimura, S., 2015. Diffusive fractionation of H2O and CO2 during magma degassing. Chem. Geol. 411, 172–181.
Zadnik, M., Jeffery, P., 1985. Radiogenic neon in an Archaean anorthosite. Chem. Geol. Isot. Geosci. Sect. 52, 119–125.
Zhang, Y., Ni, H., Chen, Y., 2010. Diffusion data in silicate melts. Rev. Mineral. Geochem. 72, 311–408.
Zhang, Y., Xu, Z., 1995. Atomic radii of noble gas elements in condensed phases. Am. Mineral. 80, 670–675.
Zhang, Y., Xu, Z., Zhu, M., Wang, H., 2007. Silicate melt properties and volcanic eruptions. Rev. Geophys. 45.
Zhang, Y., Zindler, A., 1989. Noble gas constraints on the evolution of the Earth's atmosphere. J. Geophys. Res. Solid Earth 94, 13719–13737.

Chapitre 5 : Evolution des isotopes stables du néon pendant la dépressurisation Une série expérimentale de décompression et de "compréhension"

Les chapitres précédents ont étudié l'impact d'un flux/fusion riche en CO_2 traversant un système magmatique expérimental isobare et isotherme. L'évolution de la nucléation et de la croissance des vésicules a été observée à mesure que les échantillons expérimentaux s'approchaient de l'équilibre, et l'effet de la vésiculation sur les isotopes stables du néon a été étudié. Dans toutes les expériences analysées, les vésicules ont séparé le néon de la matière fondue, entraînant son appauvrissement, et le fractionnement des isotopes dans la phase gazeuse a été documenté à des taux différents.

Dans un système naturel, lorsque la chambre magmatique commence à se dépressuriser et qu'une masse fondue auparavant en équilibre commence à dissoudre le CO_2, la solubilité des gaz diminue, ce qui entraîne leur séparation de la phase liquide et la formation de bulles de gaz dans la masse fondue.

Comme nous l'avons vu aux chapitres 3 et 4, les vésicules générées en profondeur peuvent avoir des conséquences importantes sur le fractionnement isotopique du néon et sur le CO_2 avant la décompression de la chambre magmatique et l'éruption. Cependant, une génération distincte de bulles se produit pendant la décompression de la chambre magmatique. La croissance des vésicules est produite par (i) l'expansion des gaz à l'intérieur d'un magma ascendant et (ii) la diffusion des volatiles vers les bulles (Sparks, 1978).

La question principale de ce chapitre est de déterminer l'effet de la saturation en CO_2 sur les isotopes néon. Les isotopes du néon peuvent-ils être fractionnés lors de la nucléation ou lors de la croissance des bulles ? Et si oui, par quel paramètre sont-ils le plus affectés ?

Ce résumé synthétise les principales conclusions et implications des expériences ainsi que leur comparaison avec les systèmes naturels, en soulignant l'importance du facteur temps dans les processus magmatiques et le fractionnement isotopique des gaz rares.

Chapter 5: Evolution of neon stable isotopes during decompression. An experimental series of decompression and "comprehension"

5.1. Introduction:

The previous chapters investigated the impact of a CO_2-rich flow/melt passing through an experimental isobaric and isothermal magmatic system. The evolution of nucleation and growth of the vesicles were observed as the experimental samples approached the equilibrium and the effect that vesiculation has on the stable isotopes of neon was investigated. In all the analysed experiments, vesicles partitioned neon from the melt, leading to its depletion, and fractionation of isotopes in the gas phase was documented at different rates.

In a natural system, when the magmatic chamber starts to depressurize and a melt that previously was in equilibrium starts to exsolve CO_2 the solubility of gases decreases, causing them to separate from the liquid phase and to form gas bubbles in the melt.

As discussed in *Chapters 3* and *4*, vesicles generated at depth may have significant implications for neon isotopic fractionation and for CO_2 before magma chamber decompression and eruption. However, a distinct bubble generation takes place during the decompression of the magma chamber. The growth of the vesicles is produced by (i) the expansion of gases within a rising magma and (ii) the diffusion of volatiles towards bubbles (Sparks, 1978).

The main question of this chapter is to determine the effect of CO_2 saturation on the stable isotopes of neon. Could neon stable isotopes be fractionated during nucleation or during the growth of the bubbles? and if so, by which parameter are they affected more?

5.2. Experimental technique:

To ensure a different perspective, the new experimental capsules series will start from a melt-in equilibrium, letting the products in the capsule run the experiment for at least 24 hours (Pichavant et al., 2013), to create a uniform distribution of CO_2 and neon

(which diffuses faster than CO_2 as seen in *Chapter 4* in the melt, and then start the decompression.

Several factors influence the saturation of CO_2 in the melt. In addition to crystal and water content (Aubaud et al., 2004), when the rate of nucleation and growth of vesicles is too high to maintain equilibrium the carbon saturation occurs and it will evolve regarding to the magma chamber depth (pressure) and eruption rates (decompression rates). In this series of experiments, the factors of crystallization and water have been eliminated. The only source of water in the system will come from the reduction of iron in the oxidised starting material during the run of the experiment at its maximum.

Unlike in the previous experiments, where the bubbles grew due to inward diffusion of CO_2, in the decompression experiments it must be considered that the bubbles will also grow because of the expansion of the gas. During an isothermal ascent, from pressure P_1 (before decompression start) to pressure P_2 (quench pressure), vesicles will expand as:

$$\frac{V_2}{V_1} = \left(\frac{r_2}{r_1}\right)^3$$

where V is the molar volume of CO_2 and r is the radius of the vesicles at pressures $P_{(t=t1)}$ and $P_{(t=t2)}$ (Sparks, 1978; Sarda and Graham, 1990).

The aim of these experiments was to recreate the natural conditions leading up to an eruption using our composition (the same than experiments developed in *Chapters 3* and *4*). To achieve this, we limited the CO_2 concentration to a maximum of 2700 ppm for the basanitic melt according to Jiménez-Mejías et al. (2021) for 2 kbar and 1200ºC. Two ascension rates were chosen to compare similarities and differences in vesicle size distribution as well as neon partitioning. Finally, the products were quenched at different pressures (see **Table 5.1.**).

Sample	Run	Ne added (wt.%)	CO_2 added (wt.%)	T (°C)	P_{exp} (bar)	Pq_{exp} (bar)	/R. rate/ (bar/min)	Exp.time (min)
EN-E3	Fasnia Ne 7	3.76E-06	0.27	1200	2015	2015	0	1800
EN-E4	Fasnia Ne 10	4.37E-06	0.27	1200	2009	116	50	2610
EN-E6	Fasnia Ne 8	4.47E-06	0.28	1200	1899	519	50	1830
EN-E8	Fasnia Ne 8	4.22E-06	0.39	1200	1899	519	50	1830
EN-E9	Fasnia Ne 9	4.44E-06	0.32	1200	2147	247	50	3020
EN-E10	Fasnia Ne 9	4.36E-06	0.28	1200	2147	247	50	3020
EN-D1	Fasnia Ne 11	4.42E-06	0.27	1200	1983	250	5	4560

EN-D2	Fasnia Ne 11	4.40E-06	0.27	1200	1983	250	5	4560
EN-D4	Fasnia Ne 11	4.47E-06	0.27	1200	1983	250	5	4560

Table 5.1: Experimental conditions for decompression experiments. CO_{2added} and Ne_{added} are the CO_2 and Ne loaded into the capsule; P_{exp} indicates the pressure at which the experiment was equilibrated; P_Q is the pressure at which the experiment was quenched; */R. rate/* indicate the decompression rate of the experiment; Exp.time is the total duration of the experiments including time equilibrating and decompression.

5.3. Analytical method:

The analytical method used for the experimental glasses follows the same protocol described in previous chapters (*Chapters 2, 3* and *4*). All analyses were conducted at the Institute of Earth Sciences of Orleans, France.

5.3.1. Instrumental analysis:

Nine experimental capsules were analysed for CO_2 and water contents, as well as 2D image scanning (SEM) to verify the composition of the micro-oxides crystallised in the glass (present in a limited manner), and 3D (micro-CT) for vesicle size distribution and previous mass spectrometry analysis.

For the reasons given below, three out of the nine samples were chosen for noble gas analysis using mass spectrometry. The gas extraction of the vesicles previously the analysis was conducted by either bubble-by-bubble laser ablation or by crushing (more details in *Chapter 2*), both of which were performed under ultra-high vacuum conditions.

The selection of the samples for the analysis of neon samples was done based on the quench pressure and the decompression rate. Due to the small size of the vesicles and low vesicularity of the samples with the highest quench pressure (500 and 250 bar), piercing bubbles with the laser was a hard and long time-consuming task, taking several months to analyse only two bubbles (for sample *EN-E9*) and without success for the others. The results presented here focus on the sample quenched at shallower depths (*EN-E4*) using the bubble-by-bubble laser ablation technique, along with a bubble of the sample (*EN-E9*), and three samples analysed using the crushing method for comparison with the laser results.

Several analyses of the matrix glass where also done to test neon matrix contribution during the ablation. However, the result showed to be more than 92% of the analytical blank, even for ablation time longer than 5 minutes, so the correction of the

samples was made concerning the analytical blank. The results of the matrix will be provided in the manuscript's *Appendix*.

5.3.2. Textural analysis in 2D, readjusting parameters for VSD:

Two parameters will change in the calculations for this chapter. Since these are decompression experiments, the new bubbles will have a different origin than the bubbles formed during the static experiments. Therefore, it is necessary to readjust the residence time of these bubbles in the magma, τ, which will be set to the decompression rate. Additionally, the bubble growth rate, G, which is a parameter independent of bubble size and calculated from the slope of the bubble population density (as explained in *Chapter 3*, Watson et al. (1982); Sarda and Graham (1990); Chavrit (2010)) needs to be readjusted on the basis of the residence time.

5.4. Results:

5.4.1. Major elements:

The major elements of the bulk glass determined by electron microprobe analysis are reported in **Table 5.2.** No significant changes were observed in the composition of the decompression samples compared to the starting material.

	SiO2	TiO2	Al2O3	FeO	MnO	MgO	CaO	Na2O	K2O	P2O5	Na2O+K2O	total
EN-E3	44.84	3.76	14.86	12.26	0.23	7.67	10.65	3.66	1.38	0.69	5.04	100.00
	0.32	*0.15*	*0.10*	*0.35*	*0.04*	*0.09*	*0.08*	*0.10*	*0.12*	*0.04*		
EN-E4	44.35	3.80	15.05	11.93	0.22	7.99	10.55	3.72	1.55	0.84	5.27	100.00
	0.20	*0.06*	*0.12*	*0.24*	*0.07*	*0.07*	*0.12*	*0.08*	*0.09*	*0.06*		
EN-E6	44.62	3.74	14.77	12.64	0.12	7.71	10.46	3.68	1.45	0.82	5.13	100.00
	1.02	*0.10*	*0.23*	*1.63*	*0.04*	*0.12*	*0.30*	*0.05*	*0.09*	*0.08*		
EN-E8	46.24	3.77	15.06	10.15	0.17	7.60	11.03	3.77	1.41	0.80	5.18	100.00
	0.24	*0.10*	*0.15*	*0.29*	*0.08*	*0.07*	*0.17*	*0.09*	*0.05*	*0.07*		
EN-E9	44.24	3.77	14.70	12.68	0.25	7.89	10.68	3.60	1.38	0.81	4.97	100.00
	0.21	*0.13*	*0.17*	*0.24*	*0.06*	*0.06*	*0.08*	*0.04*	*0.04*	*0.04*		
EN-E10	44.78	3.77	14.80	12.13	0.17	7.83	10.60	3.68	1.48	0.77	5.15	100.00
	0.31	*0.07*	*0.24*	*0.27*	*0.05*	*0.08*	*0.08*	*0.04*	*0.04*	*0.06*		
EN-D1	44.75	3.82	14.98	11.66	0.18	7.92	10.55	3.74	1.57	0.83	5.31	100.00
	0.29	*0.14*	*0.12*	*0.25*	*0.05*	*0.10*	*0.08*	*0.06*	*0.08*	*0.06*		
EN-D2	44.76	3.75	14.96	11.69	0.16	7.94	10.58	3.73	1.61	0.83	5.34	100.00
	0.23	*0.11*	*0.18*	*0.18*	*0.07*	*0.11*	*0.07*	*0.08*	*0.05*	*0.08*		

EN-D4	44.41	3.78	15.08	11.93	0.14	7.93	10.58	3.76	1.56	0.82	5.32	100.00
	0.32	*0.15*	*0.15*	*0.32*	*0.06*	*0.07*	*0.12*	*0.08*	*0.08*	*0.09*		

Table 5.2: Major elements for the decompression experimental samples. Compositions normalized to 100% anhydrous melt. Oxide concentrations were measured by EPMA at ISTO-CNRS. Standard deviations are italicized. Total iron expressed as FeO.

5.4.2. FTIR:

No issues were found with oxides absorbing the infrared signal in the decompression samples. The results for CO_3^2 and OH^- in the run products are reported in **Table 5.3**. Similar to the previous experimental series, water was not added to the capsules during preparation. It is present in all experimental samples, although in quantities of < 1wt.% due to iron reduction of the oxidised starting material.

The CO_3^{2-} content ranges from 2385 to 237 ppm decreasing in the experiments quenched at shallower pressures (**Figure 5.1**). The samples plot close to the theoretical CO_3^{2-} dissolved (Jiménez-Mejías et al., 2021) with a slight excess towards the quenched samples at lower pressure.

Sample	P_Q (bar)	ρ ($g \cdot l^{-1}$)	sd	Thickness (cm)	sd	$[CO_2]$ (ppm)	sd	H_2O (wt.%)	sd
EN-E3	2015	2770	6	4.76E-03	1.7E-04	2385	162	0.91	0.06
EN-E4	116	2769	4	1.08E-02	2.6E-04	541	179	0.60	0.03
EN-E6	519	2774	27	4.00E-03	1.4E-04	799	143	0.32	0.03
EN-E8	519	2734	3	3.28E-03	1.1E-04	961	181	0.31	0.04
EN-E9	247	2784	4	6.90E-03	3.1E-04	457	42	0.34	0.02
EN-E10	247	2772	5	5.74E-03	3.9E-04	569	123	0.67	0.08
EN-D1	250	2762	4	7.74E-03	1.1E-04	237	80	0.67	0.02
EN-D2	250	2762	5	8.10E-03	2.1E-04	350	41	0.65	0.04
EN-D4	250	2768	5	9.33E-03	5.1E-04	411	143	0.67	0.03

Table 5.3: FTIR data. Average of H_2O and CO_2 concentrations calculated from the number of analytical spots in each sample after error propagation for every point. *sd* is the standard deviation.

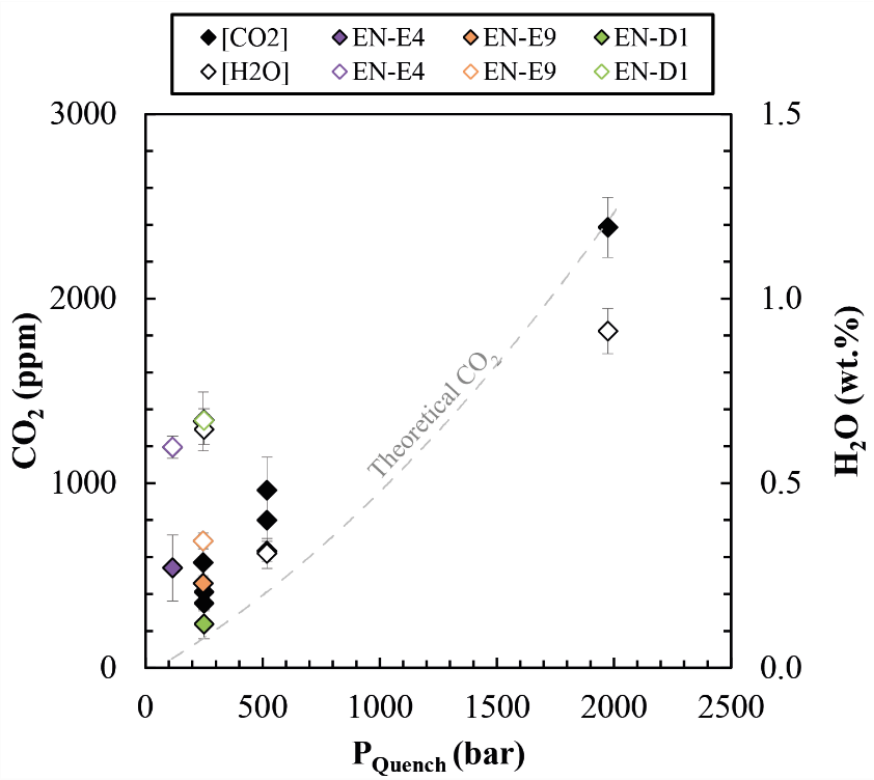

Figure 5.1: CO_3^{2-} and OH^- dissolved in the experimental glass vs the pressure at which they were quenched. The full diamonds represent the CO_3^{2-} dissolved, coloured for those that were analysed for neon concentration and isotopic ratios and black for the others. The empty diamonds represent the water dissolved, following the same legend as CO_3^{2-}. The error bar shows the standard deviation obtained after calculating the error propagation. The dashed line represents the theoretical CO_2 for the pressure at which the glass was quenched (from Jiménez-Mejías et al. (2021)).

5.4.3. Vesicle size distribution and vesicularity:

5.4.3.1. 3D-image scanning:

The recovery of the experimental glass from the run products was successful for the decompression samples. The extracted glass pieces were large enough for microtomography analysis. This success may be attributed to the lower amounts of CO_2 compared to the static experiments, for which a higher vesicularity promoted the fragility of recovered glasses.

Figure 5.2. displays the 3D images obtained for each sample, along with the corresponding experimental pressures, and a schematic drawing of the natural system.

- *EN-E3*: After 30 hours of experimentation at 1200°C and 2kbar, the *EN-E3* sample produced a bubble-free glass. This sample will serve as a representative of the starting sample for the decompression experiments and as the limit for the previously studied static samples. The equilibrium is confirmed by the CO_2 content and its homogeneous distribution across sample (**Table 5.3**).
  The experiments followed two paths: either a slow decompression at 5 bars per minute, or a fast decompression one at 50 bars per minute, and whose distinctive varying parameter will be the pressure at which the experiments were stopped.

Slow decompression samples:

This group comprises three samples (*EN-D1*, *EN-D2* and *EN-D4*) produced during the same experiment in the autoclave, all quenched at 250 bars. The vesicles are distributed homogeneously within the glass, without any preference for the upper or lower edges of the capsule. However, there seems to be a nucleation tendency towards the central vertical axis of the capsule. This group of samples has the lowest vesicularity of the decompression samples, ranging from 0.06% to 0.31%.

Fast decompression samples:

This group includes the experiments ended at pressures of 519, 247 and 116 bars. As with the previous group, the vesicles in the samples, regardless of the pressure at which they were quenched, exhibit a homogeneous distribution with two exceptions. For sample *EN-E8*, there is a greater accumulation of vesicles at one of the lateral ends of the capsule (**Figure 5.2**). Similarly, sample *EN-E9* shows a slight accumulation of larger vesicles at the upper end of the capsule, with at least three large vesicles standing out above all the others. These vesicles are at the melt-capsule interface (**Figure 5.3**).

- *Experiments quenched at 519 bars (EN-E6 and EN-E8):* they showed the smallest vesicle size among the group, mere nucleus when compared to other experiments conducted so far. Both capsules present the same characteristics.
- *Experiments quenched at 247 bars (EN-E9 and EN-E10):* The size of the bubbles and vesicularity increase in these experiments. The bubbles are distributed homogeneously throughout the glass, except for sample *EN-E9*, which has four larger bubbles located at the top of the capsule with some accumulation (**Figure 5.3**).

- *Experiments quenched at 116 bars (EN-E4):* This sample has the highest vesicularity and largest bubble sizes in the series. It is important to note that the samples are not scaled in the visual appreciation presented here. Further details will be discussed in the section where the images were treated with *ImageJ*.

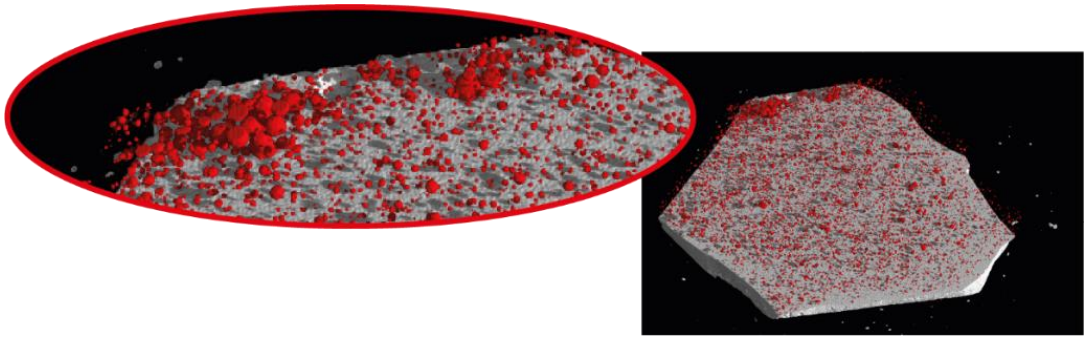

Figure 5.2: Sample EN-E8 showing accumulation of vesicles close to one of the lateral ends of the capsule.

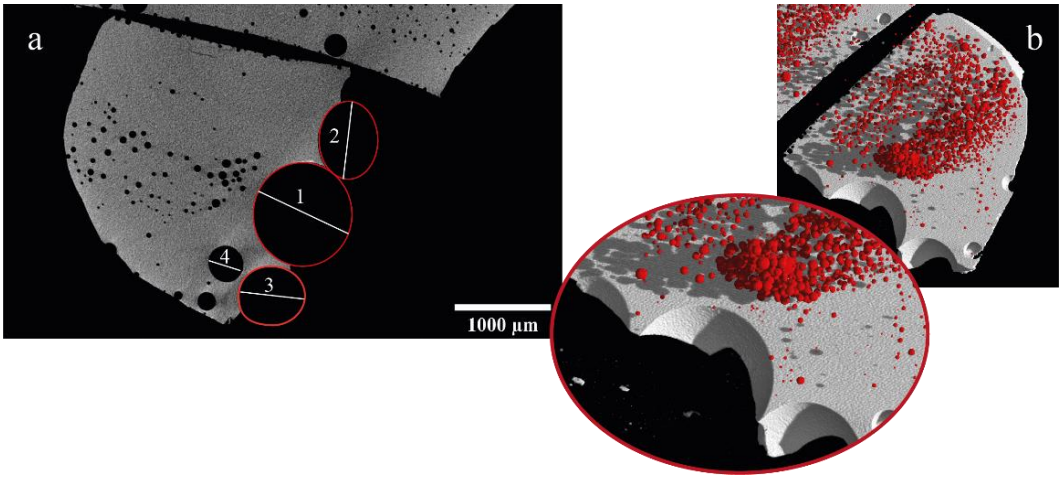

Figure 5.3: Sample *EN-E9* showing a. the maximum diameter of four vesicles trapped between the glass interface and the capsule with radius of: 1 = 987µm, 2 = 717µm, 2 = 567µm and 4 = 395µm. The diameter of the vesicles was measured individually using *ImageJ* and taking in to account the maximum diameter, b. A group of vesicles accumulated close to the top of the capsule.

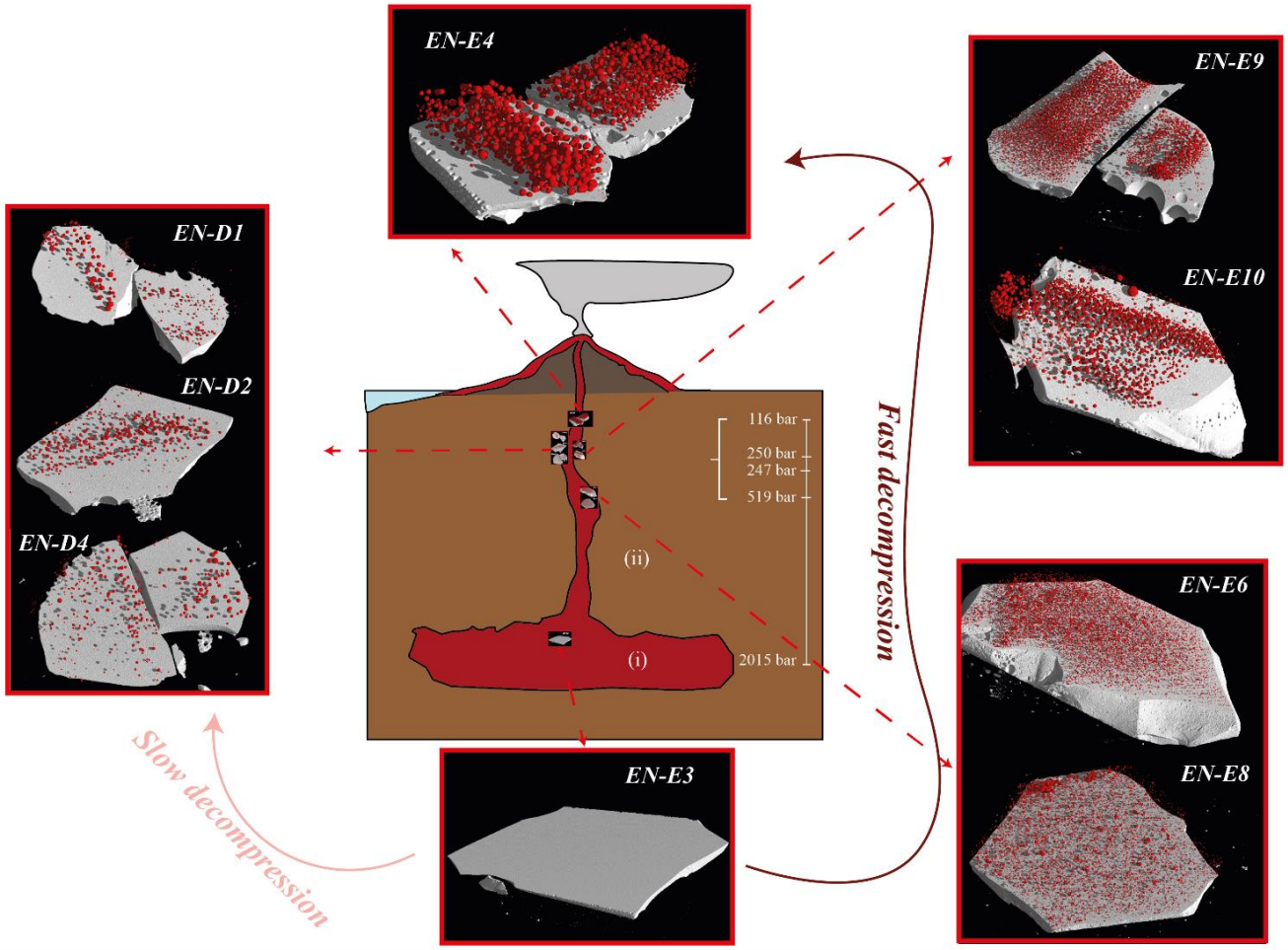

Figure 5.4: Representative diagram of the run product showing partially the glass (grey colours) and the distribution of the vesicles (red spheres) at the corresponding depth according to the pressure of quench. Fron the equilibrium starting sample, EN-E3, the decompressed samples follow two paths depending on the ascent rate (5 or 50 bar·min^{-1}).

5.4.3.2. Sorting by VSD type:

The several types of vesicle-size distribution are illustrated in **Figure 5.5**. The experimental series lacks the presence of VSD type I, which is characterised by a correlation coefficient, *R*, exceeding 0.9 and the presence of a single bubble population, as evidenced by the observation of a straight line in the diagram. Even though the correlation coefficient for some samples is larger than 0.9 (*EN-E6*, *EN-E8* and *EN-E9*), the absence of any intermediate vesicle population size or the vesicle coalescence that curbs the trend toward the smaller population of vesicles, discard this group type from the decompression samples.

The experimental group that underwent slow decompression (*EN-D1*, *EN-D2* and *EN-D4*) exhibits the greatest absence of vesicle clusters, classified as *VSD type VIb* with the absence of up to five intermediate sizes. This effect is associated with the low vesicularity of the sample, (only 52 bubbles; Chavrit, 2010).

This group is followed by the *EN-E6* sample, classified as *Type VIa* due to the absence of one of the smallest populations, but with a great correlation ratio, R=0.97.

The Ostwald ripening effect is more pronounced in the faster decompression samples, particularly in the *EN-E10* sample, sorting them in the *VSD type III*. This is evident from the accumulation and growth of bubbles at the expense of smaller bubbles towards one end (top or side) of the glass, as observed in the 3D images.

Finally, sample EN-E4 quenched at lower pressure presents a full population classification, reaching up to twice the average diameter compared to the samples of the entire experimental series (D = 0.21mm). The correlation coefficient is lowered due to the presence of a high number of bubbles belonging to the smaller average vesicle population. This sample is classified as *VSD type II*.

5.4.3.3. VSD parameters:

The results of the VSD analysis are shown in **Table 5.4.** The bubble density was calculated for all the experimental samples. The population density of the decompression samples ranges from Ln(n) = 8.91 and 14.99mm^{-4}. The samples quenched at higher pressure, except for *EN-E3*, which does not present vesicles, had the highest population density. This is related to the number of μm-size vesicles per mm^3 present in the samples,

up to n_0 = 2341 μm-size nuclei per mm^3 (**Table 5.4** and **Figure 5.6.a**). The lower value of the population density is for sample *EN-E4* as low as Ln(n) = 8.91 mm^{-4} and only 7.4 μm-size nuclei per mm^3. The high and low population of nuclei is also evident when we look at the 3D-images of the corresponding samples, where the quenched glasses at higher pressures show a glass full of nuclei in comparison with the other samples.

The relationship between the slope of the trend for *Ln(n)* and the maximum diameter of the sorted vesicles for each sample is similar. Specifically, the slope increases with population density (**Figure 5.6.b**).

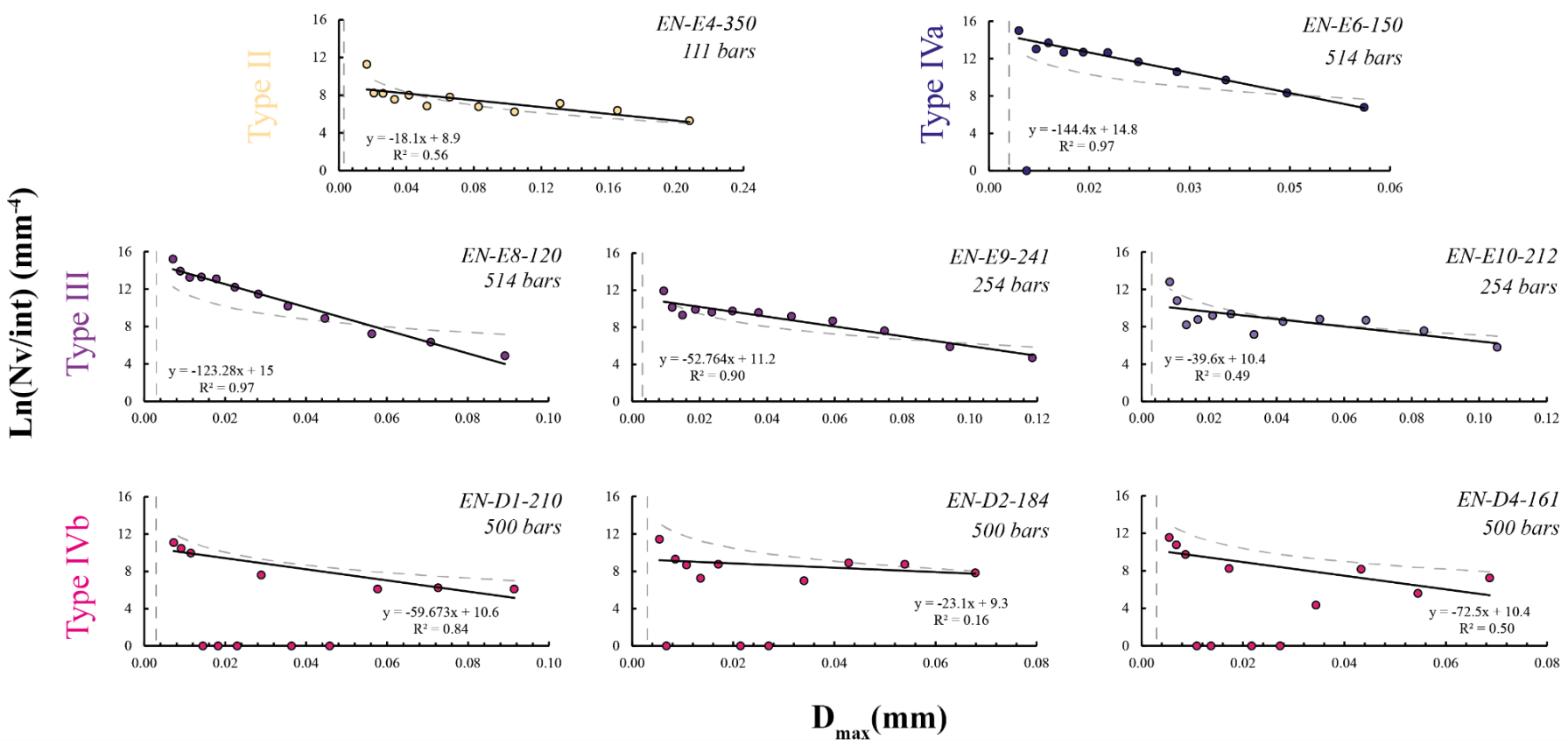

Figure 5.5: Population density plots as a function of the maximum diameter of each interval for samples grouped by VSD type. *Type I* (green dots), *VSD Type II* (salmon dots), *VSD Type III* (purple dots), *VSD Type IVa* (blue dots) and *VSD Type IVb* (pink dots). A minimum of 4 bubbles per interval is indicated by the grey dashed curve. The limit of detection for the tomography is represented by the vertical dashed grey line. The slice of the stack where the analysis was performed is indicated by the number next to the sample name. The populations where Ln(n) = 0 were not considered for the correlation coefficient.

Sample	Volume (mm^3)	Ves* (%)	Ves** (%)	Area (mm^2)	Nb	B. density (mm^{-2})	D_{max} (µm)	D_{mean} (µm)	Ln(n) (mm^{-4})	sd	a (mm-1)	sd	n_0 (mm^{-4})	R^2	$D_{mean\ th}$ (-1/a) (µm)	G (µm/min)	VSD group
EN-E3	11.8	0	0														
EN-E4	15.2	5.5	9.2	12.0	232	19.6	207.9	77.3	8.91	0.50	-18.1	5.0	7.4	0.56	55.37	1.38	II
EN-E6	9.9	0.8	1.0	11.6	997	86.5	56.1	12.3	14.82	0.23	-144.4	8.4	2717.5	0.97	6.92	0.17	IVa
EN-E8	6.6	1.2	1.9	7.7	955	149.5	89.2	12.9	14.99	0.28	-123.3	6.7	3241.0	0.97	8.11	0.20	III
EN-E9	20.1	1.3	3.4	15.3	383	23.8	118.5	42.8	11.25	0.31	-52.8	5.5	76.6	0.90	18.95	0.47	III
EN-E10	9.9	1.6	2.4	6.5	143	22.5	105.3	36.7	10.40	0.63	-39.6	12.6	32.9	0.49	25.27	0.63	III
EN-D1	6.1	0.3	0.6	8.5	26	3.5	91.4	46.3	10.61	0.59	-59.7	11.5	40.4	0.84	16.76	0.42	IVb
EN-D2	16.1	0.1	1.1	5.6	52	10.3	67.9	36.7	9.30	0.71	-23.1	20.2	10.9	0.16	43.32	0.11	IVb
EN-D4	17.9	0.1	0.5	6.1	22	4.3	68.6	38.0	10.38	1.11	-72.5	29.7	32.1	0.50	13.80	0.03	IVb

Table 5.4: VSD parameter of the experimental samples analysed by micro-CT and image treated by ImageJ and Excel. $Exp._{time}$ refers to the duration of the experiment; *Nb* represents the number of counted bubbles in the slice; D_{max} and D_{mean} correspond to the maximum and mean diameter of the vesicles in the analysed slice; $Ves_{ImageJ\ slice}$ indicates the vesicularity of the analysed area in the slice; *Ln(n)* is the density of the population of vesicles obtained by the linear trend of the graph *Ln(n)* vs (D_{max}); *a* is the slope of the trend line; n_0 is the number of µm-size vesicles nucleated per mm^3; R^2 is the correlation coefficient of the trend line; $D_{mean\ th\ (-1/a)}$ is the theoretical mean diameter for this sample obtained by the inverse of the slope; Additionally, the growth rate of the vesicles is represented by *G*. * Is the vesicularity obtained VGStudioMax and ** in the analysed slice by *ImageJ.*

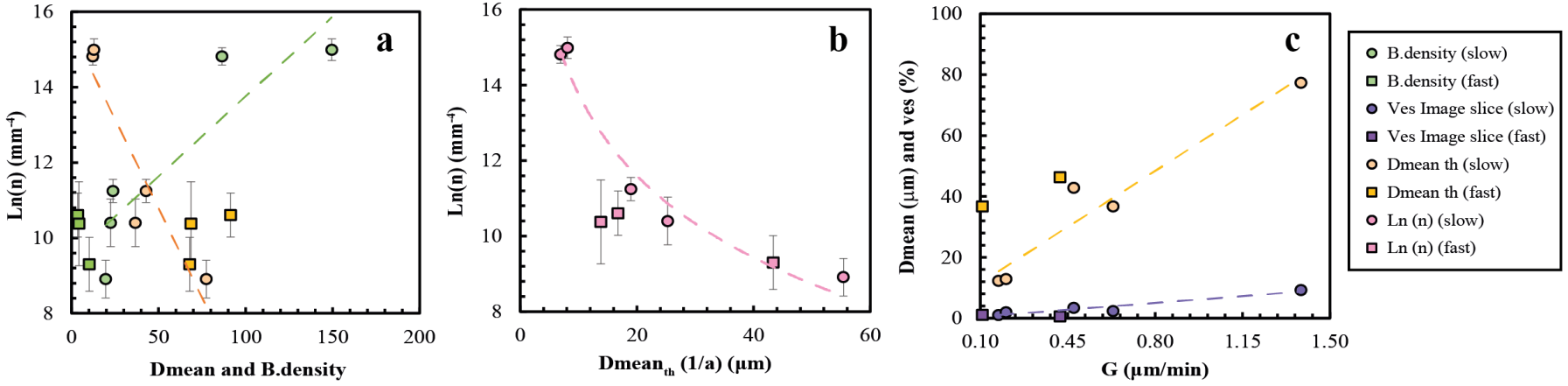

Figure 5.6: **a**. Population density, *ln(n)*, against the bubble density (green dots) and mean diameter (salmon dots) measured by *ImageJ* in single image slices. **b**. Population density, *ln(n)*, against theoretical mean diameter obtained from the slope of VSD graphic of every sample. **c**. Relationship between the vesicularity and mean diameter analysed by *ImageJ* with the growth rate, *G*, of the vesicles in each quenched glass. The dashed lines indicate the trend for each parameter. The units are shown in the legend. The standard deviation of Ln(n) is also plotted for every sample in this graph.

Samples *EN-E4*, *EN-E9* and *EN-E10* have a maximum and mean diameter greater than the other samples, *Dmax* >105µm and *Dmean* >36.7µm.

The vesicularity and vesicle diameter increase with the growth rate of the bubbles, *G*, in the decompression series (**Figure 5.6.c**). The mean diameter exhibits a steeper slope. Three samples follow the trend for the mean diameter but plot outside of it; they belong to the group that followed the slow decompression rate (*EN-D1*, *EN-D2* and *EN-D4*).

5.4.4. Neon:

5.4.4.1. Bubble by bubble laser ablation:

A total of ten vesicles were analysed for the two samples, *EN-E4* and *EN-E9*, using the bubble-by-bubble laser ablation under vacuum technique. For sample *EN-E4*, seven out of eight vesicles will be considered, as *Ves 6* represents two vesicles pierced during the same shot (as indicated by the jump in pressure in **Figure 5.7**). Only one vesicle will be considered for sample EN-E9, as Bulle 2 was observed to have high quantities of Argon during the data treatment with MATLAB (as shown in **Figure 2.30.b**).

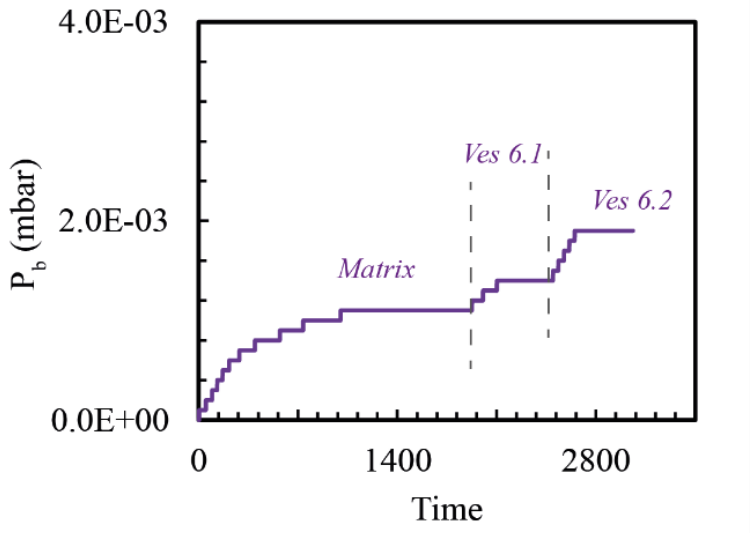

Figure 5.7: During the pressure measurement, two small vesicles were detected. The first curve stroke represents the matrix being pierced by the plasma laser and the resulting change in pressure. At time 1992, the first pressure jump due to the vesicle was observed, followed by a second jump at time 2667.

The isotopic ratios of $^{20}Ne/^{22}Ne$ and $^{21}Ne/^{22}Ne$ are remarkably close to the air standard used for developing the starting material (9.8 and 0.0290 respectively). All

vesicles plot close to each other, with $^{20}Ne/^{22}Ne$ isotopic ratios ranging between 9.62 and 9.78 (**Figure 5.8)**. The results are shown in **Table 5.5.**

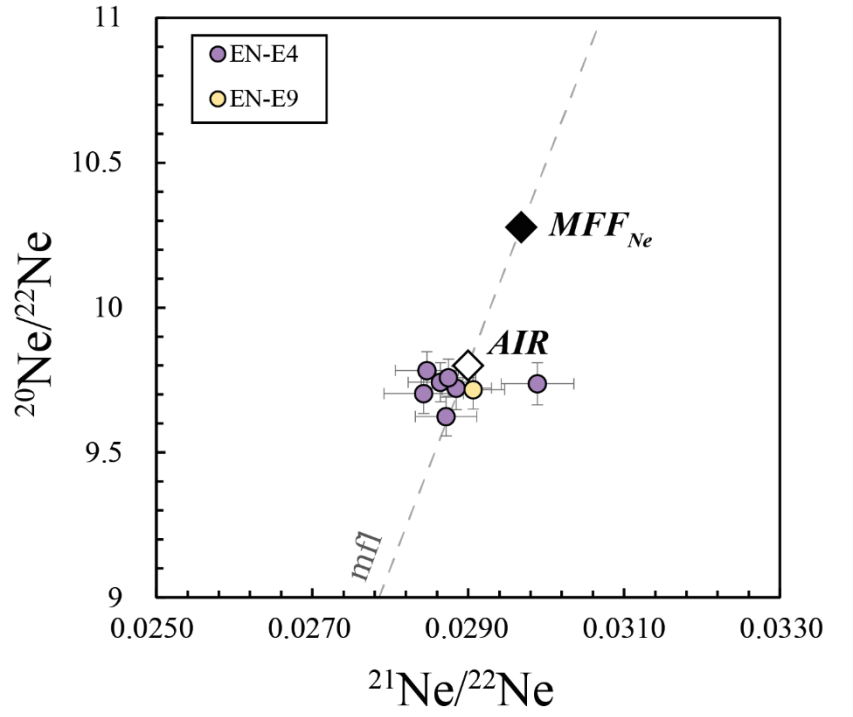

Figure 5.8: Data of singles vesicles plotted as $^{20}Ne/^{22}Ne$ vs $^{21}Ne/^{22}Ne$ diagram. The black diamond represents the maximum theoretical fractionation factor, MFF_{Ne}, expected for the reference value ($^{20}Ne/^{22}Ne$ = 10.28 and $^{21}Ne/^{22}Ne$ = 0.030); the white diamond represents the reference value taken from the standard and the starting point of the starting material. $^{20}Ne/^{22}Ne$ = 9.8 and $^{21}Ne/^{22}Ne$ = 0.029. The dashed line represents the mass fractionation line, *mfl*. The purple dots represent the vesicles pierced in sample *EN-E4*. Only one single vesicle was successful for the analysis of sample *EN-E9* (orange dot).

Regarding the volume of the vesicles and the partial pressure of CO_2 and Ne gases, the partial pressure of neon does not exhibit a clear trend when plotted against the vesicle volume obtained through the method outlined in *Section 3.3.1.2*. The vesicles' partial pressure displays a more scattered trend compared to the CO_2 partial pressure. **Figure 5.9**) displays the pressure of the pierced vesicles and the partial pressure of Ne in each vesicle.

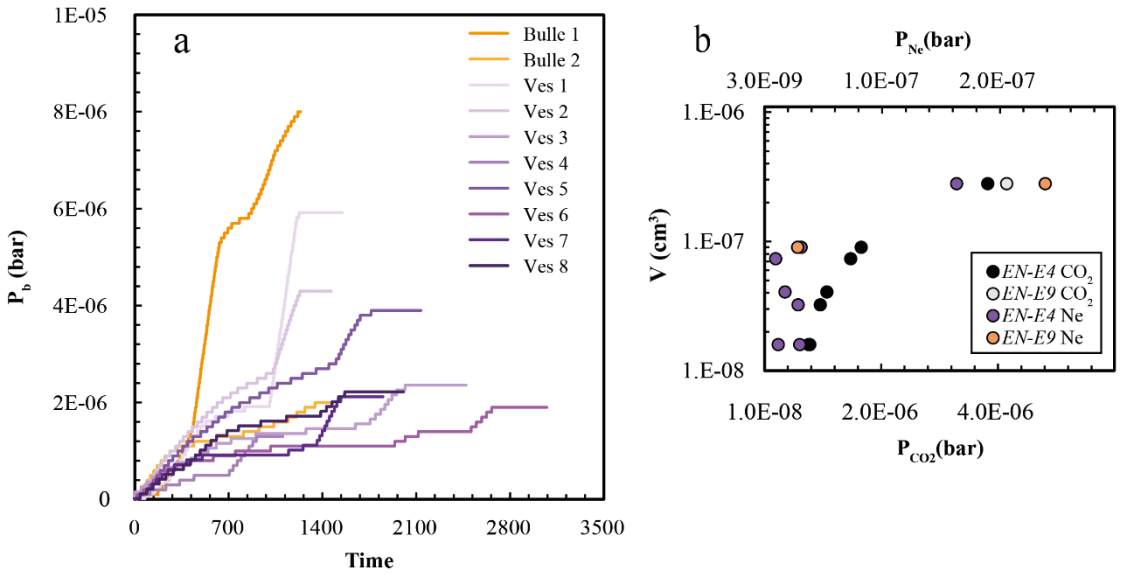

Figure 5.9: The graphic (**a)** shows in purple the vesicles ablated for sample *EN-E4* and in orange the vesicles belonging to sample *EN-E9*. For clarity only the latest part of the ablated matrix in every pierced vesicle is shown. Graphic (**b)** shows the partial pressure of every gas following the same colour scale than figure (**a)** and black and grey for CO_2 of samples *EN-E4* and *EN-E9* respectively.

5.4.4.2. Step crushing:

The $^{20}Ne/^{22}Ne$ and $^{21}Ne/^{22}Ne$ ratios obtained by crushing of samples *EN-E4*, *EN-E9* and *EN-D1* vary between 9.71 and 9.96 and 0.0283 and 0.0293 respectively, sample *EN-D1* the one with bigger values for $^{20}Ne/^{22}Ne$ ratio, as high as 9.96. Results are shown in **Table 5.5** and plotted in **Figure 5.10**.

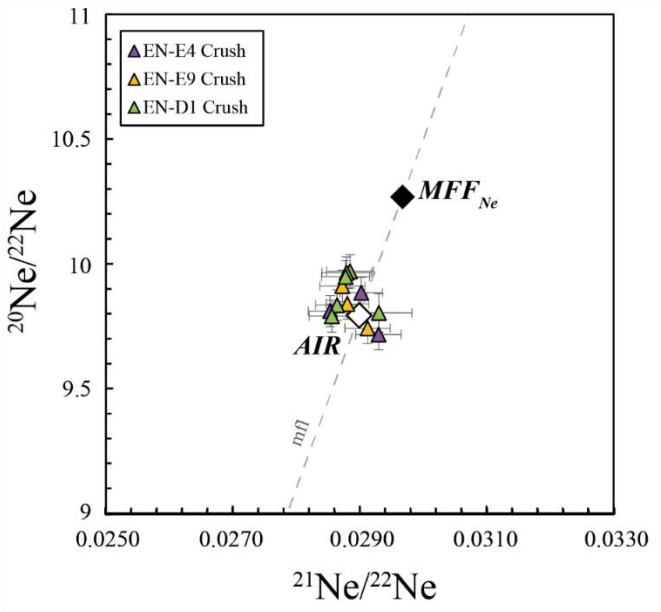

Figure 5.10: Result of neon isotopic ratios of every step crush plotted as $^{20}Ne/^{22}Ne$ vs $^{21}Ne/^{22}Ne$ diagram. The black diamond represents the maximum theoretical fractionation factor, MFF_{Ne}, expected for the reference value ($^{20}Ne/^{22}Ne$ = 10.28 and $^{21}Ne/^{22}Ne$ = 0.030); the white diamond represents the reference value taken from the standard and the starting point of the starting material $^{20}Ne/^{22}Ne$ = 9.8 and $^{21}Ne/^{22}Ne$ = 0.029. The dashed line represents the mass fractionation line, *mfl*. The purple triangles represent sample *EN-E4*, the orange triangles represent sample *EN-E9,* and the green triangles represent sample *EN-D1*.

Samples *EN-E9* and *EN-D1* showed an excess of argon when the first aliquot of every step crushing was done, so it had to be discarded in the results reported and I took a smaller volume to continue the analysis by sampling a second and even a third aliquot. Up to six steps of crushing were done in these samples taking as reference the value of the two and third aliquots of every step crush. The first aliquot of every step crushing is shown in the *appendix* of this manuscript together with the vesicles that show the same effect, and the values of several vesicles ablated at the same time by mistake.

Vesicles

EN-E4										
Experimental conditions: T = 1200^{O} C, P_Q = 116±10 bar, Decom. Rate= 50bar/min; ves = 5.5%										
	Pb_{Tot} (bar)	**D (µm)**	**Volume (cm^3)**	**^{22}Ne (cm^3STP)**	**$^{20}Ne/^{22}Ne$**	**σ**	**$^{21}Ne/^{22}Ne$**	**σ**	**P_{Ne} (bar)**	**P_{CO2} (bar)**
Ves 1 (0.95'')	4.00E-06	40.56	2.80E-07	5.25E-11	9.62	0.07	0.0287	0.0004	1.7E-07	3.83E-06
Ves 2 (1.23'')	1.70E-06	27.81	9.01E-08	1.08E-11	9.70	0.07	0.0284	0.0005	3.4E-08	1.67E-06
Ves 3 (2.04'')	8.00E-07	15.61	1.59E-08	1.04E-11	9.72	0.08	0.0288	0.0005	3.3E-08	7.67E-07
Ves 4 (0.9'')	8.00E-07	15.61	1.59E-08	4.63E-12	9.74	0.07	0.0299	0.0005	1.5E-08	7.85E-07
Ves 5 (5.4'')	1.10E-06	21.33	4.06E-08	6.47E-12	9.74	0.07	0.0286	0.0004	2.0E-08	1.08E-06
Ves 6 (5.65'') **	8.00E-07	15.61	1.59E-08	3.37E-12	9.78	0.07	0.0289	0.0005	1.1E-08	7.89E-07
Ves 7 (6.24'')	1.00E-06	19.78	3.24E-08	1.00E-11	9.76	0.06	0.0287	0.0003	3.2E-08	9.68E-07

Ves 8 (6.35'')	1.50E-06	26.00	7.36E-08	3.96E-12	9.78	0.06	0.0285	0.0004	1.3E-08	1.49E-06
EN-E9										
Experimental conditions: T = 1200° C, P_Q = 247±10 bar, Decom. Rate= 50bar/min; ves = 1.3%										
	Pb_{Tot} (bar)	**D (µm)**	**Volume (cm^3)**	**^{22}Ne (cm^3STP)**	**$^{20}Ne/^{22}Ne$**	**σ**	**$^{21}Ne/^{22}Ne$**	**σ**	**P_{Ne} (bar)**	**P_{CO2} (bar)**
Bulle 1 (1'')	4.40E-06	40.56	2.80E-07	7.62E-11	9.72	0.07	0.0291	0.0004	2.4E-07	4.16E-06
Bulle 2 (1.08'') **	1.20E-06	27.81	9.01E-08	9.82E-12	10.16	0.08	0.0313	0.0005	3.1E-08	1.17E-06
Crushing										
EN-E4										
Experimental conditions: T = 1200° C, P_Q = 116±10 bar, Decom. Rate= 50bar/min; ves = 5.5%										
step crush	**Aliquot**	**Weight (g)**	**^{22}Ne (cm^3STP/g)**	**$^{20}Ne/^{22}Ne$**	**σ**	**$^{21}Ne/^{22}Ne$**	**σ**			
1	1	0.0162	3.20E-11	9.82	0.06	0.0285	0.0003			
1	2		3.00E-11	9.72	0.06	0.0293	0.0004			
2	1		1.34E-10	9.89	0.06	0.0290	0.0003			
EN-E9										
Experimental conditions: T = 1200° C, P_Q = 247±10 bar, Decom. Rate= 50bar/min; ves = 1.3%										
step crush	**Aliquot**	**Weight (g)**	**^{22}Ne (cm^3STP/g)**	**$^{20}Ne/^{22}Ne$**	**σ**	**$^{21}Ne/^{22}Ne$**	**σ**			
1	2	0.0366	1.27E-10	9.85	0.06	0.0288	0.0003			
1	3		1.17E-10	9.92	0.06	0.0287	0.0004			
2	2		2.68E-11	9.75	0.06	0.0291	0.0004			
3	2		1.87E-10	9.92	0.07	0.0286	0.0004			
4	2		6.05E-11	9.88	0.06	0.0288	0.0003			
5	1		7.41E-12	9.73	0.07	0.0289	0.0004			
EN-D1										
Experimental conditions: T = 1200° C, P_Q = 250±10 bar, Decom. Rate= 5bar/min; ves = 0.3%										
step crush	**Aliquot**	**Weight (g)**	**^{22}Ne (cm^3STP/g)**	**$^{20}Ne/^{22}Ne$**	**σ**	**$^{21}Ne/^{22}Ne$**	**σ**			
1	2	0.0158	2.40E-11	9.98	0.07	0.0289	0.0004			
2	2		8.35E-12	9.97	0.06	0.0288	0.0004			
3	2		1.14E-11	9.96	0.07	0.0288	0.0004			
4	2		5.22E-11	9.84	0.06	0.0287	0.0003			
5	2		3.35E-11	9.80	0.06	0.0286	0.0004			
6	1		2.40E-12	9.81	0.08	0.0293	0.0005			
Air				9.80		0.029				
MFF_{Ne}				10.28		0.030				

Table 5.5: P_{bTot} is the total pressure of the gas released by the pierced vesicle, V_b is the volume of the vesicle, P_{Ne} is the partial pressure of neon in the vesicle, and P_{CO2} is the CO_2 partial pressure. Neon isotopic composition and abundances were analysed by a HELIX-SFT mass spectrometer at ISTO-France, using laser ablation of single vesicles. All experimental glasses were corrected for blank. * The gas extracted belongs to three vesicles pierced at the same time, therefore, these results were not considered for the discussion and conclusion of this work. ** The analysis of the vesicle revealed a high quantity of Ar. The units are shown in the table for each parameter.

5.5. Discussion:

5.5.1. Vesiculation parameters:

Examining the vesicularity parameters, the results demonstrate a relationship with the pressure at which the experiments were quenched, but also with the decompression rate. In **Figure 5.11.** for example, the number of nuclei per volume of magma, n_0, grows exponentially by decreasing the pressure of the quenched glass, P_Q, as:

$$n_0 = 0.7447 * e^{0.0157 * P_Q}$$

With a correlation coefficient $R^2 = 0.99$. Both the fast and slow decompression samples exhibit the same trend. However, they differ slightly in terms of "lost vesicularity", with the slower samples having slightly lower vesicularity than the faster samples for the same pressure. This can be attributed to the fact that the bubbles have more time to grow (by diffusion of CO_2 into the vesicle) and rise. Here, "lost vesicularity" refers to the difference between the vesicularity measured in the glass by 3D-image and the theoretical vesicularity calculated as described in *Chapter 3*.

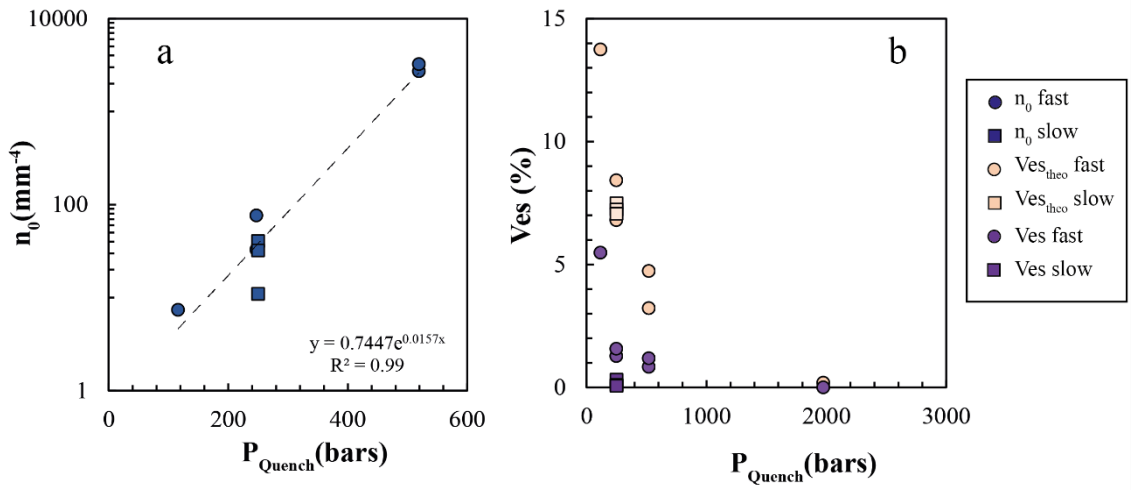

Figure 5.11. The diagram (**a)** shows the number µn-nuclei per volume of magma of the experimental glasses vs the quench at which the experiment was stopped. The diagram (**b)** shows the theoretical vesicularity (salmon dots) and the vesicularity measured in the quenched glasses by 3D-image using the software VGSudioMax.

5.5.2. CO_2 diffusion, vesicle growth, displacement, and neon fractionation?

To investigate the phenomenon observed by the vesicularity parameters, **Figure 5.12** plots the rise of the vesicles, the diffusion of CO_2 and the growth of the vesicles by

the time at which the quench was performed. This time refers to the time elapsed since the start of decompression, $rise_{time}$, and distinguishes the two groups of samples according to their decompression rate.

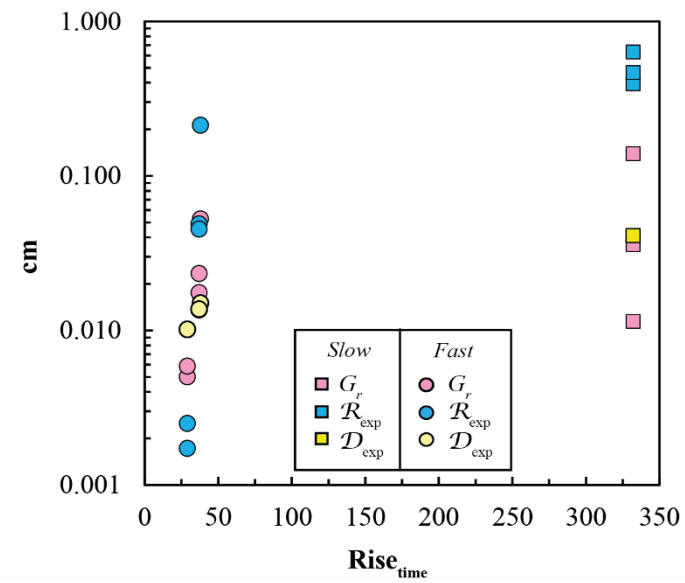

Figure 5.13.: The diagram illustrates the transport of CO_2 through diffusion (yellow) or via bubbles (blue) and the growth of the bubble radius (pink) during decompression, $Rise_{time}$. Squares points refer to the slow decompression experiments and dots to the fast decompression experiments.

The experimental capsules have a length of 1.5 cm, but the product inside barely reaches 9 mm in length. This allows even the earliest nucleated vesicles formed at the bottom of the capsule to reach the top when the capsule is quenched at 250 bars for slow decompression. In the case of fast decompression, the maximum displacement of the vesicles is ten times less at the same pressure. This explains the difference in "loss of vesicularity" compared to the theoretical vesicularity. As for the static experiments, "lost vesicularity" refers to the gas that is accumulated at the interface glass-capsule.

For the two capsules quenched at 519 bars (*EN-E6* and *EN-E8*), CO_2 diffusion is more effective in terms of CO_2 displacement than bubbles due to their small size (D < 92 μm) as vesicularity is limited to the nuclei of the vesicles. It is expected that the first nuclei formed are fractionated due to the faster diffusion of neon compared to CO_2 (Jambon et al., 1986; Lux, 1987; Zhang and Xu, 1995; Behrens and Zhang, 2001; Nowak et al., 2004; Zhang et al., 2007), see the diffusion model in *Chapter 4*. However, analysing these vesicles by laser ablation was impossible due to: (i)their tiny size; (ii) consequently the low amount of gas available and (iii) the low vesicularity of the samples (ves <1.2%).

According to this graph, fractionation of large bubbles is feasible only if they are large enough to be transported, faster than diffusion before the vesicle reaches the isotopic equilibrium. This scenario requires a bubble growth rate and therefore transport faster than diffusion.

A higher decompression rate will result in a larger expansion of the vesicles in less time. This is the scenario of samples *EN-E9 and EN-E10.* The conditions of these samples are suitable for finding fractionation in both the newly formed vesicles and in the larger vesicles since both, the growth, and the displacement of the bubbles, are faster than the diffusion of CO_2 (**Figure 5.11.** and **Table 5.6**). Moreover, the VSD of these samples (**Figure 5.5**) shows that nucleation still takes place, with at least two generations of vesicles (*EN-E9*) and three (EN-E10) with breaks in the slope of the curve towards the smallest vesicles (smaller than 20 μm of diameter) and slightly larger in the case of the *EN-E10* sample between 30 and 40 μm (**Figure 5.5**).

In details, the analytical problems are firstly, the low vesicularity of the samples (1.3 and 1.6%) presents a significant challenge in identifying individual vesicles with the laser; secondly, and more importantly, in the newly formed vesicles, the available gas is minimal due to the small size of the bubbles (D < 40 microns). Therefore, the obtained value is very low, making it hard to differentiate from the blank of the line. **Figure 5.3** shows that the larger vesicles are accumulated or lost at the interface of the melt-capsule or grouped. Therefore, finding one of them goes along with a high chance of piercing more than one vesicle at the same time due to their proximity.

In addition to the challenge of locating small bubbles in a sample with low vesicularity and avoiding multiple groups of vesicles nearby, a third issue arose when some of the bubbles were ablated, or the sample was crushed. Sample EN-E9 was found to be rich in argon, making the associated data difficult to interpret, and therefore the results had to be discarded. The manuscript's appendix displays the data that were excluded due to high and unreliable $^{20}Ne/^{22}Ne$ ratios. This signal could be affected by the significant amount of argon masking the signal, as demonstrated in *Chapter 2*.

	D_{CO2}	η_L	v_b	Q_{time}	*Rexp*	*Dexp* CO_2	G_r	*Dexp (Ne)*
Sample	**(m^2/s)**	**(Pa/s)**	**m/s**	**(min)**	**cm**	**cm**	**cm**	**cm**
EN-E3	1.18E-12	7.82	0	0	0	0	0	0

EN-E4	9.90E-12	9.54	9.34E-07	38	0.213	0.015	0.053	23.87
EN-E6	5.93E-12	14.84	1.44E-08	29	0.003	0.010	0.005	20.86
EN-E8	5.92E-12	23.38	9.91E-09	29	0.002	0.010	0.006	20.86
EN-E9	8.36E-12	12.25	2.20E-07	37	0.049	0.014	0.018	23.56
EN-E10	8.48E-12	9.64	2.04E-07	37	0.045	0.014	0.023	23.56
EN-D1	8.45E-12	9.83	3.18E-07	332	0.634	0.041	0.139	70.57
EN-D2	8.44E-12	9.94	1.98E-07	332	0.395	0.041	0.036	70.57
EN-D4	8.45E-12	9.01	2.34E-07	332	0.466	0.041	0.011	70.57

Table 5.6: Results obtained for CO_2 diffusion and bubble velocity for the composition, the CO_2 and H_2O dissolved in the glass for the respective conditions of pressure and temperature of the experimental glasses. D_{CO2} is the CO_2 diffusion; η_L is the viscosity of the melt (according to Bottinga and Richet (1981); Giordano et al.(2008), v_b is the velocity of the bubbles, R_{exp} is the distance covered by the vesicle at *R.Time*, D_{exp} is the distance covered by the CO_2 diffusion at *R.Time* and G_r is the bubble radius growth at *R.Time.*

The sample *EN-E4* was found to have the best conditions for laser ablation due to its vesicularity and vesicle size (5.5 % and 77.3µm respectively). This suggests a higher probability of finding vesicles in different equilibrium phases. However, the nuclei per mm^3 in this sample (**Table 5.4**) were too small (n_0 = 7.4µm-size per mm^3). The growth of the vesicles was comparable to that of the samples quenched at 247 bars with a faster ascent rate.

However, the displacement of the vesicles was too rapid, resulting in the “loss of the largest vesicles”. This left behind the intermediate and slower vesicles, which had enough time during the ascent to reach isotopic equilibrium.

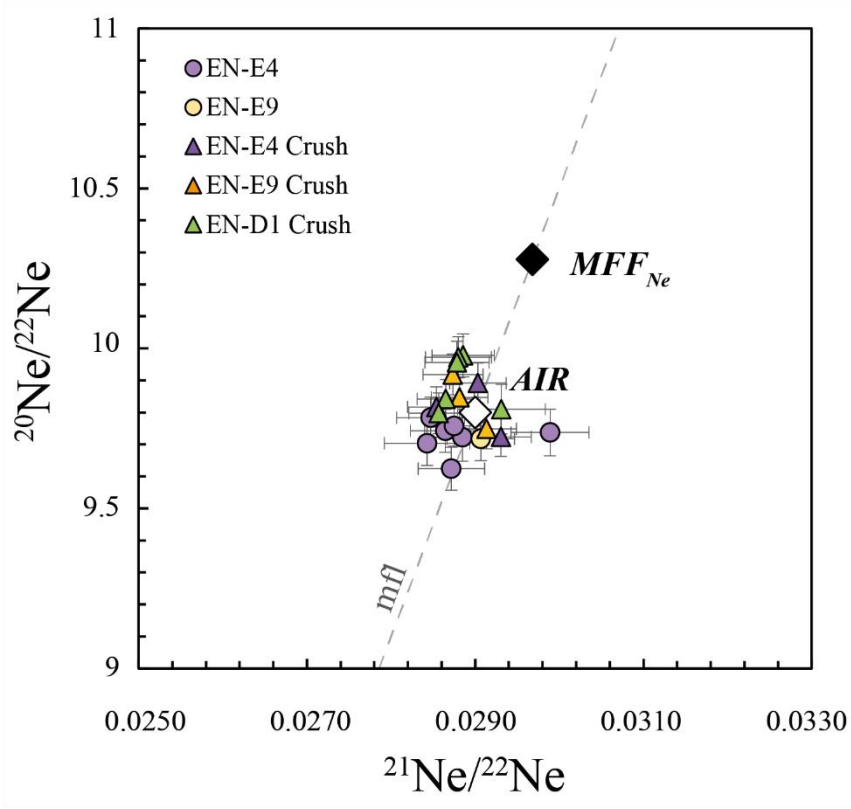

Figure 5.13: Compilation of the results obtained by the gas extraction technique Figures 5.8 and 5.10, of the decompression experiments.

About the slowly decompressed samples, it is less likely, but still possible, to find fractionation if vesicle nucleation is ongoing at the time of quenching. However, like the rapid decompression samples quenched at the same depth, the small size of the vesicles and their low vesicularity make individual analysis by laser ablation challenging. We decided to abandon the samples for this method after several weeks of unsuccessful attempts to find a bubble. Nevertheless, one of the pieces from sample *EN-D1* was analysed by extracting the gas using the crushing method.

Similar to the results obtained for its rapid decompression pressure analogue (*EN-E9*), the crushing result showed some values significantly higher than the majority of the values obtained for the isotopic ratio, as high as $^{20}Ne/^{22}Ne = 9.96$. **Figure 5.12** shows that the distance travelled by the vesicle and its growth is greater than that of CO_2 diffusion. Therefore, both the results and theory suggest that isotopic fractionation for some vesicles in sample *EN-D1* is possible. The low amount of CO_2 dissolved (237 ± 80ppm) in the glass and the small number of vesicles in this sample (26 counts in the slice taken as reference for this sample; **Table 5.4**) suggest a significant "loss of gas" before the

quenching, which is consistent with **Figure 5.5**. The absence of up to five populations of intermediate sizes and the maximum diameter of the vesicle set being 91.4μm also support this it. The *Gr* value for this sample indicates that the vesicles could grow up to 1 mm and rise to 0.9 cm within the capsule.

5.6. Conclusions:

This chapter illustrates the intricate relationship between experimental conditions, vesicle behaviour, and fractionation processes. It also highlights the challenge of accurately analysing and interpreting the data from such experiments.

5.6.1. Gas extraction in tiny vesicles: a challenge:

The most challenging part of these experiments was the technique used to extract the trapped gas from the vesicles, which involved bubble-by-bubble laser ablation. The samples contained tiny bubbles, particularly those close to the diameter of the laser beam (35μm). This, combined with the low vesicularity of the samples, resulted in several months of work. An additional gas extraction technique, i.e. crushing, was required to obtain more information of samples where the laser ablation could not arrive.

5.6.2. CO_2 and vesicularity

Carbon dioxide remains concentrated in the melt at concentrations exceeding solubility (see **Figure 5.1**), with the exception of samples decompressed at a slower rate (*EN-D1* and *EN-D2*), which are in close proximity to the equilibrium line. This phenomenon has also been observed in other experimental studies where CO_2-bearing melts exhibit disequilibrium during magma ascent. For example, Le Gall and Pichavant (2016b), Pichavant et al. (2013, 2009) and Yoshimura (2015) have all reported similar observations. They related this effect to: (i) The distance between bubbles or the distance between the gas interface (which will depend on the size and distribution of the vesicles); and (ii) the distance over which volatile diffusion occurs (which will depend on the duration of the experiment).

A significant difference is noticeable between the samples quenched during depressurisation at 500 bar and those quenched after 250 bar. The samples quenched at high pressure are characterised by a higher abundance of bubble nuclei with bubble sizes

of only a few tens of microns. Based on the laws of solubility, CO_2 diffusion, and the application of Stokes' law to these samples, the transport of CO_2 by vesicles advection to the surface is minimal, which reduces the diffusion of CO_2 and creates new bubble nuclei.

When the pressure decreases to 250 bar, the vesicles expand which allows a more efficient advective transport of CO_2 than through diffusion in both samples, fast and slow ascension. Furthermore, since the growth of the vesicles is faster than CO_2 diffusion, it can be concluded that this effect is due to depressurization, relegating the diffusion of CO_2 inward of the vesicle to a second plane.

5.6.3. Equilibrium and fractionation during decompression:

The samples analysed by both laser ablation and crushing gas extraction methods, exhibit isotopic ratios similar to the standard used in the starting material that was previously proven to be homogeneous. This is the case for sample *EN-E4* (quenched at 110 bars), where the isotopic compositions obtained for both gas extraction methods are clustered close to the standard value, indicating that equilibrium in the vesicles was reached.

Samples EN-D1 and EN-E9 were unable to undergo gas extraction by laser ablation due to the size of the vesicles, which were equal to or less than the laser diameter beam. Consequently, the samples were subjected to step crushing. The aforementioned samples exhibited higher values than those of the standards employed in the experiment, with values as high as 20Ne/22Ne = 9.92 for sample EN-E9 and 20Ne/22Ne = 9.98 for sample EN-D1.

These experimental samples demonstrate that Ne isotopic fractionation during decompression in a magma that has been previously equilibrated, if possible, occurs at higher pressures. This is corroborated by the image analysis and theoretical calculations conducted here. The observed fractionation is influenced by two factors:

- The nucleation of the bubbles: at high pressures, which is when the phenomenon of nucleation is observed to be more pronounced, it is most common to find disequilibrium since neon is going rapidly to the vesicle. While the magma is saturated in CO_2 nucleation will keep ongoing.

- The expansion of the vesicles and their higher rise rate must be faster than the diffusion of CO_2 to prevent them from reaching isotopic equilibrium. This phenomenon occurs when the decompression rate is excessively rapid. For two samples quenched at the same pressure but with different decompression rates, samples with a faster ascension rate demonstrate a closer approximation to the theoretical equilibrium in terms of CO_2 concentration in the melt.

The combination of these analytical techniques is a powerful tool for determining vesiculation, equilibrium, and fractionation processes in magmatic systems.

5.7. References:

Aiuppa, A., Federico, C., Giudice, G., Giuffrida, G., Guida, R., Gurrieri, S., Liuzzo, M., Moretti, R., Papale, P., 2009. The 2007 eruption of Stromboli volcano: insights from real-time measurement of the volcanic gas plume CO2/SO2 ratio. J. Volcanol. Geotherm. Res. 182, 221–230.

Allegre, C.J., Manhes, G., Göpel, C., 1995. The age of the Earth. Geochim. Cosmochim. Acta 59, 1445–1456.

Allègre, C.J., Staudacher, T., Sarda, P., Kurz, M., 1983. Constraints on evolution of Earth's mantle from rare gas systematics. Nature 303, 762–766. https://doi.org/10.1038/303762a0

Aubaud, C., 2022. Carbon stable isotope constraints on CO2 degassing models of ridge, hotspot and arc magmas. Chem. Geol. 605, 120962.

Aubaud, C., Pineau, F., Jambon, A., Javoy, M., 2004. Kinetic disequilibrium of C, He, Ar and carbon isotopes during degassing of mid-ocean ridge basalts. Earth Planet. Sci. Lett. 222, 391–406.

Aubry, G.J., Sator, N., Guillot, B., 2013. Vesicularity, bubble formation and noble gas fractionation during MORB degassing. Chem. Geol. 343, 85–98.

Azuma, S., Ozima, M., Hiyagon, H., 1993. Anomalous neon and xenon in an Archaean anorthosite from West Greenland. Earth Planet. Sci. Lett. 114, 341–352.

Ballentine, C.J., Barfod, D.N., 2000. The origin of air-like noble gases in MORB and OIB. Earth Planet. Sci. Lett. 180, 39–48.

Ballentine, C.J., Burgess, R., Marty, B., 2002. Tracing fluid origin, transport and interaction in the crust.

Ballentine, C.J., Burnard, P.G., 2002. Production, Release and Transport of Noble Gases in the Continental Crust. Rev. Mineral. Geochem. 47, 481–538. https://doi.org/10.2138/rmg.2002.47.12

Ballentine, C.J., Marty, B., Sherwood Lollar, B., Cassidy, M., 2005. Neon isotopes constrain convection and volatile origin in the Earth's mantle. Nature 433, 33–38.

Bauer, C.A., 1947. Production of helium in meteorites by cosmic radiation. Phys. Rev. 72, 354.

Becker, R.H., Pepin, R.O., 1994. Solar wind noble gases and nitrogen in metal from lunar soil 68501. Meteoritics 29, 724–738.

Behrens, H., 2010. Noble gas diffusion in silicate glasses and melts. Rev. Mineral. Geochem. 72, 227–267.

Behrens, H., Misiti, V., Freda, C., Vetere, F., Botcharnikov, R.E., Scarlato, P., 2009. Solubility of H2O and CO2 in ultrapotassic melts at 1200 and 1250 C and pressure from 50 to 500 MPa. Am. Mineral. 94, 105–120.

Behrens, H., Zhang, Y., 2001. Ar diffusion in hydrous silicic melts: implications for volatile diffusion mechanisms and fractionation. Earth Planet. Sci. Lett. 192, 363–376.

Black, D., Pepin, R., 1969. Trapped neon in meteorites—II. Earth Planet. Sci. Lett. 6, 395–405.

Black, D.C., 1972. On the origins of trapped helium, neon and argon isotopic variations in meteorites—I. Gas-rich meteorites, lunar soil and breccia. Geochim. Cosmochim. Acta 36, 347–375.

Blank, J.G., Brooker, R.A., 1994. Experimental studies of carbon dioxide in silicate melts; solubility, speciation, and stable carbon isotope behavior. Rev. Mineral. Geochem. 30, 157–186.

Bodmer, R., Bochsler, P., 2000. Influence of Coulomb collisions on isotopic and elemental fractionation in the solar wind acceleration process. J. Geophys. Res. Space Phys. 105, 47–60.

Bottinga, Y., Richet, P., 1981. High pressure and temperature equation of state and calculation of the thermodynamic properties of gaseous carbon dioxide. Am. J. Sci. 281, 615–660.

Bühler, F., Eberhardt, P., Geiss, J., Meister, J., Signer, P., 1969. Apollo 11 solar wind composition experiment: First results. Science 166, 1502–1503.

Burbidge, E.M., Burbidge, G.R., Fowler, W.A., Hoyle, F., 1957. Synthesis of the elements in stars. Rev. Mod. Phys. 29, 547.

Burnard, P., 2001. Correction for volatile fractionation in ascending magmas: noble gas abundances in primary mantle melts. Geochim. Cosmochim. Acta 65, 2605–2614.

Burnard, P., 1999. The bubble-by-bubble volatile evolution of two mid-ocean ridge basalts. Earth Planet. Sci. Lett. 174, 199–211.

Burnard, P., Graham, D., Turner, G., 1997. Vesicle-specific noble gas analyses of" popping rock": implications for primordial noble gases in Earth. Science 276, 568–571.

Busemann, H., Baur, H., Wieler, R., 2000. Primordial noble gases in “phase Q” in carbonaceous and ordinary chondrites studied by closed-system stepped etching. Meteorit. Planet. Sci. 35, 949–973.

Butler, W., Jeffery, P., Reynolds, J., Wasserburg, G., 1963. Isotopic variations in terrestrial xenon. J. Geophys. Res. 68, 3283–3291.

Canup, R.M., Asphaug, E., 2001. Origin of the Moon in a giant impact near the end of the Earth’s formation. Nature 412, 708–712.

Carroll, M.R., Webster, J.D., 1994. Solubilities of sulfur, noble gases, nitrogen, chlorine, and fluorine in magmas. Rev. Mineral. 30, 231–231.

Chambers, J., 2010. Planetesimal formation by turbulent concentration. Icarus 208, 505–517.

Chavrit, D., 2010. Cartographie globale des flux de CO2 à l’axe des dorsales océaniques: une approche pétrologique.

Chavrit, D., Humler, E., Morizet, Y., Laporte, D., 2012. Influence of magma ascent rate on carbon dioxide degassing at oceanic ridges: Message in a bubble. Earth Planet. Sci. Lett. 357, 376–385.

Clayton, D.D., 1983. Principles of stellar evolution and nucleosynthesis. University of Chicago press.

Colin, A., Moreira, M., Gautheron, C., Burnard, P., 2015. Constraints on the noble gas composition of the deep mantle by bubble-by-bubble analysis of a volcanic glass sample from Iceland. Chem. Geol. 417, 173–183.

Craig, H., Lupton, J., 1976. Primordial neon, helium, and hydrogen in oceanic basalts. Earth Planet. Sci. Lett. 31, 369–385.

Cuzzi, J.N., Hogan, R.C., Shariff, K., 2008. Toward planetesimals: Dense chondrule clumps in the protoplanetary nebula. Astrophys. J. 687, 1432.

Dauphas, N., Burkhardt, C., Warren, P.H., Fang-Zhen, T., 2014. Geochemical arguments for an Earth-like Moon-forming impactor. Philos. Trans. R. Soc. Math. Phys. Eng. Sci. 372, 20130244.

Dauphas, N., Chaussidon, M., 2011. A perspective from extinct radionuclides on a young stellar object: the Sun and its accretion disk. Annu. Rev. Earth Planet. Sci. 39, 351–386.

Dauphas, N., Morbidelli, A., 2013. Geochemical and planetary dynamical views on the origin of Earth's atmosphere and oceans. ArXiv Prepr. ArXiv13121202.

Dauphas, N., Pourmand, A., 2011. Hf–W–Th evidence for rapid growth of Mars and its status as a planetary embryo. Nature 473, 489–492.

D'E Atkinson, R., Houtermans, F., 1929. Transmutation of the Lighter Elements in Stars. Nature 123, 567–568.

Di Carlo, I., Pichavant, M., Rotolo, S.G., Scaillet, B., 2006. Experimental crystallization of a high-K arc basalt: the golden pumice, Stromboli volcano (Italy). J. Petrol. 47, 1317–1343.

Dickin, A.P., 2018. Radiogenic isotope geology. Cambridge university press.

Dixon, J.E., Pan, V., 1995a. Determination of the molar absorptivity of dissolved carbonate in basanitic glass. Am. Mineral. 80, 1339–1342.

Dixon, J.E., Pan, V., 1995b. Determination of the molar absorptivity of dissolved carbonate in basanitic glass. Am. Mineral. 80, 1339–1342.

Dixon, J.E., Stolper, E.M., Holloway, J.R., 1995. An experimental study of water and carbon dioxide solubilities in mid-ocean ridge basaltic liquids. Part I: calibration and solubility models. J. Petrol. 36, 1607–1631.

Donahue, T., Russell, C., 1997. The Venus atmosphere and ionosphere and their interaction with the solar wind: An overview. Venus II Geol. Geophys. Atmosphere Sol. Wind Environ. 3.

Douglass, J., Schilling, J., Fontignie, D., 1999. Plume-ridge interactions of the Discovery and Shona mantle plumes with the southern Mid-Atlantic Ridge (40°-55° S). J. Geophys. Res. Solid Earth 104, 2941–2962.

Eberhardt, P., Geiss, J., Graf, H., Grögler, N., Krähenbühl, U., Schwaller, H., Schwarzmüller, J., Stettler, A., 1970. Trapped solar wind noble gases, exposure age and K/Ar-age in Apollo 11 lunar fine material. Presented at the Geochimica et Cosmochimica Acta Supplement, Volume 1. Proceedings of the Apollo 11 Lunar Science Conference held 5-8 January, 1970 in Houston, TX. Volume 2: Chemical and Isotope Analyses. Edited by AA Levinson. New York: Pergammon Press, 1970., p. 1037, p. 1037.

Eberhardt, P., Geiss, J., Graf, H., Grögler, N., Mendia, M., Mörgeli, M., Schwaller, H., Stettler, A., Krähenbühl, U., Von Gunten, H., 1972. Trapped solar wind noble gases in Apollo 12 lunar fines 12001 and Apollo 11 breccia 10046. Bern Univ.(Switzerland).

Farrell, W.M., Hurley, D.M., Zimmerman, M.I., 2015. Solar wind implantation into lunar regolith: Hydrogen retention in a surface with defects. Icarus 255, 116–126.

Fine, G., Stolper, E., 1985. The speciation of carbon dioxide in sodium aluminosilicate glasses. Contrib. Mineral. Petrol. 91, 105–121.

Frost, B.R., 2018. Introduction to oxygen fugacity and its petrologic importance, in: Oxide Minerals. De Gruyter, pp. 1–10.

Geiss, J., Bühler, F., Cerutti, H., Eberhardt, P., Filleux, C., Meister, J., Signer, P., 2004. The Apollo SWC experiment: results, conclusions, consequences. Space Sci. Rev. 110, 307–335.

Geiss, J, Eberhardt, P., Bühler, F., Meister, J., Signer, P., 1970. Apollo 11 and 12 solar wind composition experiments: Fluxes of He and Ne isotopes. J. Geophys. Res. 75, 5972–5979.

Geiss, Johannes, Hirt, P., Leutwyler, H., 1970. On acceleration and motion of ions in corona and solar wind. Sol. Phys. 12, 458–483.

Giordano, D., Russell, J.K., Dingwell, D.B., 2008. Viscosity of magmatic liquids: a model. Earth Planet. Sci. Lett. 271, 123–134.

Gonnermann, H.M., Manga, M., 2007. The fluid mechanics inside a volcano. Annu Rev Fluid Mech 39, 321–356.

Graham, D.W., 2002. Noble Gas Isotope Geochemistry of Mid-Ocean Ridge and Ocean Island Basalts: Characterization of Mantle Source Reservoirs. Rev. Mineral. Geochem. 47, 247–317. https://doi.org/10.2138/rmg.2002.47.8

Grimberg, A., Baur, H., Bochsler, P., Bühler, F., Burnett, D.S., Hays, C.C., Heber, V.S., Jurewicz, A.J., Wieler, R., 2006. Solar wind neon from Genesis: Implications for the lunar noble gas record. Science 314, 1133–1135.

Harper Jr, C.L., Jacobsen, S.B., 1996. Noble gases and Earth's accretion. Science 273, 1814–1818.

Hashizume, K., Chaussidon, M., Marty, B., Robert, F., 2000. Solar wind record on the Moon: deciphering presolar from planetary nitrogen. Science 290, 1142–1145.

Heber, V.S., Baur, H., Bochsler, P., McKeegan, K.D., Neugebauer, M., Reisenfeld, D.B., Wieler, R., Wiens, R.C., 2012. Isotopic mass fractionation of solar wind: Evidence from fast and slow solar wind collected by the Genesis mission. Astrophys. J. 759, 121.

Heber, V.S., Wieler, R., Baur, H., Olinger, C., Friedmann, T.A., Burnett, D.S., 2009. Noble gas composition of the solar wind as collected by the Genesis mission. Geochim. Cosmochim. Acta 73, 7414–7432.

Holland, G., Ballentine, C.J., 2006a. Seawater subduction controls the heavy noble gas composition of the mantle. Nature 441, 186–191.

Holland, G., Ballentine, C.J., 2006b. Seawater subduction controls the heavy noble gas composition of the mantle. Nature 441, 186–191.

Holland, G., Cassidy, M., Ballentine, C.J., 2009. Meteorite Kr in Earth's mantle suggests a late accretionary source for the atmosphere. Science 326, 1522–1525.

Hollenbach, D.J., Yorke, H.W., Johnstone, D., 2000. Disk dispersal around young stars. Protostars Planets IV 401, 12.

Honda, M., McDougall, I., Patterson, D.B., Doulgeris, A., Clague, D.A., 1991. Possible solar noble-gas component in Hawaiian basalts. Nature 349, 149–151.

Honda, M., Reynolds, J., Roedder, E., Epstein, S., 1987. Noble gases in diamonds: Occurrences of solarlike helium and neon. J. Geophys. Res. Solid Earth 92, 12507–12521.

Iacono-Marziano, G., Paonita, A., Rizzo, A., Scaillet, B., Gaillard, F., 2010. Noble gas solubilities in silicate melts: new experimental results and a comprehensive model of the effects of liquid composition, temperature and pressure. Chem. Geol. 279, 145–157.

Jambon, A., Weber, H., Braun, O., 1986. Solubility of He, Ne, Ar, Kr and Xe in a basalt melt in the range 1250–1600 C. Geochemical implications. Geochim. Cosmochim. Acta 50, 401–408.

Jaupart, E., Charnoz, S., Moreira, M., 2017. Primordial atmosphere incorporation in planetary embryos and the origin of Neon in terrestrial planets. Icarus 293, 199–205.

Javoy, M., Pineau, F., 1991. The volatiles record of a "popping" rock from the Mid-Atlantic Ridge at 14 N: chemical and isotopic composition of gas trapped in the vesicles. Earth Planet. Sci. Lett. 107, 598–611.

Jiménez-Mejías, M., Andújar, J., Scaillet, B., Casillas, R., 2021. Experimental determination of H $ _ {{2}} $ O and CO $ _ {{2}} $ solubilities of mafic alkaline magmas from Canary Islands. Comptes Rendus Géoscience 353, 289–314.

Johansen, A., Klahr, H., 2011. Planetesimal formation through streaming and gravitational instabilities. Earth Moon Planets 108, 39–43.

Johansen, A., Klahr, H., Henning, T., 2011. High-resolution simulations of planetesimal formation in turbulent protoplanetary discs. Astron. Astrophys. 529, A62.

Johansen, A., Oishi, J.S., Low, M.-M.M., Klahr, H., Henning, T., Youdin, A., 2007. Rapid planetesimal formation in turbulent circumstellar disks. Nature 448, 1022–1025.

Kendrick, M.A., Burnard, P., 2013. Noble gases and halogens in fluid inclusions: a journey through the Earth's crust. Noble Gases Geochem. Tracers 319–369.

Kennedy, B., Hiyagon, H., Reynolds, J., 1990. Crustal neon: a striking uniformity. Earth Planet. Sci. Lett. 98, 277–286.

Kennedy, B.M., Hiyagon, H., Reynolds, J.H., 1990. Crustal neon: a striking uniformity. Earth Planet. Sci. Lett. 98, 277–286. https://doi.org/10.1016/0012-821X(90)90030-2

Kipfer, R., Aeschbach-Hertig, W., Peeters, F., Stute, M., 2002. Noble gases in lakes and ground waters. Rev. Mineral. Geochem. 47, 615–700.

Kress, V.C., Carmichael, I.S., 1991. The compressibility of silicate liquids containing Fe 2 O 3 and the effect of composition, temperature, oxygen fugacity and pressure on their redox states. Contrib. Mineral. Petrol. 108, 82–92.

Krummenacher, D., 1970. Isotopic composition of argon in modern surface volcanic rocks. Earth Planet. Sci. Lett. 8, 109–117.

Kunz, J., 1999. Is there solar argon in the Earth's mantle? Nature 399, 649–650. https://doi.org/10.1038/21352

Kuroda, P., 1960. Nuclear fission in the early history of the earth. Nature 187.

Kurz, M.D., 1986. Cosmogenic helium in a terrestrial igneous rock. Nature 320, 435–439. https://doi.org/10.1038/320435a0

Kurz, M.D., Curtice, J., Fornari, D., Geist, D., Moreira, M., 2009. Primitive neon from the center of the Galápagos hotspot. Earth Planet. Sci. Lett. 286, 23–34.

Lange, R.A., 1994a. Volatiles in Magmas, in: Carroll, M.R., Holloway, J.R. (Eds.), . De Gruyter, pp. 331–370. https://doi.org/10.1515/9781501509674-015

Lange, R.A., 1994b. Volatiles in Magmas, in: Carroll, M.R., Holloway, J.R. (Eds.), . De Gruyter, pp. 331–370. https://doi.org/10.1515/9781501509674-015

Le Gall, N., 2015. Ascension et dégazage des magmas basaltiques: approche expérimentale.

Le Gall, N., Pichavant, M., 2016a. Experimental simulation of bubble nucleation and magma ascent in basaltic systems: Implications for Stromboli volcano. Am. Mineral. 101, 1967–1985.

Le Gall, N., Pichavant, M., 2016b. Homogeneous bubble nucleation in H2O-and H2O-CO2-bearing basaltic melts: results of high temperature decompression experiments. J. Volcanol. Geotherm. Res. 327, 604–621.

Le Roux, P., Le Roex, A., Schilling, J.-G., Shimizu, N., Perkins, W., Pearce, N., 2002. Mantle heterogeneity beneath the southern Mid-Atlantic Ridge: trace element evidence for contamination of ambient asthenospheric mantle. Earth Planet. Sci. Lett. 203, 479–498.

Lensky, N.G., Niebo, R.W., Holloway, J.R., Lyakhovsky, V., Navon, O., 2006. Bubble nucleation as a trigger for xenolith entrapment in mantle melts. Earth Planet. Sci. Lett. 245, 278–288.

Lux, G., 1987. The behavior of noble gases in silicate liquids: Solution, diffusion, bubbles and surface effects, with applications to natural samples. Geochim. Cosmochim. Acta 51, 1549–1560.

Mangan, M., Sisson, T., 2000. Delayed, disequilibrium degassing in rhyolite magma: decompression experiments and implications for explosive volcanism. Earth Planet. Sci. Lett. 183, 441–455.

Marsh, B.D., 2007. Crystallization of silicate magmas deciphered using crystal size distributions. J. Am. Ceram. Soc. 90, 746–757.

Marsh, B.D., 1988. Crystal size distribution (CSD) in rocks and the kinetics and dynamics of crystallization: I. Theory. Contrib. Mineral. Petrol. 99, 277–291.

Marty, B., 2022. Meteoritic noble gas constraints on the origin of terrestrial volatiles. Icarus 381, 115020.

Marty, B., 2020. ORIGINS AND EARLY EVOLUTION OF THE ATMOSPHERE AND THE OCEANS. Geochem. Perspect. 9, 135–136.

Marty, B., 2012. The origins and concentrations of water, carbon, nitrogen and noble gases on Earth. Earth Planet. Sci. Lett. 313, 56–66.

Marty, B., Yokochi, R., 2006. Water in the early Earth. Rev. Mineral. Geochem. 62, 421–450.

Marty, B., Zimmermann, L., 1999. Volatiles (He, C, N, Ar) in mid-ocean ridge basalts: Assesment of shallow-level fractionation and characterization of source composition. Geochim. Cosmochim. Acta 63, 3619–3633.

McDonnell, J., Flavill, R., 1974. Sputter Erosion on the Lunar Surface: Measurements and Features Under Simulated Solar He+ Bombardment. Lunar Planet. Sci. V Houst. Lunar Planet Inst 478.

Mizuno, H., Nakazawa, K., Hayashi, C., 1980. Dissolution of the primordial rare gases into the molten Earth's material. Earth Planet. Sci. Lett. 50, 202–210.

Morbidelli, A., Bottke, W.F., Nesvorný, D., Levison, H.F., 2009. Asteroids were born big. Icarus 204, 558–573.

Moreira, M., 2013. Noble gas constraints on the origin and evolution of Earth's volatiles. Geochem. Perspect. 2, 229–230.

Moreira, M., Blusztajn, J., Curtice, J., Hart, S., Dick, H., Kurz, M.D., 2003. He and Ne isotopes in oceanic crust: implications for noble gas recycling in the mantle. Earth Planet. Sci. Lett. 216, 635–643.

Moreira, M., Charnoz, S., 2016. The origin of the neon isotopes in chondrites and on Earth. Earth Planet. Sci. Lett. 433, 249–256. https://doi.org/10.1016/j.epsl.2015.11.002

Moreira, M., Kunz, J., Allegre, C., 1998. Rare gas systematics in popping rock: isotopic and elemental compositions in the upper mantle. Science 279, 1178–1181.

Moreira, M., Rouchon, V., Muller, E., Noirez, S., 2018. The xenon isotopic signature of the mantle beneath Massif Central. Geochem Perspect Lett 6, 28–32.

Moreira, M., Sarda, P., 2000. Noble gas constraints on degassing processes. Earth Planet. Sci. Lett. 176, 375–386.

Moreira, M., Staudacher, T., Sarda, P., Schilling, J.-G., Allègre, C.J., 1995. A primitive plume neon component in MORB: The Shona ridge-anomaly, South Atlantic (51–52° S). Earth Planet. Sci. Lett. 133, 367–377.

Moretti, R., Papale, P., Ottonello, G., 2003. A model for the saturation of COHS fluids in silicate melts. Geol. Soc. Lond. Spec. Publ. 213, 81–101.

Mourtada-Bonnefoi, C., Laporte, D., 2002. Homogeneous bubble nucleation in rhyolitic magmas: an experimental study of the effect of H2O and CO2. J. Geophys. Res. Solid Earth 107, ECV-2.

Mourtada-Bonnefoi, C.C., Laporte, D., 2004. Kinetics of bubble nucleation in a rhyolitic melt: an experimental study of the effect of ascent rate. Earth Planet. Sci. Lett. 218, 521–537.

Mukhopadhyay, S., 2012. Early differentiation and volatile accretion recorded in deep-mantle neon and xenon. Nature 486, 101–104. https://doi.org/10.1038/nature11141

Nowak, M., Schreen, D., Spickenbom, K., 2004. Argon and CO2 on the race track in silicate melts: a tool for the development of a CO2 speciation and diffusion model. Geochim. Cosmochim. Acta 68, 5127–5138.

Nuccio, P., Paonita, A., 2001. Magmatic degassing of multicomponent vapors and assessment of magma depth: application to Vulcano Island (Italy). Earth Planet. Sci. Lett. 193, 467–481.

Nuccio, P., Paonita, A., 2000. Investigation of the noble gas solubility in H2O–CO2 bearing silicate liquids at moderate pressure II: the extended ionic porosity (EIP) model. Earth Planet. Sci. Lett. 183, 499–512.

Olson, P.L., Sharp, Z.D., 2019. Nebular atmosphere to magma ocean: a model for volatile capture during Earth accretion. Phys. Earth Planet. Inter. 294, 106294.

Ozima, M., Podosek, F.A., 2002. Noble gas geochemistry. Cambridge University Press.

Ozima, M., Zashu, S., 1991. Noble gas state of the ancient mantle as deduced from noble gases in coated diamonds. Earth Planet. Sci. Lett. 105, 13–27.

Ozima, M., Zashu, S., 1988a. Solar-type Ne in Zaire cubic diamonds. Geochim. Cosmochim. Acta 52, 19–25.

Ozima, M., Zashu, S., 1988b. Solar-type Ne in Zaire cubic diamonds. Geochim. Cosmochim. Acta 52, 19–25.

Paonita, A., 2005. Noble gas solubility in silicate melts: a review of experimentation and theory, and implications regarding magma degassing processes. Ann. Geophys.

Paonita, A., Gigli, G., Gozzi, D., Nuccio, P., Trigila, R., 2000. Investigation of the He solubility in H2O–CO2 bearing silicate liquids at moderate pressure: a new experimental method. Earth Planet. Sci. Lett. 181, 595–604.

Pepin, R., Nyquist, L., Phinney, D., Black, D.C., 1970. Isotopic composition of rare gases in lunar samples. Science 167, 550–553.

Pepin, R.O., 1991. On the origin and early evolution of terrestrial planet atmospheres and meteoritic volatiles. Icarus 92, 2–79.

Pepin, R.O., Schlutter, D.J., Becker, R.H., Reisenfeld, D.B., 2012. Helium, neon, and argon composition of the solar wind as recorded in gold and other Genesis collector materials. Geochim. Cosmochim. Acta 89, 62–80.

Péron, S., Moreira, M., Agranier, A., 2018. Origin of light noble gases (He, Ne, and Ar) on Earth: A review. Geochem. Geophys. Geosystems 19, 979–996.

Péron, S., Moreira, M., Colin, A., Arbaret, L., Putlitz, B., Kurz, M.D., 2016. Neon isotopic composition of the mantle constrained by single vesicle analyses. Earth Planet. Sci. Lett. 449, 145–154. https://doi.org/10.1016/j.epsl.2016.05.052

Péron, S., Moreira, M., Putlitz, B., Kurz, M., 2017. Solar wind implantation supplied light volatiles during the first stage of Earth accretion. Geochem. Perspect. Lett. 151–159.

Péron, S., Moreira, M.A., Kurz, M.D., Curtice, J., Blusztajn, J.S., Putlitz, B., Wanless, V.D., Jones, M.R., Soule, S.A., Mittelstaedt, E., 2019. Noble gas systematics in new popping rocks from the Mid-Atlantic Ridge (14° N): evidence for small-scale upper mantle heterogeneities. Earth Planet. Sci. Lett. 519, 70–82.

Pichavant, M., Di Carlo, I., Le Gac, Y., Rotolo, S.G., Scaillet, B., 2009. Experimental constraints on the deep magma feeding system at Stromboli volcano, Italy. J. Petrol. 50, 601–624.

Pichavant, M., Di Carlo, I., Rotolo, S.G., Scaillet, B., Burgisser, A., Le Gall, N., Martel, C., 2013. Generation of CO 2-rich melts during basalt magma ascent and degassing. Contrib. Mineral. Petrol. 166, 545–561.

Pichavant, M., Le Gall, N., Scaillet, B., 2018. Gases as precursory signals: experimental simulations, new concepts and models of magma degassing. Volcan. Unrest Adv Volcanol 139–154.

Pierre Jules César Janssen, 1908. . Mon. Not. R. Astron. Soc. 68, 245–249. https://doi.org/10.1093/mnras/68.4.245

Porcelli, D., Ballentine, C.J., Wieler, R., 2002. An overview of noble gas geochemistry and cosmochemistry. Rev. Mineral. Geochem. 47, 1–19.

Porcelli, D., Woolum, D., Cassen, P., 2001. Deep Earth rare gases: initial inventories, capture from the solar nebula, and losses during Moon formation. Earth Planet. Sci. Lett. 193, 237–251.

Poreda, R., di Brozolo, F.R., 1984. Neon isotope variations in Mid-Atlantic Ridge basalts. Earth Planet. Sci. Lett. 69, 277–289.

Raquin, A., Moreira, M., 2009. Atmospheric 38Ar/36Ar in the mantle: implications for the nature of the terrestrial parent bodies. Earth Planet. Sci. Lett. 287, 551–558.

Raquin, A., Moreira, M.A., Guillon, F., 2008. He, Ne and Ar systematics in single vesicles: mantle isotopic ratios and origin of the air component in basaltic glasses. Earth Planet. Sci. Lett. 274, 142–150.

Raymond, S.N., O'Brien, D.P., Morbidelli, A., Kaib, N.A., 2009. Building the terrestrial planets: Constrained accretion in the inner Solar System. Icarus 203, 644–662.

Reynolds, J., Hohenberg, C., Lewis, R., Davis, P., Kaiser, W., 1970. Isotopic analysis of rare gases from stepwise heating of lunar fines and rocks. Science 167, 545–548.

Reynolds, J., Turner, G., 1964. Rare gases in the chondrite Renazzo. J. Geophys. Res. 69, 3263–3281.

Rolfs, C.E., Rodney, W.S., 1988. Cauldrons in the cosmos: Nuclear astrophysics. University of Chicago press.

Roubinet, C., Moreira, M.A., 2018. Atmospheric noble gases in Mid-Ocean Ridge Basalts: identification of atmospheric contamination processes. Geochim. Cosmochim. Acta 222, 253–268.

Ruzié, L., Moreira, M., 2010. Magma degassing process during Plinian eruptions. J. Volcanol. Geotherm. Res. 192, 142–150.

Saltykov, S., 1967. Stereology: proceedings of the second international congress for stereology, chapter The determination of the size distribution of particles in an opaque material from a measurement of the size distribution of their sections.

Sarda, P., Graham, D., 1990. Mid-ocean ridge popping rocks: implications for degassing at ridge crests. Earth Planet. Sci. Lett. 97, 268–289.

Sarda, P., Moreira, M., 2002. Vesiculation and vesicle loss in mid-ocean ridge basalt glasses: He, Ne, Ar elemental fractionation and pressure influence. Geochim. Cosmochim. Acta 66, 1449–1458.

Sarda, P., Moreira, M., Staudacher, T., Schilling, J., Allègre, C.J., 2000. Rare gas systematics on the southernmost Mid-Atlantic Ridge: Constraints on the lower mantle and the Dupal source. J. Geophys. Res. Solid Earth 105, 5973–5996.

Sarda, P., Staudacher, T., Allègre, C.J., 1988. Neon isotopes in submarine basalts. Earth Planet. Sci. Lett. 91, 73–88. https://doi.org/10.1016/0012-821X(88)90152-5

Sasaki, S., 1999. Presence of a primary solar-type atmosphere around the earth: evidence of dissolved noble gas. Planet. Space Sci. 47, 1423–1431.

Sasaki, S., Nakazawa, K., 1990. Did a primary solar-type atmosphere exist around the proto-earth? Icarus 85, 21–42. https://doi.org/10.1016/0019-1035(90)90101-E

Scarpa, R., Tilling, R.I., Giggenbach, W., 1996. Chemical composition of volcanic gases. Monit. Mitig. Volcano Hazards 221–256.

Schlosser, P., Winckler, G., 2002. Noble gases in ocean waters and sediments. Rev. Mineral. Geochem. 47, 701–730.

Shinohara, H., Aiuppa, A., Giudice, G., Gurrieri, S., Liuzzo, M., 2008. Variation of H2O/CO2 and CO2/SO2 ratios of volcanic gases discharged by continuous degassing of Mount Etna volcano, Italy. J. Geophys. Res. Solid Earth 113.

Shishkina, T.A., Botcharnikov, R.E., Holtz, F., Almeev, R.R., Jazwa, A.M., Jakubiak, A.A., 2014. Compositional and pressure effects on the solubility of H2O and CO2 in mafic melts. Chem. Geol. 388, 112–129.

Sparks, R.S.J., 1978. The dynamics of bubble formation and growth in magmas: a review and analysis. J. Volcanol. Geotherm. Res. 3, 1–37.

Staudacher, T., Allègre, C.J., 1988. Recycling of oceanic crust and sediments: the noble gas subduction barrier. Earth Planet. Sci. Lett. 89, 173–183.

Staudacher, T., Sarda, P., Richardson, S., Allègre, C., Sagna, I., Dmitriev, L., 1989. Noble gases in basalt glasses from a Mid-Atlantic Ridge topographic high at 14 N: geodynamic consequences. Earth Planet. Sci. Lett. 96, 119–133.

Stolper, E., 1982. Water in silicate glasses: an infrared spectroscopic study. Contrib. Mineral. Petrol. 81, 1–17.

Stout, V.L., Gibbons, M.D., 1955. Gettering of gas by titanium. J. Appl. Phys. 26, 1488–1492.

Sumino, H., Kaneoka, I., Matsufuji, K., Sobolev, A.V., 2006. Deep mantle origin of kimberlite magmas revealed by neon isotopes. Geophys. Res. Lett. 33.

Tolstikhin, I., O'Nions, R., 1994. The Earth's missing xenon: A combination of early degassing and of rare gas loss from the atmosphere. Chem. Geol. 115, 1–6.

Trieloff, M., Kunz, J., Clague, D.A., Harrison, D., Allègre, C.J., 2000. The Nature of Pristine Noble Gases in Mantle Plumes. Science 288, 1036–1038. https://doi.org/10.1126/science.288.5468.1036

Warren, P.H., 1995. Extrapolated partial molar densities of SO3, P2O5, and other oxides in silicate melts. Am. Mineral. 80, 1085–1088.

Watson, E.B., Sneeringer, M.A., Ross, A., 1982. Diffusion of dissolved carbonate in magmas: experimental results and applications. Earth Planet. Sci. Lett. 61, 346–358.

Wetherill, G.W., 1954a. Variations in the isotopic abundances of neon and argon extracted from radioactive minerals. Phys. Rev. 96, 679.

Wetherill, G.W., 1954b. Variations in the isotopic abundances of neon and argon extracted from radioactive minerals. Phys. Rev. 96, 679.
Wetherill, G.W., 1953a. Spontaneous fission yields from uranium and thorium. Phys. Rev. 92, 907.
Wetherill, G.W., 1953b. Spontaneous fission yields from uranium and thorium. Phys. Rev. 92, 907.
Wieler, R., 2002. Cosmic-ray-produced noble gases in meteorites. Rev. Mineral. Geochem. 47, 125–170.
Wieler, R., 1998. The solar noble gas record in lunar samples and meteorites. Space Sci. Rev. 85, 303–314.
Williams, C.D., Mukhopadhyay, S., 2019. Capture of nebular gases during Earth's accretion is preserved in deep-mantle neon. Nature 565, 78–81. https://doi.org/10.1038/s41586-018-0771-1
Yatsevich, I., Honda, M., 1997a. Production of nucleogenic neon in the Earth from natural radioactive decay. J. Geophys. Res. Solid Earth 102, 10291–10298.
Yatsevich, I., Honda, M., 1997b. Production of nucleogenic neon in the Earth from natural radioactive decay. J. Geophys. Res. Solid Earth 102, 10291–10298.
Yokochi, R., Marty, B., 2004. A determination of the neon isotopic composition of the deep mantle. Earth Planet. Sci. Lett. 225, 77–88. https://doi.org/10.1016/j.epsl.2004.06.010
Yoshimura, S., 2015. Diffusive fractionation of H2O and CO2 during magma degassing. Chem. Geol. 411, 172–181.
Zadnik, M., Jeffery, P., 1985. Radiogenic neon in an Archaean anorthosite. Chem. Geol. Isot. Geosci. Sect. 52, 119–125.
Zhang, Y., Ni, H., Chen, Y., 2010. Diffusion data in silicate melts. Rev. Mineral. Geochem. 72, 311–408.
Zhang, Y., Xu, Z., 1995. Atomic radii of noble gas elements in condensed phases. Am. Mineral. 80, 670–675.
Zhang, Y., Xu, Z., Zhu, M., Wang, H., 2007. Silicate melt properties and volcanic eruptions. Rev. Geophys. 45.
Zhang, Y., Zindler, A., 1989. Noble gas constraints on the evolution of the Earth's atmosphere. J. Geophys. Res. Solid Earth 94, 13719–13737.

Chapitre 6 : Discussion générale et conclusion. Des expériences à la nature.

Ce chapitre résume les résultats des deux types d'expériences réalisées pour étudier le fractionnement du néon sous des conditions de haute pression (≈ 2 kbars) et de haute température (1200°C), avec le CO_2 comme phase volatile principale.

Pour comparer ces expériences à un système naturel, huit roches caractéristiques de la dorsale médio-atlantique ont été scannées par micro-CT. Parmi ces échantillons, les "Popping rocks" ont été utilisées comme référence en raison de leur haute vésicularité et de leur forte concentration en gaz, fournissant des indices précieux sur les processus magmatiques dans le manteau supérieur.

Les paramètres de distribution de taille de vésicule (VSD) ont été comparés entre les échantillons naturels et synthétiques, révélant des différences significatives en termes de densité de population de bulles et de pente de croissance. Les expériences ont montré que le temps est un facteur crucial pour interpréter la composition isotopique, influençant l'équilibre et la distribution hétérogène des espèces volatiles dans le magma.

Les observations indiquent que le temps de résidence des vésicules dans le magma et le temps de montée du magma influencent le fractionnement isotopique. Les expériences et les données naturelles suggèrent que les MORBs affectés par les panaches présentent des compositions isotopiques variées en raison de mécanismes de distillation et d'un mélange incomplet des systèmes impliqués.

Ce résumé synthétise les principales conclusions et implications des expériences ainsi que leur comparaison avec les systèmes naturels, en soulignant l'importance du facteur temps dans les processus magmatiques et le fractionnement isotopique des gaz rares.

Chapter 6: General discussion and conclusion. From experiments to nature.

6.1. Experimental samples:

For the development of this thesis, two types of experiments were conducted to study the fractionation of neon under high pressure (P ≈ 2 kbar) and high-temperature conditions (T = 1200ºC), with CO_2 acting as the main volatile phase.

The first series of experiments, the static experiments, had loads of 10 wt.% of Ne-bearing glass and variables CO_2 loads above 1 wt.%. being the glass the same composition as the powder used for the experiments. The experiments were conducted at different durations before the CO_2 had time to homogenise through the charge.

The second type of experiment focused on the decompression of charges of a CO_2-Ne-bearing glass prepared with initial CO_2 dissolved contents of 2700 ppm and the same amount of neon as the previous series (10 wt.% of Ne-bearing glass). The capsules were firstly brought to equilibrium (>24h at 1200ºC and 2kbars of pressure at the IHPV (Pichavant et al., 2018), and right away decompressed at two constant decompression rates and quenched at different pressures.

The two types of experiments aimed to simulate the degassing of CO_2-Ne-bearing basaltic melts resulting from recharging or during the decompression of a shallow magmatic chamber at isothermal conditions.

Either the textural analysis of the samples or the compositional analysis of the glasses and vesicles conducted in both static and decompression experiments revealed interesting observations regarding the behaviour and evolution of the volatile species involved.

Chapters 3 and *4* demonstrate that the CO_2 concentration in the different time series was highly variable throughout the experimental disequilibrium period. The range of CO_2 dissolved into the glasses ranged from 1709 down to 585 ppm, with measures differing up to 50% in the same charge showing the heterogeneity distribution of CO_2 in the glass. As the experimental time increased, the distribution of CO_2 in the glasses became more homogeneous (**Figure 6.1.a**), getting close to the equilibrium value. However, they remained still below this value (as defined by Jiménez-Mejías et al., 2021).

These static experiments revealed a previously unobserved evolution of vesicularity, as no similar experiments had been conducted before. The heterogeneous distribution of CO_2 in the glass was not related to the vesicularity (**Figure 6.1.b**) as can be observed by the correlation coefficient $R^2 = 0.04$. As the silver oxalate reaches its breakdown temperature, the CO_2 is released from the compound and passed through the micro grains of the silicate powder while they are going through the glass-melt transition. While CO_2 is being released, the gas follows two paths: (i) the nucleation and growth of bubbles by inward gas diffusion and (ii) the diffusion into the silicate melts and the capsule-melt interface.

The expected theoretical vesicularity for the amount of CO_2 introduced in the statics samples should reach up to 34% of the sample volume (*ESFa-10-CO_2;* **table 3.7**). However, due to the high rate of vesicle generation and ascension, significant CO_2 released from the silver oxalate was cumulated at the capsule-melt interface. Part of this accumulated of gas corresponds to the Type I vesicle described by (Pichavant et al., 2013), which have up to 1.5 mm diameter (for experimental samples; e.g. *ESFa-5A-CO_2+Ne* in **Figure 4.9**). Furthermore, another portion of this "*lost vesicularity*" is attributable to the experimental fragments that are unable to be analysed due to their small size, which is a consequence of the fragility of the sample during the extraction of the glass from the capsule. In this manuscript, the difference between the theoretical vesicularity and the measured in the glass is the so-called "*lost vesicularity*". As a result, the maximum measured vesicularity in the glasses was 4.15% corresponding to sample *ESFa-1B-CO_2*.

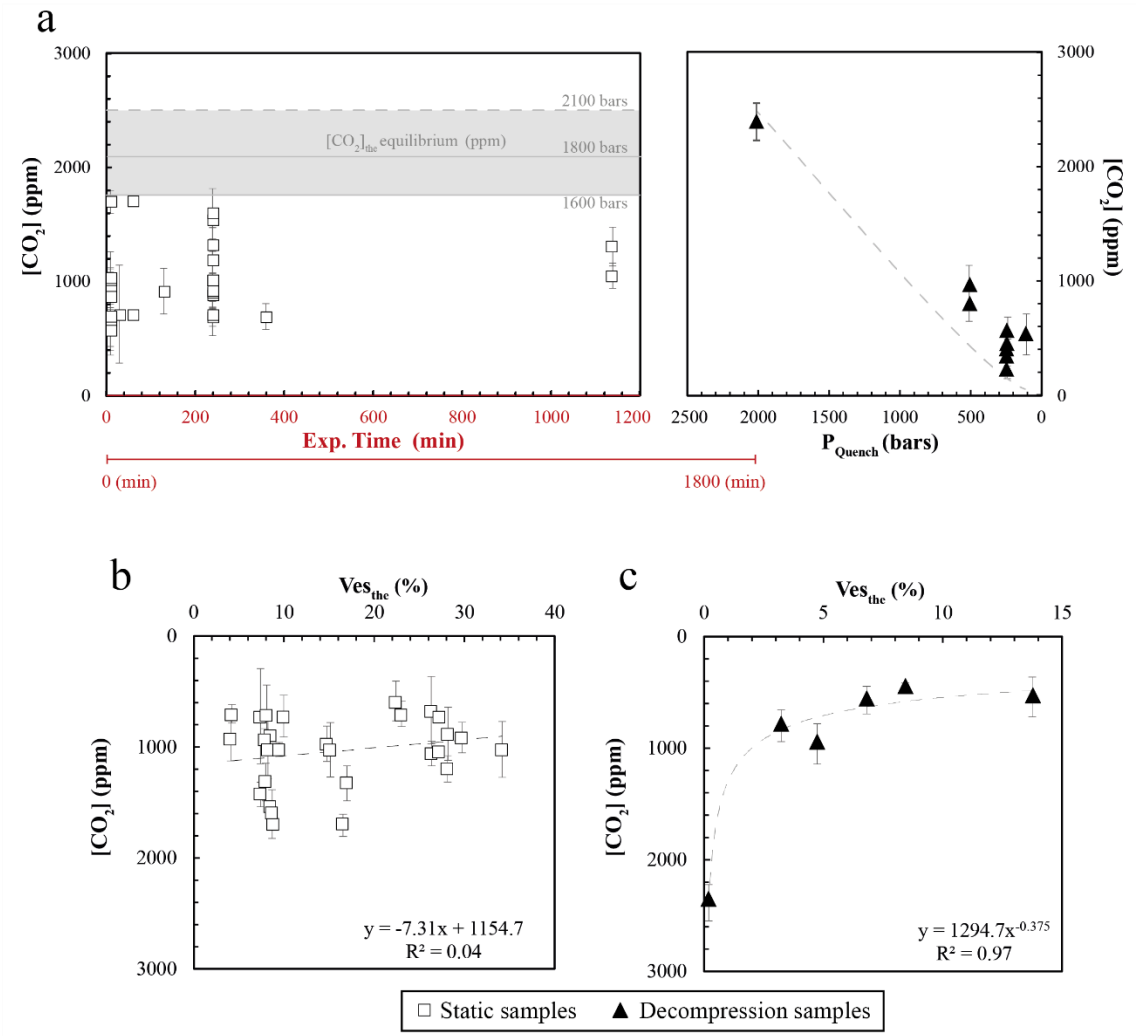

Figure 6.1: **(a)** The dissolved CO_2 evolution over time was observed for both static samples and samples lead to equilibrium and quenched at different pressures in the decompression series. The theoretical vesicularity was calculated for both the static samples **(b)** and the decompression series **(c)** in relation to the amount of dissolved CO_2. The graph displays the theoretical vesicularity of the samples, as the exsolved CO_2 to the capsule/melt interface is significant, and some glass fragments are lost. It is important to note that if the graph were shown with the vesicularity of the melt, it would exhibit the same trend.

One characteristic of this experimental series was the high representativeness of VSD types I and II (refer to *Chapter 3* and *4*) in comparison with decompression samples. For the static samples, the correlation coefficient, R^2, is above 0.83 in 35 out 39 samples. It explain that the high concentration of CO_2 loaded in the experimental capsules caused a homogeneous bubble nucleation (Pichavant et al., 2013; Le Gall and Pichavant, 2016b). That was observed for the continued nucleation of vesicles (vesicles diameter sizes <10 µm; vesicularity type 3 according to (Pichavant et al., 2013), leading straight slopes

between the population density and the diameter of the bubbles for a significant part of the experimental glasses (Sarda and Graham, 1990; Chavrit, 2010) as well as a full sort population of vesicles for such diagrams.

The most notable effect of this experimental series, in terms of textural analysis, was the effect of buoyancy as the experiment reached the equilibrium time, and this is reflected in the accumulation of bubbles towards the upper end of the capsule. The largest sizes were present at the top of the samples progressively in the longer experiments, while nucleation was increasingly low, and bubbles were absent towards the bottom of the capsules.

Pichavant et al. (2013) suggest that degassing in experimental basaltic magmas is limited kinetically by the diffusion of volatiles in the melt, occurring through the diffusion of volatiles at the gas-melt interface, either between bubbles or at the gas-melt interface. Mangan and Sisson (2000) and Pichavant et al. (2013) describe two different behaviours for CO_2 during vesiculation. At the onset of nucleation, when the bubbles are small and widely dispersed (vesicularity is still low), the diffusion of CO_2, which is the less diffusive species in their experiments, appears to have different behaviour during degassing. At the melt-gas interface, CO_2 concentration values are close to equilibrium, while in the melt away from the bubbles, CO_2 concentrations are above equilibrium. The involved volatile species are decoupled regarding the diffusivity in the melt (non-equilibrium diffusion).

Our static samples yielded intriguing results regarding the behaviour of stable neon isotopes. A significant contribution observed in these experimental series is that if the input of CO_2-rich melt/CO_2-flow generates a high enough vesicularity, such that the buoyancy (i.e. ascent rate) of the vesicles exceeds the diffusion of the slower species, it will result in out-of-equilibrium degassing within the system.

As in Pichavant et al. (2013) experiments, CO_2 remains the slowest diffusing species in our experiments. Upon replacing water by neon as a secondary volatile species, the gas phase became enriched in Ne. In addition to this enrichment, the analysis of individual vesicles in the resulting products demonstrated a significant isotopic fractionation, consistent with the kinetic model shown in *Chapter 4* (**Figure 4.5**). The heterogeneous CO_2 distribution in the magma and the high vesicularity of the samples as well as the homogeneous nucleation of the vesicles during a significant part of the static

experiment provided the power of vesicle buoyancy to outrate the diffusion of CO_2 before the attainment of equilibrium between the CO_2-rich flow and the melt.

In contrast, the volatile concentration of the decompression glasses and vesicularity of the charges are closely related (**Figure 6.1.c**) as is evident from the high correlation coefficient of the trend data R^2 =0.97. These results may indicate that degassing is controlled by vesicularity with two clear end-members marked mainly by (i) the absence of vesicles, or the onset of nucleation and homogeneous CO_2 dissolved in agreement with equilibrium values; (ii) a second end-member where vesicularities are higher than 3% and the dissolved CO_2 is low but higher than the equilibrium values (Jiménez-Mejías et al., 2021).

In the decompression experiments, CO_2 concentration in the quenched glasses exceeded the solubilities obtained (see **Figure 6.1.b**), except for the end member where no bubbles were found and for the samples quenched at 250 bars with a low decompression rate (*EN-D1* and *EN-D2*). This effect has also been observed in other experimental studies where CO_2-bearing melts exhibit disequilibrium during magma ascent, e.g. Le Gall and Pichavant (2016b); Pichavant et al. (2013, 2009); Yoshimura (2015). That may indicate the degassing process is controlled by the distance between the gas phases (either the distance between vesicles or to the capsule-melt interphase) and the volatile diffusion distance in the melt (which is dependent on each volatile species).

In Pichavant's decompression experiments, CO_2 was the slowest diffusive species, compared to water. However, in our experiments, where water was mostly absent and Ne took the role of the other volatile species, CO_2 remained the slowest diffusive species.

When decompression starts, the volatiles partition between melt and gas. The degassing occurs by diffusive volatile transfer at the gas-melt interface and is kinetically limited by the diffusivity of the volatiles in the melt, leading to CO_2-oversaturated melts (Pichavant et al., 2013) as can be observed in **Figure 6.1.a.** The post-decompression glasses evolve from those initially dissolved in the pre-decompression glasses (as sample *EN-E3*) following two paths that depend on the established ascension rate. In contrast to static samples, samples that undergo decompression exhibit more uniform neon isotopic values that are closer to the reference standard (**Figure 6.2**). These experiments demonstrate that equilibrium degassing can occur when vesicularity and the bubble size

are large enough to ensure that the distance between the gas phase and melt is smaller than the volatile diffusion of the slower gas distance in the melt.

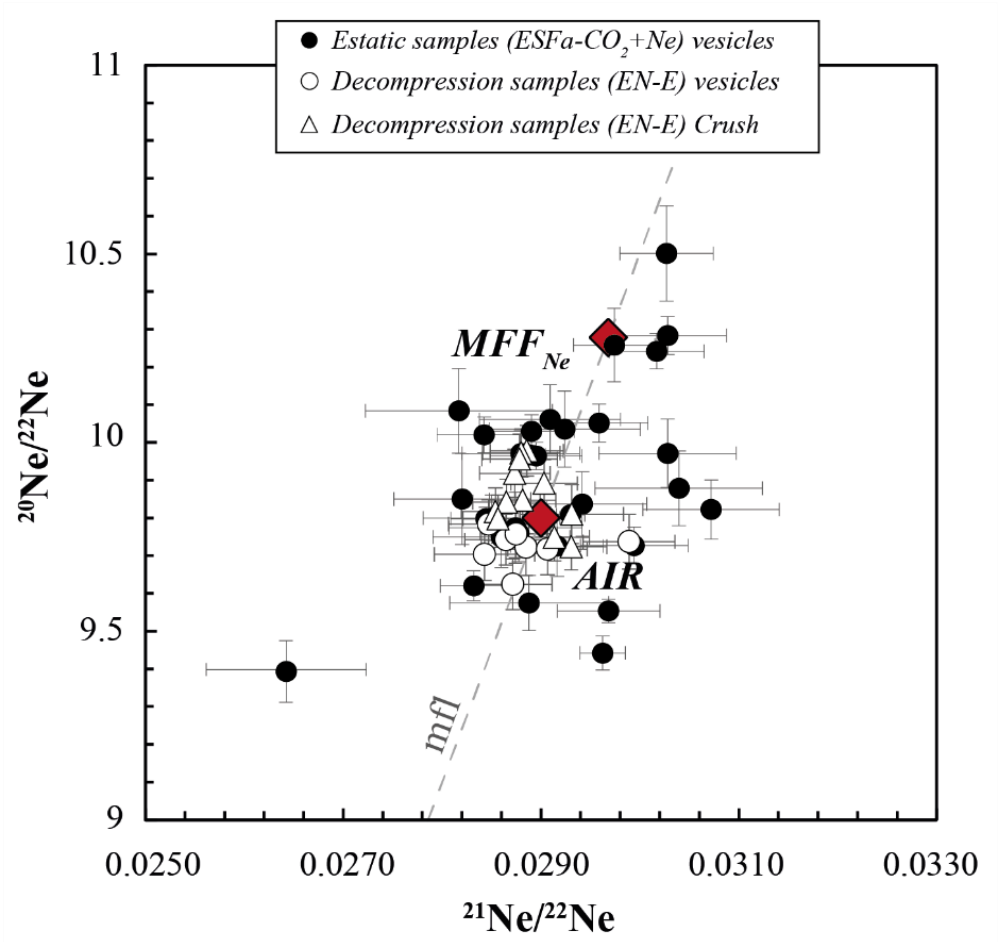

Figure 6.2: Compilation of the results obtained for the experimental series carried out in this work. The black dots represent the analysed vesicles of the static experiments, the white dots are the vesicles of the decompression experiments, and the white triangles are results obtained by the crushing technic of the decompression samples. The dashed line shows the mass fractionation line, and the theoretical maximum fractionation ratio and the Air are represented by red diamonds. Specifications about which samples corresponds the data are given in the in the corresponding chapters (Chapters 4 and 5).

The static samples exhibit a clear CO_2 heterogeneity concentration in the glass, where the CO_2 does not have enough time to dissolve to equilibrium for the given conditions of pressure and temperature. Additionally, the isotopic fractionation of Ne is significant, particularly in the initial stages of the experimental series. Due to the initial charge and short experimental time, the availability of CO_2 is high, and the magma does not have sufficient time to assimilate the CO_2 that is being released from the silver oxalate

compound. As a result, the buoyancy effect prevails over diffusion. *Sample ESFa-3B-CO_2+Ne* (10 minutes experiment) exhibited a significantly lower CO_2 concentration in the melt than its solubility. The bubbles appeared highly fractionated in neon with isotopic ratios as high as $^{20}Ne/^{22}Ne$ = 10.47, much more than the other analysed static samples *ESFa-5B-CO_2+Ne* and *ESFa-6B-CO_2+Ne*, after 240 minutes.

The decompression samples, after 1800 minutes experiment, when the magma has reached equilibrium (*EN-E3*) and with the appropriate amount of CO_2 for equilibrium saturation (2700 ppm; Jiménez-Mejías et al., (2021), the concentration in the melt follows the equilibrium trend, although not the solubility laws, since the glass is above the equilibrium values. A negative dependence is observed concerning the vesicularity of the sample (**Figure 6.1.c)** for the two paths of decompression. The vesicularity is negatively associated with decompression.

What these experimental series outlines, either the statics or the decompression, is that the longer the experiment or the slower the decompression rate, the more time has the magma to reach equilibrium. This will also allow the neon isotopes to reach equilibrium in the bubbles that have already formed.

This suggests that (i) the vesicularity and the (ii) state of vesiculation of the magma (buoyancy effect), (iii) the duration of the CO_2 flow recharging the system, (iv) and/or the duration during which CO_2 is exsolved from the magma to produce bubbles (that is the magma rising rate), directly impact the volatile species initially dissolved in the magma. The impact will depend on the diffusion and solubility of every involved species.

6.2. Volcanological implications:

6.2.1. Selection of natural samples:

To compare our experiments with a natural system, eight of the most characteristic rocks belonging to the MidAtlantic Ridge were image-scanned by micro-CT, and some of the most representative VSD-MORBs sample results were compilated.

The eight image-scanned samples included the so-called *popping rocks*, 2πd43, (Sarda and Graham, 1990; Javoy and Pineau, 1991; Moreira et al., 1998), and some of the

samples dredged at the cruise EW9309 in the South Atlantic Ridge, covering the Shona and Discovery topographical ridges anomalies (42.19º - 48.24º N) (Moreira et al., 1995; Douglass et al., 1999; Moreira and Sarda, 2000; Sarda et al., 2000; Williams and Mukhopadhyay, 2019).

Sarda and Graham, (1990) investigated the behaviour of volatiles during ridge crest volcanism using the VSD and rare gas abundances from the popping rocks (2πd43). Moreira et al. (1998) analysed the same samples to determine the rare gas and elemental isotopic composition of the upper mantle. Popping rocks have been used as a reference for the upper mantle by many authors (Staudacher et al., 1989; Javoy and Pineau, 1991; Péron et al., 2019) due to their high vesicularity and gas concentration, which offer insights into magmatic processes occurring in the upper mantle, such as degassing, partial melting, and interaction between different types of magmas. These rocks are assumed to have minimal loss of volatiles, the gases present in these vesicles are believed to be the gases present before the eruption and, therefore, serve as a testimony of degassing in a closed system.

However, the samples from the South Atlantic Ridge (Shona and Discovery anomalies) exhibit a combination of plume and MORB signatures. When plotted on the three-isotope neon diagram, the results suggest that the degassing mechanisms in these samples differ from those located further away from the anomalies, such as *EW9309-15D,18D, 19D* and *45D*, which are attributed to normal MORBs by noble gases (Moreira et al., 1995), incompatible elements (Le Roux et al., 2002) and Pb, Sr and Nd isotopes (Douglass et al., 1999). Additionally, these samples indicate that the mixture between the two components was incomplete during eruption (Moreira et al., 1995; Douglass et al., 1999; Sarda et al., 2000; Moreira and Sarda, 2000). It is important to note that magma chamber mechanisms differ between MORs and plumes, even when they are located on a ridge (Moreira and Sarda, 2000; Sarda and Moreira, 2002). Plumes are characterized by an open system behavior, where vesicles are continuously lost (*Rayleigh distillation)*, while mid-ocean ridge basalts follow a closed system, where degassing occurs after vesiculation. These samples suggested a distillation process occurring in the plumes that injected into the residual MORs chamber.

6.2.2. Relationship of synthetic samples with natural samples based on vesicularity parameters.

Firstly, we considered the parameters associated with VSD: the bubble population density, *ln(n)*, and the slope, *a*, obtained from the samples analysed in this study, including both natural and synthetic samples, as well as those from other ocean basins taken from the literature (**Figure 6.3**). The graph, which is based on the crystal size distribution of (Marsh, 2007), was previously presented by Chavrit (2010) to illustrate the growth time of bubbles in MORBs.

Figure 6.3 shows that the vesiculation trend of the experimental samples, including both static and decompression samples, is like that of the natural samples, and both plot at the Atlantic MORB field, including those influenced by plumes, which suggests that our experiments are a reliable representation of nature.

To enhance the clarity of this chapter, the vesicle size distribution results of the natural samples will be provided in the *Appendix,* although they are here discussed.

Unlike other decompression experiments, where bubble densities and vesicularities are weakly linked to decompression rates for homogeneous nucleation (Mourtada-Bonnefoi and Laporte, 2002; Mourtada-Bonnefoi and Laporte, 2004), the experimental samples of this study show a behaviour similar to the experiments of (Pichavant et al., 2013, 2018), in which the VSD parameters that characterize the experimental samples are related to (i) the pressure at which the sample was quenched; but beyond (ii) to the distance travelled between the bubble nucleation depth and the quench pressure; and (iii) the residence time of the bubble, i.e. the time spent under static conditions.

It is worth noting that the decompression samples quenched at a greater depth show a higher population density and a greater slope, *a*, which is coherent since the samples quenched at 500 bars show up to $n_0 = 3241$ μm-size bubbles per mm^3 comparing to the samples quenched at less pressure $n_0 = 7$ μm-size bubbles per mm^3 (EN-E4). Similarly, it is observed that the ln(n) in the static samples display a negative correlation with time, as the nucleation of CO_2 vesicles decreases as the experiment progresses.

In terms of decompression rate, the experimental samples show a pattern similar to that of the natural samples analysed in this study, falling on the natural trend, or plotting

above it (**Figure 6.3.b)**. However, the decompression rates between the two groups of experiments are less pronounced (6 hours) than for the natural samples, where the time to reach the oceanic floor differs by up to 70 hours (**Table 6.1**; The estimation was derived using the same methodology as in *Chapters 3, 4* and *5*).

Sample	**location**	**depth (m)**	**V (mm^3)**	**Ln(n) (mm^{-4})**	**sd**	**a (mm^{-1})**	**sd**	**n_0 ($\mu m \cdot mm^{-3}$)**	**τ_{theo} (h)**
2πD43	13.76N - 44.01W	3510	221	2.85	0.70	-2.41	0.77	0.02	76.98
EW9309-2D*	47.55S - 10.19W	2494	176	4.74	0.44	-11.22	1.93	0.11	16.51
EW9309-3D*	47.80S - 10.15W	2549	300	4.59	0.56	-9.77	2.76	0.10	18.96
EW9309-4D*	47.97S - 10.08W	2895	236	4.85	0.46	-8.27	3.00	0.13	22.39
EW9309-5D*	48.24S - 10.00W	3453	101	6.12	0.53	-22.25	5.18	0.45	8.32
EW9309-20D **	51.43S - 5.78W	1719	419	3.49	0.90	-8.18	1.98	0.03	22.63
EW9309-25D*	47.35S - 10.32W	2032	730	7.25	0.35	-23.02	3.17	1.40	8.05
EW9309-43D	42.19S - 16.08W	2925	288	4.51	0.72	-11.53	3.75	0.09	16.07

Table 6.1: main results obtained from the VSD parameters (see *Appendix*) and data presented by Douglass et al., (1999). * Are the samples dredged at the Discovery ridge-anomaly; ** is the sample dredged at the Shona ridge-anomaly. τ_{theo} calculated with $G = 1.5 \cdot 10^{-7}$ $cm \cdot s^{-1}$ (Sarda and Graham, 1990)

Both parameters (i) the pressure at which the experimental samples were quenched and (i) the decompression rate have in common the distance travelled between the bubble nucleation depth and (ii) the quenched depth/pressure for the decompression samples. The common characteristic that these processes in decompression samples have with static samples is time. The time necessary for the magma to assimilate a CO_2-rich flow/melt and the time for each volatile species to reach the equilibrium in each of the phases.

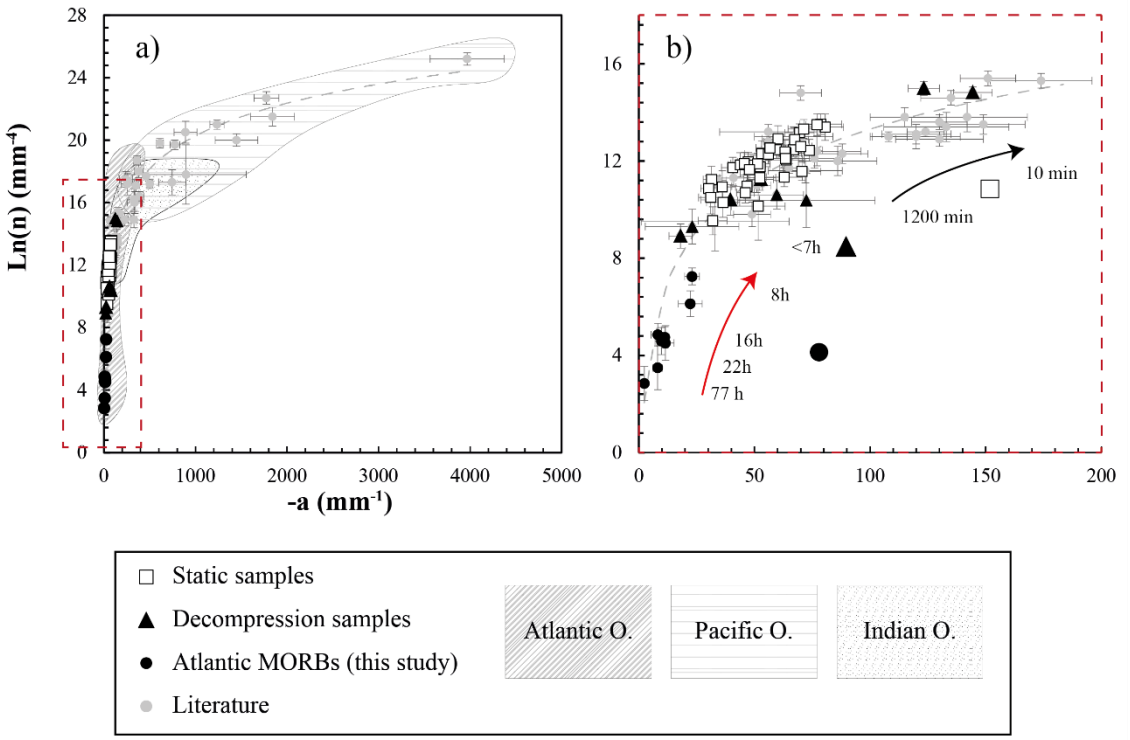

Figure 6.3: relationship between population density and slope, *-a*, as obtained for static experimental samples (white squares), decompression samples (black triangles) and natural samples (black dots, representing this study and grey dots representing literature; Chavrit 2010). (**a**) The graph also depicts the corresponding fields of origin of the MORB samples. The samples of this study, both natural and experimental, are located within the Atlantic MORB field. For clarity, **Figure b** zooms in on this field. This graph also shows the observed trend for the ascent rate of the natural and decompression samples (red arrow) and for the duration of the static experiments (black arrow), which are marked on the right with the corresponding symbols.

6.3. What could be happening to the basalts of the mid-oceanic ridges?

Assuming a melt that is initially in equilibrium in a magma chamber that, for the suitability of our experiments, is located at 10-13 km depth (sample *EN-E3*), we envision two possible scenarios to explain the resultant products of the decompression: {Citation}

6.3.1 Scenario 1: Popping Rocks and N-MORBs (not affected by plumes):

To simplify, in the first scenario, a closed system is proposed, where the most abundant volatile species are CO_2 and neon. CO_2 begins to be exsolved from the melt and nucleates vesicles when the decompression starts. Nucleation occurs homogeneously (experimental decompression series).

The evolution of this melt can be analysed by observing the several types of vesicles present within it. The bigger vesicles, Type 1, which correspond to vesicles that had already nucleated at greater depths and that grow due to gas expansion, inward diffusion, and/or coalescence of touching bubbles. The smaller vesicles, type 2, correspond to the new nuclei that are forming. The gas trapped in these two types of bubbles will tell different histories:

- Vesicles type 1, bubbles that grew, either by gas expansion and/or inward diffusion, for a sufficient period to reach isotopic equilibrium. They are expected to show an enrichment in the more diffusive volatile species. This is exemplified by neon in sample *EN-E4*, where the melt where vesicles are quenched before the gas is lost in the eruption.
- Type 2 vesicles are small nuclei that result from internal gas diffusion. They are more abundant in the early stages of decompression, making them more likely to show kinetic isotope fractionation. This occurs because the lighter isotopes move faster than the heavier isotopes (model *Section 4.2.2*; samples *EN-E9* and *EN-D1*).

If magma ascent is sufficiently slow that the bubbles reach isotopic equilibrium before the eruption and loss of bubbles occurs, the vesicles would predominantly be type 1. These bubbles would reflect the isotopic ratio of the source, as is the case for sample *2πD43* (Raquin et al., 2008; Sarda and Graham, 1990). Sample *EN-E4* shows the same characteristic as *2πD43*, vesicles in equilibrium, high vesicularity V_{the}=13.75% (or V_{ImageJ} =11.1%), and visually these samples show similar vesicle distribution and shape (**Figure 6.4**). It is noteworthy that V_{ImageJ} was employed in this instance, as it accounts for vesicles situated on the boundary of the samples and it is not possible to achieve the same degree of exact reproducibility of a natural sample. Sample *EN-E4* was the most closely matching the natural sample.

Only bubbles nucleated at the last moment before quenching (type 2 vesicles) could show fractionation, and this would be possible as long as the melt is oversaturated.

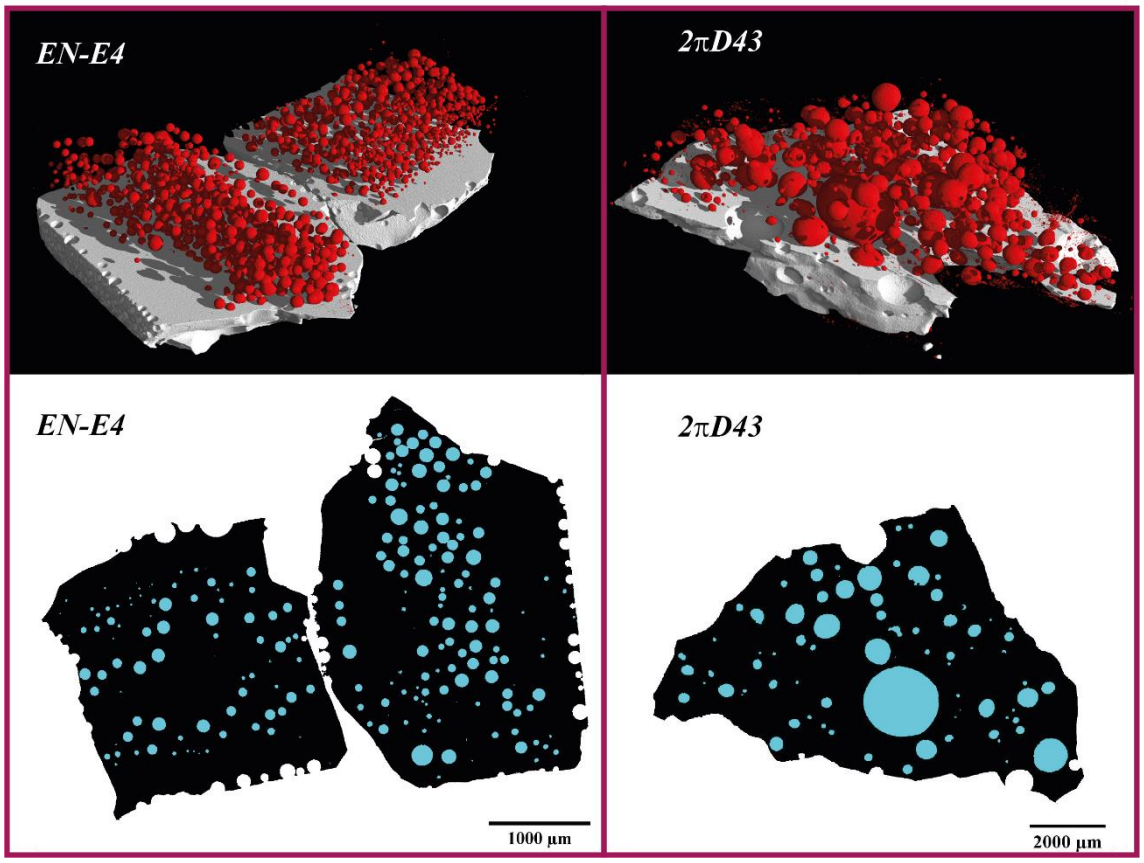

Figure 6.4: 3D images and slices sections for sample EN-E4 AND 5, and *2πD43*. The images aim to compare the vesicle distribution in the experimental and natural glasses. In these images the crystals present in sample *2πD43* are not shown. The slice without the threshold treatment for sample *2πD43* is included in the *Appendix.* Notice that given the limited dimensions of the capsule the size of the vesicles cannot go as far as for natural samples.

6.3.2. Scenario 2: MORBs affected by plumes (the case of Shona and Discovery):

If the previous scenario is replicated, assuming this time a closed-system, MOR, with homogeneous vesiculation and the same two volatile species, but including injection of a CO_2-rich melt/flow from a deeper open system, plume, which is continuously degassing and whose bubbles, as they ascend into the closed system and stored till eruption. The melts differ compositionally, therefore, when decompression starts, the resultant vesicles and melt will provide different information:

6.3.2.1. Homogeneous mix between the two involved systems before the eruption:

In the event of an ideal homogeneous mixture of the two systems before eruption, that i.e. quenched sometime before the eruption, the analysed vesicles would exhibit an

intermediate and homogeneous isotopic ratio between the two systems, with an evolution in terms of vesicles similar to that of the first scenario.

6.3.2.2. Incomplete mixture between the two involved systems:

In the case of an incomplete mixing of the two systems, before the eruption starts:

- Some vesicles would exhibit isotopic equilibrium and an intermediate composition of the two systems since they would have resided in the magma a longer time.
- If the melt is still oversaturated in CO_2, nucleation will still occur, and these vesicles, nucleated just before the quench, would show kinetic isotopic fractionation as in the first scenario.
- In addition, there would be another type of vesicle that would present a different fractionation than the nuclei formed moments before being quenched. These vesicles represent the last bubbles to emerge from the injected magma (plume), which, in contact with the resident melt (MOR), would start to fractionate and equilibrate with the composition of the closed system. As evidenced by the experimental static samples, this fractionation occurs immediately upon the vesicles entering the resident magma and persists until equilibrium is reached. Furthermore, the buoyancy effect of these vesicles is significant, as they are already formed vesicles entering the closed system. Consequently, their ascension rate prevents from complete the diffusion to the vesicles and then reach the isotopic equilibrium.

Consequently, in the first scenario and the homogeneous mixture between the two systems, the possibility of finding a fractionation would be mainly related to the size of the bubbles, as long as we take as a reference that the largest vesicles would represent the most evolved bubbles in a system in which vesiculation occurs homogeneously, i.e. while there is still CO_2 saturating the system and conditions favour the nucleation of new vesicles.

In the second scenario, isotopic fractionation of neon, as well as other volatile species, would be much more frequent as long as the CO_2 injection to the upper chamber (the resident melt) is continuous and does not achieve a homogeneous mixture prior to eruption or the system stays supersaturated (Pichavant et al., 2009, 2013; Aubaud et al.,

2004; Aubaud, 2022). This second scenario may be characteristic of those MORB affected by plumes.

Moreira et al. (1995), Moreira and Sarda (2000) and Sarda et al. (2000) observed the presence of a primitive and little degassed mantle component (with non-radiogenic helium isotopes) in the basaltic glasses dredged over the Shona and Discovery gravity and topographic anomalies on the Mid-Atlantic Ridge. The neon isotopic ratios showed an incomplete mixing between the two components (plume and MOR). These samples show a negative trend pointing towards solar values, bridging the commonly observed MORB and the Galapagos mixing lines, plotted in **Figure 6.5** as a dashed red line. These results are interpreted in terms of incomplete mixing between the upper mantle neon and the plume neon. **Figure 6.5** shows the three neon isotope results for some of these analysed samples along with the results of new analyses obtained by single vesicles of new *popping rocks* (Péron et al., 2019) and crushing samples *EW-9303-25D* and *EW-9303-5D* (Williams and Mukhopadhyay, 2019) and the results of crushing and single vesicles of sample *2πD43* (Moreira et al., 1998; Kunz, 1999; Raquin et al., 2008).

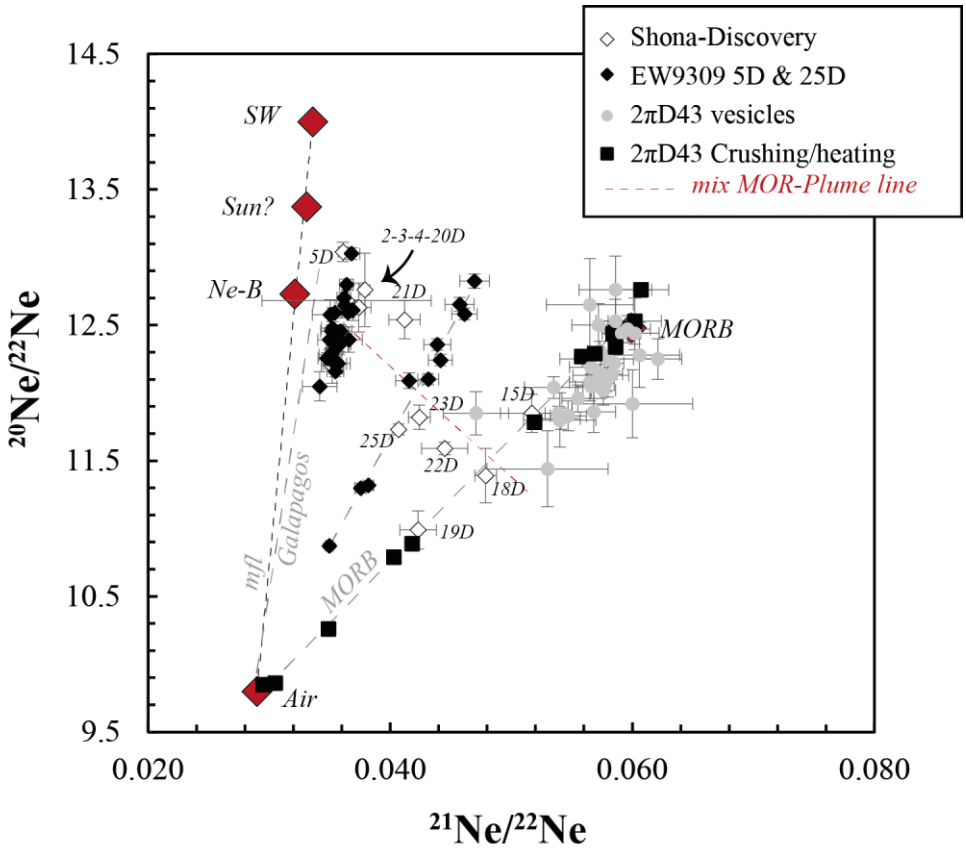

Figure 6.5: The graph displays the analytical results for the three neon isotopes obtained by (i) crushing: black squares for *2πd43,* black diamonds for the new analysis of samples 25D and 5D and white diamonds for samples analysed at and close to the Shona and Discovery anomalies and (ii) single vesicle analysis (grey dots) for *popping rocks*. Data from: (Moreira et al., 1995, 1998; Kunz, 1999; Sarda et al., 2000; Raquin et al., 2008; Péron et al., 2019; Williams and Mukhopadhyay, 2019). *Galapagos* trend from Péron et al. (2016), SW from Pepin et al. (2012), Ne-B from Moreira and Charnoz (2016) Sun from (Heber et al., 2012)

Upon examination of the samples belonging to the Discovery and Shona anomalies, it can be observed that the estimated residence time (τ_{the}; **Table 6.1**), decreases as the signal approaches the influence of both plumes.

The isotopic composition of neon was found to be correlated with the behaviour of other noble gases, including argon and helium. In their work, Sarda et al. (2000) associated this fractionation with a Rayleigh-type distillation, in which a significant portion of the MOR vesicles had been lost prior to the incorporation of the plume. Samples exhibiting the most pronounced effects of plumes, such as sample *EW-9303-5D*, exhibited this kind of fractionation, as evidenced by the high values of $^{3}He/^{22}Ne$ and $^{3}He/^{36}Ar$, which were higher than the values of the plume source at the time of mixing. The loss of vesicles is a characteristic feature of MORBs, with the exception of popping rocks, which preserve the majority of the gas (Sarda and Graham, 1990).

In *Chapter 1*, one of the hypotheses put forth was that the higher isotopic ratios ($^{20}Ne/^{22}Ne$ =13.03 ± 0.04) obtained for the samples with a mantle plume signal (*EW-9303-5D*) could indicate the primordial plume mantle with a value of 13.23 ± 0.22 (Williams and Mukhopadhyay, 2019), thereby corroborating the hypothesis that the solar nebula gas is preserved in the present-day deep mantle.

The two scenarios presented here demonstrate that time is the primary factor in interpreting the isotopic composition in both single vesicles and step crushing, as well as other methods where gas extraction is involved. Time is a fundamental factor in the coupling of several diffusion of species and different isotopes within the melt and at the gas-melt interface. Time is a crucial factor in the ascent of magma during decompression, influencing the residence time of vesicles in magma and the residence time of magma. Furthermore, the time required to create a homogeneous and in equilibrium mixture when two or more systems or components are involved must be considered.

As observed in both experimental series (**Figures 3.26**; **3.30**; **4.17**; and **5.13**) and in the fractionation model presented in *Section 4.2.2* and **Figure 4.5**, the shorter the residence time, the less time the magma has to equilibrate or the more likely it is to find isotopic fractionation or heterogeneous distribution of volatile species in the magma and gas. The younger the analysed vesicles are.

The answer to the main question posed in this thesis may lie in the *Time*. Could the highest isotopic ratios obtained from *EW-9303-5D* represent the primordial isotopic composition of the mantle and thus lend credence to the possibility that a solar nebula component remains trapped in the mantle?

This thesis does not rule out this hypothesis, but the experiments conducted do raise the possibility that the vesicles show fractionation due to (i) the rapid ascent of magma to the surface or (ii) that the incorporation of the plume to the degassed mantle source resulted in insufficient time for the two systems to complete homogeneous mixing and vesicle equilibrium leading erratic interpretation of the obtained isotopic composition.

6.4. References:

Aiuppa, A., Federico, C., Giudice, G., Giuffrida, G., Guida, R., Gurrieri, S., Liuzzo, M., Moretti, R., Papale, P., 2009. The 2007 eruption of Stromboli volcano: insights from real-time measurement of the volcanic gas plume CO2/SO2 ratio. J. Volcanol. Geotherm. Res. 182, 221–230.

Allegre, C.J., Manhes, G., Göpel, C., 1995. The age of the Earth. Geochim. Cosmochim. Acta 59, 1445–1456.

Allègre, C.J., Staudacher, T., Sarda, P., Kurz, M., 1983. Constraints on evolution of Earth's mantle from rare gas systematics. Nature 303, 762–766. https://doi.org/10.1038/303762a0

Aubaud, C., 2022. Carbon stable isotope constraints on CO2 degassing models of ridge, hotspot and arc magmas. Chem. Geol. 605, 120962.

Aubaud, C., Pineau, F., Jambon, A., Javoy, M., 2004. Kinetic disequilibrium of C, He, Ar and carbon isotopes during degassing of mid-ocean ridge basalts. Earth Planet. Sci. Lett. 222, 391–406.

Aubry, G.J., Sator, N., Guillot, B., 2013. Vesicularity, bubble formation and noble gas fractionation during MORB degassing. Chem. Geol. 343, 85–98.

Azuma, S., Ozima, M., Hiyagon, H., 1993. Anomalous neon and xenon in an Archaean anorthosite from West Greenland. Earth Planet. Sci. Lett. 114, 341–352.

Ballentine, C.J., Barfod, D.N., 2000. The origin of air-like noble gases in MORB and OIB. Earth Planet. Sci. Lett. 180, 39–48.

Ballentine, C.J., Burgess, R., Marty, B., 2002. Tracing fluid origin, transport and interaction in the crust.

Ballentine, C.J., Burnard, P.G., 2002. Production, Release and Transport of Noble Gases in the Continental Crust. Rev. Mineral. Geochem. 47, 481–538. https://doi.org/10.2138/rmg.2002.47.12

Ballentine, C.J., Marty, B., Sherwood Lollar, B., Cassidy, M., 2005. Neon isotopes constrain convection and volatile origin in the Earth's mantle. Nature 433, 33–38.

Bauer, C.A., 1947. Production of helium in meteorites by cosmic radiation. Phys. Rev. 72, 354.

Becker, R.H., Pepin, R.O., 1994. Solar wind noble gases and nitrogen in metal from lunar soil 68501. Meteoritics 29, 724–738.

Behrens, H., 2010. Noble gas diffusion in silicate glasses and melts. Rev. Mineral. Geochem. 72, 227–267.

Behrens, H., Misiti, V., Freda, C., Vetere, F., Botcharnikov, R.E., Scarlato, P., 2009. Solubility of H2O and CO2 in ultrapotassic melts at 1200 and 1250 C and pressure from 50 to 500 MPa. Am. Mineral. 94, 105–120.

Behrens, H., Zhang, Y., 2001. Ar diffusion in hydrous silicic melts: implications for volatile diffusion mechanisms and fractionation. Earth Planet. Sci. Lett. 192, 363–376.

Black, D., Pepin, R., 1969. Trapped neon in meteorites—II. Earth Planet. Sci. Lett. 6, 395–405.

Black, D.C., 1972. On the origins of trapped helium, neon and argon isotopic variations in meteorites—I. Gas-rich meteorites, lunar soil and breccia. Geochim. Cosmochim. Acta 36, 347–375.

Blank, J.G., Brooker, R.A., 1994. Experimental studies of carbon dioxide in silicate melts; solubility, speciation, and stable carbon isotope behavior. Rev. Mineral. Geochem. 30, 157–186.

Bodmer, R., Bochsler, P., 2000. Influence of Coulomb collisions on isotopic and elemental fractionation in the solar wind acceleration process. J. Geophys. Res. Space Phys. 105, 47–60.

Bottinga, Y., Richet, P., 1981. High pressure and temperature equation of state and calculation of the thermodynamic properties of gaseous carbon dioxide. Am. J. Sci. 281, 615–660.

Bühler, F., Eberhardt, P., Geiss, J., Meister, J., Signer, P., 1969. Apollo 11 solar wind composition experiment: First results. Science 166, 1502–1503.

Burbidge, E.M., Burbidge, G.R., Fowler, W.A., Hoyle, F., 1957. Synthesis of the elements in stars. Rev. Mod. Phys. 29, 547.

Burnard, P., 2001. Correction for volatile fractionation in ascending magmas: noble gas abundances in primary mantle melts. Geochim. Cosmochim. Acta 65, 2605–2614.

Burnard, P., 1999. The bubble-by-bubble volatile evolution of two mid-ocean ridge basalts. Earth Planet. Sci. Lett. 174, 199–211.

Burnard, P., Graham, D., Turner, G., 1997. Vesicle-specific noble gas analyses of" popping rock": implications for primordial noble gases in Earth. Science 276, 568–571.

Busemann, H., Baur, H., Wieler, R., 2000. Primordial noble gases in "phase Q" in carbonaceous and ordinary chondrites studied by closed-system stepped etching. Meteorit. Planet. Sci. 35, 949–973.

Butler, W., Jeffery, P., Reynolds, J., Wasserburg, G., 1963. Isotopic variations in terrestrial xenon. J. Geophys. Res. 68, 3283–3291.

Canup, R.M., Asphaug, E., 2001. Origin of the Moon in a giant impact near the end of the Earth's formation. Nature 412, 708–712.

Carroll, M.R., Webster, J.D., 1994. Solubilities of sulfur, noble gases, nitrogen, chlorine, and fluorine in magmas. Rev. Mineral. 30, 231–231.

Chambers, J., 2010. Planetesimal formation by turbulent concentration. Icarus 208, 505–517.

Chavrit, D., 2010. Cartographie globale des flux de CO2 à l'axe des dorsales océaniques: une approche pétrologique.

Chavrit, D., Humler, E., Morizet, Y., Laporte, D., 2012. Influence of magma ascent rate on carbon dioxide degassing at oceanic ridges: Message in a bubble. Earth Planet. Sci. Lett. 357, 376–385.

Clayton, D.D., 1983. Principles of stellar evolution and nucleosynthesis. University of Chicago press.

Colin, A., Moreira, M., Gautheron, C., Burnard, P., 2015. Constraints on the noble gas composition of the deep mantle by bubble-by-bubble analysis of a volcanic glass sample from Iceland. Chem. Geol. 417, 173–183.

Craig, H., Lupton, J., 1976. Primordial neon, helium, and hydrogen in oceanic basalts. Earth Planet. Sci. Lett. 31, 369–385.

Cuzzi, J.N., Hogan, R.C., Shariff, K., 2008. Toward planetesimals: Dense chondrule clumps in the protoplanetary nebula. Astrophys. J. 687, 1432.

Dauphas, N., Burkhardt, C., Warren, P.H., Fang-Zhen, T., 2014. Geochemical arguments for an Earth-like Moon-forming impactor. Philos. Trans. R. Soc. Math. Phys. Eng. Sci. 372, 20130244.

Dauphas, N., Chaussidon, M., 2011. A perspective from extinct radionuclides on a young stellar object: the Sun and its accretion disk. Annu. Rev. Earth Planet. Sci. 39, 351–386.

Dauphas, N., Morbidelli, A., 2013. Geochemical and planetary dynamical views on the origin of Earth's atmosphere and oceans. ArXiv Prepr. ArXiv13121202.

Dauphas, N., Pourmand, A., 2011. Hf–W–Th evidence for rapid growth of Mars and its status as a planetary embryo. Nature 473, 489–492.

D'E Atkinson, R., Houtermans, F., 1929. Transmutation of the Lighter Elements in Stars. Nature 123, 567–568.

Di Carlo, I., Pichavant, M., Rotolo, S.G., Scaillet, B., 2006. Experimental crystallization of a high-K arc basalt: the golden pumice, Stromboli volcano (Italy). J. Petrol. 47, 1317–1343.

Dickin, A.P., 2018. Radiogenic isotope geology. Cambridge university press.

Dixon, J.E., Pan, V., 1995a. Determination of the molar absorptivity of dissolved carbonate in basanitic glass. Am. Mineral. 80, 1339–1342.

Dixon, J.E., Pan, V., 1995b. Determination of the molar absorptivity of dissolved carbonate in basanitic glass. Am. Mineral. 80, 1339–1342.

Dixon, J.E., Stolper, E.M., Holloway, J.R., 1995. An experimental study of water and carbon dioxide solubilities in mid-ocean ridge basaltic liquids. Part I: calibration and solubility models. J. Petrol. 36, 1607–1631.

Donahue, T., Russell, C., 1997. The Venus atmosphere and ionosphere and their interaction with the solar wind: An overview. Venus II Geol. Geophys. Atmosphere Sol. Wind Environ. 3.

Douglass, J., Schilling, J., Fontignie, D., 1999. Plume-ridge interactions of the Discovery and Shona mantle plumes with the southern Mid-Atlantic Ridge (40°-55° S). J. Geophys. Res. Solid Earth 104, 2941–2962.

Eberhardt, P., Geiss, J., Graf, H., Grögler, N., Krähenbühl, U., Schwaller, H., Schwarzmüller, J., Stettler, A., 1970. Trapped solar wind noble gases, exposure age and K/Ar-age in Apollo 11 lunar fine material. Presented at the Geochimica

et Cosmochimica Acta Supplement, Volume 1. Proceedings of the Apollo 11 Lunar Science Conference held 5-8 January, 1970 in Houston, TX. Volume 2: Chemical and Isotope Analyses. Edited by AA Levinson. New York: Pergammon Press, 1970., p. 1037, p. 1037.

Eberhardt, P., Geiss, J., Graf, H., Grögler, N., Mendia, M., Mörgeli, M., Schwaller, H., Stettler, A., Krähenbühl, U., Von Gunten, H., 1972. Trapped solar wind noble gases in Apollo 12 lunar fines 12001 and Apollo 11 breccia 10046. Bern Univ.(Switzerland).

Farrell, W.M., Hurley, D.M., Zimmerman, M.I., 2015. Solar wind implantation into lunar regolith: Hydrogen retention in a surface with defects. Icarus 255, 116–126.

Fine, G., Stolper, E., 1985. The speciation of carbon dioxide in sodium aluminosilicate glasses. Contrib. Mineral. Petrol. 91, 105–121.

Frost, B.R., 2018. Introduction to oxygen fugacity and its petrologic importance, in: Oxide Minerals. De Gruyter, pp. 1–10.

Geiss, J., Bühler, F., Cerutti, H., Eberhardt, P., Filleux, C., Meister, J., Signer, P., 2004. The Apollo SWC experiment: results, conclusions, consequences. Space Sci. Rev. 110, 307–335.

Geiss, J, Eberhardt, P., Bühler, F., Meister, J., Signer, P., 1970. Apollo 11 and 12 solar wind composition experiments: Fluxes of He and Ne isotopes. J. Geophys. Res. 75, 5972–5979.

Geiss, Johannes, Hirt, P., Leutwyler, H., 1970. On acceleration and motion of ions in corona and solar wind. Sol. Phys. 12, 458–483.

Giordano, D., Russell, J.K., Dingwell, D.B., 2008. Viscosity of magmatic liquids: a model. Earth Planet. Sci. Lett. 271, 123–134.

Gonnermann, H.M., Manga, M., 2007. The fluid mechanics inside a volcano. Annu Rev Fluid Mech 39, 321–356.

Graham, D.W., 2002. Noble Gas Isotope Geochemistry of Mid-Ocean Ridge and Ocean Island Basalts: Characterization of Mantle Source Reservoirs. Rev. Mineral. Geochem. 47, 247–317. https://doi.org/10.2138/rmg.2002.47.8

Grimberg, A., Baur, H., Bochsler, P., Bühler, F., Burnett, D.S., Hays, C.C., Heber, V.S., Jurewicz, A.J., Wieler, R., 2006. Solar wind neon from Genesis: Implications for the lunar noble gas record. Science 314, 1133–1135.

Harper Jr, C.L., Jacobsen, S.B., 1996. Noble gases and Earth's accretion. Science 273, 1814–1818.

Hashizume, K., Chaussidon, M., Marty, B., Robert, F., 2000. Solar wind record on the Moon: deciphering presolar from planetary nitrogen. Science 290, 1142–1145.

Heber, V.S., Baur, H., Bochsler, P., McKeegan, K.D., Neugebauer, M., Reisenfeld, D.B., Wieler, R., Wiens, R.C., 2012. Isotopic mass fractionation of solar wind: Evidence from fast and slow solar wind collected by the Genesis mission. Astrophys. J. 759, 121.

Heber, V.S., Wieler, R., Baur, H., Olinger, C., Friedmann, T.A., Burnett, D.S., 2009. Noble gas composition of the solar wind as collected by the Genesis mission. Geochim. Cosmochim. Acta 73, 7414–7432.

Holland, G., Ballentine, C.J., 2006a. Seawater subduction controls the heavy noble gas composition of the mantle. Nature 441, 186–191.

Holland, G., Ballentine, C.J., 2006b. Seawater subduction controls the heavy noble gas composition of the mantle. Nature 441, 186–191.

Holland, G., Cassidy, M., Ballentine, C.J., 2009. Meteorite Kr in Earth's mantle suggests a late accretionary source for the atmosphere. Science 326, 1522–1525.

Hollenbach, D.J., Yorke, H.W., Johnstone, D., 2000. Disk dispersal around young stars. Protostars Planets IV 401, 12.

Honda, M., McDougall, I., Patterson, D.B., Doulgeris, A., Clague, D.A., 1991. Possible solar noble-gas component in Hawaiian basalts. Nature 349, 149–151.

Honda, M., Reynolds, J., Roedder, E., Epstein, S., 1987. Noble gases in diamonds: Occurrences of solarlike helium and neon. J. Geophys. Res. Solid Earth 92, 12507–12521.

Iacono-Marziano, G., Paonita, A., Rizzo, A., Scaillet, B., Gaillard, F., 2010. Noble gas solubilities in silicate melts: new experimental results and a comprehensive model of the effects of liquid composition, temperature and pressure. Chem. Geol. 279, 145–157.

Jambon, A., Weber, H., Braun, O., 1986. Solubility of He, Ne, Ar, Kr and Xe in a basalt melt in the range 1250–1600 C. Geochemical implications. Geochim. Cosmochim. Acta 50, 401–408.

Jaupart, E., Charnoz, S., Moreira, M., 2017. Primordial atmosphere incorporation in planetary embryos and the origin of Neon in terrestrial planets. Icarus 293, 199–205.

Javoy, M., Pineau, F., 1991. The volatiles record of a "popping" rock from the Mid-Atlantic Ridge at 14 N: chemical and isotopic composition of gas trapped in the vesicles. Earth Planet. Sci. Lett. 107, 598–611.

Jiménez-Mejías, M., Andújar, J., Scaillet, B., Casillas, R., 2021. Experimental determination of H $ _ {{2}} $ O and CO $ _ {{2}} $ solubilities of mafic alkaline magmas from Canary Islands. Comptes Rendus Géoscience 353, 289–314.

Johansen, A., Klahr, H., 2011. Planetesimal formation through streaming and gravitational instabilities. Earth Moon Planets 108, 39–43.

Johansen, A., Klahr, H., Henning, T., 2011. High-resolution simulations of planetesimal formation in turbulent protoplanetary discs. Astron. Astrophys. 529, A62.

Johansen, A., Oishi, J.S., Low, M.-M.M., Klahr, H., Henning, T., Youdin, A., 2007. Rapid planetesimal formation in turbulent circumstellar disks. Nature 448, 1022–1025.

Kendrick, M.A., Burnard, P., 2013. Noble gases and halogens in fluid inclusions: a journey through the Earth's crust. Noble Gases Geochem. Tracers 319–369.

Kennedy, B., Hiyagon, H., Reynolds, J., 1990. Crustal neon: a striking uniformity. Earth Planet. Sci. Lett. 98, 277–286.

Kennedy, B.M., Hiyagon, H., Reynolds, J.H., 1990. Crustal neon: a striking uniformity. Earth Planet. Sci. Lett. 98, 277–286. https://doi.org/10.1016/0012-821X(90)90030-2

Kipfer, R., Aeschbach-Hertig, W., Peeters, F., Stute, M., 2002. Noble gases in lakes and ground waters. Rev. Mineral. Geochem. 47, 615–700.

Kress, V.C., Carmichael, I.S., 1991. The compressibility of silicate liquids containing Fe 2 O 3 and the effect of composition, temperature, oxygen fugacity and pressure on their redox states. Contrib. Mineral. Petrol. 108, 82–92.

Krummenacher, D., 1970. Isotopic composition of argon in modern surface volcanic rocks. Earth Planet. Sci. Lett. 8, 109–117.

Kunz, J., 1999. Is there solar argon in the Earth's mantle? Nature 399, 649–650. https://doi.org/10.1038/21352

Kuroda, P., 1960. Nuclear fission in the early history of the earth. Nature 187.

Kurz, M.D., 1986. Cosmogenic helium in a terrestrial igneous rock. Nature 320, 435–439. https://doi.org/10.1038/320435a0

Kurz, M.D., Curtice, J., Fornari, D., Geist, D., Moreira, M., 2009. Primitive neon from the center of the Galápagos hotspot. Earth Planet. Sci. Lett. 286, 23–34.

Lange, R.A., 1994a. Volatiles in Magmas, in: Carroll, M.R., Holloway, J.R. (Eds.), . De Gruyter, pp. 331–370. https://doi.org/10.1515/9781501509674-015

Lange, R.A., 1994b. Volatiles in Magmas, in: Carroll, M.R., Holloway, J.R. (Eds.), . De Gruyter, pp. 331–370. https://doi.org/10.1515/9781501509674-015

Le Gall, N., 2015. Ascension et dégazage des magmas basaltiques: approche expérimentale.

Le Gall, N., Pichavant, M., 2016a. Experimental simulation of bubble nucleation and magma ascent in basaltic systems: Implications for Stromboli volcano. Am. Mineral. 101, 1967–1985.

Le Gall, N., Pichavant, M., 2016b. Homogeneous bubble nucleation in H2O-and H2O-CO2-bearing basaltic melts: results of high temperature decompression experiments. J. Volcanol. Geotherm. Res. 327, 604–621.

Le Roux, P., Le Roex, A., Schilling, J.-G., Shimizu, N., Perkins, W., Pearce, N., 2002. Mantle heterogeneity beneath the southern Mid-Atlantic Ridge: trace element evidence for contamination of ambient asthenospheric mantle. Earth Planet. Sci. Lett. 203, 479–498.

Lensky, N.G., Niebo, R.W., Holloway, J.R., Lyakhovsky, V., Navon, O., 2006. Bubble nucleation as a trigger for xenolith entrapment in mantle melts. Earth Planet. Sci. Lett. 245, 278–288.

Lux, G., 1987. The behavior of noble gases in silicate liquids: Solution, diffusion, bubbles and surface effects, with applications to natural samples. Geochim. Cosmochim. Acta 51, 1549–1560.

Mangan, M., Sisson, T., 2000. Delayed, disequilibrium degassing in rhyolite magma: decompression experiments and implications for explosive volcanism. Earth Planet. Sci. Lett. 183, 441–455.

Marsh, B.D., 2007. Crystallization of silicate magmas deciphered using crystal size distributions. J. Am. Ceram. Soc. 90, 746–757.

Marsh, B.D., 1988. Crystal size distribution (CSD) in rocks and the kinetics and dynamics of crystallization: I. Theory. Contrib. Mineral. Petrol. 99, 277–291.

Marty, B., 2022. Meteoritic noble gas constraints on the origin of terrestrial volatiles. Icarus 381, 115020.

Marty, B., 2020. ORIGINS AND EARLY EVOLUTION OF THE ATMOSPHERE AND THE OCEANS. Geochem. Perspect. 9, 135–136.

Marty, B., 2012. The origins and concentrations of water, carbon, nitrogen and noble gases on Earth. Earth Planet. Sci. Lett. 313, 56–66.

Marty, B., Yokochi, R., 2006. Water in the early Earth. Rev. Mineral. Geochem. 62, 421–450.

Marty, B., Zimmermann, L., 1999. Volatiles (He, C, N, Ar) in mid-ocean ridge basalts: Assesment of shallow-level fractionation and characterization of source composition. Geochim. Cosmochim. Acta 63, 3619–3633.

McDonnell, J., Flavill, R., 1974. Sputter Erosion on the Lunar Surface: Measurements and Features Under Simulated Solar He+ Bombardment. Lunar Planet. Sci. V Houst. Lunar Planet Inst 478.

Mizuno, H., Nakazawa, K., Hayashi, C., 1980. Dissolution of the primordial rare gases into the molten Earth's material. Earth Planet. Sci. Lett. 50, 202–210.

Morbidelli, A., Bottke, W.F., Nesvorný, D., Levison, H.F., 2009. Asteroids were born big. Icarus 204, 558–573.

Moreira, M., 2013. Noble gas constraints on the origin and evolution of Earth's volatiles. Geochem. Perspect. 2, 229–230.

Moreira, M., Blusztajn, J., Curtice, J., Hart, S., Dick, H., Kurz, M.D., 2003. He and Ne isotopes in oceanic crust: implications for noble gas recycling in the mantle. Earth Planet. Sci. Lett. 216, 635–643.

Moreira, M., Charnoz, S., 2016. The origin of the neon isotopes in chondrites and on Earth. Earth Planet. Sci. Lett. 433, 249–256. https://doi.org/10.1016/j.epsl.2015.11.002

Moreira, M., Kunz, J., Allegre, C., 1998. Rare gas systematics in popping rock: isotopic and elemental compositions in the upper mantle. Science 279, 1178–1181.

Moreira, M., Rouchon, V., Muller, E., Noirez, S., 2018. The xenon isotopic signature of the mantle beneath Massif Central. Geochem Perspect Lett 6, 28–32.

Moreira, M., Sarda, P., 2000. Noble gas constraints on degassing processes. Earth Planet. Sci. Lett. 176, 375–386.

Moreira, M., Staudacher, T., Sarda, P., Schilling, J.-G., Allègre, C.J., 1995. A primitive plume neon component in MORB: The Shona ridge-anomaly, South Atlantic (51–52° S). Earth Planet. Sci. Lett. 133, 367–377.

Moretti, R., Papale, P., Ottonello, G., 2003. A model for the saturation of COHS fluids in silicate melts. Geol. Soc. Lond. Spec. Publ. 213, 81–101.

Mourtada-Bonnefoi, C., Laporte, D., 2002. Homogeneous bubble nucleation in rhyolitic magmas: an experimental study of the effect of H2O and CO2. J. Geophys. Res. Solid Earth 107, ECV-2.

Mourtada-Bonnefoi, C.C., Laporte, D., 2004. Kinetics of bubble nucleation in a rhyolitic melt: an experimental study of the effect of ascent rate. Earth Planet. Sci. Lett. 218, 521–537.

Mukhopadhyay, S., 2012. Early differentiation and volatile accretion recorded in deep-mantle neon and xenon. Nature 486, 101–104. https://doi.org/10.1038/nature11141

Nowak, M., Schreen, D., Spickenbom, K., 2004. Argon and CO2 on the race track in silicate melts: a tool for the development of a CO2 speciation and diffusion model. Geochim. Cosmochim. Acta 68, 5127–5138.

Nuccio, P., Paonita, A., 2001. Magmatic degassing of multicomponent vapors and assessment of magma depth: application to Vulcano Island (Italy). Earth Planet. Sci. Lett. 193, 467–481.

Nuccio, P., Paonita, A., 2000. Investigation of the noble gas solubility in H2O–CO2 bearing silicate liquids at moderate pressure II: the extended ionic porosity (EIP) model. Earth Planet. Sci. Lett. 183, 499–512.

Olson, P.L., Sharp, Z.D., 2019. Nebular atmosphere to magma ocean: a model for volatile capture during Earth accretion. Phys. Earth Planet. Inter. 294, 106294.

Ozima, M., Podosek, F.A., 2002. Noble gas geochemistry. Cambridge University Press.

Ozima, M., Zashu, S., 1991. Noble gas state of the ancient mantle as deduced from noble gases in coated diamonds. Earth Planet. Sci. Lett. 105, 13–27.

Ozima, M., Zashu, S., 1988a. Solar-type Ne in Zaire cubic diamonds. Geochim. Cosmochim. Acta 52, 19–25.

Ozima, M., Zashu, S., 1988b. Solar-type Ne in Zaire cubic diamonds. Geochim. Cosmochim. Acta 52, 19–25.

Paonita, A., 2005. Noble gas solubility in silicate melts: a review of experimentation and theory, and implications regarding magma degassing processes. Ann. Geophys.

Paonita, A., Gigli, G., Gozzi, D., Nuccio, P., Trigila, R., 2000. Investigation of the He solubility in H2O–CO2 bearing silicate liquids at moderate pressure: a new experimental method. Earth Planet. Sci. Lett. 181, 595–604.

Pepin, R., Nyquist, L., Phinney, D., Black, D.C., 1970. Isotopic composition of rare gases in lunar samples. Science 167, 550–553.

Pepin, R.O., 1991. On the origin and early evolution of terrestrial planet atmospheres and meteoritic volatiles. Icarus 92, 2–79.

Pepin, R.O., Schlutter, D.J., Becker, R.H., Reisenfeld, D.B., 2012. Helium, neon, and argon composition of the solar wind as recorded in gold and other Genesis collector materials. Geochim. Cosmochim. Acta 89, 62–80.

Péron, S., Moreira, M., Agranier, A., 2018. Origin of light noble gases (He, Ne, and Ar) on Earth: A review. Geochem. Geophys. Geosystems 19, 979–996.

Péron, S., Moreira, M., Colin, A., Arbaret, L., Putlitz, B., Kurz, M.D., 2016. Neon isotopic composition of the mantle constrained by single vesicle analyses. Earth Planet. Sci. Lett. 449, 145–154. https://doi.org/10.1016/j.epsl.2016.05.052

Péron, S., Moreira, M., Putlitz, B., Kurz, M., 2017. Solar wind implantation supplied light volatiles during the first stage of Earth accretion. Geochem. Perspect. Lett. 151–159.

Péron, S., Moreira, M.A., Kurz, M.D., Curtice, J., Blusztajn, J.S., Putlitz, B., Wanless, V.D., Jones, M.R., Soule, S.A., Mittelstaedt, E., 2019. Noble gas systematics in new popping rocks from the Mid-Atlantic Ridge (14° N): evidence for small-scale upper mantle heterogeneities. Earth Planet. Sci. Lett. 519, 70–82.

Pichavant, M., Di Carlo, I., Le Gac, Y., Rotolo, S.G., Scaillet, B., 2009. Experimental constraints on the deep magma feeding system at Stromboli volcano, Italy. J. Petrol. 50, 601–624.

Pichavant, M., Di Carlo, I., Rotolo, S.G., Scaillet, B., Burgisser, A., Le Gall, N., Martel, C., 2013. Generation of CO 2-rich melts during basalt magma ascent and degassing. Contrib. Mineral. Petrol. 166, 545–561.

Pichavant, M., Le Gall, N., Scaillet, B., 2018. Gases as precursory signals: experimental simulations, new concepts and models of magma degassing. Volcan. Unrest Adv Volcanol 139–154.

Pierre Jules César Janssen, 1908. . Mon. Not. R. Astron. Soc. 68, 245–249. https://doi.org/10.1093/mnras/68.4.245

Porcelli, D., Ballentine, C.J., Wieler, R., 2002. An overview of noble gas geochemistry and cosmochemistry. Rev. Mineral. Geochem. 47, 1–19.

Porcelli, D., Woolum, D., Cassen, P., 2001. Deep Earth rare gases: initial inventories, capture from the solar nebula, and losses during Moon formation. Earth Planet. Sci. Lett. 193, 237–251.

Poreda, R., di Brozolo, F.R., 1984. Neon isotope variations in Mid-Atlantic Ridge basalts. Earth Planet. Sci. Lett. 69, 277–289.

Raquin, A., Moreira, M., 2009. Atmospheric 38Ar/36Ar in the mantle: implications for the nature of the terrestrial parent bodies. Earth Planet. Sci. Lett. 287, 551–558.

Raquin, A., Moreira, M.A., Guillon, F., 2008. He, Ne and Ar systematics in single vesicles: mantle isotopic ratios and origin of the air component in basaltic glasses. Earth Planet. Sci. Lett. 274, 142–150.

Raymond, S.N., O'Brien, D.P., Morbidelli, A., Kaib, N.A., 2009. Building the terrestrial planets: Constrained accretion in the inner Solar System. Icarus 203, 644–662.

Reynolds, J., Hohenberg, C., Lewis, R., Davis, P., Kaiser, W., 1970. Isotopic analysis of rare gases from stepwise heating of lunar fines and rocks. Science 167, 545–548.

Reynolds, J., Turner, G., 1964. Rare gases in the chondrite Renazzo. J. Geophys. Res. 69, 3263–3281.

Rolfs, C.E., Rodney, W.S., 1988. Cauldrons in the cosmos: Nuclear astrophysics. University of Chicago press.

Roubinet, C., Moreira, M.A., 2018. Atmospheric noble gases in Mid-Ocean Ridge Basalts: identification of atmospheric contamination processes. Geochim. Cosmochim. Acta 222, 253–268.

Ruzié, L., Moreira, M., 2010. Magma degassing process during Plinian eruptions. J. Volcanol. Geotherm. Res. 192, 142–150.

Saltykov, S., 1967. Stereology: proceedings of the second international congress for stereology, chapter The determination of the size distribution of particles in an opaque material from a measurement of the size distribution of their sections.

Sarda, P., Graham, D., 1990. Mid-ocean ridge popping rocks: implications for degassing at ridge crests. Earth Planet. Sci. Lett. 97, 268–289.

Sarda, P., Moreira, M., 2002. Vesiculation and vesicle loss in mid-ocean ridge basalt glasses: He, Ne, Ar elemental fractionation and pressure influence. Geochim. Cosmochim. Acta 66, 1449–1458.

Sarda, P., Moreira, M., Staudacher, T., Schilling, J., Allègre, C.J., 2000. Rare gas systematics on the southernmost Mid-Atlantic Ridge: Constraints on the lower mantle and the Dupal source. J. Geophys. Res. Solid Earth 105, 5973–5996.

Sarda, P., Staudacher, T., Allègre, C.J., 1988. Neon isotopes in submarine basalts. Earth Planet. Sci. Lett. 91, 73–88. https://doi.org/10.1016/0012-821X(88)90152-5

Sasaki, S., 1999. Presence of a primary solar-type atmosphere around the earth: evidence of dissolved noble gas. Planet. Space Sci. 47, 1423–1431.

Sasaki, S., Nakazawa, K., 1990. Did a primary solar-type atmosphere exist around the proto-earth? Icarus 85, 21–42. https://doi.org/10.1016/0019-1035(90)90101-E

Scarpa, R., Tilling, R.I., Giggenbach, W., 1996. Chemical composition of volcanic gases. Monit. Mitig. Volcano Hazards 221–256.

Schlosser, P., Winckler, G., 2002. Noble gases in ocean waters and sediments. Rev. Mineral. Geochem. 47, 701–730.

Shinohara, H., Aiuppa, A., Giudice, G., Gurrieri, S., Liuzzo, M., 2008. Variation of H2O/CO2 and CO2/SO2 ratios of volcanic gases discharged by continuous degassing of Mount Etna volcano, Italy. J. Geophys. Res. Solid Earth 113.

Shishkina, T.A., Botcharnikov, R.E., Holtz, F., Almeev, R.R., Jazwa, A.M., Jakubiak, A.A., 2014. Compositional and pressure effects on the solubility of H2O and CO2 in mafic melts. Chem. Geol. 388, 112–129.

Sparks, R.S.J., 1978. The dynamics of bubble formation and growth in magmas: a review and analysis. J. Volcanol. Geotherm. Res. 3, 1–37.

Staudacher, T., Allègre, C.J., 1988. Recycling of oceanic crust and sediments: the noble gas subduction barrier. Earth Planet. Sci. Lett. 89, 173–183.

Staudacher, T., Sarda, P., Richardson, S., Allègre, C., Sagna, I., Dmitriev, L., 1989. Noble gases in basalt glasses from a Mid-Atlantic Ridge topographic high at 14 N: geodynamic consequences. Earth Planet. Sci. Lett. 96, 119–133.

Stolper, E., 1982. Water in silicate glasses: an infrared spectroscopic study. Contrib. Mineral. Petrol. 81, 1–17.

Stout, V.L., Gibbons, M.D., 1955. Gettering of gas by titanium. J. Appl. Phys. 26, 1488–1492.

Sumino, H., Kaneoka, I., Matsufuji, K., Sobolev, A.V., 2006. Deep mantle origin of kimberlite magmas revealed by neon isotopes. Geophys. Res. Lett. 33.

Tolstikhin, I., O'Nions, R., 1994. The Earth's missing xenon: A combination of early degassing and of rare gas loss from the atmosphere. Chem. Geol. 115, 1–6.

Trieloff, M., Kunz, J., Clague, D.A., Harrison, D., Allègre, C.J., 2000. The Nature of Pristine Noble Gases in Mantle Plumes. Science 288, 1036–1038. https://doi.org/10.1126/science.288.5468.1036

Warren, P.H., 1995. Extrapolated partial molar densities of SO3, P2O5, and other oxides in silicate melts. Am. Mineral. 80, 1085–1088.

Watson, E.B., Sneeringer, M.A., Ross, A., 1982. Diffusion of dissolved carbonate in magmas: experimental results and applications. Earth Planet. Sci. Lett. 61, 346–358.

Wetherill, G.W., 1954a. Variations in the isotopic abundances of neon and argon extracted from radioactive minerals. Phys. Rev. 96, 679.

Wetherill, G.W., 1954b. Variations in the isotopic abundances of neon and argon extracted from radioactive minerals. Phys. Rev. 96, 679.

Wetherill, G.W., 1953a. Spontaneous fission yields from uranium and thorium. Phys. Rev. 92, 907.

Wetherill, G.W., 1953b. Spontaneous fission yields from uranium and thorium. Phys. Rev. 92, 907.

Wieler, R., 2002. Cosmic-ray-produced noble gases in meteorites. Rev. Mineral. Geochem. 47, 125–170.

Wieler, R., 1998. The solar noble gas record in lunar samples and meteorites. Space Sci. Rev. 85, 303–314.

Williams, C.D., Mukhopadhyay, S., 2019. Capture of nebular gases during Earth's accretion is preserved in deep-mantle neon. Nature 565, 78–81. https://doi.org/10.1038/s41586-018-0771-1

Yatsevich, I., Honda, M., 1997a. Production of nucleogenic neon in the Earth from natural radioactive decay. J. Geophys. Res. Solid Earth 102, 10291–10298.

Yatsevich, I., Honda, M., 1997b. Production of nucleogenic neon in the Earth from natural radioactive decay. J. Geophys. Res. Solid Earth 102, 10291–10298.

Yokochi, R., Marty, B., 2004. A determination of the neon isotopic composition of the deep mantle. Earth Planet. Sci. Lett. 225, 77–88. https://doi.org/10.1016/j.epsl.2004.06.010

Yoshimura, S., 2015. Diffusive fractionation of H2O and CO2 during magma degassing. Chem. Geol. 411, 172–181.

Zadnik, M., Jeffery, P., 1985. Radiogenic neon in an Archaean anorthosite. Chem. Geol. Isot. Geosci. Sect. 52, 119–125.

Zhang, Y., Ni, H., Chen, Y., 2010. Diffusion data in silicate melts. Rev. Mineral. Geochem. 72, 311–408.

Zhang, Y., Xu, Z., 1995. Atomic radii of noble gas elements in condensed phases. Am. Mineral. 80, 670–675.

Zhang, Y., Xu, Z., Zhu, M., Wang, H., 2007. Silicate melt properties and volcanic eruptions. Rev. Geophys. 45.

Zhang, Y., Zindler, A., 1989. Noble gas constraints on the evolution of the Earth's atmosphere. J. Geophys. Res. Solid Earth 94, 13719–13737.

General perspective

This thesis presents pioneering research on synthetic samples whose only volatiles are carbon dioxide (CO_2) and neon. The primary goal was to determine whether the isotopic composition of gas bubbles in natural samples reflects the isotopic composition of their source or if it is influenced by physical processes during degassing (i.e. kinetic fractionation).

Several simple models of degassing in a closed system are explored: (i) a depleted melt affected by a CO_2-rich flux/melt and (ii) saturation of CO_2 due to decompression of the melt. The research finds a notable similarity between the isotopic composition of neon in synthetic samples and the values observed in Mid-Ocean Ridge Basalts (MORBs).

The observed isotopic similarity in natural samples, with values midway between the solar isotopic values and those of solar wind implantation, supports the hypothesis that the Earth's mantle may have captured a primordial nebula during the early stages of the planet's formation. Nevertheless, this study presents compelling evidence that isotopic fractionation can occur during various stages of vesicle evolution in magma, suggesting that high isotopic ratios values in natural samples should be interpreted with caution.

Further technological advancements are necessary to progress in this field. One challenge is determining the isotopic composition of vesicle nuclei in decompressed samples quenched at higher pressures. Both samples decompressed at 50 bars per minute and those at 5 bars per minute, quenched at 500 bars, had bubble sizes smaller than the laser beam diameter. This, combined with the low pressure detected during gas expansion in the line of the mass spectrometer, makes analysis difficult. Improved techniques are needed for analysing these experimental samples.

Currently, the gas trapped between the capsule and the intermediate melt cannot be analysed due to limited resources. Analysing the isotopic composition of this gas would enhance our understanding of the "lost gas" in the melt. Some experimental capsules have been preserved for future study, which will be facilitated by a new tool designed for the capsule opening under vacuum in the extraction and purification line of the mass spectrometer.

The study also presents unique textural observations using tomography, offering new insights into the evolution of gases. In such experiments, 3D vesicularity studies

typically involve small sample volumes due to the high resolution required. Consequently, a study of the full volume using tools such as ImageJ would demand a powerful processor. Consequently, the concurrent utilisation of 3D and 2D imaging techniques on the same sample enables a more comprehensive analysis of the textural characteristics associated with vesicularity.

This research represents a significant step forward in understanding the isotopic composition of gas bubbles in natural samples thought experimental petrology. Continued technological innovation and further studies are essential for advancing this field.

This methodology can also be extended to the analysis of $^{38}Ar/^{36}Ar$ ratios, as well as to other elemental ratios. The examination of $^{4}He/^{40}Ar$ and $^{3}He/^{22}Ne$ elemental ratios offers a valuable framework for investigating distillation processes frequently observed in oceanic island basalts (Moreira and Sarda, 2000).

References:

Moreira, M., Sarda, P., 2000. Noble gas constraints on degassing processes. Earth Planet. Sci. Lett. 176, 375–386.

APPENDIX I

Vesicle Size Distribution (VSD)

Appendix I: Vesicularity Size Distribution:

The vesicular size distribution is typically employed on a portion of a natural sample in order to gain insight into the distribution of vesicles, the different populations, and the state of evolution of bubble nucleation from the magma chamber until fragmentation occurs at the crustal surface. A statistical analysis of a natural sample provides an overview of the large-scale conditions of magma evolution. The use of VDS in experimental samples allows for a more detailed examination of this process.

3D tomography enables the observation of the internal structure of the experimental vesiculated glass without compromising the integrity of the sample. In certain instances, it may not be feasible to recover the entirety of the sample. The capsule, made of gold-palladium, presents a significant challenge due to its inherent hardness, which can impede the recovery of the entire sample. In certain instances, the fragmentation of the glass can further complicate the process.

This section of the appendix provides a detailed characterization of all the experimental samples conducted during the course of the thesis, categorised into two distinct scenarios. (i) Experimental samples In non-equilibrium conditions (< 24h) at 1200 ºC and 2000 bar supersaturated in CO2 (more than 0.6 wt.% added) where CO2 and neon are the gas phase; and (ii) samples with CO2 (2700 ppm added) and neon as the gas phase, which have been decompressed and quenched after reaching equilibrium (more than 30h at 1200 ºC and 2 kbar before starting decompression) at pressures between 2000 and 110 bar.

The buoyancy effect causes vesicles in most quenched glasses to accumulate at the top of the capsule (in the position of the capsule inside the IHPV while the experiment is running). Additionally, some experiments show vesicles are more likely to nucleate on the boundaries of the capsule. This phenomenon was previously observed by Lux (1987) where a surface of adhesion was found to be more prevalent than buoyancy. Consequently, the total volume of the glass is considered in order to study the VSD in each quenched glass.

The size of the resulting tomographic image set for every sample is such that full 3D sample analysis with *ImageJ* is only possible on a powerful computer in addition to a time-consuming process. The image analysis was conducted on each slice in 2D, with the most representative slices selected for the VSD study (see **Figure S-1**).

For the final VSD characterisation, it was necessary to select the range of images used for the calculations (black square in **Figure S-1a**). In the statistics, the images of the edge of the sample were avoided, as these contain the vesicles that were trapped at the capsule-glass interface when quenched. An example of vesicularity at the capsule-glass interface for the same sample as **Figure S-1** is presented in **Figure S-2**.

Furthermore, slices containing artefacts and the boundaries of the glass, where external vesicles were located, were excluded from the analysis (they will be represented as a gap of dots in the diagrams). The image processing was conducted with a consistent reference axis for each sample, with a cross-sectional view of the sample where the top and bottom of the sample during the experiment are always present.

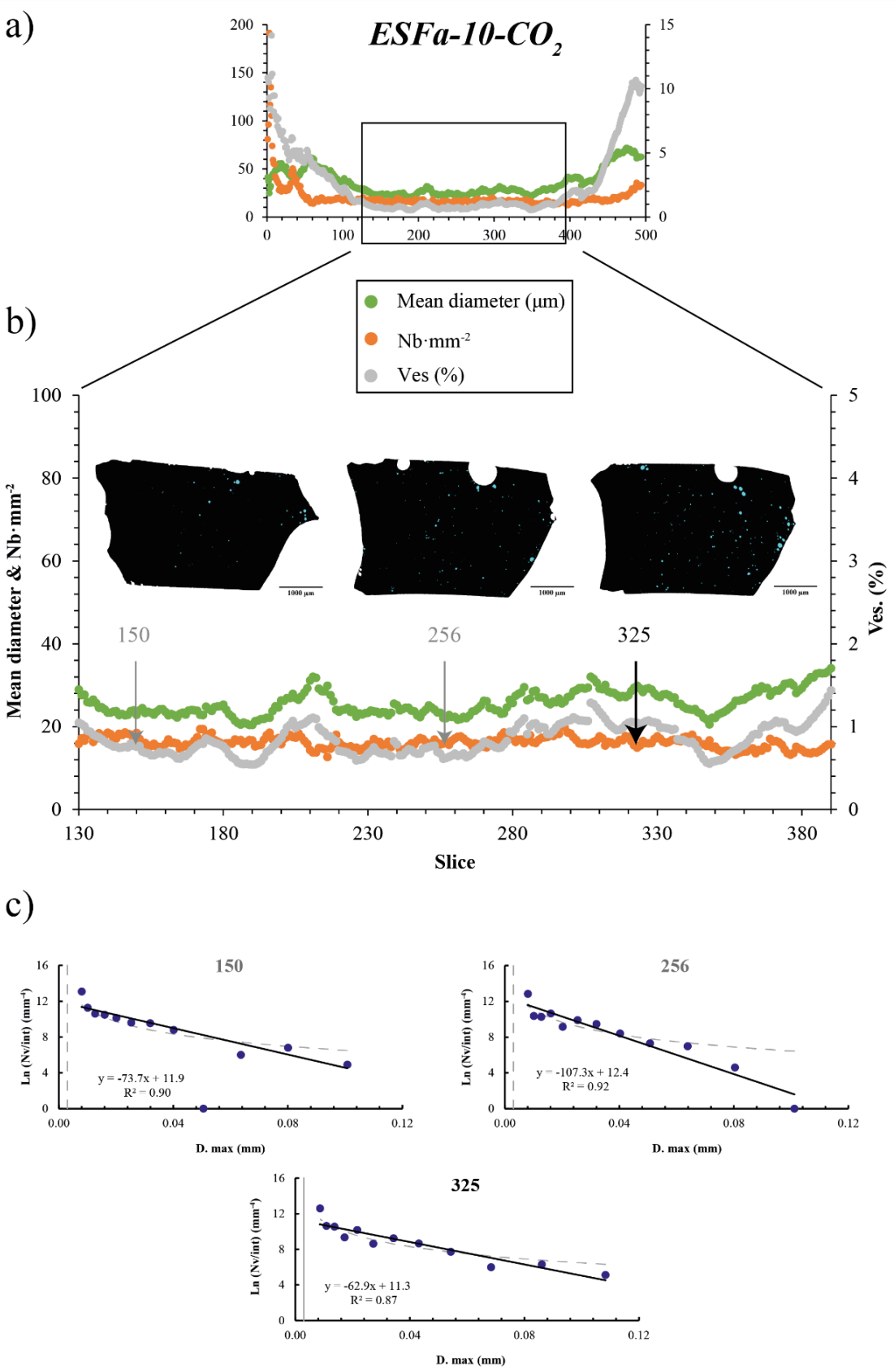

Figure S-1: (a) Selection of image range for ImageJ processing; (b) Example of three images selected from the range; (c) diagrams of ln(n) as a function of the maximum diameter of each class

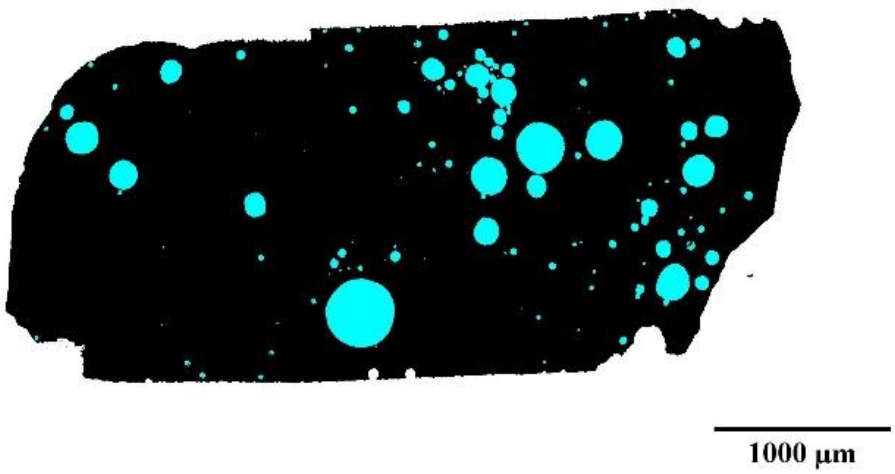

Figure S-2: Slice 471 Sample ESFa-10-CO_2 belonging to the capsule-glass interface exhibiting a remarkably high degree of vesicularity concerning the inner part of the sample, and a larger vesicle size (see Figure sup 1.a and Figure sup 1.b).

Three images from each entire data set were selected for the characterisation of the sample (**Figure S-1b**). As the results are similar in all three images, one of them is chosen as a representative of the experimental sample.

The description of the experimental samples is conducted according to several parameters.

- A 3D representative image of the experimental/natural sample obtained by micro-CT, where the glass is represented by grey, and the vesicles not connected to the air surface are represented by red.
- A graphical representation of the mean diameter of the vesicles, the bubble density and the vesicularity of each slice of the image stack obtained by micro-CT is provided. An arrow was positioned at the location of the selected slice for sample characterisation.
- Two 2D images of the selected slice in greyscale, accompanied by a corresponding treatment where the bubbles are coloured blue, and the glass is black. Both images have been scaled.
- A quantitative description of the experimental conditions and the image treatment, as provided by the two software packages employed (*ImageJ* and *VGStudioMax*). The volume of the samples was obtained using *VGStudioMax*. The vesicularity is quantified by *VGStudioMax* in terms of the volume occupied by each phase. The selected range of images was chosen to avoid vesicles belonging to the capsule-glass interface, and artefacts. The vesicularity is given by *VGStudioMax* regarding to the volume occupied for every phase; the range selected range of images to avoid vesicles belonging to the capsule-glass interface; and the vesicularity of the selected image for the vesicularity studio.

- The population density graphic showed in the corresponding chapters for the selected image.
- Furthermore, the VSD table for the corresponding image on which the study was conducted is provided.

Static Samples:

ESFa-4-CO_2:

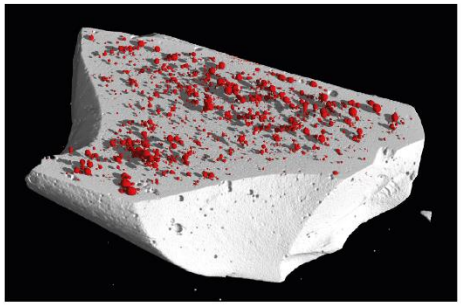

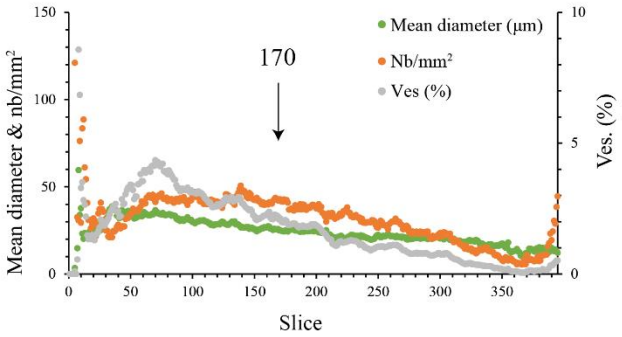

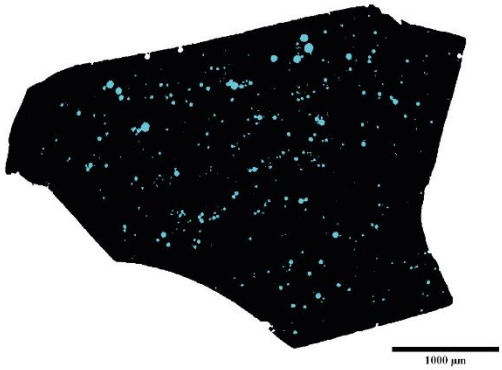

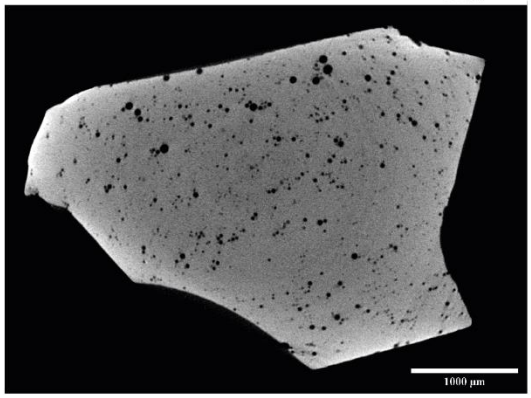

Experimental conditions	
Time (min)	30
Pressure (bars)	1598
Temperature (°C)	1200
Run	2
CO_2 added (wt.%)	1.18
Weigth (mg)	23.80
Resolution (µm)	3
Volume (mm³)	8.58
VGStudiomax treatment	
Ves (%)	0.88
ImageJ treatment	
Range	98-348
Tot. images	250
Ves. (from range volume) (%)	1.6
Area (mm²)	8.98
Bub. mean diameter	25.04
Nb/mm²	42.11
Ves. slice (%)	2.07

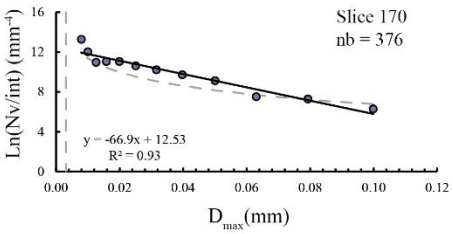

Class Number	Interval	D.max	Nb	Na (Nb/mm²)	Nv (mm⁻³)	Ln (Nv/int) (mm⁻⁴)
1	0.02054	0.100	6	0.7	11	6.28
2	0.01631	0.079	12	1.3	24	7.29
3	0.01296	0.063	12	1.3	24	7.52
4	0.01029	0.050	30	3.3	94	9.12
5	0.00818	0.040	39	4.3	136	9.72
6	0.00649	0.032	44	4.9	178	10.22
7	0.00516	0.025	45	5.0	213	10.63
8	0.00410	0.020	45	5.0	258	11.05
9	0.00325	0.016	35	3.9	204	11.05
10	0.00259	0.013	25	2.8	150	10.97
11	0.00205	0.010	30	3.3	343	12.02
12	0.00163	0.008	53	5.9	952	13.28
		Total	376			

ESFa-6-CO_2:

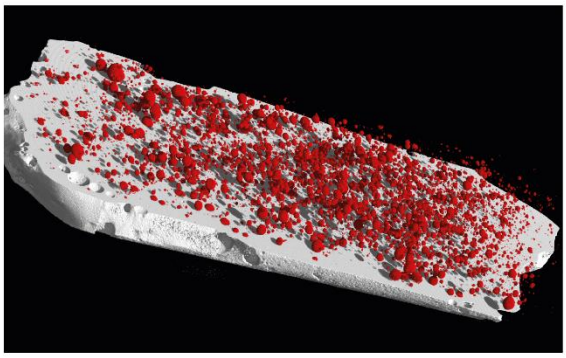

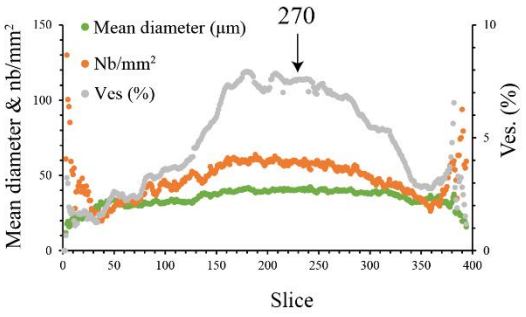

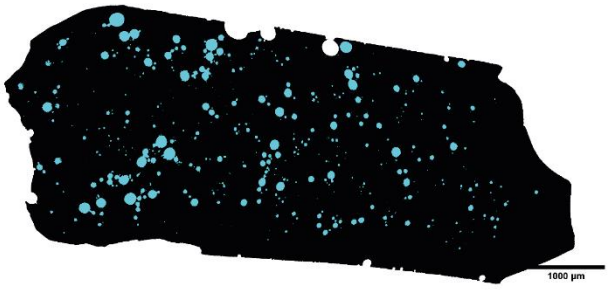

Experimental conditions	
Time (min)	30
Pressure (bars)	1598
Temperature (ºC)	1200
Run	2
CO_2 added (wt.%)	2.34
Weigth (mg)	50.6
Resolution (µm)	3
Volume (mm^3)	11.94
VGStudiomax treatment	
Ves (%)	2.68
ImageJ treatment	
Range	160-320
Tot. images	160
Ves. (from range volume) (%)	6.9
Area (mm^2)	13.36
Bub. mean diameter	40.05
Nb/mm^2	53.75
Ves. slice (%)	6.77

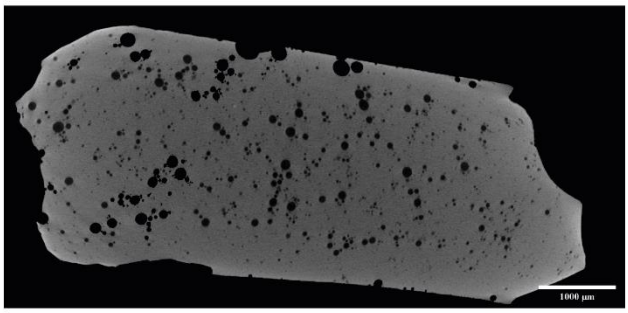

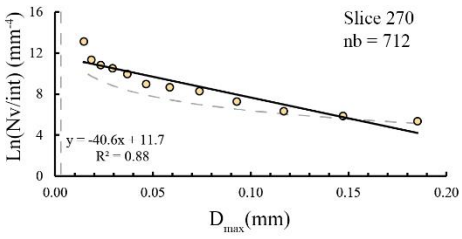

Class Number	Interval	D.max	Nb	Na (Nb/mm^2)	Nv (mm^{-3})	Ln (Nv/int) (mm^{-4})
1	0.03810	0.185	12	0.9	8	5.34
2	0.03027	0.147	16	1.2	11	5.86
3	0.02404	0.117	18	1.3	13	6.32
4	0.01910	0.093	27	2.0	27	7.27
5	0.01517	0.074	45	3.4	60	8.28
6	0.01205	0.059	48	3.6	69	8.66
7	0.00957	0.047	46	3.4	76	8.97
8	0.00760	0.037	65	4.9	158	9.94
9	0.00604	0.029	76	5.7	222	10.51
10	0.00480	0.023	73	5.5	240	10.82
11	0.00381	0.019	76	5.7	319	11.33
12	0.00303	0.015	210	15.7	1514	13.12
		Total	712			

ESFa-7-CO_2:

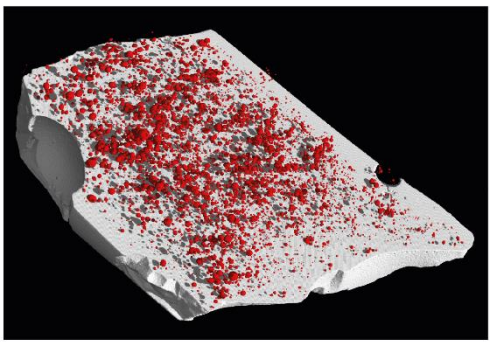

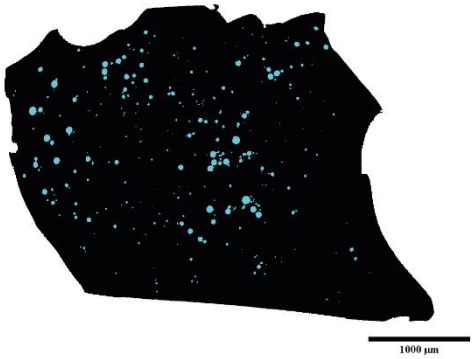

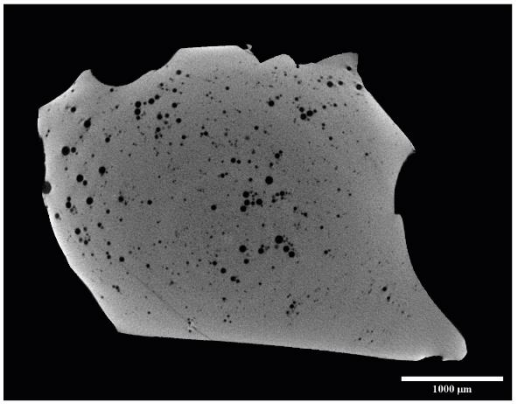

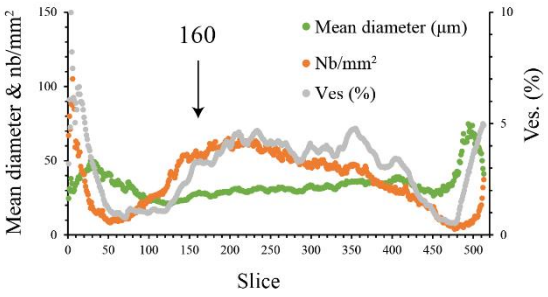

Experimental conditions	
Time (min)	30
Pressure (bars)	1598
Temperature (°C)	1200
Run	2
CO_2 added (wt.%)	6.11
Weigth (mg)	34.80
Resolution (µm)	3
Volume (mm^3)	11.05
VGStudiomax treatment	
Ves (%)	1.70
ImageJ treatment	
Range	160-340
Tot. images	180
Ves. (from range volume) (%)	3.9
Area (mm^2)	9.06
Bub. mean diameter	28.06
Nb/mm^2	52.54
Ves. slice (%)	3.25

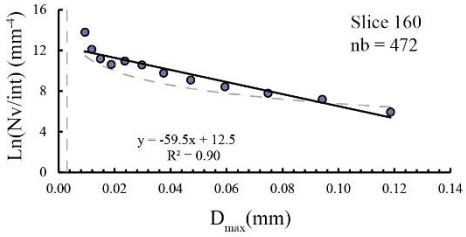

Class Number	Interval	D.max	Nb	Na (Nb/mm^2)	Nv (mm^{-3})	Ln (Nv/int) (mm^{-4})
1	0.02439	0.119	6	0.7	9	5.93
2	0.01937	0.094	15	1.7	26	7.19
3	0.01539	0.075	20	2.2	37	7.80
4	0.01222	0.059	25	2.8	56	8.43
5	0.00971	0.047	31	3.4	86	9.08
6	0.00771	0.037	39	4.3	135	9.77
7	0.00613	0.030	53	5.8	238	10.57
8	0.00487	0.024	55	6.1	279	10.96
9	0.00387	0.019	37	4.1	160	10.63
10	0.00307	0.015	34	3.8	218	11.17
11	0.00244	0.012	43	4.7	440	12.10
12	0.00194	0.009	114	12.6	1886	13.79
		Total	472			

ESFa-8-CO_2:

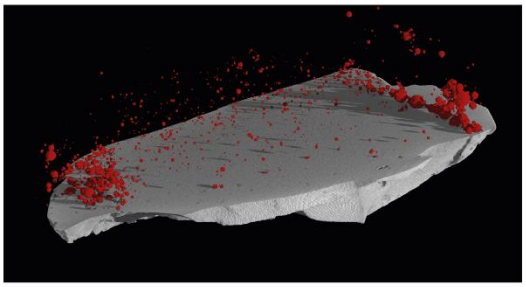

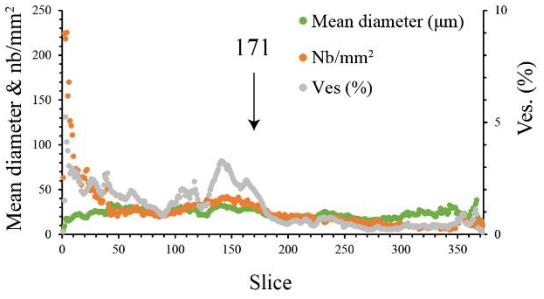

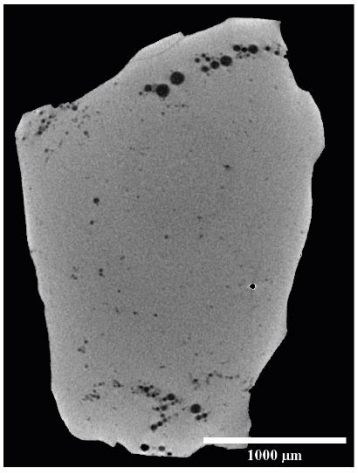

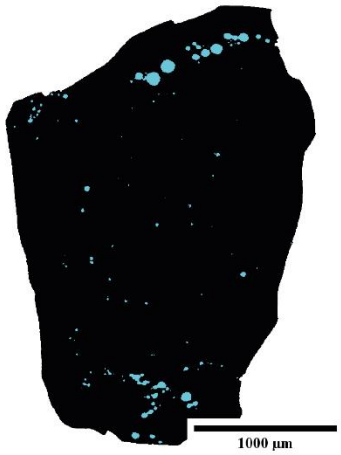

Experimental conditions

Time (min)	240
Pressure (bars)	1609
Temperature (°C)	1200
Run	3
CO_2 added (wt.%)	1.38
Weigth (mg)	7.2 (after polishing)
Resolution (µm)	3
Volume (mm³)	4.11

VGStudiomax treatment

Ves (%)	0.46

ImageJ treatment

Range	121-213
Tot. images	92
Ves. (from range volume) (%)	1.6
Area (mm²)	4.82
Bub. mean diameter	28.03
Nb/mm²	30.71
Ves. slice (%)	1.90

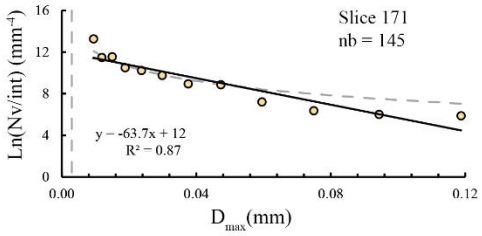

Class Number	Interval	D.max	Nb	Na (Nb/mm²)	Nv (mm ³)	Ln (Nv/int) (mm ⁴)
1	0.02443	0.119	3	0.6	9	5.87
2	0.01940	0.094	3	0.6	8	6.00
3	0.01541	0.075	3	0.6	9	6.36
4	0.01224	0.060	4	0.8	17	7.21
5	0.00972	0.047	11	2.3	69	8.87
6	0.00772	0.038	10	2.1	60	8.95
7	0.00614	0.030	13	2.7	106	9.76
8	0.00487	0.024	14	2.9	135	10.23
9	0.00387	0.019	13	2.7	142	10.51
10	0.00308	0.015	19	3.9	318	11.55
11	0.00244	0.012	15	3.1	237	11.48
12	0.00194	0.009	37	7.7	1120	13.27
		Total	145			

ESFa-9-CO_2:

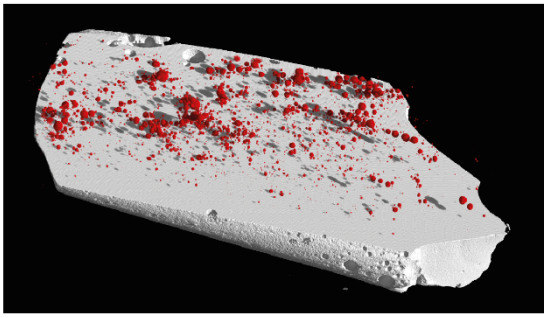

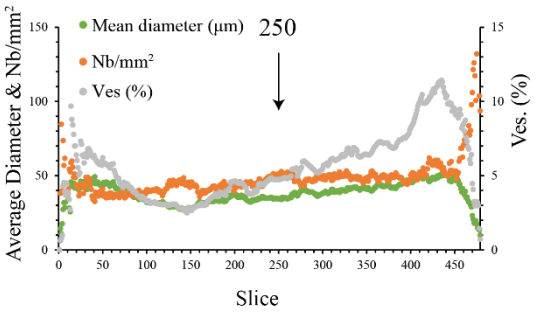

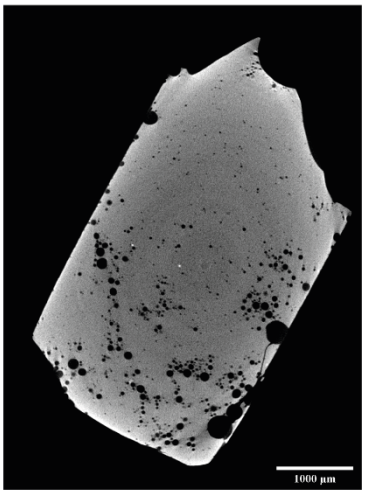

Experimental conditions

Time (min)	240
Pressure (bars)	1609
Temperature (°C)	1200
Run	3
CO_2 added (wt.%)	2.72
Weigth (mg)	37.00
Resolution (µm)	3
Volume (mm^3)	13.83

VGStudiomax treatment

Ves (%)	2.51

ImageJ treatment

Range	98-394
Tot. images	296
Ves. (from range volume) (%)	4.9
Area (mm^2)	12.54
Bub. mean diameter	34.28
Nb/mm^2	51.35
Ves. slice (%)	4.74

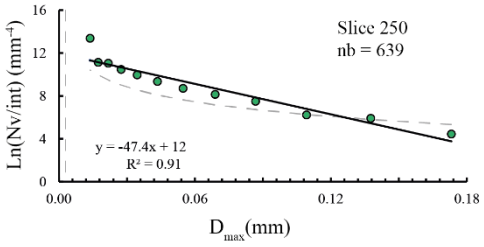

Class Number	Interval	D.max	Nb	Na (Nb/mm^2)	Nv (mm^{-3})	Ln (Nv/int) (mm^{-4})
1	0.03562	0.173	4	0.3	3	4.44
2	0.02830	0.138	12	1.0	10	5.91
3	0.02248	0.109	13	1.0	11	6.22
4	0.01785	0.087	26	2.1	32	7.50
5	0.01418	0.069	34	2.7	49	8.14
6	0.01127	0.055	40	3.2	68	8.70
7	0.00895	0.044	48	3.8	102	9.34
8	0.00711	0.035	57	4.5	151	9.96
9	0.00565	0.027	62	4.9	197	10.46
10	0.00448	0.022	70	5.6	283	11.05
11	0.00356	0.017	58	4.6	242	11.13
12	0.00283	0.014	215	17.1	1827	13.38
		Total	639			

ESFa-10-CO_2:

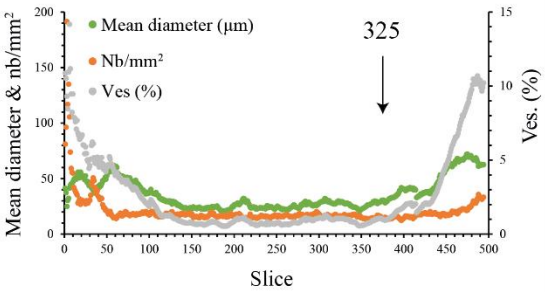

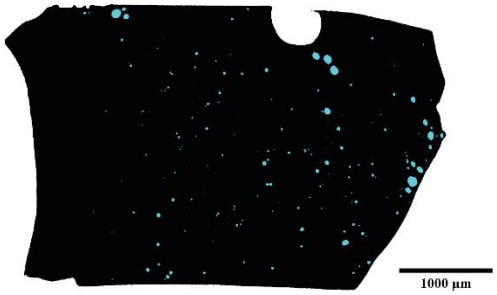

Experimental conditions	
Time (min)	240
Pressure (bars)	1609
Temperature (°C)	1200
Run	3
CO_2 added (wt.%)	7.18
Weigth (mg)	41.70
Resolution (µm)	3
Volume (mm³)	14.68
VGStudiomax treatment	
Ves (%)	0.65
ImageJ treatment	
Range	130-390
Tot. images	260
Ves. (from range volume) (%)	0.8
Area (mm²)	12.11
Bub. mean diameter	28.36
Nb/mm²	16.52
Ves. slice (%)	1.04

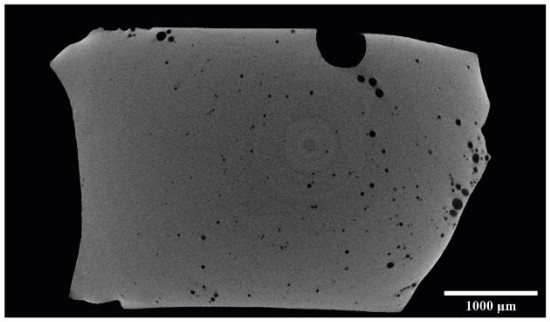

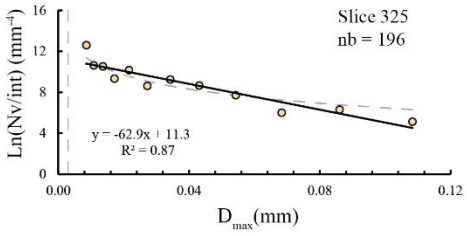

Class Number	Interval	D.max	Nb	Na (Nb/mm²)	Nv (mm⁻³)	Ln (Nv/int) (mm⁻⁴)
1	0.02228	0.108	3	0.2	4	5.13
2	0.01770	0.086	7	0.6	10	6.31
3	0.01406	0.068	5	0.4	6	6.00
4	0.01117	0.054	12	1.0	25	7.72
5	0.00887	0.043	20	1.7	51	8.65
6	0.00705	0.034	25	2.1	73	9.25
7	0.00560	0.027	15	1.2	31	8.63
8	0.00445	0.022	25	2.1	116	10.17
9	0.00353	0.017	14	1.2	40	9.34
10	0.00280	0.014	17	1.4	105	10.54
11	0.00223	0.011	14	1.2	92	10.63
12	0.00177	0.009	39	3.2	524	12.60
		Total	196			

ESFa-7E-CO_2:

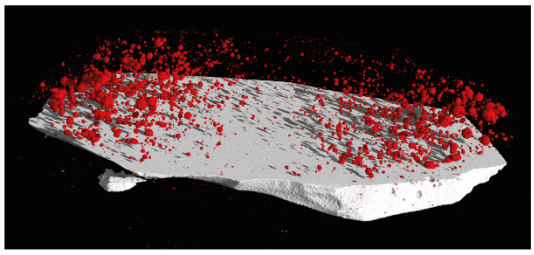

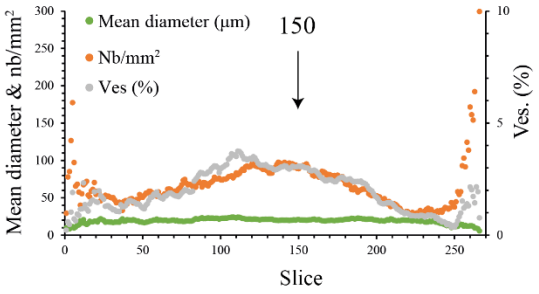

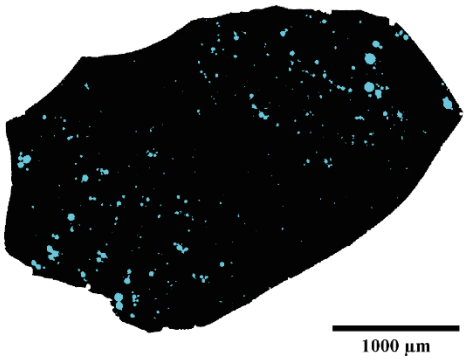

Experimental conditions	
Time (min)	10
Pressure (bars)	1794
Temperature (°C)	1200
Run	6
CO_2 added (wt.%)	1.15
Weigth (mg)	9.60
Resolution (µm)	3
Volume (mm³)	3.38
VGStudiomax treatment	
Ves (%)	0.67
ImageJ treatment	
Range	144-197
Tot. images	266
Ves. (from range volume) (%)	2.6
Area (mm²)	6.28
Bub. mean diameter	21.02
Nb/mm²	88.95
Ves. slice (%)	3.09

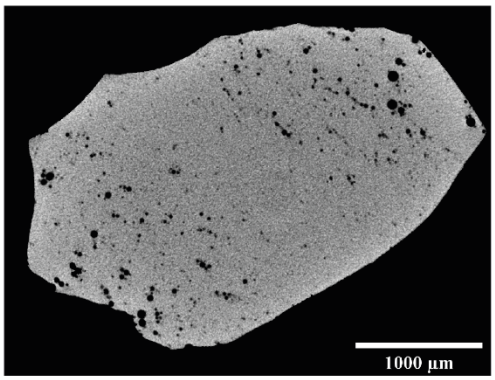

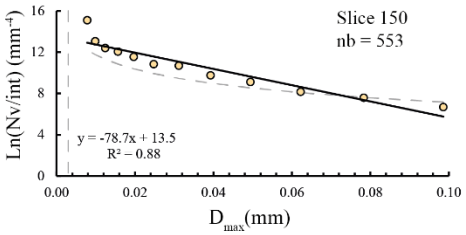

Class Number	Interval	D.max	Nb	Na (Nb/mm²)	Nv (mm⁻³)	Ln (Nv/int) (mm⁻⁴)
1	0.02027	0.099	6	1.0	16	6.67
2	0.01610	0.078	11	1.8	31	7.57
3	0.01279	0.062	14	2.2	44	8.15
4	0.01016	0.049	22	3.5	91	9.10
5	0.00807	0.039	28	4.5	137	9.74
6	0.00641	0.031	43	6.8	279	10.68
7	0.00509	0.025	39	6.2	258	10.83
8	0.00405	0.020	46	7.3	415	11.54
9	0.00321	0.016	50	8.0	553	12.06
10	0.00255	0.012	48	7.6	618	12.40
11	0.00203	0.010	54	8.6	939	13.05
12	0.00161	0.008	192	30.6	5744	15.09
		Total	553			

ESFa-8E-CO_2:

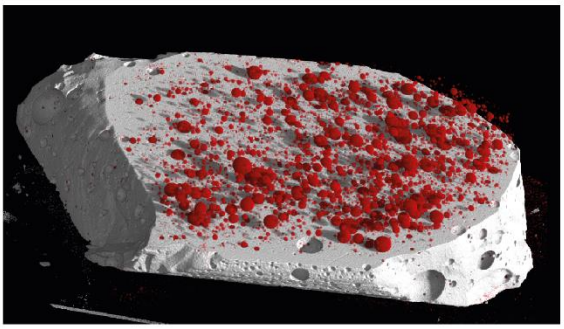

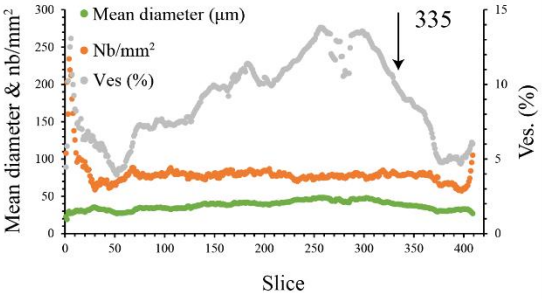

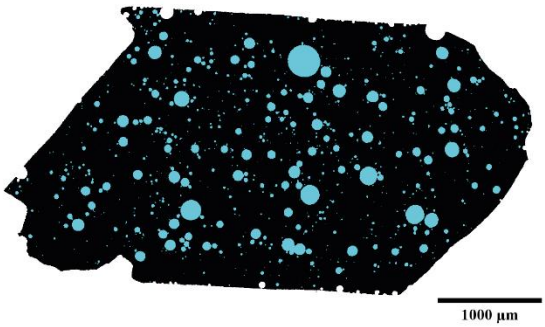

Experimental conditions	
Time (min)	10
Pressure (bars)	1794
Temperature (°C)	1200
Run	6
CO_2 added (wt.%)	3.02
Weigth (mg)	46.90
Resolution (µm)	3
Volume (mm³)	10.35
VGStudiomax treatment	
Ves (%)	7.28
ImageJ treatment	
Range	75-350
Tot. images	275
Ves. (from range volume) (%)	9.3
Area (mm²)	9.57
Bub. mean diameter	39.43
Nb/mm²	78.62
Ves. slice (%)	9.60

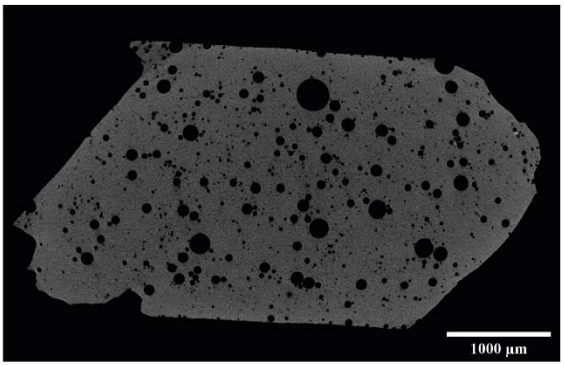

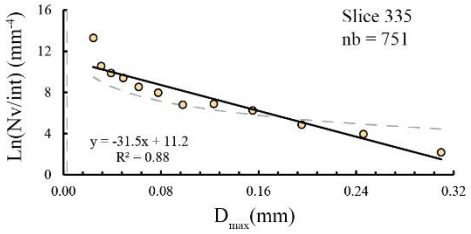

Class Number	Interval	D.max	Nb	Na (Nb/mm²)	Nv (mm⁻³)	Ln (Nv/int) (mm⁻⁴)
1	0.06368	0.310	1	0.1	1	2.17
2	0.05058	0.246	4	0.4	3	3.94
3	0.04018	0.195	7	0.7	5	4.85
4	0.03191	0.155	17	1.8	16	6.24
5	0.02535	0.123	23	2.4	25	6.88
6	0.02014	0.098	18	1.9	18	6.79
7	0.01599	0.078	28	2.9	46	7.97
8	0.01271	0.062	33	3.4	65	8.53
9	0.01009	0.049	47	4.9	123	9.41
10	0.00802	0.039	52	5.4	157	9.88
11	0.00637	0.031	63	6.6	244	10.56
12	0.00506	0.025	458	47.9	3043	13.31
		Total	751			

ESFa-9E-CO_2:

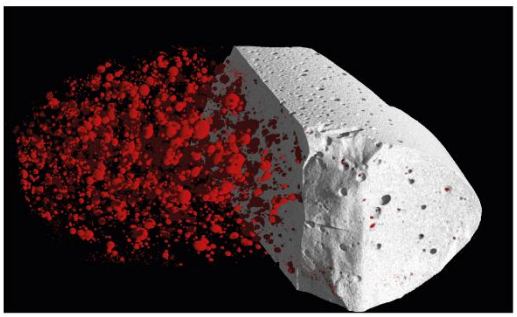

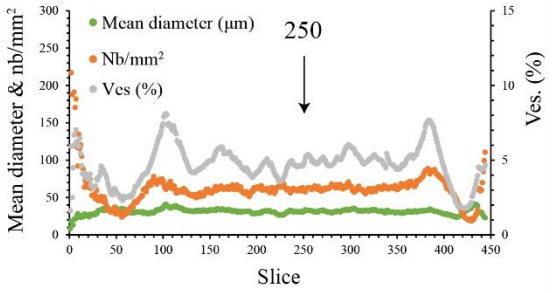

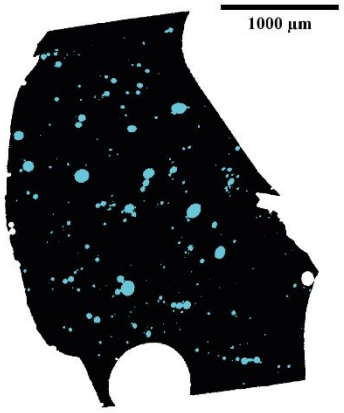

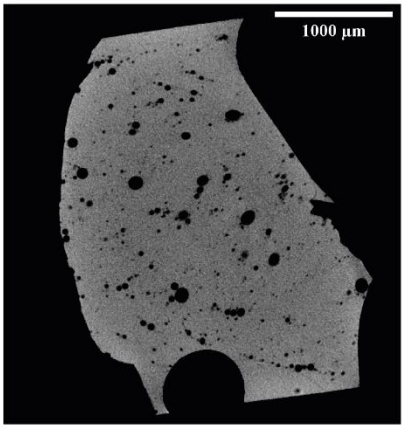

Experimental conditions	
Time (min)	10
Pressure (bars)	1794
Temperature (°C)	1200
Run	6
CO_2 added (wt.%)	4.99
Weigth (mg)	18.00
Resolution (µm)	3
Volume (mm^3)	6.49
VGStudiomax treatment	
Ves (%)	2.53
ImageJ treatment	
Range	120-370
Tot. images	250
Ves. (from range volume) (%)	4.9
Area (mm^2)	5.69
Bub. mean diameter	31.07
Nb/mm^2	62.59
Ves. slice (%)	4.74

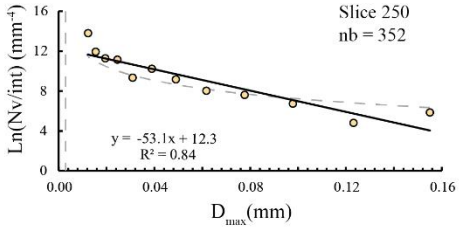

Class Number	Interval	D.max	Nb	Na (Nb/mm^2)	Nv (mm^{-3})	Ln (Nv/int) (mm^{-4})
1	0.03189	0.155	6	1.1	11	5.86
2	0.02533	0.123	3	0.5	3	4.82
3	0.02012	0.098	7	1.2	17	6.74
4	0.01598	0.078	11	1.9	32	7.61
5	0.01270	0.062	12	2.1	39	8.03
6	0.01008	0.049	21	3.7	98	9.18
7	0.00801	0.039	37	6.5	223	10.23
8	0.00636	0.031	20	3.5	73	9.35
9	0.00505	0.025	39	6.9	355	11.16
10	0.00401	0.020	35	6.2	319	11.28
11	0.00319	0.016	40	7.0	495	11.95
12	0.00253	0.012	121	21.3	2490	13.80
		Total	352			

ESFa-10E-CO_2:

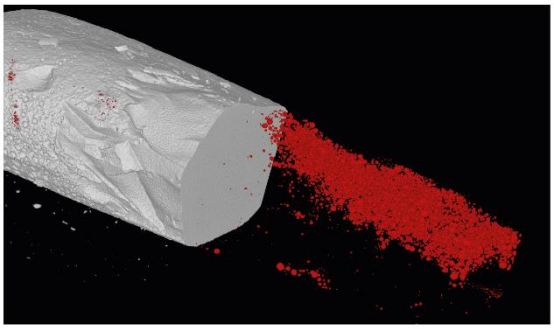

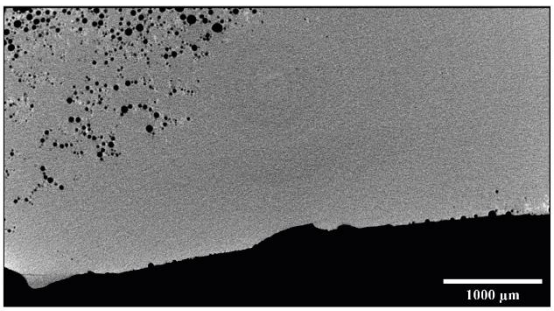

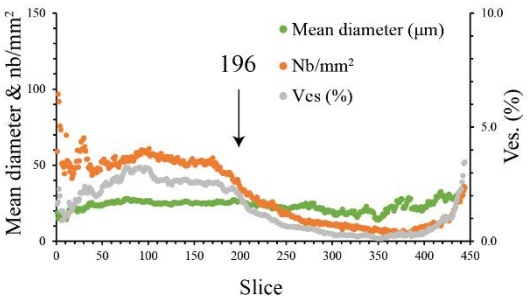

Experimental conditions	
Time (min)	1140
Pressure (bars)	1726
Temperature (ºC)	1200
Run	7
CO_2 added (wt.%)	1.38
Weigth (mg)	27.20
Resolution (µm)	3
Volume (mm³)	14.56
VGStudiomax treatment	
Ves (%)	0.69
ImageJ treatment	
Range	44-425
Tot. images	381
Ves. (from range volume) (%)	1.4
Area (mm²)	12.83
Bub. mean diameter	26.42
Nb/mm²	39.04
Ves. slice (%)	2.14

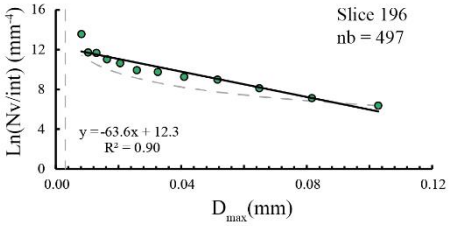

Class Number	Interval	D.max	Nb	Na (Nb/mm²)	Nv (mm ³)	Ln (Nv/int) (mm ⁴)
1	0.02114	0.103	10	0.8	12	6.38
2	0.01679	0.082	16	1.2	21	7.12
3	0.01334	0.065	28	2.2	45	8.13
4	0.01060	0.052	43	3.4	84	8.98
5	0.00842	0.041	43	3.4	90	9.27
6	0.00669	0.033	45	3.5	115	9.75
7	0.00531	0.026	39	3.0	109	9.93
8	0.00422	0.021	44	3.4	177	10.64
9	0.00335	0.016	43	3.4	206	11.03
10	0.00266	0.013	48	3.7	309	11.66
11	0.00211	0.010	39	3.0	259	11.72
12	0.00168	0.008	99	7.7	1303	13.56
		Total	497			

ESFa-2D-CO_2:

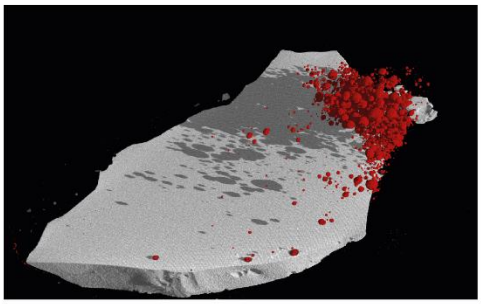

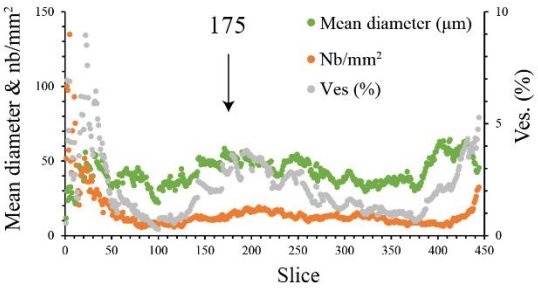

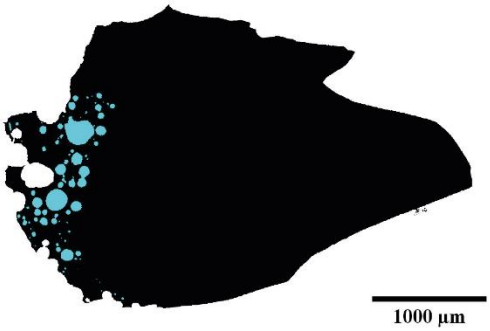

Experimental conditions	
Time (min)	1140
Pressure (bars)	1726
Temperature (°C)	1200
Run	7
CO_2 added (wt.%)	5.45
Weigth (mg)	21.00
Resolution (µm)	3
Volume (mm³)	7.6
VGStudiomax treatment	
Ves (%)	0.83
ImageJ treatment	
Range	145-365
Tot. images	220
Ves. (from range volume) (%)	2.1
Area (mm²)	2.93
Bub. mean diameter	39.99
Nb/mm²	10.83
Ves. slice (%)	1.36

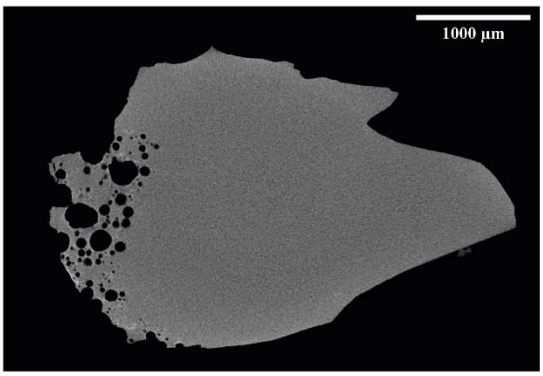

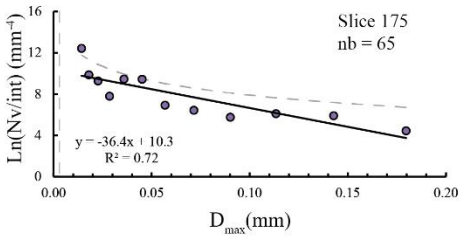

Class Number	Interval	D.max	Nb	Na (Nb/mm²)	Nv (mm⁻³)	Ln (Nv/int) (mm⁻⁴)
1	0.03696	0.180	1	0.3	3	4.44
2	0.02936	0.143	3	1.0	11	5.90
3	0.02332	0.113	3	1.0	10	6.10
4	0.01852	0.090	2	0.7	6	5.75
5	0.01471	0.072	2	0.7	9	6.42
6	0.01169	0.057	2	0.7	12	6.92
7	0.00928	0.045	10	3.4	115	9.42
8	0.00737	0.036	9	3.1	94	9.45
9	0.00586	0.028	4	1.4	14	7.78
10	0.00465	0.023	4	1.4	49	9.26
11	0.00370	0.018	4	1.4	71	9.86
12	0.00294	0.014	20	6.8	723	12.41
		Total	64			

ESFa-3D-CO_2:

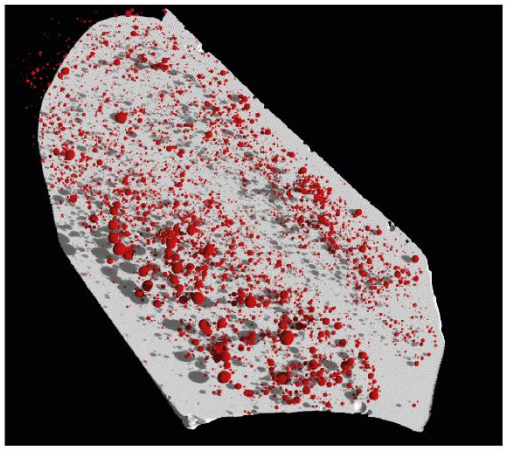

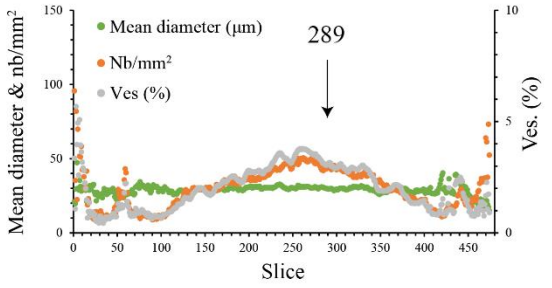

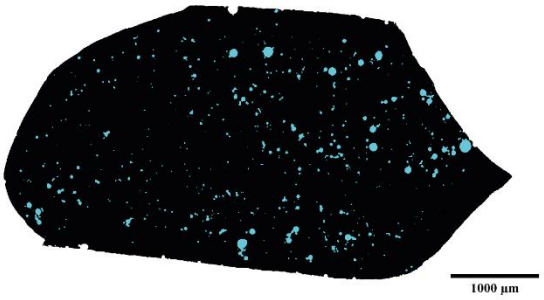

Experimental conditions	
Time (min)	130
Pressure (bars)	1725
Temperature (°C)	1200
Run	8+9
CO_2 added (wt.%)	0.68
Weigth (mg)	34.30
Resolution (µm)	3
Volume (mm³)	12.40
VGStudiomax treatment	
Ves (%)	0.86
ImageJ treatment	
Range	150-375
Tot. images	225
Ves. (from range volume) (%)	2.5
Area (mm²)	11.42
Bub. mean diameter	28.99
Nb/mm²	39.14
Ves. slice (%)	2.58

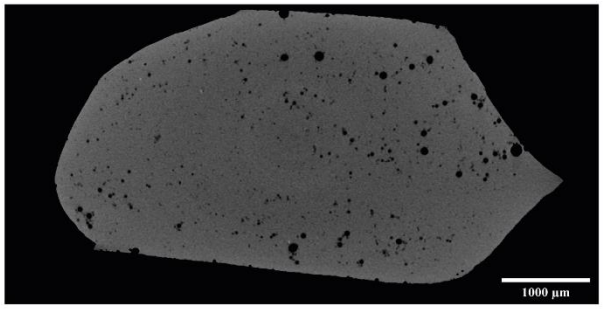

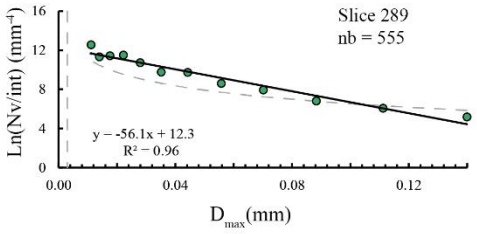

Class Number	Interval	D.max	Nb	Na (Nb/mm²)	Nv (mm ³)	Ln (Nv/int) (mm ⁴)
1	0.02879	0.140	5	0.4	5	5.19
2	0.02287	0.111	9	0.8	10	6.07
3	0.01817	0.088	13	1.1	17	6.82
4	0.01443	0.070	24	2.1	40	7.94
5	0.01146	0.056	32	2.8	62	8.60
6	0.00910	0.044	58	5.1	153	9.73
7	0.00723	0.035	50	4.4	127	9.77
8	0.00574	0.028	70	6.1	263	10.73
9	0.00456	0.022	94	8.2	449	11.50
10	0.00362	0.018	74	6.5	335	11.43
11	0.00288	0.014	53	4.6	239	11.33
12	0.00229	0.011	73	6.4	643	12.55
		Total	555			

ESFa-4D-CO_2:

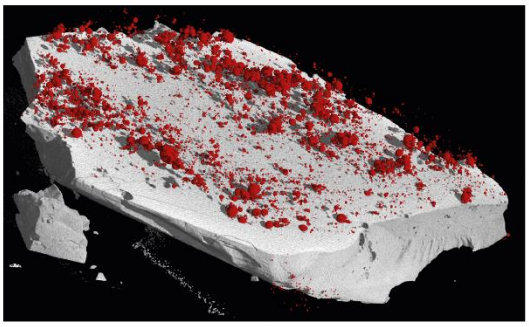

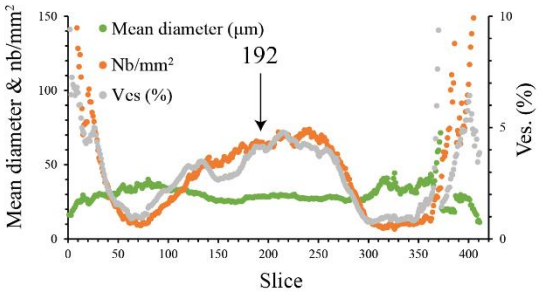

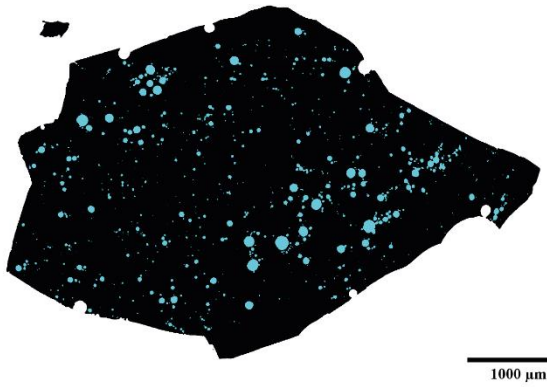

Experimental conditions	
Time (min)	130
Pressure (bars)	1725
Temperature (°C)	1200
Run	8+9
CO_2 added (wt.%)	0.68
Weigth (mg)	34.30
Resolution (µm)	3
Volume (mm^3)	10.40
VGStudiomax treatment	
Ves (%)	1.85
ImageJ treatment	
Range	125-268
Tot. images	143
Ves. (from range volume) (%)	3.7
Area (mm^2)	10.38
Bub. mean diameter	28.70
Nb/mm^2	63.61
Ves. slice (%)	4.12

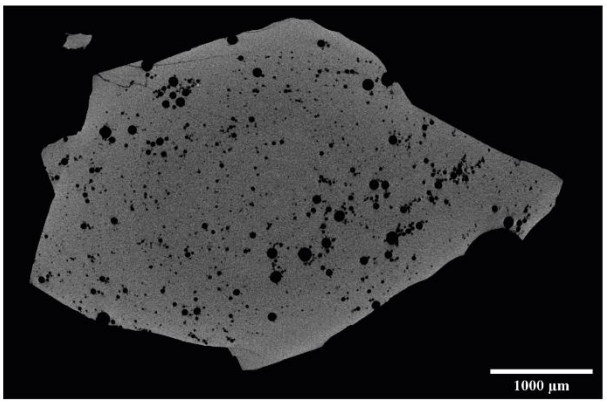

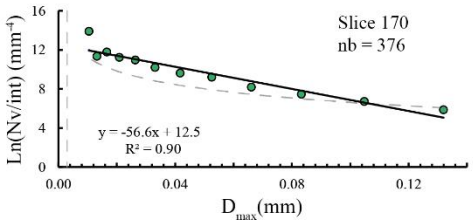

Class Number	Interval	D.max	Nb	Na (Nb/mm^2)	Nv (mm^{-3})	Ln (Nv/int) (mm^{-4})
1	0.02714	0.132	8	0.8	10	5.87
2	0.02155	0.105	14	1.3	18	6.72
3	0.01712	0.083	20	1.9	30	7.46
4	0.01360	0.066	27	2.6	49	8.18
5	0.01080	0.053	45	4.3	108	9.21
6	0.00858	0.042	49	4.7	129	9.62
7	0.00682	0.033	56	5.4	183	10.20
8	0.00541	0.026	72	6.9	310	10.96
9	0.00430	0.021	69	6.6	328	11.24
10	0.00342	0.017	73	7.0	445	11.78
11	0.00271	0.013	47	4.5	230	11.35
12	0.00216	0.010	175	16.9	2329	13.89
		Total	655			

ESFa-5D-CO_2:

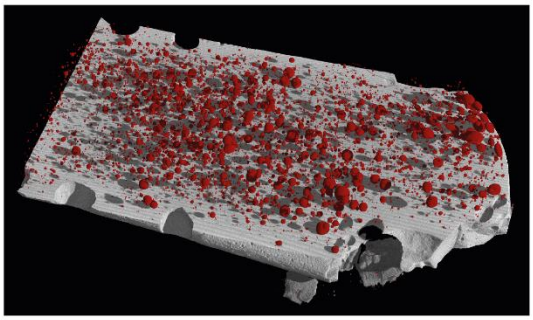

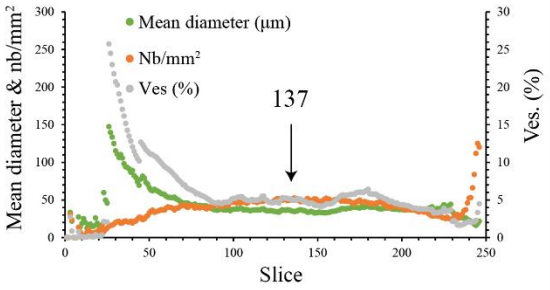

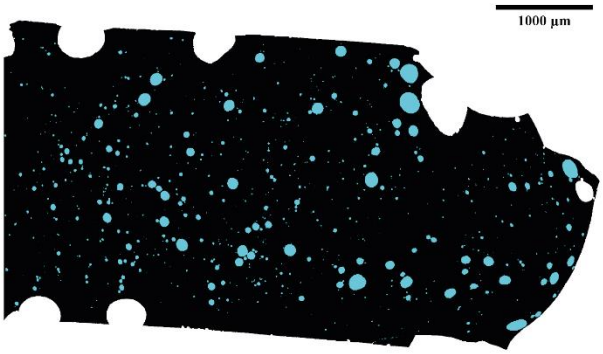

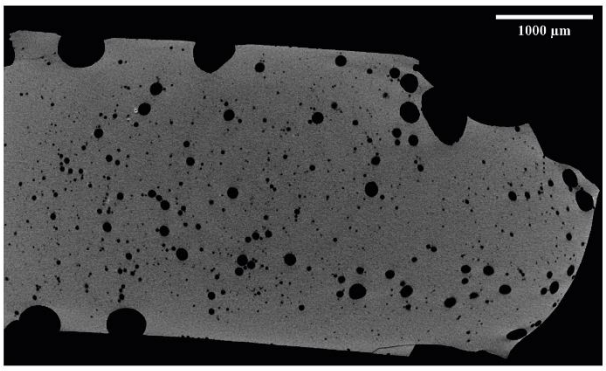

Experimental conditions	
Time (min)	130
Pressure (bars)	1725
Temperature (°C)	1200
Run	8+9
CO_2 added (wt.%)	5.07
Weigth (mg)	52.40
Resolution (µm)	3
Volume (mm³)	17.52
VGStudiomax treatment	
Ves (%)	2.49
ImageJ treatment	
Range	90-205
Tot. images	115
Ves. (from range volume) (%)	5.0
Area (mm²)	15.29
Bub. mean diameter	34.84
Nb/mm²	51.87
Ves. slice (%)	4.94

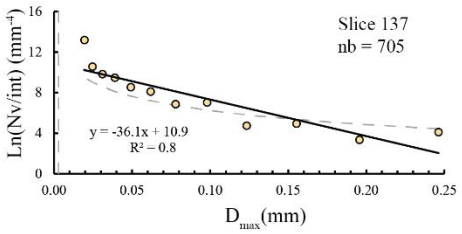

Class Number	Interval	D.max	Nb	Na (Nb/mm²)	Nv (mm⁻³)	Ln (Nv/int) (mm⁻⁴)
1	0.05065	0.246	7	0.5	3	4.10
2	0.04023	0.196	4	0.3	1	3.34
3	0.03196	0.155	8	0.5	4	4.93
4	0.02538	0.123	6	0.4	3	4.74
5	0.02016	0.098	23	1.5	23	7.02
6	0.01602	0.078	18	1.2	15	6.85
7	0.01272	0.062	31	2.0	42	8.10
8	0.01011	0.049	34	2.2	51	8.53
9	0.00803	0.039	50	3.3	104	9.47
10	0.00638	0.031	51	3.3	117	9.82
11	0.00506	0.025	63	4.1	192	10.54
12	0.00402	0.020	410	26.8	2131	13.18
		Total	705			

ESFa-6D-CO_2:

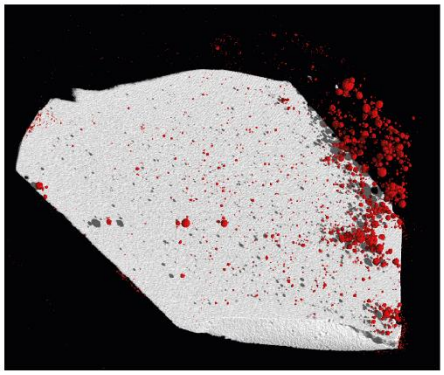

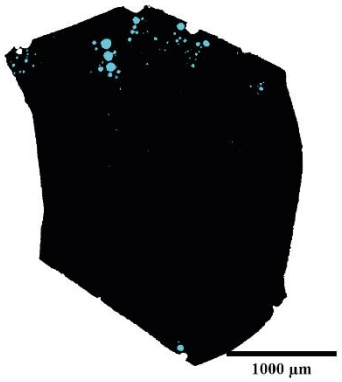

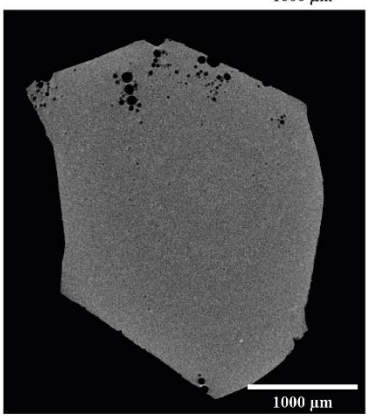

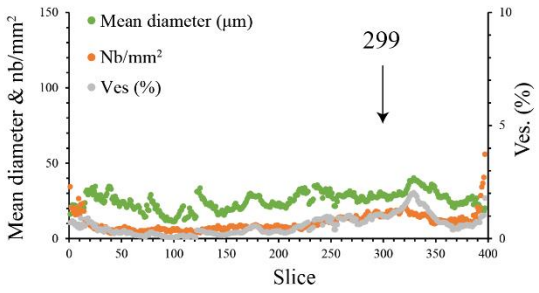

Experimental conditions	
Time (min)	360
Pressure (bars)	1674
Temperature (°C)	1200
Run	10+11
CO_2 added (wt.%)	0.97
Weigth (mg)	19.80
Resolution (µm)	3
Volume (mm³)	6.99
VGStudiomax treatment	
Ves (%)	0.35
ImageJ treatment	
Range	83-363
Tot. images	283
Ves. (from range volume) (%)	0.6
Area (mm²)	6.15
Bub. mean diameter	28.32
Nb/mm²	16.09
Ves. slice (%)	1.01

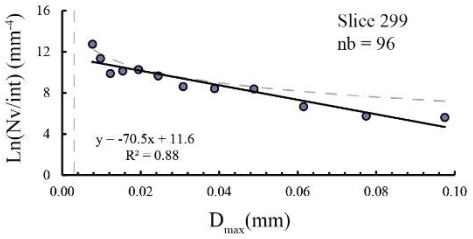

Class Number	Interval	D.max	Nb	Na (Nb/mm²)	Nv (mm⁻³)	Ln (Nv/int) (mm⁻⁴)
1	0.02005	0.097	2	0.3	5	5.61
2	0.01592	0.077	2	0.3	5	5.75
3	0.01265	0.061	3	0.5	10	6.68
4	0.01005	0.049	9	1.5	44	8.38
5	0.00798	0.039	8	1.3	36	8.42
6	0.00634	0.031	7	1.1	35	8.62
7	0.00504	0.024	10	1.6	79	9.66
8	0.00400	0.019	12	2.0	116	10.27
9	0.00318	0.015	9	1.5	81	10.14
10	0.00252	0.012	6	1.0	50	9.88
11	0.00200	0.010	9	1.5	171	11.35
12	0.00159	0.008	19	3.1	541	12.74
		Total	96			

ESFa-7D-CO_2:

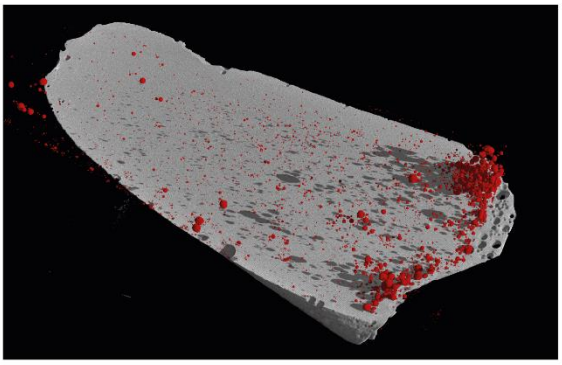

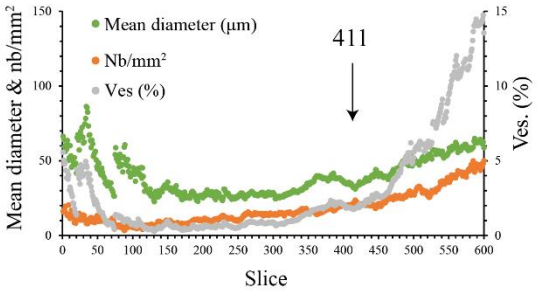

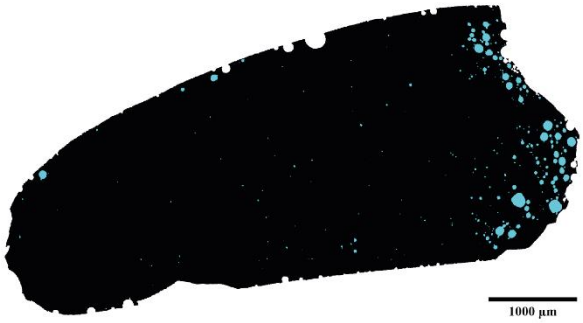

Experimental conditions	
Time (min)	360
Pressure (bars)	1674
Temperature (°C)	1200
Run	10+11
CO_2 added (wt.%)	1.94
Weigth (mg)	51.80
Resolution (µm)	3
Volume (mm³)	18.48
VGStudiomax treatment	
Ves (%)	0.67
ImageJ treatment	
Range	256-456
Tot. images	200
Ves. (from range volume) (%)	1.2
Area (mm²)	14.57
Bub. mean diameter	34.68
Nb/mm²	19.49
Ves. slice (%)	1.84

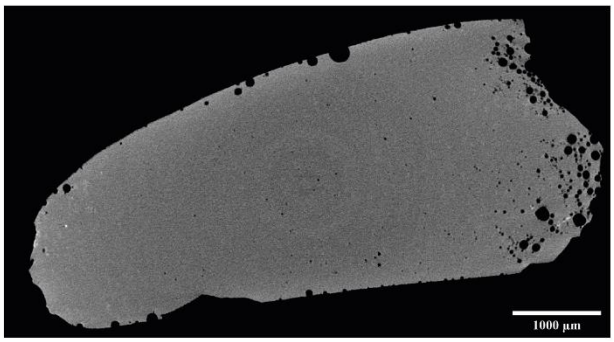

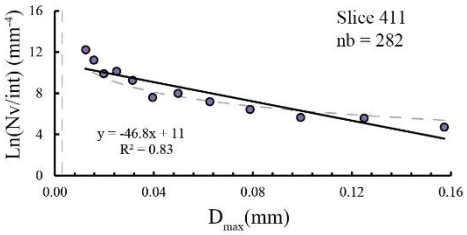

Class Number	Interval	D.max	Nb	Na (Nb/mm²)	Nv (mm⁻³)	Ln (Nv/int) (mm⁻⁴)
1	0.03237	0.157	5	0.3	4	4.71
2	0.02571	0.125	9	0.6	7	5.59
3	0.02042	0.099	8	0.5	6	5.66
4	0.01622	0.079	10	0.7	10	6.43
5	0.01288	0.063	13	0.9	17	7.18
6	0.01023	0.050	18	1.2	30	8.00
7	0.00813	0.040	12	0.8	16	7.60
8	0.00646	0.031	24	1.6	68	9.26
9	0.00513	0.025	37	2.5	131	10.15
10	0.00407	0.020	27	1.9	82	9.92
11	0.00324	0.016	45	3.1	244	11.23
12	0.00257	0.012	74	5.1	527	12.23
		Total	282			

ESFa-8D-CO_2:

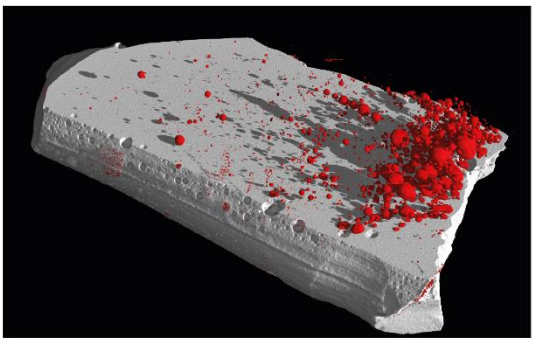

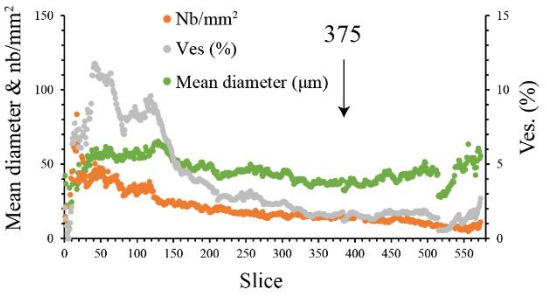

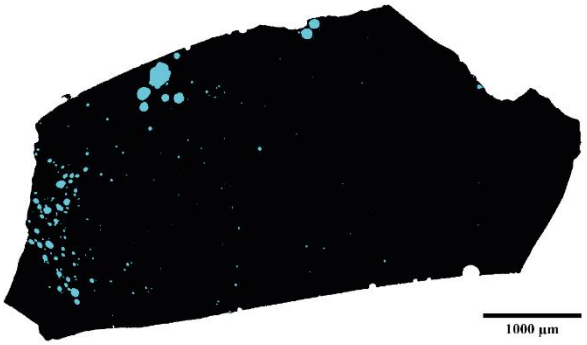

Experimental conditions	
Time (min)	360
Pressure (bars)	1674
Temperature (°C)	1200
Run	10+11
CO_2 added (wt.%)	4.43
Weigth (mg)	45.50
Resolution (µm)	3
Volume (mm³)	16.2
VGStudiomax treatment	
Ves (%)	1.41
ImageJ treatment	
Range	159-449
Tot. images	290
Ves. (from range volume) (%)	2.4
Area (mm²)	13.39
Bub. mean diameter	36.51
Nb/mm²	15.68
Ves. slice (%)	1.64

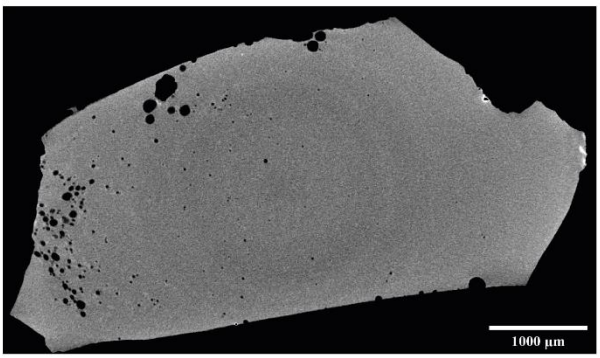

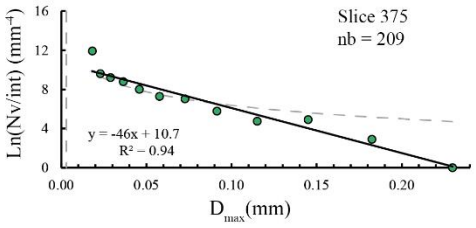

Class Number	Interval	D.max	Nb	Na (Nb/mm²)	Nv (mm⁻³)	Ln (Nv/int) (mm⁻⁴)
1	0.04725	0.230	0	0.0	0	0.00
2	0.03753	0.182	1	0.1	1	2.89
3	0.02981	0.145	5	0.4	4	4.90
4	0.02368	0.115	4	0.3	3	4.74
5	0.01881	0.091	6	0.4	6	5.78
6	0.01494	0.073	12	0.9	17	7.02
7	0.01187	0.058	12	0.9	17	7.28
8	0.00943	0.046	15	1.1	28	8.01
9	0.00749	0.036	20	1.5	49	8.79
10	0.00595	0.029	21	1.6	59	9.21
11	0.00473	0.023	21	1.6	71	9.61
12	0.00375	0.018	92	6.9	565	11.92
		Total	209			

ESFa-10D-CO_2:

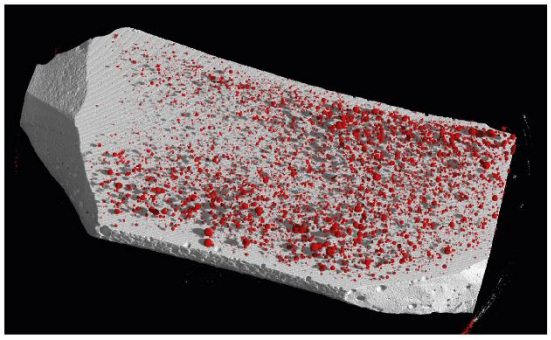

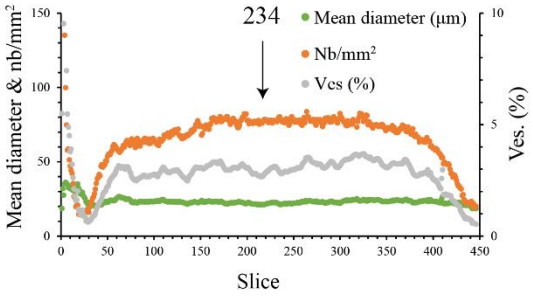

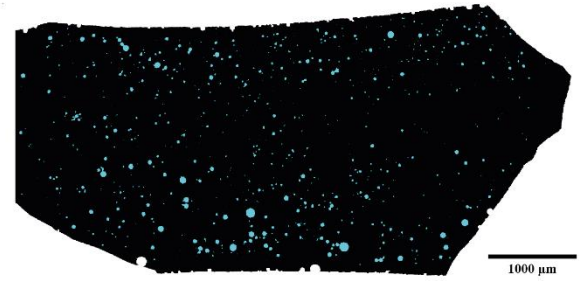

Experimental conditions	
Time (min)	10
Pressure (bars)	1671
Temperature (°C)	1200
Run	12
CO_2 added (wt.%)	1.03
Weigth (mg)	37.30
Resolution (µm)	3
Volume (mm³)	15.9
VGStudiomax treatment	
Ves (%)	1.56
ImageJ treatment	
Range	60-395
Tot. images	335
Ves. (from range volume) (%)	3.1
Area (mm²)	15.12
Bub. mean diameter	21.61
Nb/mm²	79.95
Ves. slice (%)	2.93

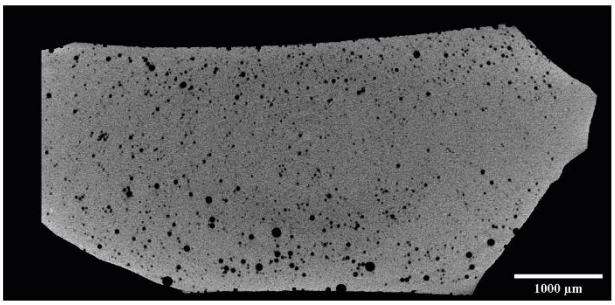

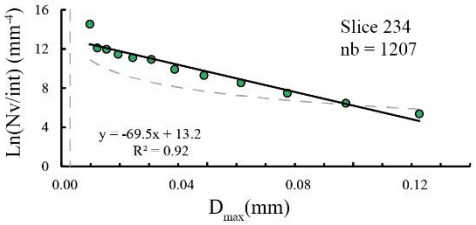

Class Number	Interval	D.max	Nb	Na (Nb/mm²)	Nv (mm ³)	Ln (Nv/int) (mm ⁴)
1	0.02523	0.123	6	0.4	5	5.35
2	0.02004	0.097	13	0.9	13	6.45
3	0.01592	0.077	24	1.6	28	7.48
4	0.01264	0.061	44	2.9	64	8.53
5	0.01004	0.049	63	4.2	109	9.29
6	0.00798	0.039	79	5.2	162	9.92
7	0.00634	0.031	127	8.4	351	10.92
8	0.00503	0.024	119	7.9	338	11.12
9	0.00400	0.019	112	7.4	376	11.45
10	0.00318	0.015	115	7.6	501	11.97
11	0.00252	0.012	96	6.3	455	12.10
12	0.00200	0.010	409	27.1	4127	14.54
		Total	1207			

ESFa-1C-CO_2:

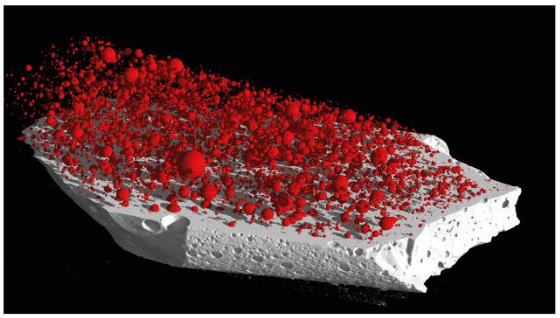

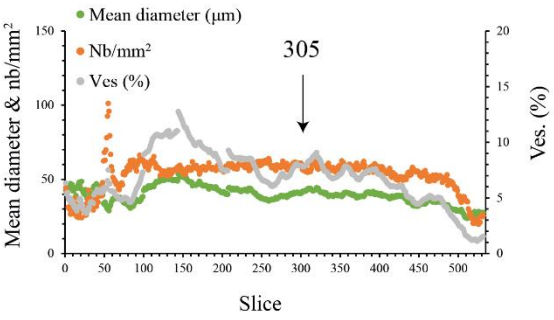

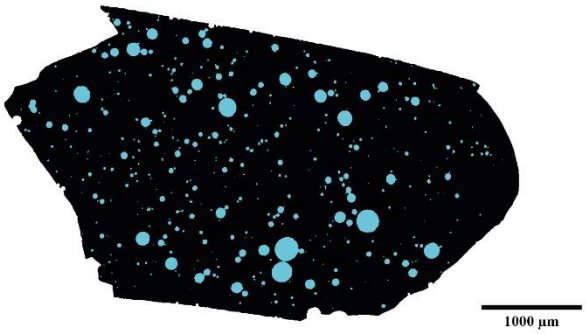

Experimental conditions	
Time (min)	10
Pressure (bars)	1671
Temperature (°C)	1200
Run	12
CO_2 added (wt.%)	2.59
Weigth (mg)	35.40
Resolution (µm)	3
Volume (mm³)	13.5
VGStudiomax treatment	
Ves (%)	4.15
ImageJ treatment	
Range	200-433
Tot. images	233
Ves. (from range volume) (%)	7.4
Area (mm²)	10.40
Bub. mean diameter	42.28
Nb/mm²	56.13
Ves. slice (%)	7.88

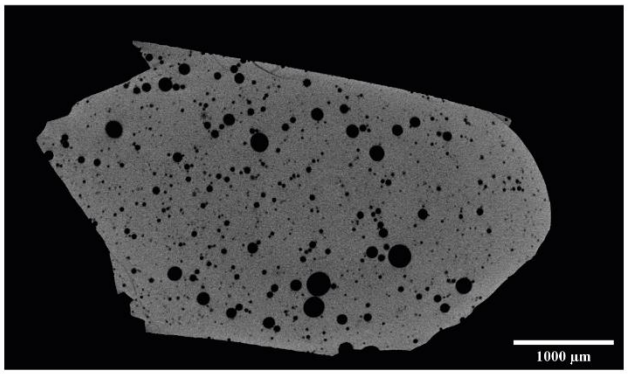

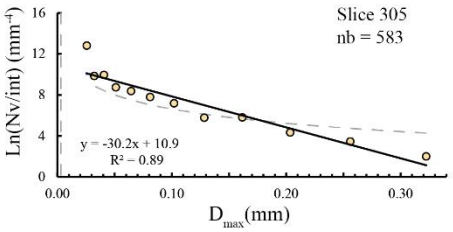

Class Number	Interval	D.max	Nb	Na (Nb/mm²)	Nv (mm⁻³)	Ln (Nv/int) (mm⁻⁴)
1	0.06629	0.322	1	0.1	0	2.00
2	0.05265	0.256	3	0.3	2	3.46
3	0.04182	0.203	5	0.5	3	4.33
4	0.03322	0.162	13	1.3	11	5.82
5	0.02639	0.128	11	1.1	9	5.78
6	0.02096	0.102	22	2.1	28	7.19
7	0.01665	0.081	28	2.7	41	7.80
8	0.01323	0.064	33	3.2	57	8.37
9	0.01051	0.051	33	3.2	65	8.74
10	0.00835	0.041	57	5.5	174	9.94
11	0.00663	0.032	45	4.3	126	9.85
12	0.00527	0.026	332	31.9	1942	12.82
		Total	583			

ESFa-2C-CO_2:

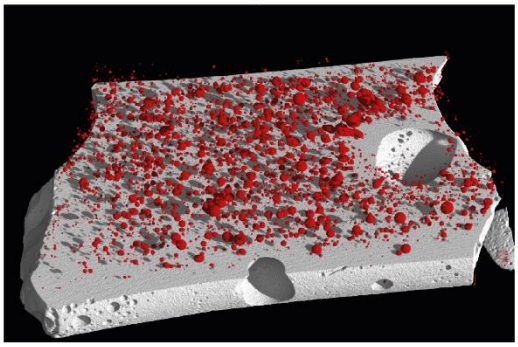

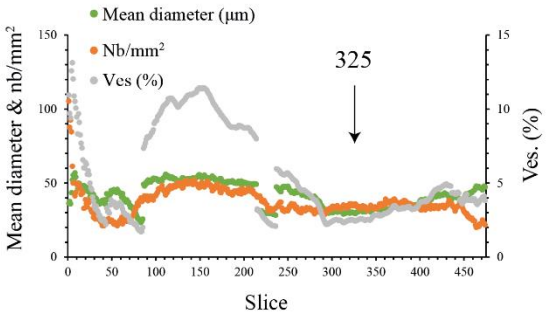

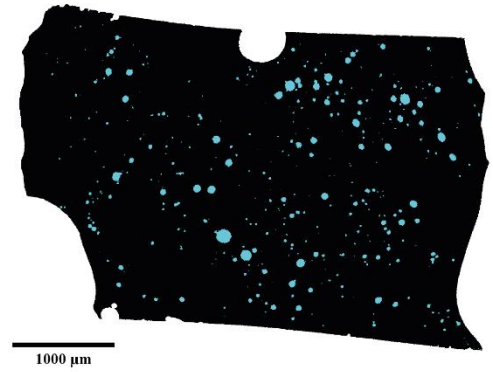

Experimental conditions	
Time (min)	10
Pressure (bars)	1671
Temperature (°C)	1200
Run	12
CO_2 added (wt.%)	5.20
Weigth (mg)	37.80
Resolution (µm)	3
Volume (mm^3)	13.2
VGStudiomax treatment	
Ves (%)	0.19
ImageJ treatment	
Range	307-448
Tot. images	141
Ves. (from range volume) (%)	3.4
Area (mm^2)	11.82
Bub. mean diameter	29.87
Nb/mm^2	35.20
Ves. slice (%)	2.47

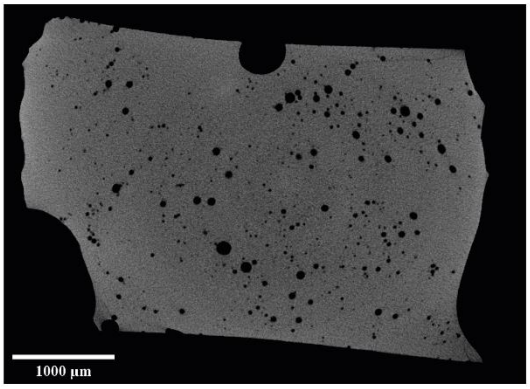

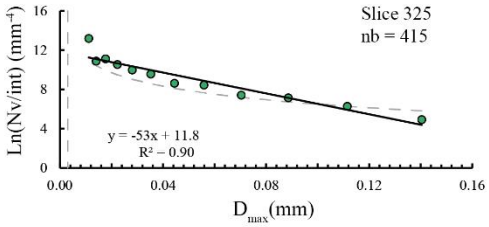

Class Number	Interval	D.max	Nb	Na (Nb/mm^2)	Nv (mm^{-3})	Ln (Nv/int) (mm^{-4})
1	0.02888	0.140	4	0.3	4	4.92
2	0.02294	0.112	11	0.9	12	6.29
3	0.01822	0.089	18	1.5	23	7.14
4	0.01448	0.070	18	1.5	24	7.41
5	0.01150	0.056	28	2.4	53	8.44
6	0.00913	0.044	26	2.2	51	8.63
7	0.00726	0.035	36	3.0	103	9.56
8	0.00576	0.028	38	3.2	125	9.99
9	0.00458	0.022	42	3.6	174	10.55
10	0.00364	0.018	47	4.0	247	11.12
11	0.00289	0.014	33	2.8	153	10.88
12	0.00229	0.011	114	9.6	1246	13.21
		Total	415			

ESFa-4C-CO_2:

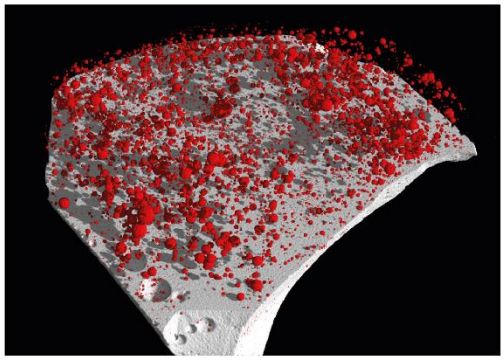

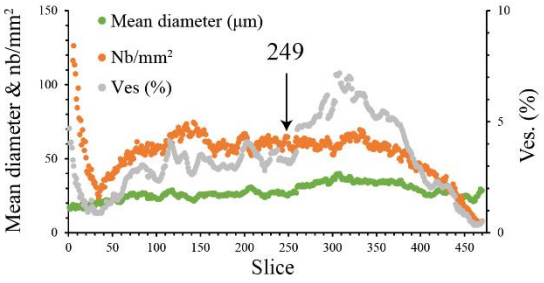

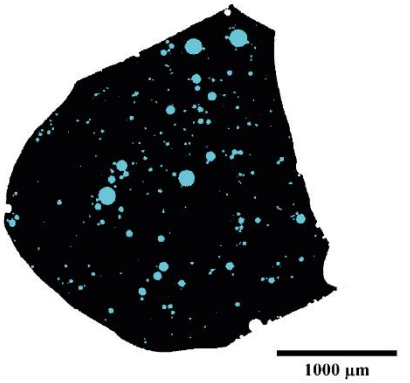

Experimental conditions	
Time (min)	60
Pressure (bars)	1683
Temperature (°C)	1200
Run	13
CO_2 added (wt.%)	1.48
Weigth (mg)	17.30
Resolution (µm)	3
Volume (mm^3)	6.2
VGStudiomax treatment	
Ves (%)	2.01
ImageJ treatment	
Range	300-640
Tot. images	340
Ves. (from range volume) (%)	4.0
Area (mm^2)	5.15
Bub. mean diameter	24.87
Nb/mm^2	64.66
Ves. slice (%)	3.14

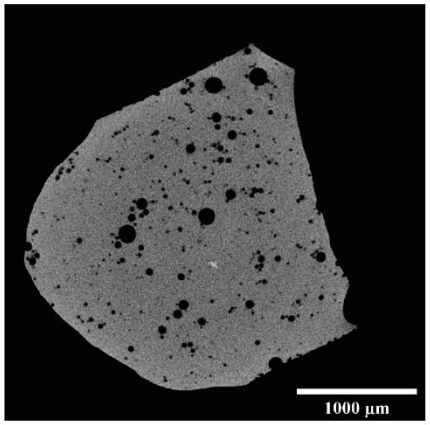

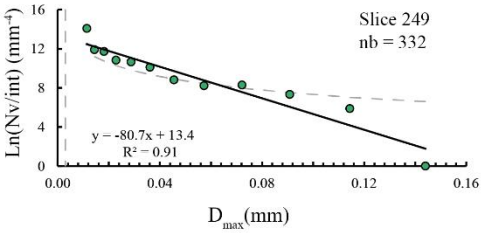

Class Number	Interval	D.max	Nb	Na (Nb/mm^2)	Nv (mm^{-3})	Ln (Nv/int) (mm^{-4})
1	0.02961	0.144	0	0.0	0	0.00
2	0.02352	0.114	3	0.6	8	5.88
3	0.01868	0.091	9	1.7	29	7.34
4	0.01484	0.072	16	3.1	59	8.29
5	0.01179	0.057	13	2.5	44	8.22
6	0.00936	0.046	14	2.7	63	8.82
7	0.00744	0.036	26	5.0	183	10.11
8	0.00591	0.029	31	6.0	248	10.64
9	0.00469	0.023	28	5.4	238	10.83
10	0.00373	0.018	37	7.2	461	11.73
11	0.00296	0.014	33	6.4	435	11.90
12	0.00235	0.011	122	23.7	3047	14.07
		Total	332			

ESFa-5C-CO_2:

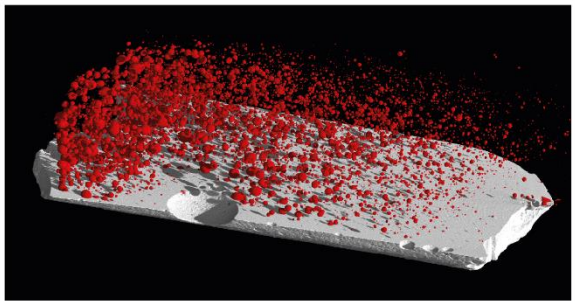

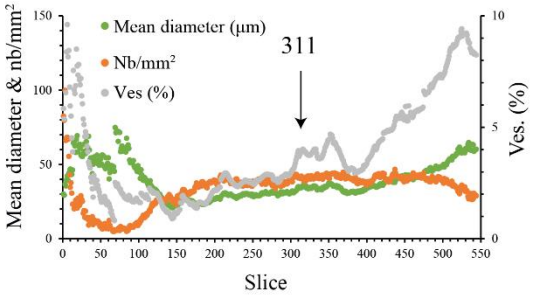

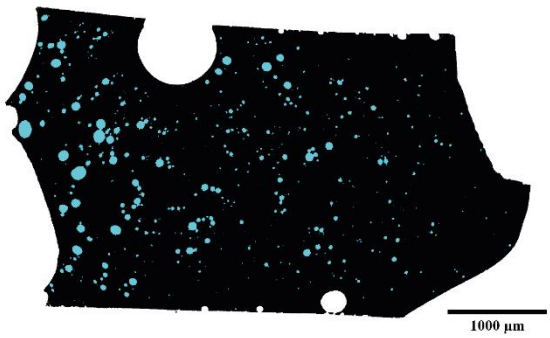

Experimental conditions	
Time (min)	60
Pressure (bars)	1683
Temperature (°C)	1200
Run	13
CO_2 added (wt.%)	5.45
Weigth (mg)	45.30
Resolution (µm)	3
Volume (mm^3)	15.9
VGStudiomax treatment	
Ves (%)	1.61
ImageJ treatment	
Range	195-474
Tot. images	279
Ves. (from range volume) (%)	2.6
Area (mm^2)	12.00
Bub. mean diameter	33.83
Nb/mm^2	41.09
Ves. slice (%)	3.69

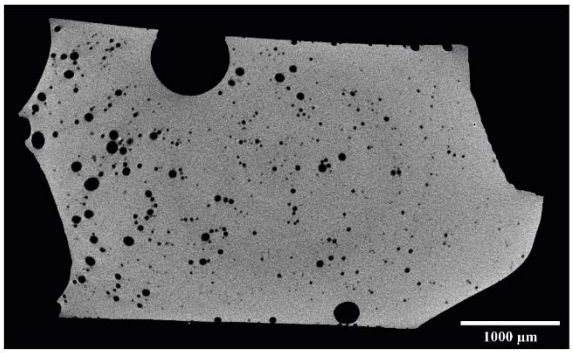

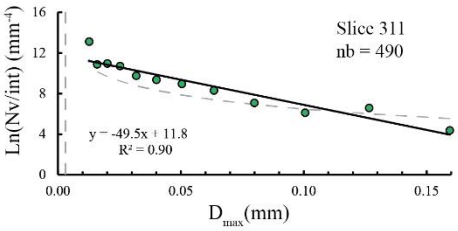

Class Number	Interval	D.max	Nb	Na (Nb/mm^2)	Nv (mm^{-3})	Ln (Nv/int) (mm^{-4})
1	0.03278	0.159	3	0.3	3	4.37
2	0.02604	0.127	18	1.5	19	6.57
3	0.02068	0.101	12	1.0	9	6.11
4	0.01643	0.080	16	1.3	19	7.08
5	0.01305	0.063	30	2.5	52	8.30
6	0.01037	0.050	39	3.3	79	8.94
7	0.00823	0.040	41	3.4	94	9.34
8	0.00654	0.032	41	3.4	112	9.74
9	0.00520	0.025	58	4.8	230	10.70
10	0.00413	0.020	55	4.6	235	10.95
11	0.00328	0.016	41	3.4	171	10.86
12	0.00260	0.013	136	11.3	1284	13.11
		Total	490			

ESFa-6C-CO_2:

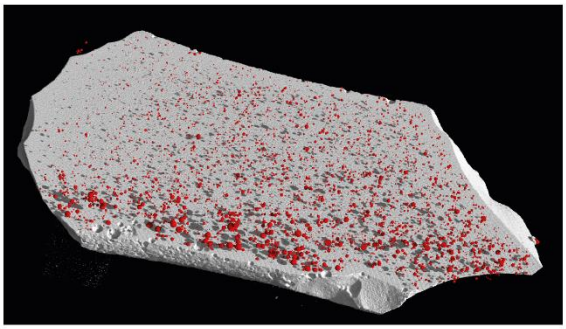

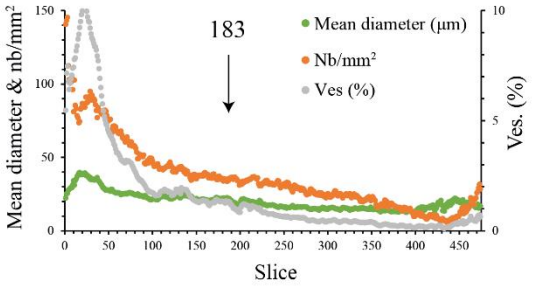

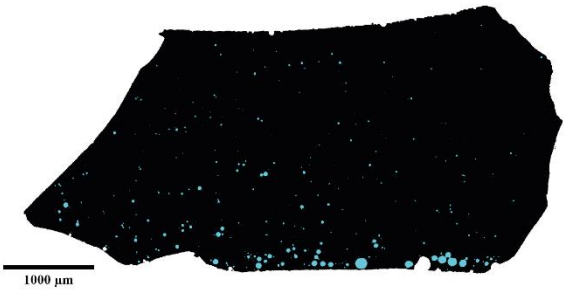

Experimental conditions	
Time (min)	240
Pressure (bars)	1605
Temperature (°C)	1200
Run	15
CO_2 added (wt.%)	0.69
Weigth (mg)	39.40
Resolution (µm)	3
Volume (mm³)	14.0
VGStudiomax treatment	
Ves (%)	0.46
ImageJ treatment	
Range	47-423
Tot. images	376
Ves. (from range volume) (%)	1.1
Area (mm²)	12.88
Bub. mean diameter	21.38
Nb/mm²	35.08
Ves. slice (%)	1.26

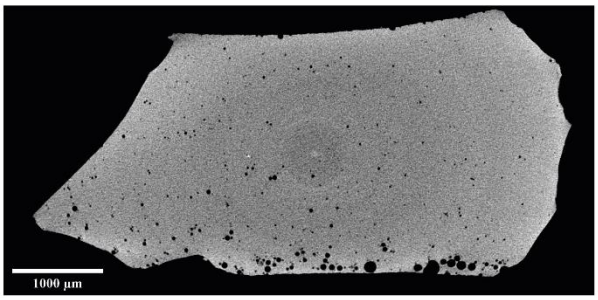

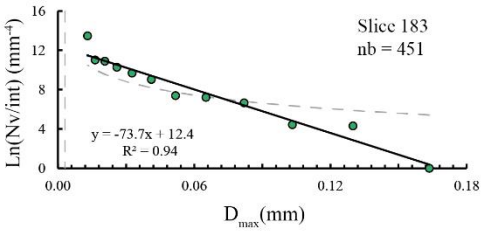

Class Number	Interval	D.max	Nb	Na (Nb/mm²)	Nv (mm⁻³)	Ln (Nv/int) (mm⁻⁴)
1	0.03364	0.164	0	0.0	0	0.00
2	0.02672	0.130	2	0.2	2	4.30
3	0.02122	0.103	2	0.2	2	4.44
4	0.01686	0.082	9	0.7	13	6.64
5	0.01339	0.065	12	0.9	18	7.22
6	0.01064	0.052	11	0.9	17	7.39
7	0.00845	0.041	27	2.1	71	9.04
8	0.00671	0.033	36	2.8	107	9.68
9	0.00533	0.026	44	3.4	156	10.28
10	0.00423	0.021	52	4.0	226	10.88
11	0.00336	0.016	45	3.5	205	11.02
12	0.00267	0.013	211	16.4	1901	13.48
		Total	451			

ESFa-7C-CO_2:

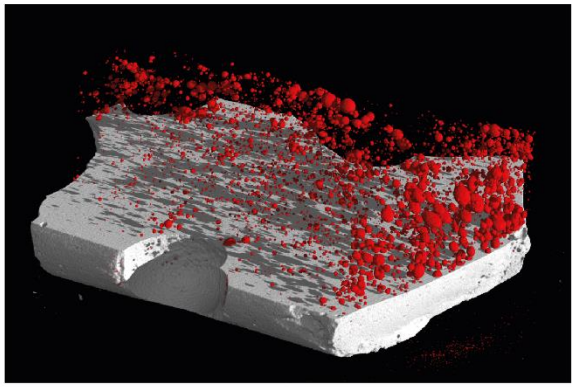

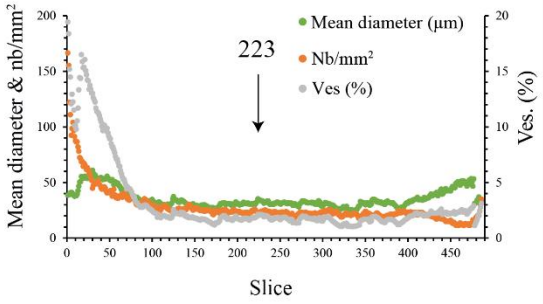

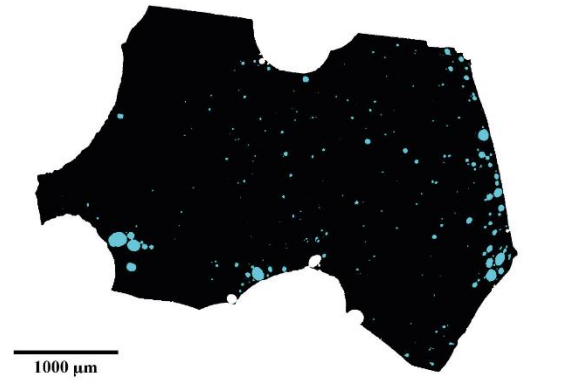

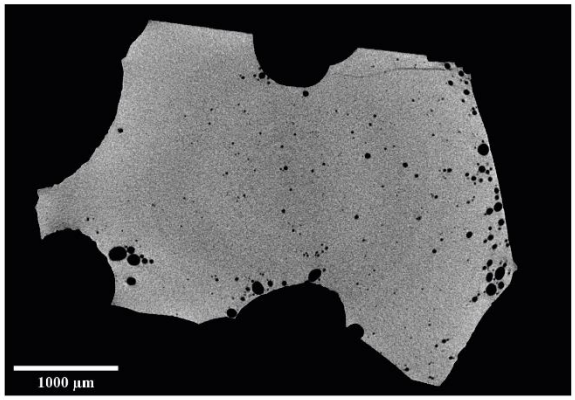

Experimental conditions	
Time (min)	240
Pressure (bars)	1605
Temperature (°C)	1200
Run	15
CO_2 added (wt.%)	6.12
Weigth (mg)	35.10
Resolution (µm)	3
Volume (mm³)	12.4
VGStudiomax treatment	
Ves (%)	1.14
ImageJ treatment	
Range	90-391
Tot. images	301
Ves. (from range volume) (%)	2.2
Area (mm²)	9.76
Bub. mean diameter	32.91
Nb/mm²	23.04
Ves. slice (%)	1.96

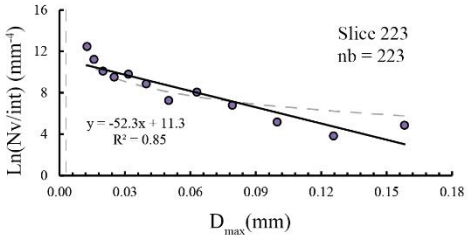

Class Number	Interval	D.max	Nb	Na (Nb/mm²)	Nv (mm⁻³)	Ln (Nv/int) (mm⁻⁴)
1	0.03252	0.158	4	0.4	4	4.88
2	0.02583	0.126	2	0.2	1	3.84
3	0.02052	0.100	3	0.3	4	5.18
4	0.01630	0.079	8	0.8	15	6.81
5	0.01295	0.063	18	1.8	41	8.07
6	0.01028	0.050	10	1.0	15	7.26
7	0.00817	0.040	18	1.8	58	8.87
8	0.00649	0.032	28	2.9	116	9.79
9	0.00515	0.025	20	2.0	71	9.52
10	0.00409	0.020	20	2.0	100	10.10
11	0.00325	0.016	31	3.2	246	11.23
12	0.00258	0.013	61	6.3	672	12.47
		Total	223			

ESFa-8C-CO_2:

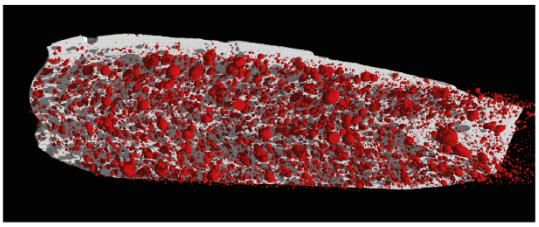

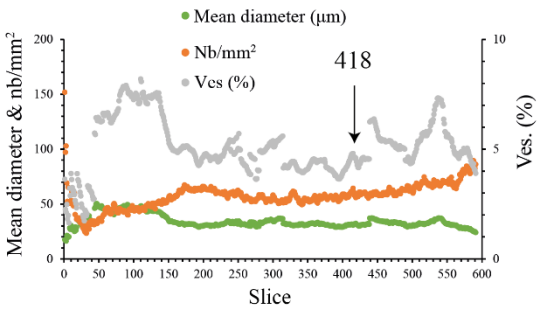

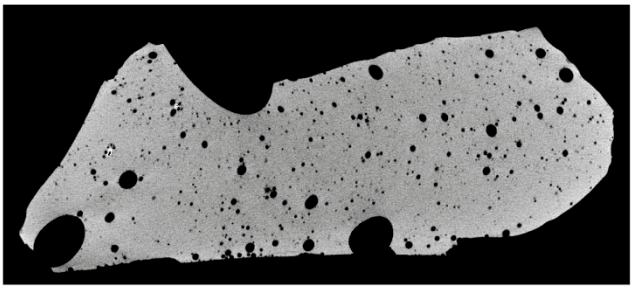

Experimental conditions	
Time (min)	10
Pressure (bars)	1660
Temperature (°C)	1200
Run	14
CO_2 added (wt.%)	4.20
Weigth (mg)	42.30
Resolution (µm)	3
Volume (mm^3)	15.7
VGStudiomax treatment	
Ves (%)	2.54
ImageJ treatment	
Range	185-475
Tot. images	290
Ves. (from range volume) (%)	4.7
Area (mm^2)	10.93
Bub. mean diameter	31.84
Nb/mm^2	57.99
Ves. slice (%)	4.62

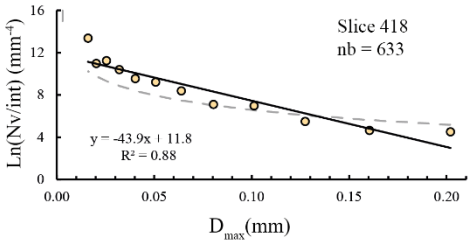

Class Number	Interval	D.max	Nb	Na (Nb/mm^2)	Nv (mm^{-3})	Ln (Nv/int) (mm^{-4})
1	0.04153	0.202	5	0.5	4	4.50
2	0.03299	0.160	5	0.5	3	4.63
3	0.02620	0.127	7	0.6	6	5.47
4	0.02081	0.101	17	1.6	22	6.95
5	0.01653	0.080	16	1.5	20	7.09
6	0.01313	0.064	30	2.7	57	8.37
7	0.01043	0.051	45	4.1	104	9.21
8	0.00829	0.040	46	4.2	115	9.54
9	0.00658	0.032	62	5.7	212	10.38
10	0.00523	0.025	89	8.1	397	11.24
11	0.00415	0.020	63	5.8	240	10.96
12	0.00330	0.016	248	22.7	2084	13.36
		Total	633			

ESFa-9C-CO_2:

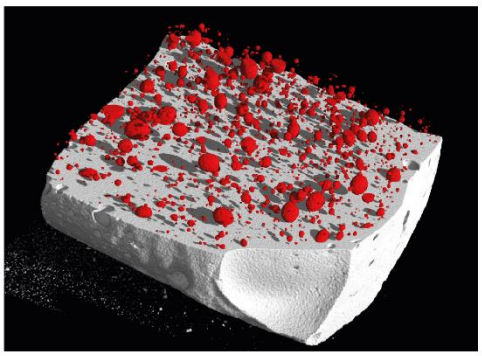

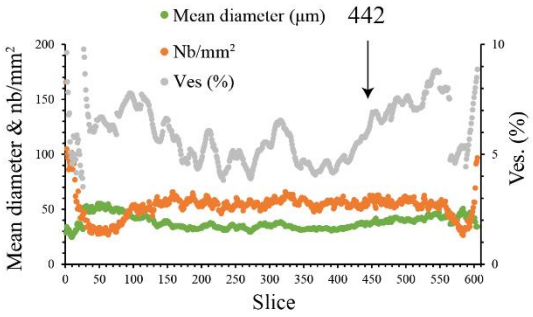

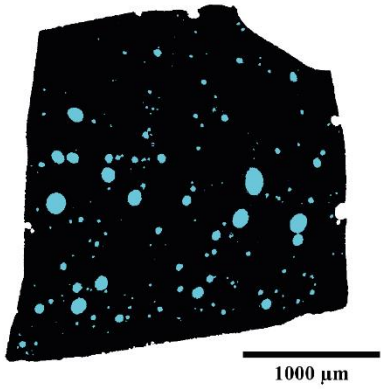

Experimental conditions	
Time (min)	10
Pressure (bars)	1660
Temperature (°C)	1200
Run	14
CO_2 added (wt.%)	4.19
Weigth (mg)	22.30
Resolution (µm)	3
Volume (mm^3)	8.1
VGStudiomax treatment	
Ves (%)	3.12
ImageJ treatment	
Range	205-573
Tot. images	370
Ves. (from range volume) (%)	5.4
Area (mm^2)	4.94
Bub. mean diameter	37.87
Nb/mm^2	52.61
Ves. slice (%)	5.93

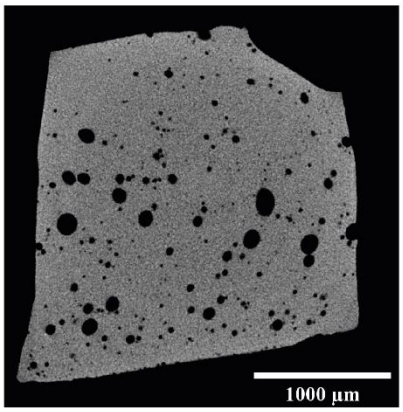

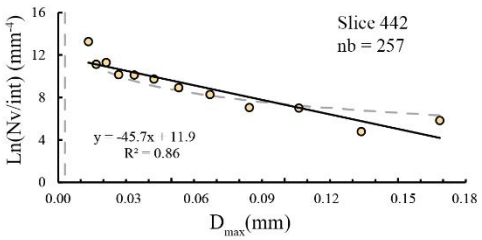

Class Number	Interval	D.max	Nb	Na (Nb/mm^2)	Nv (mm^{-3})	Ln (Nv/int) (mm^{-4})
1	0.03465	0.168	6	1.2	12	5.84
2	0.02752	0.134	3	0.6	3	4.80
3	0.02186	0.106	9	1.8	24	7.01
4	0.01737	0.084	8	1.6	20	7.06
5	0.01379	0.067	14	2.8	55	8.29
6	0.01096	0.053	18	3.6	83	8.93
7	0.00870	0.042	25	5.1	147	9.74
8	0.00691	0.034	26	5.3	172	10.12
9	0.00549	0.027	21	4.3	142	10.16
10	0.00436	0.021	31	6.3	352	11.30
11	0.00347	0.017	23	4.7	235	11.12
12	0.00275	0.013	73	14.8	1580	13.26
		Total	257			

ESFa-10C-CO_2:

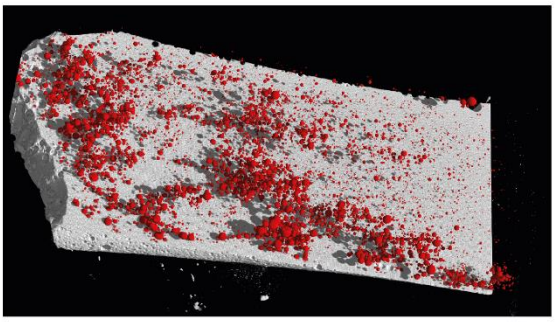

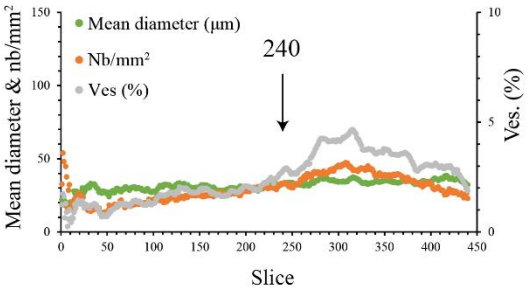

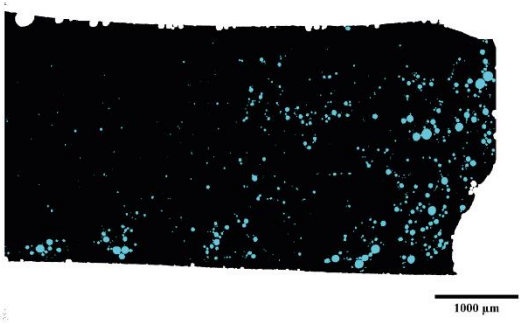

Experimental conditions	
Time (min)	240
Pressure (bars)	1605
Temperature (°C)	1200
Run	15
CO_2 added (wt.%)	1.30
Weigth (mg)	32.60
Resolution (µm)	3
Volume (mm³)	16.9
VGStudiomax treatment	
Ves (%)	2.23
ImageJ treatment	
Range	108-382
Tot. images	274
Ves. (from range volume) (%)	2.8
Area (mm²)	16.09
Bub. mean diameter	32.86
Nb/mm²	32.81
Ves. slice (%)	2.78

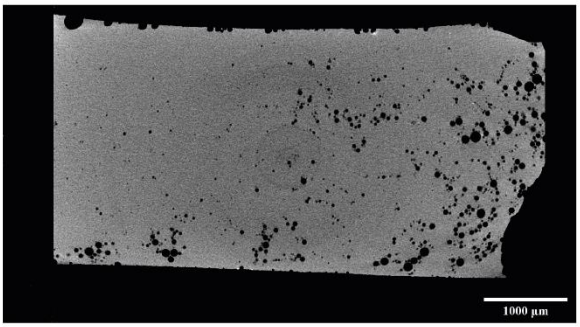

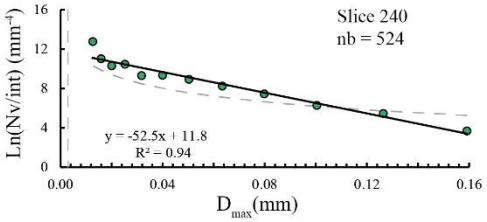

Class Number	Interval	D.max	Nb	Na (Nb/mm²)	Nv (mm⁻³)	Ln (Nv/int) (mm⁻⁴)
1	0.03274	0.159	2	0.1	1	3.67
2	0.02600	0.126	8	0.5	6	5.45
3	0.02066	0.100	13	0.8	11	6.26
4	0.01641	0.080	26	1.6	28	7.44
5	0.01303	0.063	39	2.4	49	8.24
6	0.01035	0.050	51	3.2	77	8.92
7	0.00822	0.040	54	3.4	93	9.33
8	0.00653	0.032	42	2.6	71	9.30
9	0.00519	0.025	62	3.9	181	10.46
10	0.00412	0.020	46	2.9	121	10.29
11	0.00327	0.016	50	3.1	199	11.01
12	0.00260	0.013	131	8.1	902	12.76
		Total	524			

ESFa-1B-CO_2:

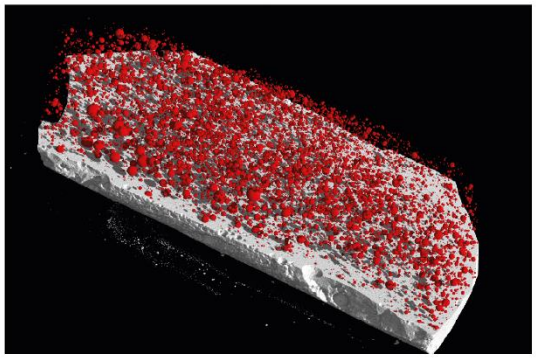

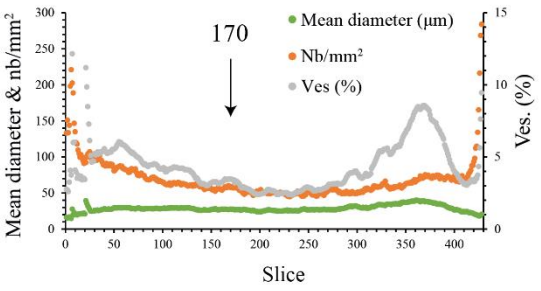

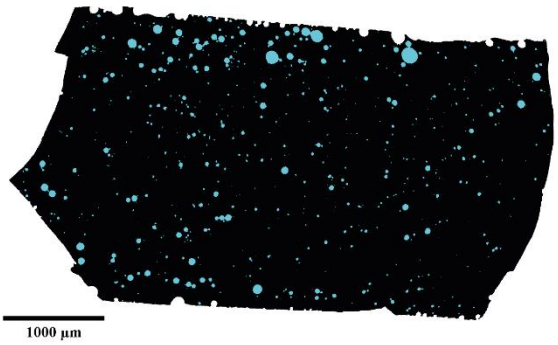

Experimental conditions

Time (min)	10
Pressure (bars)	1660
Temperature (°C)	1200
Run	14
CO_2 added (wt.%)	1.33
Weigth (mg)	37.80
Resolution (µm)	3
Volume (mm^3)	13.8

VGStudiomax treatment

Ves (%)	2.00

ImageJ treatment

Range	84-350
Tot. images	266
Ves. (from range volume) (%)	3.3
Area (mm^2)	12.77
Bub. mean diameter	27.71
Nb/mm^2	57.56
Ves. slice (%)	3.47

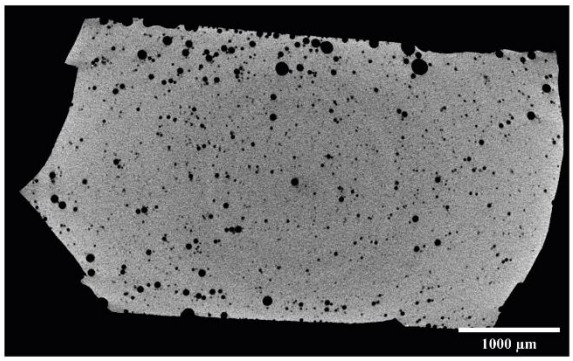

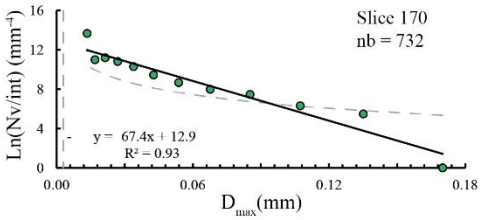

Class Number	Interval	D.max	Nb	Na (Nb/mm^2)	Nv (mm^{-3})	Ln (Nv/int) (mm^{-4})
1	0.03498	0.170	0	0.0	0	0.00
2	0.02779	0.135	7	0.5	7	5.48
3	0.02207	0.107	12	0.9	12	6.31
4	0.01753	0.085	24	1.9	31	7.46
5	0.01393	0.068	29	2.3	41	7.98
6	0.01106	0.054	37	2.9	64	8.67
7	0.00879	0.043	50	3.9	111	9.45
8	0.00698	0.034	72	5.6	207	10.30
9	0.00554	0.027	82	6.4	273	10.81
10	0.00440	0.021	83	6.5	321	11.20
11	0.00350	0.017	59	4.6	209	11.00
12	0.00278	0.014	277	21.7	2400	13.67
		Total	732			

ESFa-3A-CO_2:

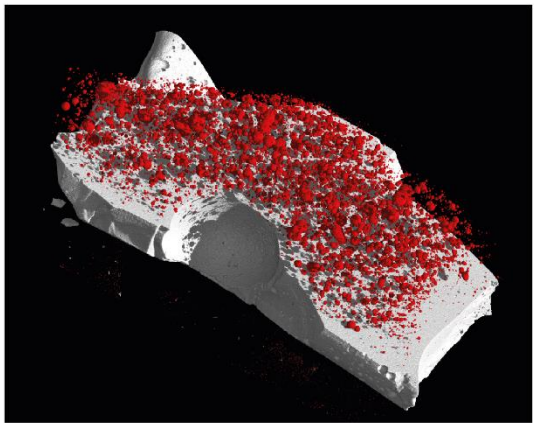

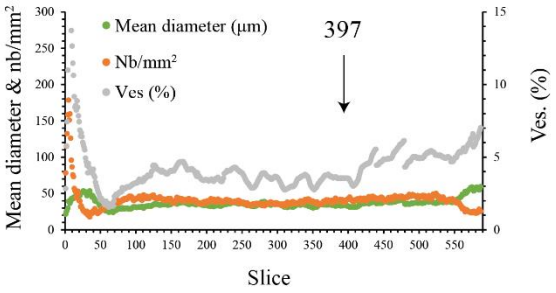

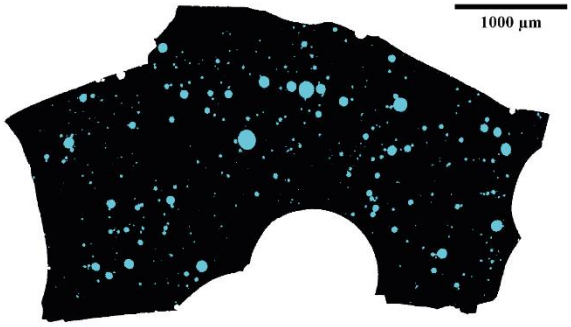

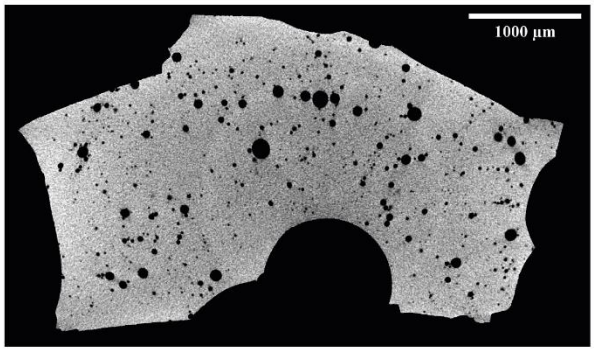

Experimental conditions	
Time (min)	10
Pressure (bars)	1669
Temperature (°C)	1200
Run	16
CO_2 added (wt.%)	5.16
Weigth (mg)	35.70
Resolution (µm)	3
Volume (mm³)	12.8
VGStudiomax treatment	
Ves (%)	3.48
ImageJ treatment	
Range	73-435
Tot. images	362
Ves. (from range volume) (%)	3.6
Area (mm²)	8.62
Bub. mean diameter	33.38
Nb/mm²	40.72
Ves. slice (%)	3.56

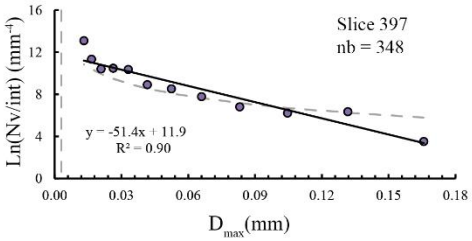

Class Number	Interval	D.max	Nb	Na (Nb/mm²)	Nv (mm⁻³)	Ln (Nv/int) (mm⁻⁴)
1	0.03410	0.166	1	0.1	1	3.52
2	0.02709	0.132	11	1.3	16	6.35
3	0.02152	0.105	9	1.0	11	6.21
4	0.01709	0.083	10	1.2	15	6.80
5	0.01358	0.066	15	1.7	33	7.79
6	0.01078	0.052	20	2.3	54	8.52
7	0.00857	0.042	21	2.4	64	8.92
8	0.00680	0.033	45	5.2	215	10.36
9	0.00540	0.026	41	4.8	191	10.47
10	0.00429	0.021	31	3.6	143	10.41
11	0.00341	0.017	38	4.4	288	11.34
12	0.00271	0.013	106	12.3	1328	13.10
		Total	348			

ESFa-1B-CO_2+Ne:

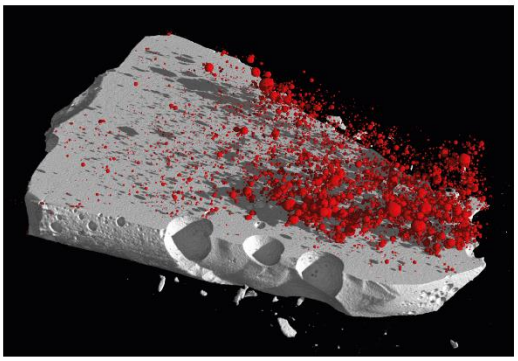

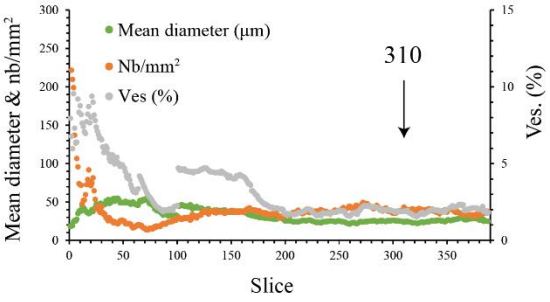

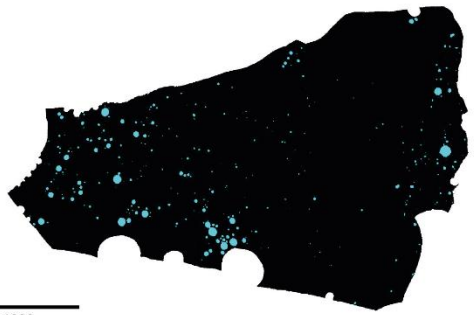

Experimental conditions	
Time (min)	240
Pressure (bars)	1535
Temperature (°C)	1200
Run	#1
CO_2 added (wt.%)	2.92
Weigth (mg)	22.60
Resolution (µm)	3
Volume (mm³)	12.8
VGStudiomax treatment	
Ves (%)	1.46
ImageJ treatment	
Range	184-321
Tot. images	137
Ves. (from range volume) (%)	1.9
Area (mm²)	9.33
Bub. mean diameter	23.51
Nb/mm²	43.30
Ves. slice (%)	1.88

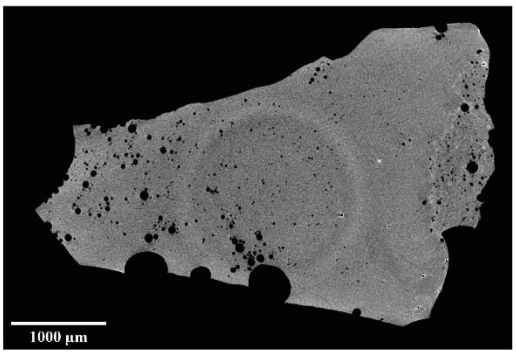

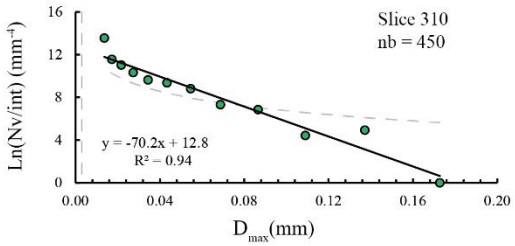

Class Number	Interval	D.max	Nb	Na (Nb/mm²)	Nv (mm⁻³)	Ln (Nv/int) (mm⁻⁴)
1	0.03553	0.173	0	0.0	0	0.00
2	0.02822	0.137	3	0.3	4	4.92
3	0.02242	0.109	2	0.2	2	4.44
4	0.01781	0.087	9	1.0	17	6.85
5	0.01414	0.069	11	1.2	21	7.32
6	0.01123	0.055	27	2.9	75	8.81
7	0.00892	0.043	34	3.6	104	9.36
8	0.00709	0.034	33	3.5	109	9.64
9	0.00563	0.027	39	4.2	171	10.32
10	0.00447	0.022	48	5.1	273	11.02
11	0.00355	0.017	54	5.8	374	11.56
12	0.00282	0.014	190	20.4	2187	13.56
		Total	450			

ESFa-2B-CO_2+Ne:

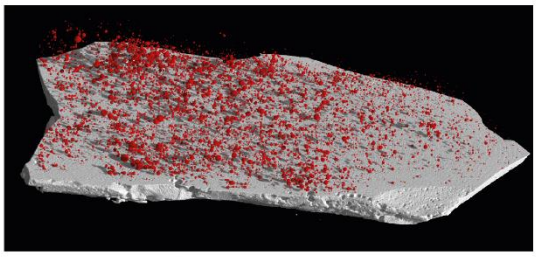

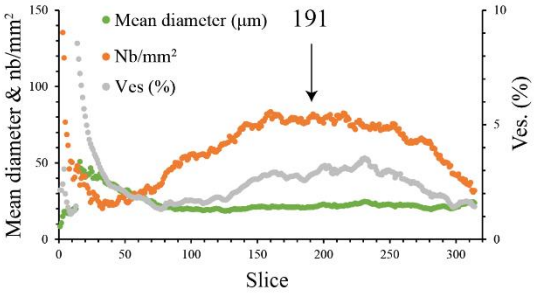

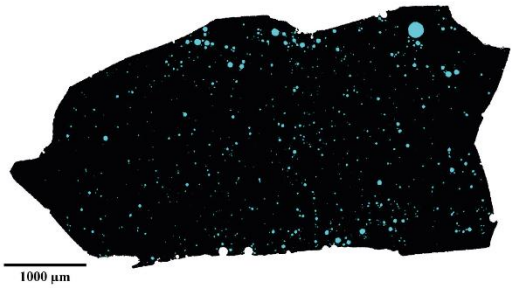

Experimental conditions	
Time (min)	240
Pressure (bars)	1535
Temperature (°C)	1200
Run	#1
CO_2 added (wt.%)	1.30
Weigth (mg)	26.30
Resolution (µm)	3
Volume (mm³)	10.4
VGStudiomax treatment	
Ves (%)	1.23
ImageJ treatment	
Range	146-525
Tot. images	106
Ves. (from range volume) (%)	2.4
Area (mm²)	13.86
Bub. mean diameter	21.23
Nb/mm²	80.25
Ves. slice (%)	2.84

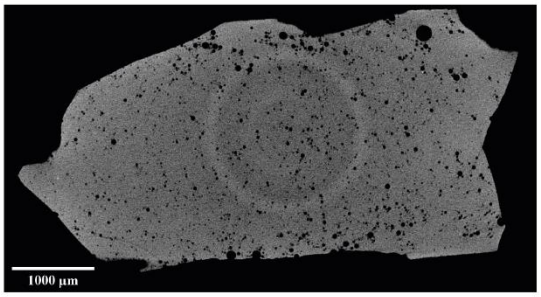

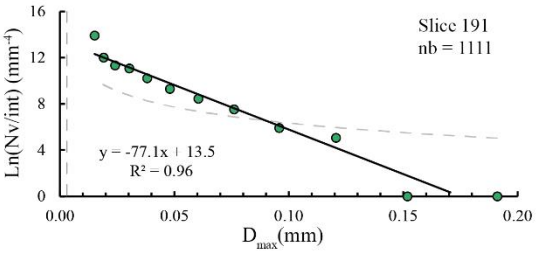

Class Number	Interval	D.max	Nb	Na (Nb/mm²)	Nv (mm⁻³)	Ln (Nv/int) (mm⁻⁴)
1	0.15182	0.191	0	0.0	0	0.00
2	0.12060	0.152	0	0.0	0	0.00
3	0.09579	0.121	4	0.3	4	5.07
4	0.07609	0.096	7	0.5	7	5.92
5	0.06044	0.076	21	1.5	29	7.54
6	0.04801	0.060	36	2.6	58	8.45
7	0.03814	0.048	55	4.0	107	9.29
8	0.03029	0.038	87	6.3	214	10.21
9	0.02406	0.030	130	9.4	395	11.06
10	0.01911	0.024	127	9.2	409	11.32
11	0.01518	0.019	151	10.9	644	12.01
12	0.01206	0.015	493	35.6	3424	13.91
		Total	1111			

ESFa-3B-CO_2+Ne:

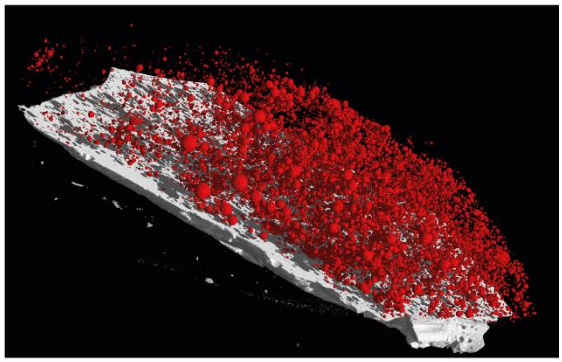

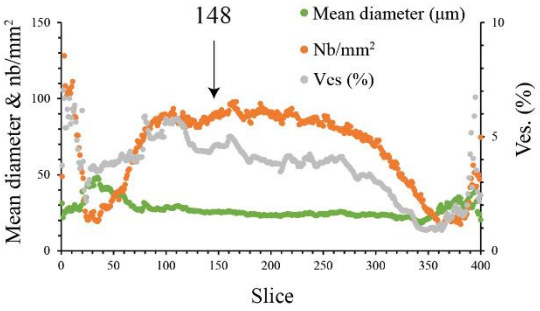

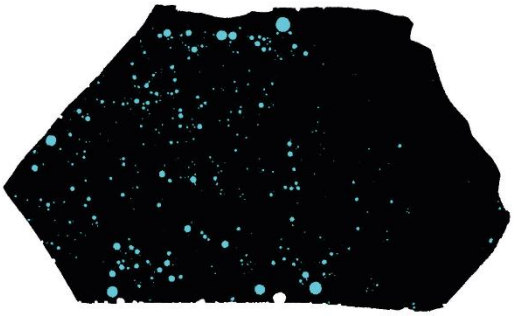

1000 µm

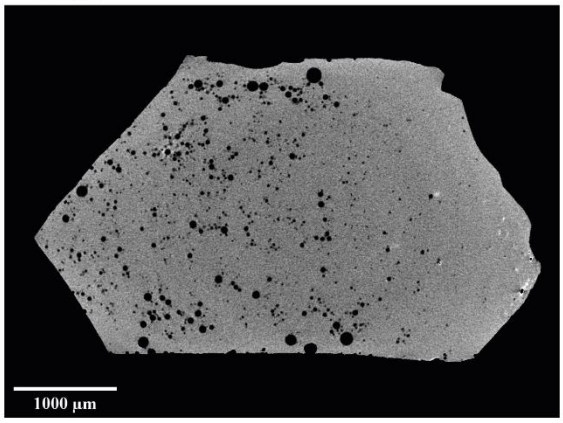

1000 µm

Experimental conditions	
Time (min)	240
Pressure (bars)	1535
Temperature (°C)	1200
Run	#1
CO_2 added (wt.%)	1.60
Weigth (mg)	21.30
Resolution (µm)	3
Volume (mm³)	10.8
VGStudiomax treatment	
Ves (%)	1.73
ImageJ treatment	
Range	105-285
Tot. images	180
Ves. (from range volume) (%)	4.20
Area (mm²)	10.63
Bub. mean diameter	25.63
Nb/mm²	89.83
Ves. slice (%)	4.63

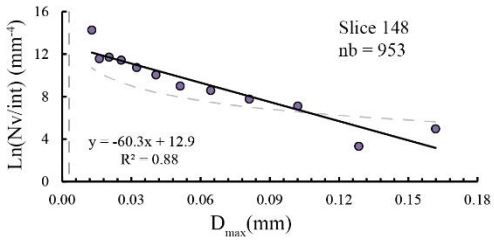

Class Number	Interval	D.max	Nb	Na (Nb/mm²)	Nv (mm⁻³)	Ln (Nv/int) (mm⁻⁴)
1	0.03327	0.162	5	0.5	5	4.97
2	0.02643	0.129	2	0.2	1	3.33
3	0.02099	0.102	18	1.7	26	7.12
4	0.01668	0.081	26	2.4	40	7.77
5	0.01325	0.064	38	3.6	71	8.58
6	0.01052	0.051	41	3.9	85	9.00
7	0.00836	0.041	66	6.2	195	10.06
8	0.00664	0.032	86	8.1	305	10.73
9	0.00527	0.026	111	10.4	489	11.44
10	0.00419	0.020	106	10.0	508	11.71
11	0.00333	0.016	77	7.2	350	11.56
12	0.00264	0.013	377	35.5	4146	14.27
		Total	953			

ESFa-5B-CO_2+Ne:

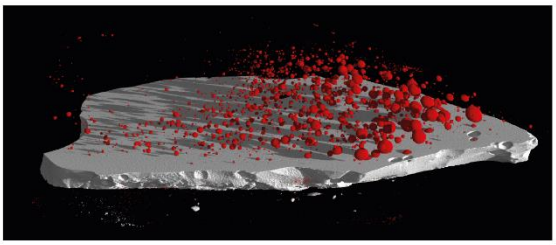

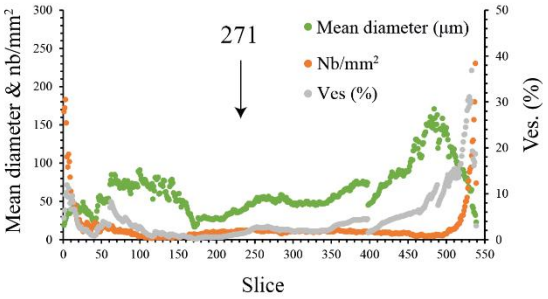

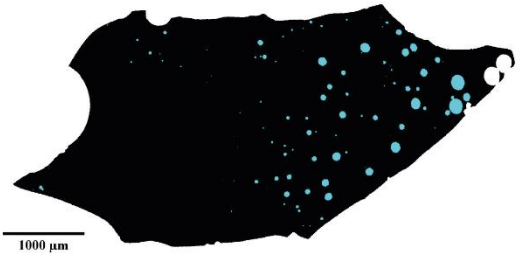

Experimental conditions	
Time (min)	10
Pressure (bars)	1573
Temperature (°C)	1200
Run	#2
CO_2 added (wt.%)	2.90
Weigth (mg)	22.90
Resolution (µm)	3
Volume (mm^3)	8.2
VGStudiomax treatment	
Ves (%)	1.50
ImageJ treatment	
Range	169-342
Tot. images	173
Ves. (from range volume) (%)	1.6
Area (mm^2)	11.26
Bub. mean diameter	52.67
Nb/mm^2	11.99
Ves. slice (%)	2.61

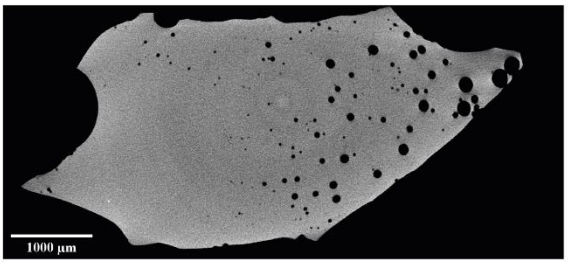

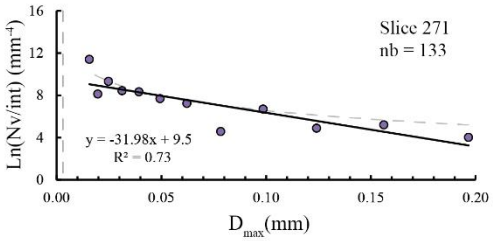

Class Number	Interval	D.max	Nb	Na (Nb/mm^2)	Nv (mm^{-3})	Ln (Nv/int) (mm^{-4})
1	0.15614	0.197	3	0.3	2	4.01
2	0.12403	0.156	7	0.6	6	5.19
3	0.09852	0.124	5	0.4	3	4.88
4	0.07826	0.099	13	1.2	16	6.70
5	0.06216	0.078	5	0.4	2	4.58
6	0.04938	0.062	10	0.9	18	7.23
7	0.03922	0.049	11	1.0	22	7.68
8	0.03115	0.039	13	1.2	33	8.33
9	0.02475	0.031	11	1.0	29	8.43
10	0.01966	0.025	14	1.2	57	9.32
11	0.01561	0.020	7	0.6	14	8.12
12	0.01240	0.016	34	3.0	286	11.40
		Total	133			

ESFa-6B-CO_2+Ne:

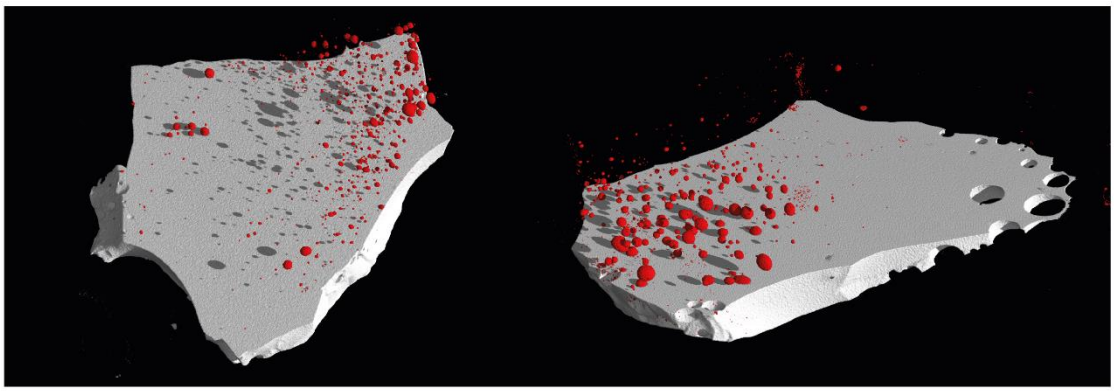

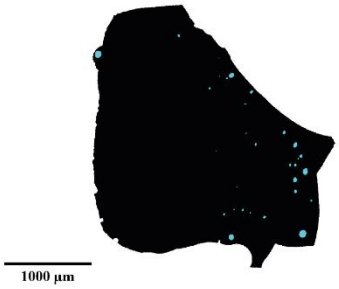

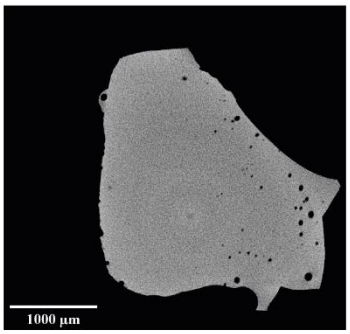

Experimental conditions	
Time (min)	10
Pressure (bars)	1573
Temperature (°C)	1200
Run	#2
CO_2 added (wt.%)	5.60
Weigth (mg)	37.50
Resolution (µm)	3
Volume (mm^3)	14.7
VGStudiomax treatment	
Ves (%)	0.41
ImageJ treatment	
Range	220-366 / 626-884
Tot. images	374
Ves. (from range volume) (%)	1.6
Area (mm^2)	5.64
Bub. mean diameter	36.67
Nb/mm^2	7.47
Ves. slice (%)	0.79

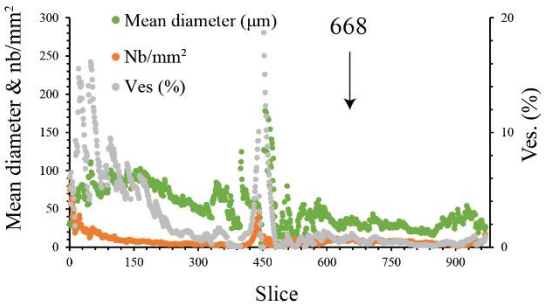

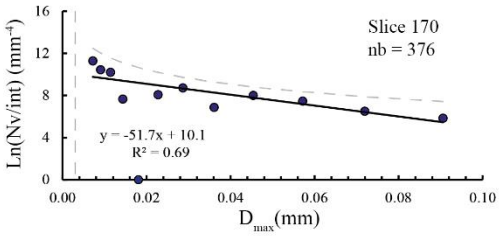

Class Number	Interval	D.max	Nb	Na (Nb/mm^2)	Nv (mm^{-3})	Ln (Nv/int) (mm^{-4})
1	0.07195	0.091	2	0.4	6	5.85
2	0.05715	0.072	3	0.5	10	6.51
3	0.04540	0.057	5	0.9	21	7.47
4	0.03606	0.045	6	1.1	28	8.01
5	0.02864	0.036	3	0.5	7	6.88
6	0.02275	0.029	5	0.9	36	8.73
7	0.01807	0.023	3	0.5	15	8.08
8	0.01436	0.018	1	0.2	-6	0.00
9	0.01140	0.014	1	0.2	6	7.67
10	0.00906	0.011	3	0.5	64	10.21
11	0.00720	0.009	3	0.5	64	10.45
12	0.00572	0.007	4	0.7	117	11.28
		Total	39			

ESFa-7B-CO_2+Ne:

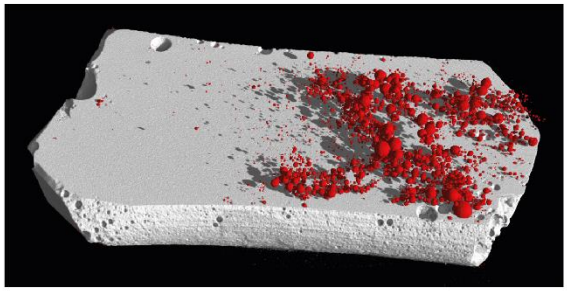

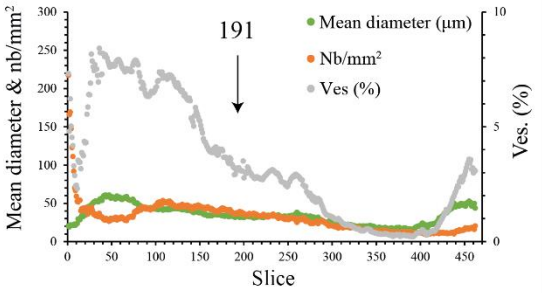

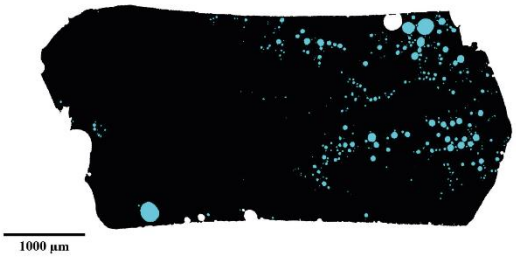

Experimental conditions	
Time (min)	240
Pressure (bars)	1605
Temperature (°C)	1200
Run	#4
CO_2 added (wt.%)	1.40
Weigth (mg)	41.20
Resolution (µm)	3
Volume (mm³)	14.7
VGStudiomax treatment	
Ves (%)	1.24
ImageJ treatment	
Range	96-298
Tot. images	462
Ves. (from range volume) (%)	3.1
Area (mm²)	13.30
Bub. mean diameter	32.63
Nb/mm²	37.37
Ves. slice (%)	3.13

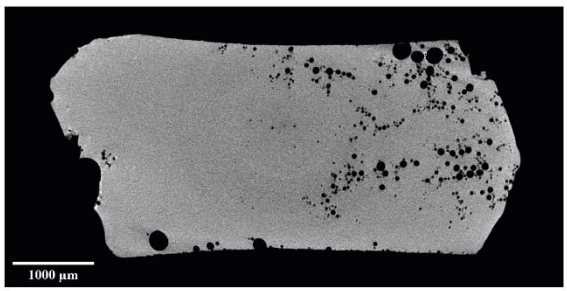

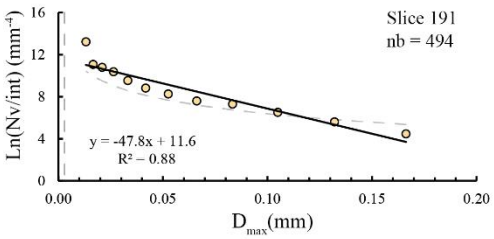

Class Number	Interval	D.max	Nb	Na (Nb/mm²)	Nv (mm⁻³)	Ln (Nv/int) (mm⁻⁴)
1	0.13203	0.166	4	0.3	3	4.47
2	0.10488	0.132	9	0.7	7	5.61
3	0.08331	0.105	15	1.1	14	6.51
4	0.06617	0.083	22	1.7	25	7.30
5	0.05256	0.066	22	1.7	27	7.60
6	0.04175	0.053	26	2.0	42	8.27
7	0.03316	0.042	29	2.2	58	8.81
8	0.02634	0.033	36	2.7	94	9.53
9	0.02093	0.026	50	3.8	174	10.37
10	0.01662	0.021	53	4.0	210	10.79
11	0.01320	0.017	49	3.7	219	11.07
12	0.01049	0.013	179	13.5	1498	13.22
		Total	494			

ESFa-10B-CO_2+Ne:

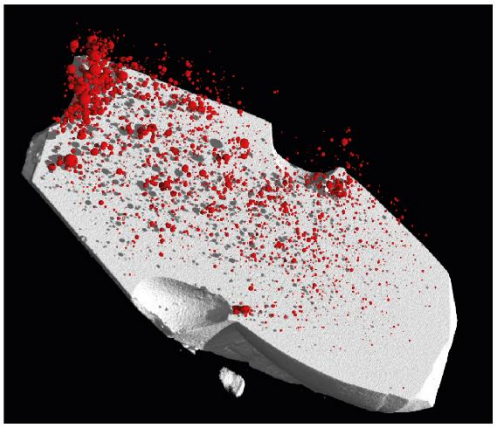

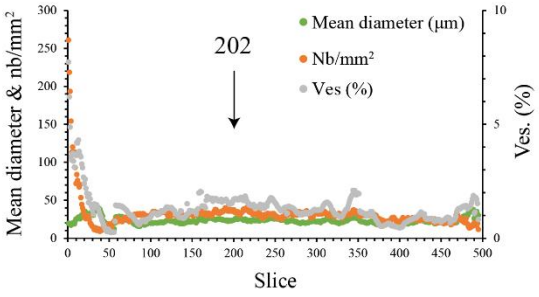

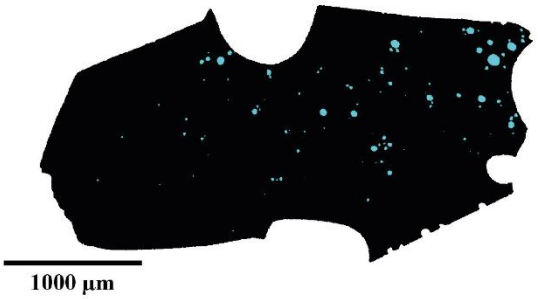

Experimental conditions	
Time (min)	240
Pressure (bars)	1605.0
Temperature (°C)	1200
Run	#4
CO_2 added (wt.%)	5.63
Weigth (mg)	17.50
Resolution (µm)	3
Volume (mm³)	14.7
VGStudiomax treatment	
Ves (%)	0.52
ImageJ treatment	
Range	116-430
Tot. images	314
Ves. (from range volume) (%)	1.2
Area (mm²)	4.71
Bub. mean diameter	25.59
Nb/mm²	33.57
Ves. slice (%)	1.73

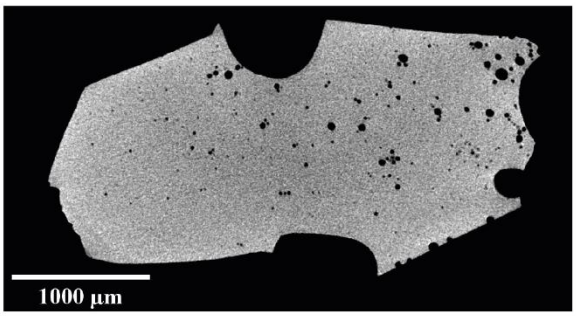

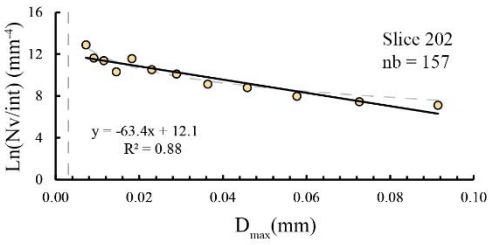

Class Number	Interval	D.max	Nb	Na (Nb/mm²)	Nv (mm⁻³)	Ln (Nv/int) (mm⁻⁴)
1	0.07260	0.091	6	1.3	23	7.11
2	0.05767	0.073	7	1.5	26	7.45
3	0.04581	0.058	8	1.7	34	7.97
4	0.03639	0.046	11	2.3	62	8.79
5	0.02890	0.036	11	2.3	69	9.12
6	0.02296	0.029	16	3.4	144	10.09
7	0.01824	0.023	17	3.6	173	10.51
8	0.01449	0.018	27	5.7	397	11.57
9	0.01151	0.014	13	2.8	90	10.31
10	0.00914	0.012	13	2.8	207	11.38
11	0.00726	0.009	11	2.3	210	11.63
12	0.00577	0.007	17	3.6	591	12.89
		Total	157			

ESFa-1A-CO_2+Ne:

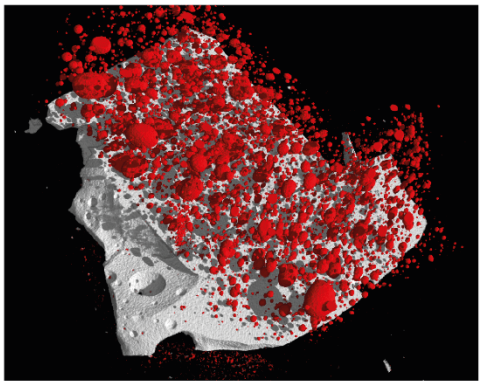

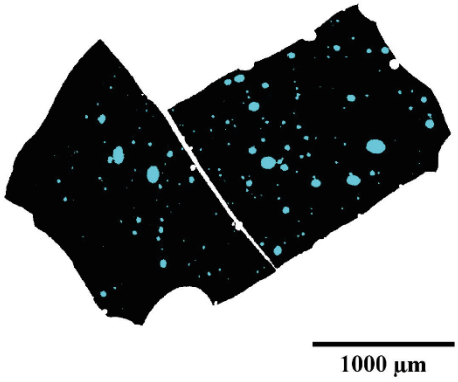

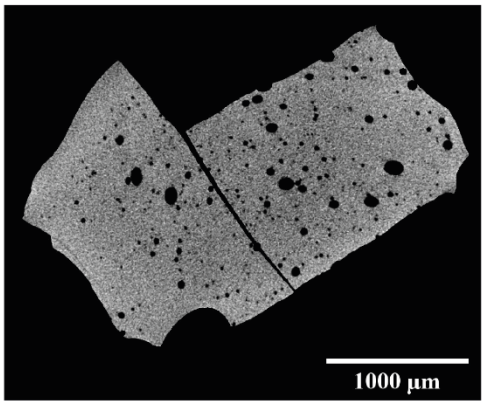

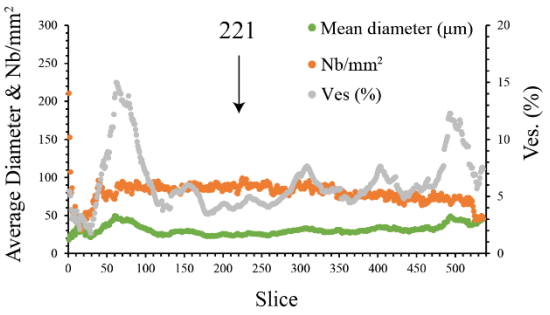

Experimental conditions	
Time (min)	10
Pressure (bars)	1660
Temperature (°C)	1200
Run	#3
CO_2 added (wt.%)	5.19
Weigth (mg)	30.40
Resolution (µm)	3
Volume (mm^3)	3.2
VGStudiomax treatment	
Ves (%)	3.95
ImageJ treatment	
Range	101-388
Tot. images	287
Ves. (from range volume) (%)	5.1
Area (mm^2)	3.73
Bub. mean diameter	24.26
Nb/mm^2	88.94
Ves. slice (%)	4.11

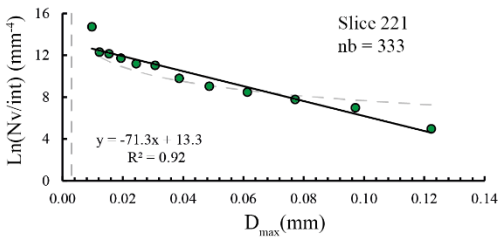

Class Number	Interval	D.max	Nb	Na (Nb/mm^2)	Nv (mm^{-3})	Ln (Nv/int) (mm^{-4})
1	0.09714	0.122	1	0.3	4	4.97
2	0.07716	0.097	5	1.3	21	6.98
3	0.06129	0.077	8	2.1	37	7.77
4	0.04868	0.061	11	2.9	61	8.48
5	0.03867	0.049	13	3.5	84	9.03
6	0.03072	0.039	17	4.6	141	9.78
7	0.02440	0.031	33	8.8	388	11.02
8	0.01938	0.024	31	8.3	365	11.19
9	0.01540	0.019	33	8.8	488	11.72
10	0.01223	0.015	33	8.8	589	12.13
11	0.00971	0.012	28	7.5	551	12.30
12	0.00772	0.010	120	32.2	4931	14.72
		Total	333			

ESFa-2A-CO_2+Ne:

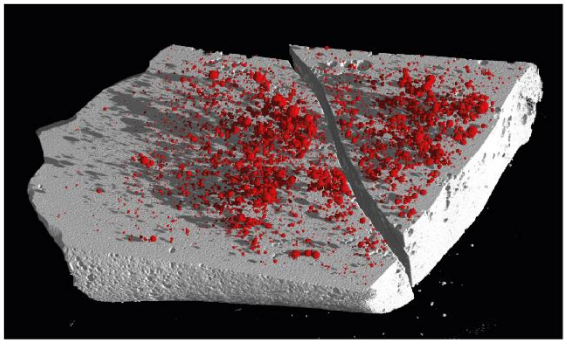

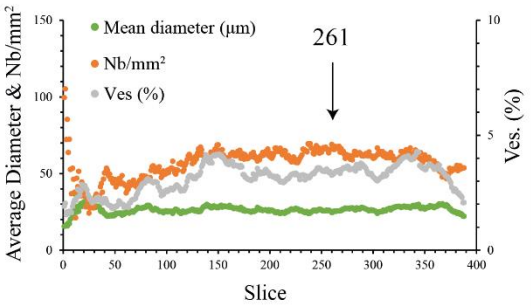

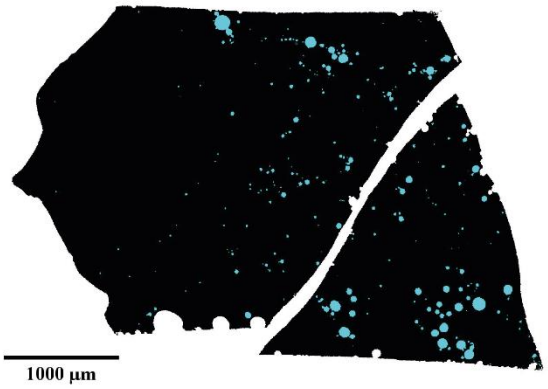

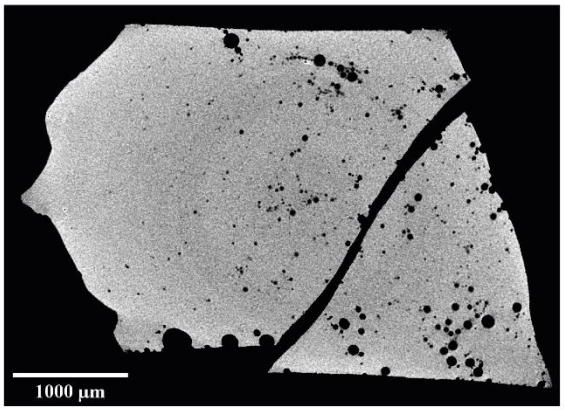

Experimental conditions	
Time (min)	240
Pressure (bars)	1605
Temperature (°C)	1200
Run	#4
CO_2 added (wt.%)	1.57
Weigth (mg)	36.40
Resolution (µm)	3
Volume (mm³)	11.9
VGStudiomax treatment	
Ves (%)	0.78
ImageJ treatment	
Range	60-344
Tot. images	498
Ves. (from range volume) (%)	3.4
Area (mm²)	10.32
Bub. mean diameter	27.73
Nb/mm²	61.43
Ves. slice (%)	3.71

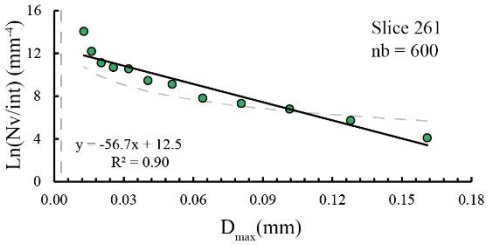

Class Number	Interval	D.max	Nb	Na (Nb/mm²)	Nv (mm⁻³)	Ln (Nv/int) (mm⁻⁴)
1	0.13466	0.170	3	0.3	3	4.40
2	0.10696	0.135	4	0.4	4	4.91
3	0.08497	0.107	15	1.5	21	6.84
4	0.06749	0.085	18	1.8	25	7.28
5	0.05361	0.067	19	1.9	30	7.69
6	0.04258	0.054	27	2.6	60	8.60
7	0.03383	0.043	39	3.8	111	9.45
8	0.02687	0.034	51	5.0	178	10.15
9	0.02134	0.027	50	4.9	192	10.45
10	0.01695	0.021	45	4.4	196	10.71
11	0.01347	0.017	68	6.6	474	11.82
12	0.01070	0.013	261	25.4	2823	13.83
		Total	600			

ESFa-5A-CO_2+Ne:

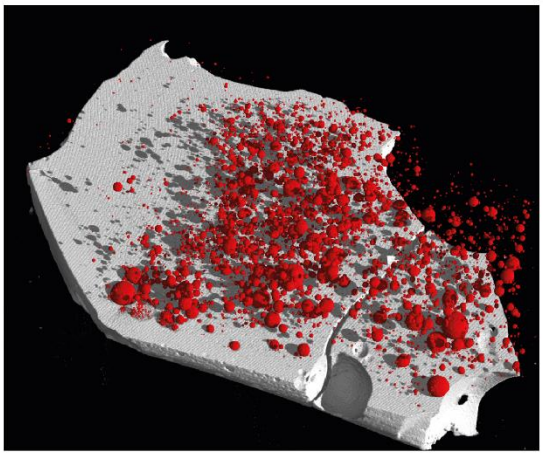

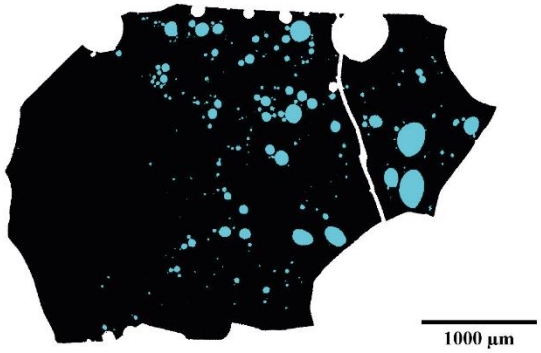

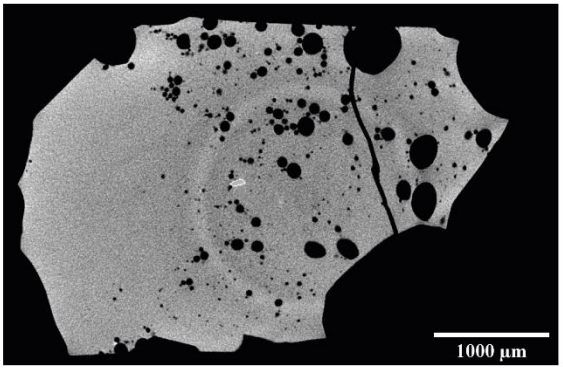

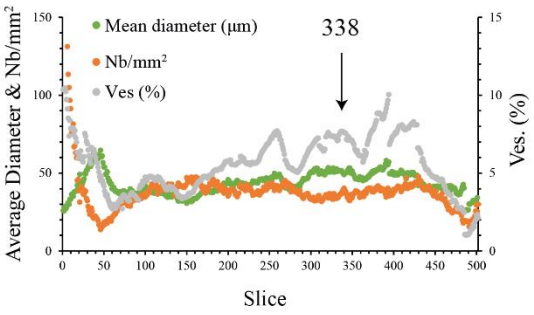

Experimental conditions	
Time (min)	10
Pressure (bars)	1669
Temperature (ºC)	1200
Run	#5
CO_2 added (wt.%)	5.52
Weigth (mg)	18.20
Resolution (µm)	3
Volume (mm^3)	11.3
VGStudiomax treatment	
Ves (%)	2.46
ImageJ treatment	
Range	145-234 316-356
Tot. images	129
Ves. (from range volume) (%)	5.7
Area (mm^2)	8.12
Bub. mean diameter	50.50
Nb/mm^2	38.30
Ves. slice (%)	7.67

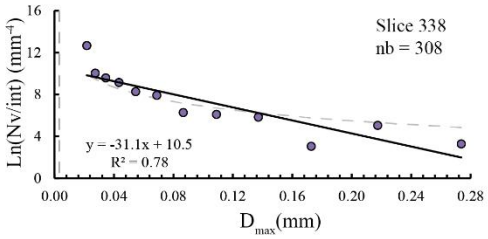

Class Number	Interval	D.max	Nb	Na (Nb/mm^2)	Nv (mm^{-3})	Ln (Nv/int) (mm^{-4})
1	0.21739	0.274	2	0.2	1	3.27
2	0.17268	0.217	8	1.0	7	5.05
3	0.13716	0.173	3	0.4	1	3.06
4	0.10895	0.137	8	1.0	10	5.84
5	0.08654	0.109	8	1.0	10	6.10
6	0.06874	0.087	7	0.9	9	6.28
7	0.05460	0.069	16	2.0	39	7.92
8	0.04337	0.055	17	2.1	44	8.26
9	0.03445	0.043	24	3.0	83	9.14
10	0.02737	0.034	26	3.2	104	9.59
11	0.02174	0.027	27	3.3	129	10.04
12	0.01727	0.022	162	20.0	1416	12.67
		Total	308			

Decompression Samples:

EN-E4:

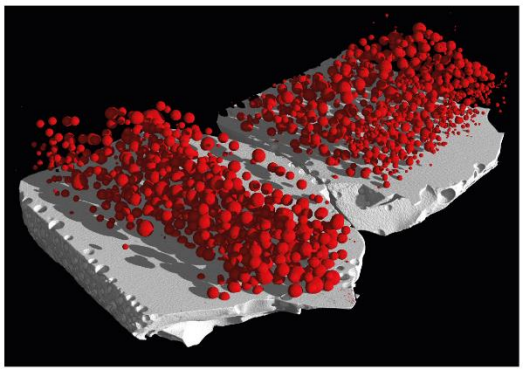

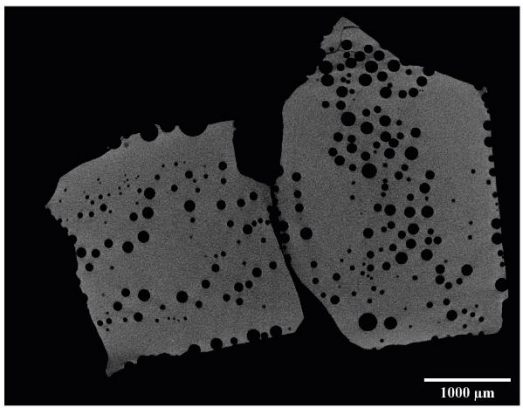

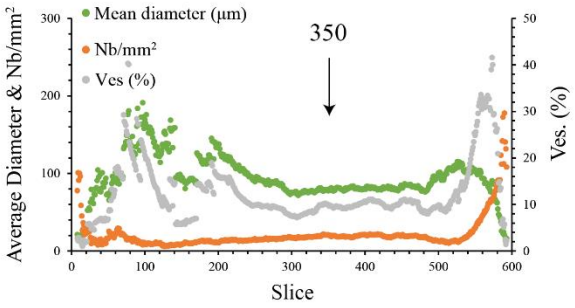

Experimental conditions	
Time (min)	2610
Pressure (bars)	2009
P_{quench} (bars)	116
D_{rate} (bar·min^{-1})	50
Temperature (°C)	1200
Run	Fasnia Ne 10
CO_2 added (wt.%)	0.27
Weigth (mg)	16.20
Resolution (µm)	3
Volume (mm³)	14.37
VGStudiomax treatment	
Ves (%)	5.49
ImageJ treatment	
Range	279-452
Tot. images	173
Ves. (from range volume) (%)	9.4
Area (mm²)	11.97
Bub. mean diameter	77.35
Nb/mm²	19.63
Ves. slice (%)	9.23

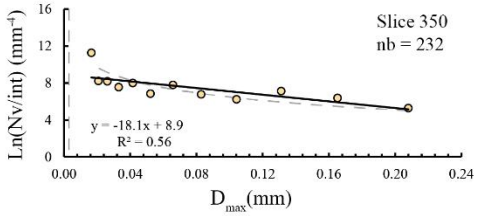

Class Number	Interval	D.max	Nb	Na (Nb/mm²)	Nv (mm⁻³)	Ln (Nv/int) (mm⁻⁴)
1	0.16517	0.208	13	1.1	9	5.30
2	0.13120	0.165	28	2.3	20	6.39
3	0.10421	0.131	41	3.4	34	7.14
4	0.08278	0.104	22	1.8	11	6.24
5	0.06575	0.083	19	1.6	15	6.80
6	0.05223	0.066	24	2.0	33	7.80
7	0.04149	0.052	13	1.1	10	6.85
8	0.03295	0.041	14	1.2	26	8.01
9	0.02618	0.033	9	0.8	13	7.58
10	0.02079	0.026	8	0.7	20	8.20
11	0.01652	0.021	6	0.5	16	8.24
12	0.01312	0.017	35	2.9	268	11.28
		Total	232			

EN-E6:

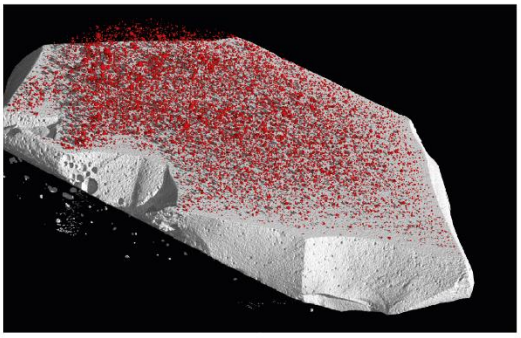

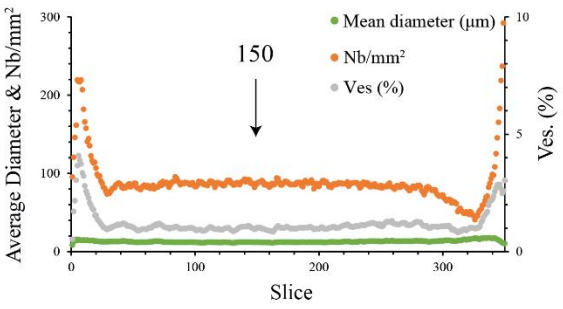

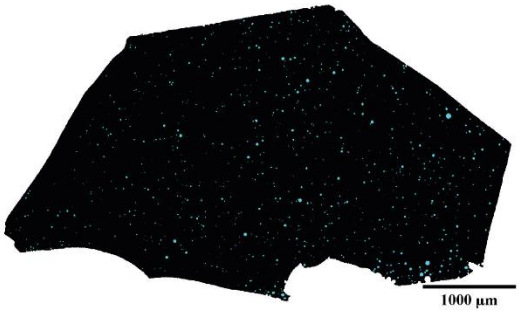

Experimental conditions

Time (min)	1830
Pressure (bars)	1899
P_{qnench} (bars)	519
D_{rate} (bar·min^{-1})	50
Temperature (°C)	1200
Run	Fasnia Ne 8
CO_2 added (wt.%)	0.28
Weigth (mg)	22.30
Resolution (µm)	3
Volume (mm³)	9.90

VGStudiomax treatment

Ves (%)	0.84

ImageJ treatment

Range	54-300
Tot. images	246
Ves. (from range volume) (%)	1.05
Area (mm²)	11.55
Bub. mean diameter	12.26
Nb/mm²	86.47
Ves. slice (%)	1.02

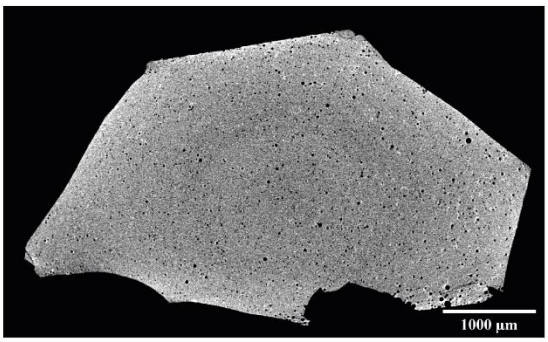

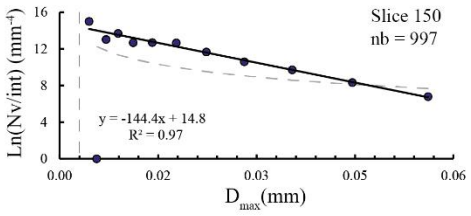

Class Number	Interval	D.max	Nb	Na (Nb/mm²)	Nv (mm⁻³)	Ln (Nv/int) (mm⁻⁴)
1	0.04459	0.056	4	0.3	10	6.78
2	0.03542	0.045	13	1.1	38	8.33
3	0.02813	0.035	34	2.9	121	9.72
4	0.02235	0.028	56	4.8	231	10.59
5	0.01775	0.022	102	8.8	534	11.66
6	0.01410	0.018	176	15.2	1146	12.66
7	0.01120	0.014	152	13.2	952	12.70
8	0.00890	0.011	116	10.0	739	12.68
9	0.00707	0.009	149	12.9	1606	13.69
10	0.00561	0.007	89	7.7	669	13.04
11	0.00446	0.006	0	0.0	-1037	0.00
12	0.00354	0.004	106	9.2	2988	15.00
		Total	997			

EN-E8:

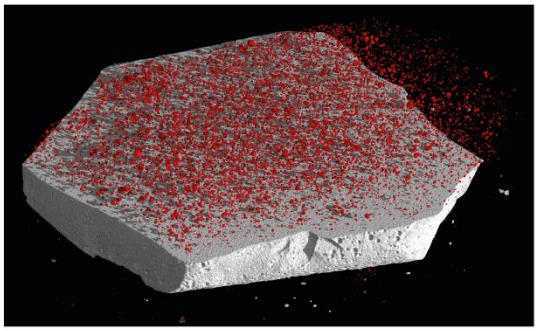

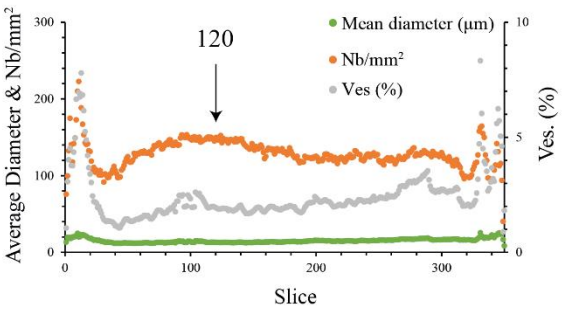

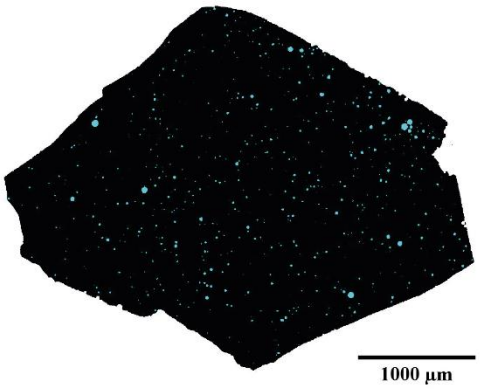

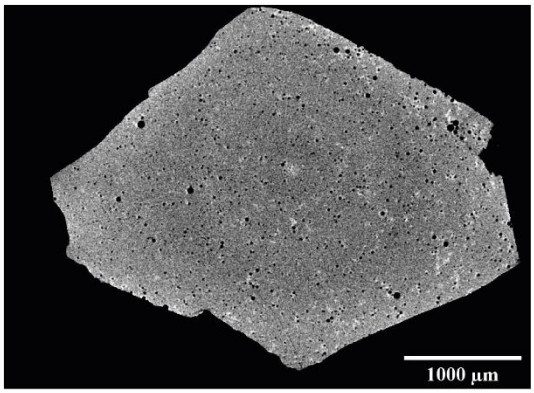

Experimental conditions	
Time (min)	1830
Pressure (bars)	1899
P_{quench} (bars)	519
D_{rate} (bar·min^{-1})	50
Temperature (°C)	1200
Run	Fasnia Ne 8
CO_2 added (wt.%)	0.39
Weigth (mg)	13.20
Resolution (µm)	3
Volume (mm³)	6.51
VGStudiomax treatment	
Ves (%)	1.19
ImageJ treatment	
Range	41-302
Tot. images	261
Ves. (from range volume) (%)	2.12
Area (mm²)	7.64
Bub. mean diameter	12.87
Nb/mm²	149.54
Ves. slice (%)	1.95

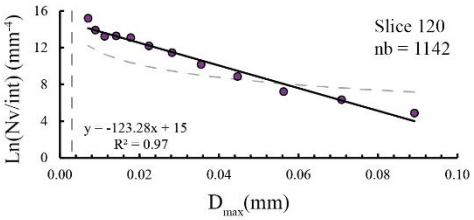

Class Number	Interval	D.max	Nb	Na (Nb/mm²)	Nv (mm⁻³)	Ln (Nv/int) (mm⁻⁴)
1	0.07084	0.089	1	0.1	2	4.88
2	0.05627	0.071	3	0.4	8	6.34
3	0.04469	0.056	5	0.7	16	7.21
4	0.03550	0.045	15	2.0	64	8.86
5	0.02820	0.036	36	4.7	191	10.17
6	0.02240	0.028	83	10.9	548	11.46
7	0.01779	0.022	120	15.7	904	12.19
8	0.01413	0.018	186	24.3	1765	13.09
9	0.01123	0.014	174	22.8	1698	13.28
10	0.00892	0.011	133	17.4	1296	13.24
11	0.00708	0.009	139	18.2	2015	13.91
12	0.00563	0.007	247	32.3	5836	15.20
		Total	1142			

EN-E9:

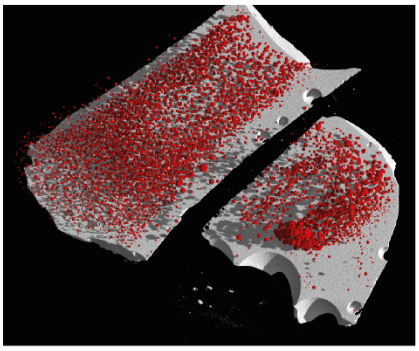

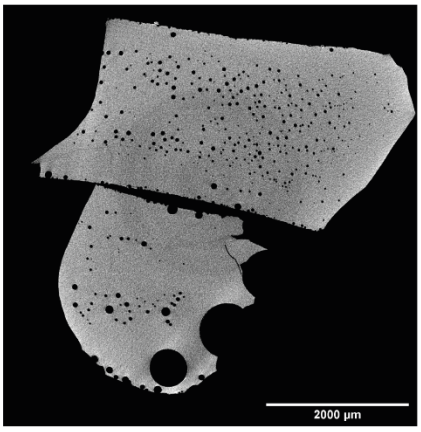

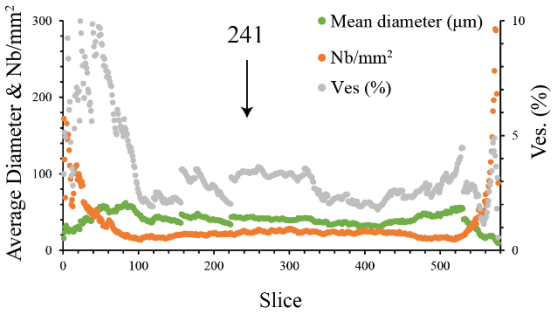

Experimental conditions	
Time (min)	3020
Pressure (bars)	2147
P_{quench} (bars)	247
D_{rate} (bar·min^{-1})	50
Temperature (°C)	1200
Run	Fasnia Ne 9
CO_2 added (wt.%)	0.32
Weigth (mg)	51.10
Resolution (µm)	3
Volume (mm³)	19.80
VGStudiomax treatment	
Ves (%)	1.27
ImageJ treatment	
Range	121-481
Tot. images	360
Ves. (from range volume) (%)	2.71
Area (mm²)	15.30
Bub. mean diameter	42.83
Nb/mm²	23.79
Ves. slice (%)	3.43

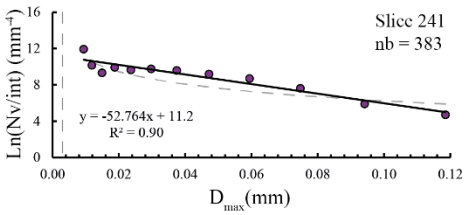

Class Number	Interval	D.max	Nb	Na (Nb/mm²)	Nv (mm ³)	Ln (Nv/int) (mm ⁴)
1	0.09415	0.119	3	0.2	3	4.72
2	0.07479	0.094	7	0.5	7	5.90
3	0.05940	0.075	24	1.6	31	7.62
4	0.04719	0.059	48	3.1	74	8.71
5	0.03748	0.047	57	3.7	95	9.19
6	0.02977	0.037	59	3.9	112	9.59
7	0.02365	0.030	51	3.3	105	9.75
8	0.01879	0.024	37	2.4	76	9.65
9	0.01492	0.019	30	2.0	79	9.92
10	0.01185	0.015	18	1.2	34	9.32
11	0.00942	0.012	16	1.0	63	10.16
12	0.00748	0.009	33	2.2	293	11.93
		Total	383			

EN-E10:

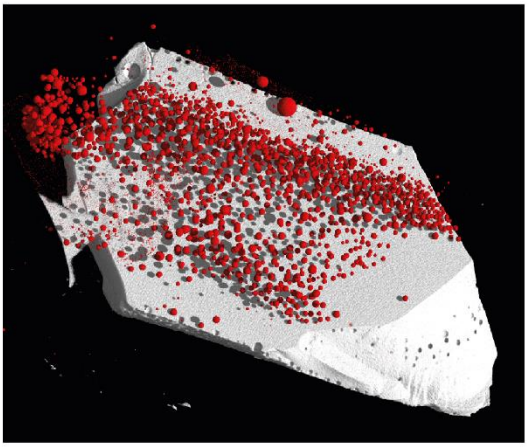

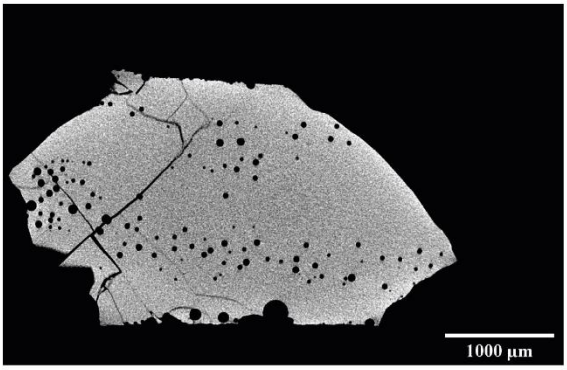

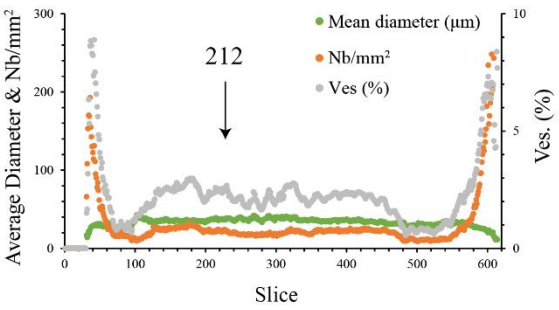

Experimental conditions

Time (min)	3020
Pressure (bars)	2147
P_{quench} (bars)	247
D_{rate} (bar·min^{-1})	50
Temperature (°C)	1200
Run	Fasnia Ne 9
CO_2 added (wt.%)	0.28
Weigth (mg)	22.50
Resolution (µm)	3
Volume (mm³)	9.88

VGStudiomax treatment

Ves (%)	1.57

ImageJ treatment

Range	119-482
Tot. images	363
Ves. (from range volume) (%)	2.21
Area (mm²)	6.50
Bub. mean diameter	36.70
Nb/mm²	22.46
Ves. slice (%)	2.38

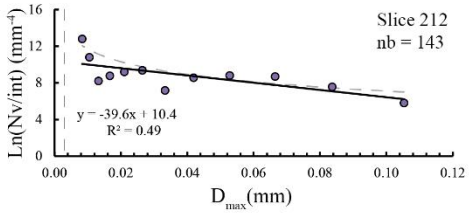

Class Number	Interval	D.max	Nb	Na (Nb/mm²)	Nv (mm ³)	Ln (Nv/int) (mm ⁴)
1	0.08366	0.105	3	0.5	7	5.81
2	0.06645	0.084	12	1.8	34	7.58
3	0.05279	0.066	25	3.8	82	8.70
4	0.04193	0.053	23	3.5	73	8.81
5	0.03331	0.042	16	2.5	45	8.57
6	0.02646	0.033	8	1.2	9	7.17
7	0.02101	0.026	11	1.7	65	9.38
8	0.01669	0.021	8	1.2	43	9.21
9	0.01326	0.017	5	0.8	22	8.77
10	0.01053	0.013	3	0.5	10	8.21
11	0.00837	0.011	6	0.9	105	10.79
12	0.00665	0.008	23	3.5	630	12.81
		Total	143			

EN-D1:

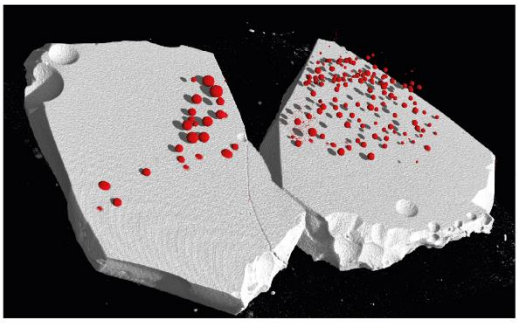

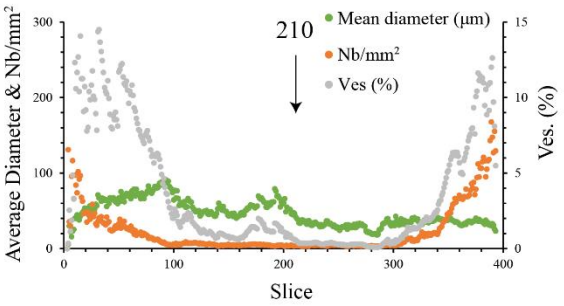

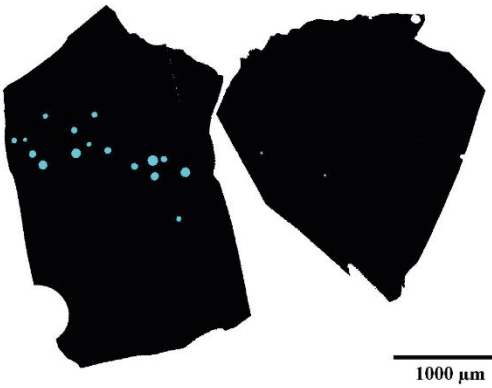

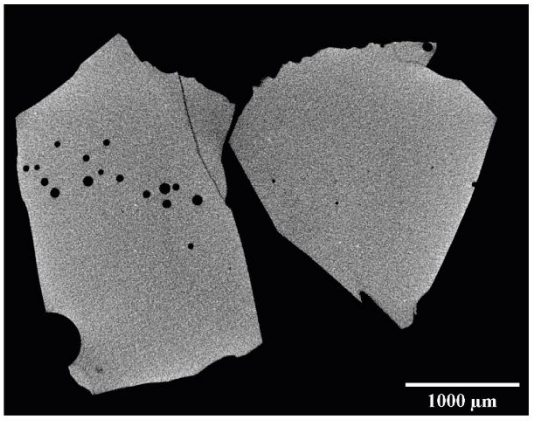

Experimental conditions	
Time (min)	4560
Pressure (bars)	1983
P_{quench} (bars)	250
D_{rate} (bar·min^{-1})	5
Temperature (°C)	1200
Run	Fasnia Ne 11
CO_2 added (wt.%)	0.27
Weigth (mg)	23.60
Resolution (µm)	3
Volume (mm^3)	6.12
VGStudiomax treatment	
Ves (%)	0.31
ImageJ treatment	
Range	130-300
Tot. images	170
Ves. (from range volume) (%)	0.65
Area (mm^2)	8.48
Bub. mean diameter	46.33
Nb/mm^2	3.54
Ves. slice (%)	0.60

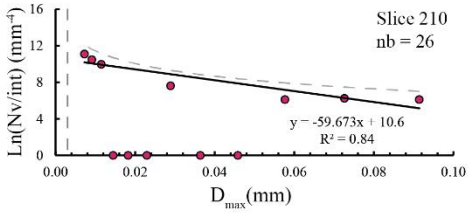

Class Number	Interval	D.max	Nb	Na (Nb/mm²)	Nv (mm⁻³)	Ln (Nv/int) (mm⁻⁴)
1	0.07260	0.091	4	0.5	8	6.11
2	0.05767	0.073	4	0.5	8	6.25
3	0.04581	0.058	3	0.4	5	6.12
4	0.03639	0.046	1	0.1	-1	0.00
5	0.02890	0.036	0	0.0	-3	0.00
6	0.02296	0.029	2	0.2	12	7.61
7	0.01824	0.023	0	0.0	-5	0.00
8	0.01449	0.018	0	0.0	-2	0.00
9	0.01151	0.014	0	0.0	-1	0.00
10	0.00914	0.012	3	0.4	50	9.96
11	0.00726	0.009	4	0.5	67	10.48
12	0.00577	0.007	5	0.6	98	11.09
		Total	26			

EN-D2:

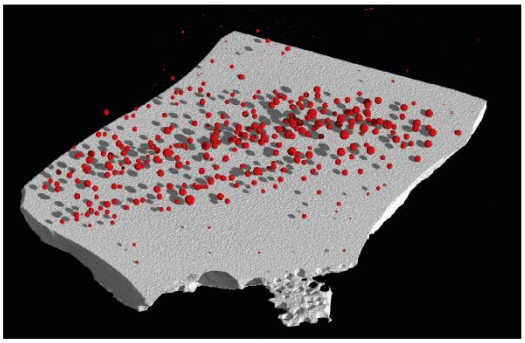

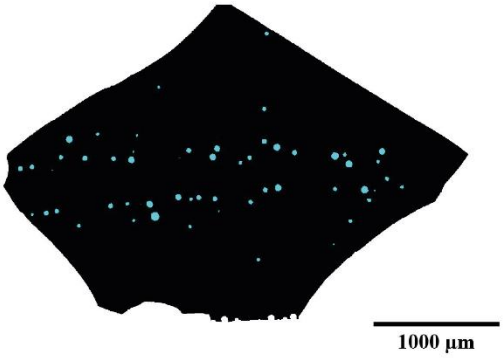

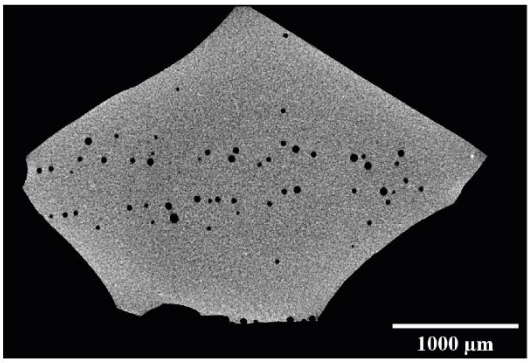

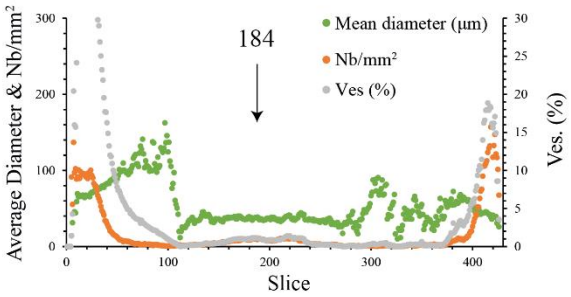

Experimental conditions

Time (min)	4560
Pressure (bars)	1983
P_{qnench} (bars)	250
D_{rate} (bar·min^{-1})	5
Temperature (°C)	1200
Run	Fasnia Ne 11
CO_2 added (wt.%)	0.27
Weigth (mg)	
Resolution (µm)	3
Volume (mm³)	16.13

VGStudiomax treatment

Ves (%)	0.31

ImageJ treatment

Range	130-370
Tot. images	240
Ves. (from range volume) (%)	0.65
Area (mm²)	5.55
Bub. mean diameter	36.73
Nb/mm²	10.28
Ves. slice (%)	1.09

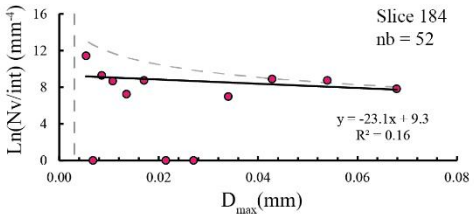

Class Number	Interval	D.max	Nb	Na (Nb/mm²)	Nv (mm ³)	Ln (Nv/int) (mm ⁴)
1	0.05391	0.068	8	1.4	35	7.83
2	0.04282	0.054	15	2.7	70	8.76
3	0.03402	0.043	14	2.5	64	8.90
4	0.02702	0.034	6	1.1	8	6.98
5	0.02146	0.027	1	0.2	-23	0.00
6	0.01705	0.021	1	0.2	-3	0.00
7	0.01354	0.017	2	0.4	22	8.74
8	0.01076	0.014	1	0.2	4	7.25
9	0.00854	0.011	1	0.2	13	8.67
10	0.00679	0.009	1	0.2	19	9.29
11	0.00539	0.007	0	0.0	-18	0.00
12	0.00428	0.005	2	0.4	103	11.44
		Total	52			

EN-D4:

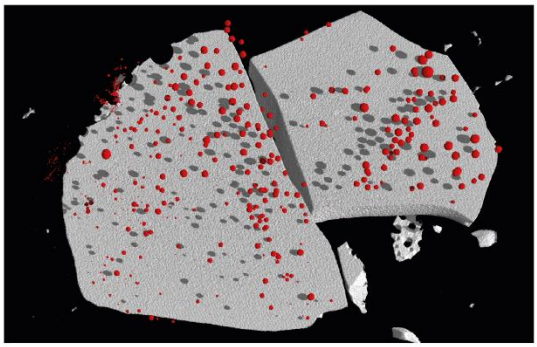

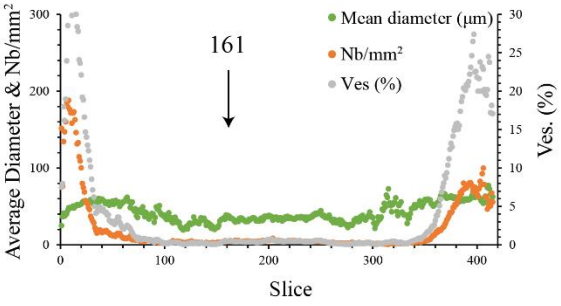

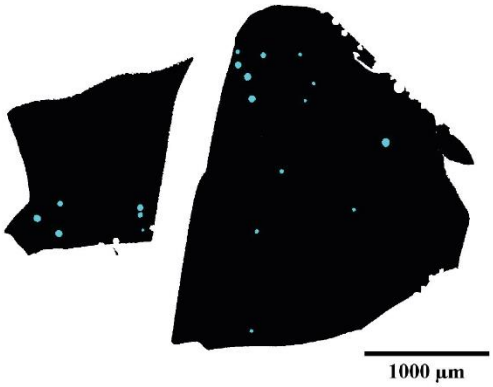

Experimental conditions

Time (min)	4560
Pressure (bars)	1983
P_{quench} (bars)	250
D_{rate} (bar·min^{-1})	5
Temperature (°C)	1200
Run	Fasnia Ne 11
CO_2 added (wt.%)	0.27
Weigth (mg)	15.30
Resolution (µm)	3
Volume (mm³)	5.44

VGStudiomax treatment

Ves (%)	0.06

ImageJ treatment

Range	100-331
Tot. images	231
Ves. (from range volume) (%)	0.32
Area (mm²)	6.09
Bub. mean diameter	37.98
Nb/mm²	4.27
Ves. slice (%)	0.48

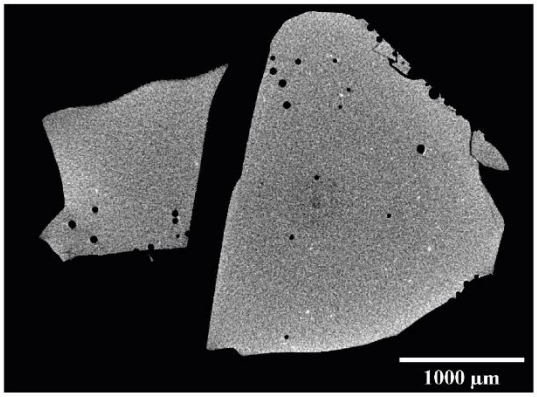

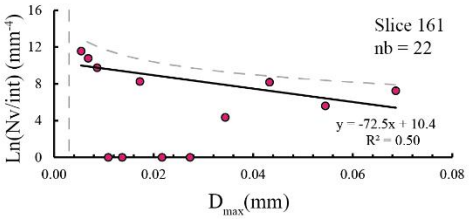

Class Number	Interval	D.max	Nb	Na (Nb/mm²)	Nv (mm⁻³)	Ln (Nv/int) (mm⁻⁴)
1	0.05451	0.069	5	0.8	20	7.24
2	0.04330	0.055	2	0.3	3	5.61
3	0.03440	0.043	6	1.0	32	8.18
4	0.02732	0.034	2	0.3	1	4.36
5	0.02170	0.027	0	0.0	-11	0.00
6	0.01724	0.022	0	0.0	-4	0.00
7	0.01369	0.017	1	0.2	14	8.25
8	0.01088	0.014	0	0.0	-7	0.00
9	0.00864	0.011	0	0.0	-2	0.00
10	0.00686	0.009	1	0.2	30	9.74
11	0.00545	0.007	2	0.3	67	10.77
12	0.00433	0.005	3	0.5	117	11.56
		Total	22			

Natural Samples:

2πD43:

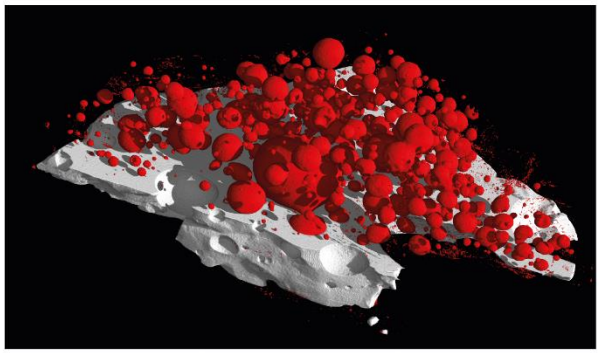

Location	13.76N - 44.01W
Depth (m)	3510
Weigth (mg)	524.8
Resolution (µm)	10
Volume (mm³)	221
VGStudio max treatment	
Ves (%)	8.89
ImageJ treatment	
tot. images	129
Ves (from volume) (%)	16.9
Area (mm²)	44.64
Bub. mean diameter (µm)	367.74
Nb/mm²	1.75
ves (slice) (%)	18.56

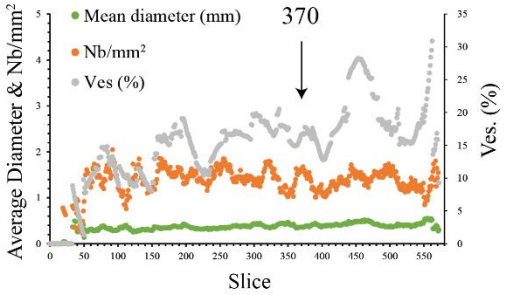

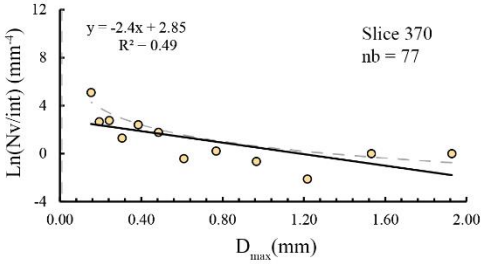

Class Number	Interval	D.max	Nb	Na (Nb/mm²)	Nv (mm⁻³)	Ln (Nv/int) (mm⁻⁴)
1	0.39660	1.928	0	0.0	0	0.00
2	0.31503	1.532	0	0.0	0	0.00
3	0.25024	1.217	1	0.0	0	-2.11
4	0.19877	0.966	3	0.1	0	-0.65
5	0.15789	0.768	5	0.1	0	0.22
6	0.12542	0.610	3	0.1	0	-0.41
7	0.09962	0.484	9	0.2	1	1.78
8	0.07913	0.385	12	0.3	1	2.40
9	0.06286	0.306	6	0.1	0	1.29
10	0.04993	0.243	8	0.2	1	2.76
11	0.03966	0.193	6	0.1	1	2.65
12	0.03150	0.153	24	0.5	5	5.10
		Total	77			

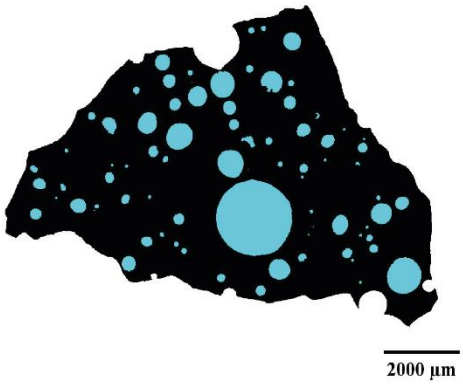

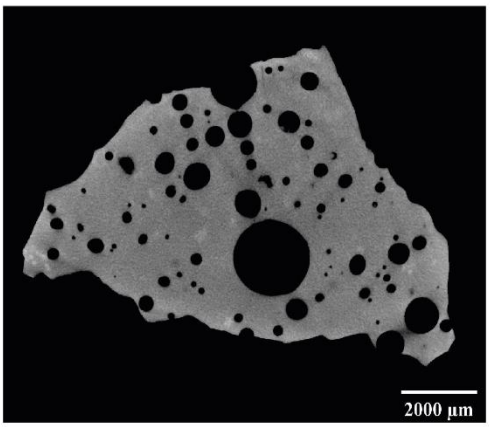

EW-9309-2D:

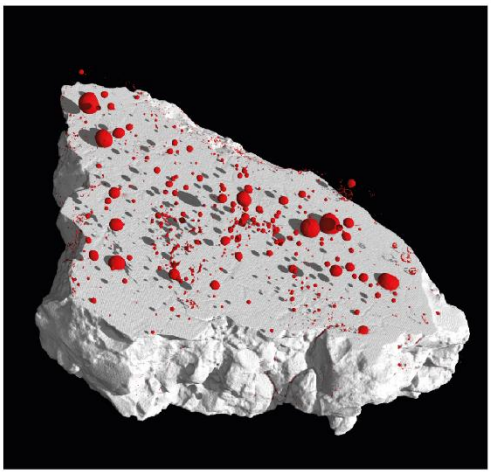

Location	47.55S - 10.19W
Depth (m)	2494
Weigth (mg)	497.4
Resolution (µm)	10
Volume (mm³)	176
VGStudio max treatment	
Ves (%)	0.74
ImageJ treatment	
tot. images	472
Ves (from volume) (%)	0.8
Area (mm²)	54.12
Bub. mean diameter (µm)	107.93
Nb/mm²	0.65
ves (slice) (%)	0.59

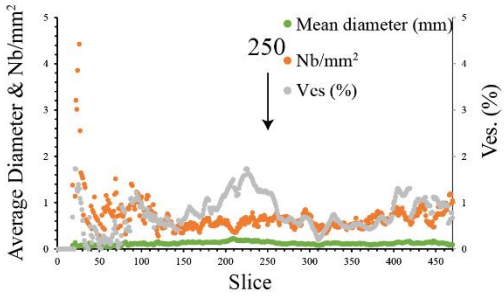

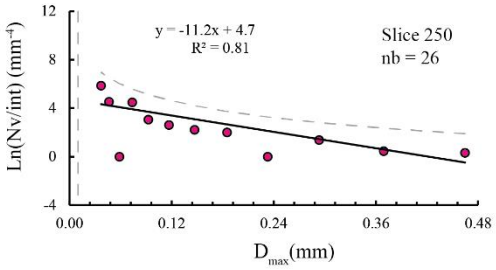

Class Number	Interval	D.max	Nb	Na (Nb/mm²)	Nv (mm ³)	Ln (Nv/int) (mm ⁴)
1	0.09557	0.465	2	0.0	0	0.31
2	0.07592	0.369	2	0.0	0	0.45
3	0.06030	0.293	3	0.1	0	1.38
4	0.04790	0.233	0	0.0	0	0.00
5	0.03805	0.185	2	0.0	0	2.00
6	0.03022	0.147	2	0.0	0	2.22
7	0.02401	0.117	2	0.0	0	2.62
8	0.01907	0.093	2	0.0	0	3.05
9	0.01515	0.074	4	0.1	1	4.48
10	0.01203	0.059	1	0.0	0	0.00
11	0.00956	0.046	2	0.0	1	4.53
12	0.00759	0.037	4	0.1	3	5.86
		Total	26			

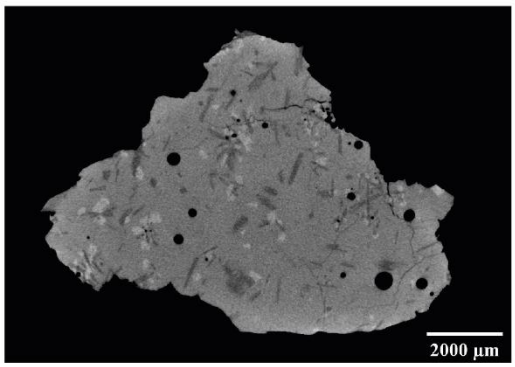

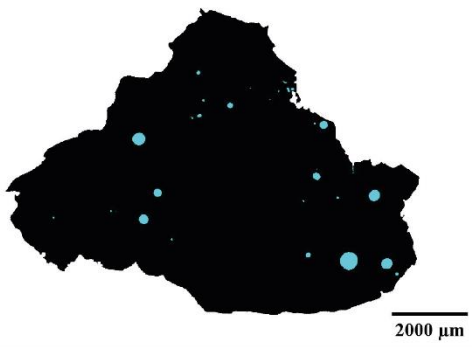

EW-9309-3D:

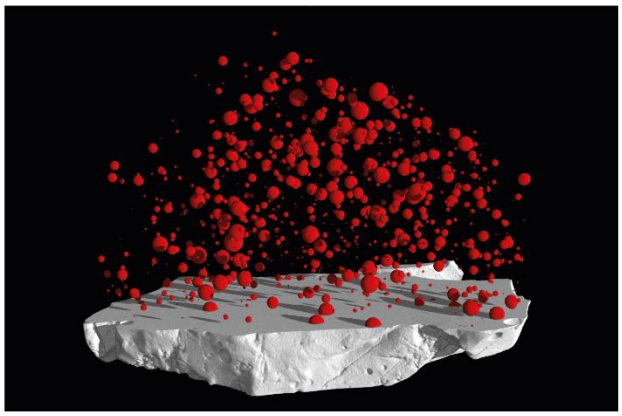

Location	47.80S - 10.15W
Depth (m)	2549
Weigth (mg)	800.9
Resolution (µm)	10
Volume (mm³)	300
VGStudio max treatment	
Ves (%)	1.24
ImageJ treatment	
tot. images	806
Ves (from volume) (%)	1.7
Area (mm²)	43.42
Bub. mean diameter (µm)	176.76
Nb/mm²	0.78
ves (slice) (%)	1.92

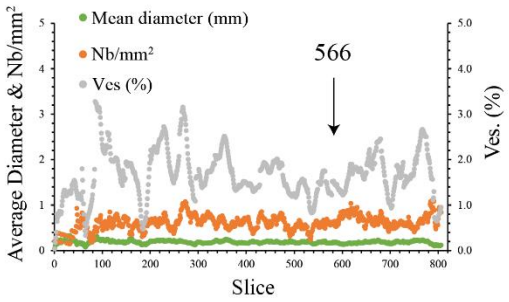

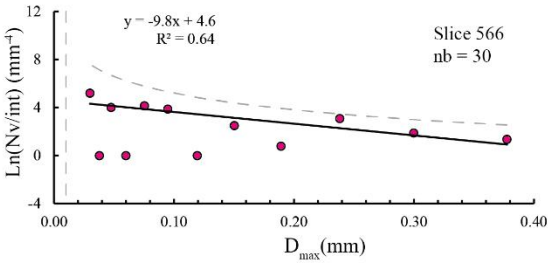

Class Number	Interval	D.max	Nb	Na (Nb/mm²)	Nv (mm ³)	Ln (Nv/int) (mm ⁴)
1	0.07763	0.377	3	0.1	0	1.36
2	0.06167	0.300	4	0.1	0	1.87
3	0.04898	0.238	8	0.2	1	3.08
4	0.03891	0.189	3	0.1	0	0.78
5	0.03091	0.150	3	0.1	0	2.49
6	0.02455	0.119	1	0.0	0	0.00
7	0.01950	0.095	3	0.1	1	3.86
8	0.01549	0.075	3	0.1	1	4.14
9	0.01230	0.060	0	0.0	-1	0.00
10	0.00977	0.048	1	0.0	1	4.00
11	0.00776	0.038	0	0.0	0	0.00
12	0.00617	0.030	1	0.0	1	5.19
		Total	30			

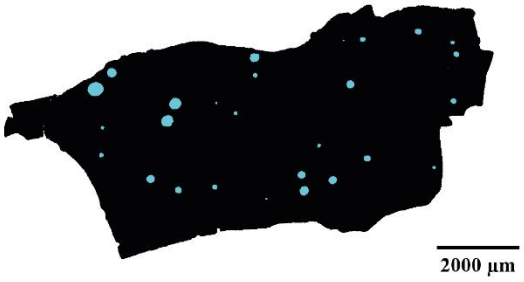

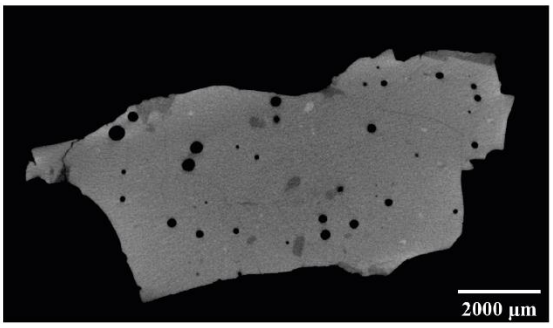

EW-9309-4D:

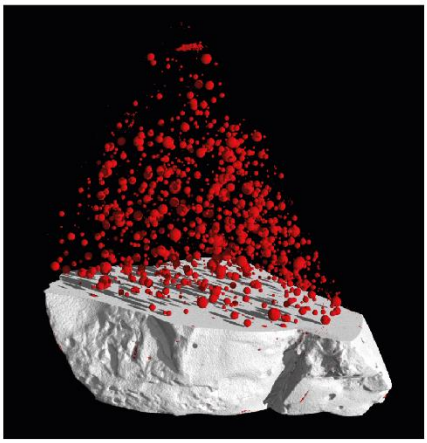

Location	47.97S - 10.08W
Depth (m)	2895
Weigth (mg)	668.2
Resolution (µm)	10
Volume (mm³)	236
VGStudio max treatment	
Ves (%)	1.23
ImageJ treatment	
tot. images	970
Ves (from volume) (%)	1.3
Area (mm²)	36.62
Bub. mean diameter (µm)	150.31
Nb/mm²	1.23
ves (slice) (%)	2.18

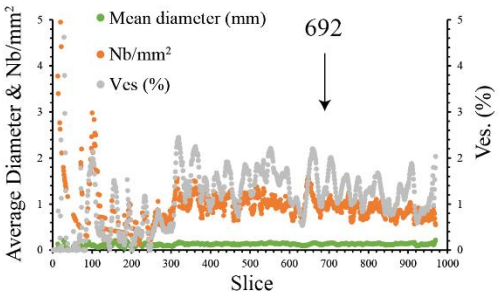

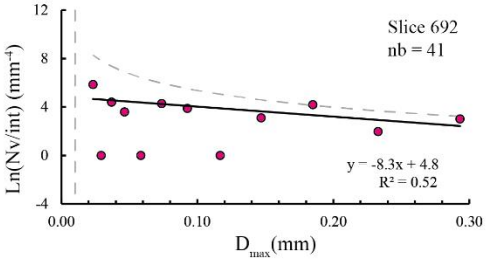

Class Number	Interval	D.max	Nb	Na (Nb/mm²)	Nv (mm⁻³)	Ln (Nv/int) (mm⁻⁴)
1	0.06030	0.293	8	0.2	1	3.01
2	0.04789	0.233	4	0.1	0	1.97
3	0.03804	0.185	12	0.3	3	4.19
4	0.03022	0.147	6	0.2	1	3.10
5	0.02400	0.117	1	0.0	-1	0.00
6	0.01907	0.093	3	0.1	1	3.89
7	0.01515	0.074	3	0.1	1	4.28
8	0.01203	0.058	1	0.0	0	0.00
9	0.00956	0.046	1	0.0	0	3.60
10	0.00759	0.037	1	0.0	1	4.40
11	0.00603	0.029	0	0.0	-1	0.00
12	0.00479	0.023	1	0.0	2	5.85
		Total	41			

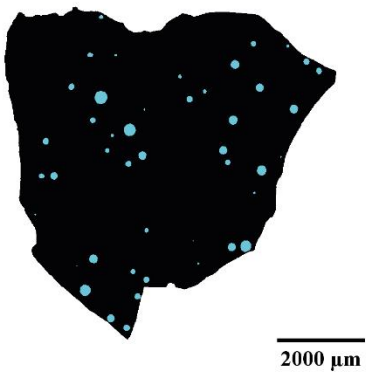

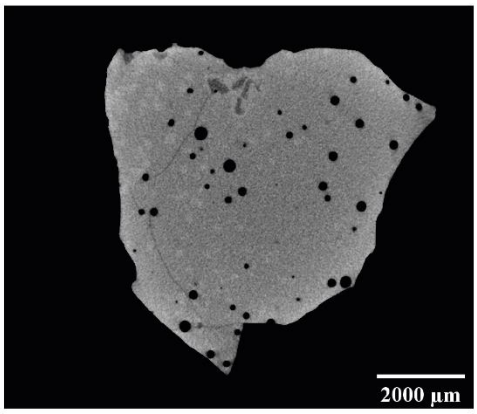

EW-9309-5D:

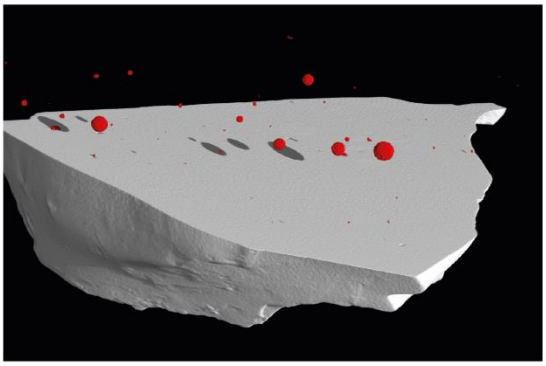

Location	48.24S - 10.00W
Depth (m)	3453
Weigth (mg)	284.8
Resolution (µm)	10
Volume (mm³)	101
VGStudio max treatment	
Ves (%)	0.03
ImageJ treatment	
tot. images	381
Ves (from volume) (%)	0.04
Area (mm²)	42.44
Bub. mean diameter (µm)	88.81
Nb/mm²	0.42
ves (slice) (%)	0.26

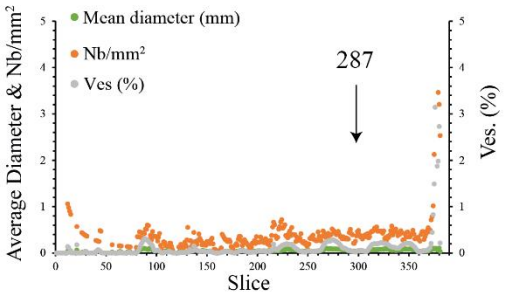

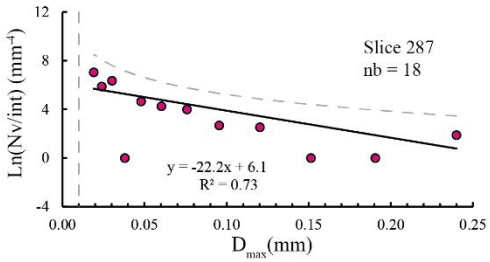

Class Number	Interval	D.max	Nb	Na (Nb/mm²)	Nv (mm⁻³)	Ln (Nv/int) (mm⁻⁴)
1	0.04934	0.240	2	0.0	0	1.88
2	0.03919	0.191	0	0.0	0	0.00
3	0.03113	0.151	0	0.0	0	0.00
4	0.02473	0.120	1	0.0	0	2.52
5	0.01964	0.096	1	0.0	0	2.68
6	0.01560	0.076	2	0.0	1	3.99
7	0.01239	0.060	2	0.0	1	4.25
8	0.00984	0.048	2	0.0	1	4.65
9	0.00782	0.038	0	0.0	-1	0.00
10	0.00621	0.030	3	0.1	4	6.35
11	0.00493	0.024	2	0.0	2	5.87
12	0.00392	0.019	3	0.1	4	7.04
		Total	**18**			

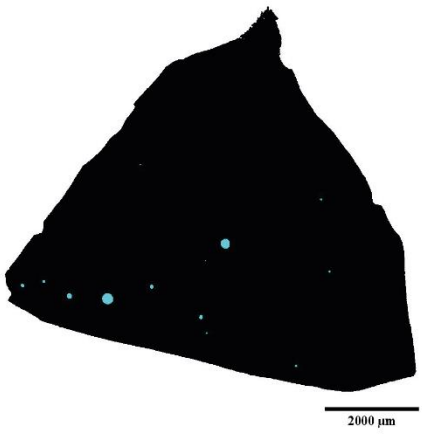

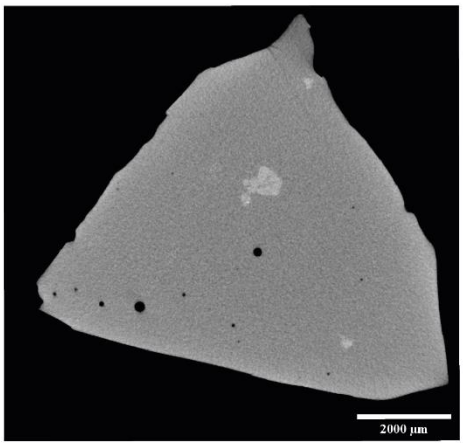

EW-9309-20D:

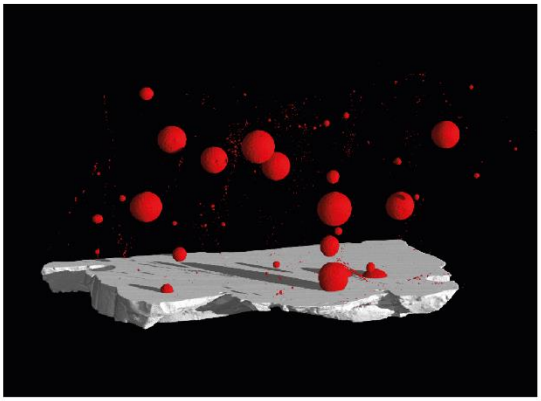

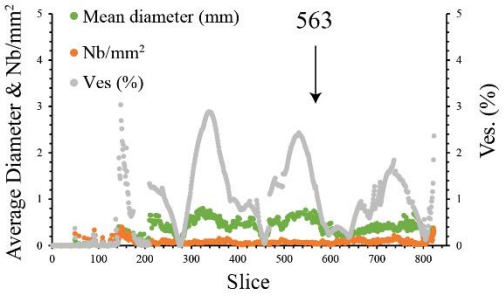

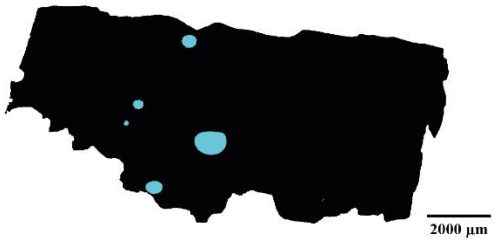

Location	51.43S - 5.78W
Depth (m)	1719
Weigth (mg)	1171.1
Resolution (µm)	10
Volume (mm³)	419
VGStudio max treatment	
Ves (%)	0.88
ImageJ treatment	
tot. images	823
Ves (from volume) (%)	1.07
Area (mm²)	66.35
Bub. mean diameter (µm)	430.88
Nb/mm²	0.11
ves (slice) (%)	1.54

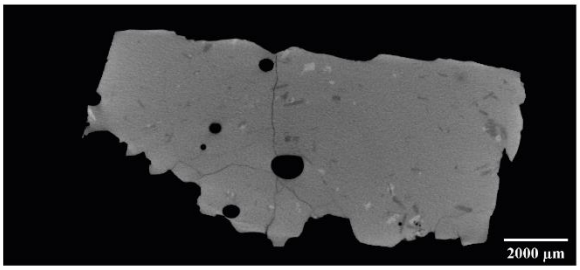

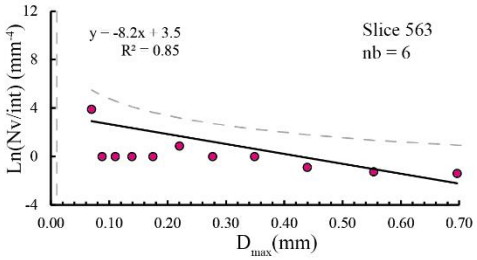

Class Number	Interval	D.max	Nb	Na (Nb/mm²)	Nv (mm⁻³)	Ln (Nv/int) (mm⁻⁴)
1	0.18033	0.877	0	0.0	0	0.00
2	0.14324	0.696	1	0.0	0	-1.39
3	0.11378	0.553	1	0.0	0	-1.26
4	0.09038	0.439	1	0.0	0	-0.90
5	0.07179	0.349	0	0.0	0	0.00
6	0.05703	0.277	0	0.0	0	0.00
7	0.04530	0.220	1	0.0	0	0.87
8	0.03598	0.175	0	0.0	0	0.00
9	0.02858	0.139	0	0.0	0	0.00
10	0.02270	0.110	0	0.0	0	0.00
11	0.01803	0.088	0	0.0	0	0.00
12	0.01432	0.070	2	0.0	1	3.90
		Total	*6*			

EW-9309-25D:

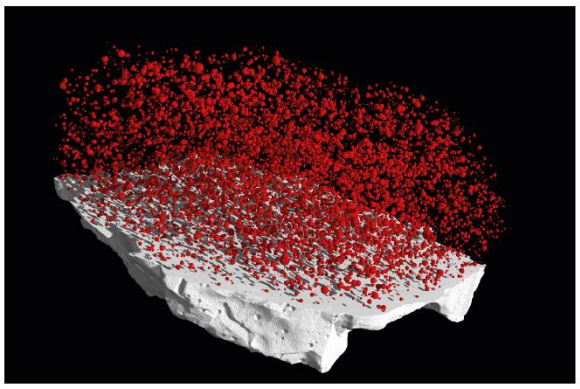

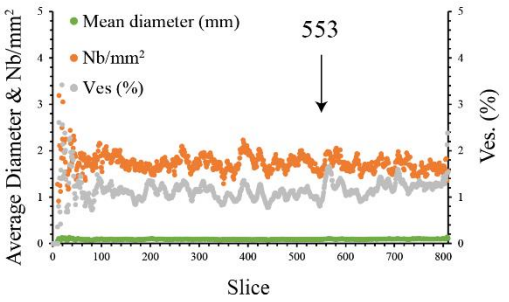

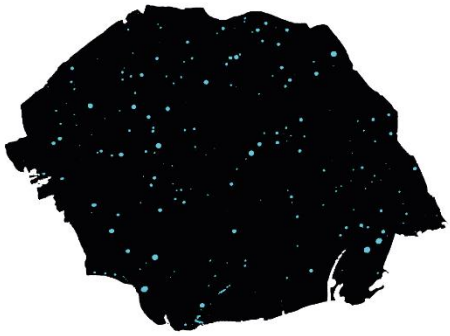

Location	47.35S - 10.32W
Depth (m)	2032
Weigth (mg)	1973.1
Resolution (µm)	10
Volume (mm³)	730
VGStudio max treatment	
Ves (%)	1.04
ImageJ treatment	
tot. images	815
Ves (from volume) (%)	1.13
Area (mm²)	114.00
Bub. mean diameter (µm)	86.07
Nb/mm²	1.92
ves (slice) (%)	1.12

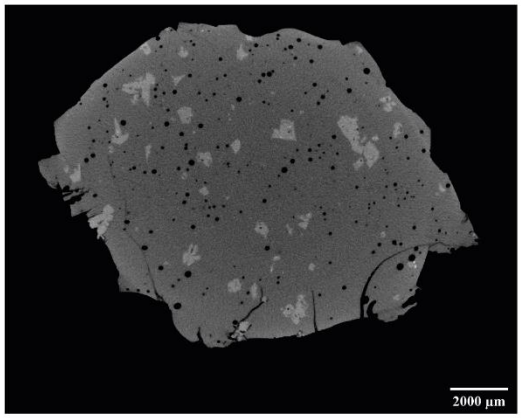

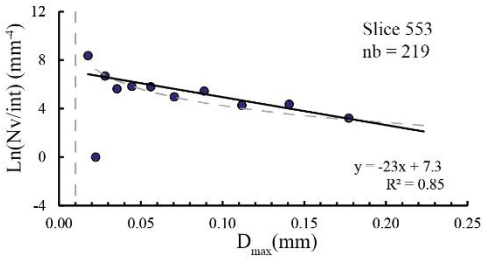

Class Number	Interval	D.max	Nb	Na (Nb/mm²)	Nv (mm⁻³)	Ln (Nv/int) (mm⁻⁴)
1	0.04589	0.223	7	0.1	0	2.29
2	0.03645	0.177	13	0.1	1	3.21
3	0.02895	0.141	26	0.2	2	4.35
4	0.02300	0.112	21	0.2	2	4.27
5	0.01827	0.089	34	0.3	4	5.44
6	0.01451	0.071	22	0.2	2	4.98
7	0.01153	0.056	24	0.2	4	5.79
8	0.00916	0.045	19	0.2	3	5.82
9	0.00727	0.035	13	0.1	2	5.63
10	0.00578	0.028	15	0.1	5	6.68
11	0.00459	0.022	3	0.0	-2	0.00
12	0.00365	0.018	22	0.2	16	8.37
		Total	219			

EW-9309-43D:

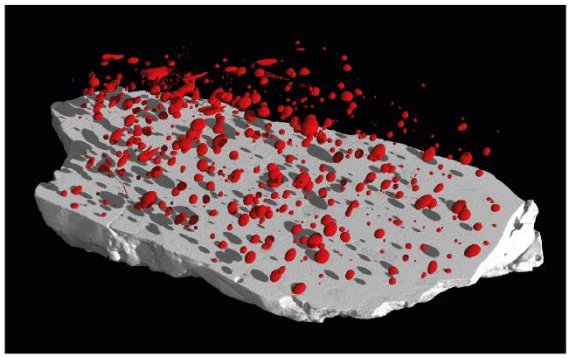

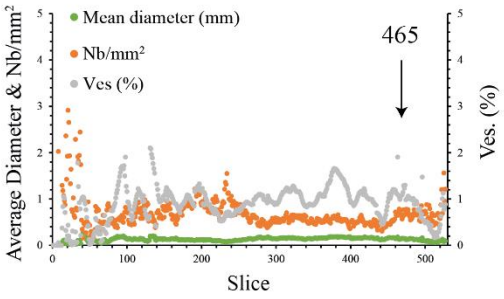

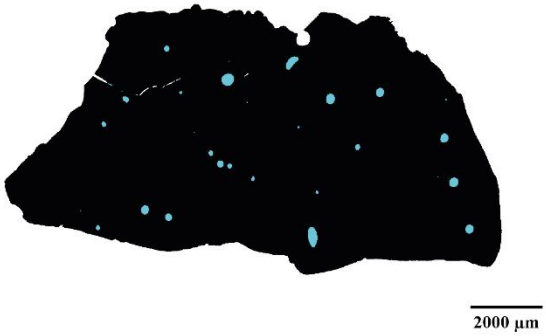

Location	42.19S - 16.08W
Depth (m)	2925
Weigth (mg)	790.1
Resolution (µm)	10
Volume (mm³)	288
VGStudio max treatment	
Ves (%)	0.84
ImageJ treatment	
tot. images	527
Ves (from volume) (%)	0.98
Area (mm²)	73.29
Bub. mean diameter (µm)	166.87
Nb/mm²	0.49
ves (slice) (%)	1.07

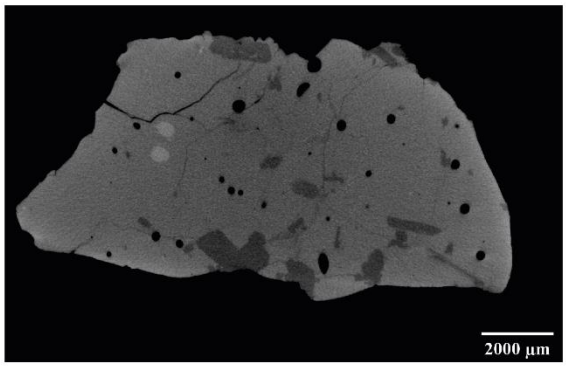

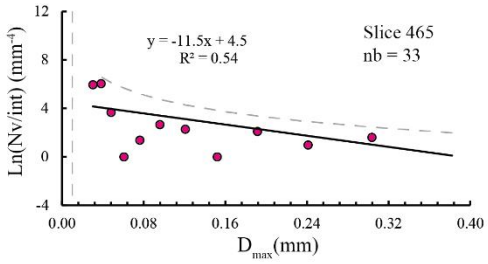

Class Number	Interval	D.max	Nb	Na (Nb/mm²)	Nv (mm⁻³)	Ln (Nv/int) (mm⁻⁴)
1	0.0786	0.382	3	0.0	0	0.81
2	0.0624	0.304	5	0.1	0	1.60
3	0.0496	0.241	3	0.0	0	0.97
4	0.0394	0.192	4	0.1	0	2.10
5	0.0313	0.152	1	0.0	0	0.00
6	0.0249	0.121	2	0.0	0	2.27
7	0.0197	0.096	2	0.0	0	2.67
8	0.0157	0.076	1	0.0	0	1.37
9	0.0125	0.061	0	0.0	0	0.00
10	0.0099	0.048	1	0.0	0	3.68
11	0.0079	0.038	6	0.1	3	6.05
12	0.0062	0.030	5	0.1	2	5.95
		Total	33			

References:

Lux, G., 1987. The behavior of noble gases in silicate liquids: Solution, diffusion, bubbles and surface effects, with applications to natural samples. Geochim. Cosmochim. Acta 51, 1549–1560.

APPENDIX II

Scanning Electron Microscopy (SEM):

Appendix II: Scanning Electron Microscopy (SEM):

This section presents some of the raw data obtained by scanning electron microscopy. Some of the points analysed for the oxides are so small that the signal recorded by the scanner also assimilated the signal from the glass. These data were subsequently processed, and only the points where the analysis represented 100% of the oxide or glass were taken for the composition. The data presented here are composed of the composition of the points, the sweep plot obtained by the SEM, and the value at each point.

ESFa-5:

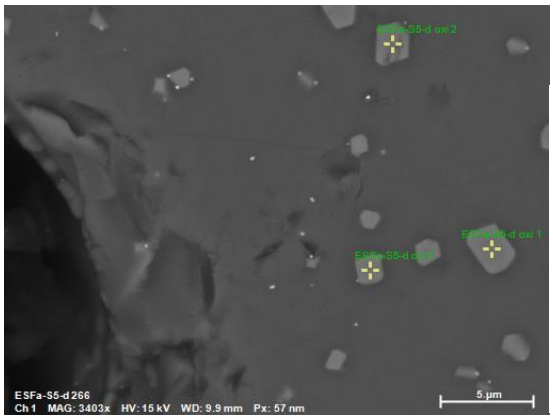

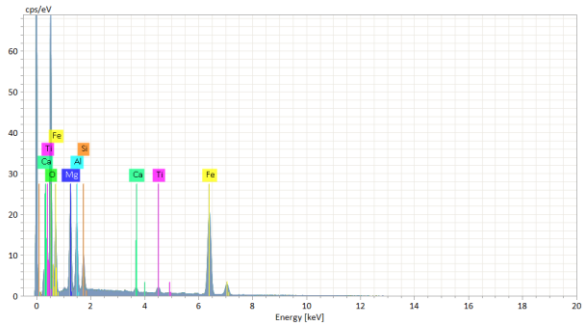

ESFa-5 oxi	MgO	Al2O3	TiO2	FeO
ESFa-5.1	16.22	11.93	2.68	68.11
ESFa-5.2	14.79	12.03	2.54	65.16
ESFa-5.3	14.79	12.41	2.52	62.45
mean	15.27	12.12	2.58	65.24
sigma	0.83	0.25	0.09	2.83
sigma mean	0.48	0.15	0.05	1.63

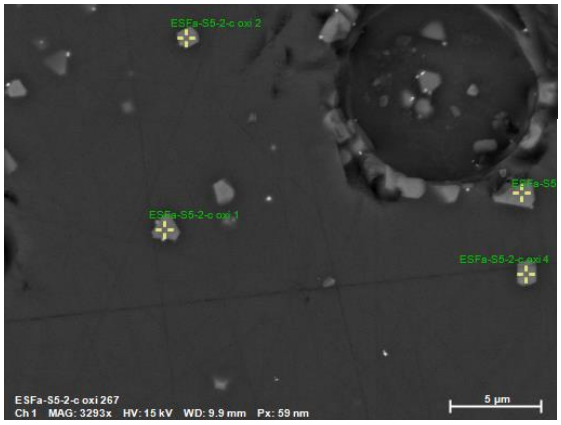

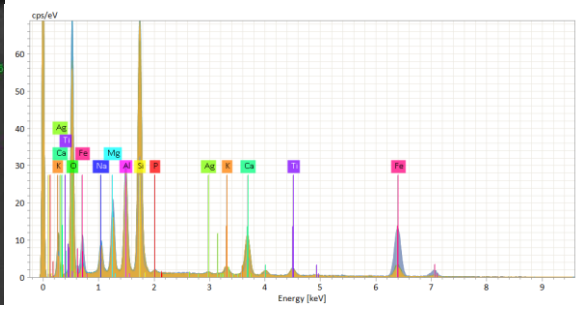

ESFa-5 oxi	Na2O	MgO	Al2O3	SiO2	K2O	CaO	TiO2	FeO
ESFa-5.1	4.22	7.36	16.1	46.62	1.43	10.32	3.59	8.86
ESFa-5.2	3.85	7.34	15.74	44.8	1.62	9.95	3.55	11.74
ESFa-5.3	2.48	11.46	12.79	22.2	0.85	4.08	3.06	42.47
ESFa-5.4	3.76	7.11	15.59	46.65	1.66	10.98	3.94	8.84
Mean	3.58	8.32	15.05	40.07	1.39	8.83	3.54	17.98
Sigma	0.76	2.1	1.53	11.94	0.37	3.2	0.36	16.39
Sigma Mean	0.38	1.05	0.76	5.97	0.19	1.6	0.18	8.19

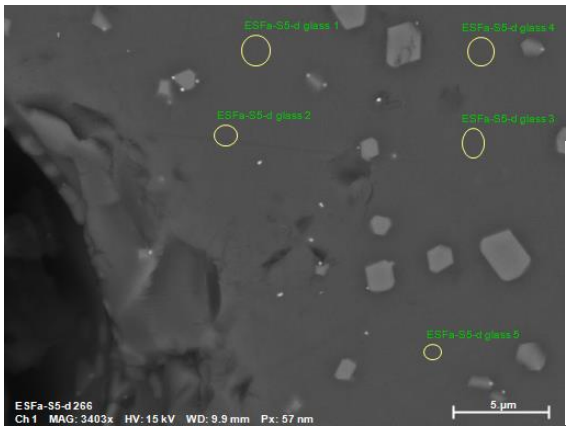

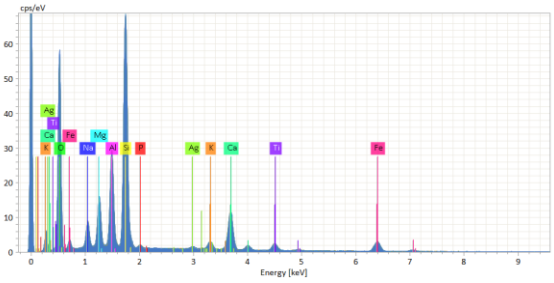

ESFa-5 glass	Na2O	MgO	Al2O3	SiO2	K2O	CaO	TiO2	FeO
ESFa-5-dglass1	3.82	6.92	15.6	46.24	1.65	10.93	3.86	9.46
ESFa-5-dglass2	3.83	6.95	15.68	46.21	1.66	10.79	3.94	9.35
ESFa-5-dglass3	3.95	6.96	15.72	46.02	1.61	10.92	3.69	9.54
ESFa-5-dglass4	3.78	6.83	15.34	46.51	1.65	10.99	3.84	9.28
ESFa-5-dglass5	3.86	7.07	15.73	46.16	1.61	10.83	3.92	9.33
Mean	3.85	6.95	15.61	46.23	1.64	10.89	3.85	9.39
Sigma	0.06	0.08	0.16	0.18	0.02	0.08	0.1	0.11
Sigma Mean	0.03	0.04	0.07	0.08	0.01	0.04	0.04	0.05

ESFa-3C:

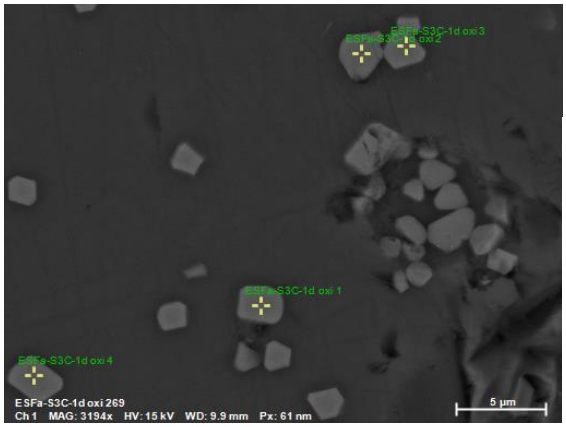

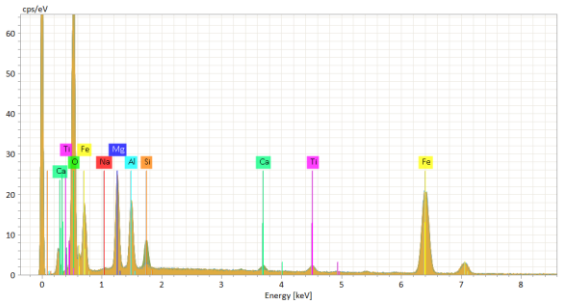

ESFa-3C	MgO	Al2O3	TiO2	FeO
ESFa-3C-1d.1	15.06	12.2	2.64	68.8
ESFa-3C-1d.2	13.96	12.12	2.62	63.72
ESFa-3C-1d.3	14.84	12.22	2.63	68.37
ESFa-3C-1d.4	15.56	12.51	2.72	67.99
Mean	14.86	12.26	2.65	67.22
Sigma	0.67	0.17	0.04	2.36
Sigma Mean	0.33	0.09	0.02	1.18

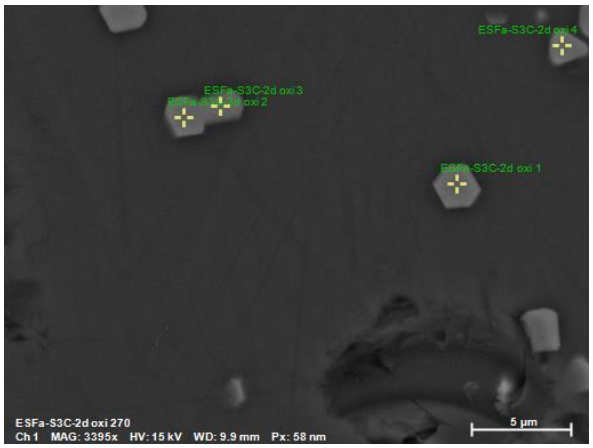

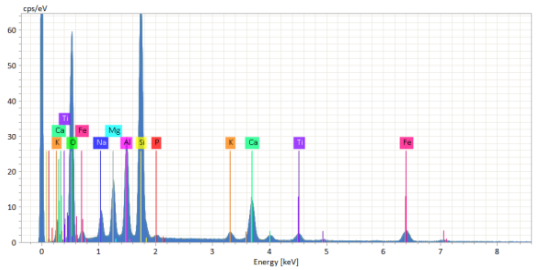

ESFa-3C oxi	MgO	Al2O3	TiO2	FeO
ESFa-3C-2d.1	15.29	12.63	2.92	69.16
ESFa-3C-2d.2	15.25	12.21	2.8	69.74
ESFa-3C-2d.3	13.11	12.78	2.65	53.03
ESFa-3C-2d.4	15.94	13.24	2.86	67.96
Mean	14.9	12.71	2.81	64.97
Sigma	1.23	0.43	0.12	7.99
Sigma Mean	0.62	0.21	0.06	4

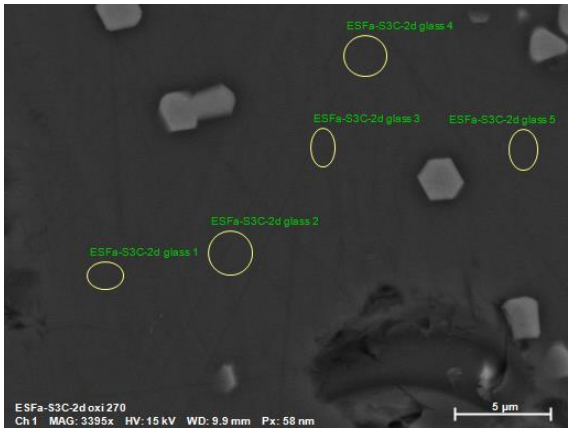

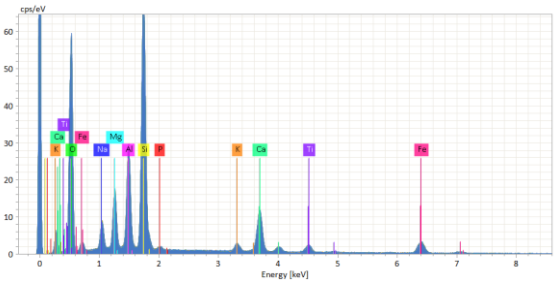

ESFa-3C glass	Na2O	MgO	Al2O3	SiO2	K2O	CaO	TiO2	FeO	P2O5
ESFa-S3C-2d1	3.74	7.58	15.72	46.47	1.6	10.5	3.63	10.18	0.58
ESFa-S3C-2d2	3.82	7.25	15.64	46.58	1.54	10.66	3.84	10.06	0.62
ESFa-S3C-2d3	3.72	7.32	15.74	46.31	1.59	10.79	3.89	9.94	0.7
ESFa-S3C-2d4	3.75	7.4	15.94	46.57	1.48	10.51	3.83	9.8	0.71
ESFa-S3C-2d5	3.75	7.27	15.67	46.6	1.5	11.02	3.83	9.77	0.59
Mean	3.76	7.36	15.74	46.51	1.54	10.7	3.81	9.95	0.64
Sigma	0.04	0.14	0.12	0.12	0.05	0.22	0.1	0.17	0.06
Sigma Mean	0.02	0.06	0.05	0.05	0.02	0.1	0.04	0.08	0.03

ESFa-10:

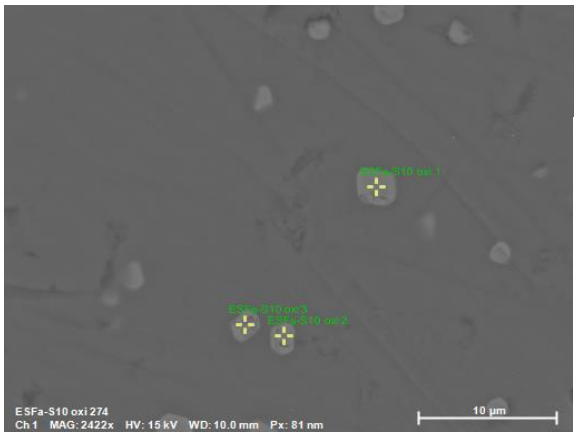

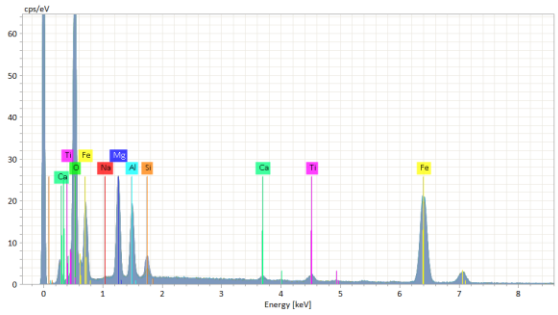

ESFa-S10 oxi	MgO	Al2O3	TiO2	FeO
ESFa-10.1	16	11.74	2.72	68.64
ESFa-10.2	16.06	12.57	2.64	66.35
ESFa-10.3	16.04	12.38	2.54	63.64
Mean	16.03	12.23	2.63	66.21
Sigma	0.03	0.44	0.09	2.51
Sigma Mean	0.02	0.25	0.05	1.45

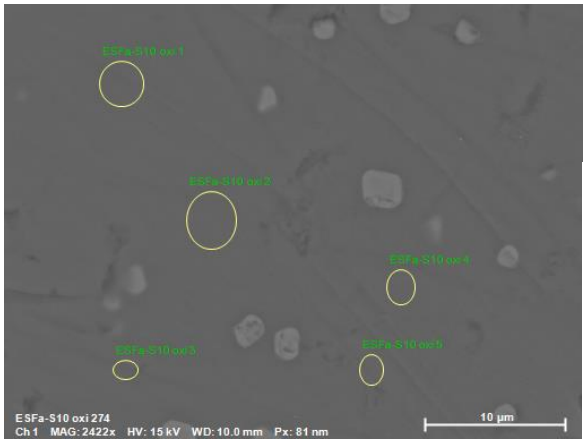

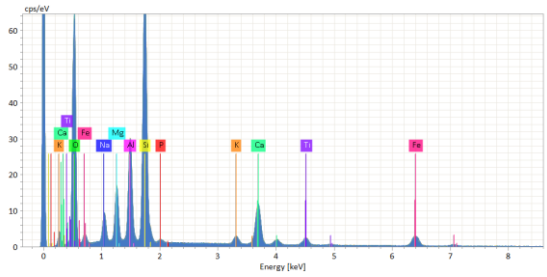

ESFa-10 glass	Na2O	MgO	Al2O3	SiO2	K2O	CaO	TiO2	FeO	P2O5
ESFa-10.oxi.1	4.04	7.08	15.85	47.26	1.62	10.91	3.46	8.97	0.82
ESFa-10.oxi.2	3.97	7.12	16.08	46.7	1.57	10.9	3.72	9.27	0.68
ESFa-10.oxi.3	3.83	6.94	15.83	47.01	1.58	11.1	3.9	9.21	0.6
ESFa-10.oxi.4	3.81	7.08	15.41	47.53	1.6	10.93	3.73	9.12	0.8
ESFa-10.oxi.5	3.85	7	15.77	47.14	1.59	10.88	3.82	9.28	0.67
Mean	3.9	7.04	15.79	47.13	1.59	10.94	3.72	9.17	0.71
Sigma	0.1	0.07	0.24	0.31	0.02	0.09	0.17	0.13	0.09
Sigma Mean	0.04	0.03	0.11	0.14	0.01	0.04	0.07	0.06	0.04

ESFa-9C:

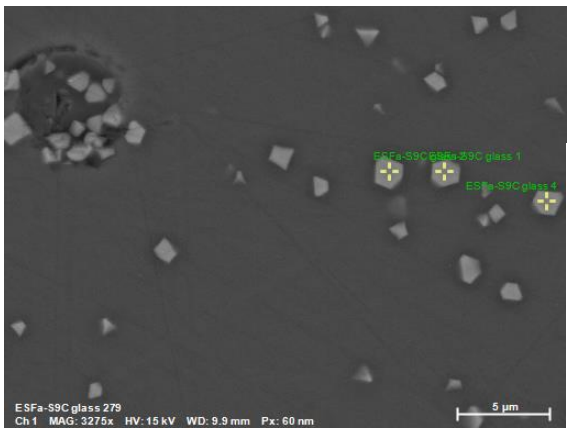

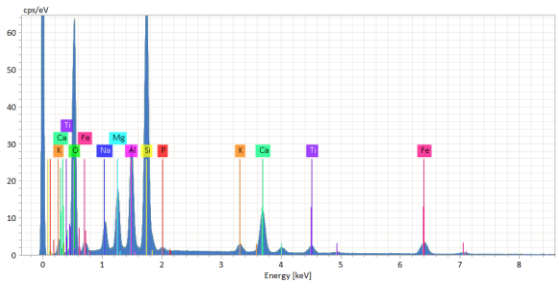

ESFa-9C oxi	MgO	Al2O3	TiO	FeO
ESFa-9C.1	12.22	12.66	3.64	60.29
ESFa-9C.2	12.89	12.3	3.36	65.61
ESFa-9C.4	12.84	12.49	3.41	64.22
Mean	12.65	12.48	3.47	63.37
Sigma	0.37	0.18	0.15	2.76
Sigma Mean	0.21	0.1	0.08	1.59

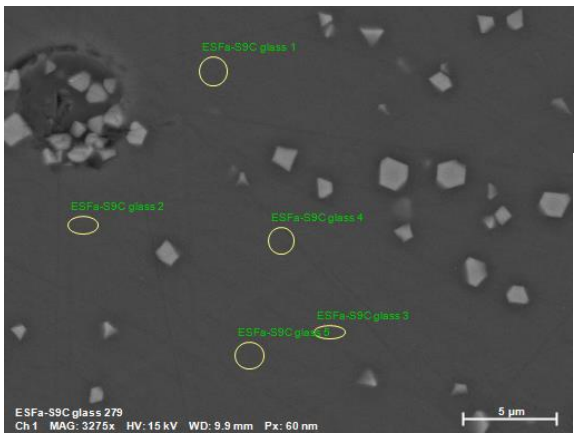

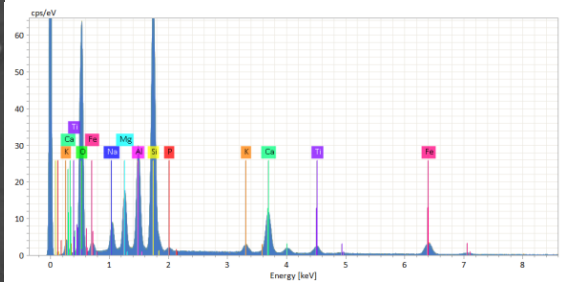

SFa-9C glass	Na2O	MgO	Al2O3	SiO2	K2O	CaO	TiO2	FeO	P2O5
ESFa-9Cglass.1	3.87	7.32	15.91	46.33	1.56	10.71	3.71	9.95	0.64
ESFa-9Cglass.2	3.89	7.39	16.04	46.54	1.47	10.5	3.71	9.76	0.71
ESFa-9Cglass.3	3.97	7.38	15.77	46.49	1.55	10.63	3.71	9.83	0.67
ESFa-9Cglass.4	3.82	7.5	15.81	46.14	1.52	10.7	3.81	10.24	0.46
ESFa-9Cglass.5	3.75	7.59	15.71	46.06	1.54	10.79	3.73	10.2	0.62
Mean	3.86	7.44	15.85	46.31	1.53	10.67	3.73	10	0.62
Sigma	0.08	0.11	0.13	0.21	0.04	0.11	0.04	0.22	0.09
Sigma Mean	0.04	0.05	0.06	0.09	0.02	0.05	0.02	0.1	0.04

EN-E3:

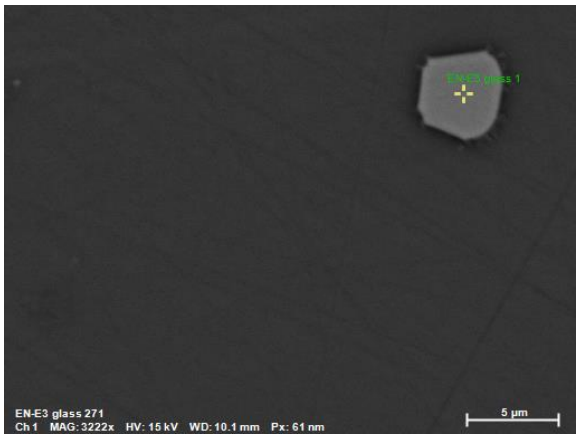

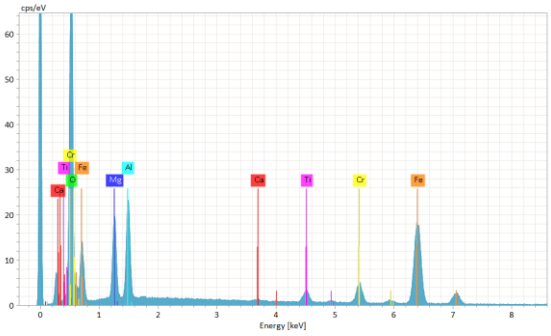

EN-E3 oxi	Sto. [%]	Norm. [%]	abs. error [%] (1 sigma)	rel. error [%] (1 sigma)
Oxygen	0	0	3.46	12.83
MgO	10.68	11.84	0.27	4.14
Al2O3	14.07	15.6	0.28	3.76
CaO	0.35	0.39	0.03	10.32
TiO2	4.1	4.54	0.08	3.37

Cr2O3	8.12	9	0.16	2.95
FeO	52.87	58.63	1.07	2.6

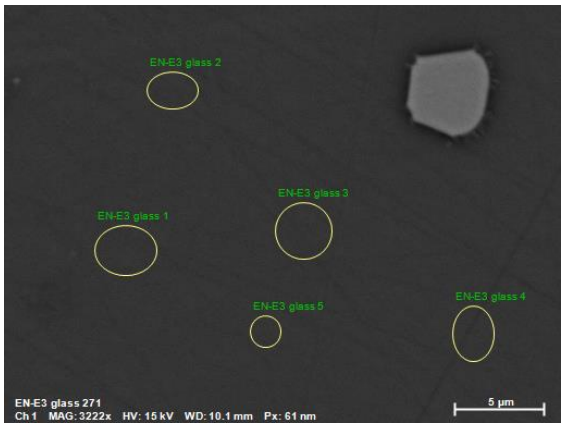

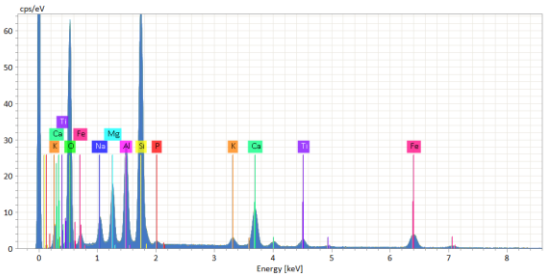

EN-E3 glass	**Na2O**	**MgO**	**Al2O3**	**SiO2**	**K2O**	**CaO**	**TiO2**	**FeO**	**P2O5**
EN-E3glass.1	3.74	7.4	15.74	45.08	1.52	10.16	3.61	11.96	0.78
EN-E3glass.2	3.87	7.59	15.56	44.66	1.61	10.05	3.73	12.29	0.64
EN-E3glass.3	3.79	7.75	15.66	44.76	1.59	10.11	3.66	12.03	0.67
EN-E3glass.4	3.73	7.61	15.81	44.82	1.45	10.16	3.79	12.07	0.55
EN-E3glass.5	3.72	7.64	15.65	45.2	1.56	10.11	3.77	11.7	0.65
Mean	3.77	7.6	15.68	44.9	1.55	10.12	3.71	12.01	0.66
Sigma	0.06	0.13	0.1	0.23	0.06	0.05	0.08	0.21	0.08
Sigma Mean	0.03	0.06	0.04	0.1	0.03	0.02	0.03	0.1	0.04

APPENDIX III

Electron probe micro-analyser (EPMA):

Appendix III: Electron probe micro-analyser (EPMA):

This section presents the major element composition of all experimental samples obtained with the electron probe micro-analyser (EPMA) spread in three tables:

(i) Static samples with CO_2-bearing glass (Table S-1).

(ii) Static samples with CO_2+Ne-bearing glass (Table S-2).

(iii) Decompression Samples (Table S-3).

	Na_2O	sd	MgO	sd	SiO_2	sd	Al_2O_3	sd	CaO	sd	K_2O	sd	TiO_2	sd	FeO	sd	MnO	sd	P_2O_5	sd	$Na_2O + K_2O$	Total
ESFa-4-CO₂	3.80	0.23	7.49	0.74	44.23	4.21	15.13	0.36	10.58	1.51	1.57	0.13	3.73	0.28	12.55	6.05	0.09	0.04	0.84	0.16	5.37	100.00
ESFa-5-CO2	3.71	0.23	7.28	0.37	45.71	0.33	14.88	0.23	10.96	0.13	1.40	0.09	3.90	0.09	11.23	0.34	0.17	0.05	0.76	0.06	5.12	100.00
ESFa-6-CO2	3.72	0.04	7.40	0.14	45.38	0.47	14.80	0.08	10.98	0.15	1.42	0.04	3.74	0.04	11.63	0.61	0.16	0.05	0.77	0.05	5.14	100.00
ESFa-7-CO2	3.84	0.08	7.04	0.23	46.11	1.48	15.34	0.24	10.98	0.50	1.59	0.11	3.65	0.20	10.44	2.05	0.13	0.04	0.88	0.08	5.43	100.00
ESFa-8-CO2	3.81	0.08	7.19	0.02	46.67	0.39	15.28	0.08	11.13	0.13	1.53	0.06	3.55	0.13	9.77	0.42	0.21	0.07	0.87	0.05	5.34	100.00
ESFa-9-CO2	3.79	0.17	7.15	0.24	45.89	1.87	15.53	0.27	10.77	0.70	1.61	0.11	3.64	0.28	10.58	2.88	0.19	0.05	0.87	0.05	5.40	100.00
ESFa-10-CO2	3.81	0.05	7.46	0.20	45.12	1.19	14.64	0.03	10.96	0.39	1.45	0.16	3.79	0.12	11.87	1.72	0.16	0.09	0.74	0.04	5.26	100.00
ESFa-7E-CO2	3.81	0.08	7.14	0.27	46.16	1.50	15.42	0.24	10.85	0.58	1.61	0.04	3.63	0.14	10.35	2.16	0.14	0.12	0.89	0.09	5.42	100.00
ESFa-8E-CO2	3.83	0.05	7.50	0.10	45.28	0.62	14.77	0.13	10.96	0.24	1.43	0.08	3.83	0.18	11.43	0.94	0.18	0.09	0.81	0.16	5.26	100.00
ESFa-9E-CO2	3.73	0.09	7.36	0.49	44.36	2.21	15.40	0.48	10.50	0.70	1.62	0.06	3.63	0.14	12.37	3.05	0.20	0.06	0.82	0.12	5.36	100.00
ESFa-10E-CO2	3.77	0.06	7.36	0.10	45.39	0.30	15.53	0.08	10.84	0.10	1.61	0.07	3.67	0.18	10.77	0.15	0.21	0.10	0.86	0.06	5.38	100.00
ESFa-1D-CO2	3.78	0.08	7.44	0.12	45.02	0.12	15.25	0.06	10.63	0.13	1.58	0.10	3.71	0.20	11.54	0.26	0.17	0.10	0.87	0.06	5.37	100.00
ESFa-2D-CO2	3.85	0.13	7.59	0.14	44.91	0.52	15.37	0.12	10.84	0.12	1.51	0.09	3.47	0.09	11.43	0.37	0.17	0.11	0.86	0.03	5.36	100.00
ESFa-3D-CO2	3.73	0.08	7.57	0.15	44.23	1.80	15.15	0.16	10.47	0.74	1.54	0.11	3.49	0.17	12.80	2.65	0.20	0.08	0.82	0.11	5.28	100.00
ESFa-4D-CO2	3.77	0.19	7.55	0.65	44.73	3.27	15.13	0.51	10.68	1.07	1.53	0.11	3.61	0.22	12.03	4.68	0.14	0.06	0.83	0.12	5.29	100.00
ESFa-5D-CO2	3.70	0.11	7.38	0.11	44.91	0.49	14.85	0.12	10.79	0.29	1.40	0.04	3.65	0.12	12.36	0.82	0.21	0.07	0.75	0.08	5.10	100.00
ESFa-6D-CO2	3.77	0.15	7.42	0.69	45.25	3.79	15.14	0.47	10.81	0.99	1.54	0.12	3.62	0.20	11.44	4.87	0.12	0.08	0.89	0.06	5.32	100.00
ESFa-7D-CO2	3.76	0.03	7.44	0.12	45.10	0.41	14.93	0.20	10.95	0.19	1.45	0.08	3.77	0.08	11.56	0.69	0.21	0.06	0.83	0.03	5.21	100.00
ESFa-8D-CO2	3.87	0.16	7.41	0.54	44.67	2.88	15.31	0.33	10.25	1.18	1.60	0.08	3.50	0.27	12.34	3.92	0.23	0.09	0.82	0.10	5.47	100.00
ESFa-10D-CO2	3.78	0.11	7.48	0.12	45.74	0.97	15.48	0.22	10.71	0.38	1.60	0.07	3.57	0.07	10.57	1.36	0.16	0.10	0.91	0.10	5.39	100.00
ESFa-1C-CO2	3.82	0.19	7.59	0.18	44.52	2.25	15.17	0.04	10.28	0.82	1.60	0.07	3.52	0.18	12.36	3.33	0.24	0.06	0.90	0.16	5.42	100.00
ESFa-2C-CO2	3.79	0.08	7.75	0.24	44.63	1.28	15.01	0.13	10.34	0.44	1.62	0.09	3.58	0.19	12.21	1.74	0.21	0.03	0.85	0.09	5.42	100.00
ESFa-3C-CO2	3.73	0.07	7.54	0.02	45.39	0.53	15.14	0.17	10.62	0.21	1.37	0.07	3.53	0.09	11.74	0.78	0.20	0.08	0.74	0.05	5.10	100.00
ESFa-4C-CO2	3.90	0.07	7.65	0.13	45.35	0.84	15.07	0.13	10.60	0.34	1.63	0.08	3.57	0.12	11.14	1.09	0.23	0.06	0.87	0.06	5.53	100.00
ESFa-5C-CO2	3.75	0.11	7.61	0.12	45.41	1.29	14.81	0.18	10.60	0.26	1.38	0.09	3.74	0.15	11.73	1.58	0.19	0.06	0.78	0.05	5.14	100.00
ESFa-6C-CO2	3.95	0.02	7.52	0.10	45.87	0.98	14.96	0.08	10.71	0.26	1.67	0.08	3.63	0.17	10.58	1.16	0.23	0.04	0.87	0.08	5.62	100.00
ESFa-7C-CO2	3.82	0.18	7.92	0.40	44.07	2.41	14.93	0.23	10.23	0.73	1.61	0.10	3.60	0.16	12.82	3.12	0.17	0.13	0.83	0.07	5.42	100.00
ESFa-8C-CO2	3.59	0.31	7.82	0.54	42.88	4.40	14.92	0.47	9.91	1.22	1.46	0.11	3.48	0.02	14.89	5.97	0.22	0.06	0.84	0.06	5.04	100.00

ESFa-9C-CO2	3.71	0.08	7.68	0.07	45.08	0.29	14.76	0.18	10.55	0.41	1.37	0.04	3.70	0.19	12.21	0.95	0.15	0.07	0.79	0.08	5.08	100.00
ESFa-10C-CO2	3.91	0.06	7.57	0.13	45.77	0.52	15.06	0.14	10.79	0.14	1.70	0.02	3.56	0.18	10.59	0.75	0.19	0.06	0.87	0.12	5.60	100.00
ESFa-1B-CO2	3.98	0.07	7.72	0.10	45.67	0.50	15.14	0.11	10.84	0.18	1.62	0.11	3.66	0.11	10.29	0.81	0.21	0.11	0.86	0.05	5.60	100.00
ESFa-3A-CO2	3.93	0.10	7.76	0.12	44.91	0.55	14.98	0.03	10.51	0.22	1.60	0.05	3.57	0.08	11.63	0.74	0.24	0.08	0.87	0.05	5.54	100.00
ESFa-4A-CO2	4.01	0.06	7.61	0.21	45.92	0.91	14.97	0.25	10.65	0.25	1.65	0.06	3.60	0.13	10.62	1.17	0.20	0.05	0.77	0.06	5.66	100.00
Starting mat	3.63	0.06	7.80	0.04	44.86	0.20	14.87	0.16	10.38	0.09	1.47	0.13	3.70	0.16	12.39	0.22	0.17	0.06	0.73	0.08	5.10	100.00

Table S-1: Major element composition of the static samples with CO_2-bearing glass

	SiO_2	sd	**TiO_2**	**sd**	**Al_2O_3**	**sd**	**FeO**	**sd**	**MnO**	**sd**	**MgO**	**sd**	**CaO**	**sd**	**Na_2O**	**sd**	**K_2O**	**sd**	**P_2O5**	**sd**	**$Na_2O + K_2O$**	**Total**
ESFa-1B-CO2+Ne	45.17	2.37	4.15	0.59	20.12	1.92	7.54	2.36	0.18	0.08	5.98	1.30	9.38	1.26	3.93	0.24	2.52	0.40	1.03	0.23	6.44	100
ESFa-2B-CO2+Ne	45.15	3.01	3.76	0.05	15.81	0.16	10.97	4.11	0.22	0.06	7.36	0.35	10.31	0.83	3.83	0.24	1.73	0.18	0.87	0.08	5.55	100
ESFa-3B-CO2+Ne	47.51	0.25	3.57	0.08	15.31	0.12	8.52	0.41	0.21	0.05	7.09	0.16	11.15	0.09	4.09	0.10	1.76	0.03	0.80	0.10	5.85	100
ESFa-4B-CO2+Ne	44.51	0.23	3.60	0.16	15.09	0.14	12.18	0.19	0.24	0.03	7.76	0.13	10.43	0.08	3.78	0.08	1.62	0.09	0.78	0.09	5.40	100
ESFa-5B-CO2+Ne	44.92	0.13	3.80	0.09	15.25	0.24	11.86	0.23	0.19	0.06	7.68	0.09	10.32	0.09	3.55	0.10	1.65	0.07	0.79	0.05	5.19	100
ESFa-6B-CO2+Ne	44.59	0.20	3.58	0.10	15.16	0.22	12.08	0.12	0.23	0.06	7.74	0.06	10.41	0.12	3.72	0.08	1.64	0.03	0.85	0.04	5.37	100
ESFa-1A-CO2+Ne	45.13	1.83	3.63	0.19	15.26	0.21	11.34	2.43	0.19	0.06	7.48	0.16	10.72	0.53	3.81	0.04	1.63	0.09	0.80	0.07	5.44	100
ESFa-2A-CO2+Ne	46.48	0.72	3.70	0.06	15.57	0.22	9.71	1.19	0.18	0.03	7.15	0.12	10.81	0.22	3.84	0.18	1.63	0.08	0.93	0.11	5.47	100
ESFa-7B-CO2+Ne	45.96	0.30	3.70	0.10	14.99	0.09	10.43	0.39	0.18	0.11	7.45	0.15	10.80	0.18	4.02	0.04	1.62	0.05	0.84	0.07	5.64	100
ESFa-10B-CO2+Ne	46.97	0.37	3.73	0.09	15.41	0.16	9.23	0.26	0.20	0.08	7.18	0.06	10.96	0.09	3.77	0.07	1.61	0.03	0.94	0.07	5.38	100
ESFa-5A-CO2+Ne	46.26	1.60	3.67	0.14	15.37	0.23	9.74	2.03	0.21	0.04	7.42	0.23	10.89	0.50	3.91	0.10	1.63	0.10	0.90	0.04	5.55	100
ESFa-6A-CO2+Ne	44.46	0.36	3.49	0.15	15.20	0.10	12.24	0.26	0.18	0.06	7.75	0.06	10.45	0.10	3.79	0.08	1.62	0.05	0.81	0.08	5.41	100
Ne-bearing glass	45.47	0.15	3.78	0.14	14.94	0.17	11.49	0.43	0.11	0.06	7.80	0.11	10.43	0.16	3.77	0.08	1.49	0.04	0.71	0.05	5.26	100

Table S-2: Major element composition of the static samples with Ne+CO_2-bearing glass

	SiO2	sd	TiO2	sd	Al2O3	sd	FeO	sd	MnO	sd	MgO	sd	CaO	sd	Na2O	sd	K2O	sd	P2O5	sd	Na2O+K2O	total
EN-E3	44.84	0.32	3.76	0.15	14.86	0.10	12.26	0.35	0.23	0.04	7.67	0.09	10.65	0.08	3.66	0.10	1.38	0.12	0.69	0.04	5.04	100
EN-E4	44.35	0.20	3.80	0.06	15.05	0.12	11.93	0.24	0.22	0.07	7.99	0.07	10.55	0.12	3.72	0.08	1.55	0.09	0.84	0.06	5.27	100
EN-E6	44.62	1.02	3.74	0.10	14.77	0.23	12.64	1.63	0.12	0.04	7.71	0.12	10.46	0.30	3.68	0.05	1.45	0.09	0.82	0.08	5.13	100
EN-E8	46.24	0.24	3.77	0.10	15.06	0.15	10.15	0.29	0.17	0.08	7.60	0.07	11.03	0.17	3.77	0.09	1.41	0.05	0.80	0.07	5.18	100
EN-E9	44.24	0.21	3.77	0.13	14.70	0.17	12.68	0.24	0.25	0.06	7.89	0.06	10.68	0.08	3.60	0.04	1.38	0.04	0.81	0.04	4.97	100
EN-E10	44.78	0.31	3.77	0.07	14.80	0.24	12.13	0.27	0.17	0.05	7.83	0.08	10.60	0.08	3.68	0.04	1.48	0.04	0.77	0.06	5.15	100
EN-D1	44.75	0.29	3.82	0.14	14.98	0.12	11.66	0.25	0.18	0.05	7.92	0.10	10.55	0.08	3.74	0.06	1.57	0.08	0.83	0.06	5.31	100
EN-D2	44.76	0.23	3.75	0.11	14.96	0.18	11.69	0.18	0.16	0.07	7.94	0.11	10.58	0.07	3.73	0.08	1.61	0.05	0.83	0.08	5.34	100
EN-D4	44.41	0.32	3.78	0.15	15.08	0.15	11.93	0.32	0.14	0.06	7.93	0.07	10.58	0.12	3.76	0.08	1.56	0.08	0.82	0.09	5.32	100

Table S-3: Major element composition of the decompression samples.

APPENDIX IV

Fourier-transform infrared spectroscopy (FTIR):

Appendix IV: Fourier-transform infrared spectroscopy (FTIR):

This section presents the CO_2 and water content of all experimental samples obtained with FTIR spread in three tables:

(i) Static samples with CO2-bearing glass (**Table S-4**).

(ii) Static samples with CO2+Ne-bearing glass (**Table S-5**).

(iii) Decompression Samples (**Table S-6**).

(iv) Natural samples (**Table S-7**).

Some of the points taken for the analysis are shown below (**Fig. S-3**).

Sample	Thickness (cm)	sd	Density (g · l^{-1})	sd	A_{1430}	sd	A_{3525}	sd	[CO_2] (ppm)	sd	H_2O (wt.%)	sd
ESFa-4.3	3.3E-03	3.6E-04	2722	15	0.060	0.002			722	429		
ESFa-4.4	5.1E-03	4.0E-04	2722	15	0.037	0.003						
ESFa-8.1	5.6E-03	1.3E-04	2717	7	0.087	0.005	0.063	0.002	893	0	0.13	0.00
ESFa-10.1	5.0E-03	1.8E-04	2734	41	0.114	0.004	0.064	0.003	1022	252	0.10	0.03
ESFa-10.2	6.2E-03	2.1E-04	2734	41	0.088	0.003	0.044	0.002				
ESFa-10.3	5.6E-03	1.3E-04	2734	41	0.095	0.005	0.044	0.003				
ESFa-10E.1	6.1E-03	2.4E-04	2739	4	0.121	0.007	0.239	0.003	1315	169	0.47	0.04
ESFa-10E.4	4.9E-03	3.6E-04	2739	4	0.117	0.004	0.231	0.001				
ESFa-10E.5	4.9E-03	2.5E-04	2739	4	0.136	0.002	0.217	0.002				
ESFa-10E.6	5.5E-03	2.0E-04	2739	4	0.118	0.006	0.217	0.001				
ESFa-2D.1	8.5E-03	1.9E-04	2751	7	0.162	0.006	0.303	0.002	1059	111	0.39	0.04
ESFa-2D.2	8.7E-03	3.4E-04	2751	7	0.144	0.007	0.274	0.002				
ESFa-2D.3	8.6E-03	3.1E-04	2751	7	0.175	0.004	0.336	0.002				
ESFa-3D.1	3.0E-03	6.7E-04	2772	44	0.063	0.002			925	200		
ESFa-3D.2	5.9E-03	4.7E-04	2772	44	0.085	0.002						
ESFa-3D.3	5.9E-03	4.7E-04	2772	44	0.086	0.002						
ESFa-8D.1	9.7E-03	1.1E-04	2735	43	0.111	0.005			702	114		
ESFa-8D.3	9.2E-03	1.7E-04	2735	43	0.113	0.004						
ESFa-8D.4	9.4E-03	1.6E-04	2735	43	0.126	0.009						
ESFa-8D.4.2	9.7E-03	1.1E-04	2735	43	0.117	0.004						
ESFa-8D.5	1.1E-02	3.8E-04	2735	43	0.164	0.005						
ESFa-8D.6	9.6E-03	1.8E-04	2735	43	0.090	0.002						
ESFa-1C.1	5.5E-03	2.4E-04	2762	56	0.086	0.002			971	159		
ESFa-1C.2	5.4E-03	1.3E-04	2762	56	0.084	0.003						
ESFa-1C.3	6.7E-03	4.1E-04	2762	56	0.137	0.004						
ESFa-2C.1	3.7E-03	2.9E-04	2761	31	0.024	0.003			668	304		
ESFa-2C.2	4.2E-03	2.7E-04	2761	31	0.049	0.003						
ESFa-2C.3	4.3E-03	8.1E-04	2761	31	0.074	0.006						

ESFa-4C.2	2.6E-03	1.9E-04	2742	18	0.080	0.005			1710	3		
ESFa-5C.1	5.0E-03	1.9E-04	2754	32	0.063	0.003			722	0		
ESFa-6C.1.1	6.7E-03	3.3E-04	2730	21	0.089	0.005			700	84		
ESFa-6C.1.2	6.7E-03	1.9E-04	2730	21	0.086	0.004						
ESFa-6C.2.1	7.0E-03	3.5E-04	2730	21	0.081	0.004						
ESFa-6C.2.2	7.0E-03	3.5E-04	2730	21	0.071	0.004						
ESFa-6C.2.3	7.0E-03	2.2E-04	2730	21	0.096	0.006						
ESFa-7C.1	7.2E-03	3.1E-04	2773	57	0.106	0.006			915	137		
ESFa-7C.2	5.8E-03	3.6E-04	2773	57	0.088	0.010						
ESFa-7C.3	5.7E-03	1.9E-04	2773	57	0.109	0.006						
ESFa-7C.4	5.8E-03	3.6E-04	2773	57	0.108	0.007						
ESFa-7C.5	7.8E-03	2.2E-04	2773	57	0.107	0.013						
ESFa-9C.1	5.0E-03	2.1E-04	2762	12	0.064	0.003	0.082	0.004	585	178	0.21	0.04
ESFa-9C.2	4.6E-03	5.5E-05	2762	12	0.026	0.002	0.082	0.002				
ESFa-9C.3	4.6E-03	5.5E-05	2762	12	0.052	0.002	0.081	0.002				
ESFa-9C.4	3.7E-03	1.6E-04	2762	12	0.043	0.003	0.093	0.002				
ESFa-10C.1	5.2E-03	2.6E-04	2731	13	0.078	0.006			931	97		
ESFa-10C.2	5.2E-03	2.6E-04	2731	13	0.083	0.007						
ESFa-10C.3	5.4E-03	2.1E-04	2731	13	0.098	0.007						
ESFa-1B-CO2.1	4.4E-03	1.7E-04	2731	13	0.034	0.003	0.099	0.009	707	267	0.24	0.04
ESFa-1B-CO2.2	4.9E-03	1.6E-04	2731	13	0.060	0.003	0.124	0.006				
ESFa-1B-CO2.3	4.9E-03	1.6E-04	2731	13	0.085	0.004	0.086	0.006				

Table S-4: CO2 and water content of the static samples with CO2-bearing glass.

Sample	Thickness (cm)	sd	Density (g · l^{-1})	sd	A_{1430}	sd	A_{3525}	sd	[CO_2] (ppm)	sd	H_2O (wt.%)	sd
ESFa-1B-CO2+Ne.1	5.0E-03	2.5E-04	2678	46	0.105	0.010			1328	158		
ESFa-1B-CO2+Ne.2	4.9E-03	2.7E-04	2678	46	0.122	0.006						

ESFa-2B-CO2+Ne.1	3.5E-03	1.9E-04	2739	75	0.079	0.004			1023	259		
ESFa-2B-CO2+Ne.2	3.5E-03	1.9E-04	2739	75	0.064	0.006						
ESFa-2B-CO2+Ne.3	4.1E-03	3.0E-04	2739	75	0.055	0.004						
ESFa-3B-CO2+Ne.1	8.2E-03	1.1E-04	2691	7	0.099	0.003			721	188		
ESFa-3B-CO2+Ne.2	8.2E-03	1.1E-04	2691	7	0.108	0.001						
ESFa-3B-CO2+Ne.3	8.2E-03	1.1E-04	2691	7	0.128	0.002						
ESFa-3B-CO2+Ne.4	7.3E-03	1.9E-04	2691	7	0.053	0.009						
ESFa-3B-CO2+Ne.5	5.7E-03	2.8E-04	2691	7	0.082	0.003						
ESFa-5B-CO2+Ne.1	2.6E-03	2.5E-04	2755	4	0.081	0.004			1705	101		
ESFa-5B-CO2+Ne.2	2.7E-03	2.2E-04	2755	4	0.077	0.004						
ESFa-6B-CO2+Ne.1	4.2E-03	3.8E-04	2758	3	0.052	0.002	0.120	0.000	880	240	0.30	0.02
ESFa-6B-CO2+Ne.2	4.2E-03	3.8E-04	2758	3	0.077	0.001	0.107	0.001				
ESFa-7B-CO2+Ne.1	3.4E-03	2.2E-04	2728	8	0.090	0.002			1546	66		
ESFa-7B-CO2+Ne.2	3.4E-03	4.3E-04	2728	8	0.095	0.003						
ESFa-10B-CO2+Ne.1	3.9E-03	2.2E-04	2707	5	0.087	0.004			1197	119		
ESFa-10B-CO2+Ne.2	4.2E-03	1.8E-04	2707	5	0.081	0.003						
ESFa-2A-CO2+Ne.1	6.4E-03	2.0E-04	2715	20	0.120	0.004			1023	63		
ESFa-2A-CO2+Ne.6	3.3E-03	1.3E-04	2715	20	0.056	0.002						
ESFa-5A-CO2+Ne.1	3.4E-03	8.4E-05	2720	36	0.064	0.003			1043	47		
ESFa-5A-CO2+Ne.2	3.4E-03	7.1E-05	2720	36	0.060	0.005						

Table S-5: CO2 and water content of the static samples with Ne+CO2-bearing glass.

Sample	Thickness (cm)	sd	Density (g · l^{-1})	sd	A_{1430}	sd	A_{3525}	sd	[CO_2] (ppm)	sd	H_2O (wt.%)	sd
EN-E3.1	4.8E-03	1.7E-04	2770	6	0.213	0.001	0.4330	0.0019	2385	162	0.91	0.06
EN-E3.2	4.8E-03	1.7E-04	2770	6	0.187	0.003	0.3600	0.0007				
EN-E3.3	4.8E-03	1.7E-04	2770	6	0.189	0.003	0.3932	0.0016				
EN-E3.4	4.8E-03	1.7E-04	2770	6	0.205	0.004	0.3864	0.0009				

EN-E3.5	4.8E-03	1.7E-04	2770	6	0.217	0.004	0.4038	0.0013				
EN-E6.1	4.0E-03	1.4E-04	2774	27	0.056	0.001	0.1174	0.0024	799	143	0.32	0.03
EN-E6.2	4.0E-03	1.4E-04	2774	27	0.052	0.001	0.1014	0.0011				
EN-E6.3	4.0E-03	1.4E-04	2774	27	0.053	0.001	0.1186	0.0011				
EN-E6.4	4.0E-03	1.4E-04	2774	27	0.060	0.001	0.1254	0.0125				
EN-E6.5	4.0E-03	1.4E-04	2774	27	0.078	0.002	0.1242	0.0008				
EN-E6.6	4.0E-03	1.4E-04	2774	27	0.051	0.001	0.1174	0.0015				
EN-E6.7	4.0E-03	1.4E-04	2774	27	0.048	0.006	0.1018	0.0024				
EN-E8.1	3.3E-03	1.1E-04	2734	3	0.045	0.002	0.0774	0.0005	961	181	0.31	0.04
EN-E8.2	3.3E-03	1.1E-04	2734	3	0.055	0.001	0.0994	0.0011				
EN-E8.3	3.3E-03	1.1E-04	2734	3	0.066	0.002	0.0970	0.0012				
EN-E9.1	3.5E-03	2.2E-04	2784	4	0.092	0.001	0.2886	0.0009	457	42	0.34	0.02
EN-E9.2	3.5E-03	2.2E-04	2784	4	0.070	0.002	0.3034	0.0005				
EN-E9.3	6.9E-03	3.1E-04	2784	4	0.053	0.002	0.2264	0.0005				
EN-E9.4	6.9E-03	3.1E-04	2784	4	0.060	0.001	0.2074	0.0005				
EN-E10.1	5.7E-03	3.9E-04	2772	5	0.051	0.002	0.3622	0.0004	569	123	0.67	0.08
EN-E10.2	5.7E-03	3.9E-04	2772	5	0.068	0.002	0.2872	0.0022				
EN-E10.3	5.7E-03	3.9E-04	2772	5	0.044	0.014	0.3712	0.0016				
EN-E10.4	5.5E-03	2.3E-04	2772	5	0.067	0.001	0.3612	0.0015				
EN-D1.1	7.3E-03	1.9E-04	2762	4	0.025	0.002	0.4464	0.0013	237	80	0.67	0.02
EN-D1.2	7.3E-03	1.9E-04	2762	4	0.019	0.001	0.4376	0.0011				
EN-D1.3	8.0E-03	2.8E-04	2762	4	0.041	0.002	0.4986	0.0005				
EN-D1.4	7.7E-03	1.1E-04	2762	4	0.044	0.001	0.4588	0.0020				
EN-D2.1	8.6E-03	2.0E-04	2762	5	0.055	0.004	0.5352	0.0027	350	41	0.65	0.04
EN-D2.2	9.8E-03	3.0E-04	2762	5	0.052	0.001	0.5218	0.0022				
EN-D2.3	9.5E-03	2.2E-04	2762	5	0.067	0.004	0.5616	0.0011				
EN-D2.4	9.4E-03	2.6E-04	2762	5	0.057	0.002	0.5636	0.0009				
EN-D4.1	8.3E-03	3.5E-04	2768	5	0.083	0.002	0.5326	0.0011	411	143	0.67	0.03
EN-D4.2	8.1E-03	2.1E-04	2768	5	0.054	0.002	0.5072	0.0018				

EN-D4.3	8.0E-03	1.9E-04	2768	5	0.033	0.001	0.4628	0.0016				
EN-D4.4	8.0E-03	1.9E-04	2768	5	0.068	0.001	0.4800	0.0246				
EN-E4.1	9.9E-03	5.1E-04	2769	4	0.140	0.003	0.5654	0.0005	541	179	0.60	0.03
EN-E4.2	9.9E-03	5.1E-04	2769	4	0.090	0.004	0.5652	0.0041				
EN-E4.3	1.1E-02	2.6E-04	2769	4	0.122	0.002	0.5608	0.0013				
EN-E4.4	1.1E-02	2.6E-04	2769	4	0.079	0.004	0.5728	0.0018				
EN-E4.5	1.1E-02	2.6E-04	2769	4	0.068	0.003	0.5608	0.0008				

Table S-6: CO_2 and water content of the decompression samples.

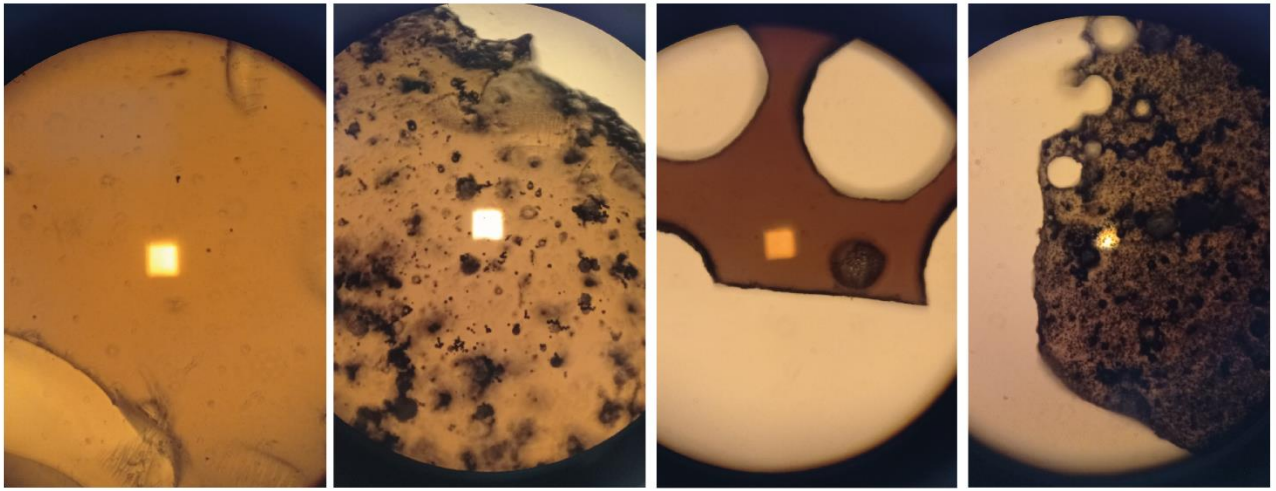

Figure S-3: Set points for FTIR analysis with apertures of 40x40 and 20x20 in quenched glasses. The presence of oxides absorbing the signal precludes the use of a larger aperture, a smaller aperture is required.

APPENDIX V

HELIX SFT Supplementary

Appendix V: HELIX SFT Supplementary:

The following section presents the abundance and isotopic composition of the blank of the line and Matrix of two analysed samples and analyses (**Table S-7, 9**), the standards (**Table S-8**) and the aliquot from the crushing gas extraction method omitted from the general results due to saturation in Ar^{++} (**Table S-10**).

	date	^{22}Ne brut	^{20}Ne/^{22}Ne	sd	^{21}Ne/^{22}Ne	sd
BLK	08/12/2021	85.64	10.46	0.19	0.0326	0.0015
BLK	13/12/2021	77.30	10.36	0.19	0.0351	0.0013
BLK	20/12/2021	70.88	11.76	0.22	0.0353	0.0018
BLK	22/12/2021	83.70	10.25	0.16	0.0313	0.0009
BLK	24/01/2022	62.66	10.69	0.19	0.0307	0.0012
BLK	02/02/2022	79.25	10.97	0.54	0.0303	0.0016
BLK	09/02/2022	84.75	10.69	0.14	0.0311	0.0007
BLK	04/03/2022	67.32	9.77	0.18	0.0298	0.0013
BLK	12/04/2022	57.72	10.82	0.14	0.0323	0.0017
BLK	04/03/2022	67.32	9.77	0.18	0.0298	0.0013
BLK	12/04/2022	57.72	10.82	0.14	0.0323	0.0017
BLK	28/04/2022	68.78	9.17	0.16	0.0286	0.0013
BLK	28/11/2022	74.57	8.56	0.12	0.0245	0.0017
BLK	22/03/2023	52.80	8.70	0.30	0.0284	0.0021
BLK	07/06/2023	172.04	9.26	0.09	0.0273	0.0009
BLK	14/06/2023	118.19	8.13	0.05	0.0214	0.0008
BLK	18/08/2023	67.57	7.64	0.12	0.0176	0.0041
BLK	07/06/2023	172.04	9.26	0.09	0.0273	0.0009
BLK	14/06/2023	118.19	8.13	0.05	0.0214	0.0008
BLK	18/08/2023	67.57	7.64	0.12	0.0176	0.0041
BLK	19/09/2023	57.00	7.78	0.10	0.0174	0.0014
BLK	21/09/2023	57.01	7.03	0.07	0.0188	0.0010
BLK	27/09/2023	113.21	8.08	0.09	0.0221	0.0013

Table S-7: ^{22}Ne abundance and isotopic composition of the blanks obtained after MATLAB© processing.

	date	^{22}Ne ccSTP	^{20}Ne/^{22}Ne	sd	^{21}Ne/^{22}Ne	sd
STD	13/12/2021	3.65E-15	10.04	0.02	0.0291	0.0003
STD	20/12/2021	3.69E-15	10.30	0.04	0.0289	0.0002
STD	04/01/2022	3.70E-15	10.23	0.03	0.0292	0.0003
STD	04/01/2022	3.67E-15	10.20	0.02	0.0290	0.0001
STD	04/01/2022	2.43E-15	10.22	0.03	0.0291	0.0003
STD	21/01/2022	3.78E-15	10.34	0.03	0.0287	0.0002
STD	21/01/2022	3.69E-15	10.31	0.03	0.0292	0.0002

STD	24/01/2022	3.70E-15	10.26	0.02	0.0288	0.0002
STD	24/01/2022	3.72E-15	10.32	0.04	0.0285	0.0002
STD	25/01/2022	3.68E-15	10.27	0.03	0.0294	0.0002
STD	25/01/2022	3.67E-15	10.26	0.03	0.0288	0.0002
STD	25/01/2022	3.61E-15	10.20	0.03	0.0290	0.0003
STD	26/01/2022	3.64E-15	10.24	0.02	0.0290	0.0003
STD	26/01/2022	3.73E-15	10.27	0.03	0.0283	0.0003
STD	31/01/2022	3.76E-15	10.22	0.03	0.0288	0.0003
STD	31/01/2022	3.73E-15	10.18	0.02	0.0286	0.0002
STD	01/02/2022	3.65E-15	10.28	0.03	0.0288	0.0003
STD	09/02/2022	3.66E-15	10.13	0.03	0.0290	0.0003
STD	09/02/2022	3.64E-15	10.02	0.04	0.0287	0.0002
STD	16/02/2022	3.69E-15	10.27	0.03	0.0288	0.0003
STD	16/02/2022	3.74E-15	10.38	0.03	0.0288	0.0003
STD	03/03/2022	3.69E-15	10.20	0.03	0.0288	0.0003
STD	03/03/2022	3.68E-15	10.29	0.03	0.0288	0.0003
STD	07/03/2022	3.67E-15	10.32	0.04	0.0293	0.0004
STD	09/03/2022	3.68E-15	10.32	0.04	0.0284	0.0003
STD	30/03/2022	3.64E-15	9.92	0.03	0.0286	0.0003
STD	30/03/2022	3.65E-15	10.03	0.04	0.0286	0.0002
STD	12/04/2022	3.66E-15	10.07	0.04	0.0289	0.0004
STD	19/04/2022	3.66E-15	10.15	0.03	0.0286	0.0002
STD	19/04/2022	3.66E-15	10.21	0.02	0.0289	0.0002
STD	20/04/2022	3.71E-15	10.09	0.04	0.0293	0.0003
STD	07/03/2022	3.67E-15	10.32	0.04	0.0293	0.0004
STD	09/03/2022	3.68E-15	10.32	0.04	0.0284	0.0003
STD	30/03/2022	3.64E-15	9.92	0.03	0.0286	0.0003
STD	30/03/2022	3.65E-15	10.03	0.04	0.0286	0.0002
STD	12/04/2022	3.66E-15	10.07	0.04	0.0289	0.0004
STD	19/04/2022	3.66E-15	10.15	0.03	0.0286	0.0002
STD	19/04/2022	3.66E-15	10.21	0.02	0.0289	0.0002
STD	20/04/2022	3.71E-15	10.09	0.04	0.0293	0.0003
STD	26/04/2022	3.70E-15	10.24	0.04	0.0291	0.0003
STD	26/04/2022	3.72E-15	10.19	0.02	0.0292	0.0004
STD	28/11/2022	3.54E-15	10.13	0.01	0.0293	0.0003
STD	02/12/2022	3.57E-15	10.10	0.02	0.0286	0.0003
STD	05/01/2023	3.50E-15	10.11	0.03	0.0285	0.0002
STD	05/01/2023	3.50E-15	10.13	0.03	0.0291	0.0002
STD	06/01/2023	3.49E-15	10.13	0.03	0.0290	0.0002
STD	06/01/2023	3.53E-15	10.10	0.02	0.0291	0.0002
STD	06/01/2023	3.49E-15	10.09	0.03	0.0288	0.0002
STD	06/01/2023	3.53E-15	10.19	0.03	0.0295	0.0003
STD	10/01/2023	3.53E-15	10.15	0.03	0.0295	0.0003
STD	10/01/2023	3.54E-15	10.15	0.03	0.0289	0.0002
STD	20/03/2023	3.51E-15	10.10	0.01	0.0297	0.0003
STD	20/03/2023	3.53E-15	9.97	0.02	0.0290	0.0002
STD	21/03/2023	3.52E-15	10.06	0.01	0.0285	0.0002
STD	21/03/2023	3.53E-15	10.02	0.01	0.0297	0.0002

STD	21/03/2023	3.56E-15	10.15	0.02	0.0282	0.0003
STD	09/06/2023	3.68E-15	9.98	0.02	0.0289	0.0003
STD	09/06/2023	3.65E-15	10.00	0.02	0.0288	0.0002
STD	09/06/2023	3.70E-15	10.04	0.02	0.0288	0.0002
STD	12/06/2023	3.75E-15	9.98	0.02	0.0291	0.0003
STD	12/06/2023	3.74E-15	9.98	0.04	0.0287	0.0005
STD	12/06/2023	3.73E-15	10.00	0.03	0.0288	0.0002
STD	13/06/2023	3.78E-15	10.04	0.02	0.0286	0.0002
STD	13/06/2023	3.80E-15	9.96	0.03	0.0292	0.0002
STD	08/08/2023	3.79E-15	10.25	0.03	0.0297	0.0002
STD	08/08/2023	3.83E-15	10.23	0.02	0.0288	0.0003
STD	08/08/2023	3.84E-15	10.28	0.03	0.0288	0.0003
STD	09/08/2023	3.83E-15	10.19	0.02	0.0293	0.0003
STD	10/08/2023	3.81E-15	10.19	0.02	0.0292	0.0002
STD	10/08/2023	3.79E-15	10.16	0.03	0.0289	0.0003
STD	10/08/2023	3.81E-15	10.24	0.02	0.0292	0.0002
STD	11/08/2023	3.83E-15	10.29	0.01	0.0291	0.0003
STD	11/08/2023	3.79E-15	10.11	0.02	0.0294	0.0003
STD	16/08/2023	3.80E-15	10.23	0.02	0.0290	0.0004
STD	16/08/2023	3.83E-15	10.24	0.02	0.0291	0.0002
STD	16/08/2023	3.82E-15	10.28	0.03	0.0289	0.0003
STD	21/08/2023	3.89E-15	10.38	0.02	0.0295	0.0003
STD	23/08/2023	3.88E-15	10.36	0.02	0.0293	0.0003
STD	23/08/2023	3.90E-15	10.27	0.02	0.0294	0.0004
STD	11/09/2023	3.90E-15	10.32	0.03	0.0296	0.0002
STD	11/09/2023	3.87E-15	10.35	0.02	0.0301	0.0003
STD	22/09/2023	4.32E-15	10.27	0.02	0.0299	0.0003
STD	22/09/2023	4.32E-15	10.24	0.02	0.0296	0.0002
STD	28/09/2023	4.43E-15	10.24	0.03	0.0293	0.0003
STD	28/09/2023	4.42E-15	10.30	0.02	0.0293	0.0004
STD	06/10/2023	4.43E-15	10.33	0.04	0.0293	0.0003
STD	12/10/2023	4.40E-15	10.28	0.01	0.0295	0.0003

Table S-8: ^{22}Ne abundance and isotopic composition of the standard obtained after MATLAB© processing.

	date	**^{22}Ne brut**	**^{20}Ne/^{22}Ne**	**sd**	**^{21}Ne/^{22}Ne**	**sd**
ESFa-3B-CO_2+Ne						
Matrix 1*	30/08/2021	626.5	10.39	0.07	0.0306	0.0006
Matrix 2	31/08/2021	189.3	10.82	0.14	0.0313	0.0007
Matrix 3	31/08/2021	270.1	9.59	0.08	0.0269	0.0010
Matrix 4	14/09/2021	169.2	10.66	0.17	0.0320	0.0010
Matrix 5*	16/09/2021	246.8	11.30	0.19	0.0304	0.0006
Matrix 6*	14/12/2021	349.3	10.26	0.04	0.0302	0.0009
EN-E4						
Matrix 1	15/06/2023	117.2	8.46	0.06	0.0235	0.0011

Matrix 2	22/08/2023	73.8	7.76	0.10	0.0190	0.0012
Matrix 3	22/08/2023	136.3	8.82	0.09	0.0258	0.0008
Matrix 4	22/08/2023	71.3	7.50	0.07	0.0208	0.0010

Table S-9: ^{22}Ne abundance and isotopic composition of the matrix obtained after MATLAB© processing. ** represents questionable results as a vesicle could be pierced.

	date	**^{22}Ne ccSTP**	**^{20}Ne/^{22}Ne**	**sd**	**^{21}Ne/^{22}Ne**	**sd**
EN-D1						
Crush1_ali1	21/09/2023	2.59E-11	10.03	0.08	0.0290	0.0004
Crush2_ali1	21/09/2023	9.26E-12	10.02	0.08	0.0293	0.0004
Crush3_ali1	25/09/2023	1.25E-11	10.06	0.07	0.0288	0.0004
Crush4_ali1	25/09/2023	8.33E-12	10.10	0.09	0.0290	0.0004
Crush5_ali1	26/09/2023	5.23E-12	9.86	0.09	0.0298	0.0004
EN-E9						
Crush1_ali1	03/10/2023	1.40E-10	10.00	0.07	0.0288	0.0003
Crush3-ali1	11/10/2023	2.99E-11	9.96	0.06	0.0287	0.0003

Table S-10: ^{22}Ne abundance and isotopic composition MATLAB© processing of the aliquot omitted from the general results due to saturation in Ar++.

Elena NUNEZ

L'origine du néon terrestre : Une étude expérimentale du fractionnement isotopique du Néon lors du dégazage des basaltes

L'origine des éléments volatils de la Terre, cruciale pour comprendre l'évolution du Système Solaire primitif, la formation de la Terre et la vie, reste débattue. Les gaz nobles, en raison de leur inertie et de leur grande volatilité, servent de traceurs clés pour les principaux volatils tels que le CO2 et le H2O dans le manteau.

Les signatures des gaz nobles dans les panaches mantelliques, en particulier ceux des Galapagos, d'Hawaï et d'Islande, suggèrent un néon de type solaire acquis lors de la formation de la Terre. Deux modèles principaux expliquent l'origine du néon dans le manteau: (i) Le néon a été incorporé dans un océan de magma à partir d'une atmosphère primaire riche en H et He, capturée par gravité ; (ii) Le néon a été acquis sur des poussières irradiées par le vent solaire Soleil et incorporées dans des planétésimaux avant l'accrétion de la Terre.

La concentration résiduelle des éléments volatils du manteau dans les roches et les minéraux volcaniques est souvent influencée par des processus secondaires plutôt que par les concentrations primaires du manteau. Dans la plupart des basaltes océaniques, la phase volatile est dominée par le CO2. Il est généralement supposé que les concentrations et les rapports isotopiques des gaz nobles dans cette phase sont homogènes à travers les vésicules et dépendent de l'ampleur et du mécanisme de la perte de gaz du magma.

Cette thèse présente une recherche pionnière sur des échantillons synthétiques dont les principaux éléments volatils sont le dioxyde de carbone (CO_2) et le néon, en explorant deux conditions de dégazage: (i) Un magma affecté par un apport de gas riche en CO2 et néon et (ii) Un magma où le dégazage est induit par la décompression.

La similitude des rapports isotopiques du néon observée dans les échantillons naturel, avec des valeurs intermédiaires entre les valeurs isotopiques solaires et celles de l'implantation du vent solaire, est en accord avec l'hypothèse que le manteau terrestre aurait pu incorporer du gaz issu d'une nébuleuse primordiale lors des premières étapes de la formation de la planète. Néanmoins, cette étude expérimentale présente des preuves convaincantes que le fractionnement isotopique peut se produire à différents stades de l'évolution des vésicules dans le magma, suggérant que les valeurs élevées des rapports isotopiques du néon dans les échantillons naturels doivent être interprétées avec prudence. Nous ne concluons qu'aucun des deux scénarios d'acquisition des volatils légers ne peut être pour l'instant rejeté.

Mots clés: **atmosphère primordiale, géochimie, cosmochimie, dégazage des magmas, pétrologie expérimentale, néon, fractionnement**

The origin of terrestrial neon: An experimental study of isotopic fractionation of Neon during basalt degassing

The origin of Earth's volatile elements, crucial for understanding the evolution of the early Solar System, Earth's formation, and life, remains debated. Noble gases, due to their inertness and high volatility, serve as key tracers for major volatiles like CO2 and H2O in the mantle.

The noble gas signatures in mantle plumes, particularly from Galapagos, Hawaii, and Iceland, suggest a solar-type neon acquired during Earth's formation.

Two main models explain neon's origin in the mantle: (i) The neon was incorporated into a magma ocean through gravitational capture of a dense primary atmosphere; (ii) The neon was acquired from planetesimals irradiated by the early Sun during Earth's accretion.

The residual concentration of mantle volatiles in volcanic rocks and minerals is often influenced by secondary processes and does not reflect primary mantle concentrations. In most oceanic basalts, the volatile phase is dominated by CO2. It's generally assumed that noble gas concentrations in this phase are similar between vesicles and depend on the extent and mechanism of gas loss from the magma.

This thesis presents pioneering research on synthetic samples whose only volatiles are carbon dioxide (CO_2) and neon by exploring simple models of degassing in a closed system such as: (i) a depleted melt affected by a CO2-rich inputs and (ii) a system where the decompression is initiated.

The observed isotopic similarity in natural samples, with values midway between the solar isotopic values and those of solar wind implantation, supports the hypothesis that the Earth's mantle may have captured a primordial nebula during the early stages of the planet's formation. Nevertheless, this experimental study presents compelling evidence that isotopic fractionation can occur during various stages of vesicle evolution in magma, suggesting that high isotopic ratios values in natural samples should be interpreted with caution. We conclude that none of the two scenarios of light-volatile acquisition can be for now rejected.

Keywords: **primordial atmosphere, geochemistry, magma degassing, experimental petrology, neon, fractionation**

.

Institut des Sciences de la Terre d'Orléans ISTO
1A Rue de la Férollerie – CS 20066
F-45071 Orléans Cedex 2